

ERDC/GSL TR-03-13

Geotechnical and Structures  
Laboratory



**US Army Corps  
of Engineers®**  
Engineer Research and  
Development Center

# **Third U.S.-Japan Workshop on Advanced Research on Earthquake Engineering for Dams, San Diego, California, 22-23 June 2002**

Edited by  
Robert L. Hall, Yoshikazu Yamaguchi,  
Enrique E. Matheu, and Ziyad H. Duron

August 2003

20031015 014

# **Third U.S.-Japan Workshop on Advanced Research on Earthquake Engineering for Dams, San Diego, California, 22-23 June 2002**

Edited by Robert L. Hall

*Geotechnical and Structures Laboratory  
U.S. Army Engineer Research and Development Center  
3909 Halls Ferry Road  
Vicksburg, MS 39180-6199*

Yoshikazu Yamaguchi

*Public Works Research Institute  
1-6, Minamihara, Tsukuba, Ibaraki, 305-8516  
JAPAN*

Enrique E. Matheu

*Louisiana State University  
Department of Civil Environmental Engineering  
Baton Rouge, LA 70803*

Ziyad H. Duron

*Harvey Mudd College  
Department of Engineering  
301 E. 12th Street  
Claremont, CA 91711*

Final report

Approved for public release; distribution is unlimited



**ABSTRACT:** This report summarizes a workshop organized by the U.S. Army Engineer Research and Development Center (ERDC), Vicksburg, MS, and the Public Works Research Institute of Japan (PWRI) under the auspices of the Task Committee on Dams of the Panel on Wind and Seismic Effects, part of the U.S.-Japan Cooperative Program in Natural Resources. The workshop was held in San Diego, CA, 22-23 June 2002, as part of the preconference activities of the 22<sup>nd</sup> U.S. Society on Dams Annual Meeting and Conference held at the same location 24-28 June 2002. Dr. Robert L. Hall, Chief, Geosciences and Structures Division, Geotechnical and Structures Laboratory (GSL), ERDC; Dr. Yoshikazu Yamaguchi, PWRI; Dr. Enrique E. Matheu, Louisiana State University, Baton Rouge, LA; and Dr. Ziyad H. Duron, Harvey Mudd College, 301 E. 12th Street, Claremont, CA, contributed in the organization of this workshop.

**DISCLAIMER:** The contents of this report are not to be used for advertising, publication, or promotional purposes. Citation of trade names does not constitute an official endorsement or approval of the use of such commercial products. All product names and trademarks cited are the property of their respective owners. The findings of this report are not to be construed as an official Department of the Army position unless so designated by other authorized documents.  
**DESTROY THIS REPORT WHEN IT IS NO LONGER NEEDED. DO NOT RETURN TO THE ORIGINATOR.**

# Contents

---

Preface .....	iv
Welcome Message.....	v
Workshop Organizing Committee.....	vii
Acknowledgements .....	viii
Workshop Participants .....	ix
Agenda .....	xiii
Resolutions .....	xx
Workshop Papers.....	xxii

# Preface

---

This report summarizes a workshop organized by the U.S. Army Engineer Research and Development Center (ERDC) Vicksburg, MS, and the Public Works Research Institute of Japan (PWRI) under the auspices of the Task Committee on Dams of the Panel on Wind and Seismic Effects, part of the U.S.-Japan Cooperative Program in Natural Resources. The workshop was held in San Diego, California, 22-23 June 2002, and it was part of the preconference activities of the 22<sup>nd</sup> U.S. Society on Dams Annual Meeting and Conference held at the same location 24-28 June 2002.

Dr. Robert L. Hall, Chief, Geosciences and Structures Division, Geotechnical and Structures Laboratory (GSL); ERDC, Dr. Yoshikazu Yamaguchi (PWRI); Dr. Enrique E. Matheu, Louisiana State University, Baton Rouge, LA; and Dr. Ziyad H. Duron, Harvey Mudd College, 301 E. 12th Street, Claremont, CA, organized and conducted the workshop. Ms. Yazmin Seda-Sanabria, ERDC, and Mr. Larry D. Stephens, U.S. Society on Dams, provided essential assistance for the successful coordination of this activity. Dr. Michael K. Sharp and Mr. Donald E. Yule, ERDC, provided additional support in several aspects related to the organization of this workshop. Mrs. Julia Baker, ERDC, and Ms. Cheri Loden, Alpha Data Corporation, ably assisted in the completion of these proceedings by consolidating and editing the technical material.

Overall direction for this report was provided by Dr. Hall and Dr. David W. Pittman, Acting Director, GSL, ERDC.

At the time of publication of this report, Commander and Executive Director of ERDC was COL James R. Rowan, EN. Director was Dr. James R. Houston.

*The contents of this report are not to be used for advertising, publication, or promotional purposes. Citation of trade names does not constitute an official endorsement or approval of the use of such commercial products.*

# Welcome Message

---

I would like to offer a warm welcome on behalf of the Task Committee on Dams of the Panel on Wind and Seismic Effects, part of the U.S.-Japan Cooperative Program in Natural Resources (UJNR).

This task committee was formed at the 25<sup>th</sup> Joint Meeting of the Panel, which was held in Tsukuba, Japan, 17-20 May 1993. We have been very active in sponsoring workshops on earthquake engineering for dams and fostering the technical exchange between the Japan and the United States. The first three workshops (including this one) have all been sponsored by the U.S. Army Engineer Research and Development Center (ERDC) (formerly Waterways Experiment Station (WES)), Vicksburg, MS, and the Public Works Research Institute (PWRI) of Japan.

The first U.S.-Japan Workshop on Advanced Research on Earthquake Engineering for Dams was held in Vicksburg, Mississippi, 12-14 November 1996, and was attended by 11 engineers and scientists from Japan and 26 from the United States. This very successful first workshop provided a most valuable opportunity for productive technical discussions and resulted in the publication of proceedings containing 25 technical papers.

The second workshop was held in Tokyo, Japan, 7-8 May 1999, and was co-sponsored by the Japan Society for Dam Engineers (JSDE). There were 110 engineers and scientists attending from Japan (from JSDE, PWRI, universities, and other agencies) and 11 from the United States. The U.S. participants represented universities, government agencies, and the private sector. This successful workshop resulted in technical discussions on a broad range of earthquake engineering issues, a detailed exchange of research results, and the publication of proceedings containing 26 technical papers.

We have now arrived at our third workshop here in San Diego. Our co-sponsor this year is the United States Society for Dams (USSD). Once again, we are honored to have some of the most highly recognized engineers and scientists in the field of dam earthquake engineering participating in this workshop. This series of workshops is continually achieving greater international recognition and we are now including participants from other countries. We welcome participants from the Republic of Panama to this year's event. Our participants represent universities, the private sector, and government and other agencies. We

hope this workshop will be as successful as past ones and will facilitate a detailed exchange of research results in the area of earthquake engineering for dams.

Dr. Yoshikazu Yamaguchi, PWRI, and Dr. Robert L. Hall, ERDC, (the Japan-side and U.S.-side chairs of the UJNR Task Committee on Dams) are very grateful to all those who have worked so diligently to plan this workshop. We would like to specially thank our other members of the workshop organizing committee: Dr. Enrique E. Matheu (Louisiana State University) and Dr. Ziyad H. Duron (Harvey Mudd College).

We hope you enjoy your time here in sunny San Diego.

Robert L. Hall, Ph.D.  
U.S.-Side Chairman,  
Task Committee on Dams,  
UJNR Panel on Wind and Seismic Effects

# Workshop Organizing Committee

---

## **Organizing Committee:**

Robert L. Hall (ERDC)  
Yoshikazu Yamaguchi (PWRI)  
Enrique Matheu (Louisiana State University)  
Ziyad Duron (Harvey Mudd College)

## **General Secretariat:**

Yazmin Seda-Sanabria (ERDC)

# Acknowledgements

---

We would like to gratefully acknowledge the generous support and assistance provided by:

Julia C. Baker (ERDC)  
Cheri T. Loden (Alpha Data Corporation)  
Yazmin Seda-Sanabria (ERDC)  
Michael K. Sharp (ERDC)  
Larry D. Stephens (USSD)  
Donald E. Yule (ERDC)

Special thanks to the following students:

Jorge Ayala (University of Puerto Rico – ERDC Internship Program)  
Gene Lee (Harvey Mudd College)  
Arturo Llavona (University of Puerto Rico – ERDC Internship Program)  
Daniel Sutoyo (Harvey Mudd College)  
Aidcer Vidot (University of Puerto Rico – ERDC Internship Program)

# Workshop Participants

---

ABREGO, Antonio (Panama Canal Authority)  
ADALIER, Korhan (Rensselaer Polytechnic Institute)  
ALVES, Steven (Caltech)  
ASLAM, Mohammad (Pacific Gas and Electric Company)  
BABBITT, Donald H. (GENTERRA Consultants, Inc.)  
BAYERS, Jeffrey (Corps of Engineers)  
BERGA, Luis (Spanish National Committee on Large Dams)  
BOULANGER, Ross (University of California)  
BRAND, Bruce (Federal Energy Regulatory Commission)  
CASTRO, Alvaro (Ingetec S.A.)  
CHARLWOOD, Robin G. (Acres International Corporation)  
CHOPRA, Anil K. (University of California, Berkeley)  
COLE, Perry (INCA Engineers, Inc.)  
COLLINS, Steve (Federal Energy Regulatory Commission)  
DEPUY, Maximiliano (Panama Canal Authority)  
DOVE, Richard C. (Corps of Engineers)  
DURON, Ziyad H. (Harvey Mudd College)  
EHASZ, Joseph L. (Washington Infrastructure Services Inc.)  
FERGUSON, Keith Allen (GEI Consultants, Inc.)  
FONG, Frank C. (State of California, Department of Water Resources)  
GALLEGOS, Humberto A. (Corps of Engineers)  
GHANAAT, Yusof (Quest Structures)  
GILLON, Murray (Dam Watch Services Ltd.)  
HALL, Robert L. (Corps of Engineers)  
HARDER, Leslie (State of California, Department of Water Resources)  
HARLAN, Richard C. (Consulting Engineer)



HARRIS, David W. (Bureau of Reclamation)  
HOROWITZ, George (Consulting)  
HRADILEK, Peter J. (HDR Engineering, Inc.)  
HUMPHRIES, Richard W. (Golder Associates Inc.)  
HUTTON, Charles C. (ECI, an AECOM Company)  
JONES, Adam N. (Framatome ANP DE&S)  
KANENAWA, Kenichi (Independent Administrative Institution - Public Works  
Research Institute)  
KIM, Woo-gu (Korean Water Resources Corporation)  
KNARR, C. Michael (Outten Engineering Company)  
KOH, Deuk-koo (Korean Water Resources Corporation)  
KOLLGAARD, Eric B. (Consultant)  
KONNO, Hisashi (Japan Dam Engineering Center)  
LAVASSAR, Jerald (Washington Department of Ecology Dam Safety Office)  
LEE, Gene (Harvey Mudd College)  
LEGAS, James (Consulting Civil Engineer)  
LEMONS, Ronnie M. (Freese and Nichols, Inc.)  
LEUNG, Ken (Pacific Gas and Electric Company)  
LIU, T. C. (State of California, Department of Water Resources)  
MACARI, Emir J. (National Science Foundation)  
MAKDISI, Faiz I. (Geomatrix Consultants, Inc.)  
MALVICK, Erik J. (University of California, Davis)  
MARTIN, Arthur C. (Cornforth Consultants, Inc.)  
MARULANDA, Alberto (Ingetec S.A.)  
MATHEU, Enrique E. (Corps of Engineers)  
MATSUMOTO, Norihisa (Japan Dam Engineering Center)  
MCLEAN, Francis G. (Bureau of Reclamation)  
MEAD, Randel J. (Corps of Engineers)  
MEEHAN, Christopher (Virginia Tech)  
MILLIKAN, Donald L. (Southern California Edison Company)  
MOORE, Rodney R. (Consultant)  
NAKAMURA, Yoshio (Aichi Institute of Technology)  
NGUYEN, Van Kha (Hydro-Quebec)  
NUSS, Larry K. (Bureau of Reclamation)

OGAWA, Naoto (Japan Dam Engineering Center)  
OH, Byung-hyun (Korean Water Resources Corporation)  
OHNE, Yoshio (Aichi Institute of Technology)  
OSKOOROUCHI, Ali M. (ATI Architects and Engineers)  
PEARRE, Charles M. (Corps of Engineers)  
PERLEA, Vlad (Corps of Engineers)  
PETERSEN, Helen (Corps of Engineers)  
PEZZA, David A. (Corps of Engineers)  
POEPELMAN, Rick L. (Corps of Engineers)  
RUBIANO, Nestor R. (Ingetec S.A.)  
SAKAMOTO, Tadahiko (Independent Administrative Institution - Public Works  
Research Institute)  
SASAKI, Takashi (Independent Administrative Institution - Public Works  
Research Institute)  
SATO, Hiroyuki (Independent Administrative Institution - Public Works  
Research Institute)  
SCHULTZ, Mark (State of California, Department of Water Resources)  
SEDA-SANABRIA, Yazmin (Corps of Engineers)  
SHARP, Michael K. (Corps of Engineers)  
SHEN, Chonggang (Chinese National Committee on Large Dams)  
SOMERVILLE, Paul (URS Group Inc.)  
STACY, Samuel T. (Corps of Engineers)  
STEELE, Kenneth A. (San Diego County Water Authority)  
SUAREZ, Luis E. (University of Puerto Rico)  
SUTOYO, Daniel (Harvey Mudd College)  
SWAISGOOD, James R. (Swaigood Consulting)  
TAVAREZ, Victor (INDRHI)  
VEILLEUX, Mario (Hydro-Quebec)  
WANG, Zhi-Liang (Geomatrix Consultants, Inc.)  
WIGHTMAN, Adrian (Klohn Crippen Consultants Ltd.)  
YAMAGUCHI, Yoshikazu (Independent Administrative Institution - Public  
Works Research Institute)  
YAN, Li (BC Hydro)  
YULE, Donald E. (Corps of Engineers)  
ZHOU, Jim (San Diego County Water Authority)



Workshop Presenters



Workshop Participants

# Agenda

---

---

**3rd U.S.-Japan Workshop on Advanced Research on Earthquake Engineering For Dams**

***“Future Directions in Seismic Design and Evaluation of Dams”***

San Diego, California – June 22-23, 2002

---

**TECHNICAL PROGRAM**

**JUNE 22, 2002 (Saturday)**

8:00-8:30 AM    **Registration**

8:30-9:00 AM    **Opening Ceremony**

Call to order by Enrique E. MATHEU (Louisiana State University)

**Welcoming Remarks**

Robert L. HALL (U.S. Army Corps of Engineers; US-side Chairman of UJNR Task Committee on Dams)

Yoshikazu YAMAGUCHI (IAI-PWRI; Japan-side Chairman of UJNR Task Committee on Dams)

**Opening Remarks**

Tadahiko SAKAMOTO (Independent Administrative Institution - Public Works Research Institute)

William B. BINGHAM (President, USSD; and Gannett Fleming, Inc.)

9:00-9:30        **Keynote Lecture**

**“Current activities on construction and maintenance of dams in Japan”**

Tadahiko SAKAMOTO (Independent Administrative Institution - Public Works Research Institute)

9:30-10:00     **Keynote Lecture**

**“Earthquake Analysis, Design, and Safety Evaluation of Concrete Arch Dams”**

Anil K. CHOPRA (University of California at Berkeley)

10:00-10:15    *Coffee Break*

10:15-10:30    Group Photograph

- 10:30-11:50      **Technical Session No. 1 - Concrete Dams I**  
Chairman: Yusof GHANAAT (QUEST Structures)
- 10:30-10:50      **"Analyses using Program EACD3D96 For Morrow Point Dam"**  
Larry NUSS\* (U.S. Bureau of Reclamation) and Anil K. CHOPRA (University of California at Berkeley)
- 10:50-11:10      **"Seismic hazard assessment, analysis and post-construction evaluation for Olmsted Locks and Dam, Ohio River"**  
Anjana CHUDGAR and Jeffrey E. BAYERS\* (U.S. Army Corps of Engineers)
- 11:10-11:30      **"Investigation on the seismic adequacy of the Gatun spillway at the Panama Canal"**  
Antonio A. ABREGO\* M. and Maximiliano DePUY (Panama Canal Authority)
- 11:30-11:50      **"Damage to dams caused by the 2000 Western Tottori-prefecture earthquake and stability evaluation of concrete gravity dam"**  
Yoshikazu YAMAGUCHI, Takashi SASAKI, and Ken-ichi KANENAWA\* (Independent Administrative Institution - Public Works Research Institute)
- 11:50-13:15      *Lunch*
- 13:15-13:45      **Keynote Lecture**  
  
**"Evaluation of concrete dams for seismic loading"**  
Yusof GHANAAT (QUEST Structures)
- 13:45-13:50      *Short Break*
- 13:50-15:10      **Technical Session No. 2 - Embankment Dams I**  
Chairman: Michael K. SHARP (U.S. Army Corps of Engineers)
- 13:50-14:10      **"Development and applications of a nonlinear approach to the analysis of earthquake performance of dams"**  
Zhi-Liang WANG, Faiz I. MAKDISI\*, and John EGAN (Geomatrix Consultants)
- 14:10-14:30      **"Numerical simulation of sliding of an earth dam during the 1995 Kobe earthquake"**  
Tadahiko SAKAMOTO, Hitoshi YOSHIDA, Tomoya IWASHITA, Yoshikazu YAMAGUCHI, and Hiroyuki SATOH\* (Independent Administrative Institution - Public Works Research Institute)
- 14:30-14:50      **"Dynamic properties of cohesive soil in foundation of an embankment dam"**  
Gonzalo CASTRO (GEI Consultants, Inc.), Francke C. WALBERG and Vlad G. PERLEA\* (U.S. Army Corps of Engineers)

- 14:50-15:10      **"Identification of non-cohesive filters to prevent migration of impervious materials for embankment dams due to large earthquakes (fault movement)"**  
Tadahiko SAKAMOTO, Yoshikazu YAMAGUCHI\*, and Hiroyuki SATOH  
(Independent Administrative Institution - Public Works Research Institute)
- 15:10-15:25      *Coffee Break*
- 15:25-17:05      **Technical Session No. 3 – Concrete Dams II**  
  
Chairman: Takashi SASAKI (IAI-PWRI)
- 15:25-15:45      **"Seismic performance evaluation and damage criteria for concrete dams"**  
Yusuf GHANAAT (QUEST Structures)
- 15:45-16:05      **"Preliminary seismic stress analysis of Folsom Dam"**  
Chung F. WONG, Rick POEPPelman\*, and Stephen GRAFF (U.S. Army Corps of Engineers)
- 16:05-16:25      **"Comparison of the nonlinear behavior of concrete arch dams using physical and numerical models"**  
David W. HARRIS\*, Terry L. PAYNE and Larry NUSS (U.S. Bureau of Reclamation)
- 16:25-16:45      **"Nonlinear seismic analysis of Stony Gorge Dam"**  
Barbara MILLS-BRIA (U.S. Bureau of Reclamation). Presented by Larry NUSS (U.S. Bureau of Reclamation)
- 16:45-17:05      **"Properties obtained from dam cores"**  
David W. HARRIS\*, Timothy P. DOLEN, Caroline E. MOHOROVIC, and Phoebe MITCHELL (U.S. Bureau of Reclamation)
- 17:05-17:10      *Short Break*
- 17:10-17:30      **"Field testing of concrete dams - iDAMS Demonstration"**  
Ziyad DURON\* (Harvey Mudd College), Robert L. HALL (U.S. Army Corps of Engineers, and Enrique E. MATHEU (Louisiana State University)
- 19:00-20:30      *Dinner*

**Invited Presentation**

**"Internationalization of earthquake engineering research: leveraging funding opportunities between countries"**  
Emir J. MACARI (National Science Foundation)

**JUNE 23, 2002 (Sunday)**

9:00-9:30

**Keynote Lecture**

**"The FERC Approach to Dam Safety under Seismic Loading"**

Bruce BRAND (Federal Energy Regulatory Commission)

9:30-10:00

**Keynote Lecture**

**"Earthquake damage and its remedial measure for earth dam with an asphalt facing"**

Yoshio OHNE\*, Kunitomo NARITA, Tetsuo OKUMURA, and Yoshio NAKAMURA  
(Aichi Institute of Technology)

10:00-10:15

*Coffee Break*

10:15-11:55

**Technical Session No. 4 - Embankment Dams II**

Chairman: Robert L. HALL (U.S. Army Corps of Engineers; US-side Chairman of UJNR Task Committee on Dams)

10:15-10:35

**"Evaluating liquefaction potential at high overburden stresses"**

Ross W. BOULANGER (University of California, Davis)

10:35-10:55

**"Dynamic centrifuge modeling of earth dams on liquefiable foundation"**

Korhan ADALIER\* (Rensselaer Polytechnic Institute) and Michael K. SHARP (U.S. Army Corps of Engineers)

10:55-11:15

**"Evaluation of permanent displacement in seismic analysis of fill dams"**

Norihisa MATSUMOTO (Japan Dam Engineering Center)

11:15-11:35

**"Post-earthquake residual shear strength of liquefiable cohesive soils"**

Samuel T. STACY (U.S. Army Corps of Engineers)

11:35-11:55

**"Design criteria for rounded/angular rock riprap in overtopping flow"**

Humberto GALLEGOS (U.S. Army Corps of Engineers) and Steven R. Abt (Colorado State University)

11:55-13:15

*Lunch*

13:15-14:35

**Technical Session No. 5 – Powerhouses and Appurtenant Structures**

Chairman: Ziyad DURON (Harvey Mudd College)

13:15-13:35

**"Seismic assessment of reinforced concrete powerhouse superstructures"**

Helen PETERSEN (U.S. Army Corps of Engineers)



- 13:35-13:55      **“Seismic response of lightly reinforced concrete intake towers”**  
Richard C. DOVE\* (U.S. Army Corps of Engineers) and Enrique E. MATHEU  
(Louisiana State University)
- 13:55-14:15      **“Earthquake analysis of radial gates/dam including fluid-structure interaction”**  
Mohammad ASLAM\* (PG&E), Edward L. WILSON (University of California,  
Berkeley), Martin BUTTON (EAC), and Charles AHLGREN (PG&E)
- 14:15-14:35      **“Seismic assessment of nonstructural issues in powerhouses”**  
Hellen PETERSEN (U.S. Army Corps of Engineers)
- 14:35-14:50      *Coffee Break*
- 14:50-16:30      **Technical Session No. 6 – Ground Motions**  
  
Chairman: Yoshikazu YAMAGUCHI (IAI-PWRI; Japan-side Chairman of UJNR Task  
Committee on Dams)
- 14:50-15:10      **“Present state of acceleration measurement and nation-wide network of  
observation at dam sites in Japan”**  
Takashi SASAKI\*, Syuji TAKASU, Hitoshi YOSHIDA, and Kenji INAGAKI  
(Independent Administrative Institution - Public Works Research Institute)
- 15:10-15:30      **“Issues for consideration in selection of design ground motions for dams”**  
Donald E. YULE (U.S. Army Corps of Engineers)
- 15:30-15:50      **“Seismic hazard analysis and selection of design earthquake for a dam in Kansas”**  
Paul G. SOMERVILLE\* (URS Group, Inc.), Francke C. WALBERG, and Vlad G.  
PERLEA (U.S. Army Corps of Engineers)
- 15:50-16:10      **“Simulation of a strong motion at Kasho Dam site during the 2000 Tottori-Ken  
Seib earthquake”**  
Nobuteru SATO and Fumio YONEZAKI (Water Resources Development Public  
Corporation). Presented by Naoto OGAWA (Japan Dam Engineering Center)
- 16:10-16:30      **“Permanent displacement and change of reservoir water level at Kasho Dam  
caused by the 2000 Western Tottori-prefecture, Japan earthquake”**  
Tatsuo OHMACHI, Naoyuki KOJIMA, and Atsushi MURAKAMI (Tokyo Institute of  
Technology). Presented by Norihisa MATSUMOTO (Japan Dam Engineering Center)
- 16:30-16:45      *Short Break*
- 16:45-17:30      **Workshop Plenary Session**
- 17:30-17:45      **Closing Ceremony**  
  
Call to order by Ziyad DURON (Harvey Mudd College)

### **Closing Remarks**

David A. PEZZA (Headquarters, U.S. Army Corps of Engineers)

Yoshikazu YAMAGUCHI (IAI-PWRI; Japan-side Chairman of UJNR Task Committee on Dams)

17:45

*Adjourn*

19:00-20:30

*Dinner*

### **Final Remarks**

Tadahiko SAKAMOTO (Independent Administrative Institution - Public Works Research Institute)

Robert L. HALL (U.S. Army Corps of Engineers; US-side Chairman of UJNR Task Committee on Dams)

# Resolutions

---

The Third U.S.-Japan Workshop on Advanced Research on Earthquake Engineering for Dams was held under the sponsorship of the U.S. Army Engineer Research and Development Center (ERDC) and the Public Works Research Institute of Japan (PWRI) under the auspices of Task Committee on Dams (T/C C), part of the UJNR Panel on Wind and Seismic Effects at the San Diego Marriott Mission Valley Hotel in San Diego, California, USA, on June 22-23, 2002.

To efficiently use this Workshop as a mechanism for wider technology transfer and to enhance the technical exchange among scientists, engineers, and specialists, the U.S. Society on Dams (USSD) agreed to co-sponsor this Workshop. This Workshop was part of the pre-conference activities of the **22<sup>nd</sup> USSD Annual Meeting and Conference** held at the same location on June 24-28, 2002.

The Workshop provided a valuable forum for the exchange of technical information related to seismic evaluation criteria for dams, numerical techniques for seismic analysis, seismic design and evaluation of appurtenant structures, instrumentation, condition assessment, seismic upgrade and rehabilitation, foundation problems, case studies, as well as many other general topics of interest. The workshop was attended by 64 U.S. participants, 10 Japanese participants, and 16 participants from other countries (Canada, China, Colombia, Dominican Republic, New Zealand, Republic of Korea, Republic of Panama, and Spain).

The following resolutions were adopted by the Workshop participants:

1. Workshop participants recognized the importance of continued exchange of research personnel, technical data and information, and the joint use of available research facilities in both countries. It was also recognized the importance of developing new means for future technology transfer, seeking the support and collaboration from other engineering societies with similar interests.
2. The following topics relevant to dam earthquake engineering were identified for the further cooperative research programs:
  - a. Develop improved methods of analysis for seismic design of dams including outlet works;

- b. Perform research to better understand the dynamic characteristics of dam construction materials and site conditions;
  - c. Evaluate observed performance of dams and outlet works during earthquakes.
- 3. Following large earthquakes in the US or Japan, this Task Committee will assemble an international reconnaissance team to jointly investigate the performance of dams and outlet works.
- 4. In view of the importance of cooperative research programs on earthquake engineering for dams, it is recommended to hold the **Fourth U.S.-Japan Workshop on Advanced Research on Earthquake Engineering for Dams** in the year 2004 in Japan. Specific location and time of the Workshop will be determined through correspondence between the Chairs of the Task Committee on Dams of the UJNR Panel on Wind and Seismic Effects.

# Workshop Papers

---

1.	<u>“Current Activities on Construction and Maintenance of Dams in Japan,”</u> Tadahiko SAKAMOTO .....	1
2.	<u>“Analyses Using EACD3D96 for Morrow Point Dam,”</u> Larry NUSS and Anil K. CHOPRA .....	27
3.	<u>“Seismic Hazard Assessment and Post-Construction Evaluation for Olmsted Locks and Dam,”</u> Jeffrey E. BAYERS .....	37
4.	<u>“Seismic Adequacy of the Gatun Spillway at the Panama Canal,”</u> Antonio A. MALOFF and Maximiliano DePUY .....	47
5.	<u>“Damages of Dams Caused by the Western Tottori-Prefecture Earthquake in 2000 and Stability Evaluation Analysis about Kasho Dam,”</u> Yoshikazu YAMAGUCHI, Takashi SASAKI, and Ken-ichi KANENAWA .....	67
6.	<u>“Development and Application of a Nonlinear Approach to the Analysis of Earthquake Performance of Dams,”</u> Zhi-Liang WANG, Faiz I. MAKDISI, and John EGAN .....	83
7.	<u>“Numerical Simulation of Sliding of an Earth Dam during the 1995 Kobe Earthquake,”</u> Tadahiko SAKAMOTO, Hitoshi YOSHIDA, Yoshikazu YAMAGUCHI, Hiroyuki SATOH, Tomoya IWASHITA, and Norihisa MATSUMOTO .....	111
8.	<u>“Dynamic Properties of Cohesive Soil in Foundation of an Embankment Dam,”</u> Gonzalo CASTRO, Francke C. WALBERG, and Vlad G. PERLEA .....	123
9.	<u>“Identification of Non-Cohesive Filters to Prevent Migration of Impervious Materials for Embankment Dams due to Large Earthquakes (Fault Movement),”</u> Tadahiko SAKAMOTO, Yoshikazu YAMAGUCHI, and Hiroyuki SATOH .....	139
10.	<u>“Seismic Performance and Damage Criteria for Concrete Dams,”</u> Yusof GHANAAT .....	151

11. <u>"Preliminary Earthquake Response Analysis of Folsom Dam Spillway Monoliths,"</u> Chung F. WONG, Rick POEPPELMAN, and Stephen GRAFF .....	167
12. <u>"Comparison of the Nonlinear Behavior of Concrete Arch Dams using Physical and Numerical Models,"</u> David W. HARRIS, Terry L. PAYNE, and Larry K. NUSS .....	193
13. <u>"Non-linear Seismic Analysis of Stony Gorge Dam,"</u> Barbara L. MILLS-BRIA .....	201
14. <u>"Properties Obtained from Dam Cores,"</u> David W. HARRIS, Timothy P. DOLEN, Carrolline E. MOHOROVIC, and Phoebe MITCHELL .....	215
15. <u>"Earthquake Damage and its Remedial Measure for Earth Dam with an Asphalt Facing,"</u> Yoshio OHNE, Kunitomo NARITA, Tetsuo OKUMURA, and Yoshio NAKAMURA .....	229
16. <u>"Evaluating Liquefaction Resistance at High Overburden Stresses,"</u> Ross W. BOULANGER .....	241
17. <u>"Dynamic Centrifuge Modeling of Earth Dams on Liquefiable Foundation,"</u> Korhan ADALIER and Michael K. SHARP .....	253
18. <u>"Evaluation of Permanent Displacement in Seismic Analysis of Fill Dams,"</u> Norihisa MATSUMOTO .....	269
19. <u>"Post Earthquake Residual Strength of Liquefiable Cohesive Soils,"</u> Samuel T. STACY .....	281
20. <u>"Design Criteria for Rounded/Angular Rock Riprap in Overtopping Flow,"</u> Humberto GALLEGOS and Steven R. ABT .....	291
21. <u>"Dynamic Response of Lightly Reinforced Concrete Intake Towers,"</u> Richard C. DOVE and Enrique E. MATHEU .....	299
22. <u>"Earthquake Analysis of Radial Gates/Dam Including Fluid-Structure Interaction,"</u> Mohammad ASLAM, Edward L. WILSON, Martin BUTTON, and Charles AHLGREN .....	311
23. <u>"Present State of Acceleration Measurement and Nationwide Network of Observation at Dam Sites in Japan,"</u> Takashi SASAKI, Syuji TAKASU, Hitoshi YOSHIDA, and Kenji INAGAKI .....	325
24. <u>"Seismic Hazard Analysis and Selection of Design Earthquake for a Dam in Kansas,"</u> Paul G. SOMERVILLE, Francke C. WALBERG, and Vlad G. PERLEA .....	343

25. “Simulation of Strong Ground Motion at Kasyo Dam Site during the 2000 Tottori-Ken Seibu Earthquake,” Nobuteru SATO and Fumio YONEZAKI .....361
26. “Permanent Ground Displacement at a Dam Site and Change in Reservoir Water Level Caused by the 2000 Western Tottori-Prefecture, Japan Earthquake,” Tatsuo OHMACHI, Naoyuki KOJIMA, and Atsushi MURAKAMI .....379

## Current Activities on Construction and Management of Dams in Japan

by

Tadahiko Sakamoto<sup>1</sup>

### ABSTRACT

Dam construction in Japan is still much needed as it provides an effective method of maintaining and harnessing water resources while controlling floods. Since Japan is densely populated, upon dam construction there has been the expenditure of utmost efforts with the participation of local residents and in harmony with the natural environment. Furthermore, in regard to construction and operational management, not to mention safety and economy, there is a strong demand for technologies that lessen the environmental impact as much as possible. Thus, the following three technological developments are primarily being promoted in Japan.

*a.* Technological development for maintaining the quality and safety of structures under difficult natural, social, and labor conditions.

*b.* Technological development for maintaining economic efficiency and technical reliability despite limited information, land space, materials, and human resources.

*c.* Technological development for maintaining environmental integrity that meets the diversified sense of values in the area of the environment.

This paper introduces the latest topics in Japan related to construction and operational management technologies for dams.

**KEYWORDS:** Dam, Earthquake, Environmental Conservation, Maintenance, Redevelopment

### 1 INTRODUCTION

Japan, a narrow landmass with 75 percent being mountainous terrain, is situated within the Asian monsoon zone. Japanese rivers are steep in gradient and short in length, and some 120 million people populate the river basin densely. During the rainy season, heavy precipitation results in rainwater gushing toward the sea rapidly. Because of such features, dam construction in Japan is still much needed as it provides an effective method of maintaining and harnessing water resources while controlling floods.

Moreover, since Japan is densely populated, upon dam construction there has been the expenditure of utmost efforts with the participation of local residents and in harmony with the natural environment. Particularly in recent years, there has been an increased awareness of local residents concerning the natural environment, which requires dam planners to provide and clarify, in addition to measures for resettlement of affected residents in the dam site areas, the future regional promotion program and natural environmental protection measures in the dam and reservoir areas.

Furthermore, in regard to construction and operational management, not to mention safety and economy, there is a strong demand for technologies that lessen the environmental impact as much as possible. Thus, the following three technological developments are primarily being promoted in Japan.

*a.* Technological development for maintaining the quality and safety of structures under difficult natural, social, and labor conditions.

---

<sup>1</sup> Chief Executive, Independent Administrative Institution Public Works Research Institute (IAI-PWRI), JAPAN.



b. Technological development for maintaining economic efficiency and technical reliability despite limited information, land space, materials and human resources.

c. Technological development for maintaining environmental integrity that meets the diversified sense of values in the area of the environment.

This paper introduces the latest topics in Japan related to construction and operational management technologies for dams.

## 2 NEEDS OF DAMS IN JAPAN AND RELATED ISSUES

### 2.1 Issues relating to water in Japan

Some 80 percent of Japan's municipalities have been victims of flooding over the past decade. This is primarily because flooding occurs as soon as it rains and the flood tends to peak at a high level due to the nature of the water pathways in Japan. The difference between ordinary water amount and that during floods is fairly large, occasionally surpassing the 100 to 1 ratio. Secondly, low-lying land in Japan that comprises some 10 percent of the entire landmass is densely populated. Perhaps this is because due to geological reasons, about half of Japan's entire population and 75 percent of her assets has to be concentrated in such locations. In

recent years, although such areas have in fact been reduced thanks to the effects of dams and fluvial improvements, the assets contained in such regions have increased due to urbanization and modernization. As a result, the damage potential from flooding has been growing over the years. Thus, a reduction in such damage is a vital issue.

Ironically, water shortage occurs in many areas of Japan. Over the past 16 years, most of the prefectures in Japan have experienced water shortage. This is because, to begin with, although the amount of water stock in Japan (1,714 mm/year) is approximately double the global average (973 mm/year), per capita amount of water (5,241 m<sup>3</sup>/year/person) is only one-fifth (26,871 m<sup>3</sup>/year/person) that of the global average (see Figure 1).

Various industrial activities including production of chemicals, precision machinery and paper among others is dependent upon major industries that use a large amount of water. Recycling of industrial-use water has been promoted to the point of having a 77 percent recycling rate in 1996, which has also reduced the effluvial amount.

However, even this improved recycling rate has a limit and thus points to the need to establish a stable water supply.

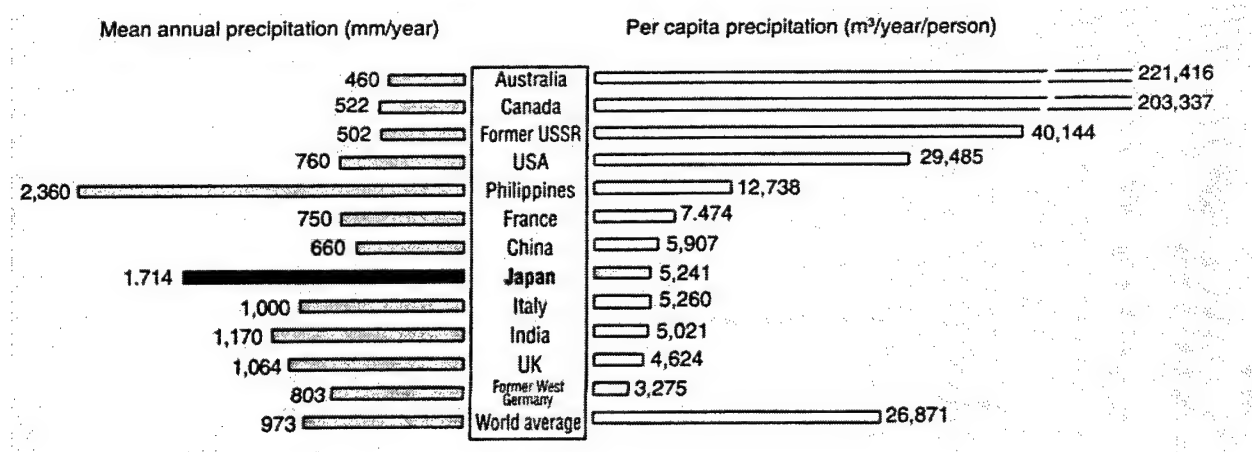


Figure 1. Precipitation around the world

The increase in urbanization has resulted in reductions in underground water. This is because of the increase in areas covered and in the demand for water. Moreover, in rural areas, the increased urbanization and other trends have resulted in the loss of the environmental functions they played. For forests that make up most of the water source areas, furtherance of development and roughshod harvesting of trees by the economically stricken forestry industry has reduced the water retention level. Thus, overall there are ill effects being shown on the water environment that requires action to revive and maintain a healthy water environment.

## **2.2 Necessity and role of dams**

As noted in 1.1, as problems concerning the management of rivers basins in Japan, there are the need to deal with weaknesses against flooding, need to maintain stability of water resources and the need to maintain the water environment that constitutes an important part of the global environment. Important upon solving such problems are the solution of management among the requirements of anti-flooding measures, water usage (water storage for tap water, agricultural and industrial uses as well as for hydropower), environmental preservation, recreation and shipping-use canals, among others. What is now needed is an understanding thereof from the standpoint of the dam as a choice for the overall management of rivers upon dealing with current Japanese riparian problems and future development. This can be accomplished by offering: (1) as many choices, including dams, to deal with the management issue; (2) an evaluation through combination of such choices; and (3) an effective management regimen, through inclusion of processes such as selection of choices that enables participation of the residents.

Upon establishing a policy for preventing flooding, different types of structural and non-structural approaches are fully considered in order to evaluate the best mix of both approaches prior to implementation. Upon this consideration, the dam as a structural approach is offered as a choice. One important reason for

selection of the dam as optimal choice in Japan is the fact that the country is situated in the Asian monsoon zone. In Japan, this leads to heavy pinpoint rainfalls and typhoons as well as a geography that lends itself to quick water build-up in the river path. The second reason is that the dam flood control can cover all river areas located downstream to the structure.

Upon planning water use, all types of structural and non-structural approaches are fully considered in order to evaluate the best mix of both approaches prior to implementation. Upon this consideration as well, a comparison of the flood control capability with other choices is of importance.

One of the most important reasons upon the selection of the dam as an optimal choice in Japan is the fact that the country is that it can adjust conditions according to changes supply and demand concerning the water resource depending upon the season and location.

Meanwhile, dams are facilities used to store water, used to store water to control flooding or when demand for water is small, while being used to meet seasonal demand variations during dry spells that cause water shortages or when demand for water is large. Furthermore, by transporting stored water to areas with difficulties in finding water, dams are used to adjust the regional demand for water. Japan, is situated within the Asian monsoon zone which has great seasonal variations as to the rainfall amount and is topographically highly variegated. These limit the amount of aquifer water content. This in turn makes it difficult to distribute water resources. There are also large seasonal temperature differences resulting in huge summertime demand for residential-use water. In addition, social conditions require a large amount of water to be used at certain periods of the year for rice cultivation in the paddy fields.

Based upon a dam's water storage amount, this dam not only offers flood control or water supply capability but also new possibilities for the stored water. By blocking the river path, a dam interrupts the continuity of water flow and

thereby alters the water environment prior to dam construction.

Thus, there is a need to aggressively pursue a choice that reduces the impact on the natural environment. On the other hand, the presence of a new reservoir through dam construction can offer a large recreational space in addition to often creating a resting place for migratory birds or promoting diversity in waterborne organisms due to seasonal changes of the water surface. Moreover, hydropower generation provides a clean energy source that does not emit carbon dioxide or sulfuric acid compounds.

Therefore, when considering the environmental impact of dams, it is important to consider not only the temporary impact on the environment in areas near the dam site but the impact over the long term on the overall environment with an eye to the global environment as well.

### **2.3 Requirement technologies of dams in Japan**

The role to be played by dam technology in Japan is, as noted in 1.2, a great one when considering Japan's unique natural and social conditions. On the other hand, such things as the diversification of values as regards dams makes it necessary deal appropriately with the issue. Moreover, dam projects are large scale construction activities which takes a long period of time while exerting a huge impact on the area to be submerged underwater and impact the lives of those living in the areas nearby. Thus, for the construction and management of dams henceforth, the following must be targeted for improved efficiency thereof.

*a.* Safety under difficult natural, social, and labor conditions.

*b.* Reliability and economic efficiency regardless of limited information, land, material, and human resources.

*c.* Sound environment that meets various requirements of parties that act on different sets

of conditions. In addition, technology development that reduces the impact of dams must also be promoted vigorously.

While dam sites with good geological conditions are starting to run short in Japan, it is necessary to ensure safety of dams against earthquakes from the design stage. Moreover, keeping in mind the high peak level of floodwater due to Japanese climatic conditions and the short period of time it takes for flooding to occur, the concept of controlled flooding and control of dam maintenance facilities especially from the standpoint of ensuring safety is a must. Furthermore, climatic conditions such as the great differences in temperature by season and time of the day requires a detailed eye as to the quality of soil materials upon design as well as the pursuit of reliable implementation of construction work and quality control.

The economic efficiency and reliability for the dam project must be ensured, which requires measures that must ensure quality under differing conditions. That is, in recent years, the aging of the skilled workforce needed for the project makes it difficult to bring together the human resources, thereby adding to the labor, material and equipment cost greatly. Therefore, it is important to consider the wide range of impact rather than the limited impact a new technology would have upon technology development. Moreover, during construction, not only a reduction in the cost or time required due to technology development can be brought about but also the realization of early operational results would improve the entire project's effectiveness. Furthermore, enhanced flood control capability and development of new water resources will effect not only new dam construction, but also such items to be considered for effective use of the dam facilities such as the removal of dam water silt and reduction of incoming soil and silt flow as well as structural additions.

Dam projects require that a full look at the impact on the environment surrounding the construction, which is large in scale and extended in terms of the time required.

Moreover, when environmental impact cannot be avoided, implementation of a mitigation scheme to reduce such impact takes place. For example, comprehensive regimen for ameliorating the situation, such as dealing appropriately with turbid water and refuse materials that emanate from the project, as well as promoting the greening of areas directly effected by the construction work, must be adopted. In addition, a reduction in activities involved and implementation of seedling plantings as well as establishment of biotopes taking place.

Furthermore, such improved water environment can be used for recreational purposes, thus having a positive effect not only on the direct beneficiaries of the dam project but for everyone, for a proper recognition of the value of the project.

### 3 TOPICS IN THE STATE-OF-THE-ART TECHNOLOGIES FOR DAM CONSTRUCTION

#### 3.1 Development of concrete preparation technologies

Conventional concrete preparation equipment uses a batch mixer to knead materials. The equipment repeats a batch cycle where measured materials are put into and kneaded by the mixer, and the uniform mass is taken out. The process is intermitted every time a batch is finished. It is inefficient in working time.

To reduce waste time, a new technology was developed to continuously knead materials. The new system continuously kneads materials, and yields a finished mixture with good qualities (see Figure 2). In addition, the new system can shorten the process time if its kneading units are set one on the top of another, because a continuous kneading of material is performed by gravity with no extra energy supply.

#### 3.2 Application of self-compacted concrete to dams

In recent years, fewer and fewer skilled workers were available in the Japanese construction

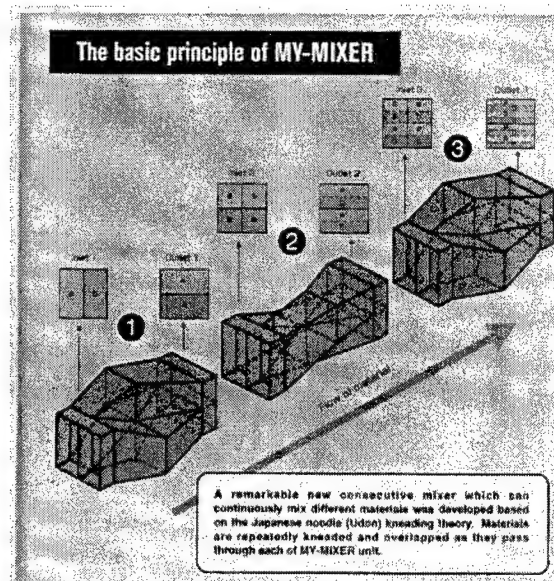


Figure 2. New technology of concrete mixing

industry. Specifically for concrete dam construction, skilled workers have been required to build, among other parts, reinforced concrete structures around outlet conduits and other steel members, galleries and gate doorstops in the dam body. During this task, workers needed to be adept in putting together or setting up steel members, iron rods and frameworks while being obliged to place concrete in confined space surrounded by the steel and iron structure. The concrete placement method must be streamlined to save labor while maintaining safety. A possible solution is to make partial use of self-compacted concrete in dam construction, and such cases are growing in number.

“Self-compacted concrete” is concrete that has been prepared with highly enhanced fluidity and resistance to material separation compared with conventional types of concrete. With good self-filling property, the new concrete requires no internal vibrator to fill up a framework and thus leaving no vacancy (see Figure 3).

The new concrete is advantageous for dam construction use in that it can fully fill up a framework without the need for the piping of the concrete placement in narrow rooms and internal vibrator compaction. This feature leads to the



**Figure 3.** Slump flow using a large cylinder

construction endowed with greater reliability, and to the lower need for labor skill and activities on site.

Self-compacted concrete was used to support precast galleries, parts around outlet conduits and concrete placed secondarily in intake gate block out.

Spillways and other large outlet works are often seated on an installing platform as seen in Figure 4. Besides, iron rods and dowels are crowded around outlet works. Concrete to be placed there thus should be self-compacted. Figure 4 shows self-compacted concrete placed under outlet works of Hinachi Dam (PG, Height = 70.5 m, Volume = 426,000 m<sup>3</sup>).

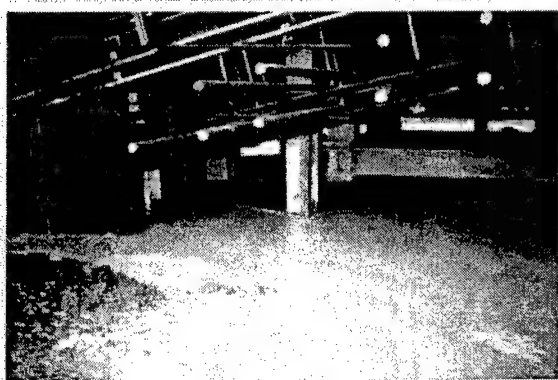


**Figure 4.** Placing of self-compacting concrete (Hinachi Dam)

Those cases were just concerned with a small part of the dam body. However underway is

research of self-compacted concrete with so large maximal aggregate size ( $G_{max}80\text{mm}$ ) that it will make up the whole dam body.

### 3.3 CSG method

Economical dam construction involves effectively using materials as well as streamlining design and building works. As a promising solution, the CSG (Cemented Sand and Gravel) method was developed, and, in 1991, was employed in building an upstream cofferdam (Height = 14.9 m, Volume = 22,900 m<sup>3</sup>) for Nagashima Dam (PG, Height = 109 m, Volume = 842,000 m<sup>3</sup>). In the CSG method, cement is added to such locally yielded materials as bed sand and gravel dug at or around the dam site and muck produced by the dam excavation and the roadwork. They are mixed, and the mixture is carried, applied and compacted as is the material of rock-fill dams. The method is effective not only in using materials, but also in enhancing economical construction and shortening the period of works.

In the CSG method, locally yielded materials to be mixed with cement are cleared of rocks larger than 150 mm across. It is different from the rockfill-dam material in containing cement, and from concrete in evading the size control of aggregate. The CSG material is thus poorer than the concrete in strength, uniformity of quality, and imperviousness, but much more advantageous over the rockfill-dam material in strength and overflow resistance.

Here are steps of the method:

- a. Rocks 150 mm across or larger are removed by a grizzly from raw material produced at the site.
- b. Cement is added to the material by a backhoe or other conventional means.
- c. The mixture is carried by a dump truck or other measures to a banking yard.
- d. The dumped mixture is laid out by a bulldozer and compacted by a vibratory roller.



Steps c and d are similar to what is done by the RCD (Roller Compacted Dam Concrete) method. In the early implementation of the CSG method, Step c relied on a backhoe, though a simple mixing plant is increasingly employed today to get greater blending power and homogeneity of the product.

Among advantages of the CSG method are cost reduction and shortened term with no large investment of equipment, saved resource because of effectively procuring materials at the site, and accelerating the construction. Unfortunately, researchers of the new method still have to solve some technical challenges: (1) the product quality differs according to properties of the materials gained at the site; (2) its strength and imperviousness vary in a low and rather wide range; and (3) there is as of yet no control system for ascertaining construction and quality.

With those features and merits, the CSG method was applied to rather small temporary constructions such as cofferdams (Nagashima Dam, Surikamigawa Dam, Chubetsu Dam, Kubusugawa Dam, Tokuyama Dam, Takizawa Dam, etc.), temporary revetments (Tomisato Dam and Tokuyama Dam) and check dams (Mizunashi River No. 1 Dam at Mt. Unzen Fugen in Nagasaki Pref.).

For example, Surikamigawa Dam (ER, Height = 111 m, Volume = 8,900,000 m<sup>3</sup>) employed a material made of tunnel muck (Figure 5). Tokuyama Dam (ER, Height = 161 m, Volume 13,900,000 m<sup>3</sup>) is placed to be built with sediment material of the existing Yokoyama Dam (PG, Height = 80.8 m, Volume = 320,000 m<sup>3</sup>, completed in 1964) lying downstream. At the same time, the removal of sediment material restored the validity of Yokoyama Dam.

At the sediment trap dam (PG, Height = 34 m) placed near the most upstream point of the reservoir of the above-mentioned Nagashima Dam, an inner part was built with the CSG concrete so that the construction work was accelerated at a lower cost (Figure 6).

### 3.4 Using precast concrete products

To streamline the construction of concrete dams, the RCD and ELCM methods have been implemented to place concrete effectively. But form work and steel bar placing require lots of time and skills in structural blocks such as galleries, elevator shafts and gate control room. Such difficulties seriously affect the lift schedule of concrete. Besides, there are dangerous manual

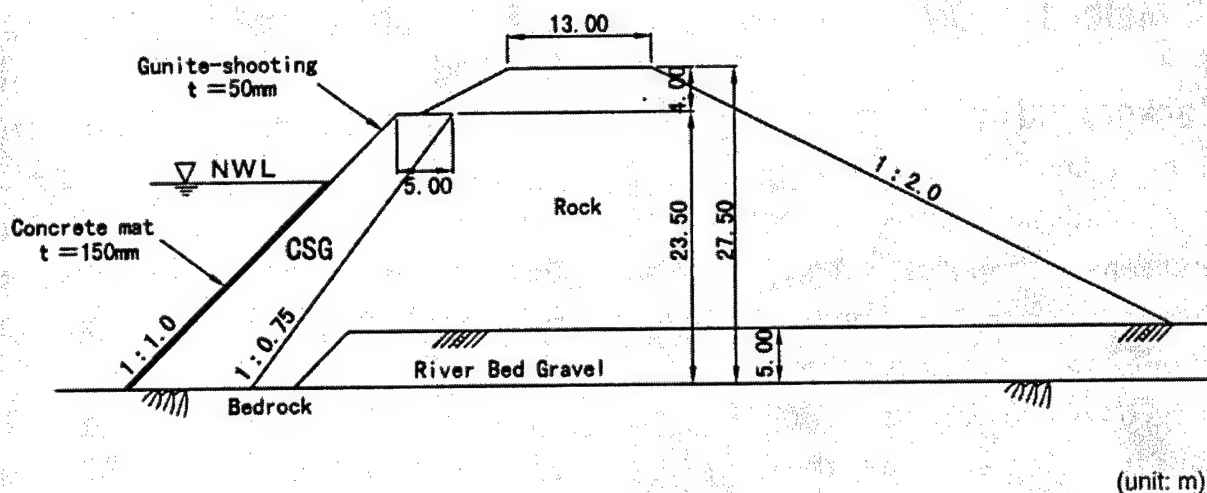
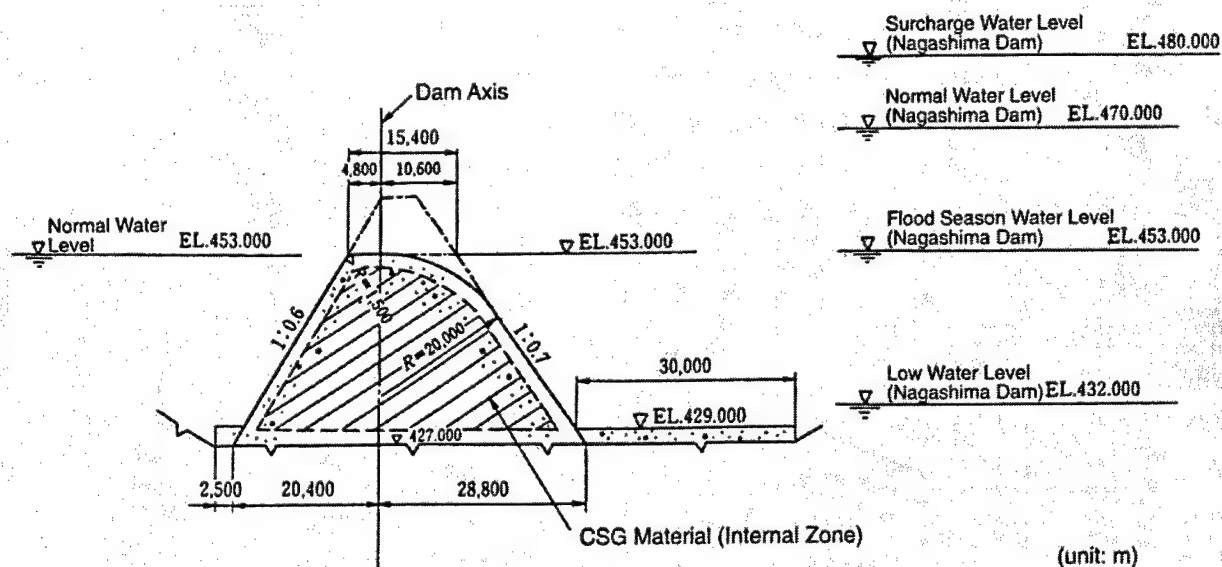


Figure 5. Typical cross section of coffer dam (Surikamigawa Dam)



**Figure 6.** Check dam used CSG material to inner part (Nagashima Dam)

works on a hanging scaffold such as installing a hanging form.

In those cases, precast concrete products (factory-made) are used to streamline the installation of forms and steel bars, and to secure the safety.

A precast concrete product should be reinforced, in case it should be strengthened to incorporate with the dam body.

#### Merits of Using Precast Concrete Products:

- a. Shortening work period. The period of construction is shortened because only placing ready-made products is necessary without form work and steel bar placing.
- b. Securing safety. Construction works are made safer because such dangerous works as assembling forms or timbering at heights are less required.
- c. Securing quality. Factory-made precast concrete products secure reliable quality.
- d. Simplifying concrete works.

Less form work and steel bar placing simplify concrete work so that non-skilled workers can make it.

For example, Unazuki Dam (PG, Height = 97 m, Volume = 510,000 m<sup>3</sup>) and Tsunakigawa Dam (ER, Height = 74 m, Volume = 2,160,000 m<sup>3</sup>) used precast concrete products for their galleries (see Figures 7, 8, and 9).

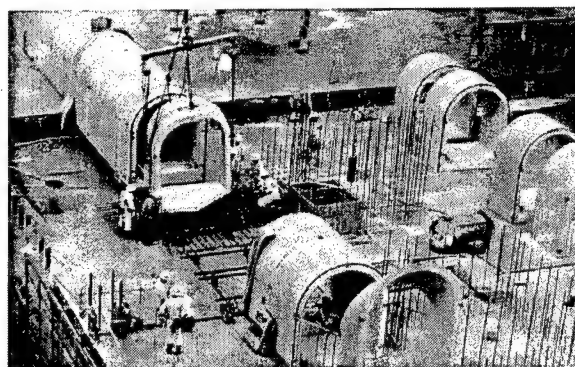


**Figure 7.** Example of using precast gallery (Unazuki Dam)

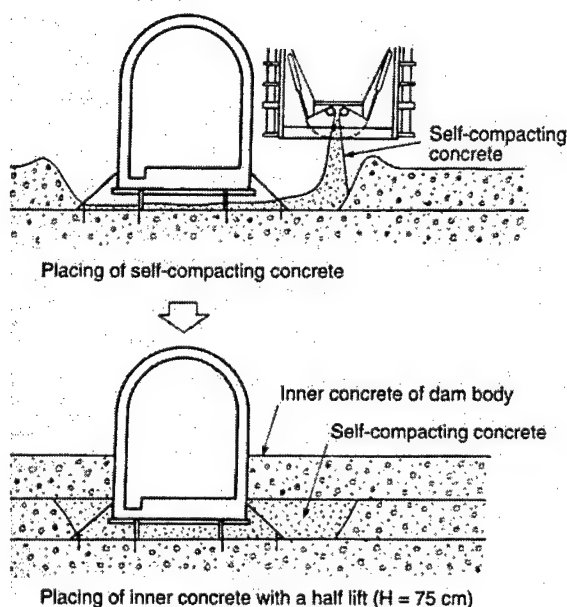


**Figure 8.** Steps of placing concrete gallery (Unazuki Dam)

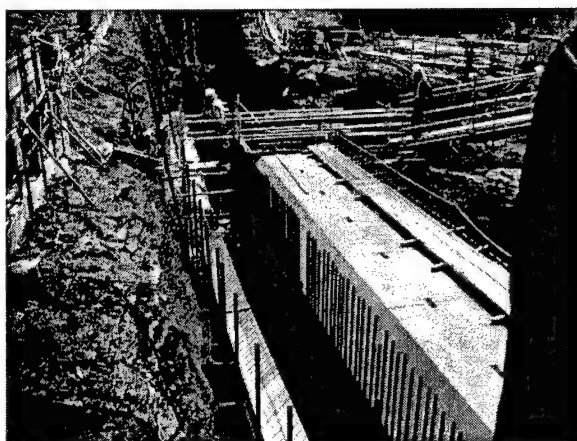


**Figure 9.** Example of using precast gallery (Tokuyama Dam)

### 3.5 Remote sensing for reservoir management

There is a wide spectrum of investigations concerned with dam construction: hydrologic, meteorological and environmental to be done beforehand as well as those performed during construction works, and those for the dam maintenance and administration.

Those investigation technologies have been remarkably advanced with the dam construction. The advancement these days is, however, particularly great because of the dam information technology newly exploited and provision of information equipment in implementing such technology.

It is important to obtain actual information accurately on the water quality of reservoirs and lakes in order to retain their water quality.

It is desirable to have actual three-dimensional information data to keep track of the water quality of reservoirs and lakes at aiming to forecast the trend in water quality.

As measurement activities involved upon doing this, site observation at the reservoirs extended to vertical and horizontal directions should be surveyed in order to make a better water quality movement model.

In conducting the survey, it is possible to monitor the water quality alterations in reservoirs by getting information on distribution data extending to the water surface.

Thus, it is most efficient to utilize the satellite remote sensing system to widely survey the extension of surface water quality.

With technological progress, the observation by remote sensing enables judgment of objects (such as water surface, plants, soil and so on) and the surveying of the surface distribution water quality, through analyses of detailed data on reflection or radiation of electromagnetic waves from objects.

The measurement of water quality by remote sensing system is more effective upon measuring water temperature, suspended solids and generation of algae (chlorophyll "a"), in accordance with experimental results.

Figure 10 shows outline of the system and Figure 11 shows results of the observation on water quality at the Lake Biwa.



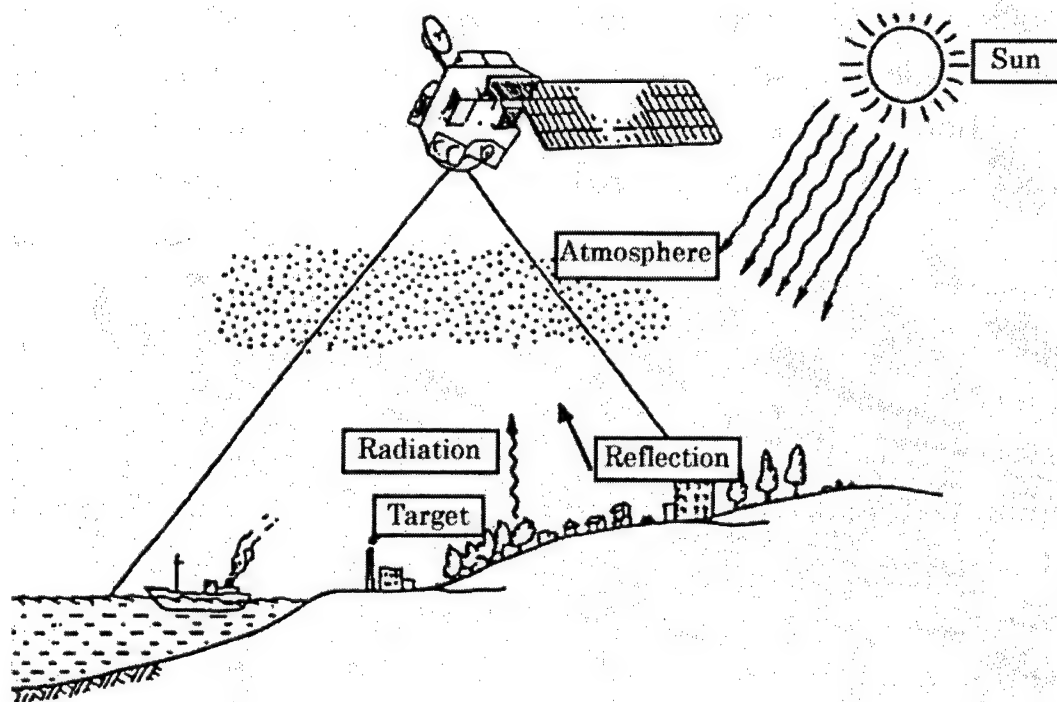


Figure 10. Outline of the system of the water management on reservoirs

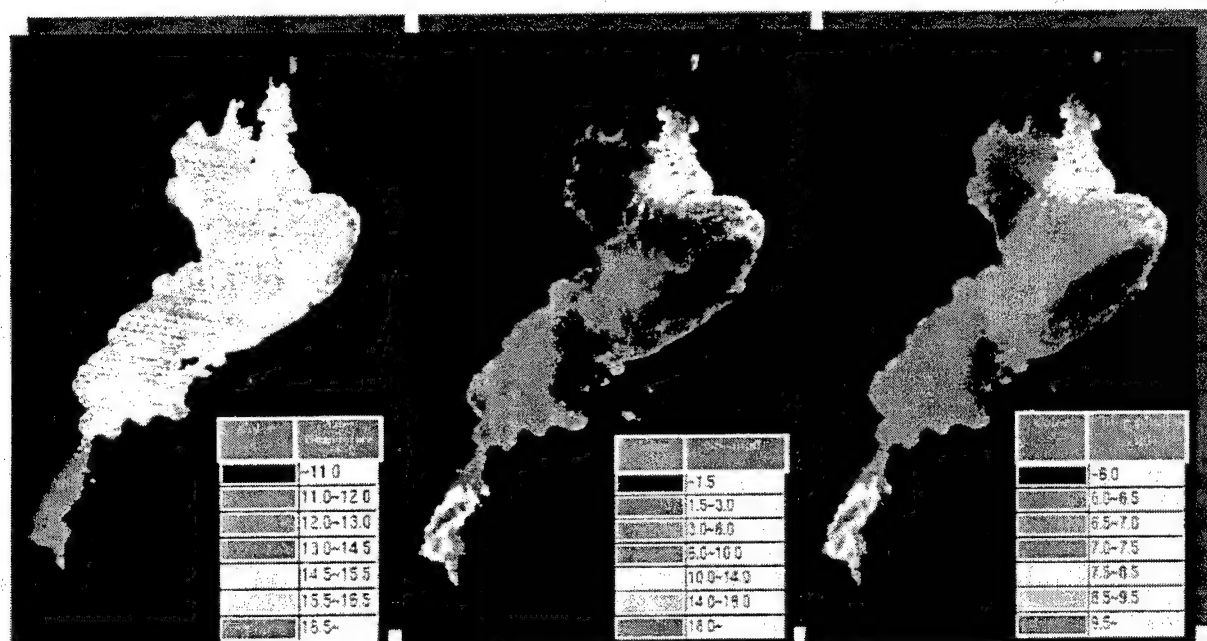


Figure 11. Results of the observation on water quality at Lake Biwa

## 4 DAM RESERVOIR REDEVELOPMENT

### 4.1 Background to dam redevelopment in Japan

As social constraints concerning dam construction increases while on the other hand locations available for dam sites dwindle, there is still a strong demand as regards dam constructions.

Such a background has led to the attempt at redevelopment of dams in existence, with the concomitant effects being larger than new dam constructions, thereby resulting in recent attempts to be put in place on several occasions.

### 4.2 Dam redevelopment ways

There are three ways for redevelopment of existing dams, as follows.

#### a. Increasing storage capacity of reservoir.

By raising the existing dam instead of constructing a new one, use of more water, with the water volume becoming relatively large in comparison with the level of the heightening, is made possible. This method offers the merit of enabling the forecast of various changes, thanks to the fact that topological surveys have been carried out when the existing dam was constructed which has led to such attempts becoming more often implemented in Japan.

Two examples of the heightening, Shin-Maruyama Dam and San-noukai Dam, are introduced.

Maruyama Dam (PG, 98 m high, dam volume,  $500,000 \text{ m}^3$ ) was completed as a multipurpose dam in 1956. Redevelopment is in progress for the enhancement of flood control function and protected flow of the river. The dam is to be raising some 24 m, with the current active storage capacity of  $38,390,000 \text{ m}^3$  to be raised to some  $6,700,000 \text{ m}^3$ .

Upon construction work, because the dam is used for flood control more than 40 times a year and two hydroelectric power stations with a total capacity of 188,000 kW are installed, there are restrictions. Namely, the current dam water

provision (maximum  $4,800 \text{ m}^3/\text{s}$ ) is to be carried out even during the work; the water level is to be maintained as under the existing design. This is in order to prevent the stop or reducing of the two power stations and to maintain the dam stability.

Under such restrictions, a new dam axis some 47.5 m downstream of the existing dam axis is to be constructed with nine flood control outlet works gates (conduit gate W 5.0 m  $\times$  H 6.5 m) for letting out  $5,700 \text{ m}^3/\text{s}$  of the designed  $10,000 \text{ m}^3/\text{s}$  amount to be added and to construct 10 uncontrolled spillways for letting  $15,000 \text{ m}^3/\text{s}$  combined with flood control outlet works (Figure 12).

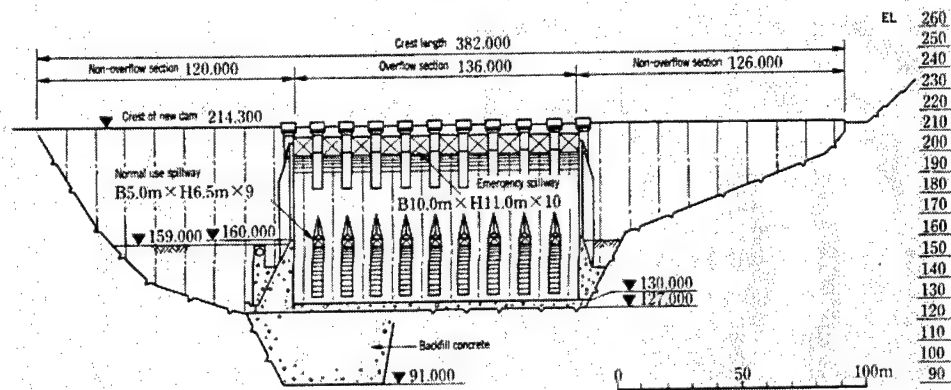
Sannohkai Dam (ER, 37.4 m height, 150 m crest length, total reservoir storage capacity  $9,600,000 \text{ m}^3$ ) is an earthfill dam. This dam for irrigation purpose was completed in 1952. In the four decades that have passed since the dam was constructed, the expansion of agricultural land including farmland by redevelopment has created a shortage of irrigation water. To cope with this situation and to assure stable supply of water, it was decided to heighten the existing dam. A new dam under construction, (trial water discharge date set during fiscal 2000) is a rock-fill structure with center impervious zone, 61.5 m high, 242 m long along the crest and gross storage volume of about  $38.4 \text{ million m}^3$ , which is almost four times the storage volume of the existing dam (Figure 13).

As a method of raising the existing dam level, the possibility of using the old waterfill zone was considered, but at Sannohkai Dam (i) using the old zone would mean that construction that makes use of the old structure would be difficult and (ii) the actual zone is not clearly identifiable, so it was decided that a new dam axis would be built downstream to the old axis.

#### b. Changing operation system of the dam reservoir.

This changing operating system of the dam reservoir reconstruction the intake work and outlet work without changing the scale of existing

(a) Downstream Face of Dam



(b) Standard Section Shin-Maruyama Dam

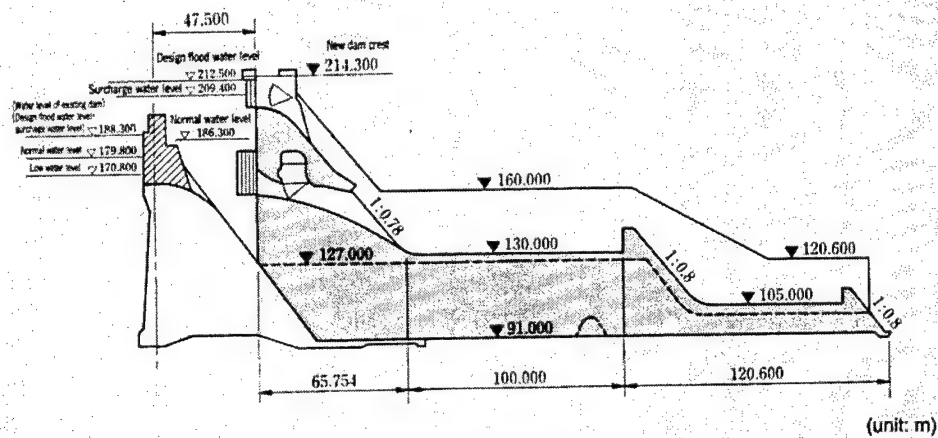


Figure 12. Section of the Shin-Maruyama Dam

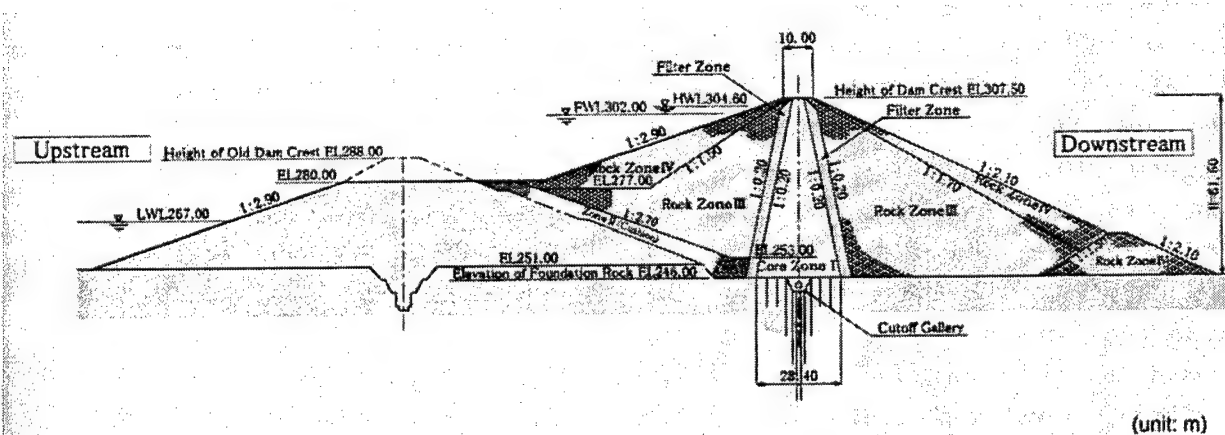


Figure 13. Typical section of the Sannohkai Dam

dam, or adding new outlet work that can correspond to top priority objectives; this is the most common redevelopment way in Japan today.

Moreover, there is also a case where the effective use of water by networking several reservoirs with a new channel, thereby altering the operation system for these.

The Dams Networking Project of Upper Kinugawa river entails water being shared through connection via waterways of dams with differing capacities, Ikari Dam (PG, 112.0 m height, crest length 261.8 m, dam volume 468,000 m<sup>3</sup>, active storage capacity 46,000,000 m<sup>3</sup> and drainage area 271.2 km<sup>2</sup>) and Kawaji Dam (VA, 140.0 m height, crest length 320.0 m, dam volume 650,000 m<sup>3</sup>, active storage capacity 76,000,000 m<sup>3</sup>, and drainage area 144.2 km<sup>2</sup>), to

enable combined operation of the reservoirs and improve the flow in the Oga River and the Kinugawa River proper.

The overflow from Ikari Dam being added to the Kawaji Dam's available capacity would mean a maximum of 20 m<sup>3</sup>/s being added; on the other hand, should the flow from Ikari Dam fall short, it can be supplemented with water from Kawaji Dam.

c. Improving the supplying water quality of dam and reservoir.

As required, the water quality is improved as per (2) where the intake and outlet work are altered or new one added, often seen in the case of old dams. 5-3 provides an example.

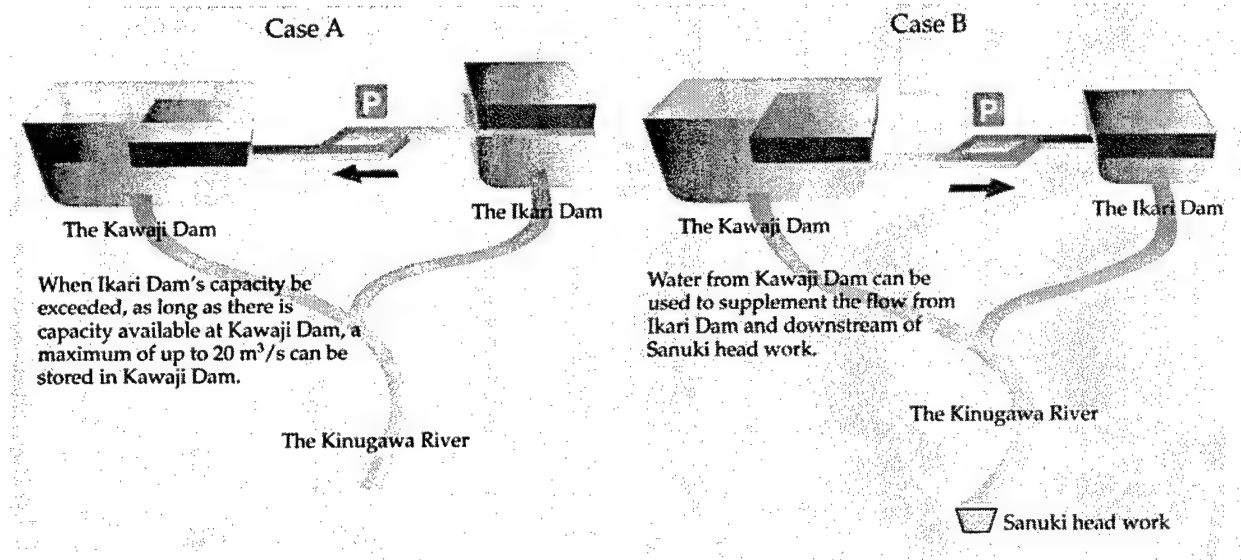


Figure 14. Dam networking system sequence

## 5 MANAGEMENT FOR DAMS AND RESERVOIRS

### 5.1 Countermeasures against sedimentation in dams and reservoirs

Countermeasures against sedimentation in the reservoir can roughly be divided into two

methods. One is the excavation and dredging method and the other is the sediment flushing facilities by the tractive force of flowing water. The countermeasures by the excavation and dredging are difficult to be adopted as the reservoir-managing plan on the grounds that the disposal area for the machinery of dredging and transportation, and for a large amount of

dredged sediment in case of a large quantity of sediment inflow. On the other hand, if the conditions are settled, the sediment flushing facilities is possible to be adopted as the permanent reservoir-managing plan. In this section, the sediment flushing facilities are described.

#### a. Sediment flushing gate.

A dam, which enables the water level to lower below the sediment level in the reservoir operation, makes sediment flushing possible by sediment flushing gates. There are some examples so far.

Here, an example of the sediment flushing gate of Unatsuki Dam is introduced.

A specific sedimentation rate is adopted  $3,300 \text{ m}^3/\text{km}^2/\text{year}$  which is obtained by the stochastic method from the relationship between results of sediment volume in Kurobe dam located upstream side Unatsuki dam and the annual floods. As estimated inflow sediment volume of  $140,000,000 \text{ m}^3$  is extremely large

and spoils the function of the dam, therefore, the installation of sediment flushing facilities was decided.

A reservoir operation is examined to secure the necessary sediment volume on the basis of the discharge in the last 25 years. An annual mean discharge of the bedload and suspended load records are estimated as the annual sediment of  $800,000 \text{ m}^3$  with three times operations of the sediment flushing a year. Sediment flushing is done during the flood taking the influence of the downstream area into consideration and after finishing the function of flood control, the water level is lowered and discharge of sediment is carried out.

Figure 15 shows standard cross section of sediment flushing facility in Unazuki Dam. Basic structure of sediment flushing facilities meets the structural criteria for outlets and its members are repairable and exchangeable, as the need arises, taking the environment of the maintenance works into consideration to keep necessary functions.

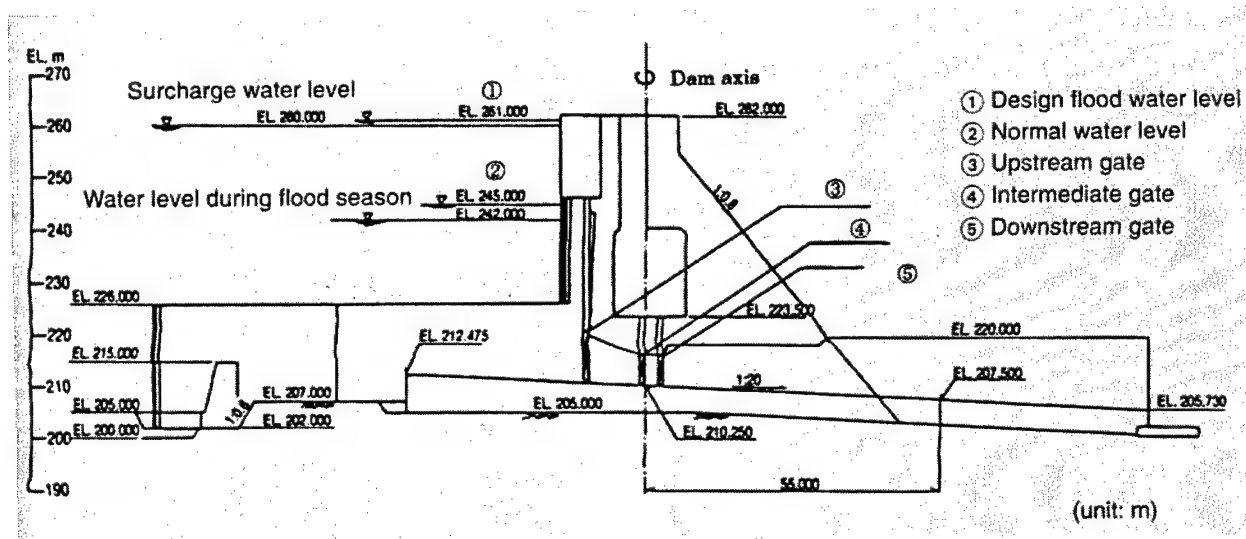


**Figure 15.** Typical section of sediment flushing facility at Unazuki Dam

For channels and open channel-type tunnels in the dam body, the lining materials are fixed on the surface with exchangeable members to avoid a bad influence by a large-scale repair was

adopted. Stainless materials are for the reason of the maintenance and the economical point. A life of lining materials of 30 mm thick is presumed of to be 30 years.

b. Sediment bypass.

In a dam, which cannot lower the water level below the sediment level, even if a sediment flushing gate is open in the high water level in the reservoir, the are of flushing would be limited only near gates and there is no restoration effect for the active storage capacity of the reservoir.

In case of the above situation, there is a countermeasure against the sedimentation to construct a bypass tunnel detouring the reservoir. Concretely, a check dam is constructed in the upstream end of the reservoir and the bedload of large grain size is settled there. From an intake located in the upstream check dam, the suspended sediment and the wash load are flushed out downstream through a channel that detours the reservoir.

Here, an example of the sediment bypass of Miwa Dam is introduced.

Miwa dam (PG, dam height = 86.1 m, dam volume =  $147,300 \text{ m}^3$ , catchment area =  $39.2 \text{ km}^2$ ) was constructed on the Mitsumine river in the Tenryu river system. The dam works started in 1953 and completed in 1959. The dam is a multipurpose dam for the flood control, the irrigation and the power generation.

In the drainage basin of the Mitsumine river, there have been repeated and large flood such as that of 1959, 1961, 1982, and 1983. Therefore,

unexpected sediment flows into the reservoir. An active storage capacity is secured by gravel gathering in the upstream end of the reservoir. However, there is the possibility to deteriorate the functions of the dam if this situation leaves as it is. Accordingly the works of sediment excavation and removal have been executed for the purpose to secure a storage capacity for 100-years sediment volume and a new storage capacity for the flood control and the industrial water. Furthermore, the sediment bypass system which is composed of the weir for diversion and the flood bypass tunnel is planned, as the permanent countermeasures to restrain the sedimentation in the reservoir.

A mean annual inflow sediment in the reservoir of Miwa dam is the bedload and suspended sediment of approximately  $160,000 \text{ m}^3$  and the wash load of  $525,000 \text{ m}^3$ . A rate of wash load portion is 76 percentage. Therefore, the flushing wash load leads to the reduction of the sediment in the reservoir.

As the bypass system is for the wash load only, it is composed of the check dam and the weir dam for diversion which has the functions of diverting the flood and capturing the bedload and the suspended sediment, and the bypass channel (side flow weir), the bypass tunnel and the energy dissipater (Figure 16). It is necessary, however, to excavate and remove in the accumulated sediment in the check dam.

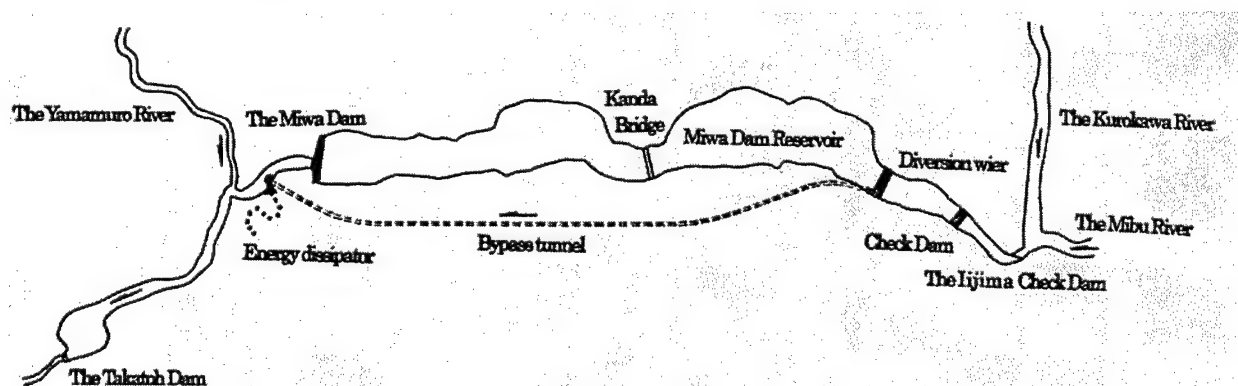


Figure 16. Structural layout of bypass system

c. Check dam.

A check dam is applied when the actual sediment inflow is considerably larger than the expected quantity in the dam planning stage.

For the purpose to capture the inflow sediment, a check dam is constructed in the upstream end of the reservoir and captures the inflow sediment. As a result it stops the inflow sediment into the reservoir and after flood, the sand deposit is excavated and dredged.

Mainly, its purpose is to capture the sand deposit more than grain size of the bedload. Partials of suspended and fine fraction of the wash load are difficult to be captured. Therefore most of them are discharged into the reservoir.

## 5.2 Dam management

Although most dams in Japan were constructed in modern times, there have been dams that were constructed by the monk Kobodaishi (774-835, one of the introducers of Buddhism into Japan). Many of these dams have been renewed until today, making them an important water resource for the respective regions.

On the other hand, there are some earlier dams from this century that have become antiquated and have seen their seismic resistance degraded, making it necessary to renew and to ensure the safety of these dams.

Here are some examples of dam refurbishment.

a. Yamaguchi Chouseichi Dam.

Yamaguchi Reservoir dam is located on the Tokyo-Saitama boundary, located within three cities and one town; construction work on the dam (TE, 34.6 m high, 691 m crest length, active storage capacity 19,528,000 m<sup>3</sup>) was begun in 1927 and completed in 1934, and has since then continued to supply Tokyo with a stable supply of water.

The structure is an integrated earthfill dam and its seismic structure has been recognized;

however, with the occurrence of the 1995 Hanshin-Awaji earthquake, surveys conducted showed that should a direct quake (magnitude 7 class) strike, although the structural integrity would be maintained, the top part of dam (bank) could be subsided.

Thus, since water supply would depend on the reservoir in the event of a natural disaster and since urbanization was proceeding downstream, measures to further enhance its seismic structure were commenced (see Figure 17).

b. Honenike Dam.

Honenike Dam (MV, 31 m high, 128 m crest length) was completed in 1930 for the purpose of supplying irrigation water. The dam has 6 arch-type buttresses built in the center. The span between 5 buttresses is enclosed by full arch structures and both ends are half-arch structures connecting to gravity sections constructed on the abutments. The dam is a masonry structure with the surface finished with stone tile facing. The spillway is a combination of uncontrolled spillway crest section and 5 siphon spillways, adopting a peculiar discharge system. As 60 years have passed since the dam was constructed, deterioration has set in with water leakage from the dam and foundation, and therefore requiring renovation work for fear of degradation of the dam's function.

In the renovation work, preservation of the peculiar shape and aesthetic value of the dam was taken into consideration, since the dam has been designated a prefectural cultural asset (Figures 18 and 19). Concrete facing for repairing the upper surface of the arch section and installing waterstops in joints prevents leakage of water. Footing was constructed in the span between buttresses to reinforce the base of the dam. As the foundation rock of the existing dam had not been treated by grouting, so, consolidation grouting and curtain-grouting were implemented, and drainholes were drilled in the footing to reduce uplift pressure.



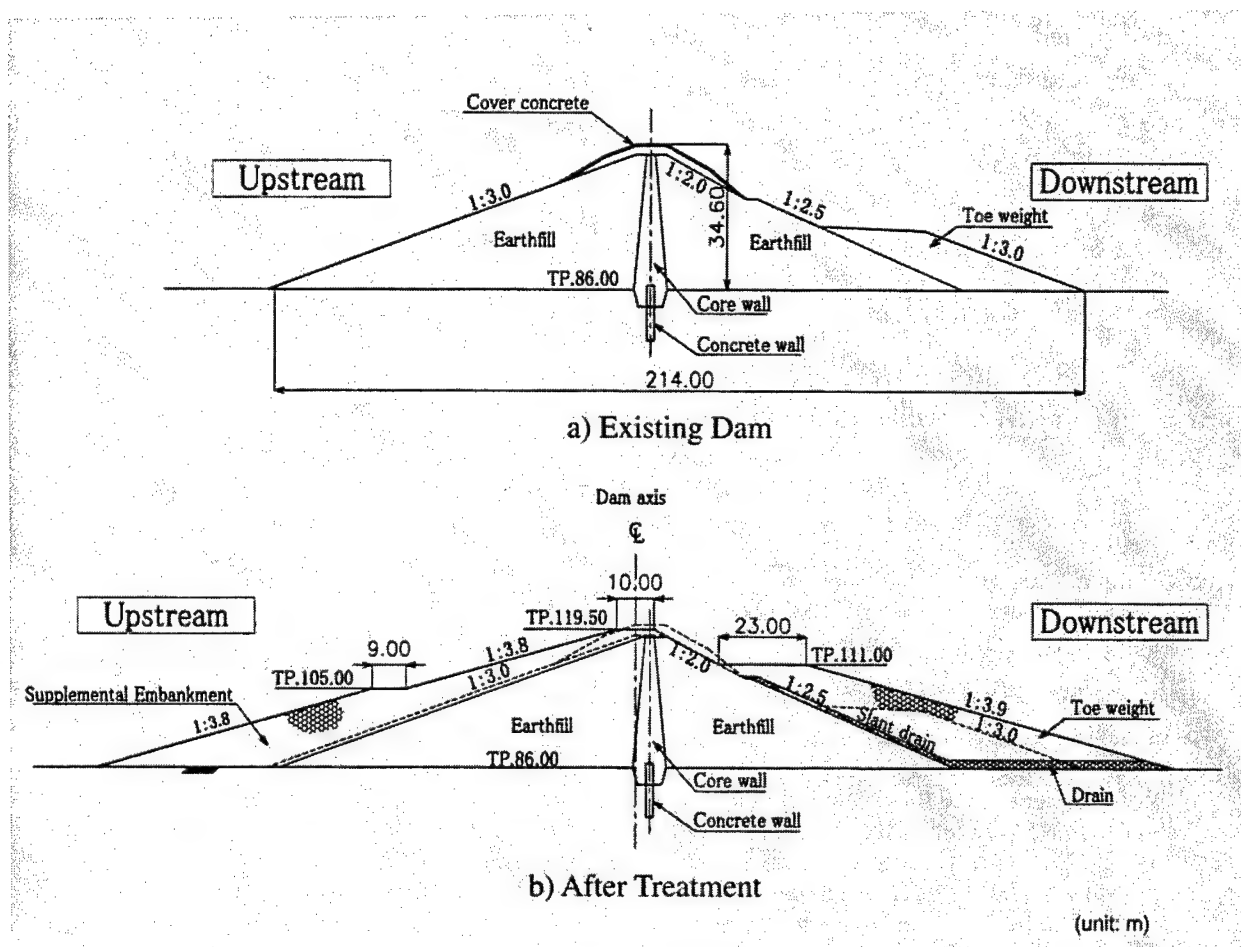


**Figure 17.** Typical section of existing and after treatment (Yamaguchi Dam)



**Figure 18.** Upstream view of Honen-ike Dam after treatment

In Japan, according to the guidelines established by Ministry of Land, Infrastructure and Transport or Japan Commission on Large Dams, dam administrators perform the comprehensive inspection periodically. At the comprehensive inspection, to confirm the safety of dams, monitoring of leakage, deformation and so on, as well as visual inspection is made. Dams, at an age of 20 or more, should be checked to evaluate the structural safety, felicity of operation and the system in an emergency by the specialist team organized by Japan Dam Engineering Center.



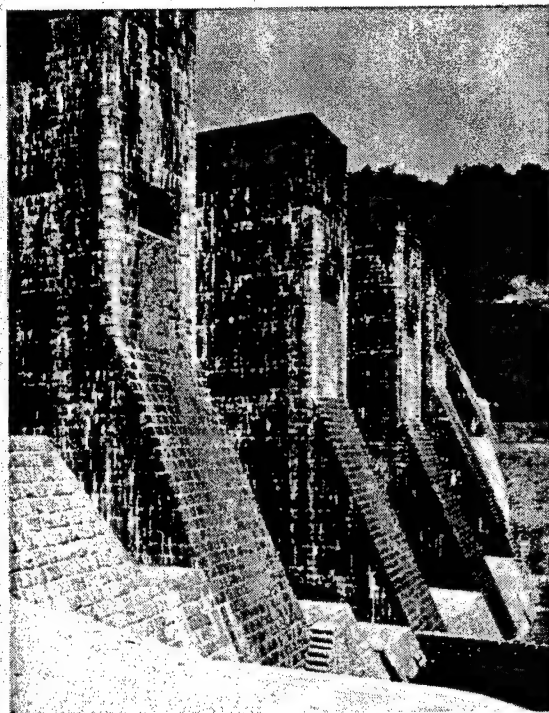


**Figure 19.** Downstream view of Honen-ike Dam after treatment

## 6 COUNTERMEASURES TO EARTHQUAKES

### 6.1 Introduction

Japan is located atop an earthquake-prone zone on the Pacific Rim, and even from a global perspective, is in an area where seismic events occur most frequently. Therefore, almost all permanent civil engineering structure design pays attention to earthquakes, furthermore dams are structures with the highest importance, it needs to be designed and constructed so that damages on dams by earthquakes may not happen. The impacts of seismic events on dams are classified roughly by two types, earthquake motion and ground displacement on the fault line. Dams in Japan have been designed after preliminary checking that there are no active faults near dam site. After the 1995 Kobe Earthquake (the 1995 Hyogoken-Nambu earthquake), measures to active faults became major topics of discussions even for construction of ordinary civil engineering structures. Concerning seismic

motions, dams are basically designed by the seismic coefficient method, and if necessary the seismic resistance of dams may be checked in detail by the modified seismic coefficient method and/or the dynamic analysis. During the Kobe Earthquake, fortunately there was little damage to large dams, but the safety of several dams that received strong seismic motion during that earthquake were reconfirmed by detailed investigations.

### 6.2 Countermeasures in investigation stage

When carrying out choosing sites for dams, in addition to the conventional study of past seismic activities, the active fault survey is always carried out. Although earthquake resistance design against seismic motion is performed, the problem of ground displacement cannot be addressed by the design process. Therefore, areas near active faults that could threaten dams are avoided when choosing dam site at present.

The objectives of active fault investigations in dam construction are summarized as below.

- a. To confirm whether or not lineaments and faults, both of which are considered to be active faults, are indeed active faults.
- b. To locate active faults with sufficient precision such that they can be avoided when building structures.
- c. To identify the activity history of active faults to predict future earthquake occurrence.

Active fault investigations for dam construction include literature research, geomorphological surveys, and geological surveys. Figure 20 shows the flow chart of investigations. Thorough comprehensive consideration of these survey results, it must be clear whether such faults requiring caution upon dam construction exist or not, and if exist, an evaluation as to the length and continuity of the existing active fault must be made.

Since the Kobe Earthquake, trenching and various investigations have been conducted on

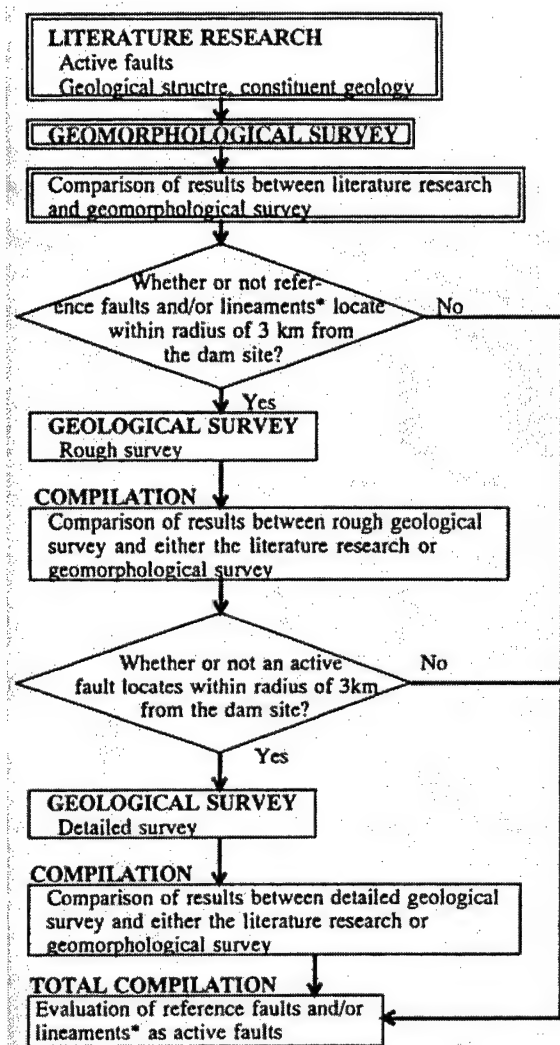


**Figure 20.** Flowchart of active fault investigation

active faults, and the location and history of activity of large-scale active faults and active faults near major cities have been obtained. However, the state of active faults in mountainous areas where many dams are planned to be constructed has not been clarified sufficiently, nor have effective methods been established for investigating and evaluating active faults in such areas where little is known about the base topographies. Existing methods for investigating and analyzing active faults for dam constructions have not been fully established; therefore, improving investigation methods and accumulating knowledge on active faults are needed to

establish the satisfactory evaluation concepts of active faults.

### 6.3 Countermeasures in design stage

Earthquake resistance designs of dams in Japan are conducted basically by the seismic coefficient method accordingly the present design criteria. There have been no large damages due to earthquakes on dams designed by the Japanese present design criteria. But, because the assumption of the acceleration distribution of the dam in the seismic coefficient method doesn't completely match to the real dynamic behavior of the dam, the investigation of the effects of earthquakes on dams are taking place in Japan in order to establish more rational earthquake resistance design methods. In this regard, the modified seismic coefficient method, which takes into account the characteristic of vibration characteristic of dams when deciding the seismic force distribution, has been proposed. In the case of fill dams, the cross section designed by the seismic coefficient method is re-checked the safety by the modified seismic coefficient method. Of course, research activities about dynamic analysis methods are being carried out at universities and public/private research institutions in Japan, and especially in areas where earthquakes may pose serious problems due to dam construction, the dynamic analysis is conducted for individual dam in order to ascertain safety against earthquakes.

### 6.4 Countermeasures in operation stage

Measurements of uplift pressure, water seepage amount, displacement, etc. are mandated for dams in Japan. Although measurement of earthquake motion is not mandated, recently constructed dams oftentimes are equipped with seismometers. In Japan, the special safety inspections should be conducted for dams where the recorded acceleration is more than 25 gal by the seismometer installed in the dam and the nearest station of Japan Meteorological Agency records a seismic event of intensity 4 or greater. The results of such special safety inspections should be informed to the river administrators by the site management offices of each dam, and

through them the river administrators can comprehensively consider the impact of an earthquake upon the dams. The special safety inspection is categorized into primary and secondary inspections, the former being based upon visual inspection immediately after an earthquake while the latter based upon a detailed visual inspection as to the external appearance and safety checks of the data recorded by the measurement equipment installed.

Due to the Kobe Earthquake, the networking of seismometers installed upon civil engineering structures and the ground surface has been rapidly promoted for forecasting earthquake damages. As regards dams, such seismometer networking is being pushed forward, with a nationwide seismometer network to be realized in the near future in order to collect various seismic data immediately after seismic events.

#### **6.5 Activities about seismic design after the 1995 Kobe Earthquake**

Japan Society of Civil Engineers has been recommending using two types of seismic motions, Level 1 and Level 2 earthquake motions, for the seismic design of civil structures after the 1995 Kobe Earthquake. Level 1 earthquake motion is equivalent to OBE (Operation Basis Earthquake), and Level 2 earthquake motion to MCE (Maximum Credible Earthquake), respectively.

In order to secure the safety of dams, it is necessary to set the Level 2 motion clearly at a dam site and to clarify the behavior of the dam during a big earthquake. In order to set Level 2 motion, it is necessary to grasp the characteristics of the earthquake motions at dam sites. Then, some researches that develop prediction formula of an acceleration spectrum have progressed using the statistical techniques based on the recorded earthquake data. Some researches have also progressed that an earthquake scenario is set and an earthquake motion derived from an active fault is estimated using semi-empirical techniques etc. Moreover, to predict the seismic behavior of a dam, analytical researches, which consider cracks of a concrete dam body generated by earthquakes, are progressed. For

embankment dams, numerical methods which consider the plastic deformation and centrifuge modeling are also progressed.

## **7 DAM AND THE ENVIRONMENT**

### **7.1 Outline**

In 1972 the environmental impact assessment (EIA) was adopted for public works. Then each organization operating the projects and local public governments also has been adopting their own regulations for environmental protection. The establishment of the Basic Environment Law in 1993 legally promoted EIA. Then the promulgation of the Environmental Impact Assessment Law in 1999 filled up the former method of assessments.

The standard items on EIA of dam projects are natural, atmospheric, water environment and abundant relations between man and nature ("Man in Nature"), and they are more enriched than the former ones.

### **7.2 Environmental preservation measures**

Upon construction of dams, it goes without saying that not only minimizing the construction area but also considering not alter the present situation of river is the most effective measures to reduce the impact on the environment. But the projects are hard to be compatible with environmental preservation, so there are many attempts to restore flora and fauna after the environment has been altered.

#### *a. Biotope.*

Biotope is a man-made marshy ground for a habitat of flora and fauna. For dam projects, there are some examples on replacing or restoring environment that have been lost due to dam construction as a part of preservation measures for natural environment. The purposes of such measures are preservation of flora and fauna habitats and their diversity, water purification and recreation.

### b. Artificial floating island.

The waterfront shore zone is an important part of the flora and fauna habitat, and has an important role to improve a diversity of flora and fauna. Dam reservoirs with changing water levels do not lead to stable shore zones, so other measures are planned to create the functions similar to the shore zone. One of the measures to provide a habitat environment and to improve the waterside landscape is to make the artificial floating island.

The effects of such an island would be providing a habitat for flora and fauna, specifically for birds that could nest and lay eggs and for fish that could spawn.

### c. Fishway.

In order to reduce the impact of dams on the migration of fish and aquatic life both upstream and downstream to the structure, fishways have been built. According to the purposes such as fish migration upstream and downstream, conservation of fishery resources and ecosystem, various fishways have been built in consideration of dam site conditions.

Currently, there are some 40 dams with fishways in existence or under planning. Table 1 shows the technical features of fishways in recent years.

In Japan, raptors protection is also important. Raptors are superior to other kind of species within the food chain of ecosystem. In order to protect the life of such birds for long time, it is necessary to be formed the food chain that provides rich feed animals constantly and to conserve the ecosystem composed of various species.

The most dams are constructed among the mountains, so golden eagles and mountain hawk eagles often become the subjects of discussion because they mainly live in such area. These birds are to be researched carefully to protect ecosystem and rare species.

Upon dam construction, based on such surveys, measures concerning birds of prey are adopted at the dam site, the temporary construction, the roads for construction and substitution, the picking site, and so on.

**Table 1.** Features of Fishways in Existence

Category	Dam/Name	Features
Pool and Weir type (Spiral fishway)	Nukibetsugawa Dam	Spiral steps allow fishway to be built without taking up space.
Denil type	Imawatari Dam	The peculiar-shaped partitions set up on the rectangular fishway increase the flow resistance and help control the flow speed.
Sector type	Nibutani Dam Meboro Dam	A float is added to part of the fishway (one side) in order to deal with changes in the water level.

## 7.3 Water quality preservation measures

At reservoirs, where river water is detained for a long period of time, the mechanism behind water quality change is different from that of rivers. There sometimes happen characteristic water quality change at dam reservoirs.

On phenomenon of water quality changes at reservoirs, especially concerned problems in Japan are discharging of cold water, prolongation of turbid water, and eutrophication, among others.

The measures for preserving water quality at reservoirs can be classified into two categories: Catchment Area Measures, which aims at reducing the influx of substances that worsen water quality of dam reservoirs; Measures in Reservoir, which aims at controlling water quality change.

#### *a. Catchment Area Measures.*

Water quality deterioration is led by influx of wastewater, and/or by influx of sediment and turbid water caused by forest denudation. Measures are taken to preserve water quality at catchment area of the Dams.

Catchment Area Measures adopted in Japan are as follows:

(1) Improvement of public water treatment facilities at upstream of the dams in order to clean wastewater flowing into reservoirs.

(2) Protection of river banks by works covering with concrete or plants, based upon projects for preserving water quality at reservoirs, in order to lessen the amount of sediment and turbid water flowing into the reservoirs; Establishment of environment preservation belts and tree zones (lakeside woods) in order to preserve quality of influx water.

(3) Planting trees and other measures are carried out at areas for reducing turbid water and for controlling influx sediment.

#### *b. Measures in Reservoir.*

##### *(1) Cold water discharges.*

Cold water has negative impact upon crop and fish growth. So, it comes to problem when the temperature of discharged water from the dam is lower than that of the river water. This problem occurs due to the relationship between the vertical distribution of water temperature in reservoirs and the relationship between the height of intakes.

To deal with this problem, the selective intake facility can be introduced. In this facility, the

height of intakes is changeable, and it is possible to discharge water that temperature would be same or higher than the influx water to reservoirs.

This selective intake facility is generally accepted among the dams that are recently constructed. It is often the case for old dams, which have not this facility, to introduce the facility newly to them, or to improve the old ones.

##### *(2) Turbid water.*

In case of flood, the turbid water flowed into reservoir mixes with existing water at reservoirs, making all the water in the reservoirs turbid.

The phenomenon that the discharging water keeps turbid for long period of time is brought by gradual discharging of turbid water after the flood.

As a measure for prolongation of turbidity, above-mentioned selective intake facility is workable.

##### *(3) Eutrophication.*

Eutrophication might happen when too much nutrient salts are added to the dam water. And depending upon conditions such as water temperature, daylight, and retention period, enormous growth of phytoplanktons follows. Such an occurrence leads to worsening water quality, problems of malodor and filtration block at water purification plant, and negative impact upon the scenery around the reservoirs, among other things.

The following are major categories of measures for eutrophication at reservoirs.

(1) Measures for reducing influx load at the upper portion of reservoir.

(2) Flow-controlling in reservoir and Bypassing of influx water, etc.

Some examples of measures against eutrophication are introduced.



(1) Measures for reducing influx load at upper portion of reservoir (Terauchi Dam).

After the dam was completed, following phenomenon appeared: Outbreak of "water blooms" formed by blue-green algae in summertime, moldy malodor, and filtration problem caused by abnormal appearance of diatomaceae, led by high percentage of nutrient salts in the river which flow into the dam; "freshwater red tides" due to flagellate algae. Thus, in order to reduce the concentration of phosphorus in the inflow rivers, various measures for this problem are to be implemented.

(a) Waterborne plants.

River water is conducted to the shallow ponds where waterborne plants uptake nutrient salts; consequently the phosphorus is reduced. Cresson is being grown as the waterborne plants in this case. (Figure 21).



**Figure 21.** Cleansing using waterborne plants (Terauchi Dam)

(b) Phosphorus absorption materials.

River water is conducted to the waterway that is parallel to the river and has phosphorus absorption materials over the bottom; consequently the phosphorus is reduced. (Figure 22)

(2) Flow-controlling at reservoir and bypassing of influx water (Miharu Dam).

At Miharu Dam, measures for water quality preservation both in inflow-river and in reservoir

are implemented. Various new technologies were adopted as measures for water quality preservation.

(a) Prestorage Pond (small sized reservoir located before the river water enters into the dam).



**Figure 22.** Phosphorus absorption materials (Terauchi Dam)

A prestorage pond was built with some 706,000 m<sup>3</sup> in capacity (for main stream + affluent). Functions of this reservoir are (a) to precipitate the suspended substances; (b) to let the phytoplanktons, at earlier stage, uptake ortho-phosphate dissolved in river water.

(b) Influx Water Bypass Duct.

A bypass duct constructed is 2.4 km long from the prestorage pond to downstream of the dam. The function is to bypassing influx water and load directly to the downstream. Thus, it is

possible to reduce the amount of nutrient salts supplied at the first stage of flood, and to repress alga growth. Furthermore, in case water quality is deteriorated within reservoirs, it is also expected to supply upstream water directly to the water purification plant.

#### (c) Aerating Circulation Facility and Selective Intake Facility.

As a new technology to deal with eutrophication, a flow control system has been designed. The flow control systems utilize Aerating Circulation Facility and Selective Intake Facility comprehensively, and bring circumstances that repress alga growth within the water surface.

Outline of the system is following:

- (i) Circulate in order to form thick upper layer whose temperature is a little higher than influx water; and conduct influx water (including nutrient salts) into deeper layer where algae can not grow.
- (ii) Circulate upper layer in order to push down algae (grown at surface layer) into middle layer.

The flow control system (Aerating Circulation Facility and Selective Intake Facility) adopted at Miharu Dam is shown in Figure 23.

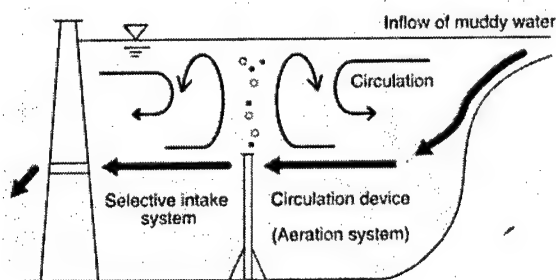


**Figure 23.** Flow control system

### 7.4 Landscape design

Dams and weirs are huge structures; the act of impounding water leads to the creation of a vast

new water surface and open space near the water. By blending this sight with nature that surrounds it, a wonderful landscape that can be accepted into the vast surrounding can be created.

Forward-looking adoption of this idea is the landscape design of dam and reservoir. The splendid view created using this idea may produce secondary benefits of tourism and recreation, in addition to improving the accessibility in and around reservoirs. Figure 24 shows an example of landscape design Kanna Dam giving an image of castle wall.

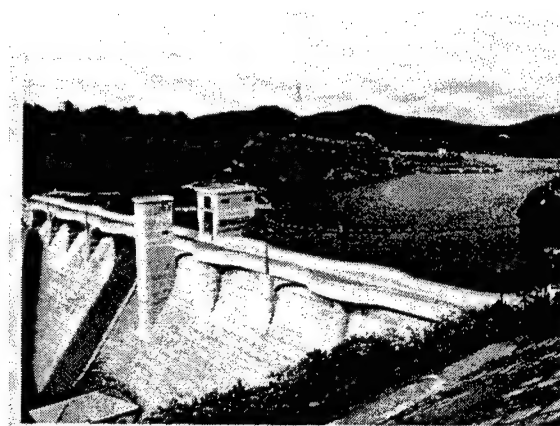


**Figure 24.** Landscape design of dam giving an image of castle wall (Kanna Dam)

### 7.5 Creating the surrounding environment

Looking to harmonize with the natural blessings in the form of the surrounding environment and reservoirs, the establishment of recreational facilities such as parks and playgrounds that act as greenbelts and open space near the water will create an atmosphere of love for water and greenery around dams (see Figure 25, Kamafusa Dam).



**Figure 25.** Colorful flower garden (Kamafusa Dam)

## 8 SUMMARY

In this paper, the latest topics were simply introduced about dam technologies of construction and maintenance/management. Although many

dams have been completed in Japan, flood damage and water shortage damage are still occurring frequently, and dam construction is one of the most effective countermeasures. It is very important both that we tackle for the technical development to secure the safety and to construct economically under the present strict conditions in natural and economical circumstances in Japan, and that we must make efforts to conserve the soundness of natural environment during construction as possible.

## ACKNOWLEDGEMENT

I would like to express my gratitude to the Japan Commission on Large Dams (JCOLD) that readily gives me the permission to quote from their publication "Current Activities on Dam in Japan (2000)" in this paper.



This page intentionally left blank.

## Analyses Using EACD3D96 for Morrow Point Dam

by

Larry K. Nuss<sup>1</sup>, Anil K. Chopra<sup>2</sup>

### ABSTRACT

The goal of any structural analysis of a concrete dam should be to provide a realistic and reliable assessment of the potential of dam failure so safety decisions can be made with confidence. To accomplish this, the dam, reservoir, and foundation should be modeled as realistically as possible. This paper reports the series of studies performed by the Bureau of Reclamation for the dynamic analysis of Morrow Point Dam, a 142-m-high (465-ft-high) thin arch dam in southwestern Colorado (USA) using computer program EACD3D96. Input parameters for EACD3D96 were adjusted to match results from vibration tests on the dam.

### 1 INTRODUCTION

In 2000, Reclamation performed both a traditional structural analysis (with a massless foundation and hydrodynamic interaction using incompressible added masses), and an analysis using EACD3D96 (with mass in the foundation and compressible water). The results were very different. Dynamic stresses computed by EACD3D96 were much lower. EACD3D96 was thought to be the more realistic analysis but additional work was needed to ensure appropriate properties were used. Studies were performed to determine appropriate properties for use in dynamic finite element analyses of Morrow Point Dam, when using EACD3D96. Acceleration response amplitudes measured at Morrow Point Dam from forces induced by eccentric-mass vibration generators attached to the crest by Duron and Hall in 1985 [1] were compared with computed results from EACD3D96. It was shown that by adjusting and

correctly choosing the appropriate material properties and reservoir-bottom reflection coefficient ( $\alpha$ ), and by using compressible water and a reservoir model that followed the topography of the reservoir canyon, the analysis produced very encouraging results that compared to the measured response of the dam to shaker tests reasonably well.

Morrow Point Dam was reanalyzed using EACD3D96 using these properties with the updated ground motions.

### 2 MORROW POINT DAM

Constructed from 1963 to 1968, Morrow Point Dam, located on the Gunnison River in Colorado, is a double-curvature thin arch dam with a structural height of 143 m (468 ft), a crest thickness of 3.7 m (12 ft), and a base thickness of 16 m (52 ft) (see Figure 1). The base of the dam was excavated 21 m (68 ft) below the ground level in the canyon to bedrock. One of the most extensive and comprehensive geologic investigations ever made by Reclamation was undertaken at Morrow Point Dam.

### 3 INITIAL DYNAMIC ANALYSIS

Material properties were obtained for the concrete from core tests conducted 10 years after construction, and for the foundation from jacking tests during construction. Material properties for the concrete and foundation were based on standard laboratory and field tests and accepted scaling factors. The average static modulus of elasticity for the concrete from laboratory tests was 29 650 MPa (4,300,000 lb/in.<sup>2</sup>).

<sup>1</sup> Structural Engineer, Bureau of Reclamation, P.O. Box 25007, Denver, CO 80225, [lnuss@do.usbr.gov](mailto:lnuss@do.usbr.gov) (USA).

<sup>2</sup> Professor, University of California, 721 Davis Hall, Berkeley, CA 94720-1710, [chopra@ce.berkeley.edu](mailto:chopra@ce.berkeley.edu) (USA).

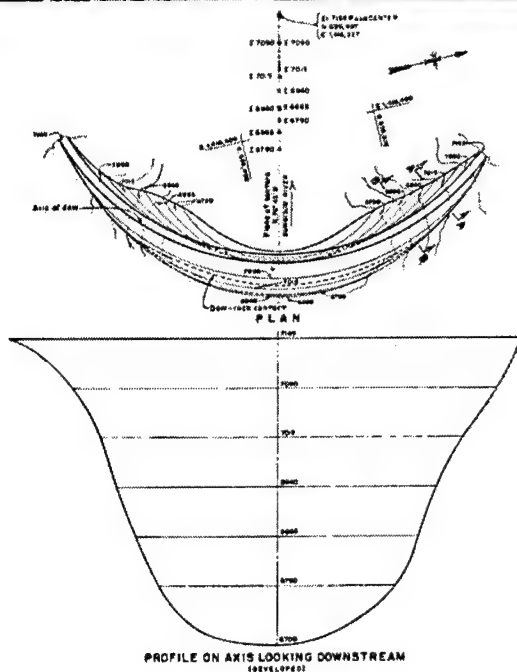
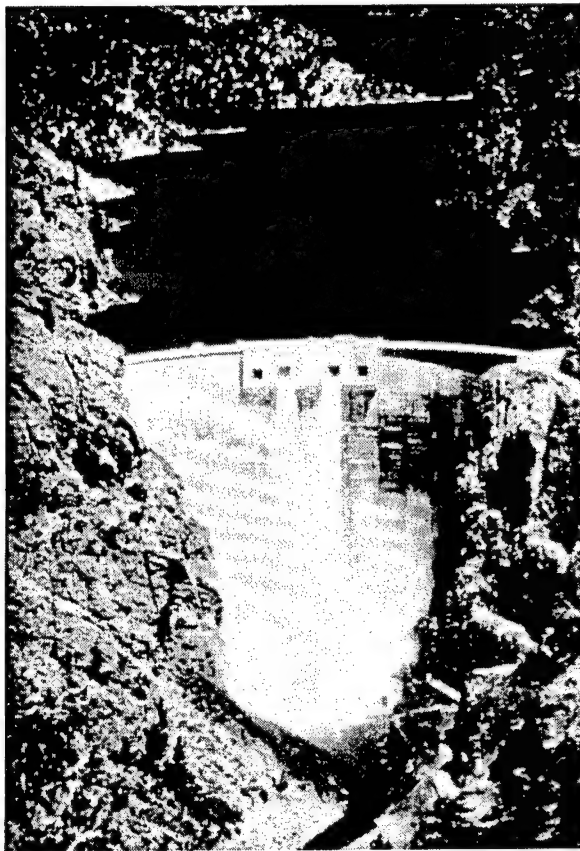


**Figure 1.** Aerial view, plan, and profile of Morrow Point Dam

For use in the analyses, the modulus of elasticity for sustained static loads was factored down to 22 410 MPa (3,250,000 lb/in.<sup>2</sup>) and for dynamic loads was factored up to 44 820 MPa (6,500,000 lb/in.<sup>2</sup>). A foundation deformation modulus of 6 340 MPa (920,000 lb/in.<sup>2</sup>) was determined from pre-construction field jacking tests [8].

For the reservoir-bottom reflection coefficient used in EACD3D96, values measured in 1995 at Morrow Point Dam by Ghanaat were used [2]. The average reservoir-bottom reflection coefficient was 0.45 using reflection surveys and 0.55 using refraction surveys. The reservoir bottom near the dam was 21 m (68 ft) above the base of the dam and rose to 30 m (100 ft) between 60 m (200 ft) and 120 m (400 ft) from the dam. The construction cofferdam was still intact 150 m (500 ft) upstream. There was relatively little silt accumulation near the dam.

Static and dynamic structural analyses of Morrow Point Dam using finite element programs SAPIV and EACD3D96 were made. Ground motions representing the recently postulated site-specific maximum credible earthquakes were used. Linear-elastic analyses using SAPIV, with a massless foundation and hydrodynamic interaction using incompressible added masses, computed maximum stress levels (arch tension of 15 550 kPa (2,255 lb/in.<sup>2</sup>), cantilever tension of 3 980 kPa (577 lb/in.<sup>2</sup>)) indicating a nonlinear response of the dam and stress levels potentially above the dynamic tensile strength of the concrete (5 515 kPa (800 lb/in.<sup>2</sup>)). Linear-elastic analyses using EACD3D96 with the same material properties, but including foundation inertia effects and hydrodynamic interaction with compressible water, computed maximum tensile stress levels (arch tension of 4 140 kPa (601 lb/in.<sup>2</sup>), cantilever tension of (1 820 kPa (264 lb/in.<sup>2</sup>)) within the tensile strength of the concrete. The response of the dam to seismic load was greatly reduced when incorporating additional damping effects in the reservoir and foundation with EACD3D96 [4,7].

EACD3D96 is thought to be the more realistic analysis, but were these large reductions in stress reliable? Could defensible conclusions about the safety of Morrow Point Dam be made by decision makers from these results?

#### 4 EACD3D96

Computer code EACD3D96 from the University of California at Berkeley enables full consideration of dam-foundation rock interaction effects in seismic analyses of arch dams. The numerical modeling of the foundation rock in EACD3D96 is based on a homogeneous rock with constant modulus for the entire unbounded domain. EACD3D96 does not model foundations with variable moduli nor does it explicitly model reservoir-foundation interaction; the latter effect is represented approximately through a reservoir-bottom reflection coefficient. EACD3D96 is an advanced analysis tool for the linear-elastic analysis of arch dams. The EACD3D96 finite element models for Morrow Point Dam, reservoir, and foundation are shown in Figure 2.

#### 5 STUDIES TO DETERMINE APPROPRIATE MATERIAL PROPERTIES WHEN USING EACD3D96

Because the analysis results were so different from the traditional analysis using massless foundation and the EACD3D96 analyses, sensitivity studies were made in 2000 using EACD3D96. These results were compared with vibration generator tests performed on the dam in 1985 by Hall and Duron [6,10]. Measured and computed response amplitudes plotted at the same normalized scale were compared for general trends and amplitudes. This would help explain why the stresses were so much lower in EACD3D96 than in the traditional and would help support or dispute the validity of these results.

Hall and Duron measured the dynamic response of Morrow Point Dam [1]. The tests used two Kinemetrics vibration generators (2 270 kg (5000 lb) force capacity each) placed side by

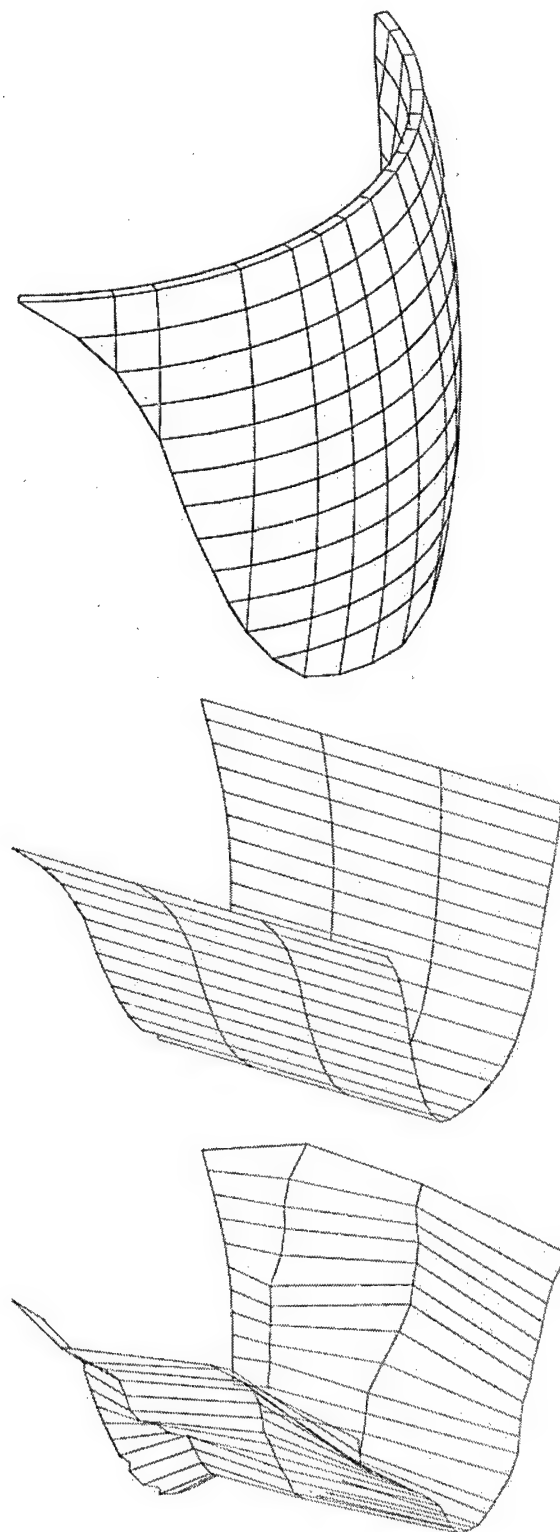


**Figure 2.** A. EACD3D96 dam model, B. Uniform reservoir model (R0), C. Reservoir matching topography (R2)

side on the dam crest at the maximum vertical section (crown cantilever, Block 10). Shaking in the upstream to downstream direction produced the symmetric modes, and shaking in the cross-canyon direction produced antisymmetric response. The reservoir elevation was 3 m (9 ft) below the top of the dam during the tests.

Measured responses obtained by Hall and Duron are shown in Figures 2a through 2c along with computed responses (plotted in frequency in cycles per second verses acceleration per unit shaker force). Only a few representative comparison studies are shown in this paper; the complete set is discussed in more detail in reference [6]. The acceleration being plotted is the radial component at the crown on the crest for a symmetric shake. Calculations verified that water compressibility is indeed important for symmetric response, and also that it is much less important for antisymmetric response.

The following material properties, listed in Table 1, were varied for the EACD3D96 comparison analyses.

- $E_c$  = modulus of elasticity of concrete,
- $d_c$  = density of concrete,
- $H_d$  = hysteretic damping of the dam,
- $E_f$  = modulus of elasticity of foundation rock,
- $d_f$  = density of foundation rock,
- $H_f$  = hysteretic damping of the foundation,
- $\alpha$  = reservoir-bottom reflection coefficient.

The J series of studies used the same material properties as the 2000 analysis. In general for study J1, the acceleration response was greatly lower in amplitude, indicating the computed system response was overly damped compared to the measured response (see Figure 3). Results from this model would be questionable.

After reviewing results from a series of tests [6] it was recommended that the material properties be adjusted so the natural frequency of the dam and foundation system (without reservoir) was computed at about 4.1 Hz. This required a concrete modulus of 34 470 MPa (5,000,000 lb/in.<sup>2</sup>) and a foundation modulus of 24 130 MPa

**Table 1. Material Properties**

Property Used in the EACD3D96 Analyses	Value
<b>- J Series -</b>	
<u>Concrete:</u>	
Modulus ( $E_c$ )	44 820 Mpa (6,500,000 lb/in. <sup>2</sup> )
Hysteretic damping	10 percent
<u>Foundation:</u>	
Modulus ( $E_f$ )	6 340 Mpa (920,000 lb/in. <sup>2</sup> )
Density	2 600 Kg (162 lb)
Hysteretic Damping	5
Reservoir reflection	0.55
<b>- Reservoir Series -</b>	
<u>Concrete:</u>	
Modulus ( $E_c$ )	34 470 Mpa (5,000,000 lb/in. <sup>2</sup> )
Hysteretic damping	3 percent
<u>Foundation:</u>	
Modulus ( $E_f$ )	24 130 Mpa (3,500,000 lb/in. <sup>2</sup> )
Density	2 730 Kg (170 lb)
Hysteretic Damping	3 percent
Reservoir reflection	0.8

(3,500,000 lb/in.<sup>2</sup>). It also appeared 0.8 was an appropriate value for reservoir-bottom reflection coefficient. The shape of the reservoir model was also varied. Initially, the shape of the reservoir model (R0) was the same shape profile as the dam and projected uniformly upstream 600 ft (see Figure 2b). The reservoir model was modified to conform to the shape of the topography (R2) (see Figure 2c). As a result, the acceleration response produced very encouraging results that matched the measured results reasonably well (see Figures 3b and 3c).

It was concluded that the results of EACD3D96 could be reliably used, but care is needed in the selection of input properties. It was shown that by adjusting and correctly choosing the appropriate material properties and reservoir-bottom reflection coefficient (alpha), and by using

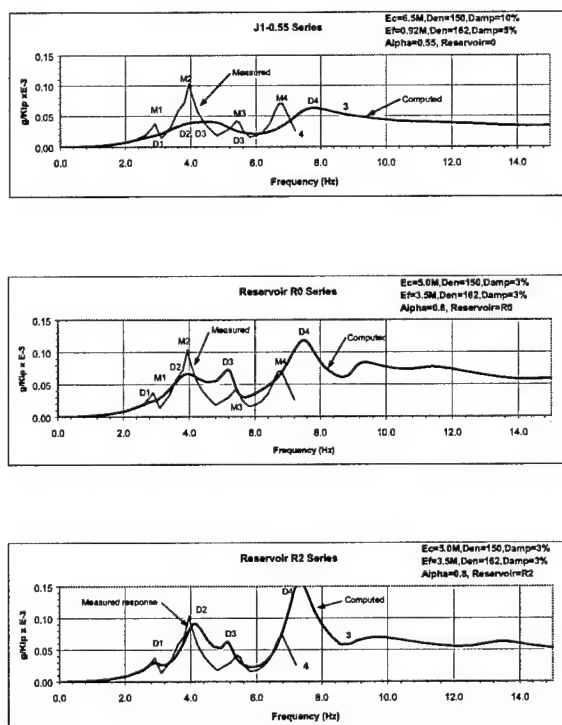


**Figure 3.** Computed and measured acceleration response amplitudes: A. J Series using initial properties, B. R Series with uniform reservoir (R0), C. R Series with reservoir matching topography (R2)

compressible water and a reservoir model that followed the topography of the reservoir canyon, the analysis produced very encouraging results that compared well with the measured response of the dam to shaker tests. Based on what was required to match the measured response, it was concluded that laboratory tests on intact concrete core tend to overestimate effective dam modulus and standard rock mechanics approaches tend to underestimate effective foundation modulus.

Other observations were:

A foundation modulus fairly close to the concrete modulus was used to obtain the good match.

Results were very sensitive to the reservoir-bottom reflection coefficient. Hydrodynamic interaction using compressible water with a large alpha (0.8) matched the acceleration response curve much better than the

incompressible formulation, and better than using measured values of alpha. High values of 0.8 to 1.0 matched the measured response amplitude relatively well below 5.0 Hz, but over-estimated the response amplitude above 5.0 Hz at certain frequencies.

Scaling up the dynamic modulus of concrete, as is typically done in the practice, from static laboratory tested modulus on intact concrete core tends to overestimate the effective dynamic dam modulus. Standard rock mechanics approaches tend to underestimate the effective foundation modulus. Lower concrete modulus, higher foundation modulus, and higher alpha values were needed to produce results from EACD3D96 that matched measured vibration generator test results. It was concluded that the revised properties and geometry would be more appropriate for safety decisions.

## 6 REANALYSIS OF MORROW POINT

Reclamation performed site-specific seismotectonic studies for Morrow Point Dam. Three ground motions were developed from the results a seismic hazard study. The postulated ground motions represented earthquakes with a return period of 1 in 50,000 years:

Representing a magnitude M 6.5 to 6.7 event on the Cimarron Fault:

1. An empirical record (cpe) developed from the Cerro Prieto recording of the M 6.5 Victoria, Mexico earthquake (see Figure 4 for the accel-erograms and the acceleration response spectra at 5 percent damping). The 045-degree component was applied in the upstream to downstream direction, the 315-degree component in the cross-canyon direction, and the UP component in the vertical direction.

2. A synthetic motion (atho) developed using a phase spectra from the Pacoima Dam foundation recording of the 1994 M 6.7 Northridge earthquake. The H2 component was applied in the upstream to downstream direction, the H1

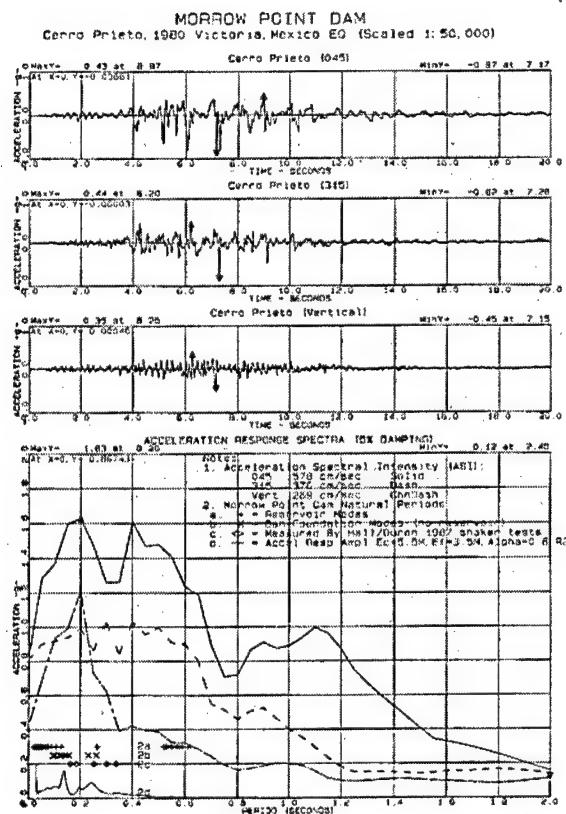


**Figure 4.** Cerro Prieto ground motions and:  
A. Upstream acceleration  
B. Cross-canyon accelerations  
C. Vertical accelerations  
D. Acceleration response spectra at 5 percent damping

component in the cross-canyon direction, and the UP component in the vertical direction.

Representing a magnitude **M** 6.0 to 6.25 background event:

1. An empirical record developed from the Convict Creek recording of the 1980 **M** 6.2 Mammoth Lakes earthquake. The 180-degree component was applied in the upstream to downstream direction, the 90-degree component in the cross-canyon direction, and the UP component in the vertical direction.

Hysteretic (material) damping used during all the EACD3D96 dynamic finite element analyses was 10 percent for the dam and 3 percent for the foundation rock. This represented a viscous

damping of 5 percent for the dam and 1.5 percent for the foundation. Hysteretic damping of 3 percent was measured by Duron and Hall during the vibration tests on the dam. This test was at a relatively low level of shaking. The higher level of damping was felt appropriate for large amplitude vibrations associated with the 1:50,000-year earthquake ground motions used in the analyses.

The first 10 natural frequencies for the dam/foundation system and for the reservoir were computed using EACD3D96 (see Figure 5). The first natural frequency was 3.815 Hz (0.262 sec period) for the dam/foundation system (no reservoir) and 3.775 Hz (0.265 sec period) for the reservoir only. The natural frequencies of the combined dam, foundation, and reservoir system were determined in EACD3D96 by computing the acceleration response amplitude for various frequencies (see Figure 3c).

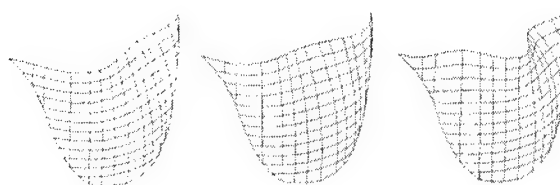


**Figure 5.** First 3 mode shapes of the dam

Contour plots of maximum and minimum arch and cantilever stresses at every location on the upstream face and downstream face of the dam at any time during the earthquake are provided (see Figure 6). The maximum arch tensile stress was 8 980 kPa (1302 lb/in.<sup>2</sup>) on the downstream face. The majority of the downstream face and the upper half of the upstream face showed positive maximum stresses (tension) indicating the relative tendency for the vertical contraction joints to open at some point during the ground motion (since the vertical contraction joints carry no tension). Large swings between tension and compression indicated possible pounding along the contraction joints with potential localized spalling and damaging the concrete around the joints. The maximum cantilever tensile stress was 4 300 kPa (624 lb/in.<sup>2</sup>) on the



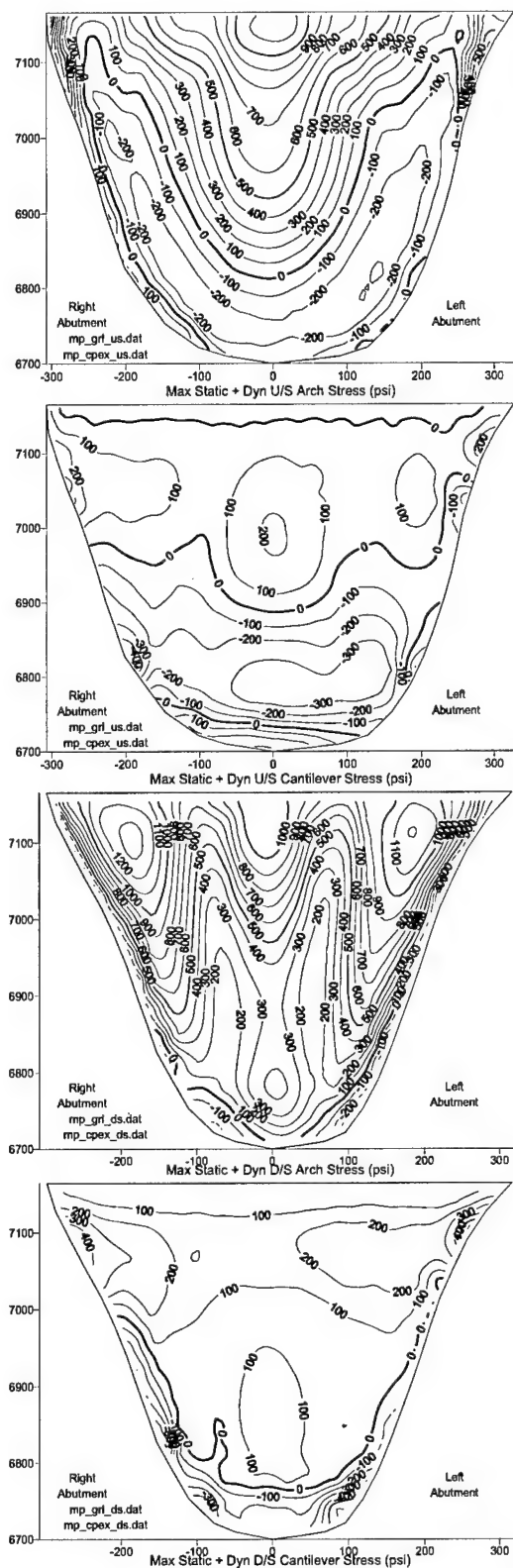


**Figure 6.** Contours of maximum arch and cantilever stresses

downstream face. These stresses were concentrated along the abutments high on the dam. The tensile stress over most of the area of both faces of the dam was below 1 380 kPa (200 lb/in.<sup>2</sup>), which was well below the 5 515 kPa (800 lb/in.<sup>2</sup>) tensile strength of the concrete.

The maximum arch compressive stress was -15 270 kPa (-2215 lb/in.<sup>2</sup>) on the downstream face and the maximum cantilever compressive stress was -8090 kPa (-1174 lb/in.<sup>2</sup>) on the upstream face. These stresses were well below the average compressive concrete strength of 51 570 kPa (7,480 lb/in.<sup>2</sup>) indicating reserve capacity for stress redistribution, if necessary.

The results from a linear-elastic analyses of a monolithic model of the dam, as in the EACD3D96 computer program, can be interpreted to examine behavior of the contraction joints. A tensile stress in the arch direction indicates opening of the vertical contraction joints. When the arch stresses on both faces of the dam were in simultaneous tension, the contraction joint was considered open through the thickness of the dam. The dam was moving upstream enough to unload the arch. Contour plots of the maximum average tension stress through the thickness, the number of excursions when both faces were in tension, the duration of tension when both faces were in tension, and the average static stress are provided in Figures 7a through 7d. In Figure 7a, the maximum average tension plot indicated the arch pulls apart to a very low elevation of about 2 087 m (6850 ft), but with only a couple excursions for less than 0.10 sec. The top of the arch pulls apart 17 times for a duration of 1.40 sec of the 14.40-sec earthquake. As the arch pulls apart, load would be transferred to the cantilevers and increase the cantilever tensile stress.

The maximum radial deflection during the ground motion was 74 mm (2.9 in.) in the upstream direction. The maximum tangential deflection was 17 mm (0.66 in.) toward the left abutment. This relatively small amount of computed deflection would not deform the arch enough to cause instability. Based on the



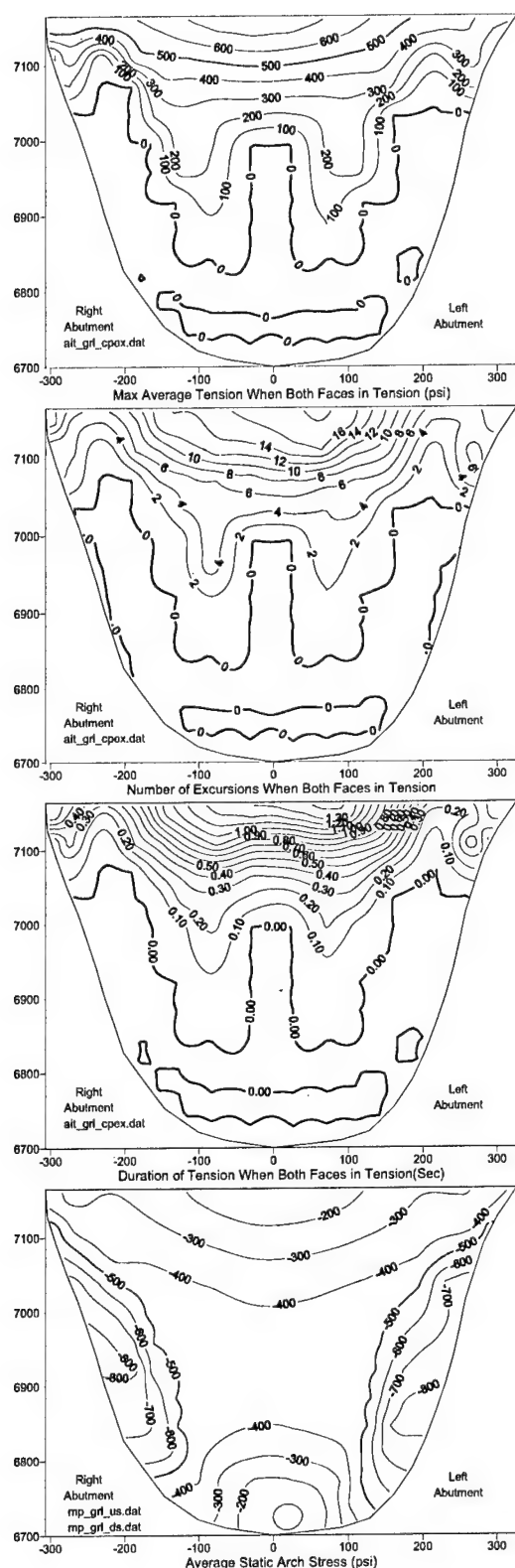


**Figure 7.** Arch-in-tension contours of average arch stress, excursions, duration, and average static arch stress

relatively low cantilever stress level and predicted minimal horizontal cracking or lift line opening, deflections experienced during the earthquake should be mainly elastic and should be largely recoverable back to the original pre-earthquake position.

The maximum radial velocity of the dam along the crown was  $-147$  cm/sec ( $-4.82$  ft/sec) in the downstream direction at the crest. The maximum radial acceleration of the dam along the crown was  $-3.94$  g in the downstream direction at the crest.

## 7 CONCLUSIONS

The following conclusions were derived from this study:

Results from dynamic analyses in this report should be more reliable than previous studies. Using EACD3D96 and correctly choosing the appropriate material properties and reservoir-bottom reflection coefficient ( $\alpha$ ) and by using compressible water and a reservoir model that matched the topography of the reservoir canyon, the analysis produced very encouraging results that matched the measured response of Morrow Point Dam to shaker tests reasonably well.

The three 1:50,000 ground motions analyzed produced about the same magnitude of maximum tensile and compression arch stress.

When using a computer program that incorporates radiation-damping mechanisms, tests to quantify the amount of radiation damping are very helpful.

Computed dynamic arch stresses in EACD3D96 showed large swings from tension to compression would open and close vertical contraction joints. This would probably damage the concrete locally along the contraction joints when the joints close, and redistribute load into the cantilevers when the contraction joints open.

Computed dynamic cantilever tensile stresses in EACD3D96 are well below the tensile strength of the concrete. There should be reserve capacity to carry redistributed load when the vertical contraction joints open.

Scaling up the dynamic modulus of concrete, as is typically done in the practice, from static laboratory tested modulus on intact concrete core tends to overestimate the effective dynamic dam modulus. Standard rock mechanics approaches tend to underestimate the effective foundation modulus.

## 8. FURTHER STUDIES

The amount of stress redistribution due to nonlinear effects from contraction joint opening in the dam is not known. Also, a foundation wedge appears unstable using an uncoupled dam/foundation sliding stability analysis. For these reasons and high estimated risks, additional structural analyses are currently being performed at Lawrence Livermore National Laboratories (LLNL). These analyses incorporate the same properties of the dam, foundation, and reservoir as in EACD3D96 but use an explicit integration of a model that incorporates nonlinear behavior of the vertical contraction joints and the foundation wedge (see Figure 8).

## 9 REFERENCES

- [1] Duron, Z. H. and Hall, J. F., 1988, "Experimental and Finite Element Studies of the Forced Vibration Response of Morrow Point Dam," *Earthquake Engineering and Structural Dynamics*, Vol. 16.
- [2] Ghanaat, Y. and Redpath, B. B., 1995, "Measurements of Reservoir-Bottom Reflection Coefficient at Seven Concrete Dams," Report to the U.S. Army Corps of Engineers and the Bureau of Reclamation.
- [3] Tan, H. and Chopra, A. K., 1995, "Earthquake Analysis and Response of Concrete Arch Dams," *Earthquake Engineering Research*

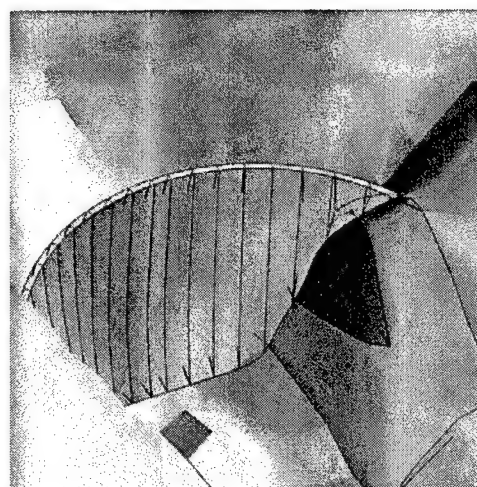
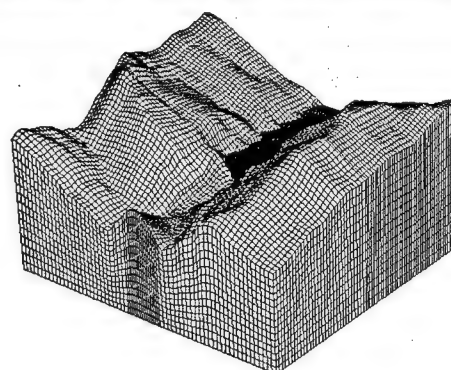
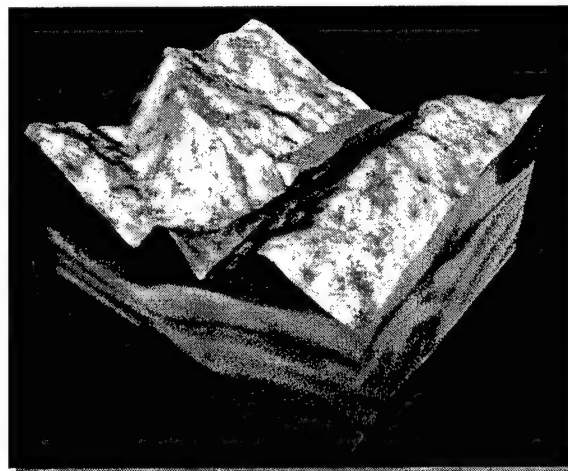


**Figure 8.** Current nonlinear analysis model incorporating vertical contraction joints and foundation wedge. A. Model geometry, B. Finite element model, C. Left abutment wedge

Center, University of California at Berkeley, Report No. UCB/EERC-95/07.

[4] Jackmauh, F. J., 2000, "Analyses Addressing Structural Issues Related to Site-Specific MCE for Morrow Point Dam," Technical Memorandum No. MPR-8110-MDA-2000-1, Bureau of Reclamation, Denver, Colorado.

[5] Bureau of Reclamation, 1983, "Morrow Point Dam and Powerplant, "Technical Record of Design and Construction.

[6] Nuss, L. K., 2001, "Comparison of EACD3D96 Computed Response to Shaker Tests on Morrow Point Dam," Technical Memorandum No. MP-D8110-IE-2001-2, Bureau of Reclamation, Denver, Colorado.

[7] Nuss, L. K., Chopra, A. K., Munoz, R. L., and Jackmauh, F. J., 2000, "Influence of Dam-Foundation Interaction in Seismic Safety Evaluation of Two Arch Dams," Paper 1113,

12<sup>th</sup> World Conference on Earthquake Engineering, Auckland, New Zealand.

[8] Powell, C, 1997, "Morrow Point Dam – Geologic and Geotechnical Issues for Modification Decision Analysis," Technical Memorandum No. MP-8312-1, Bureau of Reclamation, Denver, Colorado.

[9] Tan, H., Chopra, A. K., 1996, "EACD-3D-96: A Computer program for Three-Dimensional Earthquake Analysis of Concrete Dams," Report No. UCB/SEMM-96/06, University of California, Berkeley, California.

[10] Nuss, L. K., Chopra, A. K., and Hall, J. F., "Comparison of Vibration Generator Tests to Analyses Including Dam-Foundation-Reservoir Interaction for Morrow Point Dam," to be presented at the International Commission on Large Dams (ICOLD), Question 83, Response 6, Montreal, Canada, 2003.

## Seismic Hazard Assessment and Post-Construction Evaluation for Olmsted Locks and Dam

by

Jeffrey E. Bayers<sup>1</sup>

### ABSTRACT

The locks structure for the Olmsted Locks & Dam Project was essentially complete in the fall of 2001 and the dam is in final design stages presently with a scheduled award for fall 2002. The Olmsted site is located in an active seismic region with high potential for major earthquakes. The analysis and design at Olmsted has been significantly influenced by the necessity to design for severe earthquake loadings. The design of Olmsted Lock and Dam features in recent years has coincided with a significant evaluation and upgrading of methods, criteria and guidance on earthquake engineering by the U.S. Army Corps of Engineers. The project design and analysis has in many cases served as a model and testing ground for these methodologies and criteria.

**KEYWORDS:** Navigation Locks, Probabilistic Seismic Hazard, Seismic Capacity Evaluation, Tainter Gate Dams, Time History Analyses

### 1 INTRODUCTION

Figure 1 shows an artist's rendering of the completed project. The Olmsted Locks and Dam Project site is situated in close proximity to the New Madrid Fault Zone (NMFZ), and therefore has required a considerable amount of earthquake engineering. The design and analyses process led to time history dynamic analyses of the Olmsted Locks' dual chambered "W-frame" structure and other elements. The analyses encompassed a broad range of parametric soil-structure interaction studies and state of the art application. Additional time history analyses were utilized throughout the construction

process as changes due to Operation Division requests and new probabilistic assessments of earthquake motions were made.

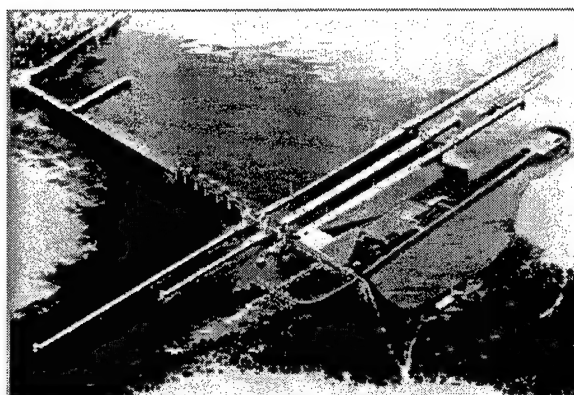


**Figure 1.** Artist rendering of project Olmsted Locks and Dam, Ohio River

The design process for the locks structure included many pseudo-static and response spectra analyses at preliminary stages, but in most cases results were considered to be conservative. At the beginning of the process the guidance described design based on an Operational Basis Earthquake (OBE) and Maximum Credible Earthquake (MCE). With this framework for criteria, it was judged that a more economical structure could be designed if better understanding of the seismic response could be obtained, especially with guidance being developed at the time that reduced load factors based on better definition of ground motions.

When it came time to analyze and design the more seismically susceptible tainter gate dam, and approach wall pylons, it was recognized that using the existing deterministic ground motions (OBE and MCE) defined for the site would yield

<sup>1</sup> U.S. Army Corps of Engineers, Louisville District, Louisville, KY 40202.

at least conservative results. During the same period the U.S. Army Corps of Engineers recognized and accepted probabilistic seismic hazard assessments. Based on new guidance and expert recommendations, the Louisville District designers decided to re-evaluate the seismic input motions based on a probabilistic approach for input on the Olmsted Dam analysis. With the new probabilistically defined OBE and Maximum Design Earthquake (MDE) the design of the Dam was initiated and the Locks structures were revisited.

During this time, the Locks were under construction and only limited (although still significant) benefit was realized with some reductions in quantities of reinforcement in the typical chamber and culvert valve monoliths while maintaining elastic response for OBE loading. Also during construction, a decision to backfill the landward wall of the Lower Miter Gate Monolith (Monolith #26) was made which was shown to be a problem in previous designs and was therefore a critical change. Increasing the backfill height by 50 ft could potentially cause adverse reactions in the foundation piles if an earthquake of high magnitude hit the site. Since this monolith was already constructed, and re-designing it was not an option, it was determined that this new loading condition of higher backfill could undergo evaluation instead of revisiting design. This approach and subsequent methodology along with the probabilistically formulated motions and an assessment of potential damage and serviceability served to yield a confident decision that the structure did not need any additional stabilization to meet the new loading conditions.

The analyses were complicated and challenging, but yielded a better understanding of the structural performance of the Olmsted Structures. The effect of this effort resulted in a more economical design based on reductions in quantities of H-piling and reinforcing steel for the locks and dam during the design process.

## 2 BACKGROUND

The Olmsted Locks and Dam Project will replace existing Locks and Dams 52 and 53 and will be located at Ohio River Mile 964.4, approximately 1.8 miles downstream of Locks and Dam 53 and 15 miles above the mouth of the Ohio River at the confluence with the Mississippi River.

The original Locks and Dam 52 project was completed in 1928. An austere 110-ft-wide by 1,200-ft-long lock was completed during 1969 as a temporary measure to reduce excessive traffic delays. The lock was constructed using sheet pile cellular structures for walls, which were never intended for long-term use. Locks and Dam 53 is very similar to 52. The original project was completed in 1929. A temporary 110-ft-wide by 1,200-ft-long lock of the same construction was completed in 1980. The wicket dams of these projects can be lowered when river flows are sufficient to provide the required navigable depth. This creates a navigable pass for tows and eliminates locking when the water is high enough. The open river condition exists at Locks and Dam 52 about 60 percent of the time and at Locks and Dam 53 about 90 percent of the time.

The Olmsted Project will provide navigation pool back to the Smithland Locks and Dam (River Mile 918.5) replacing Locks and Dams 52 and 53. Subsequent to completion of the new project, Locks and Dams 52 and 53 will be dismantled as necessary to allow safe navigation through the project areas.

The proposed site at Olmsted is situated on the northeastern boundary of the New Madrid Seismic Zone and adjacent to the southern limits of the Wabash Valley Seismic Zone, among others. These two seismic zones have the capability of producing major earthquakes. Further, the Olmsted site has experienced major earthquakes during historic time.

### 3 PROJECT DESCRIPTION

The plans for Olmsted Locks and Dam located at mile 964.4 on the Ohio River consist of two 110-ft-wide by 1,200-ft-long locks adjacent to the Illinois bank, a 1100 ft navigable pass-dam utilizing wicket gates, a six bay tainter gate dam for control, and a 426-ft-long fixed weir extending to the Kentucky bank.

The 110-ft-wide by 1,200-ft-long lock chambers are formed by twenty-six successive W-Frame monolith structures supported by a pile foundation. The entire structure is 1578 ft long and varies in width from 326 to 348 ft. The middle lock wall provides a dual filling and emptying culvert system. An overhead, vertical lift operational bulkhead system and access-bridge spans over the locks. The six bay tainter-gate dam has piers supporting gates of 110 ft width, and the total heights of the piers will be approximately 80 ft above the sill.

The Tainter Gate Piers will be founded, along with the gate sills and navigable pass sills, on 24-in.-diam, circular steel pipe piles at 7- to 14-ft spacing on center. The lock structure is supported by rows of HP 14x117 vertical piles with spacing between centers varying from 5 to 7 ft along the axis of the lock. Across the lock, piles are spaced at centers varying from 5 to 6 ft beneath walls and up to 12 ft beneath the chambers. See Figure 1 for an artist's rendering of the completed project.

### 4 ORIGINAL GROUND MOTION DEVELOPMENT/SELECTION

The Maximum Credible Earthquake (MCE) at the Olmsted site is near field, located approximately 40 to 50 km from the area of maximum micro-earthquake activity and the interpreted source area for a major New Madrid earthquake. The corresponding horizontal motions for mean plus one standard deviation are as follows:

I=MM X, near field, hard site:  
acceleration = 1200 cm/sec\*\*2;  
velocity = 125 cm/sec

duration ( $>0.05g$ ) = 30 sec

The Operating Basis Earthquake (OBE) for the New Madrid Seismic Zone at the Olmsted site was defined as an earthquake that is expected to occur during the life of the structure. This was determined based on the historic record of felt events and from recurrence estimates for the area. The corresponding horizontal motions for mean plus one standard deviation were:

I = MM VIII, near field, hard site:  
acceleration = 820 cm/sec\*\*2  
velocity = 37 cm/sec  
duration ( $>0.05g$ ) = 13 sec

Both the OBE and MCE are expected to occur in the New Madrid seismic zone. The mean values of the peak ground acceleration for the horizontal rock outcrop motion were estimated to be 0.44 g for the OBE and 1.12 g for the MCE. These values were used to derive pseudo-static coefficients and to anchor and develop acceleration time histories of rock motion used in these studies.

### 5 PROBABILISTIC SEISMIC HAZARD ASSESSMENT (PSHA) AT THE OLMSTED SITE

The original OBE and MCE motions that were utilized in studies were generated out of deterministic methodologies defined in U.S. Army Corps guidance of the period. Revised ground motions for the Olmsted project were developed following new Corps guidelines for the earthquake design and evaluation for civil works projects outlined in ER 1110-2-1806 (dated 31 July 1995). These guidelines define the OBE as ground motions that have a 50 percent chance of being exceeded during a 100-yr service life (equivalent to ground motions with a 144-yr return period). The new guidance also allows for the use of a maximum design earthquake (MDE) that may be different than the MCE. The MDE is the maximum level of ground motion for which a structure is designed or evaluated. The associated performance requirement is that the project performs without catastrophic failure,

although severe damage or limited economic loss may be tolerated. For critical features, the MDE shall be the same as the MCE. For other features, the MDE may be selected as a lesser earthquake than the MCE, which provides economic designs meeting appropriate safety standards.

A Probabilistic Seismic Hazard Analysis (PSHA) was conducted to define ground motion levels for a range of return periods in order to select revised ground motion design levels in accordance with guidelines in ER 1110-2-1806. The analysis incorporated recent geologic data concerning the recurrence of large earthquakes in the New Madrid Fault Zone, 30 km southeast of the project site. The analysis explicitly addressed the uncertainties in defining the input parameters for the PSHA in order to provide the best estimate of the hazard given the scientific uncertainty in characterizing the ground motions that they may produce. The basic formulation involves computing the frequency at which a ground motion parameter exceeds a specified level at the site of interest.

The PSHA formulation used attempts to evaluate the likelihood that various levels of seismic loading will affect a structure by using a set of probability models to model the randomness of the physical process of earthquake generation and wave propagation. Four probabilistic distributions are assessed: (1) the frequency of earthquake occurrence, (2) distribution of possible earthquake sizes, given an occurrence, (3) distribution of possible distances from the site to the rupture, given an occurrence of a particular size, and (4) distribution of possible ground motions at the site, given a particular earthquake of a certain size and location. Modeled directly in the analytical framework the scientific uncertainties in characterizing seismic sources and attenuation was modeled using logic trees and alternative attenuation relationships.

The results were used to construct a series of equal-hazard response spectra for a range of return periods. The District engineers selected the equal-hazard response spectrum with a 144-yr return period to be the OBE ground

motion and the equal-hazard response spectrum with a 1,000-yr return period to be the MDE. The resulting peak ground accelerations for base-rock outcrop motions are 0.065 g and 0.37 g, respectively. The PSHA and the equal-hazard response spectra (5 percent damping) were only accomplished for horizontal rock motion. Equal-hazard response curves from various return periods are shown in Figure 2.

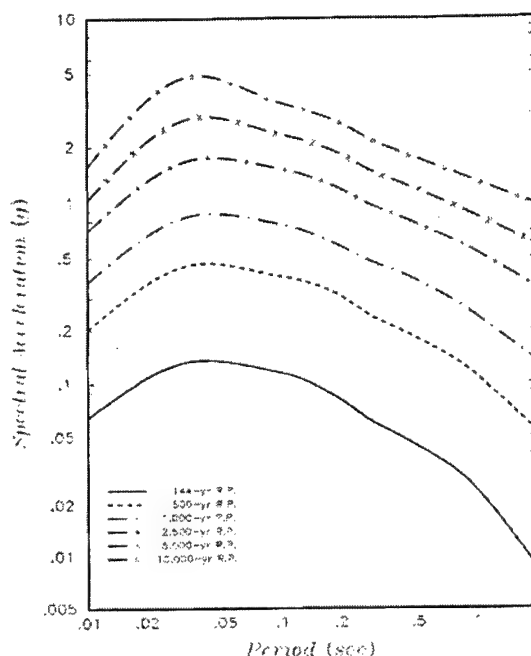


Figure 4-10 Equal-hazard response spectra (5% damping) for base rock conditions

## Figure 2. Equal hazard responses for various return periods

The peak ground accelerations used in the design of the locks structures were originally estimated to be 0.44 g for the OBE and 1.12 g for the MCE. Based on earlier studies the response spectra of the vertical motion were selected to be 70 percent of the corresponding design response spectra for the horizontal motion.

Spectrum compatible time histories were developed for the OBE and MDE conditions. These time histories were used to conduct site response analyses to develop free field ground surface motions for use in seismic analyses of the



various project components. The MDE is shown in Figure 3 plotted against the 1000-yr return spectrum.

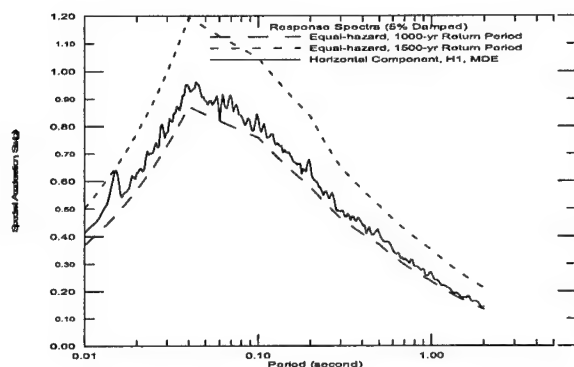


Figure 2-5 Comparison of Response Spectra (5% Damped) of Horizontal Component, H1, with Equal-hazard Spectra, MDE, Olmsted Locks and Dam

**Figure 3.** Horizontal MDE compared to 1000-yr return spectrum

## 6 SEISMIC LOADING CHANGE DURING CONSTRUCTION OF LOCKS

While the PHSA was accomplished primarily for the estimation of motions for the dam structure, the District attempted to maximize its benefit as much as possible. The typical chamber monoliths and the culvert monoliths were completely re-analyzed and significant reductions in reinforcing steel were made in the wall and slab systems. Though in the middle of construction, the new design was expedited and a total of 17 lock monoliths realized reductions in steel reinforcement of up to 15 percent by weight in some walls. While the updated design for as many monoliths as possible was being accomplished, further considerations on operability led to a decision to backfill the downstream, land-side end of the lock where the lower miter-gate monolith rests. This monolith had been designed right up to its limit with respect to pile capacity in the foundation and the OBE and MCE design earthquakes. Raising the backfill 50 ft on the landward side of the structure created a significant unbalanced load, which was predicted to cause trouble with the existing design.

This circumstance was a distinct challenge especially since, at the time, the monolith

construction had been completed. There was no convenient way to improve the foundation at this point without significant costs. There were however two things working in favor of a good solution. The PHSA and new OBE and MDE brought a reduction in peak ground acceleration for design compared to the original design motions (for what is required for elastic response). Also, the Corps had begun to consider "existing structure evaluation" performance criteria on a guidance level. Because there was some precedent on the approach, the District team, decided to pursue an "evaluation" approach for consideration of the performance of the lower miter-gate monolith for the earthquake loading. The combination of the PHSA and evaluation approach provided confidence that a solution could be resolved. A three-dimensional static model representation of the lower miter gate monolith is shown in Figure 4.

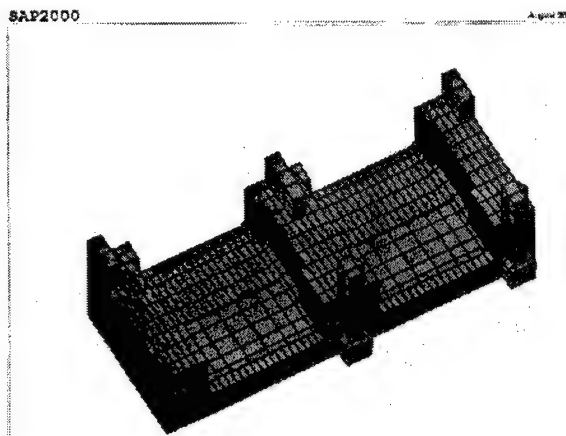


**Figure 4.** Top view of SAP2000 3-D static model of lower miter-gate monolith

## 7 FINITE-ELEMENT MODEL REPRESENTATION OF SOIL-PILE-LOCK STRUCTURE SYSTEM

To evaluate the seismic response of the lower miter-gate monolith (LMGM) lock structure, the lock structure, pile foundation and supporting soil were modeled by plane-strain finite elements. The lock structure and the foundation soil were modeled by two-dimensional solid elements. Each individual pile was modeled by a



series of beam elements. To simulate the rigidity of the connection between the pile head and the base-mat of the lock structure, the pile elements were extended two and one-half feet into the base-mat. To compute conservative values of forces and moments at pile heads, the finite element models incorporate a thin, soft-soil layer (i.e., a 3-in.-thick soil layer) beneath the base of the lock structure (to simulate the conditions that the seismic loads are carried primarily by piles).

For cross-stream section, three different cross-sectional models of the lower miter gate monolith were analyzed in the original studies. Only the first and primary "smeared" model representing the entire monolith including a reduction in mass and stiffness associated with the presence of cross-over culverts in the base slab was used in the new analyses. Energy-transmitting boundaries are specified on the riverside of the model and the outlet bucket structure is included. A displacement boundary condition exists on the landward side of the structure. The upstream-downstream model is similar in set-up and includes additional upstream monoliths to examine relative displacements and phases of motions between monoliths. The cross-stream structural model is shown in Figure 5.

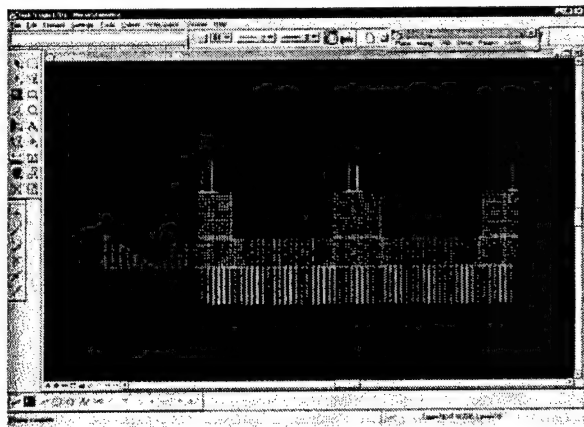


**Figure 5.** Cross-stream structural F.E.M.

## 8 APPROXIMATION FOR HYDRO-DYNAMIC FORCES

Earthquake ground motions generate two types of dynamic fluid pressures in a lock structure—

impulsive and convective. The impulsive pressure represents the effects of that portion of the fluid that moves in unison with the lock; the convective pressure represents the effects of the sloshing action of the fluid. Sloshing effects were considered negligible, but the impulsive, hydrodynamic pressures were derived with the velocity potential method. First, they were converted into nodal lumped masses according to the tributary area associated with each node. Then they were added to the lock wall nodal points as additional masses to account for the hydrodynamic forces during earthquake excitation. For the river wall, the added masses were computed for the inside and outside faces of the wall.

Impulsive pressures are exerted on the lock floor, but the added masses associated with the floor pressures must be considered only in the vertical direction. The original version of FLUSH applies the added mass assigned to a nodal point to both the horizontal and vertical translation degrees of freedom associated with that node. To appropriately apply the added masses to simulate hydrodynamic forces, the FLUSH computer program was modified for use in this study. The revised version of FLUSH allows added masses to be applied to specific degrees of freedom, either the horizontal or vertical translation degrees of freedom or both.

## 9 DYNAMIC ANALYSES OF SOIL-PILE-LOCK STRUCTURE SYSTEMS FOR HORIZONTAL AND VERTICAL EXCITATION OF OBE AND MDE

Dynamic, soil-pile-lock structure interaction (SSI) analyses conducted in this study were performed by using the computer code FLUSH. To perform the SSI analyses using FLUSH, the input motion along the bottom boundary of the model had to be specified. The motions used in the analyses were developed by conducting one-dimensional ground response analyses using the computer code SHAKE for a free-field soil column on the riverside. In these analyses, the time histories of the rock motion selected to represent the OBE and MDE described earlier were

prescribed at the rock outcrop. In both the SHAKE and FLUSH analyses, the nonlinear soil behavior (i.e., strain-dependent shear modulus and damping) was approximated by the equivalent linear method; an iterative procedure was used to obtain strain-compatible shear modulus and damping for each soil layer or element. The SSI analyses were performed separately for the horizontal and vertical excitations. The dynamic force and displacement responses from the horizontal and vertical excitations were combined in time domain to obtain the resultant total responses. In combining the responses from the horizontal and vertical excitations, possibilities of reversing the direction of excitation were considered.

## 10 PILE HEAD FORCES AND MOMENTS

Time histories of pile head forces and pile interaction values were computed from analyses of the horizontal and vertical excitations. They were combined in time domain considering possibilities of reversing the direction of excitation. Since there were two horizontal components and one vertical (to consider three dimensional effects), this amounted to eight combinations of the three components. Values of forces and moments were converted from the plane strain model to values for individual piles. Figure 6 show maximum total interaction values for individual piles at a particular cross-section for

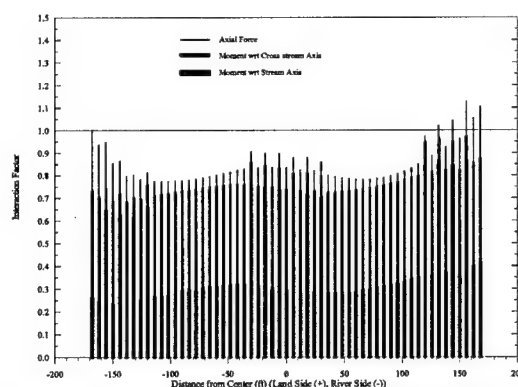


Figure 5-59 Combined Static and Dynamic Interaction Factors for H-Piles under Lower Miter Gate Mouth Subjected to MDE: Expected Yield Case; Distance to Downstream Face = 131.74 ft

**Figure 6.** Maximum pile interaction values throughout duration of time history for the expected yield condition

the entire duration of the earthquake event. These interaction values are not seen by the structure simultaneously.

As was expected, even with the new MDE input, the demand capacity ratios for the piles were high relative to criteria for design. A factor of safety of 1.15 on combined stress in the steel H-piles in the foundation was used in the original design. Interaction values plotted in time for every pile and for every force direction combination showed many excursions to be beyond the allowable design limits in the new analysis for forces in individual piles and in numerous piles at the same time increment. Unfortunately, the monolith was already constructed and options were very limited. Nonlinear analyses were considered as an approach to be used, but the technical requirements, expense and time constraints gave rise to the decision to examine other alternatives for solving the problem.

Since the monolith was already constructed and there were not many options for construction alternatives, the monolith would be evaluated as an existing structure. An assessment of the material strength of the H-piles as fabricated was judged to be the best way to gain some capacity out of the system. Records were reviewed that included the heat number and tested yield stresses of steel H-piling delivered to the job site. A statistical analysis was accomplished on the data and it was determined that the mean yield strength less one standard deviation was 41 kips/in.<sup>2</sup>. With this information the foundation piling was evaluated. Three computations for stress interaction were made. One was based on the extreme allowable condition which included a factor of safety equal to 1.15 based on 36 kips/in.<sup>2</sup> steel. The second, called minimum yield was based on the 36 kips/in.<sup>2</sup> steel with no factor of safety, and the third, named expected yield was based on the statistically determined 41 kips/in.<sup>2</sup> strength.

By examining (1) numbers and percentages of piles over the applicable interaction value limit at individual time steps, (2) the number of times an individual pile went over the limit, and (3) by assessing the duration of those

excursions, evaluation of the piled foundation was made. Noting that significant reductions in these excursions and durations were made using the higher pile strength of 41 kips/in.<sup>2</sup>, and recognizing the integrity of the concrete was not breached, the pile foundation was considered to be sufficient for the MDE condition without further stabilizing of the structure. Examples of interaction value time histories are shown in Figure 7 for the extreme allowable condition. The results indicated that for the extreme allowable case, 91 percent of the piles at different time steps had a demand capacity ratio greater than unity, while 35 percent had values greater than 1.1 and 13 percent were greater than 1.2. For the minimum yield case 69 percent were over unity while 20 percent and 9 percent were over 1.1 and 1.2, respectively. In the expected yield case, only seven percent of the piles experienced interaction values over unity.

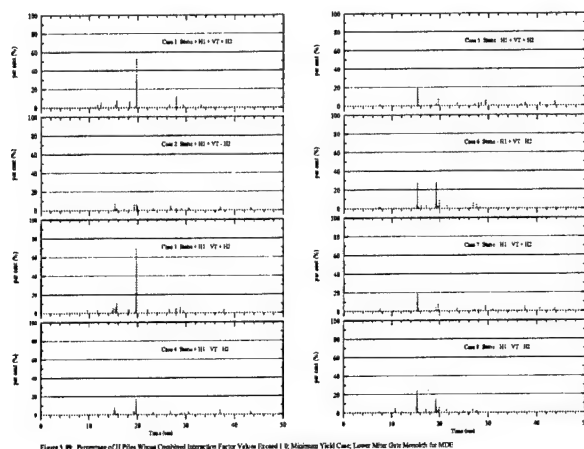


**Figure 7.** Pile interaction time histories for 8 combinations of 3-D E.Q. components for extreme allowable condition

Examples of interaction value time histories are shown in Figure 8 for the expected yield-condition.

Because the actual yield strength of the steel used for the piles installed for the locks is higher than the minimum yield strength required, either the ductility ratio slightly higher than one can be acceptable or use of the yield strength higher than 36 kips/in.<sup>2</sup> is reasonable. In addition, it

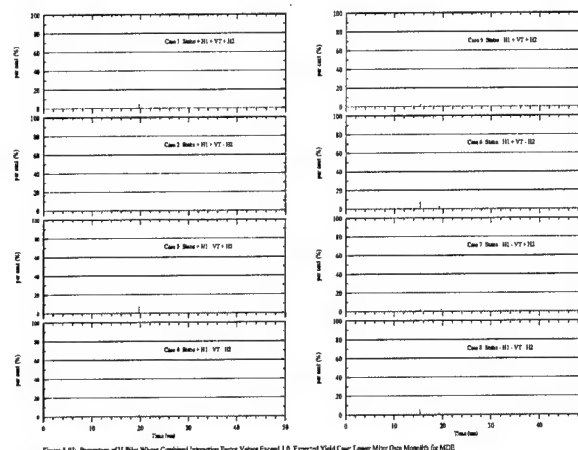


**Figure 8.** Pile interaction time histories for 8 combinations of 3-D E.Q. components for expected yield condition

was determined that if some of the piles yield during the MDE excitation, the period of the soil-pile-lock system will lengthen and result in lower demand because the free-field response spectral values decrease with an increase in period beyond the fundamental periods of the system. It is estimated that no more than 20 percent of piles would actually yield and no significant damage would be realized under the MDE loading condition due the integrity of the concrete at these loadings, ductility of the piles, pile rebound, and force redistribution with any nonlinear behavior.

## 11 REINFORCED CONCRETE SECTION FORCES AND MOMENTS

Dynamic section forces and moments were computed for selected sections on the lock structure. These values were computed from element stresses along each selected section. Dynamic element stresses were computed separately for the horizontal and vertical excitations and combined in time domain. The dynamic forces and moments were then obtained from the combined dynamic stresses and combined with static forces and moments to obtain the resulting combined static and dynamic values.

Concrete interaction diagrams were generated with scatter plots of interaction values in time for each concrete section as shown in Figure 9. These plots were generated for all eight combinations of earthquake components and in all cases show the concrete sections to be effective in resisting the effects of the earthquake motions analyzed. The integrity of the cross sections was one factor in concluding that the structure would redistribute forces stemming from any nonlinear behavior of individual piles.

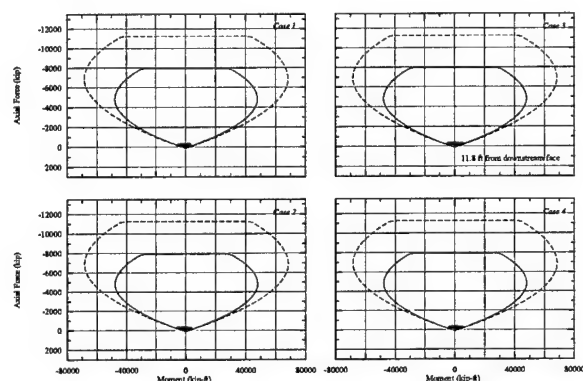


Figure 9-95: Axial Force vs. Bending Moment of Concrete Section 1 due to Combined Static, Horizontal III and Vertical Excitation for MDE, Olmsted Lower Miter Gate Monolith - Cross-Stream Model

**Figure 9.** Concrete interaction time history scatter plots for various combinations of 3-D earthquake components

## 12 RELATIVE DISPLACEMENTS

Displacements at pile heads and pile tips for selected piles and at selected nodal points on the lock base and on top of the lock walls were computed from the dynamic analyses of the soil-pile-lock structure systems. As described previously, analyses were made for the horizontal and vertical excitations separately. Acceleration time histories at selected nodal points were then combined in time domain to obtain the combined acceleration due to both horizontal and vertical excitations from which displacement time histories were obtained by double integration. Possibilities of reversing the direction of excitation were also considered. Relative displacements between two selected nodal points (between pile heads and pile tips, and between top of lock walls and lock base) were then computed. For the "smeared" lower miter gate monolith (Model 1), relative displacements were

computed between pile heads and pile tips, and between the top of the lock walls and the lock base.

## 13 CONCLUSION

The objectives of these studies included (1) selecting or developing time histories of input rock motions for the operating basis earthquake (OBE) and the maximum design earthquake (MDE); and (2) to conduct a series of dynamic analyses of the soil-pile-lock structure system. This work was accomplished to effectively yet efficiently design the locks and dam structures and foundations at Olmsted for the OBE and MDE.

Earthquake magnitude generated from deterministic assessments in original project work resulted in peak horizontal ground accelerations for the OBE and MCE. They were defined as having a magnitude M6 and as producing near-field motions within a distance of about 25 km for the OBE, and defined as an earthquake having a magnitude M8+ and occurring approximately 45 km from the site for the MCE. The mean values of the peak ground acceleration for the horizontal rock outcrop motion was estimated to be 0.44 g for the OBE and 1.12 g for the MCE.

A Probabilistic Seismic Hazard analysis was accomplished in preparation of the dam design and was utilized on the locks to the degree possible during construction. Designers selected the equal-hazard response spectrum with a 144-yr return period to be the OBE ground motion and the equal-hazard response spectrum with a 1,000-yr return period to be the MDE. The resulting peak ground accelerations for base-rock outcrop motions are 0.065 g and 0.37 g, respectively.

Dynamic soil-structure interaction (SSI) analyses were performed using the computer code FLUSH. The soil-pile-lock system was modeled using finite element plane-strain model. Based on the results from the SSI analyses, dynamic pile forces and moments and structural section

forces and moments were combined with the forces and moments under static loads. In addition, relative displacements between selected locations on the lock structure and between the pile heads and pile tips were computed. Interaction time histories were generated for evaluation of criteria.

While the work was being done to maximize design efficiency and understanding for the dam and portions of the lock that were not yet complete, a request by District Operations staff gave rise to the necessity to evaluate one of the existing structures – monolith 26, the lower miter-gate monolith. Evaluation methodology and criteria based on what was done here, and further enhanced for guidance purposes, will be available in U.S. Army Corps of Engineers guidance document EM-2-1110-6051, Time History Analysis of Hydraulic Structures, once published. Investigation of the actual tested strengths of the delivered foundation piling resulted in an assessment that the foundation piles had more capacity than they were actually designed for. By taking this into account and assessing time history results for pile force excursions, extent, and duration it was concluded that the structure had enough residual capacity that further improvements would not be necessary for what amounted to a significant additional load.

Use of these tools and methods in obtaining a more refined analysis and achieving a better understanding of the structural performance has allowed the designers to confidently improve the efficiency of the design for the structures. The PHSA and subsequent time history analyses and post construction evaluation methodology have been successful in improving understanding of the structural performance and of saving costs in construction.

## REFERENCES

U.S. Army Corps of Engineers, Geomatrix Consulting Engineers, Final Report – Probabilistic Seismic Hazard Assessment Olmsted Locks and Dam Site, October 1996.

U.S. Army Corps of Engineers, Geomatrix Consulting Engineers, Final Report – Volumes I & II, Seismic Analysis and Evaluation of Lower Miter Gate Monolith, M26 Olmsted Locks and Dam, January 1999.

U.S. Army Corps of Engineers, Quest Structures, Final Report – Three Dimensional Static Analysis of Lower Miter Gate Monolith, M26 Olmsted Locks and Dam, December, 1998.

## Seismic Adequacy of the Gatun Spillway at the Panama Canal

by

Antonio A. Abrego Maloff<sup>1</sup>, Maximiliano De Puy<sup>1</sup>

### ABSTRACT

The Panama Canal is a lock-type canal, approximately 80 km long that unites the Atlantic and Pacific Oceans. The Canal's three sets of locks serve as water lifts, which elevate ships 26 m above sea level to the Gatun Lake. The Gatun concrete spillway, which was constructed between 1908 and 1913, is an integral part of the Gatun Dam System, and together they retain the water of the Chagres, Trinidad, and Gatun Rivers to form the Gatun Lake, which regulates all the water needed for Canal operations.

Recent studies have revealed that the cities of Panama and Colon are located in areas of higher seismic activity than previously assumed. Consequently, this increased concern about the seismicity of the region motivated the Panama Canal Authority to initiate an extensive program to evaluate the seismic risk and the stability of vital structures along the Panama Canal.

The present study summarizes all the stability analyses performed on the Gatun concrete spillway, which were performed using a simplified procedure for the monolith section, and a finite element procedure for the analysis of the piers. The simplified procedure used in this report yields lateral forces associated with the fundamental vibration mode of the gated monoliths, which are estimated directly from a smoothed design spectrum.

In 1996 a seismic hazard analysis in the Gatun area was initiated to identify ground motions at the dam site. Deterministic approaches were implemented to estimate the Maximum Design Earthquake (MDE), which, due to the importance of the structure, was set equal to the maximum credible earthquake (MCE).

The procedure implemented in this report is considered to be a model for the seismic evaluation of all the other existing concrete dams in the Panama Canal.

**KEYWORDS:** Attenuation Relationships, Ground Motions, Monolith, Overturning, Peak Ground Acceleration (PGA), Piers, Response Spectrum, Simplified Procedure, Sliding

### 1 INTRODUCTION

The need to verify the seismic adequacy of most structures along the Panama Canal, has led the Panama Canal Authority to perform evaluations of the seismic stability of major structures within the Panama Canal Basin including the Gatun Spillway, work which is summarized in this paper. The objective of this study is to assess the possibility of seismically induced failures of the whole or a part of the spillway during an earthquake.

The analysis performed to the concrete spillway was divided in two sections: a simplified analysis of the dam monoliths, and a finite element procedure for the piers of the structure. The first analysis was performed using a simplified procedure developed by Chopra and Tan (1989) for gated spillway monoliths of concrete gravity dams. The second set of analyses was aimed at obtaining the response of the piers when they are subjected to ground motion acting in the cross-stream direction and were implemented through a finite element (FE) procedure using the FE software SAP 2000.

Although recent seismicity in Panama is concentrated on the borders with Costa Rica and Colombia there is evidence for consideration of

<sup>1</sup> Geotechnical Branch, Engineering Division, Panama Canal Authority, Republic of Panama.



seismicity closer to the Canal based on a significant historical earthquake in 1882 offshore, northeast of Gatun (Figure 1), with an 8.0 estimated magnitude (Mendoza and Nishenko, 1989). The Panama Canal Authority contracted the United States Geological Survey (Schweig et al., 1999) to perform a seismic hazard evaluation of the Gatun area. In addition, a comprehensive site investigation was carried out to determine the geotechnical characteristics of the Gatun Dam (earth dam and spillway).

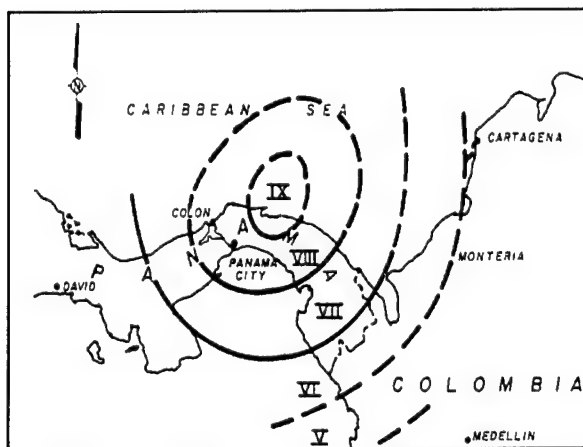


**Figure 1.** Intensity map for the 1882 San Blas Earthquake

Finally, the structure was also evaluated to verify its stability against overturning and sliding along a failure plane. Several loading conditions were selected for the analysis considering the variation of the lake and the operating conditions of the spillway. The different factors of safety obtained through this analysis were compared to the safety provisions provided by USACE (1997).

## 2 PROJECT DESCRIPTION

The Gatun Dam system was built in 1913 and is composed of a concrete gated spillway, an earth dam, and a powerhouse (Figure 2). The system is located in the north side of the Panama Canal and it retains the water of the Chagres, the Trinidad, and the Gatun Rivers to form the

Gatun Lake. The dam has an elevation of approximately 32.00 m (105 ft) above the sea level, and its total length is approximately 2,500 m (8,200 ft). The slopes of the earth dam are very flat, varying from 1:8 at the upstream face to 1:16 at the downstream face. About midway along the length of Gatun Dam system there was a rocky hill outcropping, which provided a suitable foundation for the Spillway (Figure 3). For the construction of the spillway, a cut was made through the outcropping hill. Concrete floor and sidewalls were first poured except at the location where low piers were built in the channel to key the dam to the bedrock (Figure 4). Second, the piers were used as supports for stop-planks or cofferdams, which were required to shut off the water and permit the placing of concrete (Figure 5). These sections had to be completed before the Chagres was forced into this channel, because after that it would have been necessary to reckon with the river before completing the work (Figure 6). Since the pier sections were raised before the ogee, all of the concrete for the piers, except in the extreme southern ends, was imbedded in the dam. The concrete in the ogee below was dumped from cars into chutes, and placed by gravity.



**Figure 2.** Gatun Dam and Spillway

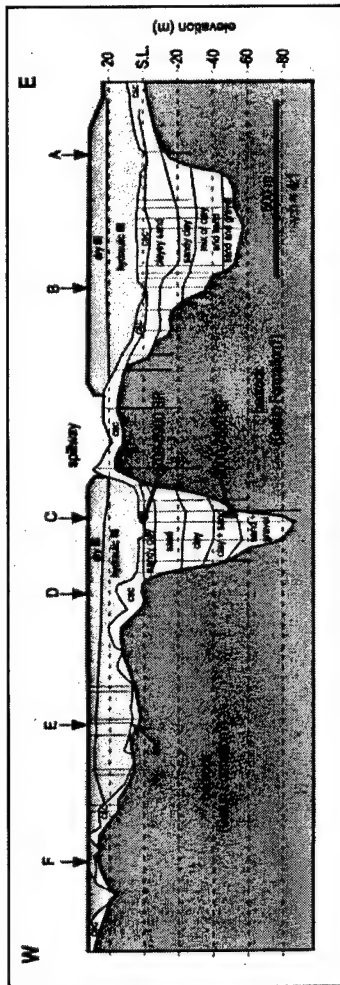


**Figure 3.** Gatun Dam longitudinal section (Pratt, 1999)

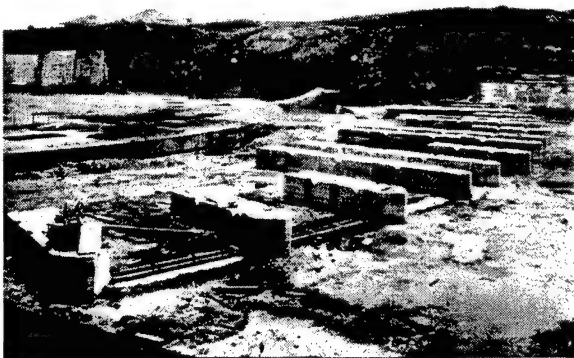


**Figure 4.** Picture from construction era showing the piers keyed to the foundation rock

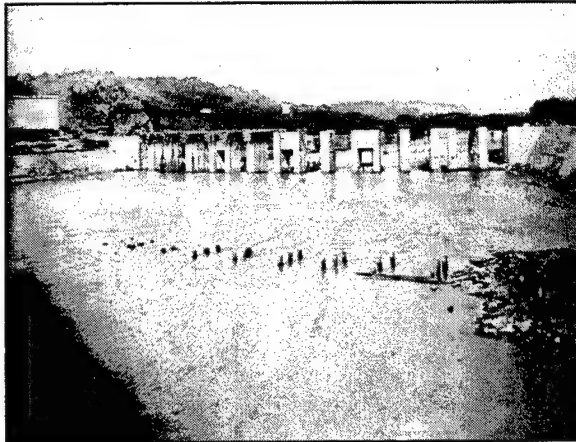


**Figure 5.** Picture from construction era showing the piers as they are raised

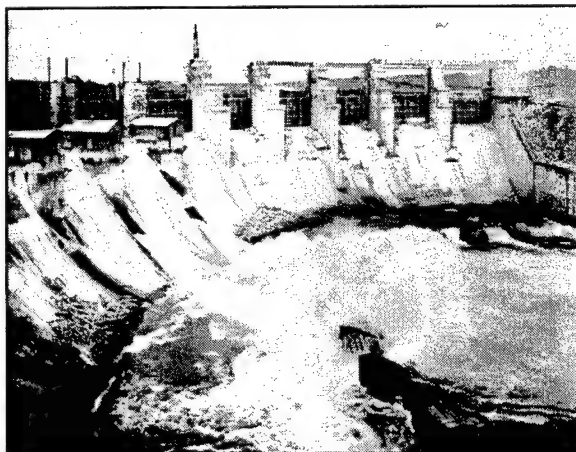


**Figure 6.** Picture from construction era showing downstream face of the spillway

The concrete spillway is an 18.60 m (61 ft) high (no piers included) gated concrete gravity dam with a horseshoe shape (Figure 7). The spillway consists of three sections: an ogee section, piers built at the top of the ogee section to hold the steel gates (Stoney Gates), and a discharge channel, which varies in thickness from 1.20 m (4 ft) at the upper end to 0.30 m (1 ft) at the lower end. However, below the ogee, where great water disturbance was expected, the thickness of the slab was increased to 3.70 m (12 ft).



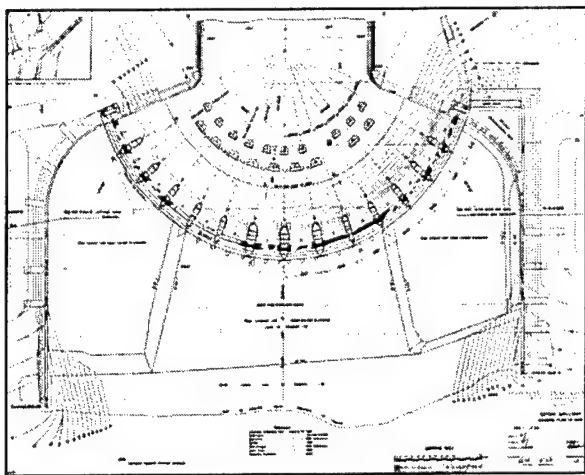


**Figure 7.** Gatun Spillway plan view

The crest of the spillway is divided into openings or bays by piers, which extend above the crest high enough to permit the stoney gates to be raised clear of the water and to allow the safe passage of drift. Each stoney gate weighs about 38.50 metric tons and are essentially steel frames, consisting of two end posts, four horizontal main girders, and three vertical cross girders with intercostals and braces. Their dimensions are approximately 13.70 m (45 ft) wide, 6.70 m (22 ft) height and 100 mm to 150 mm thick. At the back of the gates (facing the lake) the frame is covered with watertight steel plates, butt-jointed with calked cover plates. Inside the spillway (ogee) there is a machinery tunnel extending throughout its length and beyond it. This tunnel gives access to the mechanism controlling the gates.

### 3 DESIGN GROUND MOTIONS

The seismic evaluation of the Gatun spillway required the identification of appropriate design earthquakes. Since 1992, several works were carried out to elucidate the seismic hazard of the Gatun Dam area (Vergara, 1992; Schweig et al., 1999; Joyner, 1999; and Cowan, 2001) and hence obtain a predictive model for ground motions. Firstly, a deterministic approach was selected to develop the design ground motion. Three possible earthquake sources were identified (from these studies) that could affect the

Gatun Dam site (Figure 8): (1) the North Panama Deformed Belt (NPDB); (2) the Rio Gatun Fault; and (3) Caribbean Coast Faults near Gatun Dam. It was concluded that ground motions associated with the North Panama Deformed Belt be used in our seismic evaluation of the Gatun Spillway, as this is the most critical source. This was also discussed and agreed at the 8<sup>th</sup> Meeting of the Geotechnical Advisory Board (Duncan et al., 1998).

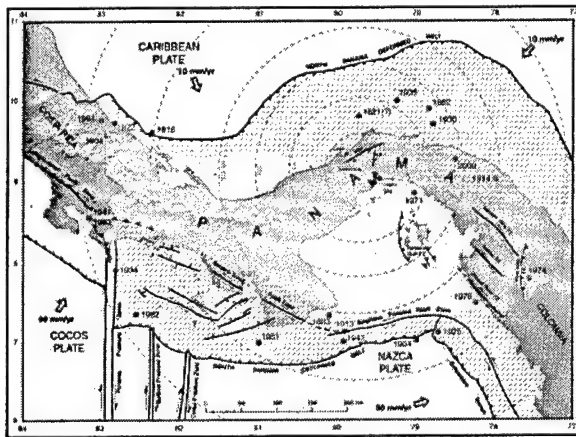


**Figure 8.** Map of Possible Earthquake Sources (Cowan, 2001)

The North Panama Deformed Belt (NPDB) is a large submarine fold-thrust belt, or an accretionary wedge that bounds the northern margin of Panama, the northeast coast of Costa Rica and extends into the Gulf of Uraba in western Colombia. It is considered the zone of convergence between the Caribbean Plate and the Panama microplate (block). Although, the NPDB is not a typical subduction zone, it should be considered as such for the purpose of choosing ground motions. Schweig et al., 1999 proposed that this source could potentially produce a shallow dipping thrust earthquake of moment magnitude M 7.7 at a distance of 35 km from the site. This is deeper than a crustal earthquake that typically occurs in the upper 20 km of the over-riding crust.

Secondly, Joyner (1999) recommended the use of an attenuation relationship based on data obtained from the 1985 Chile Earthquake, which was originated in a subduction zone and has

conditions somehow similar to the NPDB (soil type, moment magnitude and site-to-source distance). This relationship yields median and 84<sup>th</sup> percentile values of peak ground acceleration of 0.313 g and 0.544 g, respectively at a distance of 35 km, on rock for rupture propagation toward the site. Considering the Gatun Spillway an essential and critical facility for the Panama Canal, it was decided to adopt only the 84<sup>th</sup> percentile value of peak ground acceleration (mean + 1 standard deviation) as the dominating parameter for the analysis; therefore, that value was assumed as the Maximum Design Earthquake (MDE), which, in the case of Gatun spillway was set equal to the maximum credible earthquake (MCE).

Several records from the 1985 Chile earthquake data were then scaled to the 84<sup>th</sup> percentile of the design peak ground acceleration and used as input in our evaluation. Furthermore, data from the 1991 Limon Earthquake (Costa Rica), which was triggered on the NPDB, was also included in the analysis. In this case, the scaling procedure was applied to the ground motion record from Siquirres station.

These individual records, however, are site-dependent and the jaggedness in their response varies from one event to another even if they were recorded at the same site. Consequently, the peaks and valleys from the records are not necessarily at the same period and it is not possible to predict the jagged response spectrum in all its details for a ground motion that may occur in the same site. In this case, the appropriate procedure is to design a smooth response spectrum, which is a statistical combination of many earthquakes recorded at the site.

Considering the limitations of individual records and the variation of what type of earthquake motion to be considered, several ground motions' spectral acceleration relationships were used for comparison:

a. For shallow crustal earthquake, the relationship developed by Abrahamsson et al. (1997) was used.

b. For intermediate depth subducting events with specification of an interface (intermediate depth) earthquake, we included the relationship developed by Youngs et al. (1997).

c. For combined deep and shallow events for sources in Central America, the relationship developed by Climent et al. (1994) was also considered.

d. For subduction zones using earthquakes with moment magnitude greater than 7.7 in the distance range of interest, we selected the relationship modified by Joyner (1999).

Figure 9 summarizes the response spectra of all these attenuation relationships, including the response spectra of two individual records (1985 Chile Earthquake represented by the Pichilemu record and 1991 Limon earthquake represented by the deconvoluted Siquirres record). As seen in this figure, the response spectrum for the Joyner attenuation relationships has been constructed using the Newmark and Hall procedure (USACE, 1999) for a PGA of 0.544 g (mean + 1 standard deviation), since no coefficients for the attenuation relationship were available at the time this work was elaborated.

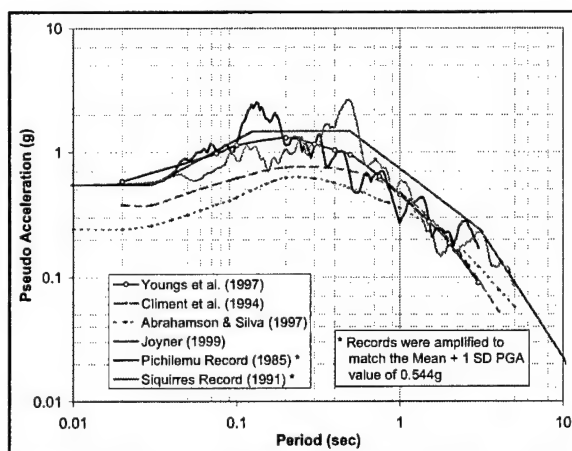


Figure 9. Response Spectrum for  $\xi = 5$  percent

Considering that the intermediate depth source is the controlling source and that the selected

accelerograms are representative of this source, the relationship by Youngs et al. (1997) provides a suitable envelope of the entire spectral ordinates of both the Pichilemu and Siquirres record. The relationship modified by Joyner also considers the maximum accelerations bracketed by the range of attenuation relationships.

#### 4 FIELD INVESTIGATION

As part of the Gatun Dam studies, a comprehensive site investigation, which included field and laboratory testing, was carried out from 1994 to 1997 (this work was summarized by Franceschi, 2001). The main objective of these investigations was to evaluate the geotechnical conditions of the earth dams (not included in this paper) and concrete structures.

First, a series of geophysical tests were performed in the earth embankments and their foundations. A second testing program was oriented to obtain the concrete properties of the spillway monolith.

##### 4.1 Geophysical tests

The geophysical investigations were originally conducted as part of the seismic stability evaluation of the Gatun Earth Dam. However, since the analysis presented in this paper takes into consideration the dam-foundation rock interaction, several soil parameters should be considered and determined beforehand. One of the most important soil parameters to be estimated is the Young's modulus of elasticity of the foundation rock ( $E_f$ ). This value should be determined from a site investigation and appropriate testing according to Chopra and Tan (1989).

During 1995 and 1996 a team from the Waterways Experiment Station (WES) conducted several field tests in the vicinity of the concrete spillway (Yule, 1996 and Olsen & Yule, 1997). They performed cone penetration tests (CPT) and shear wave velocity tests. This geophysical seismic test program consisted of crosshole and downhole seismic boreholes tests. The holes

were extended 7.60 m (25 ft) into rock, but did not exceed 92.0 m (300 ft) in depth, due to limitations of the test equipment.

Direct determination of the shear modulus ( $G'$ ) is difficult; therefore this material property was derived accurately from direct measurements of in situ shear wave velocities ( $V_s$ ). The  $G'$  is dependent of strain levels, and since the seismic velocities measurements from these in situ tests are small strain based, the calculated modulus is a maximum shear modulus,  $G'_{\max}$ .

The shear wave velocity is first related to the dynamic elastic constants of the soil according to the Theory of Elasticity as:

$$G'_{\max} = \rho V_s^2$$

where,

$$\begin{aligned} V_s &= \text{shear wave velocity} \\ \Delta &= \text{mass density} \end{aligned}$$

Then, the relationship between the shear modulus  $G'_{\max}$  and stress-strain modulus  $E_s$  is the same as for static conditions and is given by the following relationship:

$$E_s = 2(1 + \mu) G'_{\max}$$

Where,  $\mu$  is Poisson's ratio (assumed to have a value of 0.2 for the rock type present at the site).

Figure 10 shows the locations of the borings along the Gatun Dam where the shear wave velocities were taken, and Table 1 provides the resulting shear modulus and elasticity modulus respectively. It is important to note that the shear wave velocities at section C are significantly lower than those at other sections. It is believed that these lower values were influenced by the presence of highly weathered rock. However, when implementing the simplified procedure of analysis described in section 5, the response of the structure is not notably affected by considering these low values in the calculation of the modulus of elasticity.

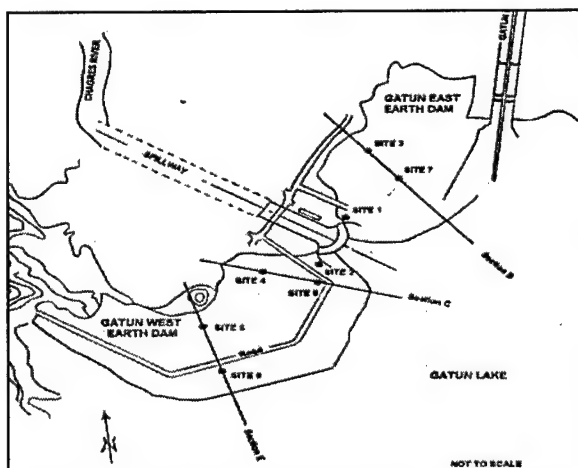


**Figure 10.** Location Map of Seismic Testing Sites at Gatun Earth Dam and Concrete Spillway

**Table 1.** Values of shear and Young's modulus for rock underlying the spillway (Yule, 1996)

Section	Site	Shear Wave Velocity $V_s$ (m/sec)	Shear Modulus ( $G' = \rho V_s^2$ ) (MPa)	$E_s$ (MPa)
1	GDV-1	747	1252	3005
2	GDV-2	810	1473	3534
Section B	GDV-3	793	1410	3384
	GDV-7	668	999	2397
Section C	GDV-4	306	210	503
	GDV-8	352	278	668
Section E	GDV-5	677	1027	2466
		695	1084	2601
	GDV-6	811	1475	3539
		698	1092	2621
	Average	655.78	1030	2472

#### 4.2 Concrete tests

The Gatun Spillway was built out of mass concrete with no reinforcing steel, although some railroad rails were placed or left inside the concrete. About 170,000 cu m. of concrete were used in Gatun Spillway, nearly all of it being 1:3:6 mixtures (Sherman, 1916). Therefore, the second part of the field investigations consisted in obtaining core samples from the spillway to obtain acceptable and reliable concrete properties from the spillway. All tested samples were obtained from the downstream face of the spillway at ten different locations and the cores were typically 150 mm (6 in.) in diameter. Figure 11 shows a typical drilling operation

performed at the spillway. Five holes were drilled horizontally and five were drilled at a 30E angle with the vertical. They were distributed along the spillway apron perimeter in an alternating fashion.

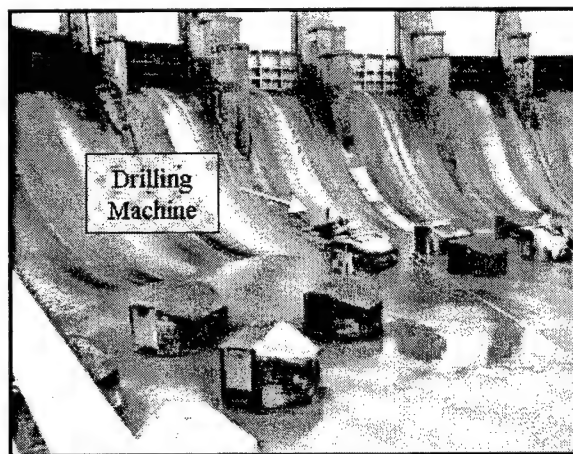


**Figure 11.** Drilling site for concrete core samples

The horizontal holes are 3.0 m in length, and the angled holes vary from 5.50 m to 6.10 m in length. The core samples obtained from the horizontal holes were used in the laboratory for standard concrete testing; the angled holes were drilled from the concrete base to the underlying rock to determine the condition of the contact between the dam and the rock foundation. All samples were tested at the Geotechnical Laboratory of the Panama Canal Authority.

The objective of this concrete testing program was to obtain three concrete properties needed for analysis: the modulus of elasticity, the compressive strength and the tensile strength. The first and second one are determined by testing to failure the 150 mm (6 in.) diameter by 300 mm (12 in.) concrete cylinders at a specific rate of load (unconfined compression test). The results of such test indicate that the mean value of the compressive strength of the specimen is  $f_c = 15,200$  kPa (2,200 psi).

On the other hand, the tensile strength of the concrete is quite difficult to measure with direct axial tension loads. As a result of these problems, the standard practice is to measure the

splitting tensile strength by testing a cylindrical core placed on its side in a testing machine and applying a compressive uniform load along the length of the cylinder (ASTM C 496). The value obtained this way is known as the static tensile strength. The mean value of the results obtained from such test is  $f'_t = 1,860$  kPa (270 psi). However, for evaluating the seismic safety of the spillway, the tensile strength of the concrete was estimated by using an empirical relation:  $f'_t = 1.7f_c^{2/3} = 2,000$  kPa (290 psi). Considering that this tensile strength is representative of the static strength but not the dynamic tensile strength, it was necessary to increase this value by multiplying it by about 4/3 to account for the nonlinear behavior of concrete near failure and then increased it by 50 percent (Figure 12) to account for rapid loading when judging the seismic safety of a concrete dam (Chopra, 1988), then:

$$f'_t = 3.4f_c^{2/3} = 4,000 \text{ kPa (580 psi)}$$

The modulus of elasticity ( $E_c$ ) of the concrete was determined according to the ASTM C 469. The test results showed that the mean value of the Modulus of Elasticity of the concrete is  $E_c = 20,800$  MPa ( $3.02 \times 10^6$  psi).

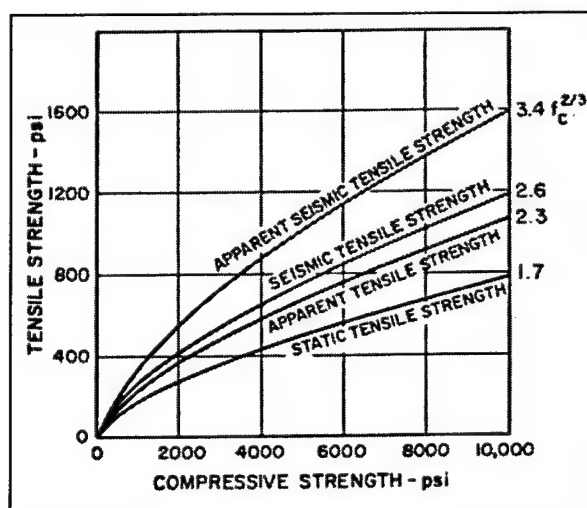


Figure 12. Design Chart for tensile strength (Raphael, 1984)

## 5 SIMPLIFIED ANALYSIS

The simplified analysis procedure was first introduced in 1978 (Chopra, 1978) and subsequently improved and extended (Chopra & Fenves, 1986) for the elastic design and safety evaluation of non-overflow concrete gravity dams. Later, the procedure was extended (Chopra & Tan, 1989) to analyze gated spillway monoliths. In this latest procedure, the lateral forces associated with the fundamental vibration mode of the gated monoliths are estimated directly from smoothed design spectrum. This procedure also considers the effects of water-dam interaction, water compressibility, absorption of hydrodynamic pressure waves in the reservoir bottom materials and underlying foundation rock, and the response contribution of higher vibration modes. The purpose of using this method in the present analysis is to determine the dynamic response of the spillway section. A 3-D analysis should only be considered if the stresses determined by the beam theory are close to, or greater than, those allowed.

### 5.1 System idealization

For the implementation of the simplified method, it was first necessary to determine the cross section to be analyzed:

#### 5.1.1 Assumptions

A three-dimensional analysis may seem necessary to predict the seismic stresses in the horse-shoe shaped Gatun Spillway with shear keys between monoliths. The approach adopted here is different. If a simpler two-dimensional analysis demonstrates that the computed stresses are less than the tensile strength of concrete, then it can be argued that a 3-D analysis is not necessary. Therefore, it was initially assumed an equivalent two-dimensional (Figure 13) system of unit thickness along the dam axis with the mass and elastic modulus of the monolith kept a their actual values, but those of the piers reduced by the ratio of monolith thickness to pier thickness.

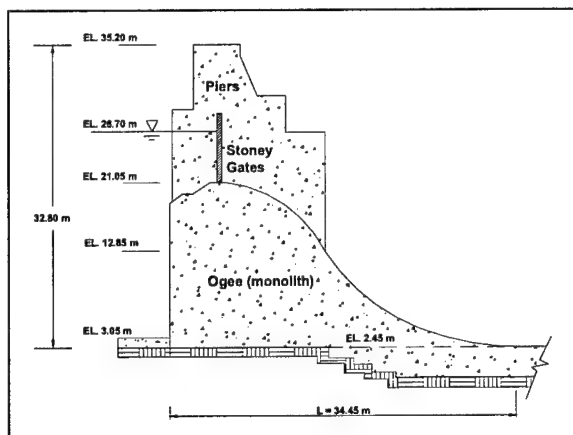


**Figure 13.** Two-dimensional model of Gatun Spillway, showing monolith and piers

Another assumption made by the simplified procedure establishes that the equivalent two-dimensional system is supported on a viscoelastic half-plane and impounding a reservoir of water, possibly with some sediments at the bottom. The dynamic effects of the tail water are neglected in the analysis because it is usually too shallow to influence the dam response, as it is in this case.

### 5.1.2 Model geometry

A two-dimensional equivalent system has been assumed and it is represented by the properties of a series of horizontal sections distributed throughout the height of the dam. A consequence of this geometric representation is that the simplified analysis procedure cannot account adequately for voids or large geometric changes in a dam, such as machinery tunnel or gate shafts.

The Gatun Spillway idealization to be used in this procedure is described as follows:

*a. Spillway cross-section:* The cross-section used in this procedure has been divided in 13 blocks (including the piers). Among these 13 blocks, 6 correspond to the monolith (equally spaced), 2 to transition blocks, and the remaining 5 to the pier section (Figure 14).

*b. Galleries and Shafts:* The voids produced by the machinery tunnel that runs in the cross-

stream direction of the spillway, as well as the shafts from the machinery to the gates have been neglected.

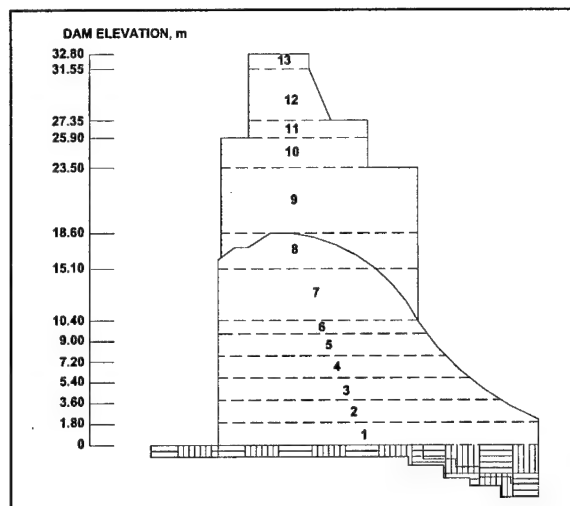


**Figure 14.** Block model of Gatun Spillway

*c. Monolith and Pier Width:* The dimensions of the monolith and piers were taken from actual values of the dam, as shown in drawings kept at the Panama Canal Authority Library. The monolith width is approximately 18.40 m (60.3 ft) and the pier width is 4.60 m (15 ft). This gives a ratio of pier width to monolith width of 0.25.

*d. Height of Model:* The height of the dam section is 18.60 m (61 ft) and the height of the piers is 14.20 m (46.5 ft) (from top of ogee to top of pier). This gives a total height for the structure of 32.80 m (107.5 ft).

*e. Stoney Gates:* The analysis has included the weight of the steel gates, which has been obtained for a 300-mm (1-ft) strip.

### 5.1.3 Pool elevation condition

Several basic loading conditions are generally used in the stability analysis of concrete gravity dams. For the implementation of the simplified analysis, however, the load case used to obtain the stresses corresponds to the "Extreme Loading Condition" case, which considers the structure under normal operating conditions with the maximum credible earthquake (MCE).



The usual pool elevation has been established for analysis purposes at an elevation of 26.70 m (87.5 ft) above the sea level, which corresponds to the normal operating level. Being the elevation of the bottom of the dam along 2.45 m (8.0 ft) above the sea level, the head of water acting against the structure is 24.25 m (79.5 ft) (see Figure 13)

## 5.2 Analysis results

The results from the analysis include the maximum hydrodynamic and inertial earthquake forces represented by equivalent lateral forces at each of the horizontal sections. The magnitude of the forces depends on the spectral acceleration evaluated at the estimated fundamental vibration period of the dam. The distribution of the earthquake forces is based on an assumed mode shape for the fundamental mode. The lateral forces associated with the fundamental vibration mode are computed to include the effects of dam-water interaction, water compressibility, reservoir bottom absorption, and dam-foundation interaction.

The total effects of the fundamental mode ( $r_1$ ) and the higher modes ( $r_{sc}$ ) are combined by the square-root-of-sum-of squares (SRSS) method. The SRSS estimate of the dynamic response is then combined with the static effect ( $r_{st}$ ) to obtain the total value of the response. The static effect includes the initial stresses in the dam prior to the earthquake due to the effects of the self-weight of the dam and the hydrostatic pressures. The combination of the static and dynamic stresses should allow for the worst case, leading to the maximum value of the total response:

$$r_{max} = r_{st} \pm (r_1^2 + r_{sc}^2)^{1/2}$$

Considering the dam monolith to be a cantilever beam, the vertical bending stresses are computed at the bottom of the blocks of the monolith (not the pier) using elementary formulas to compute beam stresses. The maximum principal stresses can then be obtained from the calculated vertical bending stresses ( $\sigma_{y1}$ ,  $\sigma_{y,sc}$ , &  $\sigma_{y,st}$ ) and by an appropriate transformation:

$$\sigma_1 = \sigma_{y1} \sec^2 \theta + p_1 \tan^2 \theta$$

where  $\theta$  is the angle of the face with respect to the vertical, and  $p_1$  is the hydrodynamic pressure. The second term can be neglected for the downstream face since no tail water is included in the analysis. In the same manner, the first term is negligible for the upstream face of the spillway since it is vertical ( $\theta = 0$ ).

The simplified procedure considers several effects that influence the behavior of the monoliths. Two of the most important are the dam-water interaction and the dam-foundation interaction. Both of them are controlled by several parameters that may influence the response of the structure to the input motion.

The reservoir level affects the dam-water interaction, therefore, two reservoir levels are considered in the analysis: (a) reservoir empty; and (b) reservoir at normal operational level. On the other hand, the dam-foundation interaction also modifies the natural vibration period and the added damping ratio of the system. This effect is highly influenced by the modulus of elasticity of the rock foundation. In the case of the Gatun Spillway, the field and laboratory tests showed that the Modulus of Elasticity ( $E_f$ ) of the rock foundation is much smaller than the one of the concrete ( $E_c$ ), therefore, the analysis can be performed considering a flexible foundation. ( $E_f/E_c < 4$ ). However, at this point it is important to note that cracks may occur in the concrete of the spillway during the earthquake, thus reducing its modulus of elasticity ( $E_c$ ). Considering this condition, the analysis has been performed assuming the following:

a. The rock foundation is considered rigid in the simplified analysis (this condition has been proved to be more conservative)

b. The Young's modulus of the concrete is 20,800 MPa ( $3.02 \times 10^6$  psi), then the Young's modulus of the rock foundation is estimated in 103,400 MPa ( $15.0 \times 10^6$  psi) to comply with the relation  $E_f > 4E_c$ .

The spillway was then analyzed for the ground motions characterized by the pseudo-acceleration response spectrum shown in Figure 9. For each analyzed case, a pseudo-acceleration value has been assigned according to the appropriate period and damping values shown in Table 2.

**Table 2.** Simplified procedure parameters and fundamental mode properties

Attenuation Relationship	Reservoir	Fundamental Mode Properties				
		Concrete $E_c$ (MPa)	Vibration Period $T_1$ (sec)	Damping Ratio $\xi_1$	PGA (g's)	$S_a$ (g's)
Joyner	Empty	20,800	0.084	0.050	0.544	1.1031
Joyner	Full	20,800	0.094	0.048	0.544	1.1862
Youngs	Empty	20,800	0.084	0.050	0.5823	1.0244
Youngs	Full	20,800	0.094	0.048	0.5823	1.0833

Considering that the natural vibration period and the added damping ratio of the system are influenced by the Young's modulus of the concrete, and because the Young's modulus can also vary considerably as function of the concrete condition, analyses were also performed using the maximum acceleration given by the attenuation relationship to obtain the maximum possible response of the structure.

For purposes of preliminary analysis of concrete gravity dams, the key property that determines the capacity of concrete dams to withstand earthquakes is the tensile strength of the concrete; although the compressive stresses should not exceed the compressive strength of the concrete either.

Figures 15, 16 and 17 compare the principal tensile stresses generated along the upstream and downstream faces of the structure under seismic loading against the tensile strength of the concrete. Because the upstream face of Gatun Spillway is vertical and the effect of the tail water at the downstream face has been neglected, the bending stresses calculated through the simplified analysis are the same as the principal stresses. It is clear that, even for the case under the conservative assumption of a rigid foundation, the dynamic stresses computed are below

the seismic tensile strength of concrete, indicative that the main cross-section of the spillway has sufficient capacity to withstand the considered ground motions.

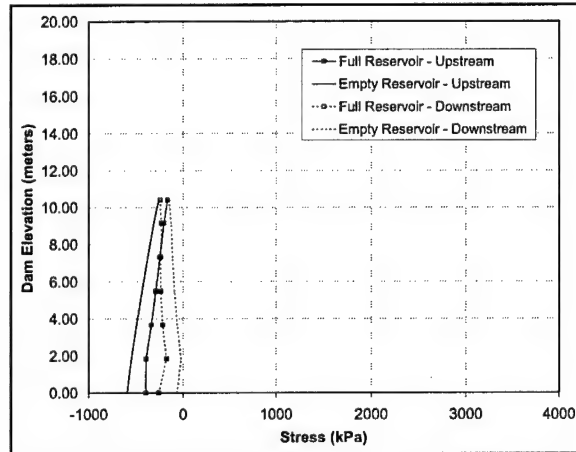


**Figure 15.** Stress distribution at both faces of spillway under usual loading condition

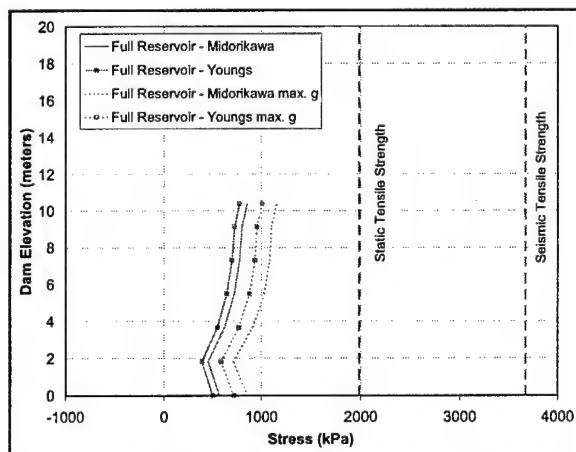


**Figure 16.** Stress distribution in upstream face of spillway under extreme loading condition

It is important to note that beam theory overestimates the stresses near the sloped downstream face of the spillway. This error depends on the slope and heightwise distribution of equivalent lateral forces on the downstream face. To overcome this problem, the method also recommends that  $\sigma_{y1}$  and  $\sigma_{y,sc}$  computed at the sloping part of the downstream face should be multiplied by a factor of 0.8. However, the results do not show



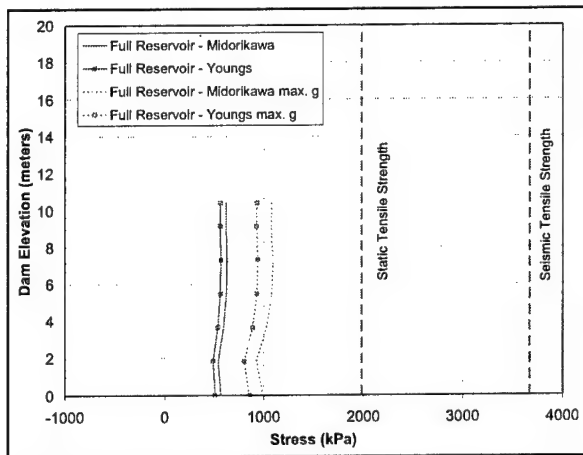


**Figure 17.** Stress distribution in downstream face under extreme loading condition

this reduction since the evaluation demonstrates that the stresses at the downstream face are well below the minimum limits.

## 6 STABILITY ANALYSIS

In addition to the dynamic analysis performed previously, the structure should be stable against overturning and sliding along a failure plane for several loading conditions.

### 6.1 Loading conditions

Several basic loading conditions are generally used in the stability analysis of concrete gravity dams. Following there is a description of the four basic loading cases analyzed:

*a. Usual Loading Condition:* The dam is operating under normal conditions, and the analysis includes the following:

- (1) Pool elevation at top of closed gates
- (2) Minimum tailwater
- (3) Silt pressure

*b. Unusual Loading Condition:* The dam is operating under the following conditions:

- (1) Pool at Standard Project Flood (SPF)
- (2) Gates at appropriate flood-control openings
- (3) Tailwater at flood elevation

- (4) Silt pressure

The SPF level of the Gatun Lake is 27.20 m (89.14 ft) above the sea level. Therefore, the head of water acting against the structure is 24.75 m (81.14 ft).

*c. Extreme Loading Condition #1:* The analysis of the dam under this case includes the following:

- (1) Maximum Credible Earthquake (MCE)
- (2) Horizontal earthquake acceleration in downstream direction
- (3) Usual pool elevation
- (4) Minimum tailwater
- (5) Uplift at pre-earthquake level

*d. Extreme Loading Condition #2:* The analysis of the dam under this case includes the following:

- (1) Pool at Probable Maximum Flood (PMF)
- (2) All gates open and tailwater at flood elevation
- (3) Uplift pressure
- (4) Tailwater pressure
- (5) Silt Pressure

The PMF level of the Gatun Lake is 28.20 m (92.55 ft) above the sea level. Therefore, the head of water acting against the structure is 25.75 m (84.55 ft).

### 6.2 Shear strength parameters

The concrete-to-rock interface of the dam foundation is generally one of the potential failure surfaces that required evaluation during the stability analysis of a dam; therefore, representative shear strength parameters are needed in the analysis of concrete-to-rock interface.

Based on various publications from the Electric Power Research Institute (1992), and recommendations from the Geosciences and Structures Division of WES (Hall, 2001), stability evaluations were performed using the following values for the angle of friction and cohesion parameter:  $\phi = 30^\circ$  and  $c = 690$  kPa (100 psi). The actual

values of these parameters typically depend on the characteristics and conditions of the contact interface, and the direction and magnitude of the relative motion. Their values are likely to change during sliding, and therefore the assumed values represent constant approximations.

The stability analysis was carried out using a sliding plane along the contact between the concrete structure and the foundation rock. This failure plane is assumed to run along the entire contact between both surfaces, and is located at an elevation of 2.45 m (8.0 ft) above the sea level.

### 6.3 Uplift pressure

The uplift pressure distribution is a very sensitive parameter for stability analysis. Therefore, an appropriate assumption of this value will result in acceptable Factors of Safety and unnecessary conservatism will not be added to the analysis. Several U.S. Design Agencies' Guidelines recommend different uplift assumptions, which are fairly consistent between them. In the case of existing dams, the guidelines allow for more appropriate uplift assumptions to be used when supported by uplift pressure monitoring data at the dam. Such is the case of the Gatun spillway, where six piezometric holes are located in the machinery tunnel of the spillway and a regular monitoring program of the gages provides information on the uplift pressures generated at the bottom of the structure (Barrelier, 2000).

The uplift pressures were assumed to act over the entire base. The distribution of the pressures were assume to have 100 percent headwater pressure at the upstream heel and varied as a straight line to 100 percent tailwater pressure at the toe of the dam. This assumption is consistent with the observed data at the dam.

### 6.4 Required factor of safety

A factor of safety is required in sliding stability analysis to provide a suitable margin of safety between the loads that can cause instability and the strength of the material along potential

failure planes that can be mobilized to prevent instability. The required factor of safety for sliding is defined by the following equation (USACE, 1997):

$$FS_{SL} = 2.00 (F_L)(F_I)(F_{SI}) > 1.10$$

where:

- $F_L$  = a loading condition factor
- $F_I$  = a structure importance factor
- $F_{SI}$  = a site information factor

For the Gatun spillway, the loading factor ( $F_L$ ) has been established as 1.0 for the normal operation condition and 0.667 for the extreme condition. The Structure importance factor ( $F_I$ ) has been established as 1.0 considering the spillway as a critical structure (a value of 0.75 is assigned to normal structures). Finally, considering the investigations performed in the area to establish the condition of the foundation rock underneath the spillway, it has been assumed that a Site Information Factor ( $F_{SI}$ ) equal to 1.0 is reasonable.

### 6.5 Seismic coefficient ( $a_h$ )

The seismic coefficient is a dimensionless unit obtained as the ratio between the acceleration for an appropriate spectral content and the response of a structure with the acceleration of the ground. In practice, coefficients are presented in maps in which areas or zones are assigned seismic coefficients. However, for the Gatun area there are no maps. Instead, from geological and seismological investigations of the dam site, it has been possible to estimate the controlling maximum credible earthquake (MCE). Following the recommendations of several reports issued by USACE (1995), the analyses were performed using a seismic coefficient equal to two-third of the peak ground acceleration selected for the MCE.

### 6.6 Forces

The forces involved the analyses are depicted in Figure 18.

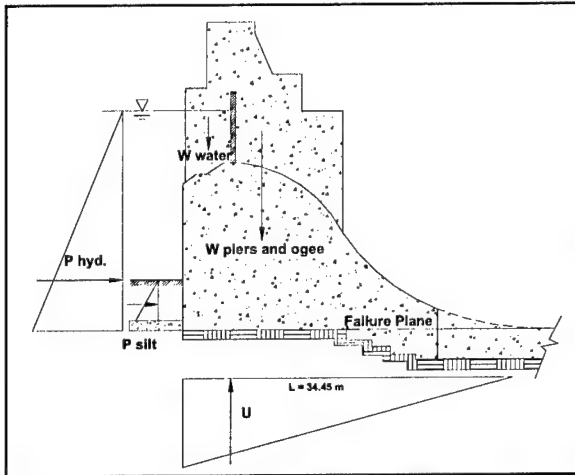


**Figure 18.** Static forces acting on the Spillway

### 6.6.1 Vertical forces

Considers all forces resisting the inertial motion transmitted to the structure by the earthquake. The main forces in this category are the following:

- Weight of the structure ( $W$ ): Includes the weight of the ogee section and the apportioned weight of the piers.
- Weight of water ( $W_{water}$ ): Includes the weight of the water portion on top of the structure.
- Uplift Pressure ( $U$ ): The pressure generated under the structure has been determined taking the initial gradient equal to the head of water in the upstream face of the dam, decreasing linearly down to zero at the downstream face of the structure. Several holes located at the end of the ogee section show very low pressure head which demonstrate that the uplift pressures have dissipated at this point.

### 6.6.2 Horizontal forces

Considers all forces acting in the direction of the motion. The main forces in this category are the following:

- Hydrostatic Force ( $H_s$ ): Force exerted in the upstream face of the spillway by the impounded water:

$$H_s = 0.5 \gamma_{water} H^2$$

- Hydrodynamic Force ( $W_{ao}$ ): Hydrodynamic water pressure resulting from the dynamic response of the body of water behind the dam estimated from Westergaard's solution for the case of a vertical, rigid dam retaining a semi-infinite reservoir of water that is excited by harmonic, horizontal motion of its base:

$$W_{ao} = 7/12 a_h / g \gamma_{water} H^2$$

- Inertial Forces ( $gW$ ,  $gW_{water}$  &  $W_{silt}$ ): These are the inertial forces induced by the horizontal acceleration of the structure, silt and water on top, which is the product of the earthquake acceleration and the masses.

## 6.7 Results

Based on limit equilibrium, the stability of the spillway was calculated using the following relationships:

### Factor of Safety against Sliding:

$$SF = \frac{\sum F_{vertical} \tan \phi + cB}{\sum F_{horizontal}}$$

### Factor of Safety against Overturning:

$$SF = \frac{\sum M_{resisting}}{\sum M_{driving}}$$

where:

- $F$  = Forces acting on the structure
- $c$  = Cohesion of the interface between the concrete dam and the rock foundation

$B$  = Length of base in compression  
(26.70 m)

$\phi$  = Friction angle of the interface  
between the concrete dam and the  
rock foundation

The results, shown in Tables 3 and 4, indicate that the spillway is structurally stable against overturning and sliding along the assumed failure plane. In addition, the fact that the contribution of the curved shape of the spillway (in plan view) to its structural capacity has been neglected, will fortify this conclusion.

**Table 3.** Factor of Safety against sliding

Loading Condition	Gatun Level (m - PLD)	Minimum F.S.	Actual F.S.
Usual	26.70	2.00	7.34
Unusual (SPF)	27.20	1.75	7.04
Extreme (PMF)	28.20	1.33	6.46
Extreme (MCE)	26.70	1.33	1.76

**Table 4.** Factor of Safety against overturning

Loading Condition	Gatun Level (m - PLD)	Requirement	Actual F.S.
Usual	26.70	Middle 1/3	1.71
Unusual (SPF)	27.20	Middle 1/2	1.67
Extreme (PMF)	28.20	Within Base	1.58
Extreme (MCE)	26.70	Within Base	1.19

## 7 PIER FINITE ELEMENT ANALYSIS

The piers of the Gatun Spillway are approximately 4.60-m- (15-ft-) thick concrete sections and raise 14.20 m (46.5 ft) above the crest of the main section of the spillway. They have an irregular shape, which varies with their height.

As previously mentioned, the piers were poured prior to the casting of the ogee section; therefore, they are embedded into the main section of the spillway. Examining old construction

drawings. It seems that no reinforcement between the spillway section and the piers was used; only massive concrete dumped from cars into chutes was used.

Due to inherent difficulties of modeling the piers in the simplified procedure, a known Finite Element Software (SAP 2000) was incorporated in the analysis to determine the response of the piers. It is also considered that this analysis is preliminary because it neglects the curvature of the spillway; the hydrodynamic effects; the dam-foundation interaction (flexibility, damping and radiation); and the effects of the gate systems.

### 7.1 Model

The preliminary evaluation of the piers was modeled assuming a rigid foundation (fixed-base model). The 3-D model (Figure 19) is then run not including the effects of the impounding water and the gate system. This means that the mass of the gates and its probable restraining effect that may be induced in the response of the pier are neglected.

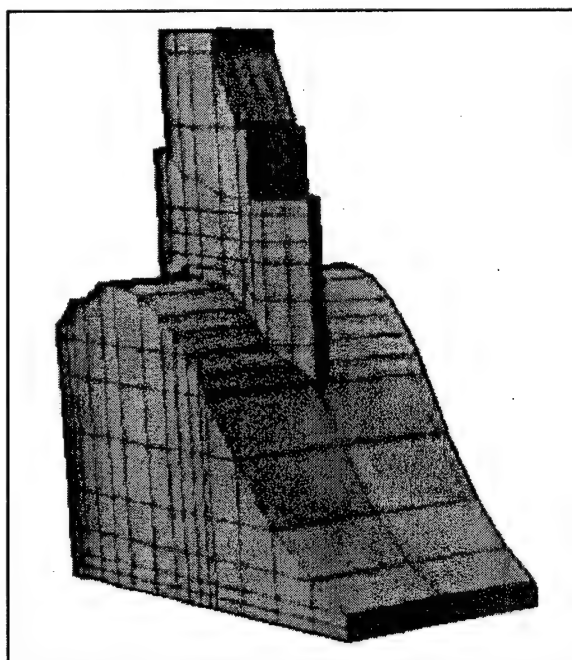


**Figure 19.** 3-D Finite Element model of the piers of the spillway

The FEM procedure for the piers is a response spectrum analysis. The total number of modes used in the analysis has been set to 30, allowing in this way to have a modal participating mass of 90 percent of the total mass in each direction. For a given direction of acceleration, the maximum displacements, forces and stresses are then computed throughout the model for each of the vibration modes. Finally, these modal values for a given response are combined to produce a single, positive result for a given direction of acceleration using the Complete Quadratic Combination rule (CQC).

The event used for the analysis is the one corresponding to a PGA of 0.544 g's (mean + 1 standard deviation). To implement the cross-stream analysis, the model has been fixed not only at the base but also at the sides, since the purpose of the run was to determine the response of the pier to ground motions in the cross-stream direction. The stresses determined at the interface were compared with the maximum tensile stresses allowed for the concrete (splitting test) to verify the capacity of the section.

## 7.2 FEM results

The results of the cross-stream analysis (Figure 20) indicate that the dynamic stresses exceeded the maximum strength capacity of the material at the pier-dam interface. Although it seems that this high stress concentration develops mainly at the outer fibers of the elements, further analysis and a mesh refinement is necessary to characterize the extension of the capacity exceedance inside the piers. Nevertheless, this analysis has served to point out that the material strength capacity of the pier-dam interface is exceeded during this critical event. The FEM analysis provides reasonable estimates of the location and occurrence of material strength exceedance, and the grid at the pier-dam interface has sufficient degrees-of-freedom to determine the likelihood of tensile stresses exceeding the material strength capacity. However, due to the limitations in the model, this analysis is considered only as preliminary, and a more refined analysis must be performed, including all the effects hereby neglected.

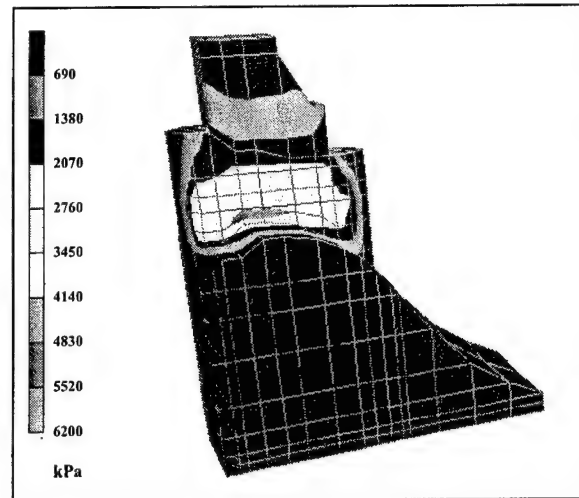


**Figure 20.** Stress contours in kPa. Pier response to cross-stream oscillation using a PGA of 0.544 g

## 8 CONCLUSIONS

The Gatun Dam System (earth dams and spillway) is the most important structure in the Canal as it impounds and regulates the Gatun Lake, which is considered the core of the Canal System.

From the results of this evaluation, it is concluded that the main cross-section of the spillway has sufficient capacity to perform in the elastic range during a 0.544 g's event, even for the case under conservative assumption of a rigid foundation. The analysis hereby presented neglected the contribution of the curved plan of the spillway to the structural capacity, which strengthens the conclusion that the Gatun Spillway main body may withstand the considered ground motions without any significant damage of the concrete. Furthermore, failure by sliding and overturning is unlikely. Therefore, the initial assumption of a structure fully coupled to the rock foundation is adequate.

On the other hand, the preliminary finite-element analysis suggests that the piers of the spillway may not have sufficient capacity to perform well in the elastic range during the most critical event. The finite-element mesh of the

piers needs to be refined, and more elements need to be added through the width and along the contact with the spillway section. Once the mesh has been refined, a response-spectrum method of analysis is recommended, using the MCE smooth response spectra developed for a mean plus one standard deviation level. Additionally, equal-hazard spectra for an appropriate return period should be used. These analyses are needed to provide estimates and extent of material capacity exceedance and possible remediation if required.

## 9 ACKNOWLEDGEMENTS

This work has been performed for the Panama Canal Authority, under its sponsoring. The authors appreciate the cooperation of Panama Canal Authority, which permitted the presentation of this study. The authors also appreciate the cooperation and participation of the Waterways Experiment Station (WES) of the U.S. Army Corps of Engineers, particularly Drs. Robert L. Hall, Enrique E. Matheu and Donald E. Yule; the United States Geological Survey (USGS), to Prof. Anil K Chopra, who peer reviewed the process, and last but not least to Dr. Luis D. Alfaro, Manager of Engineering Division of the Panama Canal Authority, who reviewed the manuscript and supported the authors throughout all the process. Permission to publish this paper was granted by the Director of the Engineering and Projects Department of the Panama Canal Authority.

## 10 REFERENCES

- Abrahamson, N. A., and Silva, W. J., (1997), "Empirical Response Attenuation Relations for Shallow Crustal Earthquakes," *Seismological Research Letters*, Vol. 68, January/February, pp. 94-109.
- Barrelier, M., (2000), "Report on the Evaluation of Uplift Pressures at Gatun Spillway," Panama Canal Authority.
- Camacho, E., Lindholm, C., Dahle, A., and Bungum, H., (1994), "Seismic Hazard for Panama Update," Technical Report, NORSAR, Norway.
- Chopra, Anil K., and Fenves, Gregory, (1986), "Simplified Analysis for Earthquake Resistant Design of Concrete Gravity Dams," Report No. UCB/EERC-85/10, Earthquake Engineering Research Center, University of California, Berkeley, CA, pp. 149.
- Chopra, A. K., (1988), "Earthquake Response Analysis of Concrete Dams," Chapter 15, *Advanced Dam Engineering for Design, Construction, and Rehabilitation*, Robert B. Jansen & Van Nostrand Reinhold, pp. 416-465.
- Chopra, A. K., and Tan, Hanchen, (1989), "Simplified Earthquake Analysis of Gated Spillway Monoliths of Concrete Gravity Dams," Report No. SL-89-4, U.S. Army Corps of Engineers, Waterways Experiment Station, 153 pp.
- Climent, A., and Taylor, W., and Ciudad Real, M., (1994), "Spectral Strong Attenuation in Central America," Report No. 2-17, NORSAR, 46 pp.
- Cowan, H., (2001), "Design Earthquakes for the Southeast Area of the Panama Canal Basin," Consulting Engineer, Final Report to the Panama Canal Authority.
- Duncan, J. M., Marcuson III, W. F., Morgenstern, N. R., Schuster, R. L., Wesson, R. L., (1998), "Report of the 8<sup>th</sup> Geotechnical Advisory Board," Internal Report for the Panama Canal Authority.
- Duncan, J. M., Marcuson III, W. F., Morgenstern, N. R., Schuster, R. L., Wesson, R. L., (1999), "Report of the 9<sup>th</sup> Geotechnical Advisory Board," Internal Report for the Panama Canal Authority.
- Electric Power Research Institute, (1992), "Uplift Pressures, Shear Strengths, and Tensile



Strengths for Stability Analysis of Concrete Gravity Dams," EPRI TR-100345, Volume I.

Franceschi, P., (1992), "Geology of the Gatún Dam Site," Panama Canal Commission, 150 pp.

Franceschi, P., and Ramesh J., (1999), "Gatún Spillway Coring and Sampling Report," Panama Canal Commission, 10 pp.

Franceschi, P., (2001), "Site Investigation at Gatún Dam," Summary Report, Panama Canal Authority.

Hall, R. L., (2001), "Review of Preliminary Report on the Seismic Adequacy of Gatun Spillway," Internal memorandum, Geotechnical and Structures Laboratory, Waterways Experiment station, Department of the Army.

Joyner, W. B., (1999), "Design Ground Motion for Seismic Evaluation of the Gatun Dam," Appendix A (in) Schweig, E., et al., "Design Earthquakes for the Evaluation of Seismic Hazard at the Gatun Dam and Vicinity," Final Report to the Panama Canal Commission.

Mendoza, C., and Nishenko, S., (1989). "The North Panama Earthquake of 7 September, 1882: Evidence for active underthrusting," Bulletin of the Seismological Society of America, Vol. 79, pp. 1264-1269.

Midorikawa, S., (1991), "Attenuation of Peak Ground Acceleration And Velocity from Large Subduction Earthquakes," Proc. Fourth International Conference on Seismic Zonation, Earthquake Engineering Research Institute, Stanford, California, Vol. 2, pp. 179-186.

Olsen, R., and Yule, D., (1997), "Cone Penetrometer Test (CPT) Field Investigation and Data Evaluation, Gatun Dam, Panama Canal, Republic of Panama," Report No. GL-97, U.S. Army Corps of Engineers, Waterways Experiment Station.

Pratt, T., Holmes, M., Stephenson, W., and Odum, J., (1999), "Results of 1997 High-Resolution Seismic Reflection Profiling for

Evaluation of the Seismic Hazard at the Gatún Dam, Republic of Panama," Final Report to the Panama Canal Commission.

Raphael, J. M., (1984), "Tensile Strength of Concrete," Title No. 81-17, ACI Journal, pp. 158-165, Mar-Apr.

Schmidt V., Dahle A., and Bungum, H., (1997), "Costa Rican Spectral Strong Motion Attenuation," Technical Report, NORSAR, Norway.

Schweig, E., Cowan, H., Gomberg, J., Pratt, T., and Tenbrink, A., (1999), "Design Earthquakes for the Evaluation of Seismic Hazard at the Gatún Dam and Vicinity," Final Report to the Panama Canal Commission, 60 pp.

Sherman, E., (1916), "The Spillway of the Panama Canal," Boston Society of Civil Engineers, Vol. III, pp. 135-150.

USACE, (1995), "The State of Practice for Determining the Stability of Existing Concrete Gravity Dams Founded on Rock," USACE Technical Report REMR-GT-22.

USACE, (1995), "Gravity Dam Design," USACE Report No. EM-1110-2-2200.

USACE, (1995), "Seismic Analysis and Design of Reinforced Concrete Locks," USACE Report No. ETL-1110-2-342.

USACE, (1997), "Stability Analysis of Concrete Structures," USACE Report No. EC-1110-2-291.

USACE, (1999), "Response Spectra & Seismic Analysis for Concrete Hydraulic Structures," USACE Report No. EM-1110-2-6050, June 30.

Yule, D., (1996), "Geophysical Site Investigation for Gatún Dam, Panama Canal, Republic of Panama," Report No. GL-96, U.S. Army Corps of Engineers, Waterways Experiment Station, 99 pp.

Yule, D., (2001), Personal Communication.

Youngs, R. Chiou, S.-J., Silva, W., and Humphrey, J., (1997), "Strong Ground Motion Attenuation Relationships for Subduction Zone

Earthquakes," Seismological Research Letters, Vol 68, No. 1, pp. 58-73.



This page intentionally left blank.

## **Damages of Dams Caused by The Western Tottori-Prefecture Earthquake in 2000 and Stability Evaluation Analysis about Kasho Dam**

By

Yoshikazu YAMAGUCHI <sup>1)</sup>, Takashi SASAKI <sup>2)</sup> and Ken-ichi KANENAWA <sup>3)</sup>

### **ABSTRACT**

The Western Tottori-Prefecture Earthquake of October 6, 2000 caused strong earthquake motion over a wide area in the western Japan. Immediately after the earthquake, dam management personnel carried out special safety inspections of dam facilities in the region. Research engineers of the Public Works Research Institute (PWRI) performed field investigation of dams near the epicenter and gathered the earthquake observation data of these dams. The results of the special safety inspections by the dam management offices and field investigation by the PWRI have confirmed that several minor damages, such as cracks in structures or dam crests, were observed, but no severe damage harming dam safety occurred. In addition, the safety of Kasho Dam, that is the nearest dam to the epicenter, was reconfirmed by linear dynamic analyses with the acceleration data observed during the Western Tottori-prefecture Earthquake in 2000.

**KEY WORDS:** the Western Tottori-prefecture Earthquake in 2000, Special Safety Inspection, Acceleration Records and Dynamic Analysis

### **1. INTRODUCTION**

On October 6, 2000, the strong earthquake occurred on the main island in Japan. The death toll due to the earthquake was none, but 132 people were injured. 28 houses were completely destroyed, 82 houses were half destroyed, and 5,050 houses were partially

damaged. Rock fall or debris slides occurred in 129 places. The strong ground shaking greater than the Japanese Seismic Intensity of 4 was experienced in the region within the radius of about 250km from the epicenter. Soil liquefaction widely took place in the reclaimed land along the Nakaumi coastal area. The water supply system failed to provide water to 2,800 families due to the damaged water distribution pipelines. Numerous aftershocks were recorded in the following months. There were one of them having a magnitude of 5, and three of them greater than 4.

### **2. SPECIFICATIONS OF EARTHQUAKE**

The specifications of the earthquake published by the Japan Meteorological Agency are summarized in Table 1.

This earthquake caused strong shaking in the Chugoku, Kinki, and Shikoku regions in Japan. It recorded a seismic intensity of 6 (strong) in Sakaiminato City and Hino Town in Tottori Prefecture, 6 (weak) in Saihaku Town, Aimi Town, Kishimoto Town, Yodoe Town, Mizokuchi Town, and Hiezu Village in Tottori Prefecture, and 5 (strong) in Yonago City in Tottori Prefecture, in Yasugi City, Nita Town, and Shinji Town in

- 
- 1) Team Leader, Dam Structures Research Team, Hydraulic Engineering Research Group, Public Works Research Institute (PWRI), 1-6 Minamihara Tsukuba City, 305-8516, JAPAN
  - 2) Senior Researcher, Dam Structures Research Team, Hydraulic Engineering Research Group, PWRI
  - 3) Researcher, Dam Structures Research Team, Hydraulic Engineering Research Group, PWRI

Shimane Prefecture, in Niimi City and Tetta Town in Okayama Prefecture, and in Tonosho Town in Kagawa Prefecture.

### 3. CHARACTERISTICS OF EARTHQUAKE MOTION AT DAM FOUNDATIONS

#### (1) Records at Kasho Dam

Figure 1 shows the time history of the acceleration measured at the lower inspection gallery of Kasho Dam that is managed by Tottori Prefecture (a concrete gravity dam with a height of 46.4 m, completed in 1989) and that is the nearest dam to the epicenter. Kasho Dam recorded the largest peak acceleration at dam foundations among observation data measured in Japan so far. Figure 2 shows the acceleration response spectrum recorded at the lower inspection gallery in case damping ratio is 5%. The response spectrum with a frequency of 0.1 seconds or less dominates in the east/west component.

#### (2) Attenuation of Peak Acceleration of Dam Sites

The acceleration records were measured at the dams whose locations are shown in Figure 3. Figure 4 shows the relationship of the peak horizontal acceleration measured at dam foundations (at the lower inspection gallery in concrete dams or at the inspection gallery beneath embankment dams) with the horizontal distance from the earthquake source fault. The peak horizontal acceleration indicates composite value of the two horizontal components. The figure also shows the peak horizontal accelerations recorded under the ground at a depth of 100 m at the Hino Observation Station and Hakuta Observation Station of the KiK-net<sup>1)</sup>. The S-wave velocities at the two underground observation sites are 790 m/s and 2,800 m/s respectively. They are hard enough to become the foundation for a dam. The solid and broken lines are the presumption values by the attenuation relationship equations by Fukushima et al.<sup>2)</sup> and

An-naka et al.<sup>3)</sup> These two attenuation relationship equations are obtained based on the data mainly collected on hard soil foundation. Accordingly, the data of dam sites seems to be small as compared with the presumption values about all over.

Figure 5 shows the relationship of the ratio of the peak vertical acceleration to the peak horizontal acceleration with the horizontal distance from the earthquake source fault. The ratio seems to become small as the horizontal distance from the earthquake source distance becomes large.

#### (3) Acceleration Response Spectrum

Figure 6 shows acceleration response spectrum for different epicentral distances. And, Figure 7 shows acceleration response magnification spectrum obtained by dividing acceleration response spectrum by the peak acceleration values. The peak value of response magnification spectrum is about 2-3 regardless of epicentral distance, and the peak values appear within the periods of 0.1-0.2 seconds except for the epicentral distance of 120-150km.

Figure 8 shows acceleration response spectrum of the dams that are located along the straight line from the epicenter, drawn in Figure 3. Near the epicenter, value for the high frequency range is strong. As dam is farther from the epicenter, value for the high frequency range becomes smaller, and the acceleration response spectrum becomes flat for wide range of periods.

### 4. DAMAGES TO DAMS

#### (1) Special Safety Inspections of Dams after Earthquake

In Japan the owner of the dam ought to make inspections of the dam, in the case the peak acceleration at the dam site is greater than 25 gal or the Japanese Seismic Intensity in the area is greater than 4. The special safety inspection includes a primary inspection that is a visual inspection immediately after the earthquake and a secondary inspection that is a detailed visual inspection

accompanied by analyzing the data measured by instruments. The results should be reported to the Ministry of Land, Infrastructure, and Transport.

According to the guidelines for the dam safety management, a total of 180 dams were included in the special safety inspections: 119 dams in the region of the Chugoku Regional Construction Bureau, 31 dams in the region of the Shikoku Regional Construction Bureau, and 30 dams in the region of the Kinki Regional Construction Bureau. The special safety inspections by dam owner did not result in any reports of damage that could threaten the safety of a dam. But the slight damages were reported from Kasho Dam and Sugawada Dam managed by the Ministry of Land, Infrastructure and Transport (main dam: a concrete gravity dam with a height of 73.5 m, saddle dam: concrete face rockfill dam with a height of 17.0 m, completed in 1968). Figure 9 explains the locations of the epicenter and the two dams.

◆ Damages to Kasho Dam

- Cracking of the walls and the foundation of the guard gate house
- Sliding of the mountain-side slope of the road on the right bank
- Settlement of pavement around the dam management office building

◆ Damages to Sugawada Dam

- Cracking of the walls and the floor of the guard gate house
- Chipped concrete on the downstream surface of the dam body (length of about 1 m and width of about 0.3 m)
- Partial rupture of the foundation work of the mooring facility
- V-shaped crack on the ground around the garage on the right bank downstream from the dam (length of about 100 m)
- Cracking of the wall of the garage shed on the right bank downstream from the dam
- V-shaped cracking on the left bank slope

upstream from the dam

- Cracking of the surface of the wall of the dam management office building on the right bank

(2) Field Investigation

We, research engineers of the PWRI, performed a field investigation of dams including small irrigation reservoir with small earth dams near the epicenter. The followings are a summary of the results of the investigation at Kasho dam and Sugawada Dam.

◆ Damages to Kasho Dam

At Kasho Dam (Photograph 1), the earthquake caused peak accelerations at the lower inspection gallery of 529 gal (north/south direction), 531 gal (east/west direction), and 485 gal (vertical direction). At the elevator tower at the crest elevation (Photograph 2), the peak accelerations were 2,051 gal (north/south direction), 1,406 gal (east/west direction), and 884 gal (vertical direction). The stream direction is 20 degrees east from north. At this dam, the wall and the foundation of the guard gate house that was a cantilever structure projecting upstream from the dam crest were cracked (Photograph 3). But the drainage from the foundation, dam body leakage, and displacement of the dam body had stabilized so that there were no problems threatening the dam's safety.

◆ Damages to Sugawada Dam

At Sugawada Dam (Photograph 4), in the lower inspection gallery of the dam, the peak accelerations were 158 gal (downstream/upstream direction), 126 gal (right bank/left bank direction), and 109 gal (vertical direction). On the walls and the floor of the guard gate house that is a cantilever structure projecting upstream from the dam crest (Photograph 5), there were cracks that appeared to be extensions of the transversal joints of the dam (Photograph 6), and concrete on the dam's downstream surface was partially chipped (Photograph 7), but the no trouble of dam body was observed. Although the drainage from the foundation slightly increased immediately

after the earthquake, it later stabilized. Near the dam and in the natural ground surrounding the reservoir, ground deformation caused cracking (Photograph 8).

### **(3) Level Measurement around Reservoir of Kasho Dam**

Figure 10 shows the time history of the water level measured by the water level gauge installed in the dam. Judging from the measurement of the water level gauge, the water level in the reservoir dropped abruptly by 6 cm immediately after the earthquake. To verify the truth of it, the leveling measurement was conducted for the surveying points around the reservoir shown in Figure 11. Figure 12 shows the projection of the measured results on the section that intersects perpendicularly with the estimated earthquake fault line (N28 degree W). The data from surveying points affected by landslides were excluded. Vertical displacement shown in Figure 12 is not absolute displacement, but is relative displacement based on the water level gauge at the dam body. From the Figure 12, the upstream end of reservoir has sunk about 20 cm as compared with the dam. The settlement of 20 cm would be a possible reason for the dropping of water level of the reservoir.

## **5. SAFTY ANALYSIS OF KASHO DAM**

Kasho Dam, that is the nearest dam to the epicenter, recorded the largest peak acceleration of the observation data measured so far at the inspection galley of dams. According to the special safety inspections and field investigation, the slight damages were reported, but no damage harming dam safety occurred. For the purpose of reconfirming the safety of Kasho Dam, linear dynamic analysis was carried out with the acceleration data observed during the Western Tottori-prefecture Earthquake in 2000.

### **(1) Analytical Condition**

The block that is installed the seismograph in was modeled 2 dimensionally. The FEM Model is illustrated in Figure 13. The model consists of the dam body and the reservoir, but the rock mass was not modeled. As the elevator tower is set up at the seismograph installation block and the drop of the stiffness due to the space of the elevator tower shaft is considered, the dam body was modeled in three parts of different thickness. The water level during the earthquake was EL112.2 (34.3m height from the bottom of the reservoir), and the normal highest water level was EL118.0 (40.0m height from the bottom of the reservoir). Reservoir part assumed non-compressible fluid with no viscosity. Dead weight and hydrostatic pressure are set as static loads.

The physical properties of materials are shown in Table 2. By the comparison of the acceleration observed with the seismograph at the crest and the calculated acceleration at the same position, the damping coefficient was set to 10%.

Earthquake motion is measured by NS and EW constituents in Kasho dam. The riverflow direction wave that was used in this analysis was calculated from the time history of the acceleration of NS and EW constituents observed at the lower inspection gallery in Kasho Dam. The riverflow direction and vertical wave was simultaneously inputted from the bottom of the dam body. The riverflow direction and vertical wave is shown in Figure 14.

### **(2) Analytical Result**

The principal stress is the sum of the stresses calculated from static analysis and dynamic analysis.

On the condition of the water level during the earthquake, the principal stress in the dam body is shown in Figure 15-(a). The maximum tensile stress was occurred at the heel of the dam, and the value was 1,489 kPa. The maximum compressive stress was occurred at the same position, and the value was -1,836 kPa.

On the condition of the normal water level, the

principal stress in the dam body is shown in Figure 15-(b). The maximum tensile stress was occurred at the heel of the dam, and the value was 2,281 kPa. The maximum compression stress was occurred at the downstream of the dam body, and the value was -1,868 kPa.

### (3) Conclusions

The safety of Kasho Dam was investigated using dynamic analyses with the observed acceleration data. Judging from the results of analyses, stresses in the dam body at the water level during the earthquake may be smaller enough than the strength of concrete for dams. Therefore, it is thought that this earthquake did not harm the safety of Kasho dam, and this agrees with the results of special safety inspections and field investigation after the earthquake. And the safety of the dam is assured even at normal water level based on the analytical results.

## 6. SUMMARY

From the results of the special safety inspections by the dam owner and the field investigation by the

PWRI after the earthquake, it was confirmed that no damage harming dam safety occurred.

At Kasho Dam, large earthquake acceleration was recorded. Through the dynamic analyses with the observed acceleration data, it is reconfirmed that there was no damage harming dam body safety. However, since there was slight damage in the crest structure, it is important to examine the earthquake resistance of the dam including not only dam body but also the attached structure.

## REFERENCES

- 1) Web page of the KiK Network of the National Research Institute for Earth Science and Disaster Prevention,  
<http://www.kik.bosai.go.jp/kik/>.
- 2) Fukushima et al.: Shimizu Tech. Res. Bull., Vol.10, 1-11, 1991 (in Japanese)
- 3) An-naka et al.: 19th JSCE Earthquake Engineering Symposium, 129-132, 1987 (in Japanese)

Table 1 Specifications of the Western Tottori-Prefecture Earthquake in 2000  
(Published by the Japan Meteorological Agency)

Name of earthquake	The Western Tottori Prefecture Earthquake in 2000
Time of occurrence	1:30 p.m. on October 6, 2000
Epicenter	35°16.5' north latitude 133°21.0' east longitude
Focal depth	11.3 km
JMA Magnitude	7.3

Table 2 Physical Properties of Materials

Material	Elastic Modulus(MPa)	Poisson Ratio	Unit Weight(t/m <sup>3</sup> )	Depth(m)	Damping Coefficient(%)
Dam body 1	30,000	0.2	2.3	15.0	10
Dam body 2	30,000	0.2	2.3	3.3	10
Dam body 3	30,000	0.2	2.3	1.0	10
Reservoir	∞	—	1.0	15.0	—

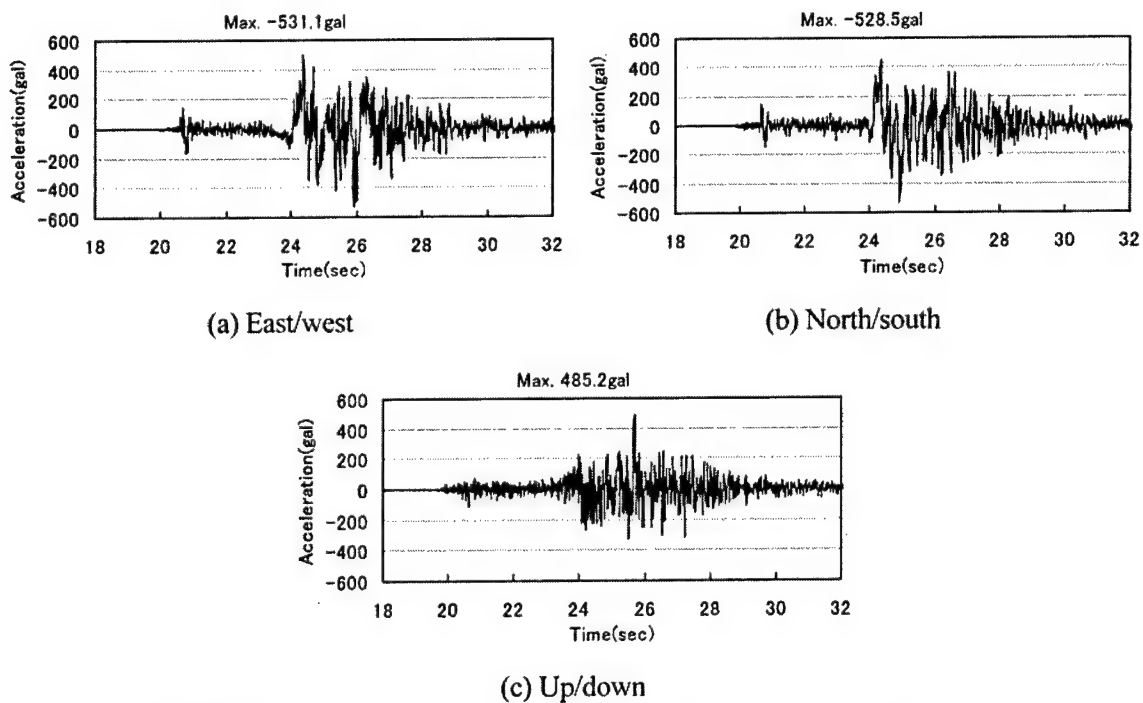


Figure 1 Earthquake Records at Kasho Dam at Lower Inspection Gallery

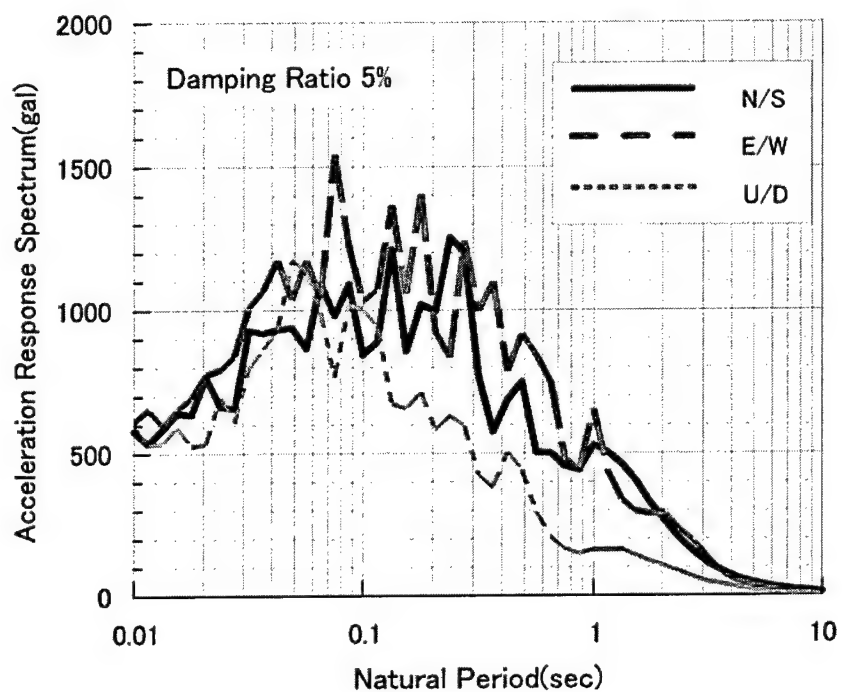


Figure 2 Acceleration Response Spectrum at Lower Inspection Gallery of Kasho Dam

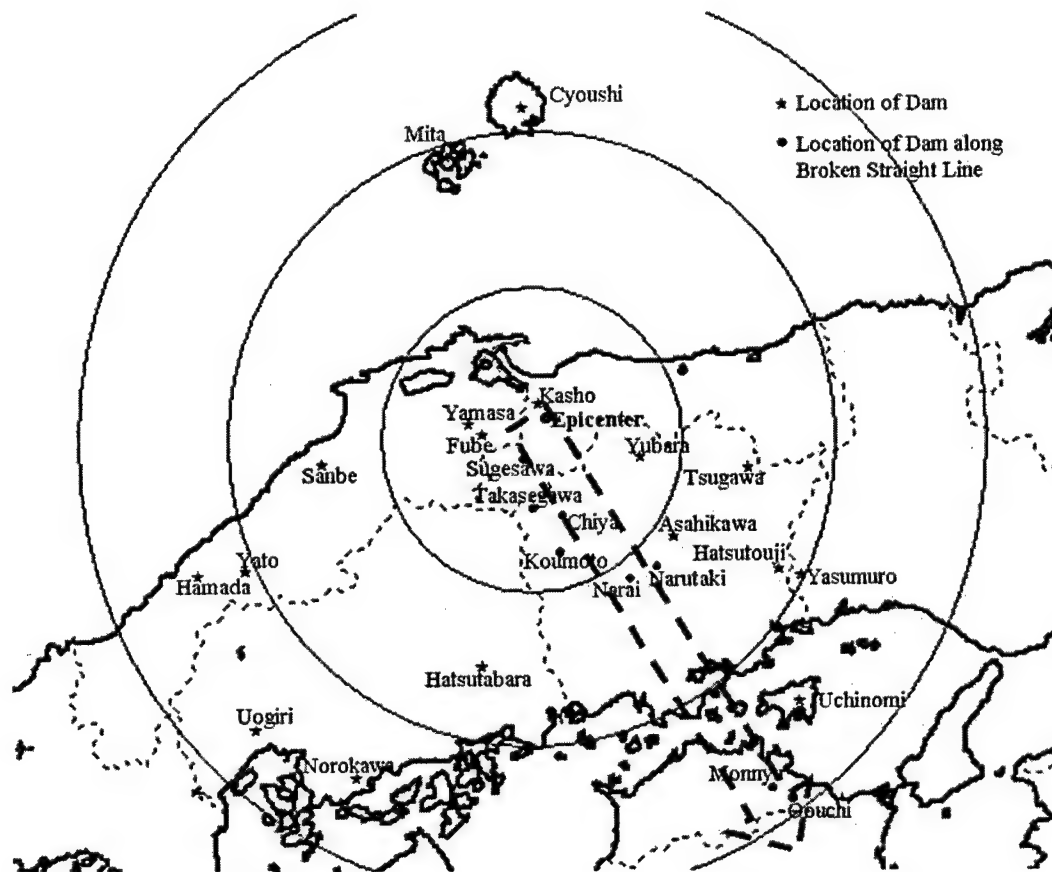


Figure 3 Location Map of the Dams that Acceleration Records were observed

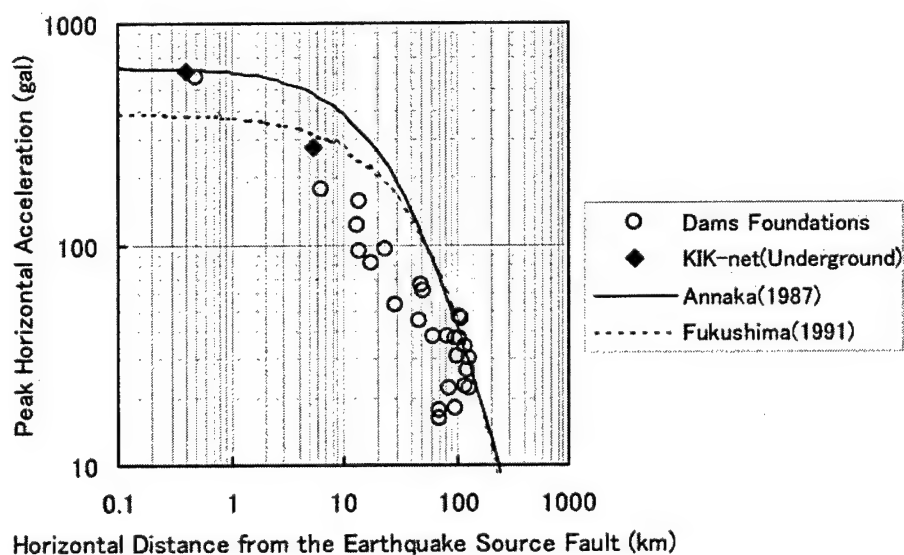


Figure 4 Attenuation of Peak Horizontal Acceleration Observed in Dam Foundations



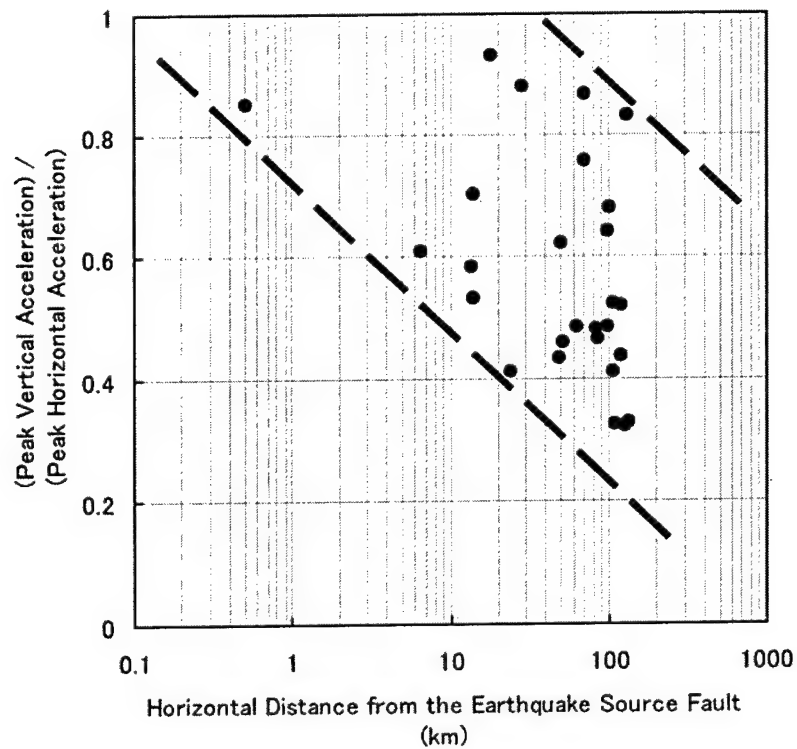


Figure 5 The Ratio of the Peak Vertical Acceleration to the Peak Horizontal Acceleration

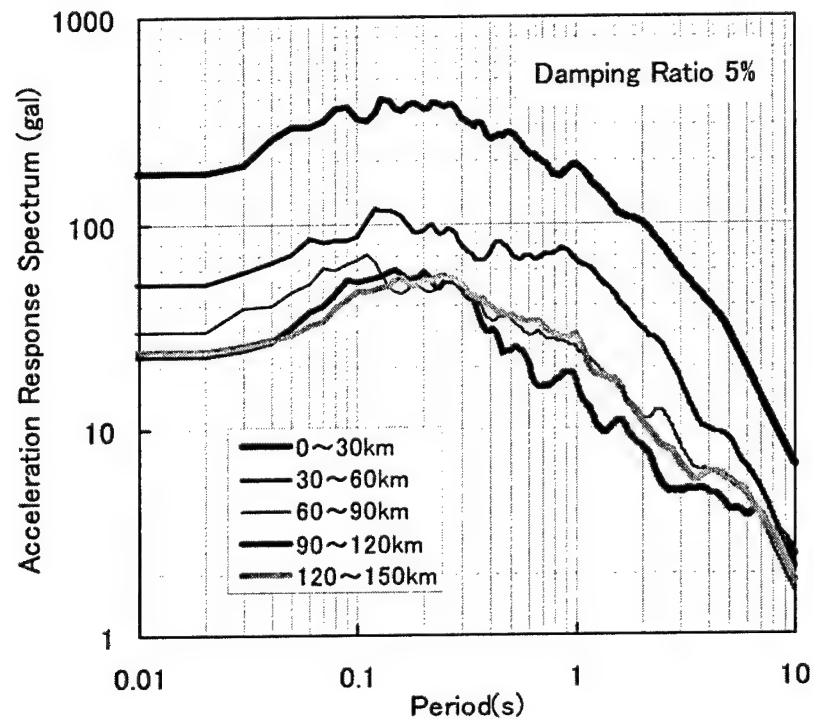


Figure 6 Acceleration Response Spectrum for Different Epicentral Distances

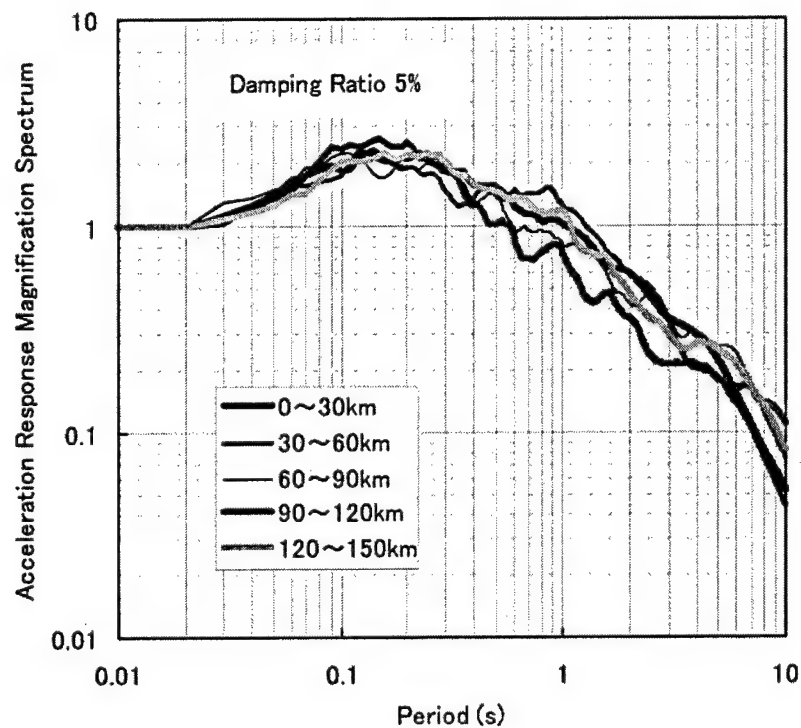


Figure 7 Acceleration Response Magnification Spectrum for Different Epicentral Distances

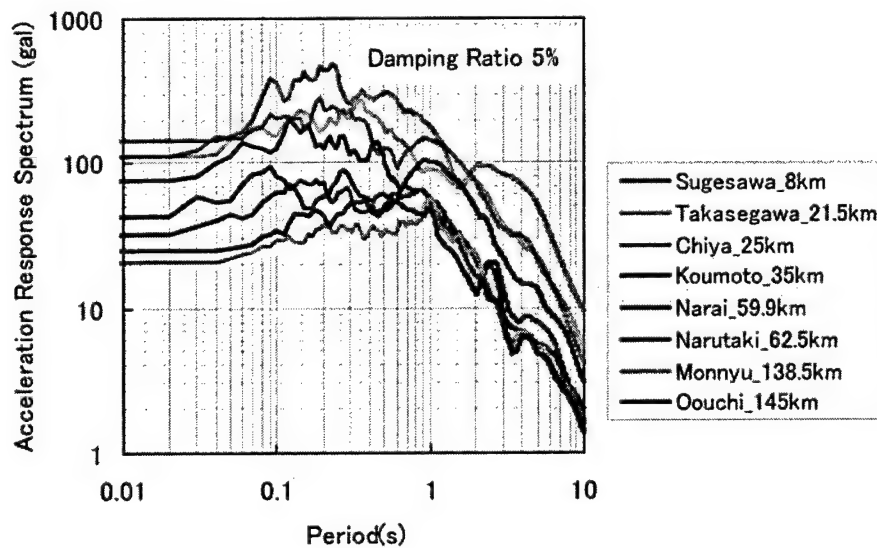


Figure 8 Acceleration Response Spectrum of the Positions that are in a Straight Line from the Epicenter

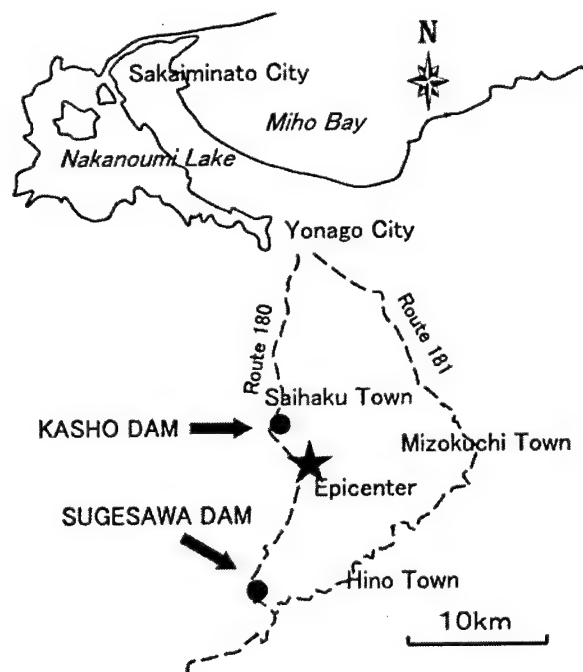


Figure 9 Locations of the Epicenter, Kasho Dam and Sugesawa Dam

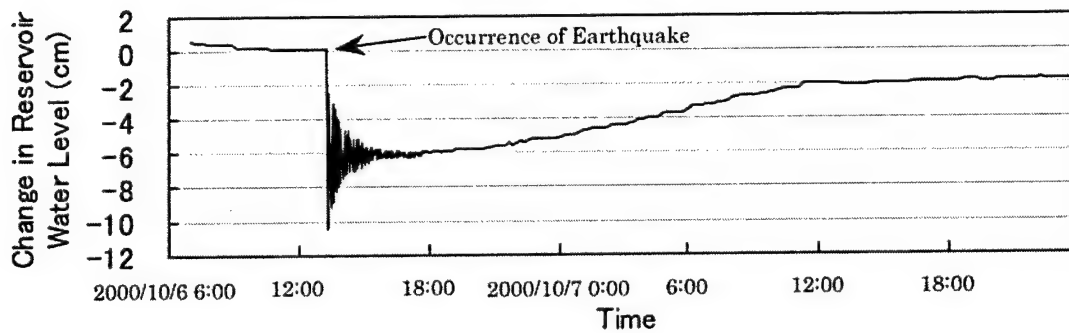


Figure 10 Time History of Reservoir Water Level at Kasho Dam

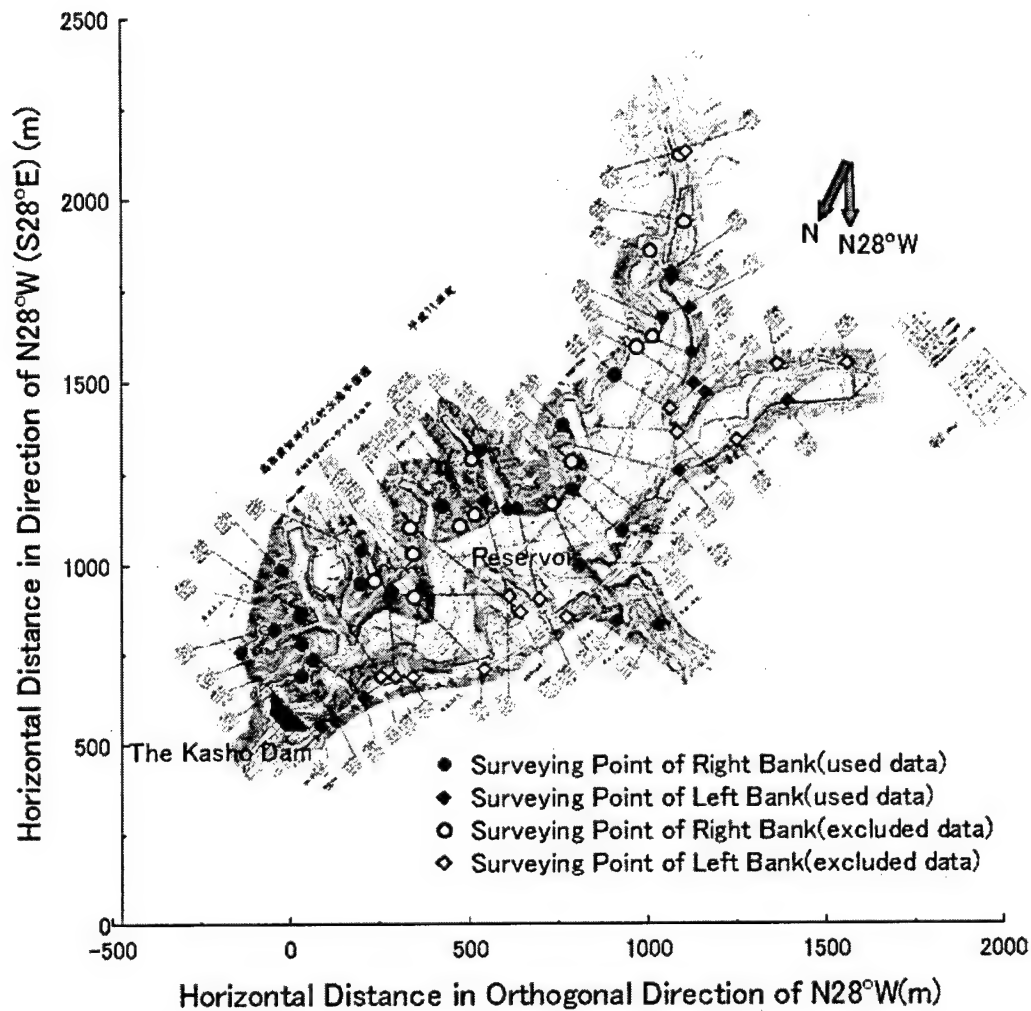


Figure 11 Surveying Points of Reservoir Circumference at Kasho Dam

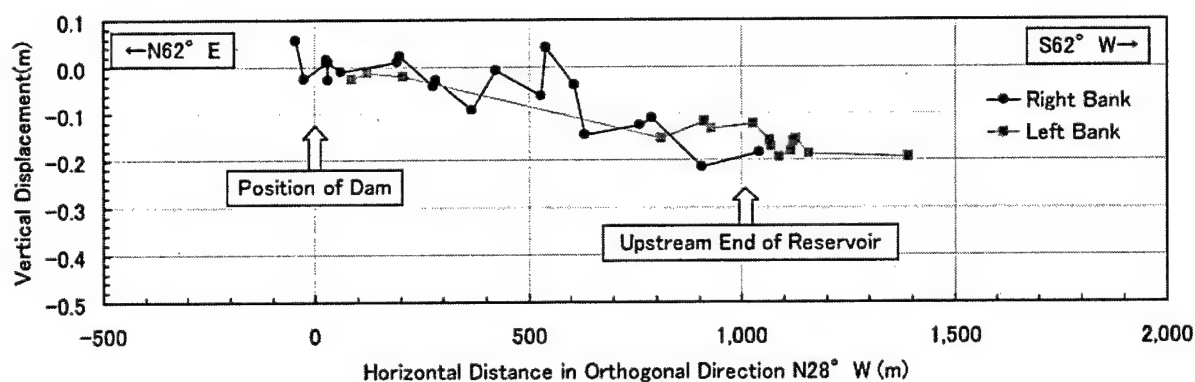


Figure 12 Results of Leveling Measurement around Reservoir of Kasho Dam

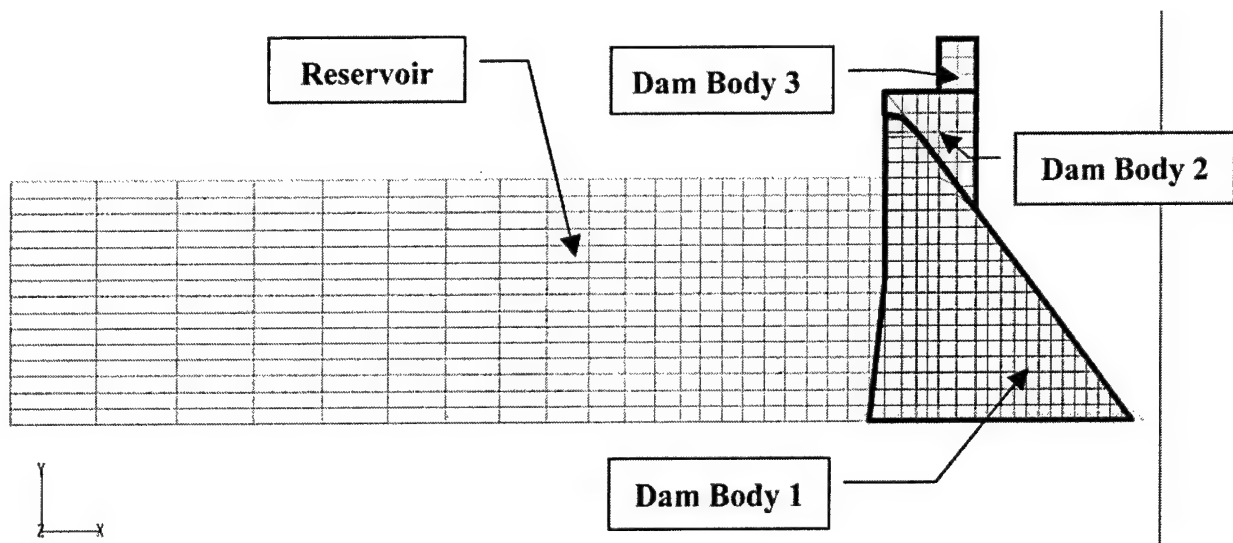
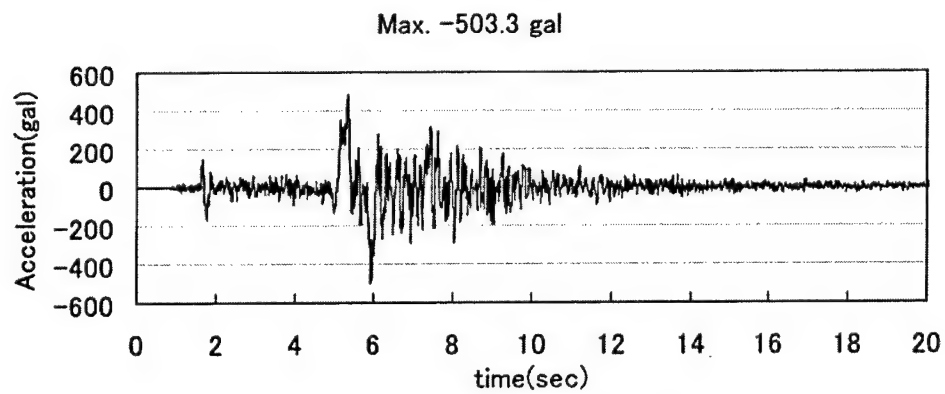
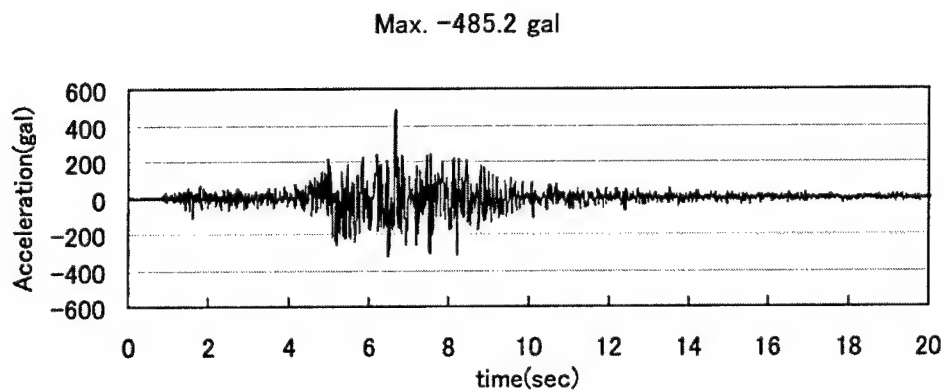


Figure 13 FEM Model

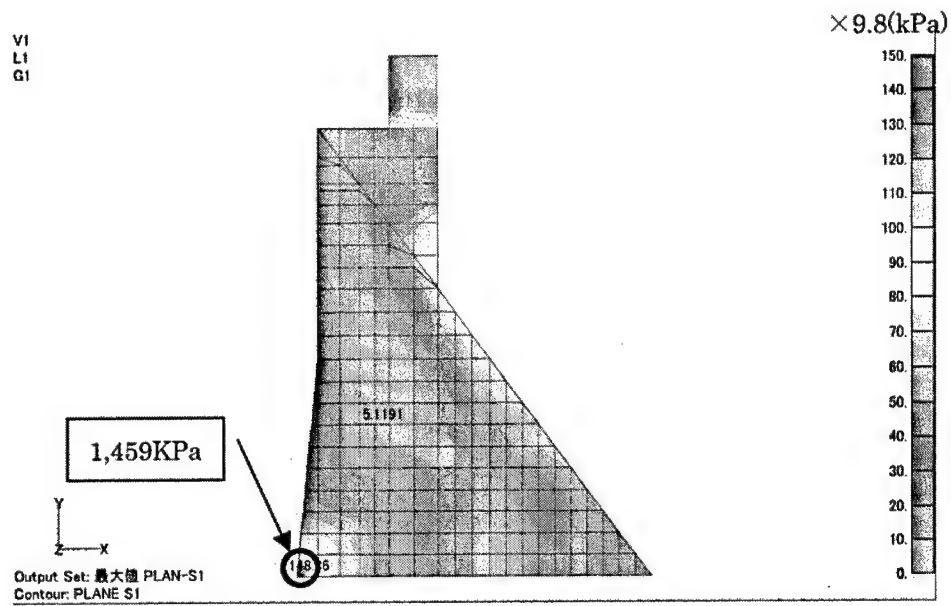


(a) River Flow Direction Component

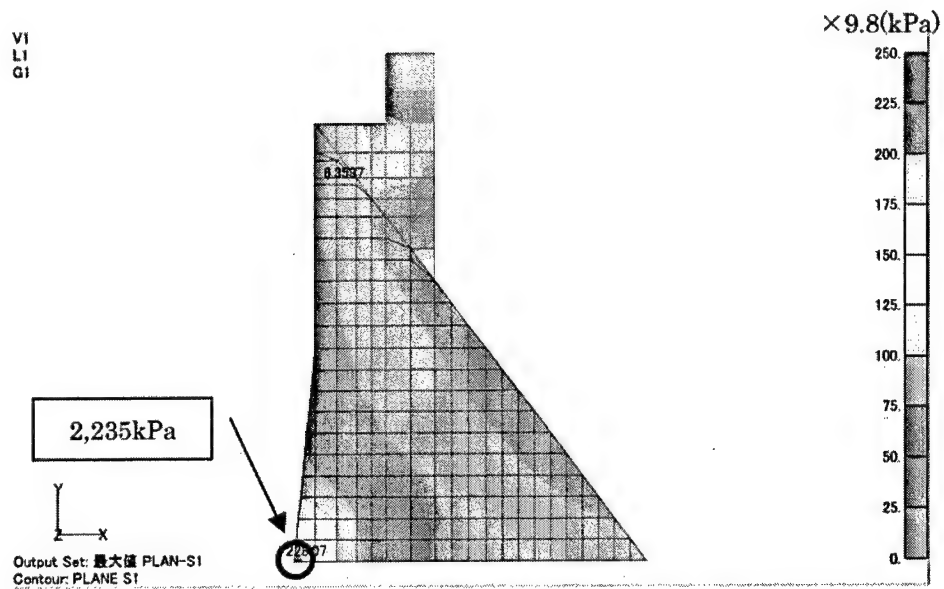


(b) Vertical Component

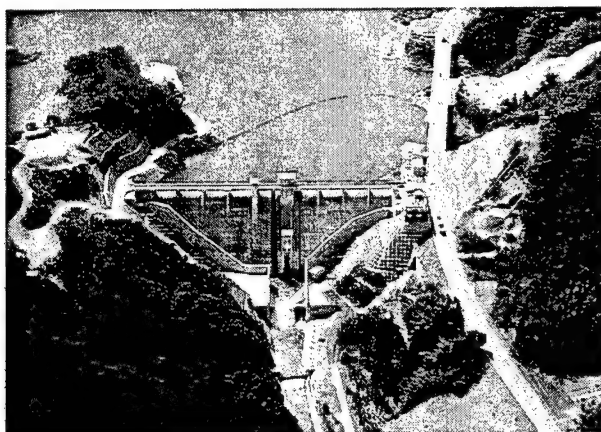
Figure 14 Horizontal and Vertical Inputted Seismic Waves



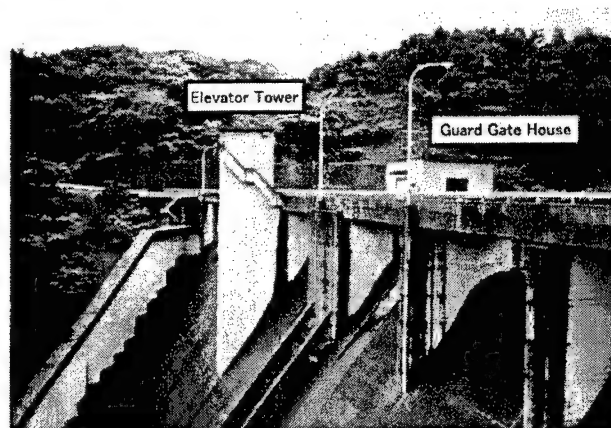
(a) On the Condition of the Water Level during the Earthquake



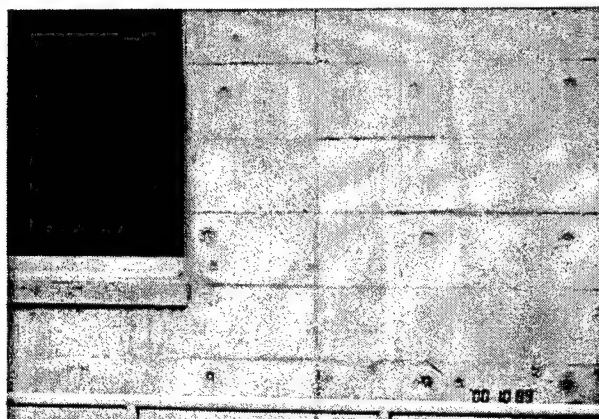
(b) On the Condition of the Normal Water Level  
Figure 15 Principal Stress (tensile side)



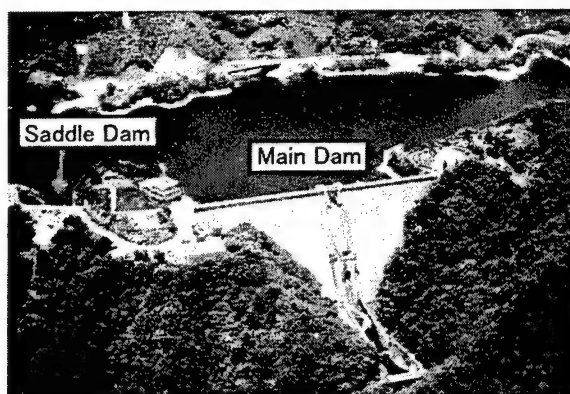
Photograph 1 View of Kasho Dam



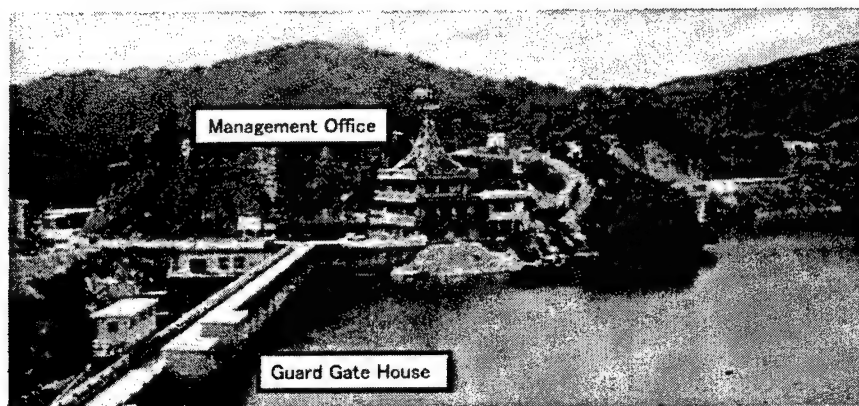
Photograph 2 Elevator Tower and Guard Gate House of Kasho Dam



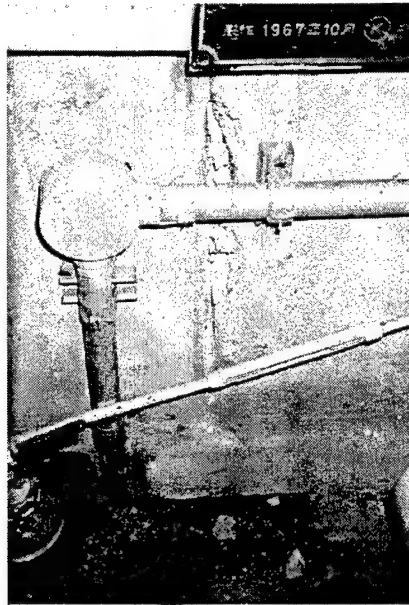
Photograph 3 An Example of Cracks on Wall of Guard Gate House of Kasho Dam (exterior wall surface on the right bank side)



Photograph 4 View of Sugesawa Dam



Photograph 5 Upstream Surface and Guard Gate House of Sugesawa Dam



Photograph 6 Cracking on Wall of Guard Gate House of Sugisawa Dam  
(interior wall surface on the downstream side)



Photograph 7 Chipped Concrete on  
Downstream Surface of Sugisawa Dam



Photograph 8 An Example of Cracks in Ground  
Near Sugisawa Dam  
(near the garage on the downstream right bank)



This page intentionally left blank.

## Development and Application of a Nonlinear Approach to the Analysis of Earthquake Performance of Dams

by

Zhi-Liang Wang<sup>1</sup>, Faiz I. Makdisi<sup>1</sup>, John Egan<sup>1</sup>

### ABSTRACT

The practice of evaluating the behavior of earth dams and embankments during earthquake shaking has evolved recently in the United States. The key element for such analyses is a comprehensive constitutive model that can simulate soil behavior under cyclic loading and liquefaction conditions. The capability of such a soil model (Wang et al., 1990) is summarized briefly before the focus shifts to applications. Recent improvements to the model are also introduced.

The second part of this paper describes our current practice in performing nonlinear, fully coupled dynamic analyses using the computer code FLAC incorporated with this constitutive soil model. The advantages of using a nonlinear approach are illustrated by comparison with results from the equivalent linear approach for a rockfill dam. The earthquake performance of a waterfront slope is evaluated to predict pore pressure generation and liquefaction in a sandy fill.

**KEYWORDS:** Earth dams, earthquake performance, nonlinearity of soils, plasticity model, liquefaction

### 1 INTRODUCTION

The state-of-practice for evaluating the seismic stability of earth dams was developed in the early and mid-1970s by the late Professor Seed and co-workers at the University of California at Berkeley (Seed et al., 1975). The basic elements of this analysis included the following steps: (a) earthquake ground motions are estimated at bedrock underlying the dam and its soil

foundation; (b) the response of the embankment to the base rock excitation is computed to estimate the dynamic stresses induced in representative elements of the embankment; (c) the cyclic strength of the embankment soils is evaluated using in situ tests and liquefaction resistance correlation curves based on observed performance during past earthquakes; (d) by comparing the dynamic induced shear stresses to the cyclic strength, the potential for liquefaction of the embankment and foundation soils is estimated; (e) for the zones of the embankment that are determined to have liquefied during the earthquake, a residual strength is assigned based on the density of the soil; (f) the stability of the embankment and its foundation is evaluated using limit equilibrium stability analyses; if the embankment is found to be stable, earthquake-induced permanent displacements are estimated using Newmark-type deformation analyses. In this procedure, the dynamic response of an embankment is estimated using an iterative equivalent linear approach (Seed and Idriss, 1970) to model the nonlinear strain-dependent modulus and damping properties of the soils. With this approach, however, the computed seismic response and shear stresses within embankment soils do not reflect the effects of induced pore pressure during earthquake shaking. The amount of induced pore pressure and the potential for liquefaction are estimated at the end of the specified duration of shaking.

In cases where an earth structure is subjected to severe ground motions, and where liquefaction may occur soon during shaking, an alternative approach to account for the effects of buildup of pore pressure and the potential for liquefaction during earthquake shaking is to use a nonlinear

<sup>1</sup> Geomatrix Consultants, Inc., 2101 Webster Street, 12th Floor, Oakland, CA 94612 (USA).

effective stress analysis. This paper describes a nonlinear, fully coupled dynamic analysis procedure for estimating the potential for buildup of pore pressure, the potential for liquefaction, and the resulting permanent deformation of earth structures. The basic elements for such analyses are: (1) an estimated site ground motion; (2) a constitutive model to simulate soil behavior under conditions of cyclic loading and liquefaction; (3) a computer program capable of performing dynamic analyses that are fully coupled (that include mechanical aspects and groundwater flow); and (4) relevant laboratory and in situ measurements of soil properties.

The procedure uses a nonlinear, bounding surface plasticity constitutive model for sand (Wang et al., 1990), incorporated into the finite-difference computer program FLAC (Itasca, 1998). Because the basis for such an analysis is a soil model, we will briefly introduce this model before shifting our focus to applications. Recent improvements to the model include: (1) a newly proposed state parameter, the state pressure index, and its use in defining a dilatancy curve; (2) simulation of the critical state behavior of sands; and (3) simulation of post-liquefaction deformation of sands. These new formulations are verified by comparing model simulations to laboratory test results.

This paper also introduces our current practice of using this bounding surface plasticity model, as incorporated into the computer program FLAC, to perform nonlinear, fully coupled dynamic analyses. The reliability of using FLAC is verified by comparison with results from other dynamic analysis programs. The advantages of using a nonlinear approach are illustrated based on comparison with results from an equivalent linear analysis for a rockfill dam. The earthquake performance of a waterfront slope is also evaluated to demonstrate the model's ability to simulate pore pressure generation and liquefaction in a sandy fill.

The procedures for using and calibrating the model and FLAC also are explained. The soil tests to support such analyses are generally similar to those currently used for equivalent linear

and simplified effective stress analyses. Given the increasing availability of high-speed personal computers, the newly formulated analytical methods are becoming more practical and attractive despite their theoretical sophistication.

## 2 BOUNDING SURFACE HYPOPLASTICITY MODEL FOR SAND

We will briefly introduce the basic features of the model and its capability to simulate sand behavior during monotonic and cyclic loading under drained and undrained conditions, focusing on the prediction of liquefaction. Then, we examine its advantages compared with using the Mohr-Coulomb or hyperbolic stress-strain relations.

### 2.1 Basic formulations

The general analytical formulation of the bounding surface hypoplasticity model for sand (Wang, 1990; Wang et al., 1990) was written in terms of tensors of stress rate and strain rate. The elastic and plastic strain rates are given as:

$$d\epsilon_{ij}^e = \frac{ds_{ij}}{2G} + \frac{dp\delta_{ij}}{3K} \quad (1)$$

$$d\epsilon_{ij}^p = \left( \frac{(n_D)_{ij}}{H_r} + \frac{\delta_{ij}}{3K_r} \right) p (dr_{kl}(n_N)_{kl}) + \left( \frac{r_{ij}}{H_p} + \frac{\delta_{ij}}{3K_p} \right) h(p - p_m) \langle dp \rangle \quad (2)$$

$G$  and  $K$  are the incremental elastic shear and bulk moduli, respectively.  $H_r$  and  $K_r$  are the plastic shear and bulk moduli, respectively, associated with the tensor of the stress ratio increment  $dr_{ij}$ . Similarly,  $H_p$  and  $K_p$  are the plastic shear and bulk moduli, respectively, associated with the mean pressure increment  $dp$ .  $n_D$  is a unit vector in stress space along the direction of the deviatoric plastic strain increment, and  $n_N$  is the associated direction of deviatoric unit loading.  $\delta_{ij}$  is a unit tensor along the  $p$  axis. Using  $J^2 = 0.5 s_{ij} s_{ij}$  and  $R = J/p$ , the failure surface ( $R - R_f g(\theta) = 0$ ) and the loading surface

( $R - R_m g(\theta) = 0$ ), as shown in Figures 1 and 2, are defined in the stress space  $J$ - $p$  with a shape function  $g(\theta)$  on  $p = \text{constant}$  plane ( $\theta$  is the Lode angle). A flat-cap surface,  $p - p_m = 0$ , is proposed for simulating consolidation and rebound. Because we will consider sand deformation under undrained conditions only and compare model simulations to a simple shear condition, for simplicity we assume that the flat cap is fixed (i.e.,  $p_m = p_{in}$ ) and  $g(\theta) = 1$ .

The elastic shear and bulk moduli are functions of  $p$ :

$$G = G_o p_a V(e) \sqrt{\frac{p}{p_a}} \quad (3)$$

in which  $V(e) = \frac{(2.973 - e)^2}{1 + e}$

$$K = p_a \frac{1 + e}{\kappa} \sqrt{\frac{p}{p_a}} \quad (4)$$

in which  $G_o$  and  $\kappa$  are model parameters that define the elastic moduli,  $e$  is void ratio, and  $p_a$  is atmospheric pressure.

The plastic modulus  $H_r$  for monotonic and cyclic loading is:

$$H_r = G h_r C(\xi) \left[ \frac{R_f}{R_m} \left( \frac{\bar{\rho}}{\rho} \right)^m - 1 \right] \quad (5)$$

where  $R = R_m$  is the maximum pre-stress bounding surface, and  $R = R_f$  is the failure bounding surface.  $\rho$  and  $\bar{\rho}$  are distances from the projection center (as shown in Figure 2) to the current stress and maximum pre-stress surfaces, respectively. Index  $m = (1 + g(\theta)) R_m / \bar{\rho}$  is state-dependent for irregular cyclic loading. For stress-controlled cyclic loading,  $m = 1$ , and the shear stress-shear strain relations derived based on Eqs. (3) and (5) conform to the well-known Masing rules.  $C(\xi)$  is a function of a hardening/softening measure; e.g., the accumulated plastic strain, volumetric and/or deviatoric.  $C(\xi)$

increases (during hardening) or decreases (during softening) with  $\xi$ .

The plastic volumetric strain rate is controlled by the plastic bulk modulus,  $K_r$ :

$$K_r = p_a \frac{1 + e}{w \kappa} \sqrt{\frac{p}{p_a}} \quad (6)$$

The variable  $w$  (for monotonic loading) will be introduced in the next section for the flow rule. For details of the model formulation for cyclic loading, readers are referred to the original publications.

## 2.2 Comparison with test results

This nonlinear, fully-coupled model has been used to simulate sand and silt behavior under various loading and saturation conditions (Wang, 1990). Yamada and Ishihara (1983) conducted extensive laboratory studies using a true triaxial device. They studied Fuji River sand under complex stress paths, as shown in Figure 3. All these test results were simulated using the model with one set of parameters. Comparisons of stress paths for three tests are presented in Figure 4. Towhata and Ishihara (1985) performed cyclic torsional shear tests for Toyoura sand. The model simulation and test results (for both the stress-strain relation and effective stress path) are compared in Figure 5. In these comparisons, the cyclic contractive and dilative behavior of the sand is well predicted by the model.

## 2.3 Comparison with other nonlinear models

Currently, two nonlinear soil models are used in the dynamic analysis of soil structures—the Mohr-Coulomb (or bilinear model), and the hyperbolic stress-strain formulation (Konder and Zelasko, 1963). Two parameters characterize these two models in the simple shear mode: the soil strength,  $\tau_m$ , and shear modulus,  $G_{max}$ . The hyperbolic stress strain relationship is defined by:

$$\tau = \frac{G_{\max} \gamma}{1 + \frac{G_{\max}}{\tau_m} \gamma} \quad (7)$$

It has an equivalent functional form as:

$$\begin{aligned} \gamma &= \tau / G \\ G / G_{\max} &= 1 - \tau / \tau_m \end{aligned} \quad (8)$$

in which  $G$  is the secant modulus and  $G/G_{\max}$  is the "modulus reduction curve."

Modulus reduction curves represent basic soil properties used for analyzing the dynamic response of soil structures. Seed and Idriss (1970) summarized laboratory tests and gave upper- and lower-bound curves for sands, as shown by the thin dashed lines in Figure 6. The thicker lines show modulus reduction curves based on the Mohr-Coulomb and hyperbolic models. For a given soil strength,  $\tau_m$ , and a shear modulus,  $G_{\max}$ , these modulus reduction curves are uniquely defined for each of the two models, as shown in Figure 6. These curves do not adequately match the ranges for sand presented by Seed and Idriss (1970). As commonly recognized, modulus reduction curves differ for different soils. Therefore it is desirable to provide constitutive models that can better fit the curves derived from the test data.

In the bounding surface hypoplasticity model, Eqs. (1) and (2) can be integrated under monotonic simple shear loading with  $p = \text{constant}$  condition. The analytical solution of the model for this loading condition is:

$$\begin{aligned} G / G_{\max} &= \left[ 1 - \frac{2\tau_m}{h_r \tau} \left( \ln \left( 1 - \frac{\tau}{\tau_m} \right) + \frac{\tau}{\tau_m} \right) \right]^{-1} \\ \gamma &= \tau / G \end{aligned} \quad (9)$$

in which  $h_r$  is a model parameter. The modulus reduction curve for this model is the first equation in Eq. (9), i.e.,  $G/G_{\max}$ .

For a given soil strength,  $\tau_m$  and shear modulus,  $G_{\max}$ , the modulus reduction curve (Eq. (9)) is a function of shear stress, and the function varies

with model parameter  $h_r$ , as shown in Figure 6. This parameter can be calibrated against a given soil modulus reduction curve to obtain a best fit. The capability of the model to fit specific modulus reduction curves enables a good comparison with results obtained using an equivalent linear model, except at large strain ranges (1 percent or higher), where the equivalent linear approach may unreasonably compute stresses that exceed the soil strength.

The original hyperbolic stress-strain relation represents nonlinear elasticity; i.e., it does not predict the volumetric changes induced by variation of shear stress variation. Several empirical formulations have been proposed to compute volumetric strains due to shear strain changes, such as (Byrne, 1991):

$$\Delta \varepsilon_{vd} = \gamma_a c_1 \exp(-c_2 \varepsilon_v / \gamma_a) \quad (10)$$

Based on this empirical equation, the volumetric strain increment per cycle is a function of the total accumulated volumetric strain,  $\varepsilon_v$ , and the amplitude of the shear strain cycle,  $\gamma_a$ . Although the relation considers the strain hardening from accumulated volumetric strain, it does not simulate the dilative behavior of sand within a cycle.

In the model of Wang (1990), the plastic volumetric strain increment (due to shear) is computed using an independently defined plastic bulk modulus— $K_r$  in Eq. (1). The ratio between the plastic bulk modulus,  $K_r$ , and plastic shear modulus,  $H_r$ , is identified (Wang et al., 2002) as:

$$\frac{d\varepsilon_v^p}{d\varepsilon_d^p} = \sqrt{\frac{3}{2}} \frac{H_r}{K_r} = \sqrt{\frac{3}{2}} \left( \frac{G h_r}{K k_r} \right) \left( \frac{p}{p_m} \right)^a \left( \frac{\eta}{M} \right)^b \left( \frac{M_p - \eta}{\eta} \right) \quad (11)$$

For a case in which model parameters  $a = 0$  and  $b = 1$ , it takes the following form:

$$d = \frac{d\varepsilon_v^p}{d\varepsilon_d^p} = A(M_p - \eta) \quad (12)$$

in which  $A$  is a constant, and  $\eta = q/p$  is the stress ratio. This is similar to the dilatancy equation first proposed by Rowe (1962) using the energy concept. In plasticity theory, the dilatancy  $d$  is

often called the "flow rule," because it is the ratio of plastic volumetric strain rate to the plastic deviatoric strain rate. It can be seen from Eqs. (11) or (12), if stress ratio  $\eta = q/p$  is greater than  $M_p$ , we have  $d\epsilon_v^p < 0$ , that is dilative behavior. Figure 7 is an example of computed volumetric strain under drained cyclic loading showing the contractive and dilative behavior of sand (Wang et al., 1990).

### 3 NONLINEAR, FULLY COUPLED DYNAMIC ANALYSES

The above is an effective stress based, fully nonlinear model that was implemented in the one-dimensional site response program SUMDES (Li et al., 1992), and the two-dimensional, large-deformation code FLAC (Itasca, 1998), to perform fully nonlinear, fully coupled dynamic analyses. We applied this approach to the following problems in geotechnical earthquake engineering: (1) seismic response analysis for a soft soil site subjected to very strong earthquake motions; (2) seismic stability analysis for soil-structure-foundation interaction involving liquefiable soils; (3) earthquake-induced deformation analysis of embankment and earth dams; and (4) estimates of periods for strength recovery and settlement in post-earthquake and post-liquefaction situations.

#### 3.1 Seismic site response using nonlinear approach

In current practice, the site response to a given earthquake input commonly is obtained using an equivalent linear approach. For low-level earthquake excitations (e.g., a peak acceleration of 0.1 g), the nonlinear and equivalent linear approaches produce essentially the same results (see Figure 8), when the model was calibrated using the same dynamic properties of soils, especially the modulus reduction curves described above. When the input motion was scaled-up to a peak acceleration of 0.56 g and applied at a depth of 6.4 m to a site having a soft clay layer at depth between 2.4 and 6.4 m, the results were different. The equivalent linear SHAKE analysis predicted a surface motion

having an amplified peak acceleration of 0.8 g, as shown in Figure 9. The nonlinear analysis based on Wang (1990) de-amplified the peak acceleration at the surface. In the nonlinear analysis a friction angle of 30 degrees was assumed for the soft clay layer. The equivalent linear approach, however, predicts shear stresses in the soft clay layer that exceed the shear strength of the layer. For instance, the ratio between peak shear stress and vertical confining pressure from the equivalent linear analysis reached 0.92 at a depth of 5.8 m.

#### 3.2 Simulation of liquefaction and post-liquefaction site response

We used records obtained from a downhole array at Port Island, Japan during the 1991 Kobe earthquake, to compute the site response and predict the observed liquefaction at this site (Wang et al., 2001b). The predicted liquefaction in the top 20 m of fill is shown in Figure 10. The computed surface acceleration time histories match the recordings reasonably well for both pre- and post-liquefaction periods, as shown in Figure 11.

#### 3.3 Predicting deformation using nonlinear models

We now will discuss using the fully nonlinear model to predict deformation. Given an infinite slope surface, the static stresses can be expressed by an element of soil having a non-zero initial shear stress (and normal stresses). Under a sinusoidal cyclic shear stress loading, the initial shear stress renders the cyclic stress strain loops asymmetric, and shear deformation accumulates during each successive cycle, as shown in Figure 12. If the soil element is saturated, pore water pressure may generate, resulting in a reduction of effective stress. Because the elastic shear modulus of the soil (Eq. (3)) is a function of the effective mean pressure, the shear modulus also will decrease. Thus, the accumulated deformation will be much greater, as shown by the dashed line in Figure 12. Incorporating the step-by-step degradation of modulus due to pore water pressure generation is

often called “fully-coupled” effective stress analysis.

### 3.4 Post-earthquake and post-liquefaction settlement and strength recovery

The seismic stability of an offshore structure foundation was analyzed given design earthquakes. A silty sand layer (No. 2 in Figure 13) except for the area directly beneath the foundation, was computed as liquefied. After the earthquake shaking, the effective stresses at locations A, B, and C (in Figure 14, A and B are located beneath the foundation) increase due to dissipation of pore water pressure. This analysis was performed to resolve a concern that the structure could become unstable if storm loading occurred after an earthquake had softened the sand layer, and before enough time had passed for the excess pore pressures to dissipate.

## 4 RECENT DEVELOPMENTS IN THE CONSTITUTIVE MODEL FOR SAND

Laboratory tests on Toyoura sand (Verdugo and Ishihara, 1996) show that sand behavior under large shear deformations can be well represented by the concept of critical state. Applications of critical-state soil mechanics to the constitutive model of sand have gained wide acceptance in geotechnical engineering. The critical state line for Toyoura sand is shown in Figure 15. To simulate the behavior of sand at the critical state, the phase transformation stress ratio originally proposed by Ishihara et al. (1975), was revised as a curved dilatancy line (Wang et al., 2002) that passes through the critical state (as shown in Figure 16). This line is defined using a “state pressure index,”  $I_p = \frac{p}{p_c}$ . Here  $p_c$  is the mean pressure at the critical state corresponding to the current void ratio.

In Figure 16 the dilatancy line is defined as:

$$q = M_d p = \left\{ M_o + (M - M_o) \frac{p}{p_c} \right\} p \quad (13)$$

Using this state-dependent dilatancy line to replace the phase transformation line (a straight line in Figure 1), the model can simulate the behavior of Toyoura sand at critical state using a unique set of parameters for different void ratios consolidated at different confining pressures. A model simulation is compared with test results in Figure 17.

Another improvement to the model of Wang (1990) is the ability to simulate post-liquefaction deformation. Recent laboratory tests (Kamerrer, 2001, personal communication) demonstrate that shear deformation develops continuously following initial liquefaction, in sands subjected to cyclic loading. The effective stress paths after liquefaction repeat dilative and contractive behaviors that are similar in each cycle, but the corresponding shear strain amplitude increases continuously. Wang and Dafalias (2002) proposed a strain-history dependence of plastic shear modulus and used an intrinsic variable to capture the reduction in the plastic shear modulus. The reduction factor from Eq. (5) is:

$$C(\xi) = \frac{1 + \xi}{1 + \alpha \xi} \quad (13)$$

and the intrinsic variable is the accumulated plastic deviatoric strain:

$$\xi = \int \sqrt{2 de_{ij}^p de_{ij}^p} \quad (14)$$

Recent results of simple shear tests for post-liquefaction deformation of Nevada sand were simulated using the model and the above Eq. (14), as shown in Figure 18.

## 5 EXAMPLES

In this section we describe applications of the above non-linear approach to evaluating the seismic stability of a rockfill dam and the performance of a waterfront slope (berth) during the Loma Prieta earthquake.



## 5.1 New Exchequer Dam

New Exchequer Dam, located on the Merced River east of Merced, California, is a 150 m high, concrete-faced, rockfill dam that impounds Lake McClure, providing a gross storage capacity of one million acre-feet at normal maximum reservoir level. The crest length is 426.7 m. The volume of rockfill is four million cubic meters. Both upstream and downstream slopes are 1.4H to 1.0V. The dam sits in a deep, relatively narrow canyon eroded in highly competent, meta-andesite rock, and all rockfill was placed on a fully stripped foundation. The seismic stability of the dam was evaluated for potential earthquake ground motions from a maximum magnitude,  $M_w$  6.5 earthquake on the Bear Mountains fault, about 1/2 km from the site. Estimated median peak horizontal accelerations at the site exceeded 0.5 g. The dam was analyzed using both equivalent linear and nonlinear approaches.

Two-dimensional dynamic finite element analyses were performed using the computer program QUAD4M (Hudson et al., 1994) for the maximum cross section of the dam (Figure 19). The variation of shear modulus and damping ratio with shear strain is shown in Figure 20. Details of this analyses are presented in Makdisi et al. (2000). Dynamic finite element analyses provide the distribution of peak accelerations within the embankment and seismic coefficient time histories within potential sliding masses for estimating permanent slope deformation. Slope stability analyses were performed to estimate factors of safety and yield accelerations,  $k_y$ , for potential sliding surfaces within the upstream and downstream slopes of the embankment. Permanent deformations were estimated using the concept of yield acceleration proposed by Newmark (1965) and modified by Makdisi and Seed (1978). The computed peak horizontal acceleration at the crest of the dam was about 0.85 g, and the greatest amplification occurred in the upper 12.2 m of the embankment. The greatest estimated earthquake-induced permanent deformation (about 18.3 cm) was for a potential "shallow" sliding surface within the upper one-fourth of the downstream slope.

The response of New Exchequer Dam also was evaluated using nonlinear analyses employing the bounding surface hypoplasticity model incorporated into the finite difference program FLAC.

Six parameters are required in dynamic response analyses that utilize the bounding surface hypoplasticity model. Three of these parameters ( $\phi$ ,  $G_o$ , and  $h_r$ ) can be estimated from parameters used in the equivalent linear analysis.  $\phi$  is the Mohr-Coulomb friction angle;  $G_o$  is related to  $K_{2max}$ ; and  $h_r$  is a model parameter that characterizes the relationship between shear modulus and shear strain. The model parameter  $h_r$  for each material zone was calibrated to provide modulus and damping relationships with shear strain similar to those used in the equivalent linear analysis (Figure 20).

The response of the maximum section of the dam was computed using the same input acceleration time history as used for the equivalent linear analysis. For simplicity the rock base was assumed rigid. This assumption may have resulted in higher computed accelerations compared to those from the equivalent linear analysis, which treated the bedrock base as an elastic half-space. The nonlinear analysis provides the time history of acceleration and displacement at any location within the embankment, as well as contours of horizontal and vertical displacement at the end of earthquake shaking. Figure 21 shows the time history of computed acceleration at the crest of the dam, along with the acceleration time history computed from the equivalent linear analysis. The computed maximum crest acceleration from the nonlinear analysis is about 1.1 g, compared to 0.85 g from the equivalent linear approach. The phases of the two time histories are in reasonable agreement.

Time histories of horizontal and vertical displacements at the crest of the embankment are presented in Figure 22. Computed peak horizontal displacements at the crest of the embankment were less than 61 cm in the downstream direction; computed vertical settlements were about 36.6 cm. Contours of computed horizontal and

vertical displacements throughout the embankment at the end of earthquake shaking are shown in Figure 23. The maximum horizontal displacements at the end of earthquake shaking (within the upper one-fourth of the downstream slope) were about 46 cm. The corresponding maximum vertical settlements at the crest were about 37 cm. The estimated permanent displacements from the equivalent linear analyses were less than 30 cm.

## 5.2 Port of Oakland Berth 40

Following the 1989  $M_w$  7 Loma Prieta earthquake in California, significant damage was observed at the site of the Port of Oakland's Seventh Street Marine Terminal (Egan et al., 1992). Damage included a slope failure along part of a dike near the southwest corner of the terminal; damage to battered, pre-stressed concrete piles in the wharf structure; settlement as great as 0.3 m of the landside crane rail; numerous cracks in the pavement in the yard area; and movement of some of the armor stone slope protection on the face of the dike. Other earthquake effects at the site included sand boils, cracks at the ground surface in unpaved areas near the dike, and lateral and vertical displacement as great as 0.3 m between the ground surface and adjacent pile-supported structures along the dike. The level of ground shaking recorded at a ground motion instrument within 2 km of the site was about 0.28 g.

The observed behavior of a typical profile at Berth 40 without the wharf structure (shown in Figure 24) during the Loma Prieta earthquake was simulated using the fully coupled, nonlinear effective stress analysis described here.

Construction records of the berth at this site indicate that after soft mud was dredged from beneath the dike area, dredged sand fill was hydraulically placed by bottom-dump barges up to the elevation of the original mud line. A small rock toe dike was constructed on top of the first sand lift. After construction of the rock toe dike, a second sand lift was placed to the elevation of the top of the toe dike. Rock spoil material was then placed by end-dumping from trucks.

Compacted sand fill was later placed on top of the rock spoil. Materials used to create the terminal yard area behind the perimeter dike are believed to consist primarily of hydraulically placed dredged sand.

A finite difference model of the wharf embankment profile is presented in Figure 25. Dynamic model parameters (maximum shear modulus and the variation of modulus and damping ratio with shear strain) were developed based on soil properties used in equivalent linear analyses. Cyclic strength model parameters were calibrated based on in situ Standard Penetration Test data (converted to  $(N_1)_{60}$ ) and the observed occurrence of liquefaction during past earthquakes. Such cyclic strength curves, shown in Figure 26, are based on the liquefaction chart of Seed et al. (1985), the magnitude scaling factors reported in Youd and Idriss (1997), and the magnitude vs. equivalent number of cycles relationship of Seed and Idriss (1982). The dashed lines in Figure 26 show the cyclic strength curves from the field data; the solid curves were predicted based on calibrated model parameters. Details of the model parameters used in the analysis are described in Wang et al. (2001a). The input ground motion used in the analysis was based on the recording from the strong motion instrument near the site. The time history recorded at the ground surface was deconvolved to compute an interface motion at the top of the stiff old clay (bay mud) layer underlying the site at a depth of about 20 m.

The analysis was performed first for the free-field zone (i.e., a one-dimensional column) representing areas away from the crest of the slope. Three layers (A, B, and C in Figure 25) located at the bottom, middle, and top of the submerged sand fill were selected to show the computed decrease in mean effective stress, the effective stress path, and the shear stress vs. shear strain variation during earthquake shaking. Figure 27 shows that the computed effective mean stress in layers A and B dropped to its lowest level after 15 seconds of shaking, indicating the occurrence of liquefaction. In contrast, the top layer, C, did not reach full liquefaction, because the

underlying layers A and B had already liquefied and fully softened, and thus could not transmit the strong shaking to the soil above. However, this layer also was softened by the significant reduction in effective stress. Figures 28a and 28b show the relationships between the shear stress and effective mean stress, as well as shear strain computed for layer B, using the bounding surface model.

Similar responses were computed for zones near the slope (locations D, E, and F in Figure 25). The effective stress time histories (Figure 29) show that the sand fill near the rock toe dike (zone F) had liquefied, while the sand fill under beneath the crest (zone D) experienced dilative behavior after initial liquefaction. The rock spoil portion (zone E) did not liquefy.

The computed time histories of displacement, both horizontal and vertical, at the crest are shown in Figure 30. The base displacement is shown as a reference for the crest movements. The computed deformed shape of the slope at the end of earthquake shaking is shown in Figure 31. The greatest displacement values (about 0.5 m) were those developed at the rock toe below the water surface. The horizontal displacement at the crest was computed to be about 37 cm. The computed settlement at the crests was about 24 cm. These computed deformations are consistent with those observed during the Loma Prieta earthquake.

## 6 CONCLUSIONS

A nonlinear approach is developed and applied to seismic stability and deformation analyses of embankments and dams that may experience strong earthquake shaking. The key element for performing such analyses is a constitutive model capable of simulating soil behavior under cyclic loading. The model's capability is demonstrated in comparison with both laboratory tests and other commonly used nonlinear models.

The advantages of using a nonlinear approach are illustrated using results for the seismic deformation analysis of New Exchequer Dam. The

earthquake performance of a waterfront slope is evaluated to demonstrate the model's ability to simulate pore pressure generation and liquefaction in a sandy fill.

Because the soil properties needed to support such analyses are generally similar to those currently used for performing equivalent linear and simplified effective stress analyses, considering the increasing availability of high-speed personal computers, the above analyses are becoming more practical and attractive.

## 7 References

- Byrne, P. M., (1991), "A Cyclic Shear-Volume Coupling and Pore Pressure Model for Sand," Proceedings, 2<sup>nd</sup> International Conference on Recent Advances in Geotechnical Earthquake Engineering and Soil Dynamics, University of Missouri at Rolla, USA, March 11-15, Vol. I, pp. 47-56.
- Egan, J. A., Hayden, R. F., Scheibel, L. L., Otus, M., and Serventi, G. M., (1992), "Seismic repair at Seventh Street Marine Terminal", in Proceedings, Grouting, Soil Improvement and Geosynthetics: v2, pp. 867-878, Eds. Borden/Holtz/Juran. ASCE, Geotechnical Special Publication No. 30.
- Hudson, M., Idriss, I. M., and Beikae, M., (1994), "User's Manual for QUAD4M: a Computer Program to Evaluate the Seismic Response of Soil Structures using Finite Element Procedures and Incorporating a Compliant Base," Center for Geotechnical Modeling, University of California, Davis, USA.
- Ishiraha, K., Tatsuoka, F., and Yasuda, S., (1975), "Undrained Deformation and Liquefaction of Sand under Cyclic Stress," Soils and Foundations, Vol. 15, No. 1, pp. 29-44.
- Itasca Consulting Group, Inc., (1998), "FLAC - Fast Lagrangian Analysis of Continua, Version 3.40 User's Manual," Minneapolis, Minnesota, USA.

- Konder, R. L., and Zelasko, J. S., (1963), "A Hyperbolic Stress-Strain Formulation for Sands," *Proceedings, 2<sup>nd</sup> Pan American Conference on Soil Mechanics and Foundation Engineering*, pp. 289-324.
- Li, X. S., Wang, Z. L., and Shen, C. K., (1992), "SUMDES: A Nonlinear Procedure for Response Analysis of Horizontally Layered Sites Subjected to Multi-Directional Earthquake Loading," *Department of Civil Engineering, University of California at Davis, USA*.
- Makdisi, F. I., and Seed, H. B., (1978), "Simplified Procedure for Estimating Dam and Embankment Earthquake-Induced Deformation," *Journal of Geotechnical Engineering Division, ASCE*, Vol. 104, No. GT7, July, pp. 849-867.
- Makdisi, F. I., Wang, Z. L., and Edwards, W. D., (2000), "Seismic Stability of New Exchequer Dam and Gated Spillway," *Twentieth Annual USCOLD Lecture Series, Seattle, Washington, USA*, pp. 437-458.
- Newmark, (1965), "Effects of Earthquakes on Dams and Embankments," *Geotechnique, Institution of Civil Engineers, London, England*, Vol. XV, No. 2, June.
- Rowe, P. W., (1962), "The Stress-Dilatancy Relation for Static Equilibrium of an Assembly of Particles in Contact," *Proceedings of the Royal Society of London, Series A* 269, pp. 500-527.
- Seed, H. B., and Idriss, I. M., (1970), "Soil Moduli and Damping Factors for Dynamic Response Analyses," *Earthquake Engineering Research Center, University of California, Berkeley, Report No. EERC 79-10*.
- Seed, H. B., and Idriss, I. M., (1982), "Ground Motion and Soil Liquefaction During Earthquakes," *Monograph Series, Earthquake Engineering Research Institute, University of California, Berkeley, California*.
- Seed, H. B., Lee, K. L., Idriss, I. M., and Makdisi, F. I., (1975), "The Slides in the San Fernando Dams During the Earthquake of February 9, 1971," *Journal of Geotechnical Engineering Division, ASCE*, Vol. 101, No. GT7, pp. 651-688.
- Seed, H. B., Tokimatsu, K., Harder, L. F., and Chung, R., (1985), "Influence of SPT Procedures in Soil Liquefaction Resistance Evaluations," *Journal of Geotechnical Engineering Division, ASCE*, Vol. 111, No. 12.
- Towhata, I., and Ishihara, K., (1985), "Undrained Strength of Sand Undergoing Cyclic Rotation of Principal Stress Axes," *Soils and Foundations*, Vol. 25, No. 2, pp. 135-147.
- Verdugo, R., and Ishihara, K. (1996). "The Steady State of Sandy Soils," *Soils and Foundations*, Vol. 36, No. 2, pp. 81-91.
- Wang, Z. L., Dafalias, Y. F., and Shen, C. K., (1987), "Simulation and Prediction of Sand Behavior Using the Bounding Surface Hypoplasticity Model," *Proceedings: International Workshop on the Constitutive Equations for Granular Non-Cohesive Soils, Cleveland, Ohio, USA*.
- Wang, Z. L., (1990), "Bounding Surface Hypoplasticity Model for Granular Soils and its Applications," *Ph.D. Dissertation, University of California at Davis, U.M.I. Dissertation Information Service, Order No. 9110679, Ann Arbor, Michigan, USA 48106*.
- Wang, Z. L., Dafalias, Y. F., and Shen, C. K., (1990), "Bounding Surface Hypoplasticity Model for Sand," *ASCE, Journal of Engineering Mechanics*, Vol. 116, No. 5, pp. 983-1001.
- Wang, Z. L., and Makdisi, F. I., (1999), "Implementing a Bounding Surface Hypoplasticity Model for Sand into the FLAC Program," *Proceedings: International Symposium on Numerical Modeling in Geomechanics, Minnesota, USA*, pp. 483-490.
- Wang, Z. L., Egan, J., Scheibel, L., and Makdisi, F. I., (2001a), "Simulation of Earthquake Performance of a Waterfront Slope using Fully

Coupled Effective Stress Approach," FLAC and Numerical Modeling in Geomechanics, Proceedings of the Second International FLAC Symposium, Lyon, France.

Wang, Z. L., Chang, C. Y., and Mok, C. M., (2001b), "Evaluation of a Site Response Using Downhole Array Data from a Liquefied Site," Third International Conference on Recent Advances in Geotechnical Earthquake Engineering and Soil Dynamics, San Diego, California, USA, Paper No. 4.30.

Wang, Z. L., Dafalias, Y. F., Li, X. S., and Makdisi, F. I., (2002), "State Pressure Index for Modeling Sand Behavior," Journal of Geotechnical and Geoenvironmental Engineering, Vol. 128, No. 6, pp. 511-519.

Wang, Z. L. and Dafalias, Y. F., (2002), "Simulation of Post-liquefaction Deformation of Sand," Paper No. 183, ASCE 15<sup>th</sup> Engineering Mechanics Conference, Columbia University, New York, NY, USA.

Yamada, Y. and Ishihara, K., (1983), "Undrained Deformation Characteristics of Sand in Multi-Directional Shear," Soils and Foundations, Vol. 23, No. 1, pp. 61-79.

Youd, T. L., and Idriss, I. M. (eds.), 1997, Summary Reports, in Proceedings of NCEER Workshop on Evaluation of Liquefaction Resistance of Soils: National Center for Earthquake Engineering Research, Technical Report NCEER-97-0022, December 31.

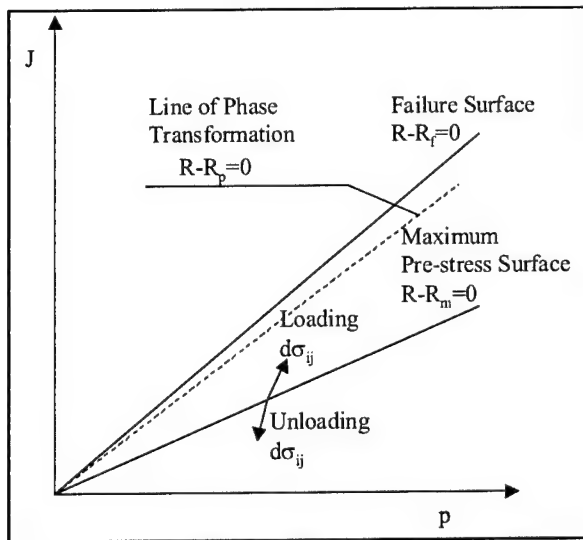


**Figure 1.** Surfaces and stress variables in J-p plane

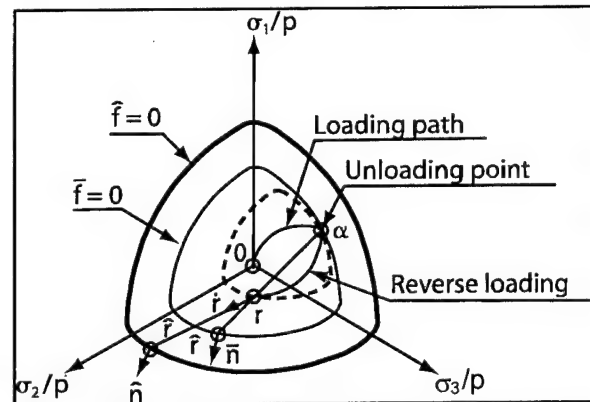


**Figure 2.** Surfaces and stress variables in  $p = \text{constant}$  plane

NAME	MONOTONIC	CYCLIC	CRISSCROSSING
STRESS PATH			
NAME	ELLIPTIC	ROTATIONAL SHEAR	
		CIRCULAR	ORIENTATIONAL
STRESS PATH			

**Figure 3.** Patterns of true triaxial stress paths tested by Yamada and Ishihara (1983)

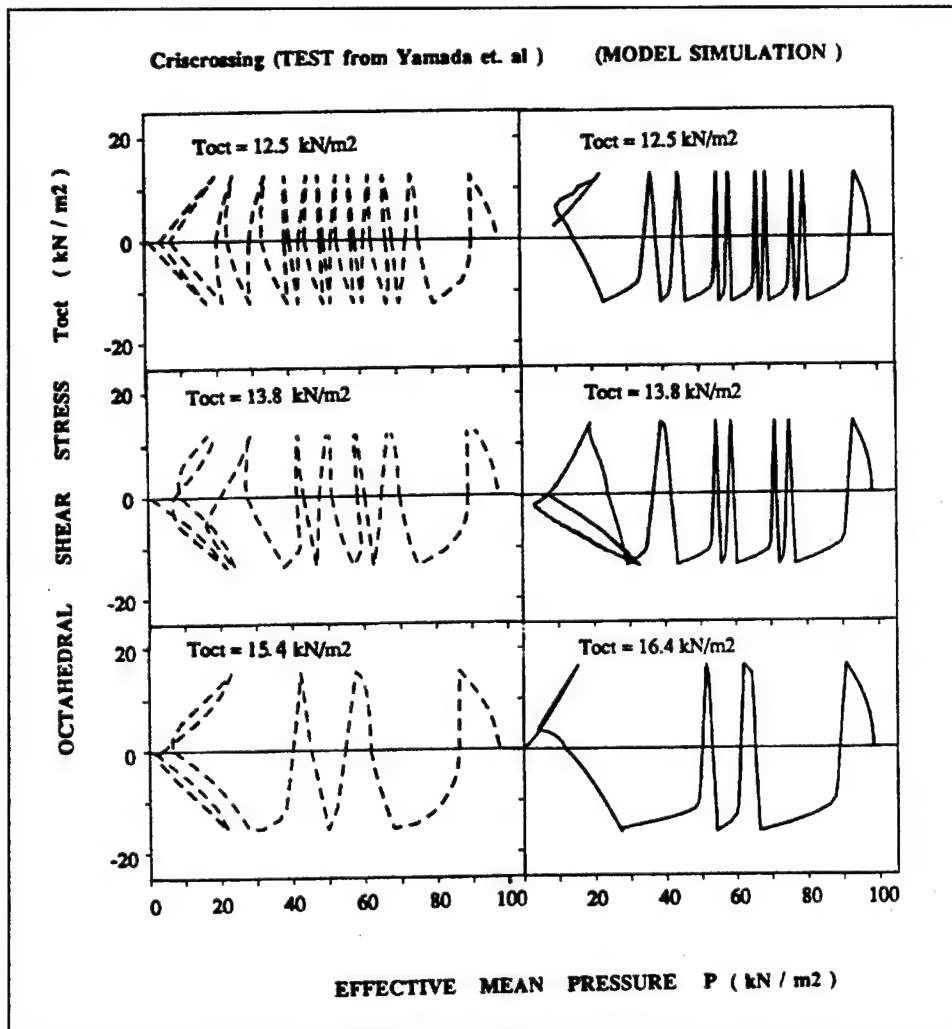


**Figure 4.** Comparison of model simulations and true triaxial test results of effective stress under undrained criss-crossing path



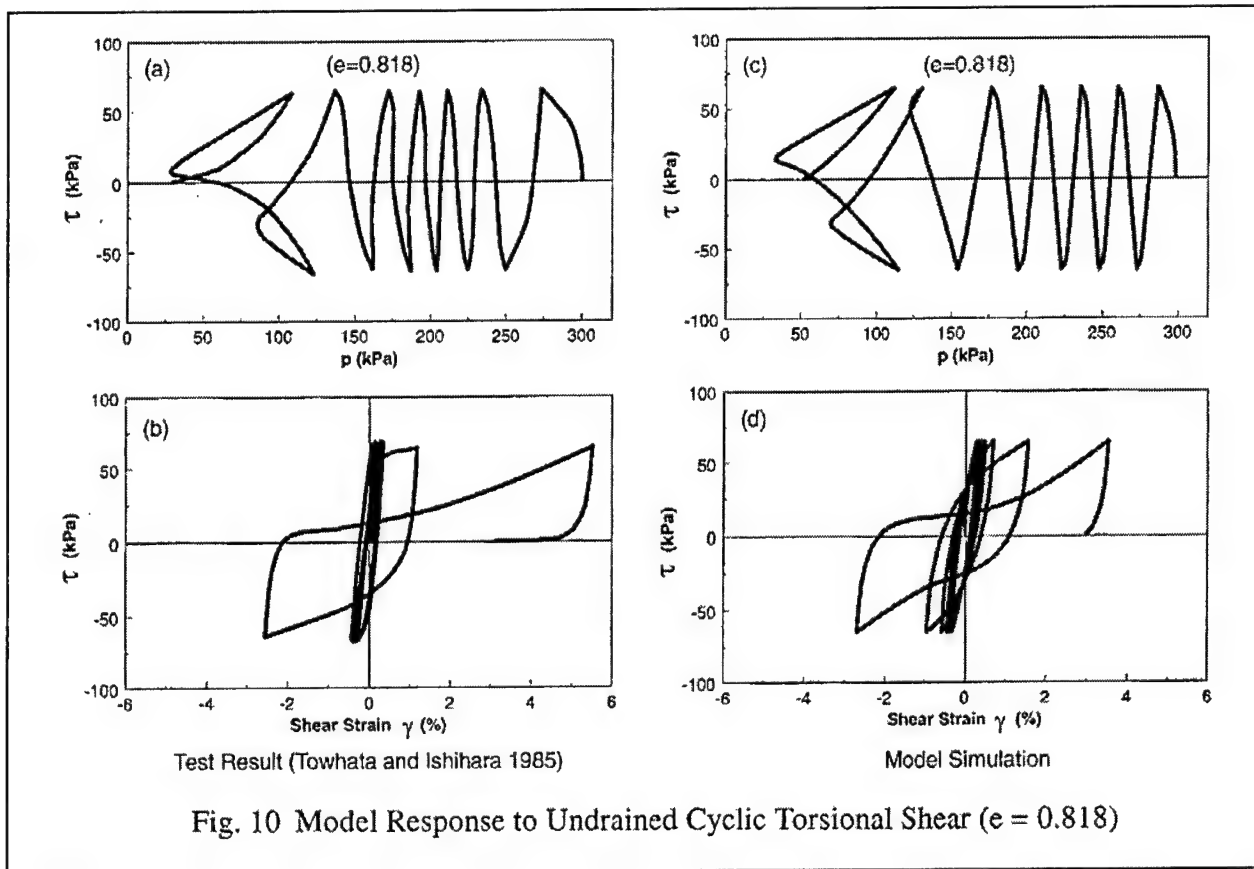


**Figure 5.** Comparison of model simulations and undrained cyclic torsional shear test results

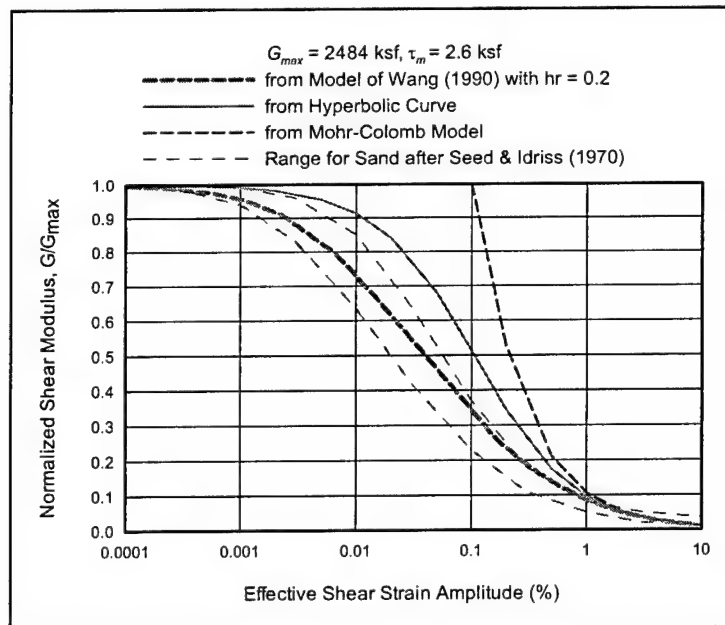


**Figure 6.** Comparison of modulus reduction curves from nonlinear models

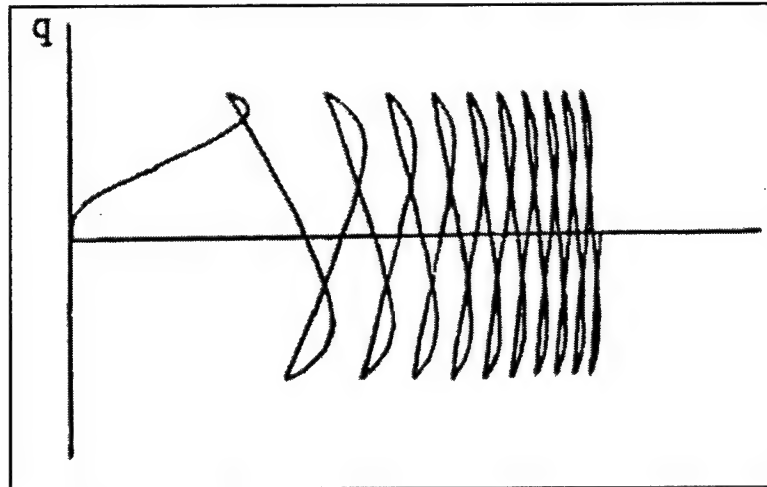


**Figure 7.** Model simulation for volumetric strain under cyclic drained shear loading

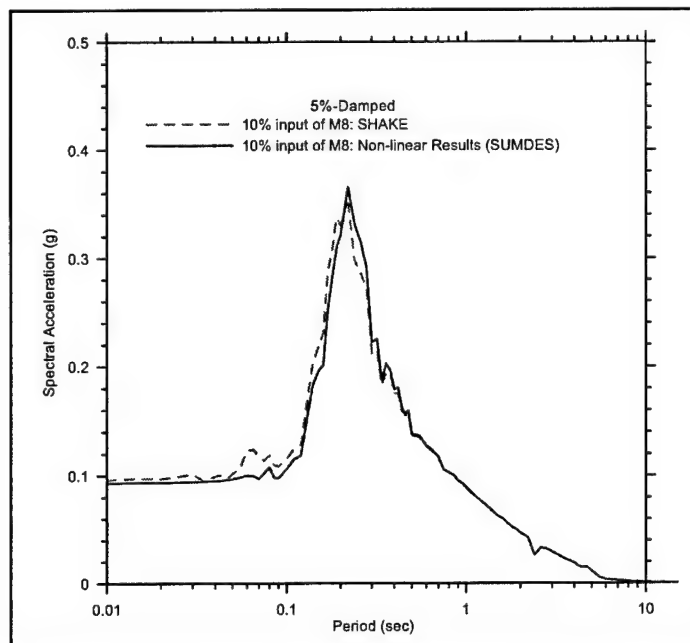


**Figure 8.** Comparison of response spectra at site surface using 10 percent of input motion (M8 event)

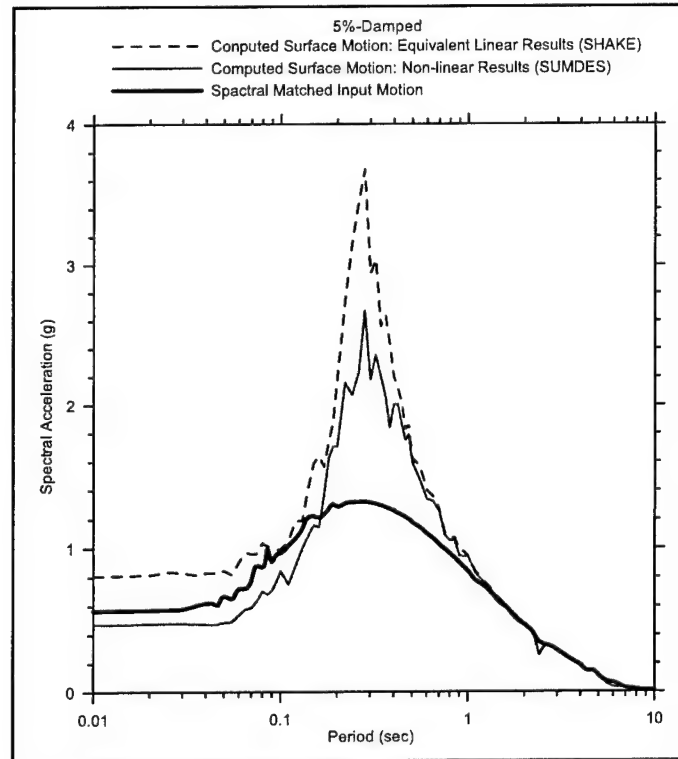


**Figure 9.** Comparison of response spectra at site surface and input motion (M8 event)

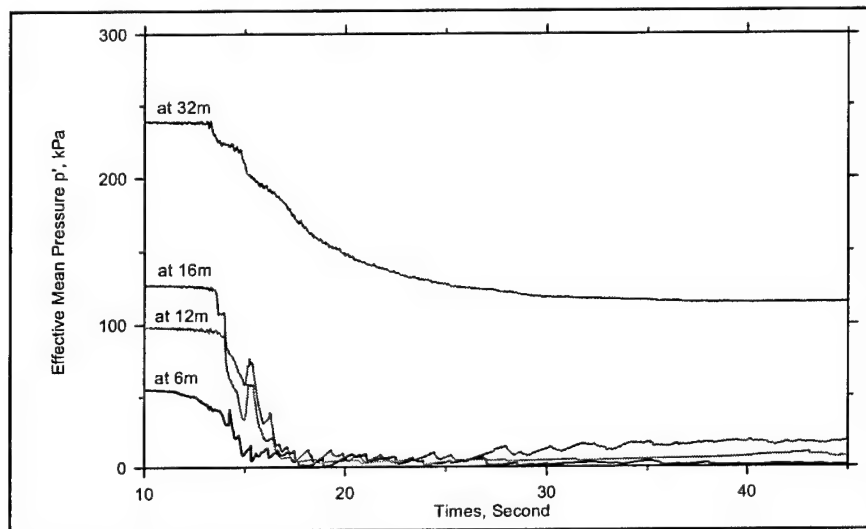


**Figure 10.** Computed time histories of effective mean pressure at Port of Island during Kobe earthquake

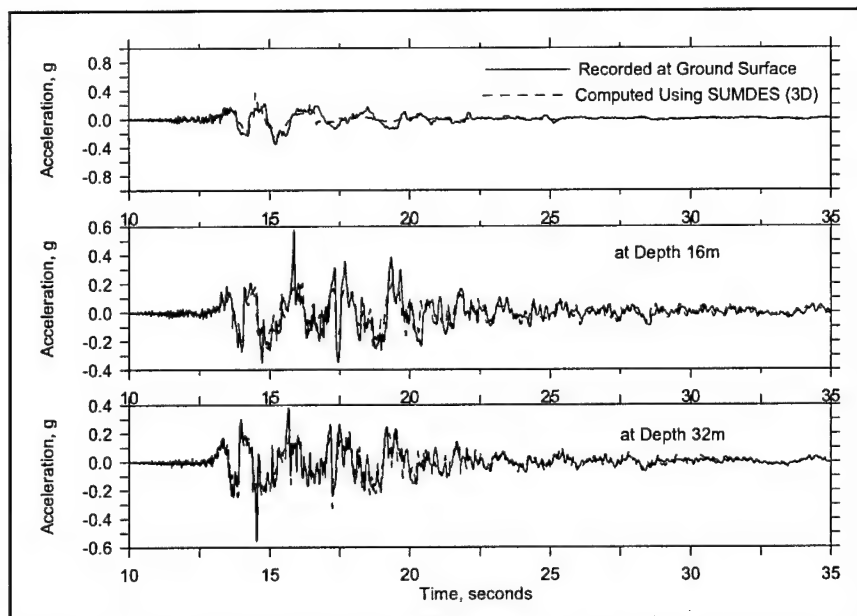


**Figure 11.** Comparison of recorded and computed acceleration time histories, N00E component at Port of Island

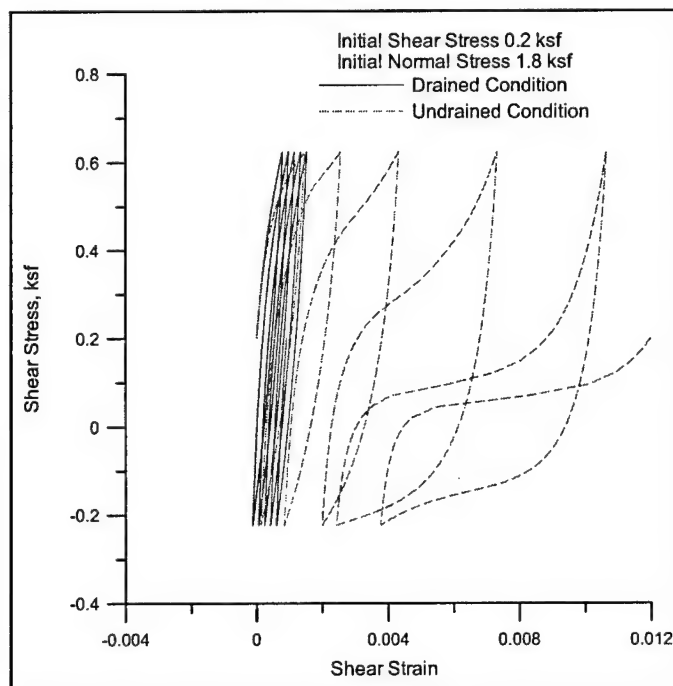


**Figure 12.** Model simulation for sand with initial shear stress under cyclic loading

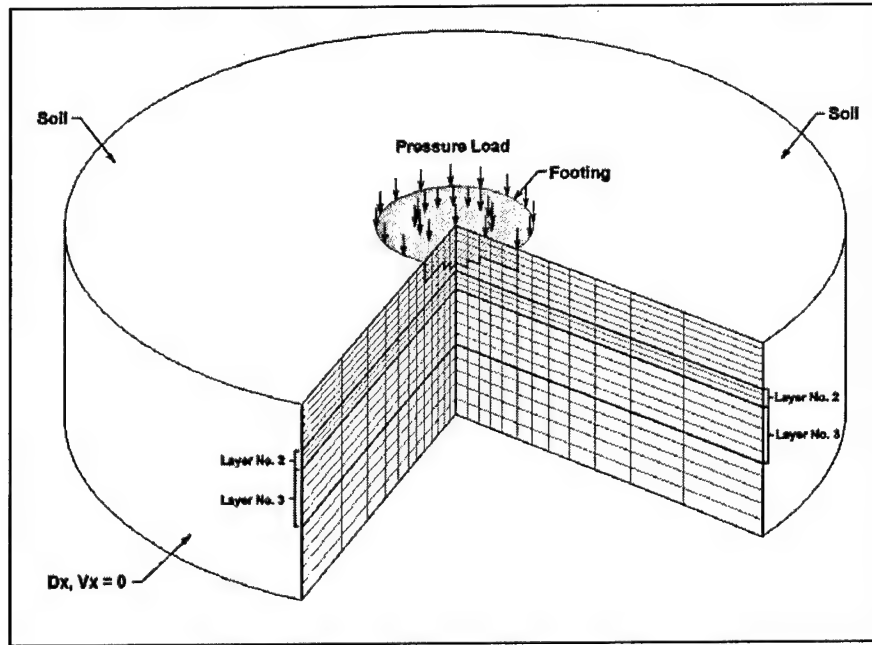


**Figure 13.** Grid and boundary conditions for axis-symmetric analysis using FLAC

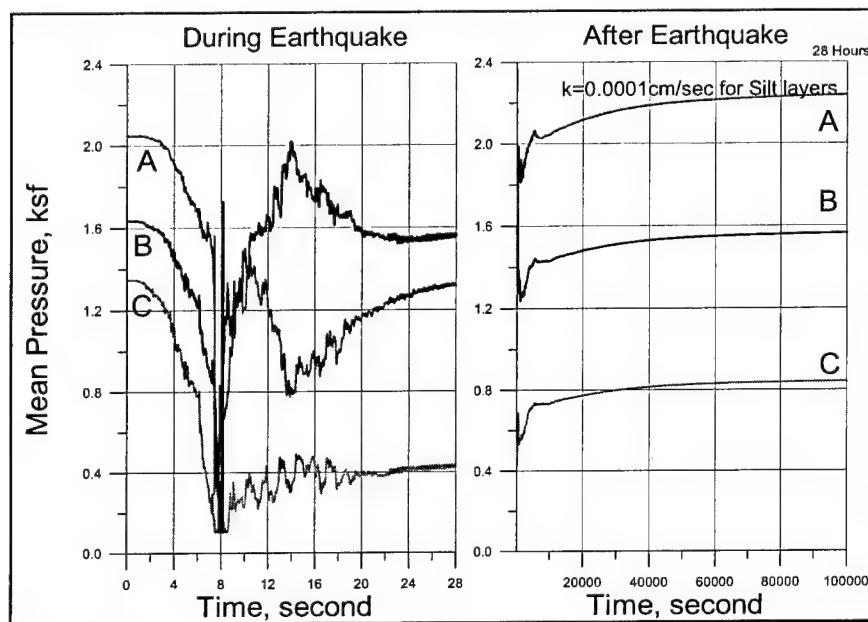


**Figure 14.** Computed times histories of mean pressure during and after earthquake

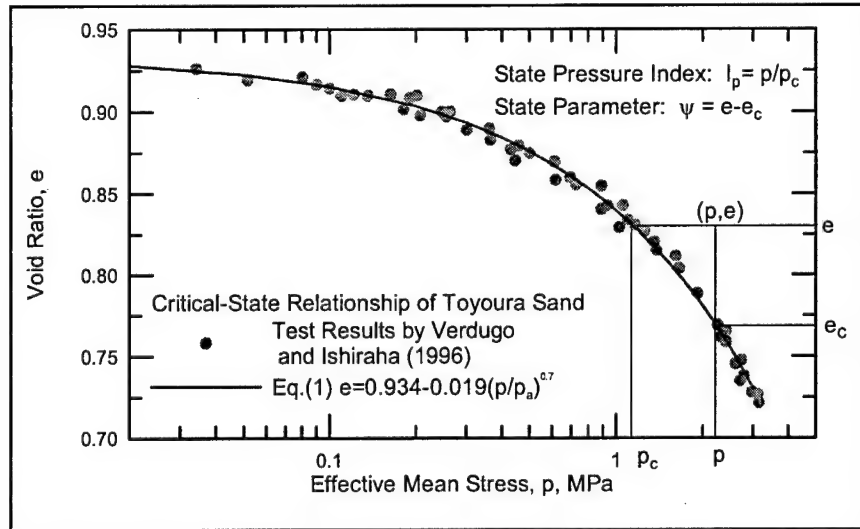


**Figure 15.** Critical-state line of Toyoura Sand (after Verdugo and Ishihara, 1996)

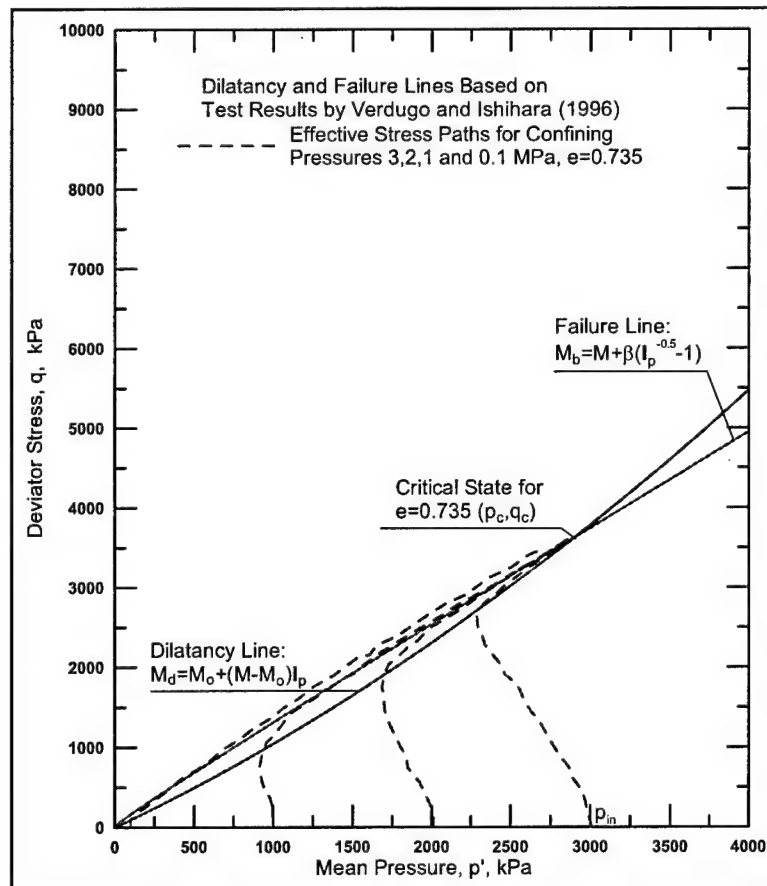


**Figure 16.** Dilatancy and failure lines as a function of  $I_p$  for  $e = 0.735$  (after Wang et al., 2002a)

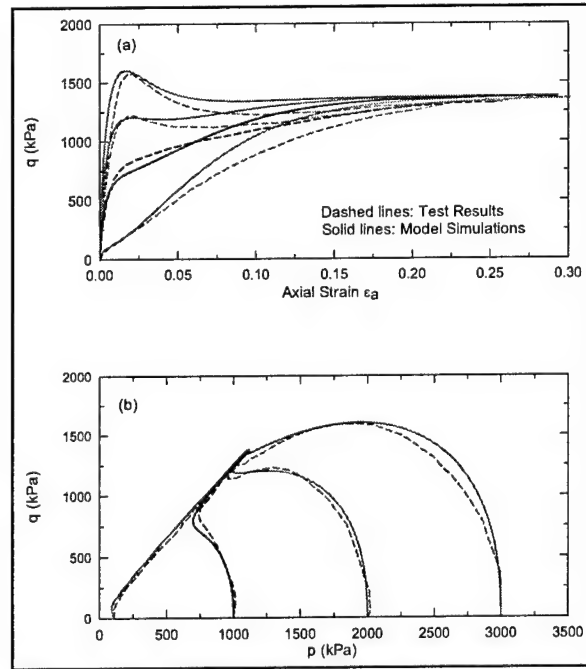


**Figure 17.** Comparison of model simulations (Wang et al., 2002) with undrained triaxial test results on Toyoura sand having void ratio of 0.833 (Verdugo and Ishihara, 1996)

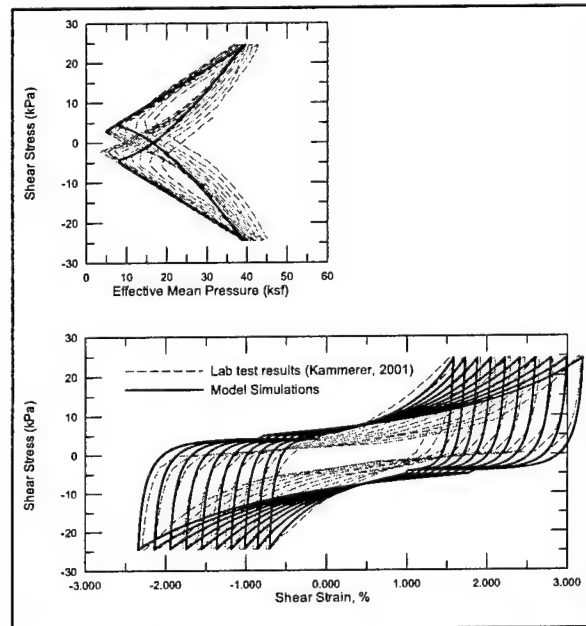


**Figure 18.** Comparison of model simulation with post-liquefaction deformation test results (Wang and Dafalias, 2002)



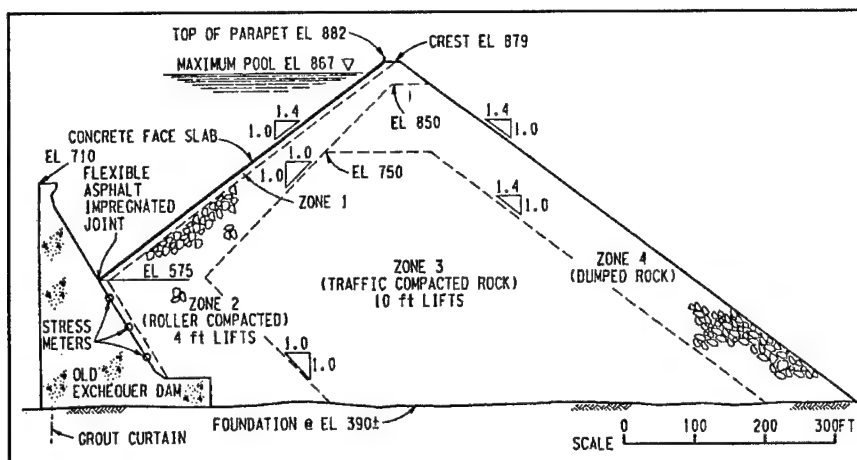


Figure 19. Maximum section of New Exchequer Dam

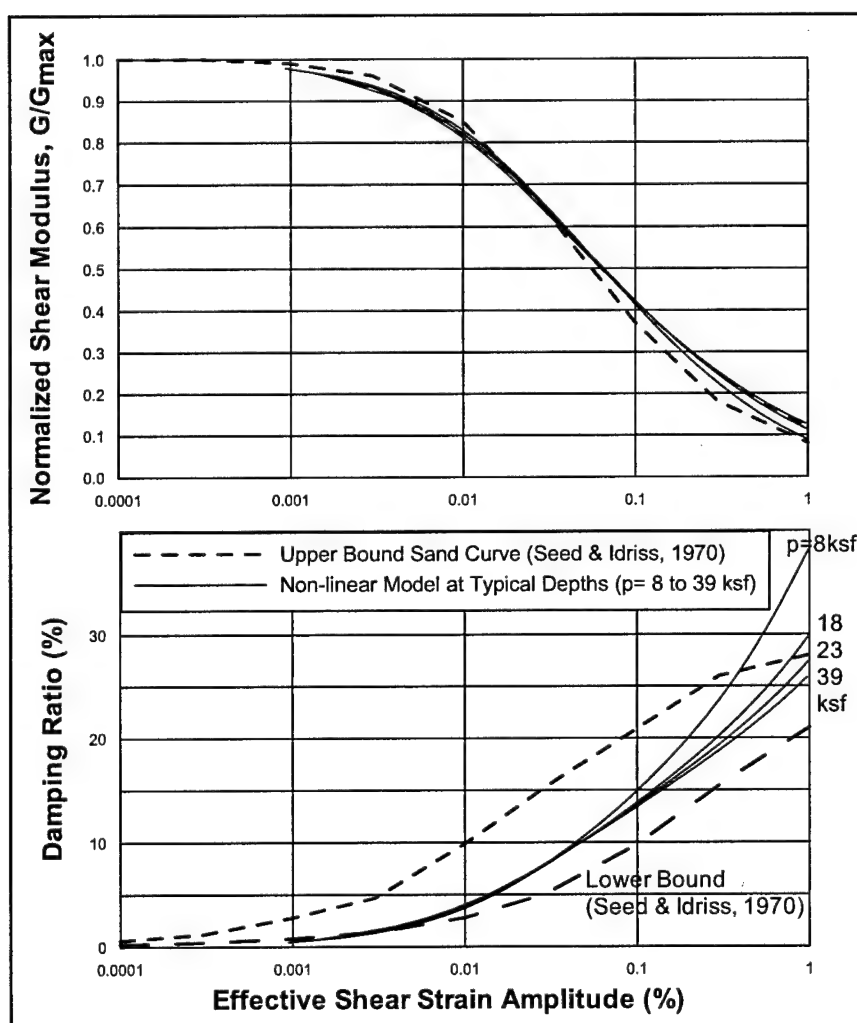
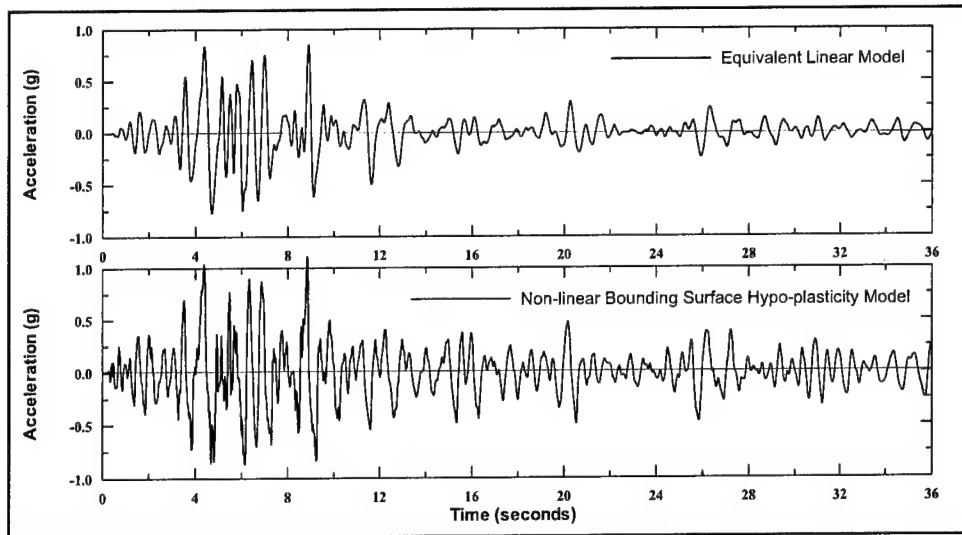
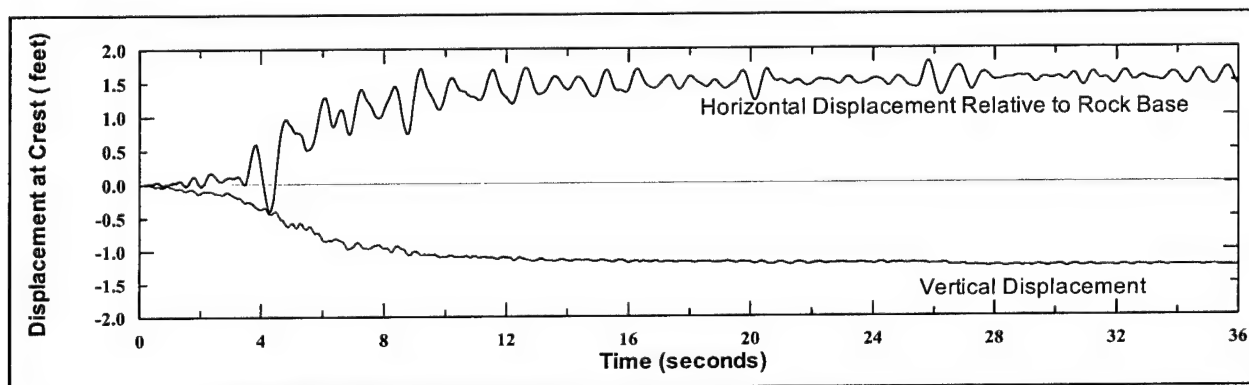


Figure 20. Relationships of normalized modulus and damping ratio with shear strain



**Figure 21.** Crest acceleration time histories computed from equivalent linear and nonlinear approaches



**Figure 22.** Computed time histories of crest displacements using FLAC and bounding surface hypoplasticity model

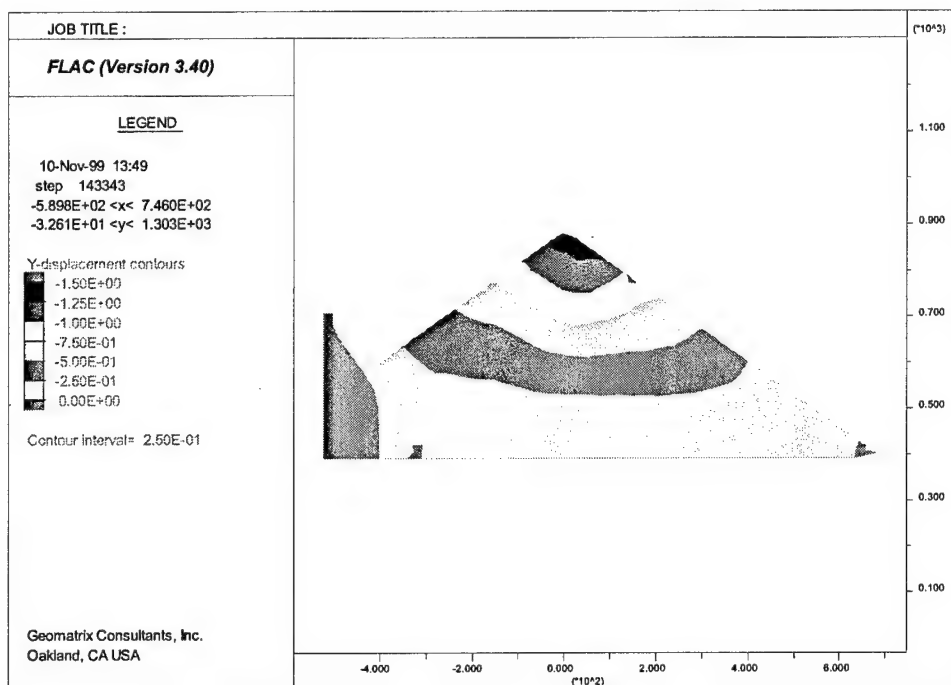
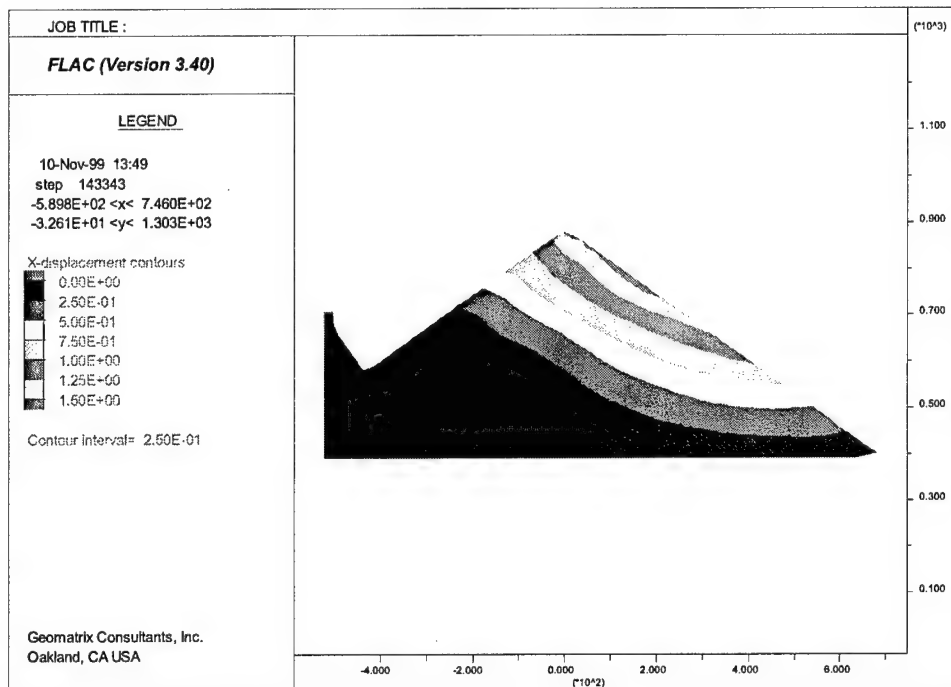


**Figure 23.** Computed displacement contours using FLAC and bounding surface hypoplasticity model

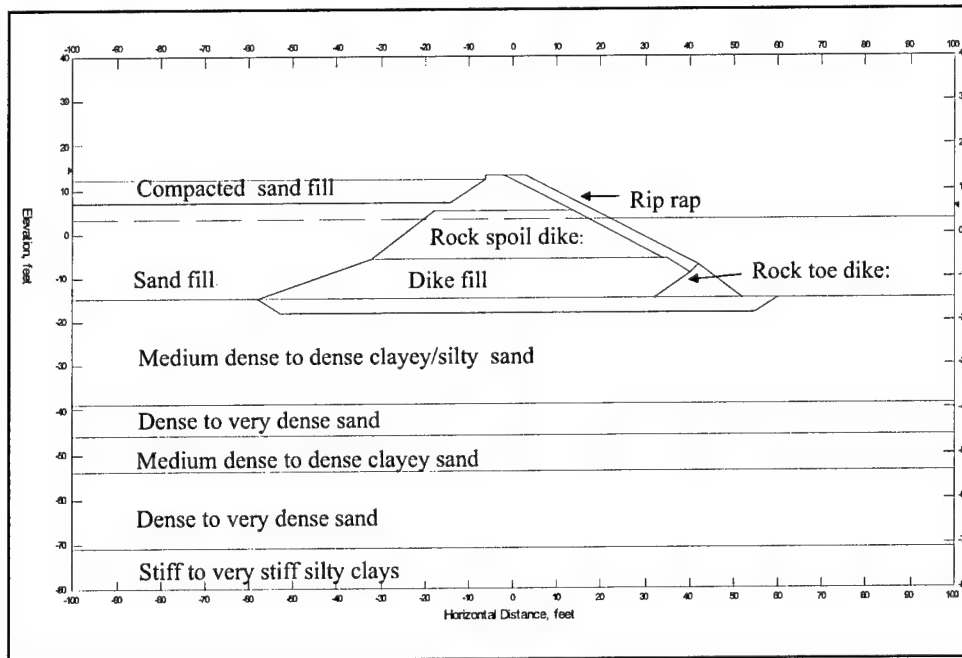


**Figure 24.** Typical cross section at Berth 40, Port of Oakland

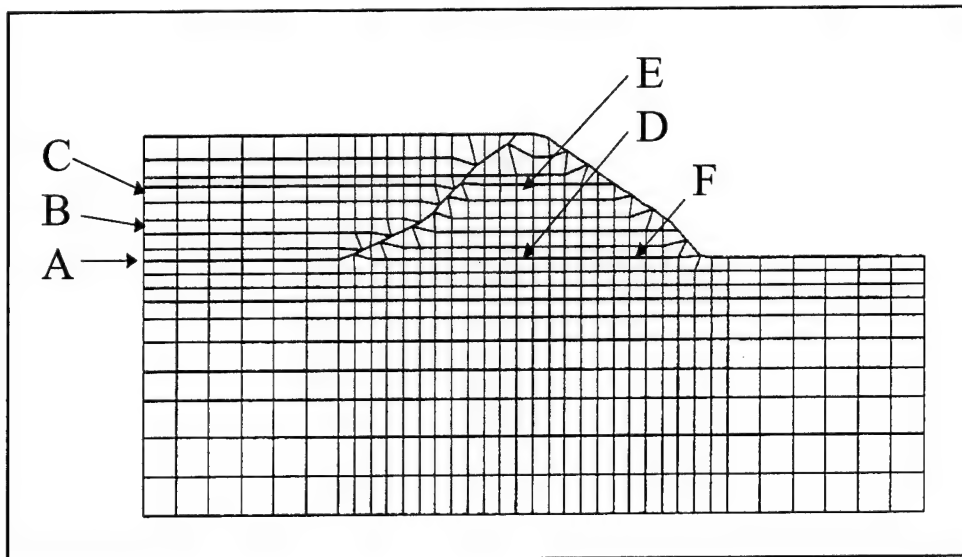


**Figure 25.** Finite difference grid and typical material zones

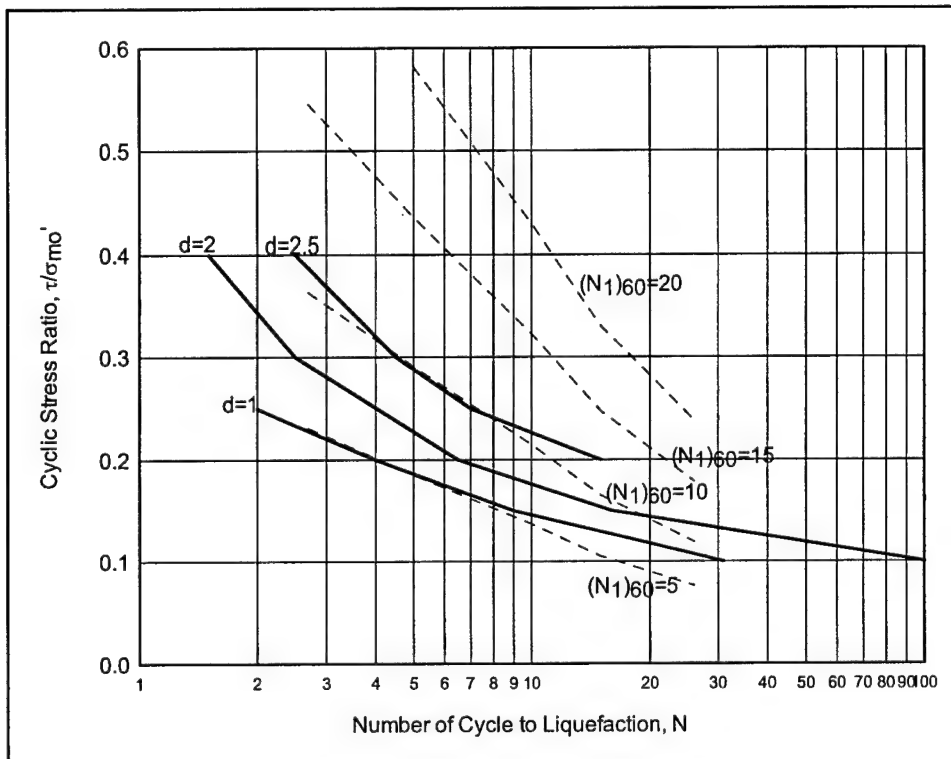


**Figure 26.** Cyclic strength of sand with 5 percent (or less) fines based on liquefaction chart of Seed et al. (1985)

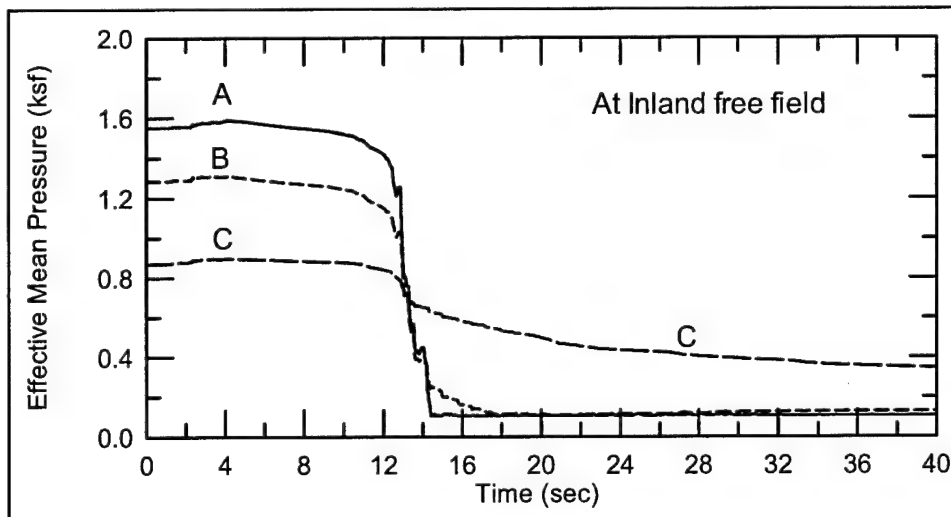


**Figure 27.** Computed effective mean pressure time histories in sand fill layers at inland free field

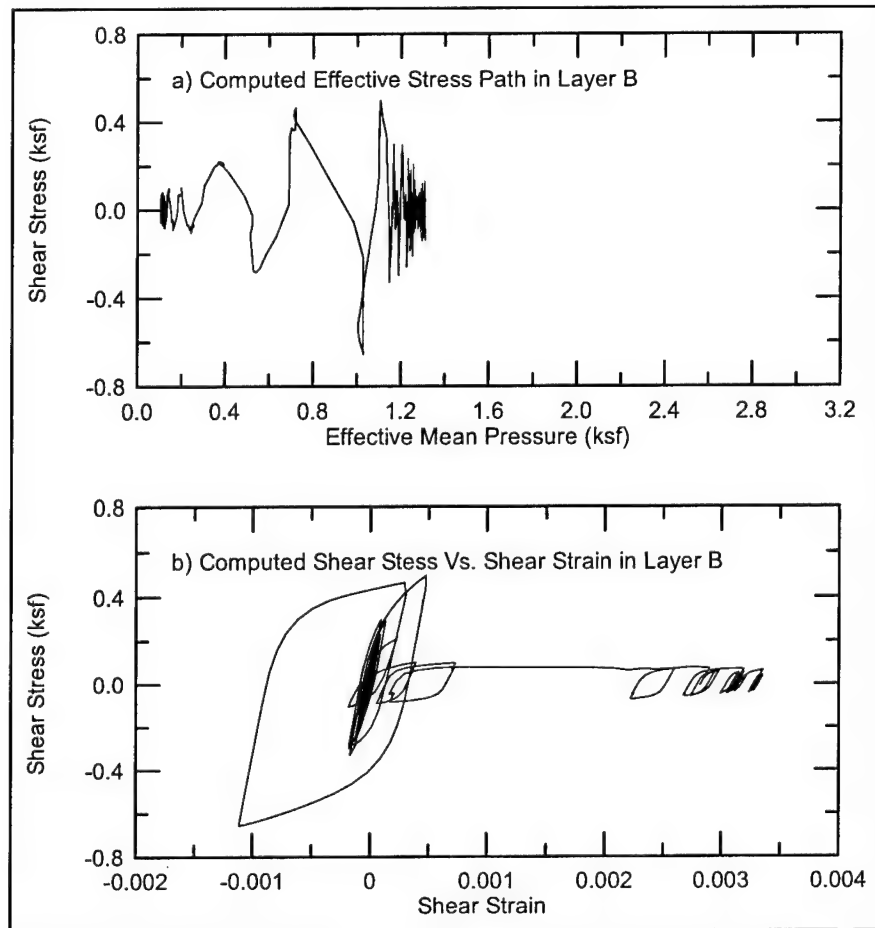


**Figure 28.** Computed effective mean pressure, shear stress and shear strain in sand fill layer B at inland free field

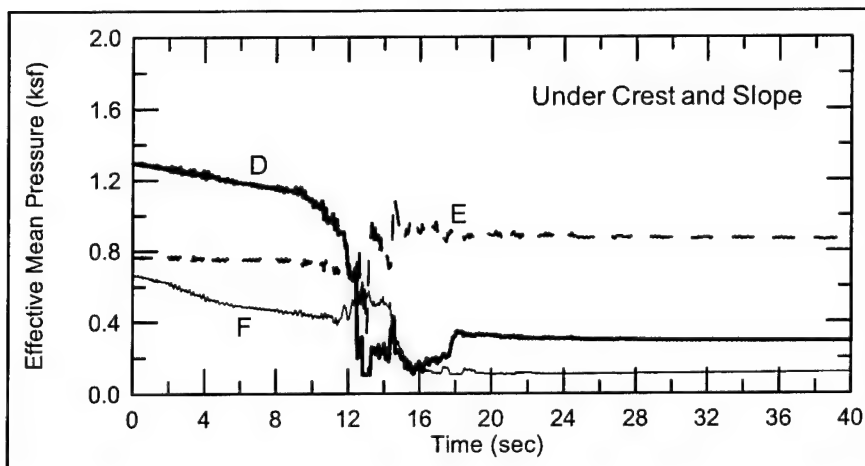


**Figure 29.** Computed mean pressure time histories in sand fill zones under crest and slope

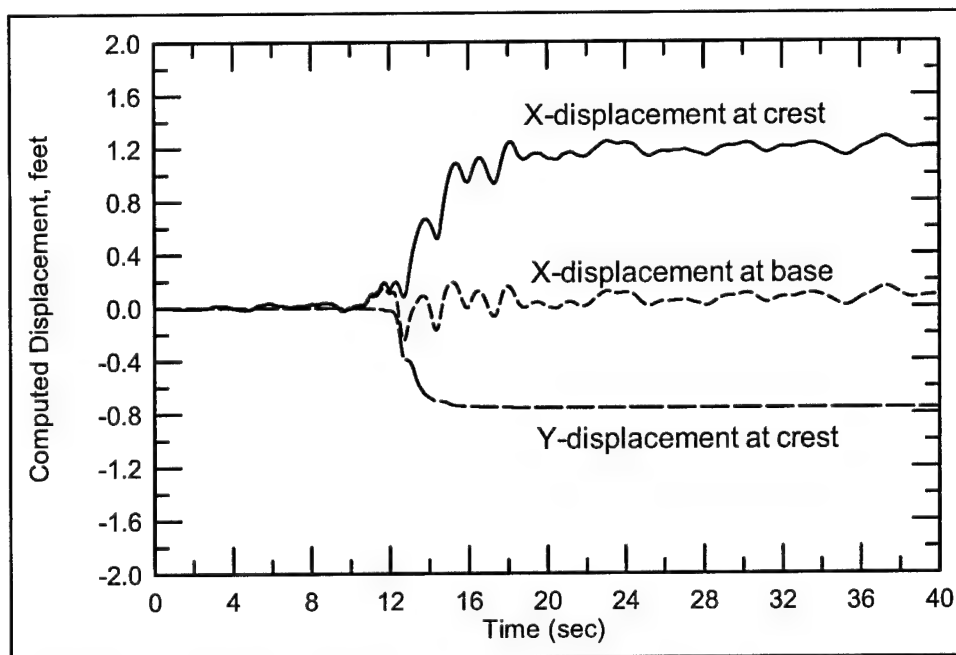


**Figure 30.** Computed horizontal and vertical displacement time histories at crest

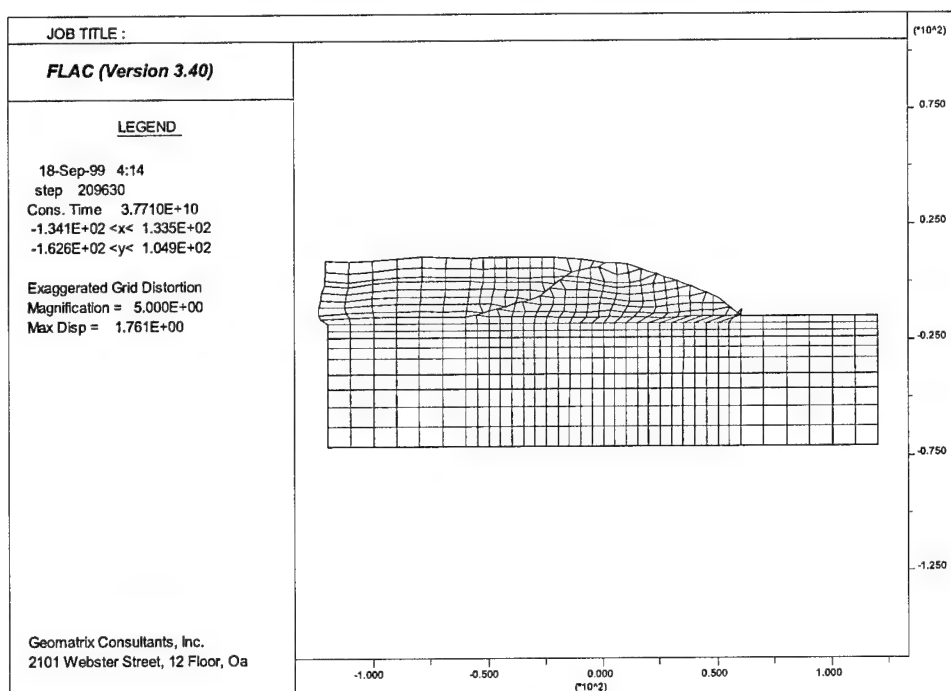


**Figure 31.** Computed deformed slope at Berth 40 (displacements shown are magnified five times)

This page intentionally left blank.



## Numerical Simulation of Sliding of an Earth Dam During the 1995 Kobe Earthquake

by

Tadahiko Sakamoto<sup>1</sup>, Hitoshi Yoshida<sup>2</sup>, Yoshikazu Yamaguchi<sup>3</sup>,  
Hiroyuki Satoh<sup>4</sup>, Tomoya Iwashita<sup>5</sup>, and Norihisa Matsumoto<sup>6</sup>

### ABSTRACT

The Kobe Earthquake in Japan caused shallow sliding on the upstream slope below the water level of the Kitayama Dam. This paper briefly stated the results of post-earthquake surveys and tests of this earth dam. The FE model of the dam was prepared based on the detailed results of in-situ tests and laboratory material tests. The numerical analysis was performed by the effective stress analysis to simulate the performance of the dam during the Kobe Earthquake. The analysis resulted in that large residual deformation and shear strain occurred at the shallow area of the upstream slope below the water level. The analysis was able to simulate the behavior and damage pattern of the dam, that is sliding deformation, during the Kobe Earthquake.

**KEYWORDS:** Earth Dam, Earthquake, In-situ Test, Dynamic Analysis

### 1 INTRODUCTION

The Kobe Earthquake of January 17, 1995 in Japan caused slides on the upstream slope of the Kitayama Dam which is an earth dam located about 33 km north-east of the epicenter. It was minor damage that did not affect the structural safety and the water storage functions of the dam. But this was the first time that an

embankment dam designed based on design standards and filled by the engineered rolling compaction was damaged in this way in Japan. Therefore, since the earthquake, we carried out detailed investigations of the dam and soil tests of the dam materials. This paper describes the numerical simulation of the behavior of the Kitayama Dam during the earthquake by the dynamic effective stress analysis. The mechanism of the earthquake damage to the Kitayama Dam is evaluated through the comparison of the computed simulation with the actual damage of the dam.

### 2 DAMAGE TO KITAYAMA DAM

#### 2.1 Description of Kitayama Dam

The Kitayama Dam is located on the Rokko granite zone and about 1.5 km from the Ashiya Fault and the Koyo Fault. The dam is an earth dam with a height of 25 m and was completed in 1968. Its standard cross section is shown in Figure 1. The dam body materials in Zones [1], [2] and [3] and counterweight fill consist mostly of decomposed Rokko granite. The material in Zone [2] of the upstream side of the dam body has a maximum particle size of 9.50 mm, a uniformity coefficient of about 300 and a percentage passing of silt and clay of about 20 percent. The dam body was compacted well

<sup>1</sup> Dr. Eng., Chief Executive, Public Works Research Institute (PWRI), 1-6 Minami-hara, Tsukuba-shi, 305-8516, JAPAN.

<sup>2</sup> Research Coordinator for Watershed Management, River Department, National Institute for Land and Infrastructure Management (NILIM), Ministry of Land, Infrastructure and Transport (MLIT), 1 Asahi, Tsukuba-shi, 305-0804, JAPAN.

<sup>3</sup> Dr. Eng., Principal Researcher, Dam Structures Team, PWRI.

<sup>4</sup> Researcher, Dam Structures Team, PWRI.

<sup>5</sup> Deputy Director, River Planning Bureau, MLIT.

<sup>6</sup> Dr. Eng., Vice President, Japan Dam Engineering Center.

by the rolled fill with a 30 cm lift: its degree of compaction, D-value, was over 100 from banking execution control tests.

The pseudo-static analysis was applied as the seismic design of the dam body. The lateral seismic coefficient was 0.15, which was determined based on the design criteria enacted in 1957 by the Japanese National Committee on Large Dams.

## 2.2 Damage to Kitayama Dam

The earthquake caused sliding failure on the upstream slope as shown in Figure 2. The length in the dam axis direction of the sliding was about 100 m. During the earthquake, the reservoir water level was at the top of the sliding failure block. The level differences on the top of the sliding block were 1 to 1.5 m. We excavated four pits (P-1 to P-4) in the sliding slope of the standard cross section to investigate the interior of the dam body. Figure 3 represents the view of the excavation of the pit P-4 close to the upstream toe. We found loose layers with high water content below the riprap and gravel layer in all 4 pits. In the pits P-2 and P-4 that were excavated earlier, an extremely loose layer was found below the loose layer. Water seeped out from this extremely loose layer and if it had been left as it was, it would have crumbled naturally. This must have happened because the rain that fell on the dam at the night before the pits were excavated remained on the sliding surface, and the pit excavation made the collected water drain from the sliding surface. Figure 4 is the cross section of the 4 pits. We confirmed the boundary between the loose layer and well-compacted (not affected) layer as the sliding layer that is indicated as a dotted line on Figure 4. The sliding failure zone with a depth of 1.5 to 2 m was confirmed. The undisturbed material samples obtained using air bubble boring revealed that there were not particularly loose zones inside the slope up from the sliding failure zone.

## 3 IN-SITU AND LABORATORY TESTS

After the earthquake, we performed several kinds of in-situ tests such as PS logging, density logging and microtremeter observations. We recovered undisturbed cores, with a diameter of 70 mm, of the dam body materials and weathered rock foundation using air bubble boring. A variety of laboratory tests were performed using the undisturbed samples in the shallow ([A]), middle ([B]), and deep ([C]) zones of the dam body. We measured the density of the cores and performed permeability tests, drained monotonic loading triaxial tests (MTX), undrained cyclic loading triaxial tests (CTX), drained cyclic torsional simple shear deformation tests, and others.

## 4 DYNAMIC ANALYSIS

### 4.1 Analysis method

We calculated the initial stress distribution of the dam body from banking analysis and seepage analysis. Twenty-six-step-banking analysis was performed with the modeling of the elastic foundation rock and weathered rock and with the modeling of the relationship between the stress and the strain of the dam body by the Duncan-Chang method (Duncan *et al.*, 1970). Saturated seepage analysis was performed and the phreatic surface and seepage flow force inside the dam body were given. We obtained the initial stress distribution by the superimposition of the seepage flow force on the stress from banking analysis.

We performed dynamic effective stress analysis of the Kitayama Dam during the Kobe Earthquake and used the program code "MuDIAN." The saturated part of the dam body (Zones [A], [B] and [C] in a part of Zones [1] and [2]) was modeled by two-phase formulations of soil (solid) and water (fluid). The unsaturated part of the dam body (a part of Zones [1] and [2],

Zone [3] and the downstream counterweight fill) was one-phase formulations of soil. Elastoplastic behavior of soil was modeled by a constitutive model "Modified Densification model" (Zienkiewicz *et al.*, 1999). This model assumes a plastic hardening by volumetric strain and that by shear strain independently. The plastic volumetric strain due to the dilatancy, which is called autogeneous volumetric strain by Zienkiewicz *et al.* (1978), can be estimated from accumulated shear strain. The incremental autogeneous volumetric strain can be a function of an accumulated damage quantity that is assumed as a function of a stress ratio and accumulated shear strain. The relation's function is determined by cyclic loading tests empirically. Excess pore pressure in the undrained condition can be determined using bulk modulus from the autogeneous volumetric strain. The plastic shear strain is calculated by the potential surface ( $\phi=0^\circ$ ) of the Mohr-Coulomb's yield criteria based on the non-associate flow rule with no plastic volumetric strain. This modified model is able to simulate cyclic mobility behavior after the stress point reaches the phase transformation line, which is the most important to simulate the dynamic behavior of dense soils.

#### 4.2 Analytical model

Figure 5 shows the material partition of the FE model of the Kitayama Dam. A riprap layer with a 70 cm thickness is modeled in one-slice-element of the upstream slope. The viscous boundary condition is adopted on the bottom and the sides of the foundation model. We determined that the depth of the weathered rock was 8 to 10 m based on the comparison of the dam's natural frequency (3.8 Hz) by microtremor measurements at the dam with that by eigenvalue analysis of the model. The material properties, shown in Table 1, are given based on the results of the in-situ tests and laboratory tests for undisturbed specimens of dam body materials. In the two-phase formulation section, the soil parameters are given for three zones partitioned into on a basis of the depth. The friction angle is given by drained monotonic loading triaxial tests (MTX), and the phase transformation angle is

determined at 0.65 times the friction angle. Figure 6 shows the distribution of S-wave velocity,  $V_s$ , within the dam body by the PS logging. The S-wave velocity distributions of the upstream side and downstream side of the dam body are almost the same. We also show the S-wave velocities converted from the initial shear moduli obtained by the cyclic torsional shear tests for undisturbed specimens. The S-wave velocity distributions by PS logging agree with the empirical equation of S-wave velocity distribution of a core zone of rockfill dams (Sawada *et al.*, 1977). The empirical equation is as follows:

$$V_s \text{ (m/s)} = 140Z^{0.34} \quad (1)$$

where  $Z$  is a depth below the surface of the dam slope (unit in meters). The initial shear moduli,  $G_0$ , within the dam body are given using the S-wave velocity obtained by equation (1). The shear moduli,  $G$ , are calculated using the follow equation.

$$G = G_0 (\sigma'_m / \sigma'_{mo})^{0.63} \quad (2)$$

Where  $\sigma'_m$  is effective mean stress and  $\sigma'_{mo}$  is the initial value of  $\sigma'_m$ . In the weathered rock and the foundation rock, the S-wave velocities of 500 and 1200 m/s respectively obtained from the PS logging are used.

We determined the soil parameters for the dilatancy in the modified Densification model based on a simulation (element analysis) of the undrained cyclic loading triaxial test (CTX) using undisturbed specimens of the Kitayama Dam material. The parameters were suited to the relationship between the number of cyclic loading and the strain in the CTX as shown in Figure 7. The element analysis simulates the undrained cyclic loading simple shear test. Hence, the shear strain from the element analysis is transformed into axial strain using Poisson's ratio for the sake of the comparison with the strain from the CTX test. Figure 8 indicates a comparison of the effective stress path of the CTX test with that simulated by this element analysis.

Small viscous damping was added for solid phase. This damper was given by Rayleigh damping: the damping factors of the dam body were assumed 0.005 for the first and second natural periods. That of the weathered rock and foundation rock was assumed 0.03.

### 4.3 Input motions

No seismometer was installed at the Kitayama Dam and no earthquake motion was also measured near the dam site. We, therefore, had no better alternative but to input the following two earthquake motions on the bottom viscous boundary of the FE model. One is the earthquake motion at the Kitayama Dam site simulated by statistical Green's function approach, and the other is the earthquake record observed at Kobe University during the Kobe Earthquake. The acceleration time histories of the input motions are shown in Figure 9. Only the horizontal input motions are taken into account. Time interval of the calculation is 0.001 sec.

We simulated the incident motion during the Kobe Earthquake on the surface of seismic bedrock ( $V_p > 5$  km/s) at the Kitayama Dam site by superimposing the weak motions of small earthquakes as statistical Green's function (Irikura, 1986). We used the causative fault model of the Kobe Earthquake (Yamada *et al.*, 1998) that was the modified model of the fault model by Kamae and Irikura (1997). The weak motions of small earthquakes on the seismic bedrock were produced by Boore's procedure (Boore, 1983), because of no measuring of aftershocks. Next, we calculated the input motion on the dam basement from the simulated motion on the seismic bedrock by the one-dimensional multiple reflected method. The peak acceleration of the simulated input motion is 215.6 gal and its duration is 14 sec.

The Kobe University motion is the earthquake motion observed during the Kobe Earthquake. The observation station is located on a weathered rock with an S-wave velocity of 340 m/s and 24 km far from the epicenter. The Kobe University motion has a peak acceleration of 270.4 gal and a duration of 20 sec, and is

stronger and longer than the simulated motion above.

### 4.4 Analysis results

The effective stress analysis resulted in the residual deformation and in the residual displacement at some nodes using vector arrows shown in Figures 10 and 11 for each input motion. These figures indicate that large deformation is restricted within the shallow area of the upstream slope below the water level. The maximum horizontal residual displacement is 87 cm for the simulated motion and 413 cm for the Kobe University motion, which occur on the slope in the vicinity of the toe. Large lateral deformation occurs at the shallow area around the toe, while at the slope surface around the water level settlement predominates over lateral displacement. The computed deformation pattern would correspond to the damage condition of the original dam as shown in Figure 2: the bulging of the sliding block around the upstream toe and the drop of the sliding block at the water level.

Figure 12 shows the time histories of the effective mean stress  $\sigma_m'$  at the three elements (E1, E2 and E3) which are designated on Figure 10 as double circle dots. The shallower the point of the element is from the slope surface, not only does a sharp drop of  $\sigma_m'$  due to cyclic mobility occur earlier, but  $\sigma_m'$  also remains smaller. The dropped effective mean stress  $\sigma_m'$  during cyclic mobility causes the decline of the shear modulus as defined in equation (2), and as a result, causes the distribution of the deformation inside the dam body. The deformation for the Kobe University motion inputted is much larger than that for simulated motion. That's caused not so much by the power of the input motion as but by its duration during cyclic mobility phenomenon.

The distribution of the maximum principal shear strain through the motion for the simulated motion inputted is shown in Figure 13. Large strain is distributed along the belt-shaped zone of a depth of 3 to 4 m near the upstream toe and also around the slope surface at the water level. The zones approximately agree with the sliding

layer confirmed in the pits excavated shown in Figures 3 and 4.

## 5 CONCLUSIONS

The Kobe Earthquake caused a shallow sliding on the upstream slope below the water level of the Kitayama Dam. This paper stated the results of post-earthquake surveys and tests of this earth dam. We prepared the FE model of the dam based on the detailed results of in-situ tests and

laboratory material tests and performed the effective stress analysis of the dam during the Kobe Earthquake. The numerical analysis results showed that large residual deformation and shear strain occur at the shallow area of the upstream slope below the water level. The numerical analysis was able to qualitatively simulate the behavior and damage pattern of the dam, that is sliding deformation, during the Kobe Earthquake.

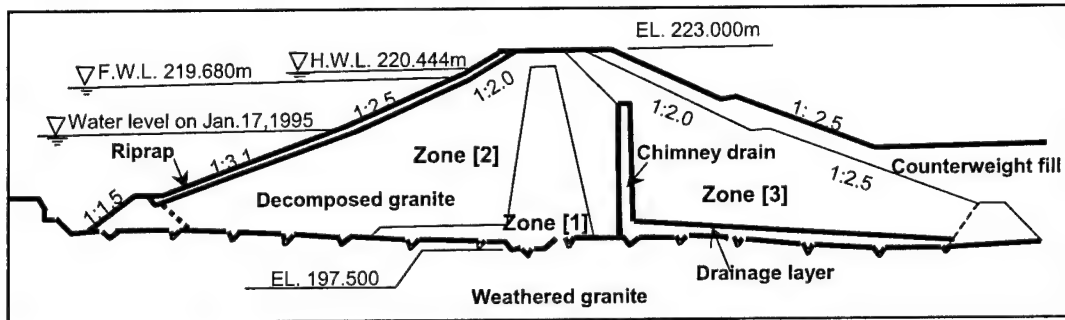


**Figure 1.** Cross section of the Kitayama Dam



**Figure 2.** Over view of damage to the Kitayama Dam due to the Kobe Earthquake



**Figure 3.** View of pit (P-4) excavated at the failure zone of the dam

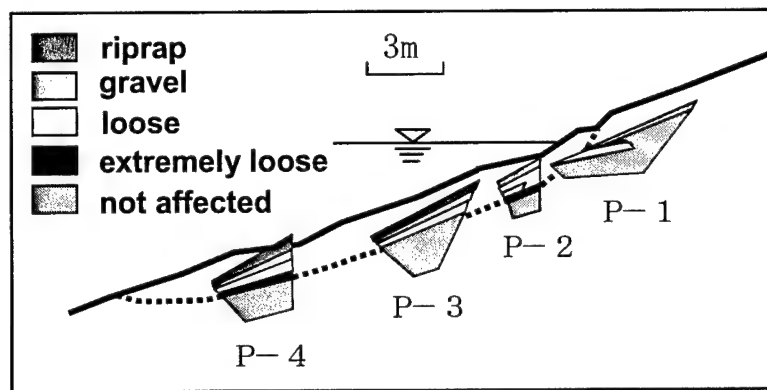


**Figure 4.** Cross section of the sliding failure by pit excavation investigation

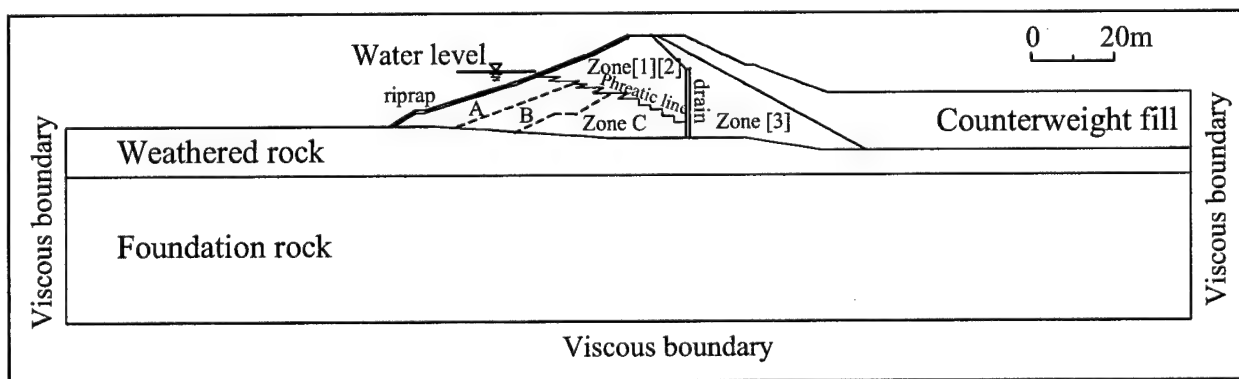


**Figure 5.** Material partition of numerical model of the Kitayama Dam

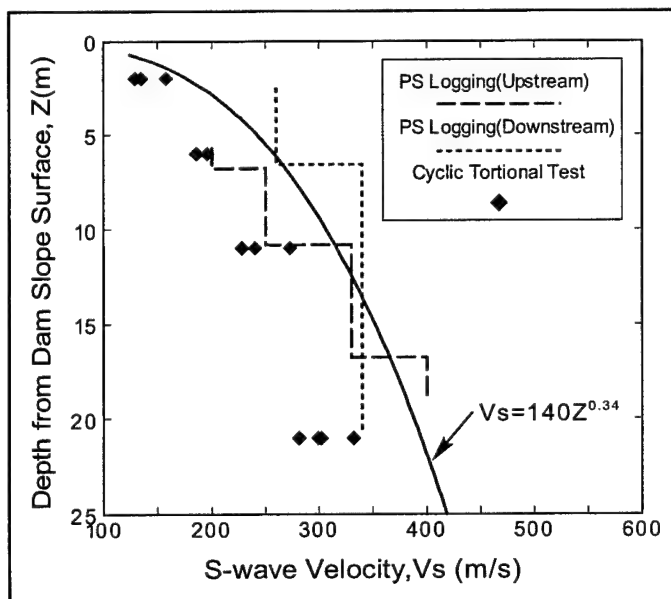


**Figure 6.** Distribution of S-wave velocity inside dam body



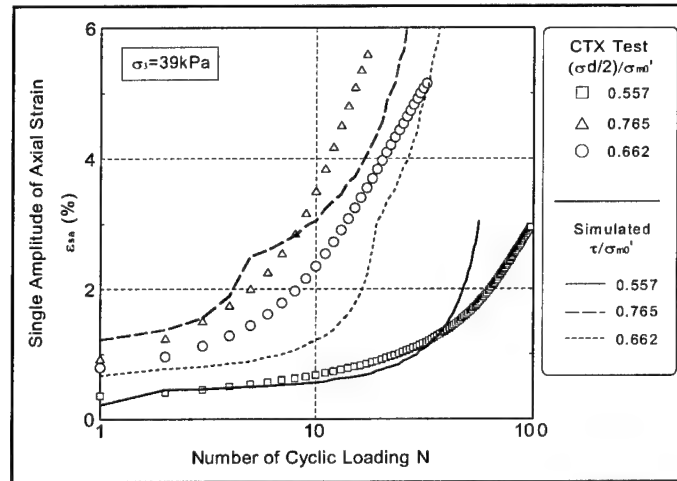


**Figure 7.** Suiting of enlargement of strain due to cyclic loading (accumulation of damage) by cyclic triaxial test (CTX) and simulation

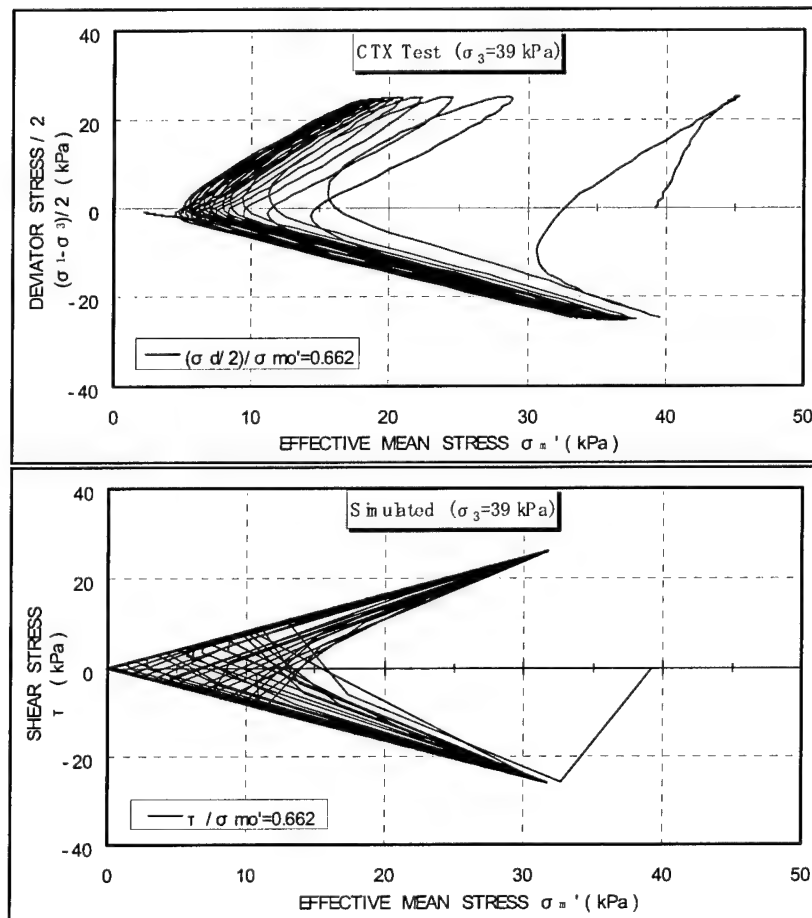


**Figure 8.** Comparison of effective stress path by undrained cyclic triaxial test (CTX) and by simulation



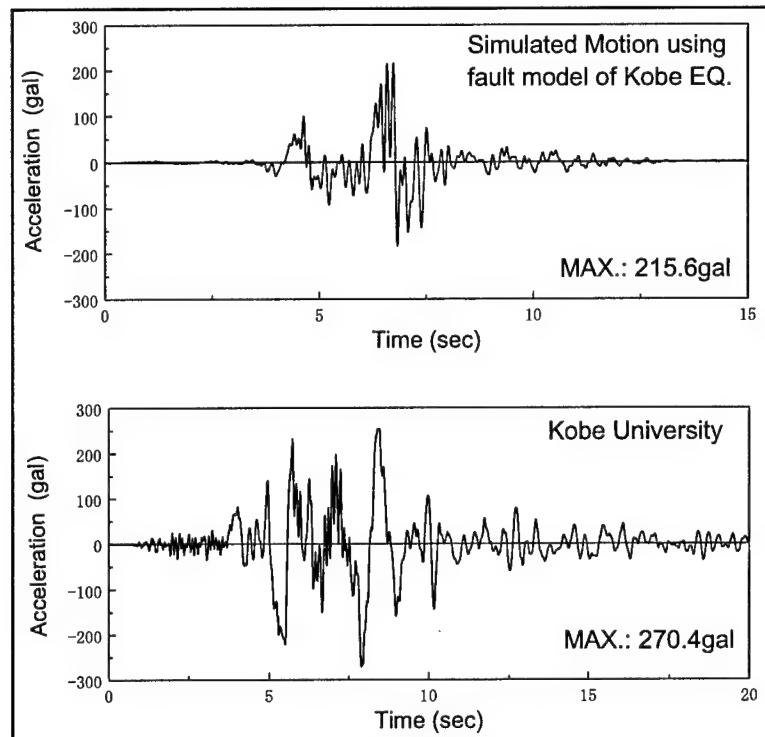


**Figure 9.** Input earthquake motions (simulated motion and Kobe University motion)

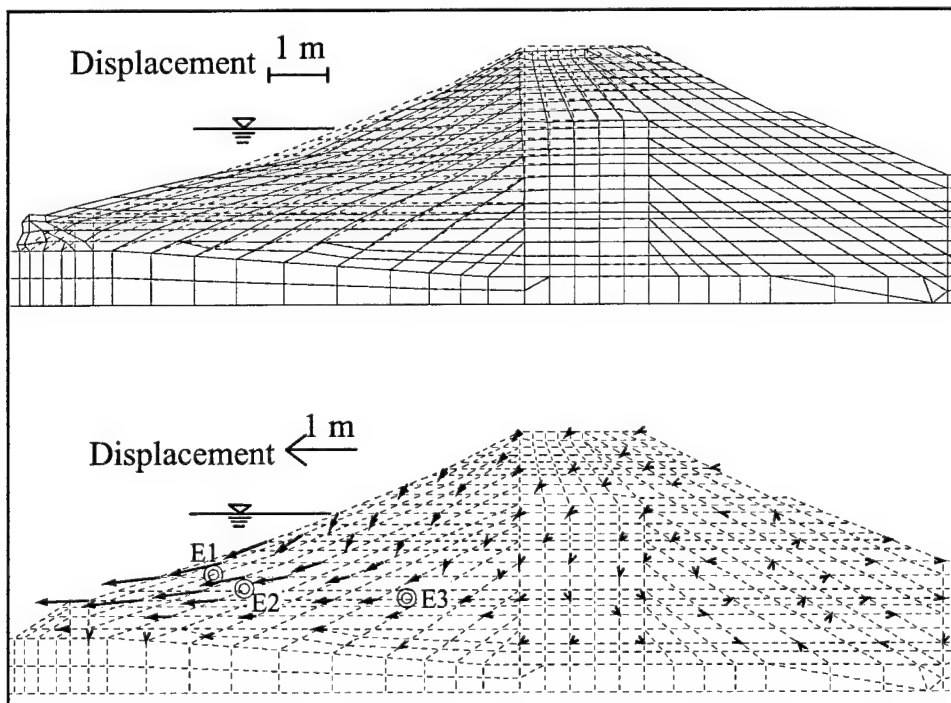


**Figure 10.** Computed deformation of the Kitayama Dam for simulated motion inputted

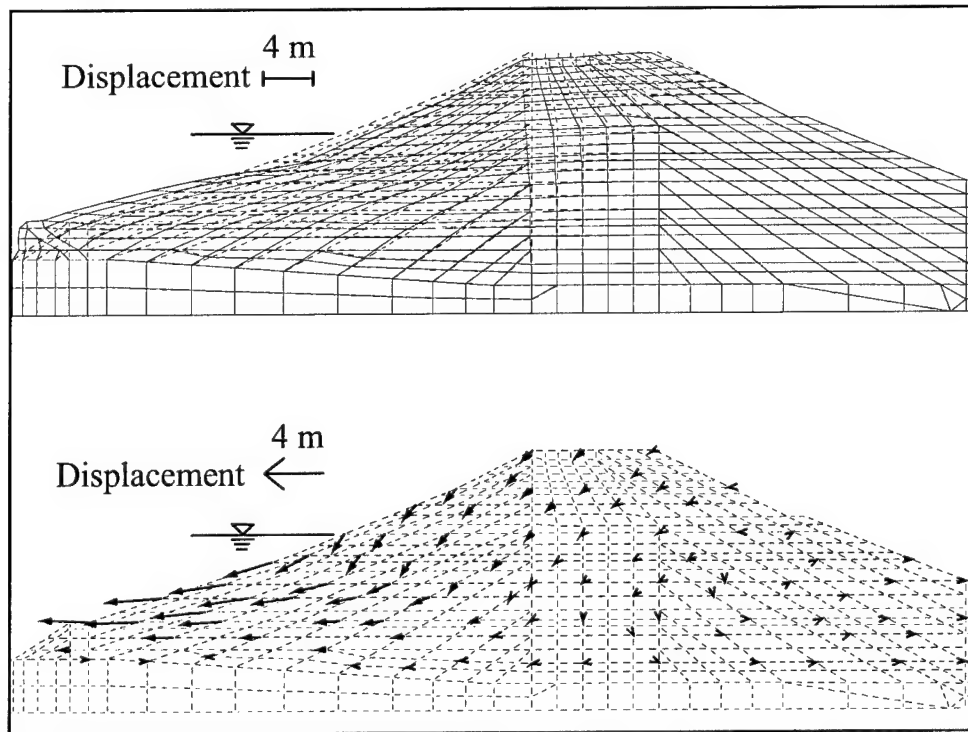


**Figure 11.** Computed deformation of the Kitayama Dam for Kobe University motion inputted

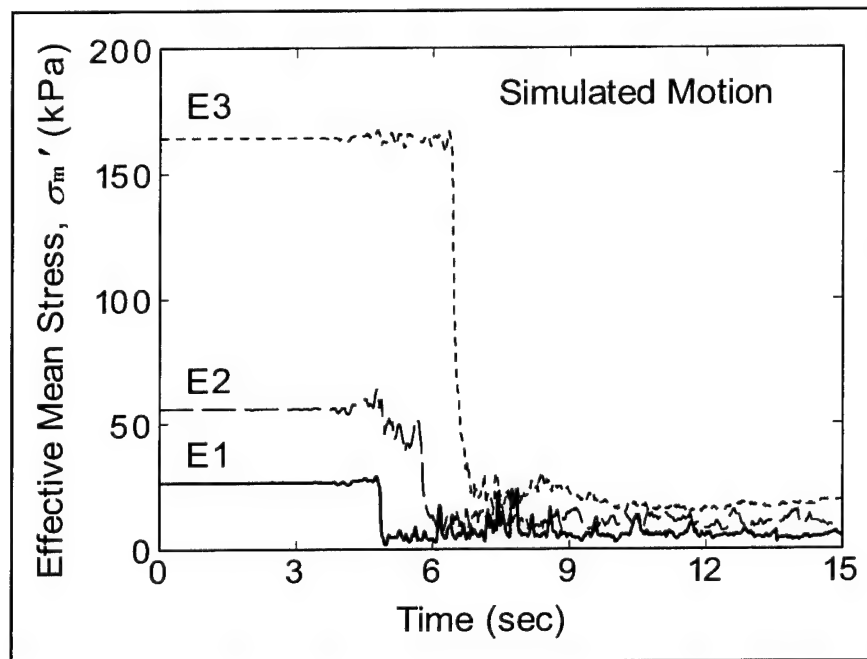


**Figure 12.** Effective mean stress time history for simulated motion inputted

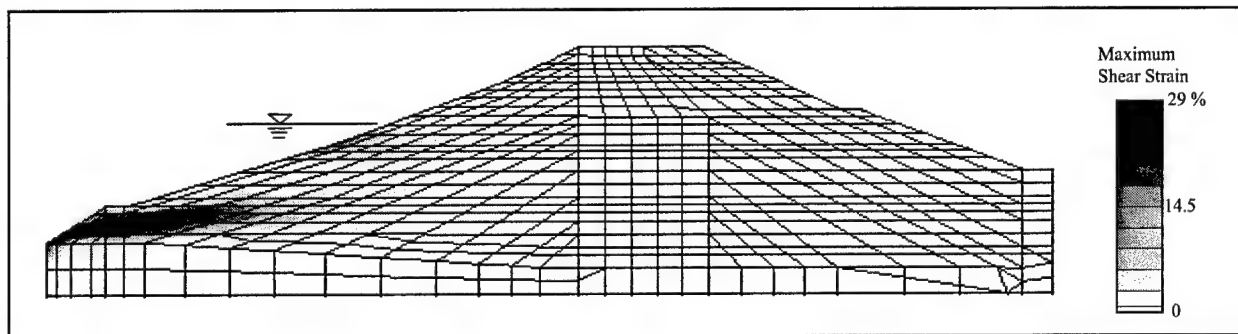


**Figure 13.** Distribution of the maximum principal shear strain through the motion for simulated motion inputted

**Table 1.** Material Properties

n			Density, ρ (g/cm <sup>3</sup> )	Porosity n	Permeability Coefficient, K (cm/s)	Poisson's ratio ν	Internal friction ϕ (deg)	Cohesion C(kPa)
Dam body Zone (1) (2)	Saturated	Riprap	2.96	0.171	1.0×10 <sup>-1</sup>	0.3	39.0	22.5
		Zone (A)	2.10	0.283	1.0×10 <sup>-4</sup>	0.3	55.0	0
		Zone (B)	2.10	0.283	1.0×10 <sup>-4</sup>	0.3	48.0	0
		Zone (C)	2.10	0.283	1.0×10 <sup>-4</sup>	0.3	45.0	0
	Unsaturated	Riprap	2.96	--	--	0.45-0.0067 <sup>0.6*</sup>	44.3	63.7
		The other	2.10	--	--	0.45-0.0067 <sup>0.6*</sup>	44.3	63.7
Dam body Zone (3)			2.08	--	--	0.45-0.0067 <sup>0.6*</sup>	44.3	63.7
Counterweight fill			1.96	--	--	0.45-0.0067 <sup>0.6*</sup>	44.3	63.7
Weathered rock			2.41	--	--	0.33	--	--
Foundation rock			2.50	--	--	0.3	--	--

This page intentionally left blank.

## Dynamic Properties of Cohesive Soil in Foundation of an Embankment Dam

by

Gonzalo Castro<sup>1</sup>, F. C. Walberg<sup>2</sup>, and Vlad Perlea<sup>2</sup>

### ABSTRACT

The post-liquefaction behavior of cohesive soils depends primarily on their dilatancy properties and the characteristics of the cyclic loading: number of cycles, amplitude, frequency, and magnitude of shear stress reversal. Taking into account the multitude of factors affecting liquefiability and post-liquefaction undrained strength of cohesive soils, the best way of evaluation of their behavior is through undisturbed sampling and testing. The recommended laboratory test is cyclic loading in undrained conditions followed immediately (without drainage permitted) by monotonic loading. Pre-existence of shear stresses on the planes of maximum applied cyclic shear stress should be given consideration, as shear stress reversal is an important factor in liquefaction triggering and evolution of strength degradation with accumulated displacement. Field tests (vane, cone penetration, shear wave velocity measurements) also may be useful in conservative evaluation of stability of non-critical structures on liquefiable soil deposits. In general, cohesive soils appear to be more resistant to liquefaction than fine sands, when their states of denseness are similar.

**KEYWORDS:** Embankment dams, seismic analysis, cohesive soils, dynamic properties

### 1 INTRODUCTION

Although it is generally believed that loss of shear strength due to dynamic loading is a phenomenon affecting primarily cohesionless soils, some categories of cohesive soils may be significantly affected by dynamic (cyclic) loading.

Observations in China following strong earthquakes that occurred from 1966 through 1976 lead to the conclusion that some clayey silts, silty clays, or lean clays are susceptible to significant loss of strength during cyclic loading, in particular due to the seismic action, leading to a phenomenon similar to liquefaction of cohesionless soils. Wang (1979) summarized these observations under the so-called "Chinese Criteria." Seed et al. (1983) acknowledged the importance of those findings and made the following recommendation: "*Consider some clay soils as being vulnerable to significant loss of strength. Based on Chinese data, these soils would appear to have the following characteristics: percent finer than 0.005 mm < 15%, liquid limit, LL < 35, and water content > 0.9 LL. The best way to handle these soils, if they plot above the A-line, would be to determine their liquefaction characteristics by tests.*" However, the Chinese practice of determining plasticity limits, moisture content, and clay fraction differs from procedures used in USA (based on ASTM standards); therefore, the U.S. Army Corps of Engineers, Vicksburg District in cooperation with Waterways Experiment Station performed a parametric study of laboratory practices and found that minor corrections should be applied to ASTM-based parameters for input in the Chinese model: decrease clay content by 5 percent, increase liquid limit by 1.5 percent, and increase moisture content by 2 percent (Koester, 1992).

Perlea et al. (1999) applied these corrections to the original model for direct use of ASTM-based parameters, as shown in Figure 1. Based on the available Chinese data, it was also considered justified to add the criterion of Plasticity Index

<sup>1</sup> GEI Consultants, Inc., Winchester, MA 01890 (USA).

<sup>2</sup> U.S. Army Corps of Engineers, Kansas City District, MO 64106 (USA).

less than or equal to 13 and the specification that the Chinese Criteria are applicable to saturated soil only.

For design purposes, the Chinese Criteria are of little help, as they are not correlated with the cyclic loading parameters, in particular the intensity and duration of shaking. All available information on the seismic loading that triggered liquefaction in the Chinese case histories is that they occurred in zones where the Modified Mercalli Intensity was from VII to IX. The criteria recommend some categories of cohesive soils for testing, but obtaining undisturbed samples and testing them is difficult. This paper presents the efforts for evaluation of the seismic response of a clayey soil meeting the Chinese Criteria, through laboratory and field tests. The soil is present in the 6-m blanket of the alluvial deposit in the foundation of an embankment dam in Kansas and is considered representative for many other fine-grained deposits in the river flood plains. The embankment dam has a maximum height of 43 m (140 ft) and the average cross section shown in Figure 2. It is located 20 km from a fault capable of generating earthquakes of 6.6 moment magnitude and peak ground acceleration of 0.3 g at the site. The normal pool is relatively low, as the major function of the dam is flood control.

The foundation consists of 15 to 21 m (50 to 70 ft) of alluvial deposits over shale and limestone. The upper zone of the alluvium of about 6 m (20 ft) consists of lean clay, silty clay, and clayey silt. The response of these soils to seismic shaking is the subject of this paper. Underneath the cohesive soil blanket are sand deposits. The upper sands are easily liquefiable (the minimum factor of safety determined with Seed-Idriss simplified procedure varied between 0.6 and 0.8 in the free field and between 0.7 and 1.1 underneath the embankment). It was assumed that the cohesive soil in direct contact with liquefiable sand is susceptible to large deformations and, therefore, to loss of strength following a strong earthquake. The threshold event, capable of inducing liquefaction in a 1.5 m (5 ft) thick layer in at least one location near the toe, was determined to have the moment magnitude 5.7.

## 2 SOIL TESTED AND TESTING PROCEDURE

Soils meeting the Chinese Criteria are probably the most susceptible cohesive soils to loss of shear strength when subjected to cyclic loading, although the range of susceptible soils is probably broader: for example, Bootlegger Cove clay (average liquid limit 39, clay size fraction in excess of 50 percent) failed during the Anchorage, Alaska earthquake in 1964 (Stark and Contreras, 1998). The studied foundation deposit in Kansas contains cohesive soil of the most susceptible category, as shown in Figure 1. For seismic stability analyses, it is important to determine the undrained shear strength immediately after the seismically induced pore pressures. Castro and Christian (1976) showed that an effective stress approach would be misleading, because of the pore pressure variation during post-earthquake undrained shear. The authors observed that when the undrained strength of a saturated soil was determined after the specimen was subjected to cyclic loading, with no drainage permitted during and between the two loading stages, the resulting strength was almost the same as obtained through monotonic loading only. This behavior was verified on a large range of soil types, from silty clays to relatively dense sand.

The static undrained shear strength was determined both in laboratory through triaxial compression and extension tests, and in the field using vane shear tests. Good agreement was obtained when the anisotropic consolidation of the specimens in laboratory tests modeled the field stress conditions. The undrained strength was determined for both samples that were and were not subjected to prior cyclic loading. Because a deformation analysis was planned, the influence of the cyclic loading on the shear modulus was also determined, which was used in the constitutive model for the deformation analysis.

### 3 FIELD VANE SHEAR TESTS

Vane shear tests were performed both in the foundation soil near the downstream toe, and in the foundation soil underneath the mid-downstream and upstream slopes of the embankment, where the additional loading corresponded to 18 to 20 m (60 to 70 ft) of embankment fill. After the determination of peak strength, the tests were carried out to at least 25 revolutions of the vane or until a constant strength was obtained. The ultimate strength was assumed to represent the in situ undrained steady state (residual) strength of the cohesive soil.

The results of the vane shear tests are plotted on Figure 3 as a function of the maximum experienced vertical effective stress, together with laboratory triaxial test results, that are presented further in the paper. The maximum vertical effective stress occurred during dam construction and lasted until seepage through the dam became established. This period lasted about 5 years, assumed to be long enough for consolidation of the foundation soil. The overconsolidation ratio of the foundation soil, where not loaded by the dam, was about equal to 1.55.

The sensitivity (ratio between peak and residual strength) was found to be low under the slopes of the embankment but increased to medium to high sensitivity at the downstream toe. (See Table 2 for average geotechnical parameters.)

Close to lower bound envelopes of the field measurements were drawn defining the following undrained shear strengths:

- a. Peak,  $s_u = 0.35 p_v'$
- b. Residual,  $s_r = 0.12 p_v'$

### 4 SEISMIC WAVE VELOCITY FIELD TESTING

Three types of seismic investigation were used at three locations (on the embankment crest, on the downstream slope, and at the downstream toe): surface refraction, down hole, and cross

hole studies. The average seismic wave velocity results, used primarily to evaluate the tangent (initial) shear modulus, are presented in Table 1.

### 5 UNDISTURBED SAMPLING AND THEIR HANDLING

Boreholes were advanced through the embankment with hollow stem augers to a short distance above the natural ground surface. The augers were removed and casing was placed and sealed into the borehole. Within the foundation soil, the boreholes were rockbitted to the sampling depths using bentonite drilling fluid. Pump pressure was kept as low as possible but enough to adequately clean the borehole.

After reaching the desired depth for sampling, mud circulation was continued for several minutes to ensure a clean hole. Tools were withdrawn as slowly as possible to prevent swabbing.

Sampling was performed with Teflon-coated 76 mm (3-in.) diameter, 0.9-mm (0.035-in. or 20 gage) thin wall stainless steel tubes, 60 cm (2-ft) long for 46 cm (1.5-ft) samples and 46 cm (1.5-ft) long for 30 cm (1-ft) samples. The samplers' clearance ratio was in the range of 0.5 percent to 0.9 percent. The longer sampler tubes were reserved for the shallower holes drilled at the embankment toe and the shorter tubes were used for the deeper holes drilled through the embankment.

A Hvorslev fixed-piston sampler was used with the Teflon-coated thin-wall sample tubes. The sampler, with the piston flush with the bottom of the tube, was placed on the bottom of the cleaned borehole. The depth of the sampler was compared with the depth of rockbitting to ensure no fall-in material was present. The piston rod was then securely clamped to the drill rig mast. The sample tube was forced into the soil by a continuous and rapid push, without impact or twisting. The tubes were pushed as fast as the hydraulic system on the drill rig permitted, while not exceeding the hydraulic pressure required to lift the drill rig.

The penetration length of each push was determined to the nearest 3 mm (0.01 ft) by measuring from the top of the surface casing to markings on the outer rods. The initial reading was taken immediately before unlocking the piston and the final reading before relocking the piston after the push. "**Penetration**" was calculated and noted, as the difference between those measurements. After pushing to the appropriate length, the tube was left at rest for a minimum of 3 min. The piston rods were then turned to lock the piston in place and the sample retrieved. The tube was not rotated for shearing the sample bottom prior to withdrawal. The sampler was carefully withdrawn from the hole, without any twisting action or excess vibration. At the surface, before the sampler was removed from the borehole, the geologist supervising the sampling placed fingers over the lower end of the sample tube to prevent loss of the sample. After removal of the sampler from the borehole, the bottom of the sample in the tube was carefully trimmed with a putty knife to a flat surface to allow insertion of a drainage packer and filter paper against the bottom sample surface. The distance from the cutting edge to the sample was recorded. It was considered essential that the filter paper and the bottom of the perforated packer be installed quickly while the piston remained sealed, to prevent the sample from slipping. After removing the head assembly, the distance from the top of the sample tube to the top of soil was measured (average of four measurements) to the nearest 3 mm (0.01 in.), to define soil "**Recovery**," as the difference between this average measurement and the length of the sampler.

The quality of the undisturbed samples was evaluated based on the computed "Recovery/Penetration" (R/P) ratio and the Volume Change ( $\Delta V/V$ , in percent) computed as follows:

$$\Delta V/V = [(1 + CR/100)^2 \times (R/P) - 1] \times 100$$

where:

$$CR = [(ID - CE) / CE] \times 100, \text{ the clearance ratio in percent,}$$

ID = inside diameter measured at 60 deg intervals (three readings) on the swagged end and just above the swagged end,

CE = cutting edge diameter, similarly measured.

The samples retained for testing had R/P in the range of 0.98 and 1.02, or  $\Delta V/V = -1.3$  percent to  $+3.4$  percent. Two samples with R/P ratios of 0.91 and 0.90 were discarded. These samples had  $\Delta V/V = -8.3$  percent and  $-8.9$  percent, respectively.

Special attention was given not to tilt the sampler to remove the drill mud on top of the sample, but using a suction bulb instead. If mud was still remained on top, the upper surface was trimmed with the trimming auger. After removing excess fluid and mud from the top of the sample a non-perforated plate (1/2 packer) was installed on top of the sample, ensuring full contact with the sample but avoiding application of pressure on the sample. The distance from top of tube to the 1/2 packer was measured (average of four measurements) and recorded on a data form, in order to be checked before extrusion of the sample from the tube in the laboratory. A non-perforated packer was installed above the plate. The sample tube was then placed in a drainage rack for at least 30 min to allow gravity drainage. In all cases the drainage was insignificant. The perforations in the bottom packer were sealed with silicone grease and a protective cap was installed on the lower end of the sample tube. The samples were packed in racks lined with elastic polyethylene foam and transported by van to the laboratory. The samples were maintained in the vertical position at all times, until after they were tested.

The sample length measurements were duplicated in the laboratory to verify the condition of the sample after transportation. No variation in length was evident with any sample, so it was concluded that no disturbance of the sample was induced during transportation.



## 6 EVALUATION OF CONSOLIDATION UNDER THE EMBANKMENT

The void ratios of the samples recovered from the site are plotted with open circles on Figure 4. Most of them were taken from the soil deposit near the downstream toe of the dam where the effective overburden pressure was in the range of 60 to 90 kPa (0.6 to 0.9 tsf); other samples were taken from the cohesive blanket under the mid-slope, where the average vertical effective stress was of the order of 380 kPa (4 tsf).

Although the scatter of data due to variability in soil type is significant, some effect of consolidation under the mid-slope is evident. The average void ratio at the toe was 0.80 and under the mid-slope it was 0.73; these average data agree well with the results of a consolidation test, presented also on Figure 4. From a linear extrapolation of the average measured void ratios, and from the consolidation test results, one can estimate an average void ratio of 0.66 for the foundation soil under the crest, where the vertical effective stress is of the order of 710 kPa (7.4 tsf).

When the soil is fully saturated, the criterion  $w \geq 0.87 \text{ LL}$  becomes  $e \geq 0.87 (\gamma_s / \gamma_w) \text{ LL}$ , where  $e$  is the void ratio. For the material with the specific gravity of  $\gamma_s / \gamma_w = 2.64$ , the "Chinese Criteria" indicate that the soil may be susceptible to a significant loss of strength under cyclic loading if its void ratio is greater than 0.69 for a liquid limit of 30, or greater than 0.60 for a liquid limit of 26 (if all the other criteria, based on liquid limit value, plasticity index, and clay fraction content are met). It is, therefore, probable that material meeting the Chinese criteria exists even under the dam crest, in spite of over 40 years of consolidation under the 43 m (140-ft) embankment.

## 7 SPECIMENS TESTED IN THE CYCLIC TRIAXIAL APPARATUS

Only samples meeting the Chinese criteria (with void ratio in excess of approximately 0.7) were scheduled for testing of both toe and mid-slope

samples. The range and median characteristics of these samples are presented in Table 2.

## 8 TRIAXIAL TESTING: PROCEDURE

Sample extrusion and set up in the triaxial cell were also done with a minimum of disturbance. Before extrusion, the upper portion of the sampler tube was cut with a pipe cutter immediately above the top of sample, so that only a triaxial specimen length was extruded, thus minimizing friction. Since the diameter of the specimen was equal to the diameter of the sample (76 mm = 3 in.) the specimen was pushed directly from the sampler tube into the rubber membrane, and no trimming was necessary except at the upper and lower end.

Slight vacuum was applied to the top cap to prevent the tendency of the sample to slump during set up. The samples were saturated using back pressure until a  $B$  value of at least 0.95 was reached. The triaxial tests and the results are discussed later in the paper.

Filter paper was installed between the specimen and the double membrane to improve the uniformity of the pore pressure within the specimen and the measurement of a representative pore pressure at the ends of the sample.

The consolidation stresses used for the triaxial specimens modeled the stress conditions at the following locations:

- At the downstream toe (on samples taken from the toe).
- Under mid-slope (on both samples from the toe and below the slope).
- Under the embankment crest (on samples taken from the foundation below mid-slope).

The in situ stress conditions were evaluated by finite element analysis using the program FEADAM84 developed by the University of California at Berkeley. In order to model the

shear stress condition on a horizontal plane (where the maximum seismic shear stresses occur) under the toe and the mid- slope, anisotropic consolidation was applied to specimens. The maximum and minimum consolidation principal stresses were selected so that the effective normal stress and the shear stress acting on a 45 deg-plane in the triaxial specimen after consolidation would be the same as the stresses acting on the horizontal plane in field. On the other hand under the crest the static shear stress is close to zero and thus the consolidation stresses in the laboratory were isotropic. Table 3 summarizes the stresses applied in the consolidation stage.

## 9 TRIAXIAL TEST RESULTS

An initial test was used to establish the best frequency of cyclic testing. It was determined that at a cyclic load frequency of about one cycle every 4.5 sec the pore pressure measured at the end of the specimens was representative, in that little change in pore pressure occurred after cyclic loading was stopped. The use of this load frequency of 4.5 sec per cycle in all cyclic tests was considered a reasonable compromise between getting representative pore pressure readings and avoiding excessive creep effects at very low frequencies.

In the anisotropically consolidated samples it was observed that the effects of cyclic loading were such that when a compressive strain of 5 percent was reached, the double amplitude strain was below 5 percent and the excess pore pressure was close to 100 percent of the initial effective stress. The peak pore pressure in each cycle occurred when the deviator stress was close to zero, not at the end of the cycle when the cyclic loading went back to the consolidation value of the deviator stress. Based on these observations, 5 percent compressive strain was used as an indicator of 100 percent pore pressure build-up. For the isotropically consolidated samples the cyclic strains in extension were larger than in compression, and when the extension strains reached about 5 percent the pore pressure

was close to 100 percent also when the deviator stress was close to zero.

When  $\pm 5$  percent axial deformation (or other desired accumulated strain) was observed, cyclic loading was stopped, the pore pressure was allowed to equalize within the specimen, and static axial loading was applied under undrained condition until failure (or 20 percent axial deformation) was reached (with pore pressure measurement).

The results of the cyclic phase of the triaxial tests are presented in Figure 5, as a plot of cyclic stress ratio (CSR) versus the number of cycles to reach 5 percent strain. The cyclic stress ratio is defined as the cyclic deviator stress amplitude divided by the consolidation minor principal stress. Note that for the anisotropically consolidated samples the 5 percent strain is reached in compression while for the isotropically consolidated samples it is reached in extension. In both cases at the 5 percent strain the pore pressure was close to 100 percent. Based on this graph, the cyclic stress ratio required to cause 5 percent strain in 10 cycles was determined, as shown in the Table 4. For simplicity, in what follows this parameter will be named cyclic resistance ratio ( $CRR_{10}$ ).

It is interesting to note that the mid-slope samples tested at slope stresses were more resistant to cyclic loading (about 30 percent) than the toe samples consolidated to the same mid-slope stresses. It is believed that this effect is due to the much longer consolidation time of the slope samples (of the order of 40 years).

Dynamic 1D and 2D analyses of the dam and its foundation, using an equivalent linear-elastic model for the soils, were used to estimate seismic shear stresses in the foundation soils. Even though there are uncertainties in comparing the CSR values estimated for the field with the CRR values obtained from the triaxial tests, it appears that the strains would approach or exceed 5 percent and the associated high pore pressures would develop in the "silt" stratum beneath the dam and in the free field. This

conclusion raises two main questions, namely: (1) what is the reduction if any of the peak undrained strength of the silt and will the dam remain stable with the reduced strength, and (2) if the dam remains stable what are the seismically induced deformations. Note that the cyclic tests were performed with load control and in reality the seismic shear stresses would be reduced as the soil strains (yields). In order to properly assess the seismically induced deformations of the dam, a 2D dynamic analysis is planned using non-linear stress strain properties for the soil that can account for yielding. One of the purposes of the work described herein is to obtain parameters to model the silt layer, in particular its undrained strength and its stiffness, and how they are affected by the seismically induced strains and pore pressures.

The increase in pore pressure versus number of cycles normalized by the number of cycles to 5 percent strain is shown in Figure 6. An average curve representative for the material tested is also plotted. It is noted that the obtained curves fall within the expected zone, between characteristic curves for sand and for clays presented in literature.

## 10 UNDRAINED SHEAR STRENGTH

The potential loss in peak undrained shear strength is related to the degree to which cyclic loading causes damage to the soil structure, which in turn is probably related to the amount of cyclic straining. The axial strain development during a typical cyclic load test is shown in Figure 7 for an anisotropically consolidated specimen. After reviewing the various options, the peak axial strain during cyclic loading ( $d_3$  in Figure 7) was used as an indicator for the cyclic loading effects. Note that the peak axial strain for the anisotropically consolidated specimens is in compression while for the isotropic tests is in extension.

The peak undrained strength was obtained for specimens consolidated to various stresses, and thus to compare test results a peak undrained

strength ratio was used, in which the strength is divided by the consolidation major principal stress which is close to the effective vertical stress in the field. The variation of the peak undrained strength ratio, mobilized during monotonic undrained loading following the cyclic phase of the triaxial test, with the maximum strain experienced by the specimen at the end of the cyclic phase, is presented in Figure 8. Tests in which no cyclic loading was applied are plotted at a maximum strain during cyclic loading of zero.

A review of Figure 8 leads to the following conclusions:

*a.* The triaxial compression tests for samples not subjected to cyclic loading showed a peak undrained strength ratio of about 0.35 after neglecting two high strength samples. This result is in agreement with the field vane tests as shown in Figure 2,a.

*b.* No reduction of the peak undrained shear strength ratio ( $s_u / \sigma_{1c}$ ) was evident until after about 5 percent strain.

*c.* At 10 percent strain there is a loss of strength that corresponds to the drop in strength ratio from 0.35 to about 0.23. Note that this reduced peak undrained strength ratio is still substantially higher than the residual undrained strength ratio measured in the vane tests of 0.12, see Figure 2,b. This conclusion is consistent with the observation that the stress strain curves for specimens not subjected to prior cyclic loading showed an approximately plastic type of behavior or a peak at a small strain followed by only a slight decrease, within the strain limitations of the triaxial test (about 20 percent strain). In other words, the soils tested exhibited a behavior that was not strain sensitive, i.e., large strains are required to reduce its strength and to ultimately reach its residual undrained strength.

*d.* It is recommended that the peak undrained strength of the soil be modeled in future deformation analysis with a strength ratio of 0.35, periodically checking the strains reached at selected time increments. If strains exceed

5 percent then appropriate reduction in strength ratio would be made.

## 11 SHEAR MODULUS DEGRADATION WITH PORE PRESSURE INCREASE

Figure 9 shows the decrease of the shear modulus,  $G$  (in kilograms per square centimeter) with the decrease in effective minor principal stress plotted as a ratio of the initial (consolidation) minor principal stress. These results are to be used only for determining the rate of decrease in shear modulus with effective stress decrease (i.e., with pore pressure increase), but not for evaluation of the initial in situ shear modulus. The latter value is better evaluated from in situ shear wave velocity measurements.

Although there is substantial scatter on the absolute values of  $G$  in Figure 9, it is evident that the shear modulus is proportional to the effective minor principal stress to the power of 1.5 (corresponding to the slope of the two parallel lines that represent the average correlation). It is recommended to consider in deformation analysis the initial value of the shear modulus from in situ shear wave velocity measurements, with a reduction in shear modulus as a result of cyclic loading based on the reduction in effective minor principal stress to the power of 1.5.

In Figure 9 the decrease in shear modulus was plotted against the decrease in effective stress, even though the reduction in modulus reflects not only the effect of the decrease in effective stress but also the effect of disturbance of the soil structure during cycling, associated with the increasing strains that accompany the pore pressure increase. Thus, the decrease in shear modulus shown in Figure 9 is only applicable to the effect of cyclic loading. The effect on the shear modulus of changes in effective stress alone, not associated with cyclic loading, has been reported in literature to be typically proportional to the effective stress to the power of 0.5, substantially lower than the power of 1.5 obtained from the presented cyclic tests.

## 12 COMPRESSION VERSUS EXTENSION MONOTONIC LOADING

Two specimens each from two samples taken from one boring located at the dam toe were comparatively tested for triaxial compression and triaxial extension. All specimens were anisotropically consolidated at stresses corresponding to the dam toe zone (free field). The four specimens tested were very similar in terms of water content and Atterberg limits, i.e., no significant strength difference would be expected based on these index properties. Three tests, two in extension and one in compression, resulted in practically the same peak undrained strength of 0.28 to 0.29 kg/cm<sup>2</sup>, while one compression test exhibited a higher strength of 0.39 kg/cm<sup>2</sup>. No significant difference between the undrained strength of extension and compression tests was evident, as the results are well within the scatter of the strength data.

All four tests showed a peak strength at about 1 percent strain followed by a slight decrease in resistance. In spite of the occurrence of necking in the extension tests, the decrease in resistance beyond the peak in the extension tests was not significantly different from the decrease in resistance in the compression tests. Also, since the peak strength developed at strains of only about 1 percent, the errors due to uneven deformation (especially due to necking) were negligible.

In Figure 10 the comparative tests were plotted together with the other triaxial tests with no prior cyclic loading, as a function of the moisture content after consolidation. Because the specimens were saturated, the moisture content is a measure of the denseness.

## 13 CONCLUSIONS

The post-liquefaction behavior of cohesive soils depends primarily on their dilatancy properties and the characteristics of the cyclic loading: number of cycles, amplitude, and frequency. Taking into account the multitude of factors

affecting liquefiability and post-liquefaction undrained strength of cohesive soils, the best way of evaluating their behavior under cyclic loading is by undisturbed sampling and laboratory test.

Major difficulties in accurately replicating the fabric of field conditions through reconstituted laboratory specimens, make testing of undisturbed samples a necessity. Variations in quality of undisturbed samples and testing methodologies make attempts to correlate data from various sources unreliable.

The recommended test is cyclic loading in undrained conditions followed immediately (without drainage permitted) by monotonic loading. Pre-existence of shear stresses on the planes of maximum applied cyclic shear stress should be given consideration, as shear stress reversal is an important factor in liquefaction triggering and evolution of strength degradation with accumulated displacement. Field tests (vane shear, cone penetration, and shear wave velocity measurements) also may be useful in conservative evaluation of stability of non-critical structures on liquefiable soil deposits.

In general, cohesive soils appear to be more resistant to liquefaction than fine sands, when their states of denseness are similar. The strength degradation is dependent on magnitude of cyclic strain magnitude or total accumulated displacement. As accumulation of displacement requires time, it is apparent that seismic action of relatively long duration is required for liquefaction of cohesive soils. However, the residual strength mobilized under large deformations

may be smaller than that of sandy soils with similar a state of denseness.

#### 14 REFERENCES

- Castro, G. and Christian, J.T., (1976), Shear strength of soils and cyclic loading. *Journ. of Geotechnical Engrg.* ASCE, Vol. 102, GT9, 887-894.
- Koester, J.P., (1992), The influence of test procedure on correlation of Atterberg limits with liquefaction in fine-grained soils. *Geotechnical Testing Journal*, 15(4), pp. 352-361.
- Perlea, V.G., J.P. Koester, and S. Prakash, (1999), How liquefiable are cohesive soils? *Proceedings of the Second International Conference on Earthquake Geotechnical Engineering, Lisboa, Portugal*, pp. 611-618.
- Seed, H.B., I.M. Idriss, and I. Arango, (1983), Evaluation of liquefaction potential using field performance data. *Journal of Geotechnical Engrg.*, ASCE, 109(3), pp. 458-482.
- Stark, T.D. and Contreras, I.A., (1998), Fourth Avenue landslide during 1964 Alaskan earthquake. *Journ. of Geotechnical and Geoenvironmental Engrg.*, ASCE, Vol. 124, No. 2, 99-109.
- Wang, W., (1979), Some findings in soil liquefaction. *Water Conservancy and Hydroelectric Power Scientific Research Institute, Beijing, China*.

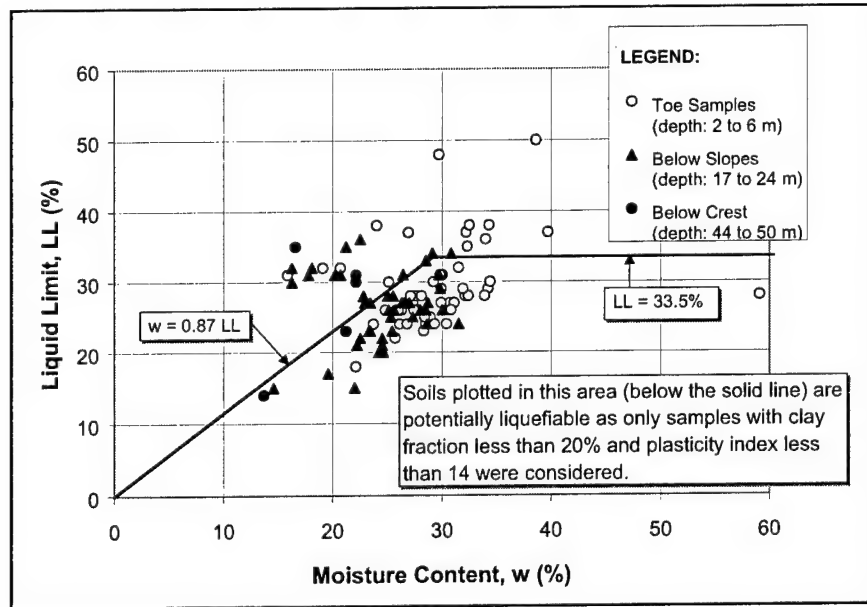


**Figure 1.** Chinese criteria adapted to ASTM definition of soil properties

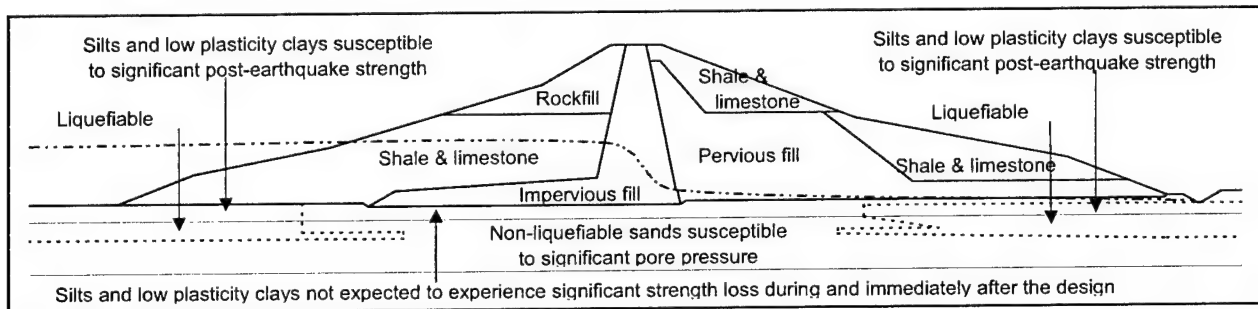


**Figure 2.** Typical cross section of the dam

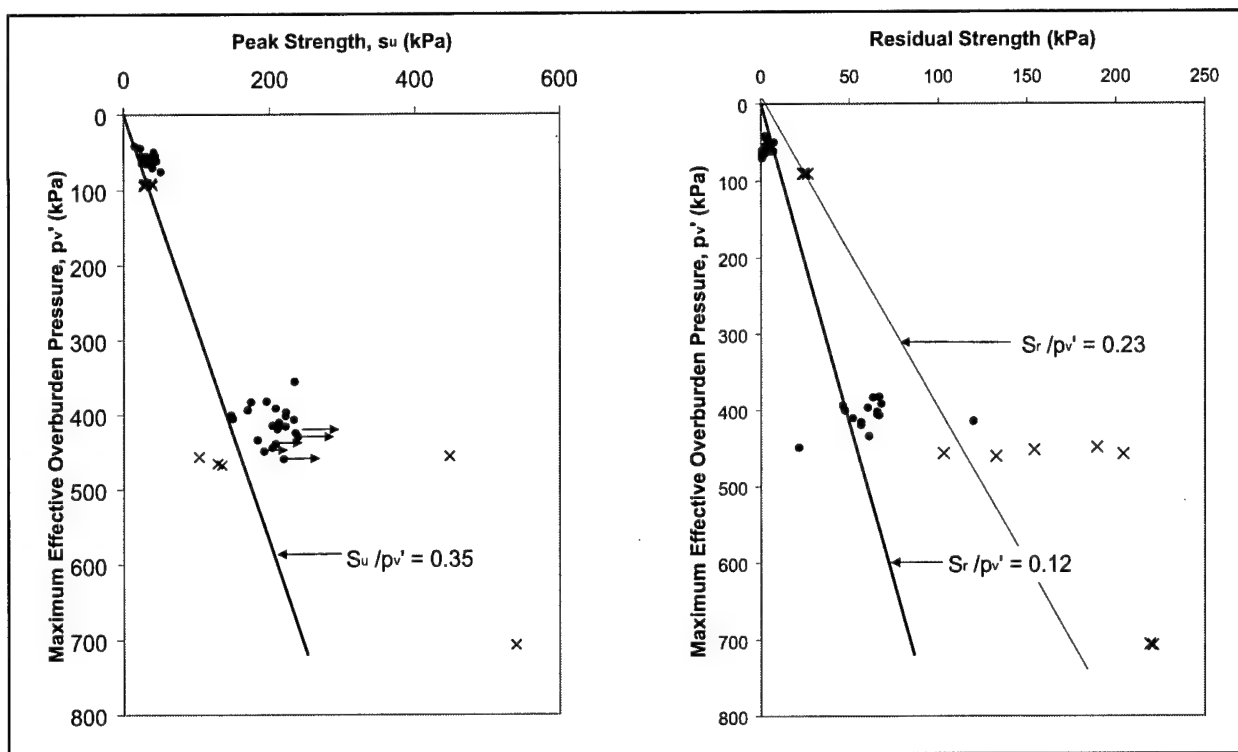


Figure 3. Undrained shear strength by vane test

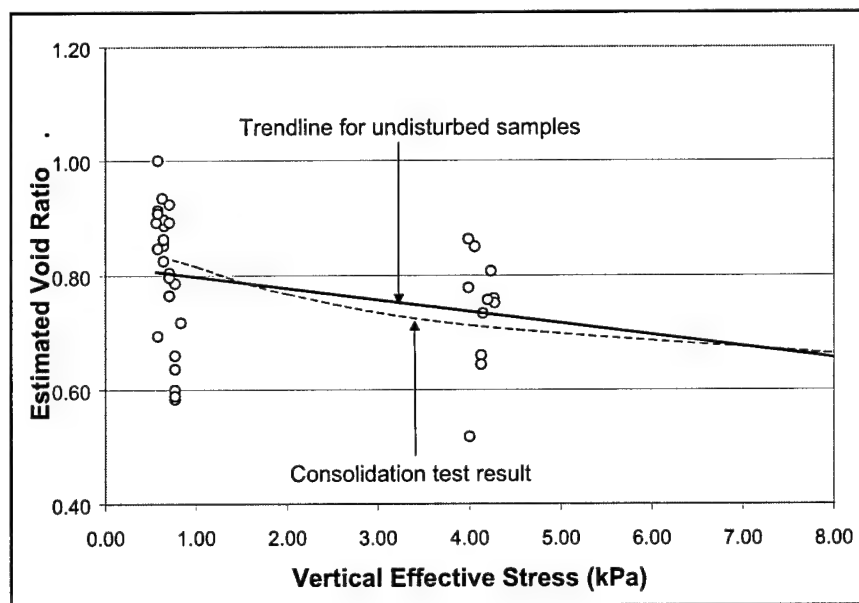
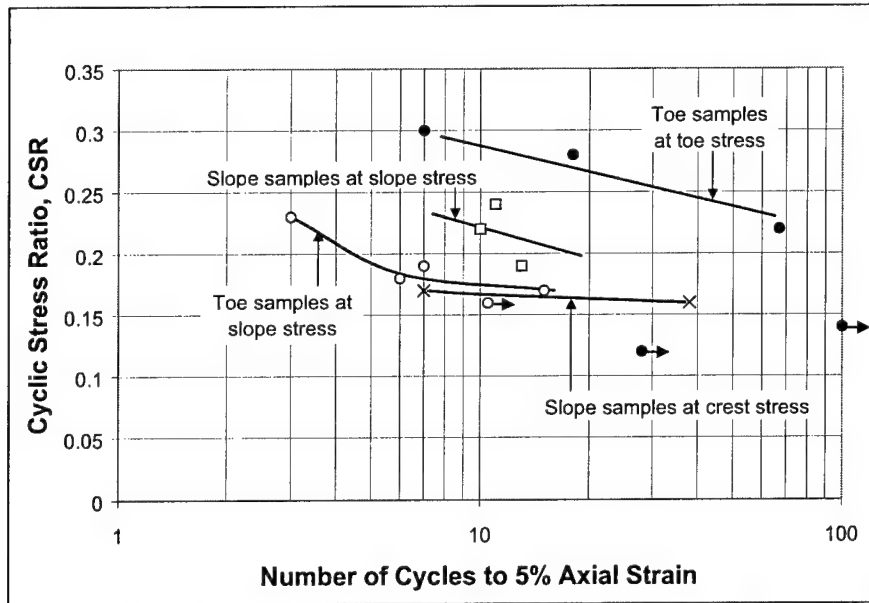
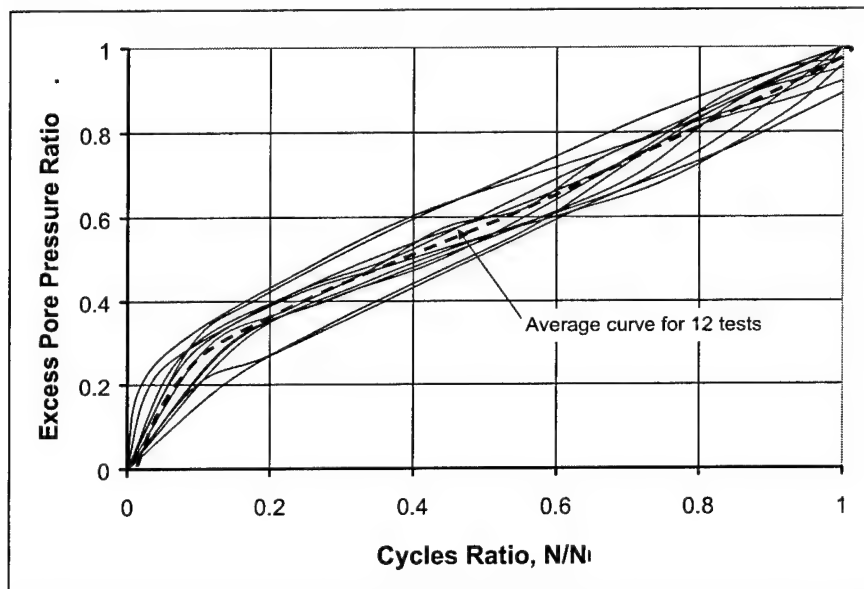


Figure 4. Evaluation of consolidation effect on the blanket soil under the embankment



**Figure 5.** Resistance to cyclic loading



**Figure 6.** Pore pressure increase with the normalized number of cycles



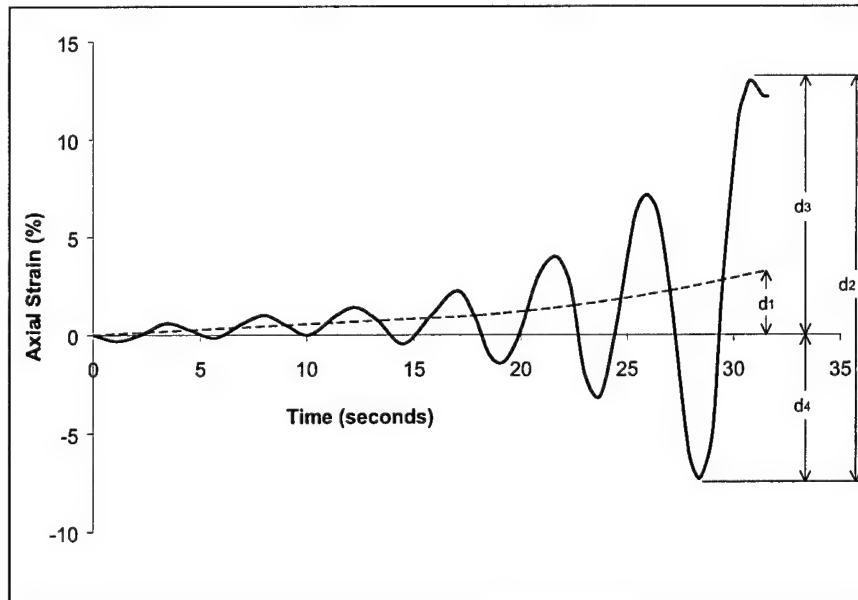


Figure 7. Alternate definitions of axial strain at the end of cyclic loading

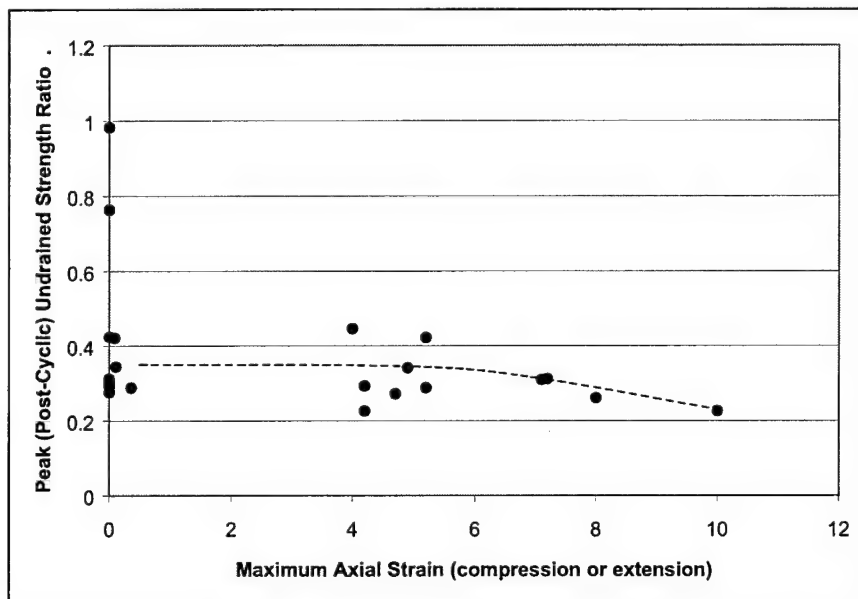
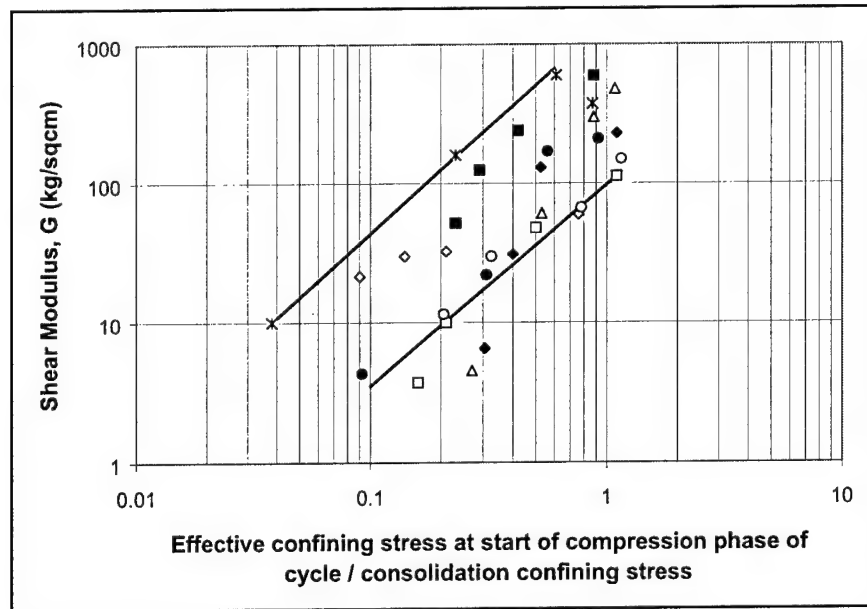
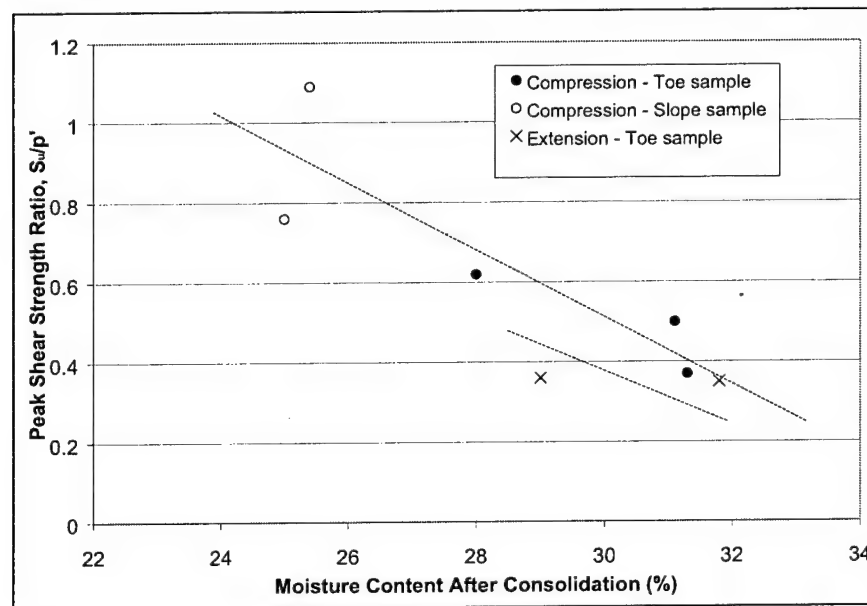


Figure 8. Peak undrained shear strength ratio vs. maximum axial strain



**Figure 9.** Moduli decrease during cyclic loading



**Figure 10.** Results of static triaxial tests

**Table 1.** Average Seismic Wave Velocities in the Foundation Cohesive Blanket (lower half, silty clay/clayey silt zone)

Location	Average Wave Velocity, m/s (1 m/s = 3.28 fps)	
	Compression Wave, P	Shear Wave, S
Embankment Crest	1,850	332
Downstream Mid-Slope	1,510	293
Downstream Toe	1,480	186

**Table 2.** Geotechnical Characteristics of Tested Samples

Characteristic	Range of Values	Median Value
Liquid Limit, LL	23 to 32	29
Plasticity Index, PI	1 to 12	6
Fines content, fraction < 0.074 mm, %	68 to 100	96
Clay content, fraction < 0.005 mm, %	10 to 20	15
Overconsolidation Ratio	1.36 to 1.75	1.55 (average)
Initial moisture content (%) of samples from foundation soil blanket located at:		
- toe	30 to 36	34
- mid-slope	25 to 30	29
Moisture content (%) after consolidation under stresses corresponding to location below:		
- toe	29 to 33	31.4
- mid-slope	23 to 32	26.1
- crest	24.5 to 26	25.0
Void ratio after consolidation under stresses corresponding to location below:		
- toe	0.77 to 0.87	0.83
- mid-slope	0.61 to 0.85	0.69
- crest	0.65 to 0.69	0.66

**Table 3.** Consolidation Stresses of Triaxial Tests

Condition modeled	Field stresses, kgf/cm <sup>2</sup>		Ratio $\alpha = \tau_{hv} / \sigma_v$	Principal Stresses for Consolidation	
	$\sigma_v$	$\tau_{hv}$		$\sigma_1 = \sigma_v(1 + \alpha)$	$\sigma_3 = \sigma_v(1 - \alpha)$
Under the downstream toe	0.79	0.13	0.17	0.93	0.65
Under mid-slope	4.19	0.46	0.11	4.65	3.72
Under crest	7.20	0	0	7.20	7.20
Note: 1 kgf/cm <sup>2</sup> = 1.0237 tsf = 98.066 kPa					

**Table 4.** Cyclic Strength Resistance

Sample Origin	Consolidation Condition	CRR10
Downstream toe	Downstream toe stresses	0.28
Downstream toe	Mid-downstream slope stresses	0.17
Mid-slope	Mid-downstream slope stresses	0.22
Mid-slope	Crest stresses	0.17

## Identification of Non-Cohesive Filters to Prevent Migration of Impervious Materials for Embankment Dams due to Large Earthquakes (Fault Movement)

by

Tadahiko SAKAMOTO<sup>1)</sup>, Yoshikazu YAMAGUCHI<sup>2)</sup> and Hiroyuki SATOH<sup>3)</sup>

### ABSTRACT

Filter materials are required to be cohesionless. They ensure safety of embankment dams against fault movement. At present, from this point of view, we have the criterion that the percentage of the filters passing the #200 sieve (0.074mm) should be less than 5%. However we can use any soil for filters, if we can confirm their high permeability and non-cohesion. We have performed Sand Castle tests proposed by P. Vaughan in order to confirm non-cohesion of filter materials. In addition, we have discussed the method of relaxing restrictions on the percentage finer than the #200 sieve of filter materials for embankment dams.

**Key Words :** *embankment dam, filter criteria, non-cohesion, Sand Castle test*

### 1. INTRODUCTION

Of most of dams built in regions of high earthquake potential, there are few in locations where faults are not recognized or suspected to exist. Any dam site located near an active fault or a potentially active fault may be subjected to strong earthquake shaking. The problems of designing the dams to withstand the accelerations imposed by strong earthquake and of making the dam safe against fault movement in the foundation are related (Sherard *et al.*, 1974). Because the design details to ensure safety against such possible fault displacement are difficult problems, a dam site with an active

fault or a potentially active fault should be avoided if possible. In Japan, to avoid a dam site with an active fault or a potentially active fault, various investigations are systematically made (Wakizaka, 1999).

In Sept. 2, 1999 Ji-Ji Earthquake in Taiwan, one branch of the activated fault crossed the northern end of the Shih-Kang Dam causing three of its spillways to be completely destroyed by vertical offsets of up to 10 meters. Besides, in Aug. 17, 1999 Kocaeli Earthquake in Turkey, the faulting and the resulting ground ruptures caused the collapse of a lot of buildings and modern engineered structures. Therefore, it is very important to comprehend how soils and rocks immediately next to active fault traces would be deformed. With this knowledge provided, damage to a variety of structures should be minimized.

In the case of dam, concrete dams on active faults, or near some major active faults, are not advisable because of their rigid and brittle bodies. On the other hand, embankment dams can be designed with confidence based on the examples of the Coyote, Ceder Springs and Palmdale Dams to withstand safely deformations imposed by fault movement (Sherard *et al.*, 1974). One of the most effective countermeasures against the damage of an impervious zone of an

1) Dr. Eng., Chief Executive, Public Works Research Institute (PWRI), 1-6 Minami-hara, Tsukuba-shi, 305-8516, JAPAN

2) Dr. Eng., Principal Researcher, Dam Structures Team, PWRI

3) Researcher, Dam Structures Team, PWRI

embankment dam imposed by foundation fault movements is a construction of thick, protective zones of cohesionless filter (transition) materials. It is impossible for an open crack to exist in the mass composed of cohesionless materials. Any open crack, which might tend to be formed momentarily by the fault displacement, must immediately close by the action of the walls of crack collapsing. Hence, internal zones of these materials acts as 'crack stoppers' in dam embankments. Sands, gravels, sand-gravel mixtures, when these materials are free of any appreciable admixtures of fine-grained soils (clays or silts) are cohesionless.

The design of filters for embankment dams in Japan is based on the criteria used throughout the world (JANCOLD, 1971, MOC, 1985) including the following rule: Filters should not contain more than about 5% of fines passing a #200 (0.074mm) sieve, and the fines should be cohesionless. Recently in Japan, we have much trouble in meeting this regulation economically. However, systematic research on identification of filter cohesion has not been made yet.

In such present condition, the applicability of the Sand Castle test (SC test) proposed by Vaughan (Vaughan, 1978, Vaughan and Soares, 1982) is examined as a testing method of identifying the non-cohesion of filter materials. In addition, the relaxation of the fine content regulation for filter materials is finally discussed based on the quantitative relation between fine content and the cohesion, and other physical properties, such as permeability and plasticity.

## 2. SAND CASTLE TEST (SC TEST)

### 2.1 Type of tests

The procedure of the SC test proposed by Vaughan is illustrated in Figure 1. Filter materials compacted in a mold are

submerged in the water, and the mold is quietly pulled out. When filter materials collapse with an angle larger than an angle of repose (AOR), they are identified to be cohesive. However, detailed specification of the test and attention in the evaluating method of the test result, are not clearly shown. In this study, three kinds of AOR tests shown in the following are carried out in order to examine procedure of the SC test and evaluation method of the test results in detail.

Test A = AOR test in the air,

Test B = AOR test in the water,

Test C = AOR test under the submerged condition.

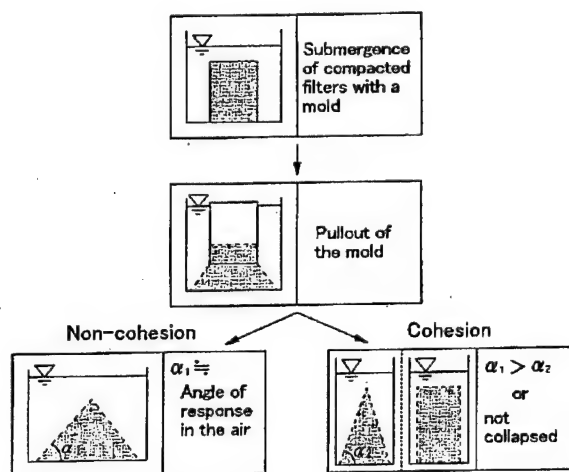


Figure 1 Procedure of SC test proposed by Vaughan

### 2.2 Test A

Using funnel or hand scoop, air-dried materials are fallen with a low falling height to form a stable conical mountain. Diameter  $D$  and height  $H$  of the conic basal plane are measured. Diameter is measured at 4 places, and the mean value is reported. AOR  $\theta$  is calculated by the substitution of  $D$  and  $H$  in the following equation.

$$\theta = \arctan(2H/D) \quad (1)$$

The mean value of the three tests for the same materials is reported as an AOR in the air, after confirming that there is not large difference among three results.

### 2.3 Test B

In a tank, which the water is poured, air-dried materials are made to fall from the water surface using funnel or hand scoop to form a stable conical mountain. Afterwards procedure is same as that of Test A. This test has no direct relation with the method proposed by Vaughan, but it is carried out for the purpose of analyzing the results of Vaughan's method in detail.

### 2.4 Test C

The specimen is prepared by compacting test materials in a mold of 150mm inner diameter and 175mm height. Compacted materials with the mold are submerged in a water tank quietly. The mold is slowly pulled out, and collapse condition of compacted materials is observed. Height of conical mountain  $H$  and diameter of the basal plane  $D$  in the final stable state are measured, and the AOR under the submerged condition is calculated by equation (1). Compaction methods of test materials for Test C are explained below.

#### (1) *Compaction method A for materials without fines*

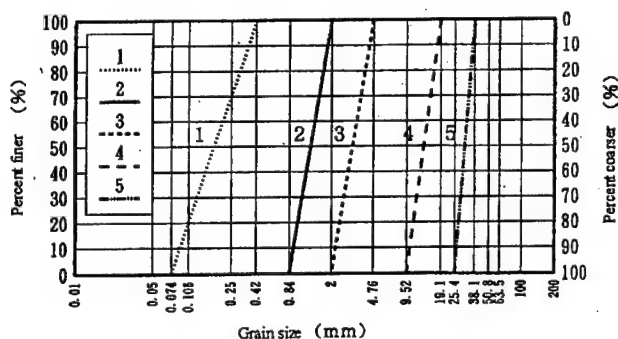
The compaction for materials without fines is performed in conformity to the JIS Standards of maximum density test (JIS-A-1224). Materials are put in a mold of 150mm inner diameter and 175mm height by dividing 10 layers, and they are compacted in respect of the outer side wall of the mold with 100 blows by a mallet (stroke plane diameter = 35mm, mass = 162.6g) for each layer. The total number of strokes becomes 1000.

#### (2) *Compaction method B for materials with fines*

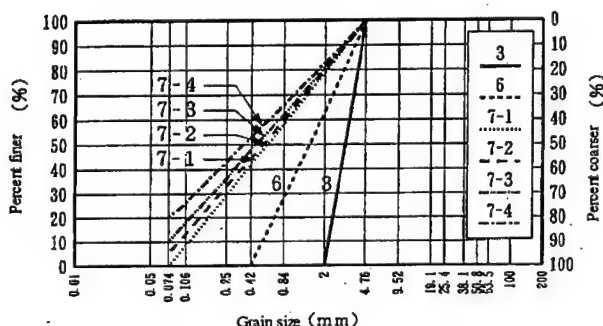
The compaction for materials with fines is performed in conformity to the JIS Standards of soil compaction test using rammer (JIS-A-1210). The water content of materials is adjusted at the optimum water content, and they are compacted in a mold of 150mm inner diameter and 175mm with an energy of 1Ec in order to prepare the specimen with a maximum dry density. Collapse of this specimen is most difficult to be generated under the same compaction energy condition. In short, this is on the safe side from the viewpoint of the identification of non-cohesion of materials.

## 3. MATERIALS AND CONDITIONS OF TEST

Gradations of test materials used in the test are shown in Figure 2. Figure 2(a) shows uniform filters (uniformity coefficient  $U_c = 1.2-2.4$ ) without fines (clays or silts) which seem to be cohesionless clearly. They are prepared for Case 1. In Figure 2(b), broadly graded filters ( $U_c = 3.4-30$ ) are shown, and are used in Case 2. Gradations ⑦-1, ⑦-2, ⑦-3 and ⑦-4 have fines of 0, 5, 10 and 20% by weight respectively. Maximum grain size of filters is set to be 38.1mm or less in consideration of an inner diameter of the mold of 150mm. Rounded and angular gravels are prepared in order to examine the effect of the particle shape on test results. In addition, the filter materials used for an existing embankment dam, the mixtures of phyllite and limestone, are also prepared. Here, rounded gravel, angular gravel and filter material for an existing dam are respectively called material A, material B and material C. Toyoura sands and glass beads are also used as uniform filters. Besides, fines with a size of 0.074mm or less, are added to materials B and C in Case 2.



(a) Uniform filters for Case 1



(b) Broadly graded filters for Case 1

Figure 2 Gradations of filters used in program

Physical properties of added fines are summarized in Table 1. In Table 2, physical test results for filter materials are shown. The results of compaction test for filters without fines are summarized in Table 3. In addition, the results of compaction and permeability tests for filters with fines are shown in Table 4 and Figure 3. Although material B and material C with gradation ⑦-1, do not contain fines, two kinds of compaction methods mentioned above are made for them. However, for material B an optimum water content and a maximum dry density could not be identified clearly from the result of compaction test B. Then, in Test C, the material B with gradation ⑦-1 is compacted by compaction method A. But two compaction methods are used to prepare the specimen of the material C with gradation ⑦-1 for Test C.

Cases and results of the SC tests are summarized in Table 5.

Table 1 Physical properties of added fines

Fines added to	Material B	Material C
Specific gravity $G_s$	2.725	2.754
Liquid limit $w_L$ (%)	42.4	52.4
Plastic limit $w_P$ (%)	20.1	30.5
Plasticity index $I_P$	22.3	21.9

Table 2 Physical properties of filter materials

Filters	Gradation #	$G_s$	$G_b$	$Q$ (%)	$w_L$ (%)	$w_P$ (%)	$I_P$
Toyoura sands	①	2.645	—	—	—	—	—
	②	2.510	—	—	—	—	—
Glass beads	④	—	2.507	—	—	—	—
	⑤	—	—	—	—	—	—
Material A	②	2.647	—	—	—	—	—
	③	2.659	—	—	—	—	—
	④	—	2.596	0.895	—	—	—
	⑤	—	2.599	0.908	—	—	—
Material B	②	2.709	—	—	—	—	—
	③	2.717	—	—	—	—	—
	④	—	2.649	1.030	—	—	—
	⑤	—	2.689	0.584	—	—	—
	⑥	2.700	—	—	—	—	—
	⑦-1	2.709	—	—	NP	NP	NP
	⑦-2	2.709	—	—	NP	NP	NP
	⑦-3	2.711	—	—	16.0	13.2	2.8
Material C	⑦-4	2.712	—	—	20.9	12.8	8.1
	①	2.750	—	—	—	—	—
	②	2.699	—	—	—	—	—
	③	2.714	—	—	—	—	—
	④	—	2.634	1.370	—	—	—
	⑤	—	2.651	0.890	—	—	—
	⑥	2.716	—	—	—	—	—
	⑦-1	2.730	—	—	NP	NP	NP
	⑦-2	2.730	—	—	NP	NP	NP
	⑦-3	2.729	—	—	18.9	15.7	3.2
	⑦-4	2.728	—	—	26.6	18.8	7.8

$G_s$  = Specific gravity of soil particle,  $G_b$  = Specific gravity of gravel,  $Q$  = Water absorption,  $w_L$  = Liquid limit,  $w_P$  = Plastic limit,  $I_P$  = Plasticity index, NP = Non plastic.

Table 3 Results of compaction test for filters without fines

Filters	Gradation #	$\rho_d$ (g/cm <sup>3</sup> )	$G_s/G_b$	$e$
Toyoura sands	①	1.625	2.645	0.628
	②	1.633	2.510	0.537
Glass beads	④	1.483	2.507	0.690
	⑤	1.654	2.647	0.600
Material A	③	1.761	2.659	0.510
	④	1.688	2.596	0.538
	⑤	1.664	2.599	0.562
	⑥	1.541	2.708	0.757
Material B	③	1.562	2.717	0.739
	④	1.559	2.649	0.699
	⑤	1.504	2.689	0.788
	⑥	1.758	2.700	0.536
Material C	⑦-1	1.894	2.709	0.430
	①	1.442	2.750	0.907
	②	1.521	2.699	0.774
	③	1.531	2.714	0.773
	④	1.536	2.634	0.715
	⑤	1.509	2.651	0.757
	⑥	1.680	2.716	0.617
	⑦-1	1.883	2.730	0.450

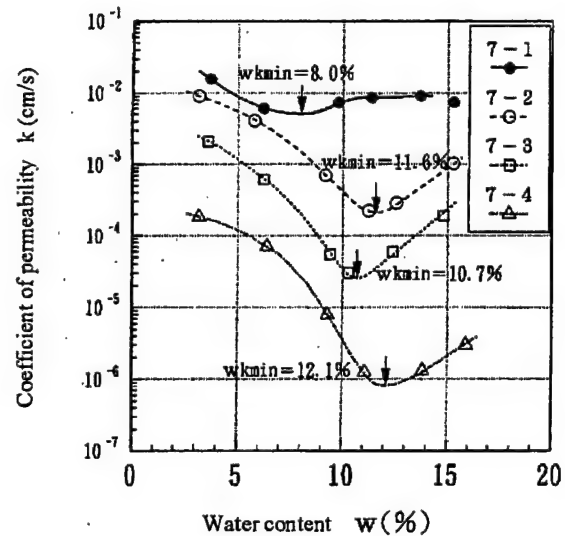
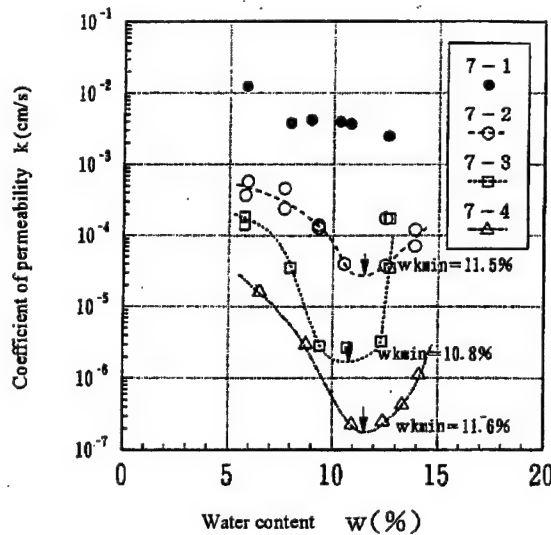
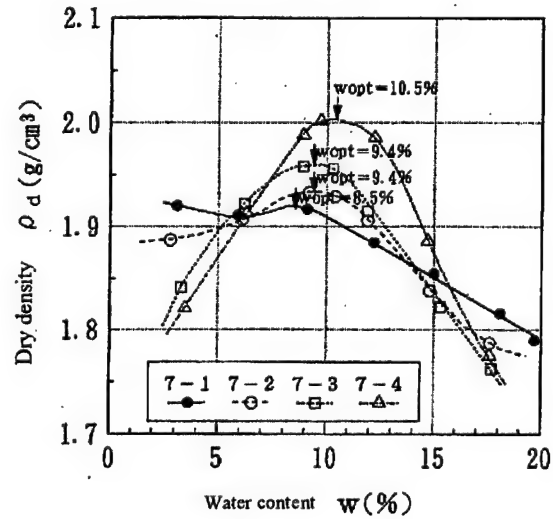
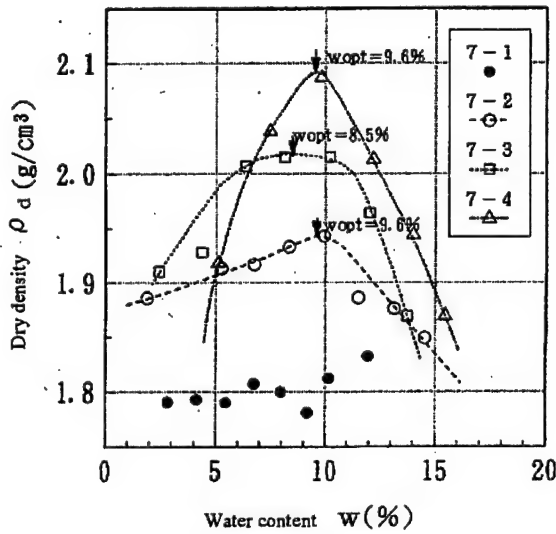
$\rho_d$  = Dry density,  $e$  = Void ratio.



Table 4 Results of compaction and permeability tests for filters with fines

Filters	Gradation #	Fine content(%)		$w_{opt}(\%)$	$\rho_{dmax}(g/cm^3)$	$k_{opt}(cm/s)$	$k_{min}(cm/s)$	$w_{kmin}(\%)$
		Before compaction	After compaction					
Material B	7-1	0.0	3.5(+3.5)	-	-	$5.1 \times 10^{-3}*$	$5.1 \times 10^{-3}*$	-
	7-2	5.0	8.5(+3.5)	9.6	1.946	$9.2 \times 10^{-5}$	$2.6 \times 10^{-5}$	11.5
	7-3	10.0	13.4(+3.4)	8.5	2.024	$1.7 \times 10^{-5}$	$1.4 \times 10^{-5}$	10.8
	7-4	20.0	21.5(+1.5)	9.6	2.092	$1.0 \times 10^{-6}$	$1.6 \times 10^{-7}$	11.6
Material C	7-1	0.0	9.3(+9.3)	8.5	1.917	$5.7 \times 10^{-3}$	$5.6 \times 10^{-3}$	8.0
	7-2	5.0	14.2(+9.2)	9.4	1.934	$6.0 \times 10^{-4}$	$2.4 \times 10^{-4}$	11.6
	7-3	10.0	18.2(+8.2)	9.4	1.960	$5.4 \times 10^{-5}$	$2.9 \times 10^{-5}$	10.7
	7-4	20.0	27.9(+7.9)	10.5	2.006	$2.7 \times 10^{-6}$	$9.0 \times 10^{-7}$	12.1

$w_{opt}$  = Optimum water content,  $\rho_{dmax}$  = Maximum dry density,  
 $k_{opt}$  = Coefficient of permeability at  $w_{opt}$ ,  $k_{min}$  = Minimum coefficient of permeability,  
 $w_{kmin}$  = Water content at  $k_{min}$ , \*) = Mean value.



(a) Material B

(b) Material C

Figure 3 Results of compaction and permeability tests

Table 5 Cases and results of SC tests

Filters	Gradation #	Test A		Test B		Test C		A-C(°)
		water content	AOR(°)	water content	AOR(°)	water content	AOR(°)	
Toyoura sands	①	Air-dried	32.3	Air-dried	30.5	Air-dried	27.6	4.7
Glass beads	②	Air-dried	20.5	Air-dried	21.8	Air-dried	18.3	2.2
	④	Air-dried	18.6	-	-	Air-dried	17.2	1.4
Material A	②	Air-dried	34.3	Air-dried	33.9	Air-dried	29.2	5.1
	③	Air-dried	32.4	-	-	Air-dried	30.6	1.8
	④	Air-dried	34.9	-	-	Air-dried	32.9	2.0
	⑤	Air-dried	34.9	-	-	Air-dried	32.5	2.4
	⑥	Air-dried	35.7	Air-dried	35.3	Air-dried	31.5	4.2
Material B	③	Air-dried	37.2	-	-	Air-dried	33.8	3.4
	④	Air-dried	39.4	Air-dried	41.8	Air-dried	38.7	0.7
	⑤	Air-dried	39.5	-	-	Air-dried	41.3	-1.8
	⑥	Air-dried	34.6	-	-	Air-dried	31.8	2.8
	⑦-1	Air-dried	35.2	-	-	Air-dried	31.3	3.9
	⑦-2	Air-dried	36.5	Air-dried	31.5	W <sub>opt</sub>	33.4	3.1
	⑦-3	Air-dried	38.1	-	-	W <sub>opt</sub>	41.7	-3.6
	⑦-4	Air-dried	39.8	-	-	W <sub>opt</sub>	43.9	-4.1
Material C	①	Air-dried	33.6	Air-dried	23.6	Air-dried	27.2	6.4
	②	Air-dried	35.0	Air-dried	35.8	Air-dried	32.4	2.6
	③	Air-dried	34.2	-	-	Air-dried	31.1	3.1
	④	Air-dried	36.7	Air-dried	38.8	Air-dried	34.5	2.2
	⑤	Air-dried	38.5	-	-	Air-dried	33.2	5.3
	⑥	Air-dried	34.2	-	-	Air-dried	31.1	3.1
	⑦-1	Air-dried	35.8	-	-	Air-dried	34.6	1.2
						W <sub>opt</sub>	32.7	3.1
	⑦-2	Air-dried	37.1	Air-dried	30.9	W <sub>opt</sub>	38.5	-1.4
	⑦-3	Air-dried	36.2	-	-	W <sub>opt</sub>	42.2	-6.0
	⑦-4	Air-dried	35.8	-	-	W <sub>opt</sub>	45.6	-9.8

## 4. TEST RESULTS

### 4.1 Results of Test A

Figure 4 shows the AOR in the air obtained from Case 1 for uniform filters without fines. Except for the AOR in the air of glass beads with only two data points, when the maximum grain size  $D_{max}$  increases, it tends to grow. The tendency of angular gravels (materials B and C) is stronger than that of rounded gravels (material A). The AOR in the air is supposed to receive the effect of the surface roughness of filters.

Next, the AOR in the air obtained from Case 2 is illustrated in Figure 5. The AOR in the air of material B without fines (gradations ③, ⑥, ⑦-1) decreases, when uniformity coefficient increases, and the AOR in the air rises with the increase of fine content. On the other hand, in the case of material C, the effect of fine content is not

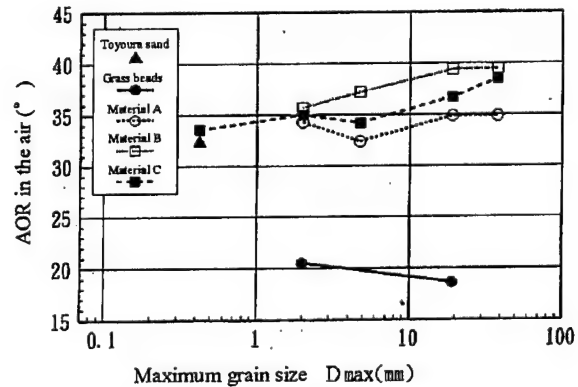


Figure 4 Angle of response in the air of Case 1

recognized in the comparison of gradations ⑦-1 to ⑦-4, but the AOR in the air tends to increase, when uniformity coefficient increases within there being no fines (gradations ③, ⑥, ⑦-1).

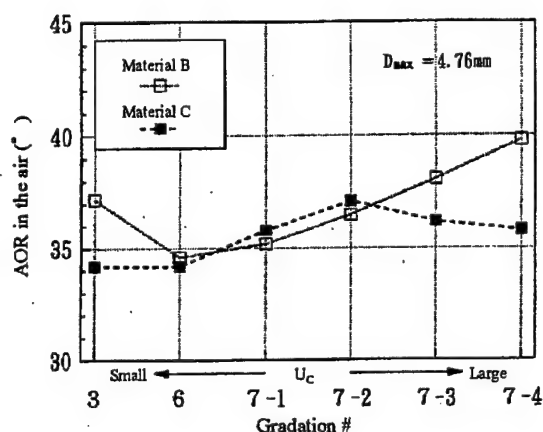


Figure 5 Angle of response in the air of Case 2

#### 4.2 Results of Test B

Figure 6 compares the AOR in the air (a) with the AOR in the water (b). In the case of uniform filters except for the material C with gradation ①, it is distributed within  $b=a \pm 2^\circ$ . Both do not have large difference. On the other hand, materials B and C with gradation ⑦-2 are broadly graded, and their AORs in the water become a little smaller because of the segregation of materials during the falling in the water. According to the hydraulic filling effect, the dry density of the conical mountain formed in Test B seems to be larger than that in Test A. In actual, this magnitude correlation could be confirmed by calculating the dry density with the weight of materials and the volume of conical mountain.

When the dry density of gravels becomes larger, the strength expressed as the AOR increases. However, because the strength of gravels under saturated condition is generally smaller than that under air-dried condition. One offsets the other, and the difference between the AOR in the air and the AOR in the water, becomes smaller as a consequence.

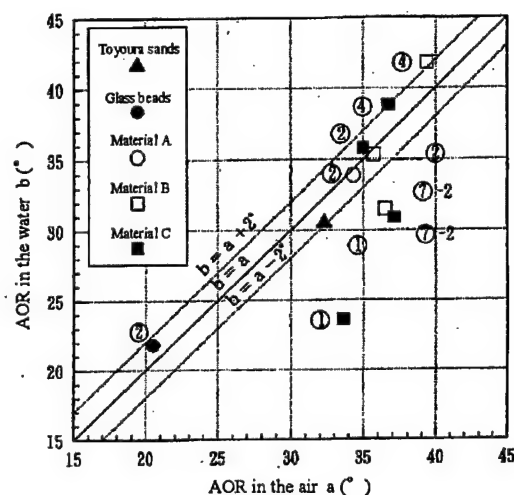


Figure 6 Comparison of AOR in the air and AOR in the water

It is found that in the case of uniform filters without fines, which are clearly cohesionless, the AOR in the water, which is considered to coincide with that in Test C introduced in the next section, is nearly equal to the AOR in the air. In short, it is guessed that identification method of non-cohesion based on the AOR in the air and the AOR under the submerged condition in the SC test proposed by Vaughan is approximately appropriate.

#### 4.3 Results of Test C and identification of non-cohesion

Figure 7 arranges the difference between the AOR in the air and the AOR under the submerged condition of uniform filters obtained from Case 1, as a relation with the maximum grain size. Though the difference between the AOR in the air and the AOR under the submerged tends to decrease, when the maximum grain size increases in the case of material B, the tendency is not clear in the case of glass beads, material A and material C. Although the material B with gradation ⑤ is identified to be cohesive according to the Vaughan's method, this seems to be the effect of the error in the size measurement of the

conical mountain because of the larger grain size. Then, the value of {(the AOR in the air)-(the AOR under the submerged condition)} (differential value) obtained from the SC test seems to become approximately  $0 \sim 6^\circ$  for cohesionless materials. With the definition of Vaughan's method, the material in which the differential value becomes 0 is evaluated to be cohesionless. However, two AORs do not exactly agree even in the test for cohesionless materials, since, strictly speaking, density, strength and stress state are different between in the air and under submerged condition. Therefore, it is considered that the differential value becomes a positive value of  $5 \sim 6^\circ$  or less in the case of cohesionless filters, when it is based on the results of Case 1 using present cohesionless materials.

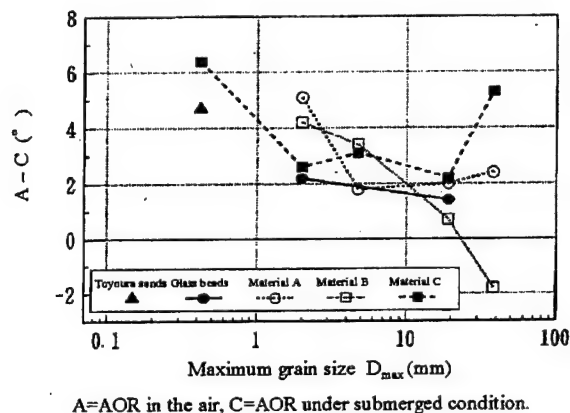


Figure 7 Difference between AOR in the air and AOR under submerged condition of Case 1

Next, the differential values obtained from Case 2 are arranged in Figure 8. From Table 5, in the case of the material C with gradation ⑦-1, it is clear that there is not large difference in AORs under submerged condition between of specimen prepared using compaction method A and of that prepared using compaction method B. Then, in drawing Figure 8, the AOR under submerged condition for the material C with

gradation ⑦-1 using the specimen prepared by compaction method B, considering that an optimum water content could be clearly defined. In the case of material B, although the differential values of gradations ⑦-1 and ⑦-2 are around  $+3 \sim +4^\circ$  and they are identified to be cohesionless, the differential values of gradations ⑦-3 and ⑦-4 are around  $-3 \sim -4^\circ$  and they are identified to be cohesive. There seems to be a boundary of whether it is cohesive or not between gradation ⑦-2 and gradation ⑦-3. In the material C, the boundary is not so clear as that in material B, but it seems to be between gradation ⑦-1 and gradation ⑦-2, since the differential value has shifted from the positive negatively at this point. Judging from the observed results of collapsing condition of compacted materials in Test C, the materials with gradation ⑦-2 or coarser started to collapse immediately after the submergence, the materials with gradations ⑦-3 and ⑦-4 did not start to collapse quickly or did not finally come to the perfect collapse. This means that the attention to collapsing condition of compacted materials as well as the differential value is very important in identifying the cohesion of filters.

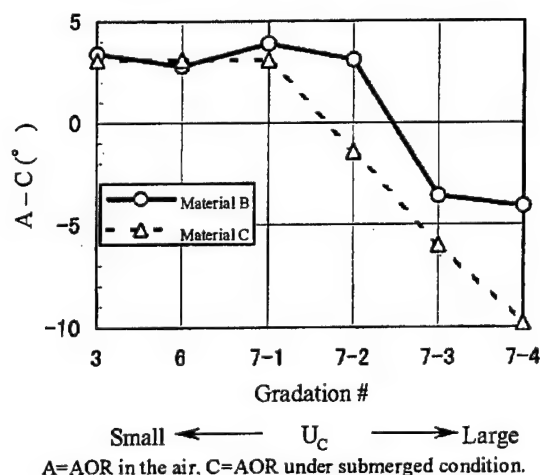


Figure 8 Difference between AOR in the air and AOR under submerged condition of Case 2

## 5. CONSIDERATIONS

The investigation on the method of the SC test and the evaluation of the test results has been carried out here. Then, the allowable maximum fine content of filters is discussed from the viewpoint of non-cohesion and permeability in consideration of the results of not only this study and previous research works.

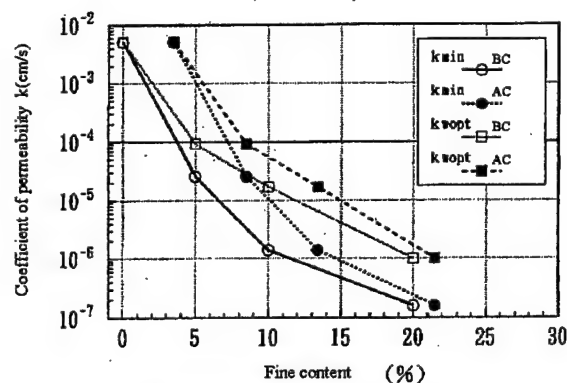
### (1) Relationship between plasticity index and cohesion

The criterion of U. S. Department of Agriculture, Soil Conservation Service (SCS) (1986) regulated that NP is the identifying condition of non-cohesion of filter materials. Based on the results of liquid and plastic limits tests, shown in Table 2, materials B and C with gradations ⑦-1 and ⑦-2 are NP, while those with gradations ⑦-3 and ⑦-4 are not NP. Liquid and plastic limits tests were carried out for filters before the compaction.

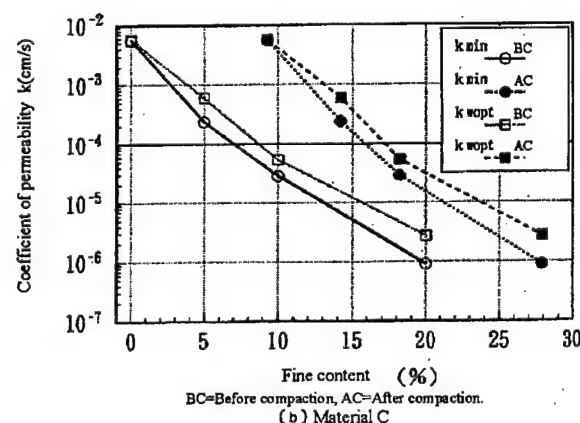
### (2) Relationship between fine content and permeability

Fine contents of gradations ⑦-1, ⑦-2, ⑦-3 and ⑦-4 are respectively set to be 0, 5, 10 and 20% before the compaction. As shown in Table 4, after the compaction, fine contents of material B increased to 3.5, 8.5, 13.4 and 21.5%, and those of material C increased to 9.3, 14.2, 18.2 and 27.9%. It is found that material C is crushed due to the compaction more easily than material B.

Figure 9 shows the relationship between fine content and the minimum permeability coefficient  $k_{min}$ , and the permeability coefficient at the optimum water content  $k_{wopt}$ . In addition, when arranging these figures, fine contents both before and after the compaction, are used. It is proven that the permeability decreases, when fine content increases in all cases.



BC=Before compaction, AC=After compaction.  
(a) Material B



BC=Before compaction, AC=After compaction.  
(b) Material C

Figure 9 Fine content vs. coefficient of permeability

The permeability of the filters is generally required to be over  $1.0 \times 10^{-4}$  cm/s in order to maintain its drainage function. At present, the fine content after the compaction should be used to evaluate the filter function, because the role of the filter zone is based on compacted filters. Then, from the viewpoint of the drainage function of filters, the allowable maximum fine contents for materials B and C are evaluated to be 7.2% and 15.8% respectively.

### (3) Total evaluation

From the results of the SC tests and physical property tests, the allowable maximum fine content to meet non-cohesion and permeability conditions for filters is

investigated. The results of the investigation are summarized in Table 6.

Table 6 Allowable maximum fine content based on filter function

Identification item		Identification criterion	Allowable maximum fine content	Before compaction After compaction
			Material B	Material C
Non-cohesion	Plasticity Index	NP	5~10% <u>≥</u>	5~10% <u>≥</u>
	SC test	(AOR in Test A)-(AOR in Test C)	8.5~13.5% <u>≥</u>	14.2~18.2% <u>≥</u>
			5~10% <u>≥</u>	0~5% <u>≥</u>
				8.5~13.5% <u>≥</u>
	Permeability		$k \geq 1 \times 10^{-4}$ cm/s	3.7% <u>≥</u> 7.2% <u>≥</u>

\*) The smallest value in allowable maximum fine contents of each item is underlined.

In the case of material B, the allowable maximum fine content is not decided from the non-cohesion condition but from the permeability condition. The allowable maximum fine content after the compaction is found to be 7.2%. In the meantime, in the case of material C, the allowable maximum fine content is decided from the results of the SC test, which is one of the non-cohesion conditions. The allowable maximum fine content after the compaction can be read to be 9.3-14.2%.

When the present Japanese filter criterion, which filters should not contain more than about 5% of fines, is met, it is found that both the non-cohesion and permeability conditions for filters are satisfied. In addition, some filters are proven to meet the non-cohesion and permeability conditions, even if they contain 7-8% of fines. Therefore, when the present filter criterion on fine content is not met, it is recommended that several tests, such as liquid and plastic limit test, the SC test and permeability test, should be made to verify the non-cohesion and permeability conditions from the viewpoint of cost reduction in dam construction.

## 6. CONCLUSIONS

In this study, for the purpose of

confirmation of the procedure of the Sand Castle (SC) test proposed by Vaughan, and examination of the evaluating method of non-cohesion of filter materials, three kinds of angle of repose (AOR) tests were carried out using uniform filters without fines and broadly graded filters with fines. The followings are found.

- (1) When maximum grain size of filters becomes larger, the AOR in the air increases. The tendency is stronger in angular gravels than rounded gravels.
- (2) In the case of the materials with the same maximum grain size, the AOR in the air becomes larger, when the fine content increases to some extent.
- (3) There is no large difference between the AOR in the air and the AOR in the water of the uniform filters without fines, which seem to be cohesionless.
- (4) The value of {(the AOR in the air)-(the AOR under the submerged condition)} (differential value) obtained from the SC test seems to become approximately  $0+6^\circ$  for cohesionless materials. From the results of the SC tests for broadly graded filters as well as uniform filters, the identification criterion of the cohesion of filters based on the positive or negative of the differential value is proposed. In addition, the attention to collapsing condition of compacted materials as well as the differential value is very important in identifying the cohesion of filters.

The investigation on the method of the SC test and the evaluation of the test results has been carried out, and the allowable maximum fine content of filters is discussed from the viewpoint of non-cohesion and permeability. The following findings are obtained.

- (5) Considering the results of the SC test, non-plastic filters can be identified to be cohesionless. There is the possibility that plasticity index is able to become an index to identify the cohesion of filters.

(6) The function of filters should be examined based on the permeability condition as well as non-cohesion condition.

Finally, this study was partially supported by Japan Society for the Promotion of Science as "Research Project 2000 Grant-in-Aid for Scientific Research (A) (No.12355020). I express thanks to Mr. Hiroyuki SATOH of Fill Dam Division, Public Works Research Institute, Ministry of Land, Infrastructure and Transportation for his great support to prepare this report.

## REFERENCES

- Japanese National Committee on Large Dams (JANCOLD) [1971] *Design Criteria for Dams*, 87-88.
- Ministry of Construction (MOC), Japanese Government [1985] *Manual for River Works in Japan -Design of Dams-*, 128-129.
- Shearad, J. L., Cluff, L. S. and Allen, C. R. [1974] "Potentially Active Faults in Dam Foundations," *Geotechnique*, 24(3), 367-428.
- U. S. Department of Agriculture Soil Conservation Service (SCS) Engineering Division [1986] "Guide for Determining the Gradation of Sand and Gravel Filters," *Soil Mechanics Note*, No.1201-V1.
- Vaughan, P. R. [1978] "Design of Filters for the Protection of Cracked Dam Cores Against Internal Erosion," *Preprint 3420 Presented to ASCE Convention*, Chicago.
- Vaughan, P. R. and Soares, H. F. [1982] "Design of Filters for Clay Cores of Dams," *Journal of Geotechnical Engineering*, ASCE, 108(GT1).
- Wakizaka, Y. [1999] "Investigations of Active Faults for Dam Construction -Present State at the Ministry of Construction-," *Proc. 31st Joint Meeting of U.S.-Japan Panel on Wind and Seismic Effects*, UJNR, 231-244.

This page intentionally left blank.



## Seismic Performance and Damage Criteria for Concrete Dams

by

Yusof Ghanaat<sup>1</sup>

### ABSTRACT

The paper describes a systematic approach for assessment of the seismic performance and probable level of damage using linear-elastic time-history analyses. The damage criterion is formulated based on magnitudes of stress demand-capacity ratios, cumulative duration of stress excursions beyond the tensile strength of the concrete, and spatial extent of overstressed regions. The level of probable damage is considered acceptable if the results from the linear-elastic time history analyses fall below a specified threshold expressed in terms of cumulative inelastic duration and demand-capacity ratios. Otherwise the damage is considered severe requiring nonlinear methods of analyses. Examples are provided to illustrate and validate the proposed criteria.

**KEYWORDS:** Concrete dams, arch dams, seismic performance, damage criteria, demand capacity ratio, tensile cracking, joint opening, failure mode

### 1. INTRODUCTION

Seismic performance of concrete dams is traditionally being conducted on the basis of simple stress checks from the linear elastic analysis combined with engineering judgment. The acceptance criterion for compressive stresses is that they should be less than the compressive strength of the concrete by a factor of 1.5 for new designs (USACE, 1994) and 1.1 for existing dams (FERC, 1999). Generally tensile stresses should not exceed tensile strength of the concrete. However, in practice up to five stress excursions above the tensile strength of the con-

crete have been considered acceptable based on engineering judgment and other considerations. This criterion neither puts limit on the magnitudes of stresses exceeding the tensile strength of the concrete nor offers any provisions regarding the spatial extent of such stresses. Rather it is left to the analyst to judge how high the magnitudes of critical tensile stresses could reach and how large an area they could occupy.

In an attempt to overcome the above shortcomings, this paper proposes a systematic approach for assessment of the seismic performance and probable level of damage using linear-elastic time history analyses. The performance evaluation and assessment of level of damage is formulated based on magnitudes of demand-capacity ratios, cumulative duration of stress excursions beyond the tensile strength of the concrete, and spatial extent of overstressed regions.

### 2. FAILURE MODES APPROACH

Although magnitudes of stresses have been used as a measure of the performance, safety of the dam should ultimately be assessed on the basis of potential modes of failure. Some of the potential modes of failure for gravity dams include: 1) overstressing due to tensile cracking, 2) sliding failure along cracked surfaces or weak planes within the foundation, and 3) overturning in the downstream direction. Studies after studies show that a typical gravity dam section may suffer tensile cracks at the base and near the upper change of slope when subjected to severe ground shaking. The cracks usually initiate from the upstream or downstream face of the dam and propagate horizontally or at an angle toward the opposite face. The cracking, if extended through

<sup>1</sup> QUEST Structures, 3 Altarinda Road, Suite 203, Orinda, CA 94563 (USA).

the dam section, could lead to sliding or rotational instability and thus failure of the dam. The goal of a seismic safety evaluation, therefore, should be to conduct appropriate analyses and evaluations that would enable the analyst to assess whether or not the above-mentioned and other modes of failure could occur.

Potentially an arch dam may fail as a result of: 1) excessive contraction joint opening combined with cantilever tensile cracking, 2) sliding along the gently sloped dam-abutment interface, and 3) movements of the abutment rock wedges formed by rock discontinuities. The contraction joint opening releases tensile arch stresses but increases tensile cantilever stresses. The increased cantilever stresses may exceed tensile strength of the concrete or lift line joints, causing horizontal cracks. The resulting cantilever blocks bounded by the opened contraction joints and cracked lift lines may become unstable leading to partial failure of the dam. Another failure scenario may involve sliding along the relatively flat dam-abutment interface where high tensile cantilever stresses have caused extensive cracking. Finally abutment foundations of an arch dam are particularly critical to the stability of the dam. Any rock wedge kinematically capable of movements should be identified and analyzed. Again, the seismic performance and acceptable level of damage for an arch dam should be assessed in view of the above-mentioned and other possible modes of failure.

### **3. EARTHQUAKE RESPONSE ANALYSIS OF CONCRETE DAMS**

The proposed seismic performance and damage criteria described in Section 4 rely on accuracy of the results of linear time-history analyses being conducted. Accurate time-history earthquake response analysis of a concrete dam for design and evaluation requires thorough understanding of the dam-water and dam-foundation mechanism and reasonable selection of material properties, seismic input parameters, and load combinations. The structural models should capture the actual dynamic characteristics of the dam-water-foundation system through accurate representation of the interaction mechanism and mass and stiffness distributions. For existing dams the

model should account for the effects of any existing cracks, deteriorated concrete, or any deficiencies that might affect the stiffness. Depending on its significance, the dam-water interaction may be modeled by simple added hydrodynamic mass coefficients, or by an elaborate solution that accounts for the effects of water compressibility and boundary absorption. Modeling of dam-foundation interaction effects may range from a simple massless finite-element mesh to more elaborate formulation involving both the inertia and damping properties of the foundation.

#### **3.1 Gravity Dams**

Relatively long and straight concrete gravity dams are usually idealized using a 2-D finite-element model including the foundation rock and the impounded water. The 2-D dam-water-foundation model may be analyzed as three separate systems in the frequency domain using the substructure method (Fenves and Chopra 1984) or as a single composite system in the time domain using the standard finite-element procedures. The substructure method may be employed if the assumption of homogeneous material properties for the foundation region can be judged reasonable and a strong coupling between the dam and water necessitates a dam-water interaction model that includes water compressibility and reservoir bottom absorption effects. Otherwise the standard composite model of the dam-foundation system with simple added hydrodynamic mass coefficients could be employed to account for the non-homogeneous material properties of the foundation rock.

#### **3.2 Arch Dams**

The complicated 3-D geometry of an arch dam requires a relatively refined 3-D model of the dam, its foundation, and the impounded water for evaluation of its response to three orthogonal components of the seismic input. The arch dam-water-foundation system may be analyzed in the time domain using the standard finite-element procedures (Ghannaat, 1993) or in the frequency domain using the substructure method (Fok and Chopra, 1985). The standard method employs a massless foundation rock modeled as part of the dam finite-element mesh in conjunction with an

incompressible liquid mesh representing the impounded water. Treating each system separately, the substructure method considers a dam model same as the standard method, a foundation model with the flexibility as well as the damping and inertia effects, and a reservoir water model that considers water compressibility and reservoir boundary absorption effects. The standard method provides reasonable results for dams built on a competent rock foundation having a deformation modulus equal or greater than that of the mass concrete and the impounded water having fundamental resonance frequency greater than twice the frequency of the dam alone. Otherwise, the more rigorous formulation of the dam-water-foundation interaction effects offered by the substructure method might be required. However, it is very important that reasonable material properties are selected for the homogeneous foundation rock to avoid unrealistic high foundation damping.

#### 4. PROPOSED PERFORMANCE AND DAMAGE CRITERIA

The proposed criteria use linear time-history analysis to formulate a systematic and rational methodology for assessment of performance and qualitative estimate of the level of damage. In linear time-history analysis, deformations, stresses, and section forces are computed in accordance with elastic stiffness characteristics of various members and components. Using acceleration time-histories as the seismic input, the linear time-history analysis computes both the magnitudes and time-varying characteristics of the seismic response. A systematic interpretation and evaluation of these results in terms of the stress demand-capacity ratios, cumulative inelastic duration, spatial extent of overstressed regions, and other considerations form the basis for an approximate and qualitative estimate of damage. If the estimated level of damage falls below the acceptance threshold for a particular dam type, the damage is considered to be low to moderate and the linear time-history analysis will suffice. Otherwise the damage is considered to be severe, requiring a nonlinear time-history analysis for more accurate estimation.

#### 4.1 Load Combination Cases

Earthquake performance of concrete dams is evaluated for three or more sets of earthquake ground motions. For each set of two- (gravity dams) or three-components (arch dams) ground motions the effects of static loads and earthquake ground motions components are combined by multiplying each earthquake component by +1 or -1 to account for the most unfavorable direction of earthquake attack.

#### 4.2 Demand-capacity Ratios

The demand-capacity ratio (DCR) for gravity dams is defined as the ratio of the calculated principal stress to tensile strength of the concrete. For arch dams where high stresses usually oriented in the arch and cantilever directions, DCR refers to ratio of the calculated arch or cantilever stress to the tensile strength of the concrete. The tensile strength of the plain concrete used in computation of DCR is obtained from the uni-axial splitting tension tests or from

$$f_t = 1.7 f_c'^{2/3}$$

proposed by Raphael (1984), where  $f_c'$  is the compressive strength of the concrete. The maximum permitted DCR for linear analysis of dams is 2. This corresponds to a stress demand twice the tensile strength of the concrete. As illustrated in Figure 1, the stress demand associated with a DCR of 2 is the same as the so called "apparent" dynamic tensile strength of the concrete, a quantity proposed by Raphael for evaluation of the results of linear dynamic analysis.

#### 4.3 Cumulative Inelastic Duration

The main problem with the traditional stress criterion is that the number of stress cycles alone is not adequate to assess damage. For example, Figure 2 shows a stress history with fewer than 5 cycles exceeding the tensile strength of the concrete. Yet the damage potential of this stress history is by far greater than stress history in Figure 3, where more than five stress cycles exceed tensile strength of the concrete. Both magnitudes and duration of stress cycles in Figure 2 are

greater than those of the Figure 3, a factor that the number of cycles alone cannot show. For this reason the proposed damage criteria employ cumulative inelastic duration, which is a measure of energy and accounts for the magnitudes, as well as duration of stress excursions.

The cumulative inelastic duration of stress excursions is defined in Figure 1. It refers to the total duration of stress excursions above a stress level associated with a  $DCR \geq 1$ . For example, a cumulative duration of 0.4 sec at DCR of 1.0 (Figure 1) indicates the total duration of stress excursions above the tensile strength of the concrete. Similarly, a cumulative duration of 0.2 sec at DCR of 1.5 is the total duration of stress excursions above the stress level equal to 1.5 times the tensile strength of the concrete. The cumulative inelastic duration may be obtained approximately by multiplying number of stress points exceeding a certain stress level by the analysis time-step. The higher the cumulative duration, the higher the possibilities for more damage. For arch dams, the allowable cumulative duration is taken equal to the duration of five harmonic stress cycles having a magnitude twice the tensile strength and an oscillation period equal to 0.2 seconds (Figure 1). This results in a cumulative duration of 0.4 seconds for a DCR of 1. The cumulative duration for a DCR of 2 is assumed zero. For gravity dams a lower cumulative duration of 0.3 is assumed, mainly because gravity dams resist loads by cantilever mechanism only, as opposed to arch dams that rely on both the arch and cantilever actions.

#### 4.4 Performance Criteria for Gravity Dams

The earthquake performance of gravity dams is evaluated on the basis of load combination cases, demand-capacity ratios, and the associated cumulative duration described in Sections 4.1 to 4.3 above. The performance is formulated for the maximum design earthquake (MDE). The MDE is defined as the maximum level of ground motion for which a structure is designed or evaluated (ER 1110-2-1806). Three performance levels are considered:

1. *Minor or no Damage.* The dam response is considered to be within the linear elastic

range of behavior with little or no possibility of damage if the computed demand-capacity ratios are less than or equal to 1.0.

2. *Acceptable Level of Damage.* The dam will exhibit nonlinear response in the form of cracking and joint opening if the estimated demand-capacity ratios exceed 1.0. The level of nonlinear response or cracking is considered acceptable if stress demand-capacity ratios are less than 2.0, overstressed regions are limited to 15 percent of the dam cross-section surface area, and the cumulative duration of stress excursions beyond a particular demand-capacity ratio falls below the performance curve given in Figure 4. Consideration should also be given to the relation between the fundamental period of the dam and peak of the earthquake response spectra. If lengthening of the period due to nonlinear behavior shifts the period to descending region of the spectra, then the nonlinear response would reduce seismic loads and thus reduce stresses as the shaking continues. Otherwise, lengthening of the period would increase seismic forces and possibly increase the level of damage.
3. *Severe Damage.* The damage is considered severe when demand-capacity ratios are greater than 2, the specified threshold being exceeded, or met marginally but the period lengthening due to nonlinear response would increase the seismic demand. In these situations a nonlinear time-history analysis may be required to assess the damage and thus the performance more accurately.

#### 4.5 Performance Criteria for Arch Dams

The earthquake performance of arch dams is evaluated on the basis of combined static and seismic stresses in accordance with the load combination cases, demand-capacity ratios, and the cumulative inelastic duration described above. The proposed arch dam performance levels for the MDE include:

1. *Minor or no Damage.* The arch dam response is considered to be within the linear elastic range of behavior with little or no damage if

computed stress demand-capacity ratios are less than or equal to 1.0. Considering that the ability of contraction joints to resist tension is limited, they are expected to open even at demand-capacity ratios  $\leq 1$ . However, the amount of joint opening would be small with little or no effects on the overall performance of the dam.

2. *Acceptable Level of Damage.* If estimated demand-capacity ratios exceed 1.0, the arch dam is expected to exhibit nonlinear response in the form of contraction joint opening and tensile cracking at the lift lines and elsewhere. The level of nonlinear response, i.e. opening and cracking of joints is considered acceptable if the demand capacity ratios  $< 2$ , overstressed region is limited to 20 percent of the dam surface area, and the cumulative duration of stress excursions above the stress level associated with a particular demand-capacity ratio falls below the performance curve given in Figure 5. As discussed previously, the relation between the fundamental period of the dam and peak of the response spectra should also be considered to determine whether the nonlinear response behavior would increase or decrease seismic demands.
3. *Severe Damage.* If the above performance criteria are not met, or met marginally but seismic demands would increase due to nonlinear behavior, then a nonlinear analysis would be required to better assess the damage and thus performance of the dam.

## 5. VALIDATION OF PERFORMANCE AND DAMAGE CRITERIA

Pacoima and Morrow Point Dams were used to validate the empirically developed performance and damage assessment curves. Both dams were analyzed for six sets of earthquake acceleration time histories covering a wide range of ground motion parameters including frequency content, duration, pulse types and pulse sequencing. For each set the effects of static loads and earthquake ground motion components were combined as described in Section 4.1, resulting in a

total of eight load cases. The earthquake response of each dam was assessed using the performance and damage criteria discussed in Section 4 as well as examining other results including periods of vibration, displacement and stress histories, and contour and vector plots of maximum stresses, minimum stresses, and critical concurrent stresses. The linear analysis of example dams was conducted using the computer program GDAP (2002).

It is important to recognize that earthquake ground motions used in this paper may not be appropriate for safety evaluation of the example dams, especially in the case of Morrow Point Dam. Therefore the results and findings of this paper should not be used to draw general conclusion about the earthquake performance of these dams.

### 5.1 Description of Example Dams

Finite element models of Pacoima and Morrow Point Dams are given in Figures 6 and 7. Located in southern California, Pacoima Dam is 111m (365 ft) high and 195 m (640 ft) long at the crest level. Its thickness varies from 3.2 m (10.4 ft) at the crest to 30.2 m (99 ft) at the base. Morrow Point Dam is a thin double-curvature arch structure in Gunnison, Colorado. It rises 142.6 m (468 ft) above the foundation and spans a length of 220.7 m (724 ft) at the crest. It is 3.7 m (12 ft) thick at the crest and 15.8 m (52 ft) at the base. The model of each dam includes three layers of solid elements through the dam thickness. The foundation models also use solid elements and are constructed on semicircles having a radius twice the dam height. The water level at Pacoima Dam is at 64 percent of the dam height and at Morrow Point at the crest level. The dam-water interaction, therefore, is less significant for Pacoima Dam than it is for Morrow Point.

### 5.2 Earthquake Ground Motions

For validation of performance and damage criteria, the example arch dams were subjected to the near field ground motions of a maximum earthquake event having a moment magnitude  $M_w$  of about 6-1/2. Five three-component sets of recorded acceleration time-histories from four re-



cent earthquakes were selected to account for sensitivity of the dam response to characteristics of earthquake ground motions. In addition, a three-component spectrum-compatible time-history derived using the 1971 Pacoima Dam record was also included. The smooth response spectra for the horizontal and vertical components of ground motion were constructed to be representative of median ground motions for an  $M_w$  6-1/2 earthquake occurring at a distance of  $R \approx 5$  km. The smooth response spectra and primary component of the selected records are shown in Figures 8 and 10, respectively. The ground motions were scaled such that the sum of ordinates for the response spectra of each natural record would match the sum for the smooth response spectra in the period range of 0.1 to 0.4 sec., a period range that includes the most significant modes of vibration for the example dams (Figure 9).

### 5.3 Earthquake Response of Pacoima Dam

The natural periods of the 10 lowest modes of vibration for Pacoima Dam vary from 0.233 to 0.088 sec, the first 5 of which are displayed in Figure 9 (shown as Dam-1) for comparison with response spectra of the earthquake input motions. The spectrum-compatible record (Pacb) induces the largest upstream-downstream (52 mm) and the 1994 Northridge Newhall record (U56) the largest vertical (9 mm) and cross-stream (20 mm) displacements. Similarly different earthquake records produce peak values for one or two stress components but not for all. Envelopes of maximum stresses for all earthquake records are nearly the same as those shown in Figure 11. High tensile arch stresses occur in the upper central region of the upstream face, and near the upper 1/4-point regions of the downstream face. High tensile cantilever stresses occur in the upper central region of the upstream face of the dam. The concurrent stress contours at the time of maximum arch stress (Figure 12) indicate that the simultaneous tensile arch stresses are developed on the upper central region of the upstream and at the upper 1/4-point regions of the downstream face. The corresponding concurrent cantilever stresses (right graphs in Figure 12) are mainly compressive on the upstream face with moderate tensile stresses on the

upper part of the downstream face of the dam. The magnitude and distribution of concurrent stresses at the time of maximum arch stress suggest that contraction joint opening, if any, would be minor, possibly involving the joints at the crown and 1/4-point locations. Figure 15 shows that maximum stress histories are quite different for each earthquake record and that the number of stress peaks beyond the assumed tensile strength of the concrete (2.95 MPa or 428 psi) is within 5 cycles for arch stresses and none for cantilever stresses.

The application of proposed damage criteria to Pacoima Dam is presented in Figure 17. The results show that demand-capacity ratios for all earthquake input records are less than 2, the cumulative inelastic duration at all demand-capacity ratios fall below the acceptance curve, and that overstressed regions are less than 20% of the dam surface area. On these bases it is concluded that Pacoima Dam exhibit minor nonlinear response in the form of contraction joint opening and closing. This performance prediction is consistent with the observed performance of the Pacoima Dam during the 1971 San Fernando and 1994 Northridge earthquakes where the main nonlinear response and damage occurred at the left abutment rock blocks but not within the body of the dam.

### 5.4 Earthquake Response of Morrow Point

The natural periods of the 10 lowest modes for Morrow Point Dam vary from 0.338 to 0.104 sec, the first 5 of which are shown in Figure 9 (shown as Dam-2) for comparison. None of the earthquake records produces the largest peak values for all displacement components at all locations. The Gilroy record (Gly) induces the largest upstream-downstream displacement (175 mm) at the center of the crest, while other records produce peak vertical (8 mm) and cross-stream (38 mm) displacements. As expected, displacement histories for different input varied significantly in terms of magnitudes and the waveforms. As in the case of Pacoima Dam, different earthquake records produce peak values for one or two stress components but not for all. Distributions of maximum stresses generally differ for different records. This is expected

since spectral ordinates for several lower modes significantly differ from one input record to another. Figure 13 shows envelopes of maximum stresses for Gilroy record, which produced the largest arch stresses. High-tensile arch stresses develop in the upper central-region of the upstream and also in the upper 1/4-point locations of the downstream face. High tensile cantilever stresses occur in the central and upper abutment regions of the upstream face. The concurrent stress contours at the time of maximum arch stress (Figure 14) indicate simultaneous tensile arch stresses in central region of the upstream and at 1/4-point locations of the downstream face. The corresponding concurrent cantilever stresses (right graphs in Figure 14) are mostly compressive on both faces of the dam. The magnitudes and distributions of concurrent stresses suggest that significant joint opening would occur. Figure 16 shows that the maximum tensile arch stress for the Gilroy record reaches 20.7 MPa (3,000 psi), but remains at 13.8 MPa (2,000 psi) for all other records. Tensile cantilever stresses reach as high as 6.9 MPa (1,000 psi) but are not concurrent with the maximum tensile arch stresses.

The application of the proposed damage criteria to Morrow Point Dam is presented in Figure 18. The results show that the arch stress demand-capacity ratios for all six ground motions exceed 2 and that the cumulative inelastic duration, especially for Pacx, Pacb, and Gly records, are substantially greater than the acceptance level. This suggests that for the ground motions used in this example, Morrow Point will experience significant and repeated joint opening and closing. The actual amount of joint opening and whether or not it could lead to local failure should be estimated by the nonlinear time-history analysis.

### 5.5 Nonlinear Earthquake Response of Morrow Point Dam

According to the proposed damage criteria, Morrow Point Dam will undergo significant nonlinear deformation requiring nonlinear analysis. To validate this aspect of the proposed damage criteria, nonlinear earthquake responses of Morrow Point Dam to the selected ground motions were

computed to assess the amount of contraction joint opening. For this purpose nonlinear joint elements were introduced at the crown section and at 1/4 points (Figure 19), where the linear analysis had indicated high tensile arch stresses are developed (Figure 14). The nonlinear analyses were conducted using the computer program QDAP (2002).

Figure 19 illustrates deflected shapes at the time of maximum joint opening. The opening is the largest at the crown section and penetrates to mid height of the dam. The openings at the 1/4 span points are much smaller and penetrating less. Figure 20 displays time history of maximum joint opening displacements for three earthquake records. The time histories show that the contraction joints repeatedly open and close during the ground shaking, but they do not stay open continuously more than 0.5 sec. The 1994 Northridge Newhall record (U56) produces the largest joint opening reaching a value of 82 mm (3.3 in.) at the crest.

The net effect of joint opening was that it released all high tensile arch stresses. However, the release of tensile arch stresses was not accompanied by unacceptable tensile cantilever or compressive stresses. At 82 mm, the joint opening is considered moderate. The cantilever blocks bounded by partially opened joints are expected to remain stable through shear-key interlocking. Consequently, excessive block movements are not expected to occur.

## 6. CONCLUSIONS

This research investigation has led to the following conclusions:

1. The proposed performance and damage criteria provide a systematic approach for assessment of the seismic performance and probable level of damage using linear time-history analysis.
2. The acceptable performance is formulated based on magnitudes of stress demand-capacity ratios, cumulative duration of stress excursions above stress levels associated for various demand-capacity ratios, and spatial

extent of overstressed regions. Therefore, it eliminates some of the shortcoming of the traditional evaluation procedures currently used in practice.

3. Threshold of acceptable damage on the basis of linear-elastic analysis is defined and therefore the need for nonlinear analysis can be determined.
4. The validation analyses indicate that the proposed criteria produce reliable conclusions regarding the performance and probable level of damage.

## 7. ACKNOWLEDGEMENTS

The US Army Corps of Engineers supported this research investigation. The author is grateful for this support. The author also appreciates the helpful comments by Donald Dressler, Robert Hall, and Anjana Chudgar who served on the research review committee for the US Army Corps of Engineers.

## 8. REFERENCES

ER 1110-2-1806

US Army Corps of Engineers' Engineer Regulations for "Earthquake Design and Evaluation of Civil Works Projects."

Fenves, G. and A.K. Chopra (1984), "*Earthquake Analysis and Response of Concrete Gravity Dams*," Earthquake Engineering Research Center, Report No. UCB/EERC-84/10, August 1984.

FERC (1999), "*Engineering Guidelines for the Evaluation of Hydropower Projects, Chapter XI, Arch Dams*," Federal Energy Regulatory Commission, Office of Energy Projects, October 1999.

Fok, K.-L., and A.K. Chopra (1985), "*Earthquake Analysis and Response of Concrete Arch Dams*," Report No. UCB/EERC-85/07, Earthquake Engineering Research Center, University of California, Berkeley.

GDAP (2002), "Graphics-based Dam Analysis Program," a linear dam analysis member of the WebDams family of programs developed by QUEST Structures ([www.webdams.com](http://www.webdams.com)).

Ghanaat, Y. (1993), "*Theoretical Manual for Analysis of Arch Dams*," Instruction Report ITL-93-1, US Army Corps of Engineers, Waterways Experiment Station.

QDAP (2002), a nonlinear dam analysis member of the WebDams family of programs developed by QUEST Structures ([www.WebDams.com](http://www.WebDams.com)).

Raphael, J.M. (1984), "*Tensile Strength of Concrete*," ACI Journal, March-April 1984.

USACE (1994), "*Arch Dam Design*," US Army Corps of Engineers EM 1110-2-2201, 31 May 1994.



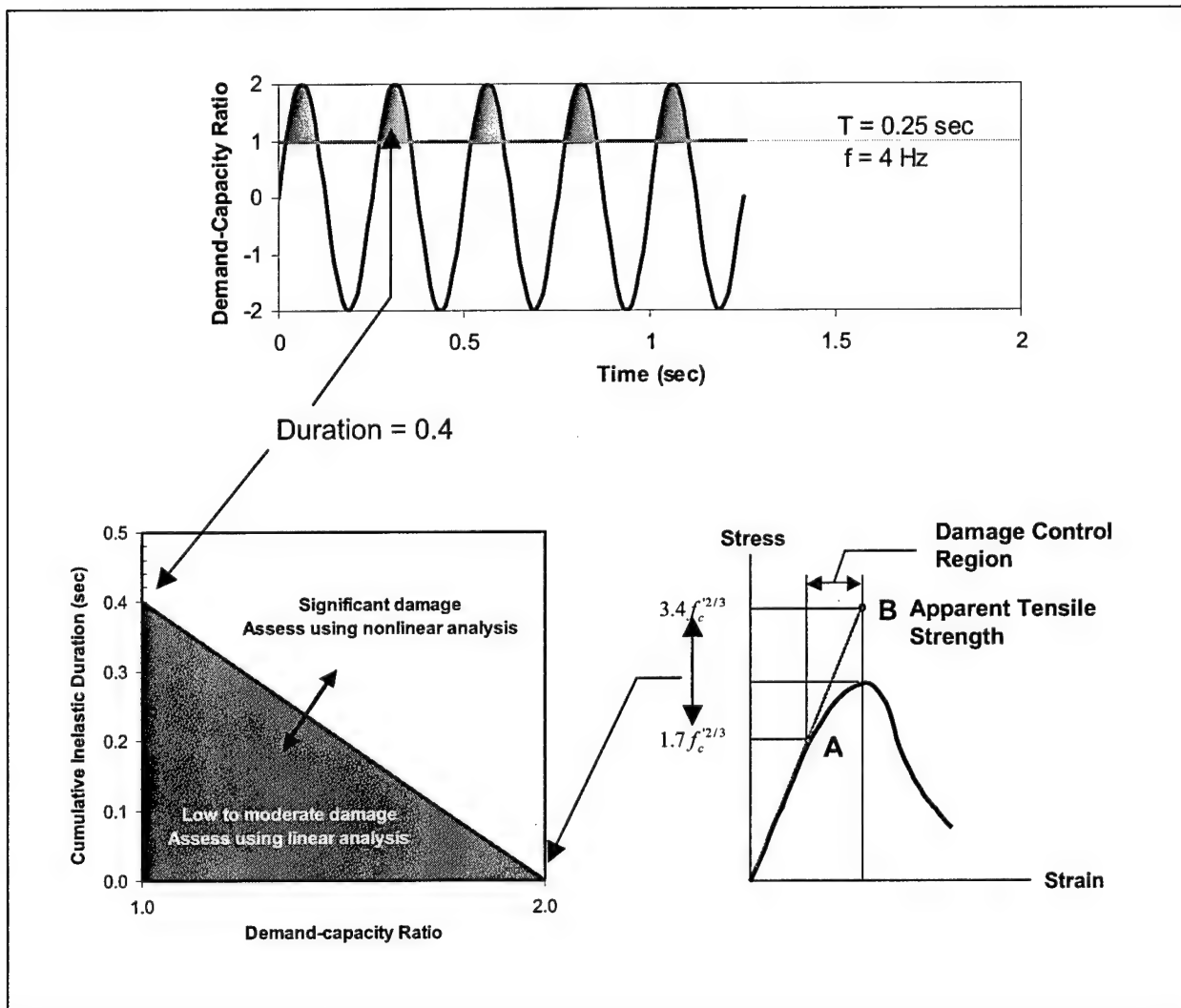


Figure 1. Basis for upper limit values of demand-capacity ratio and cumulative duration

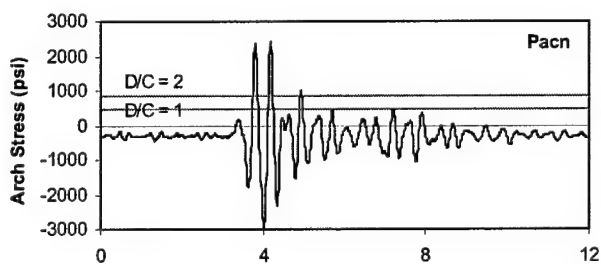


Figure 2. Fewer than five cycles exceed the capacity

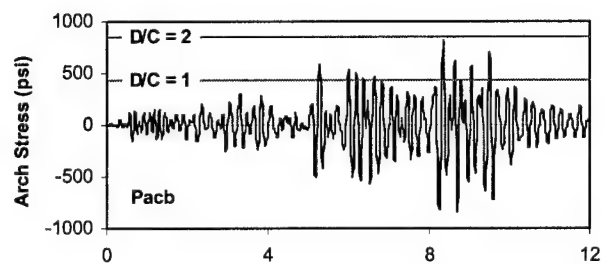


Figure 3. More than five cycles exceed the capacity

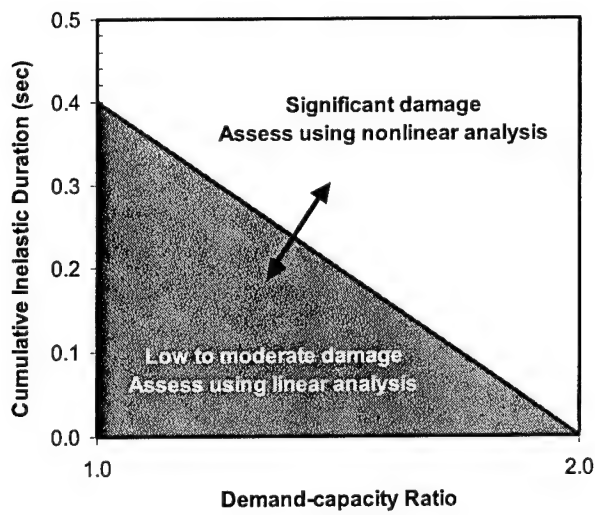


Figure 4. Performance/Damage Curve for Arch Dams

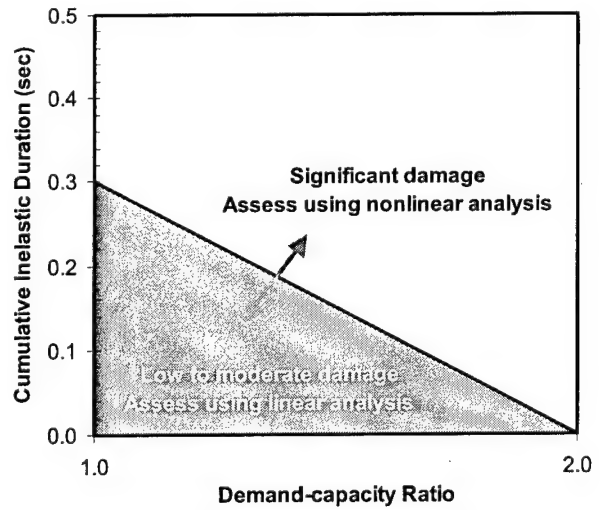


Figure 5. Performance/Damage Curve for Gravity Dams

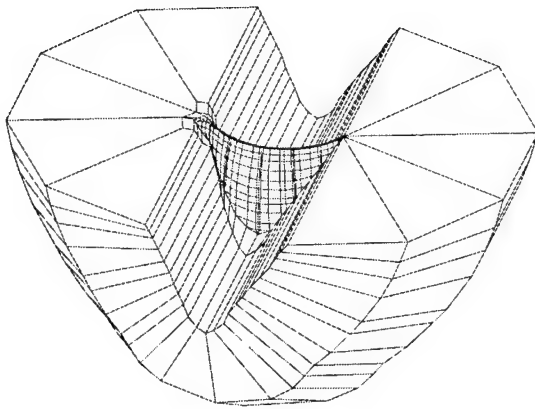


Figure 6. Pacoima Dam-Foundation model

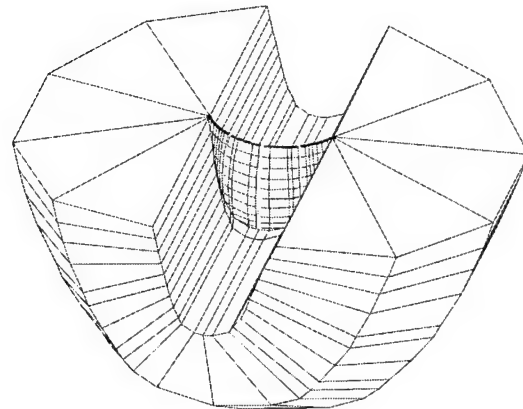


Figure 7. Morrow Point Dam-Foundation model

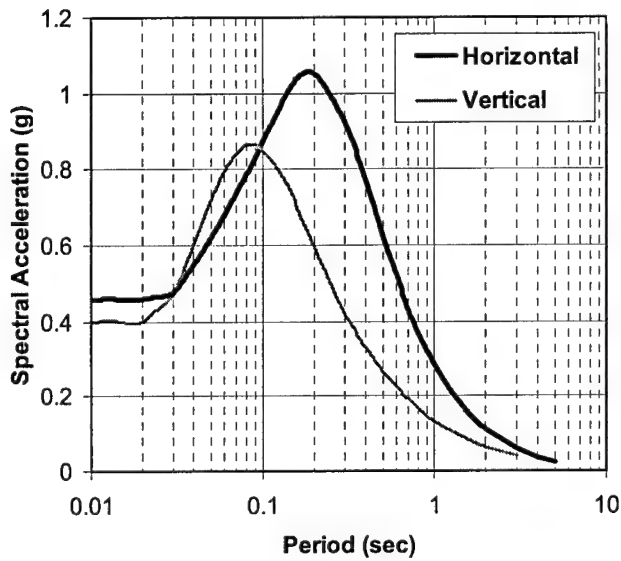


Figure 8. Horizontal and vertical response spectra for the postulated near-source,  $M_w 6.1/2$  earthquake

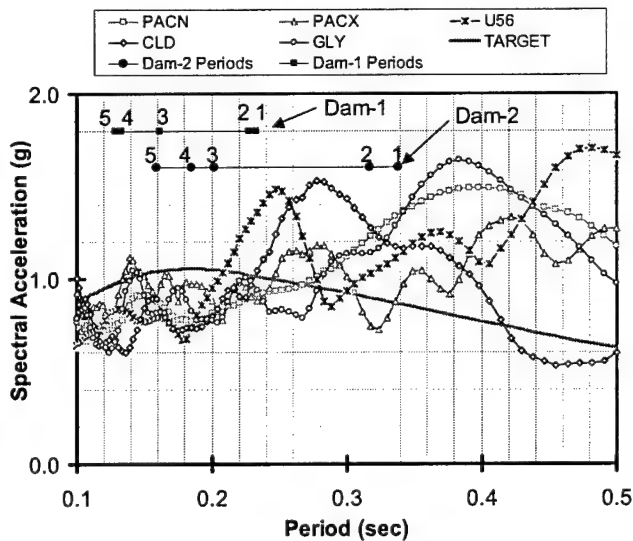


Figure 9. Comparison of design/evaluation spectrum with response spectra of scaled records

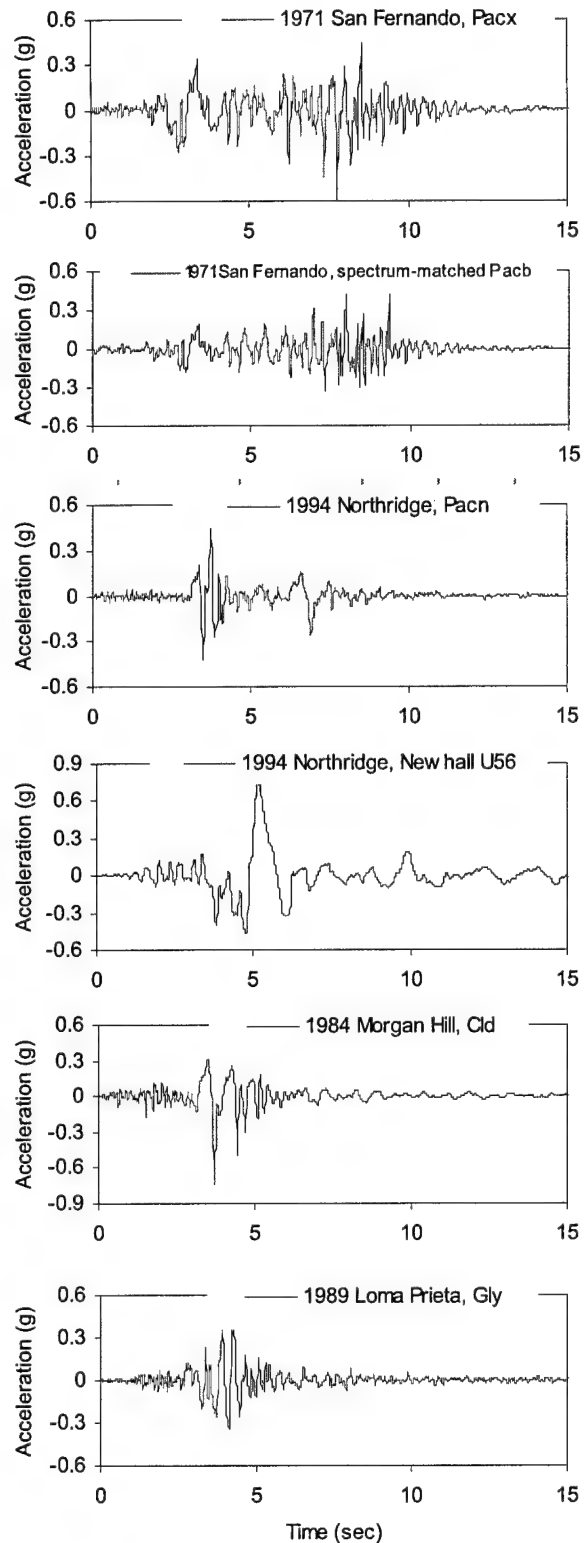


Figure 10. Scaled acceleration time-histories for near-source earthquake

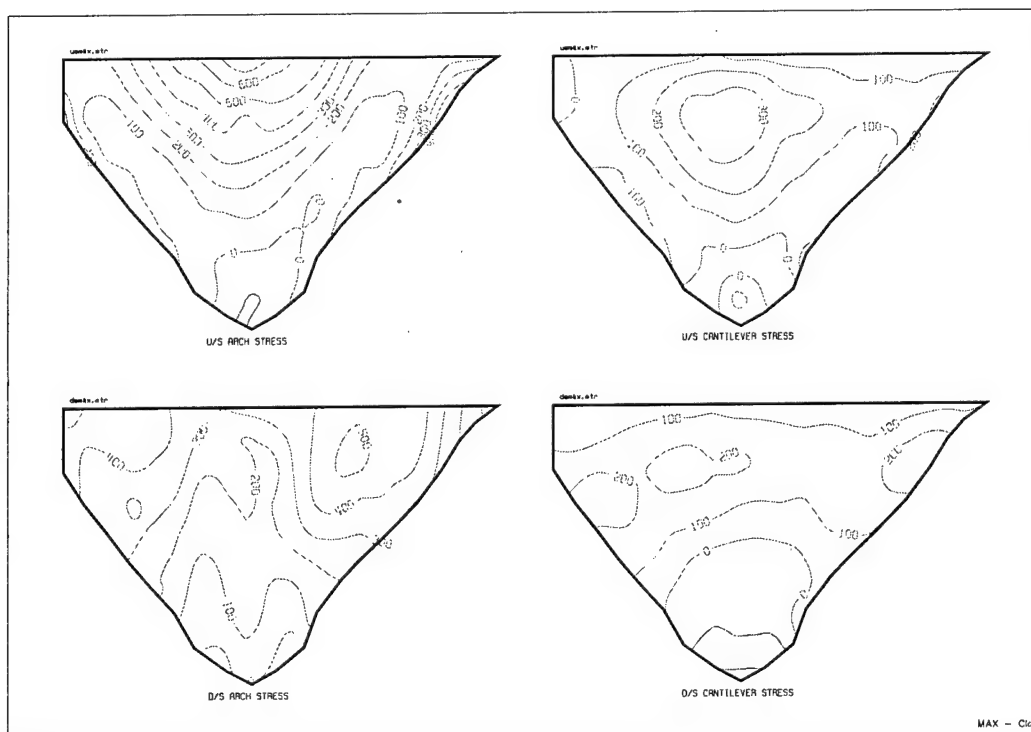


Figure 11. Envelopes of maximum arch and cantilever stresses for Pacoima Dam

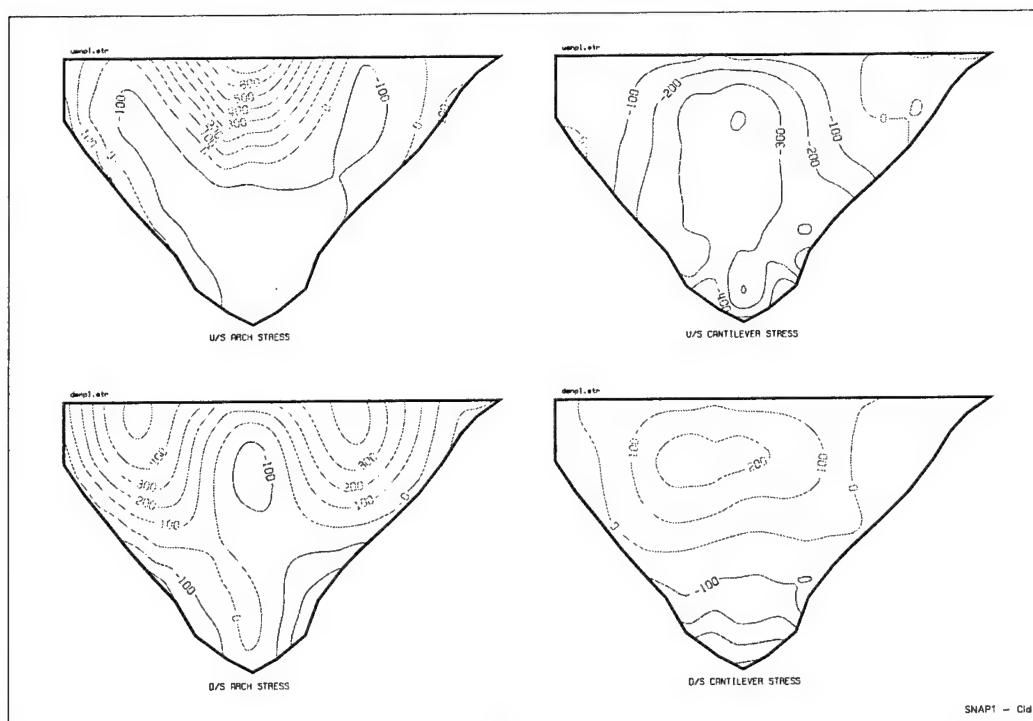


Figure 12. Concurrent stresses at the time of maximum arch stress for Pacoima Dam

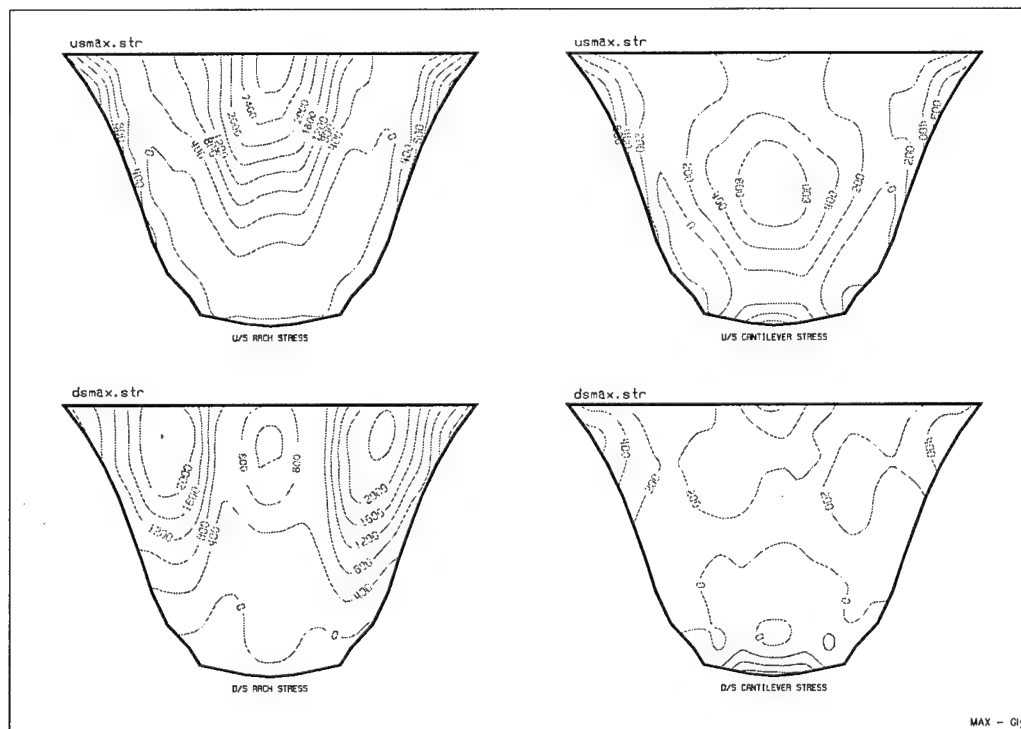


Figure 13. Envelopes of maximum stresses for Morrow Point Dam

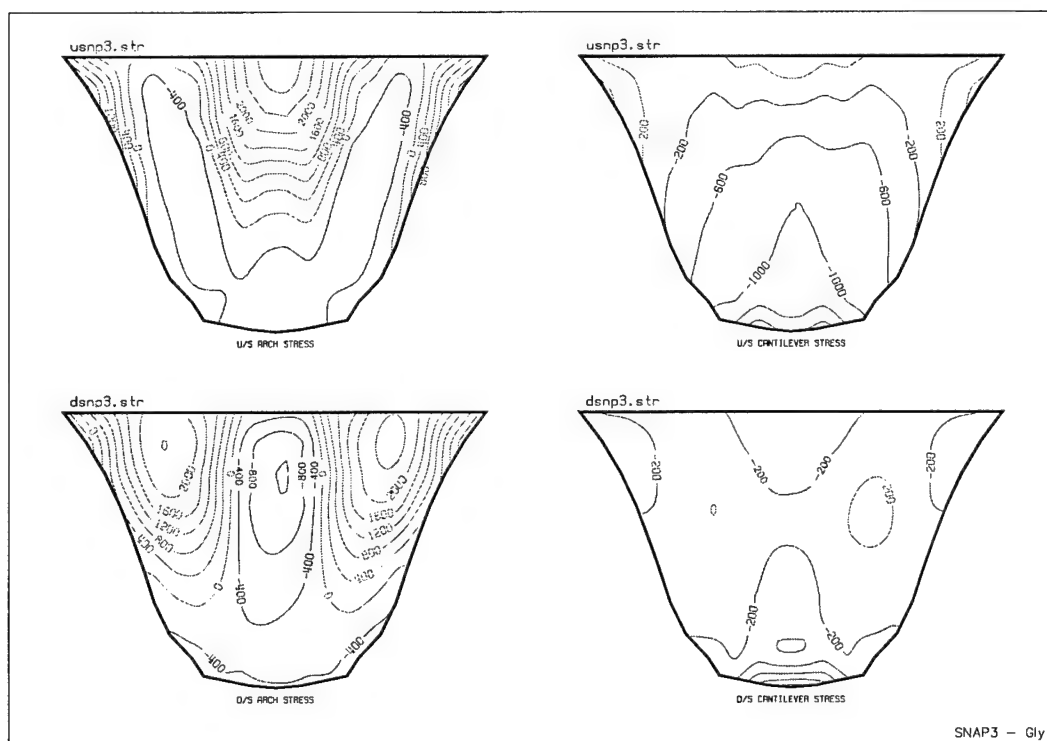


Figure 14. Concurrent Stresses at the time of maximum arch stress for Morrow Point Dam

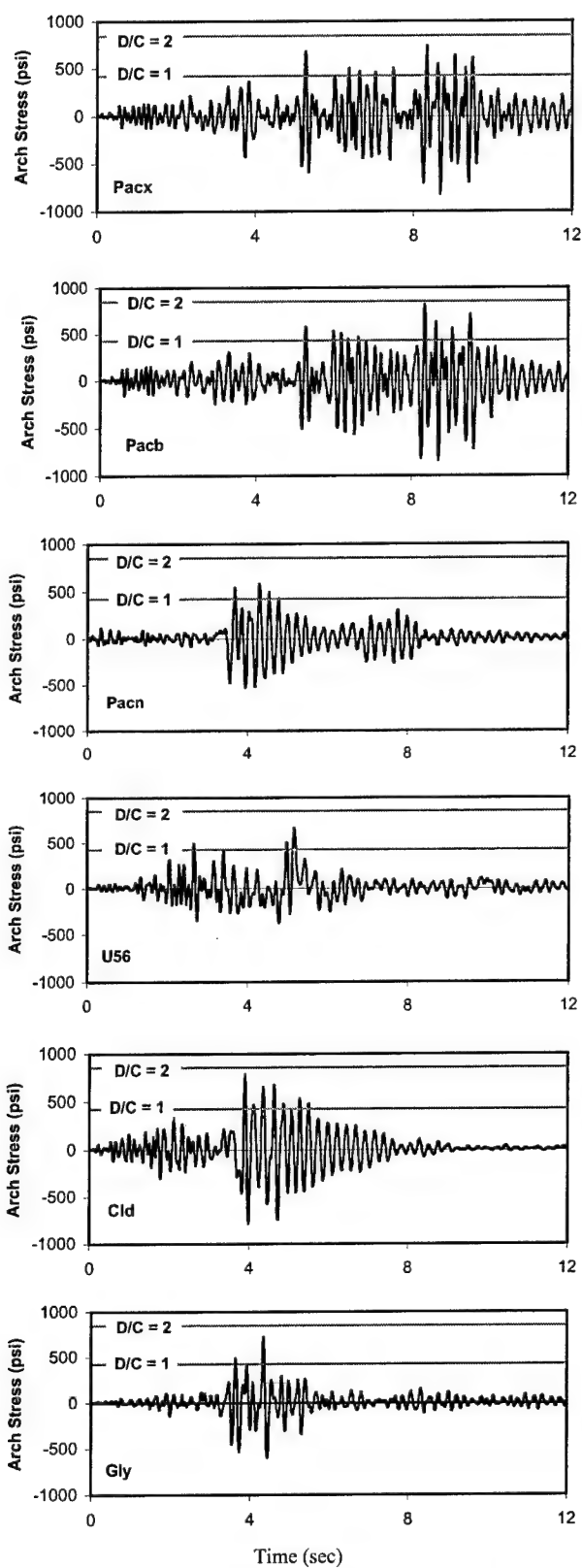


Figure 15. Stress histories for Pacoima Dam

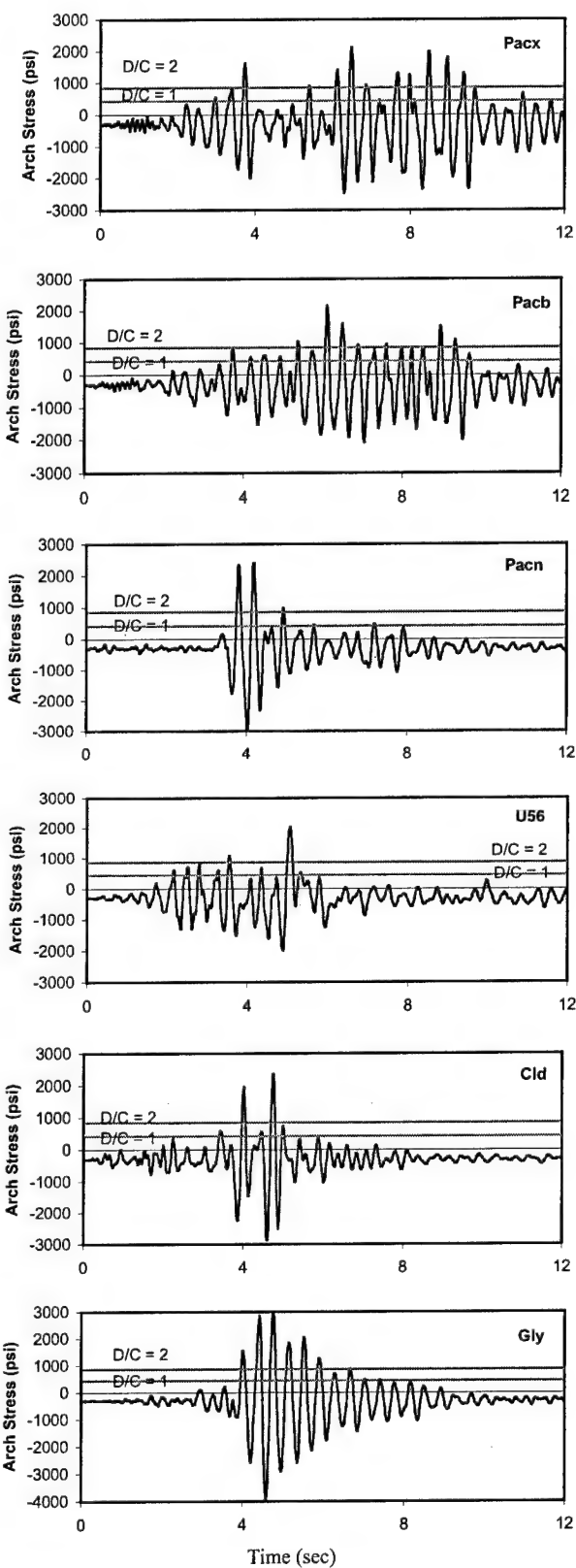


Figure 16. Stress histories for Morrow Point Dam

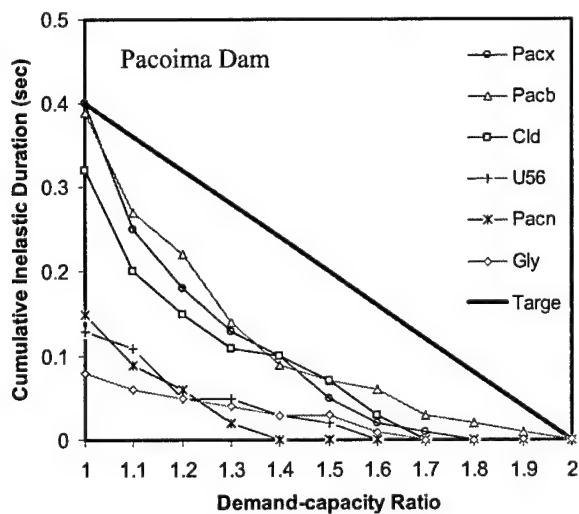


Figure 17. Performance assessment for Pacoima Dam

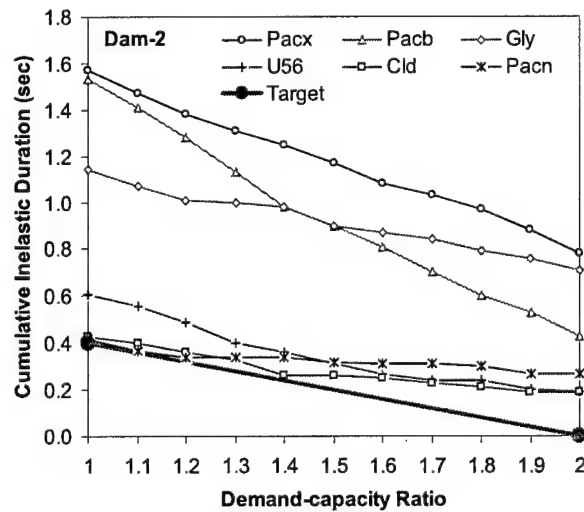


Figure 18. Performance assessment for Morrow Point Dam

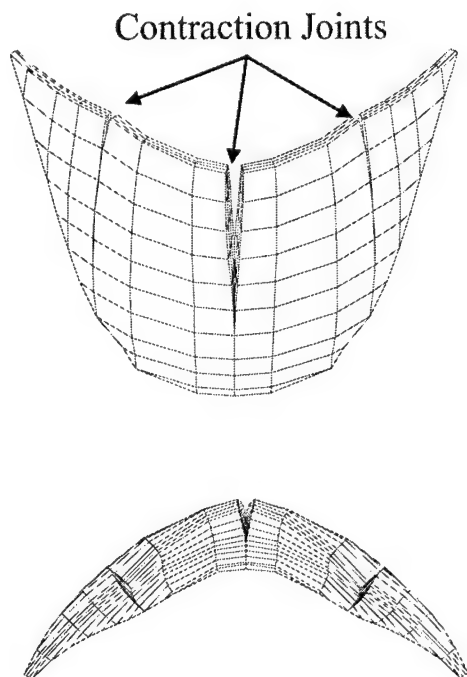


Figure 19. Deflected shape at time of maximum joint opening

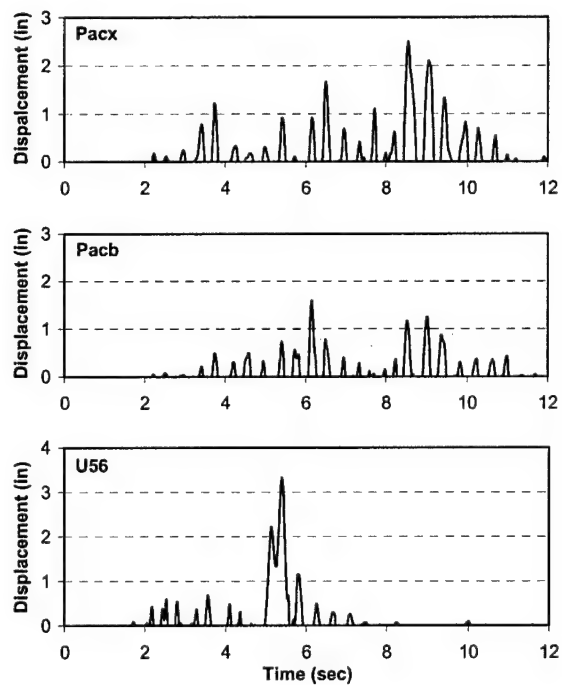


Figure 20. Time history of joint opening displacements

This page intentionally left blank.



## Preliminary Earthquake Response Analysis of Folsom Dam Spillway Monoliths

by

Chung Wong<sup>1</sup>, Rick Poeppelman<sup>1</sup>, Stephen Graff<sup>1</sup>

### ABSTRACT

Preliminary seismic stress analyses of Folsom Dam spillway monoliths were performed to provide a design basis for a significant enlargement of the existing dual-level outlet works conduits, based on a three-dimensional finite element mesh developed for the typical 50-ft wide overflow monolith. The mesh includes the spillway bridge pier, and models the gate chambers and the proposed enlargement of the conduits. The earthquake-induced lateral forces to be applied to the monolith were derived using Chopra's simplified procedure [1]; the procedure was extended to three-dimensional analysis, and considered the effects of dam-water interaction, water compressibility, reservoir bottom wave absorption, and dam foundation rock interaction. The forces were computed for a one-foot slice of dam, and applied uniformly over the monolith width. Two sets of lateral earthquake forces were computed for the Maximum Credible Earthquake (MCE) using smooth design response spectra developed by URS Corporation. One set is associated with the fundamental vibration mode, and the other set is associated with the higher vibration modes. For each set of earthquake forces, the hydrodynamic loads were applied to the upstream face as static forces, and the inertial forces due to the mass of the dam were applied as static element body forces. Analysis also included hydrostatic uplift forces at the base (foundation level).

The earthquake response was approximated by combining the response from the two sets of earthquake forces using the square-root-of-the sum-of-squares (SRSS) rule. After initial

technical review is complete, the preliminary stress analyses will be refined during the final design phase, and will consider further enhancement of the analytical approach. The procedure and results will be used as a basis for judgment regarding the need for more refined response history analysis.

**KEYWORDS:** Concrete dams, Earthquake response, Spillway monolith, Response Spectrum, Three-dimensional finite element analysis.

### 1. INTRODUCTION

Sacramento is located at the confluence of the American and Sacramento Rivers in northern California. The American River Watershed (drainage basin) covers about 2,100 square miles northeast of Sacramento and includes portions of Placer, El Dorado, and Sacramento Counties. Runoff from this basin flows through Folsom Dam and passes through Sacramento within a system of levees. The Folsom Dam and Reservoir project was originally designed and constructed by the Corps in 1955 as part of the Federal Central Valley Project (CVP), completed by the United States Bureau of Reclamation (USBR).

The current efforts to reduce the risk of flooding to the city of Sacramento from the American River began after the floods of February 1986. The U. S. Army Corps of Engineers, Sacramento District (Corps), in partnering with its non-Federal sponsors, the State of California Reclamation Board (Reclamation Board) and the Sacramento Area Flood Control Agency (SAFCA), has prepared two comprehensive studies (1992 and 1996)

<sup>1</sup> U.S. Army Corps of Engineers, Sacramento District, Structural Design Section, 1325 J Street, Sacramento, CA 95814.

and developed several alternatives for a long-term solution to the flooding problems in Sacramento, but to date none have gained overall consensus. The U.S. Congress has, however, authorized two components from these investigations, the Common Features Project and the Folsom Dam Modification Project. The Common Features Project primarily includes levee modification work along the lower American River and the Sacramento River. The Folsom Dam Modification Project consists primarily of outlet works modifications in the concrete portion of the dam. Other long-term alternatives being investigated include raising Folsom Dam, increasing the objective flood release through Folsom Dam, and making advanced flood releases based on weather forecasting. See Figure 22 for an aerial view of Folsom Dam.

The Outlet Modification project would increase the river outlet release capacity from 26,000 cubic feet per second to 115,000 cubic feet per second at the reservoir water-surface elevation corresponding to the spillway crest (Elev. 418 feet). This increased release capacity would allow the dam to pass the downstream channel capacity earlier in the flood event, thus making more efficient use of the flood reservation space, and increasing the overall level of flood protection downstream. The outlet works modifications would increase flood protection by reducing the probability of flooding in Sacramento in any one year from 1 chance in 100 to 1 chance in 140. The first cost of construction is approximately \$150 million. Construction could start as early as 2004 and be completed by 2012. The Outlet Modification project consists of enlarging the four existing upper tier river outlets from 5 feet wide by 9 feet high to 9.33 feet wide by 14 feet high, constructing two new upper tier river outlets of the same size, and enlarging the four existing lower tier river outlets from 5 feet wide by 9 feet high to 9.33 feet wide by 12 feet high. Other structural analysis and modifications involved with the project include stability analysis of all the affected spillway monoliths,

design of a concrete excavation plan and new reinforced concrete conduit liner, new outlet regulating (slide) gates and gate bodies, enlarged air intake shafts and tunnels, temporary and permanent bulkheads to allow work behind the full reservoir, and new construction (access) adits. See Figure 23 for a typical section of a spillway monolith, including a profile of the proposed enlarged outlets.

## 2. PURPOSE AND SCOPE

Preliminary stress analysis of selected spillway monoliths was performed as part of the Folsom Dam Spillway Modifications studies to provide a design basis for enlargement of the existing outlet works conduits. Dynamic response history analysis is not considered for this phase of study. Analysis results from several stress analyses for different alternatives and for different load cases are presented in this report. Stress analysis of the spillway pier in a form ready to be used for design and/or evaluation, is beyond the scope of this report.

## 3. OVERVIEW OF ANALYTICAL PROCEDURES

The analytical procedures employed for the stress analysis of the selected spillway monolith are summarized as follows:

a) Apply Chopra's simplified procedure [1] to derive the following two sets of earthquake lateral forces associated with upstream-downstream ground motion:

- The lateral earthquake forces  $f_1$  associated with the fundamental vibration mode, considering the effects of dam-water interaction, water compressibility, reservoir bottom wave absorption, and dam-foundation rock interaction
- The lateral earthquake forces  $f_{sc}$  associated with the higher vibration modes

b) Develop a three-dimensional finite element mesh of the 50-ft wide spillway monolith using GTSTRUDL.

c) Apply the two sets of earthquake-induced lateral forces (from step a) to the three-dimensional finite element dam model (from step b). For each set of earthquake-induced lateral forces, apply the hydrodynamic pressure component to the upstream face of the dam model and the force component associated with the mass of the dam concrete as body forces to all finite elements. Note that the body force is a function of elevation along the height of the dam. Perform static analysis of the three-dimensional finite element mesh subjected to the two sets of earthquake-induced lateral forces.

d) Combine the responses from the two sets of earthquake-induced forces using the square root-of-the-sum-of-squares (SRSS) rule. Combine the SRSS estimates of earthquake response with the static effects due to dead weight of spillway monolith, hydrostatic pressure and uplift.

Note that steps b, c, and d are implemented using GTSTRUDL for developing the finite element models, performing stress analysis; post-processing, and generating stress contour plots.

#### 4. COMPUTER PROGRAM

GTSTRUDL, developed by Georgia Institute of Technology, is used as the analytical tool to perform three-dimensional finite element analysis of the spillway monoliths for different alternatives and for different load cases. The program integrates sophisticated functional information processing for structural engineering modeling, analysis, design, graphical display, and database management. The types of structural analysis procedures implemented in GTSTRUDL are static stiffness analysis, nonlinear analysis, and dynamic analysis of any combination of framed structures and continuum mechanics problems of arbitrary configuration and

composition. The graphical display is useful in generating color-coded stress contour plots on planes interior to the spillway monolith as well as on its exterior faces.

#### 5. SIMPLIFIED PROCEDURE TO ESTIMATE EARTHQUAKE LOADS

Dr. Anil K. Chopra developed a simplified analysis procedure at the University of California at Berkeley for gated spillway monoliths of concrete gravity dams [1]. Basically, the maximum effects of an earthquake on a spillway monolith are represented by equivalent lateral forces in the simplified analysis procedure, associated with upstream-downstream ground motion. The maximum lateral forces associated with the fundamental vibration mode are computed to include the effects of dam-water interaction, water compressibility, reservoir bottom wave absorption, and dam-foundation rock interaction. The maximum lateral forces associated with the higher vibration modes are computed under the following assumptions: (a) the dynamic amplification of the modes is negligible; (b) the effects of dam-water interaction and water compressibility can be neglected in computing the contributions of the higher modes to the earthquake response of dams; and (c) the interaction effects between the dam and foundation rock are not significant in computing higher mode responses. These assumptions provide reasonable approximations for spillway monoliths responding to earthquake ground motions with little dynamic amplification in the higher modes because of the generally short vibration periods. Note that the use of Dr. Chopra's simplified procedure to compute earthquake-induced loads for preliminary stress analysis or feasibility level study is in compliance with EM 1110-2-2200 [2].

To calculate the equivalent lateral forces using the simplified procedure, the spillway monolith is divided into a number of horizontal blocks. Increasing the number of blocks will enhance the accuracy of the computed earthquake loads. The 'block' model

developed for Monolith 14 is shown in Figure 1. It can be observed from Figure 1 that the structural idealization of the spillway monolith consists of the spillway and pier only, but does not include the spillway bridge and tainter gate because Dr. Chopra's research has demonstrated that the fundamental vibration period and mode shape of a spillway monolith are not influenced significantly by these structural components. To account for the different width of spillway monolith and pier, the mass of the pier is reduced by a factor equal to the ratio of monolith width to pier width, for the purpose of computing the earthquake loads. The simplified procedure is applied to Monoliths 14 and 13 for computing the earthquake loads. It is assumed in the simplified procedure that the monolith is supported on a *horizontal* surface of underlying flexible foundation rock. This assumption is appropriate for Monolith 14 with a uniform dam/foundation contact. However, the dam/foundation contact varies by as much as 35 ft in elevation for Monolith 13. This monolith is idealized to have a horizontal base and the average monolith height is used in the calculations.

## 6. SYSTEM PARAMETERS FOR SIMPLIFIED PROCEDURE

The simplified procedure requires the following parameters to describe the dam-water-foundation rock system for computing the equivalent lateral earthquake loads:

- Total height of dam (monolith plus pier)  $H_s$
- Depth of impounded water  $H$
- Young's modulus of elasticity of dam concrete  $E_s$
- Unit weight of dam concrete  $\gamma_c$
- Young's modulus of elasticity of foundation rock  $E_f$
- Viscous damping ratio of dam on rigid foundation rock with empty reservoir  $\xi_1$
- Constant hysteretic damping factor for foundation rock  $\eta_f$
- Wave reflection coefficient for reservoir bottom materials  $\alpha$

For a defined geometry of spillway monolith and pier, each of the above parameters can have some effects on the computed earthquake loads.

## 7. SPILLWAY FINITE ELEMENT MODEL

A two-dimensional plane stress model, usually used for predicting earthquake response of non-overflow monoliths of a concrete gravity dam, will not be appropriate for stress analysis of spillway monoliths with big cavities due to enlargement of the conduits. A three-dimensional finite element model for the spillway monolith and pier is justified because stresses are expected to vary along the width of the monolith with high stresses around the openings. Three-dimensional finite element models have been developed for Monoliths 13 and 14. The finite element model consists of an assemblage of GTSTRU DL 'IPLS' Isoparametric Linear Solid elements and 'TRIP' Triangular Prism elements in the X, Y, and Z global coordinate system. The X-axis is horizontal and positively directed downstream; the Y-axis is vertical with the positive direction upwards, and Z-axis is horizontal along the width of the monolith following the right-hand rule. The 'IPLS' element has eight nodes and six faces with all faces being quadrilaterals. The displacement expansion associated with this element type yields a cubic field within the element and linear along the edges. The 'TRIP' element has six nodes with two triangular faces and three quadrilateral faces. The displacement expansion on the quadrilateral faces is quadratic while the expansion is linear on the triangular 4 faces. More detailed description of 'IPLS' and 'TRIP' elements are available in reference [3]. Three translational degrees of freedom in the X, Y, and Z directions per node are considered for the 'IPLS' and 'TRIP' elements. All nodes

along the dam base are fixed against translation, an appropriate boundary condition for rigid foundation rock. The flexibility effects of the foundation rock are only considered in computing the earthquake loads using the simplified procedure. Roller supports (restraints are applied to the degrees of freedom in the Z direction) are specified at the nodes on the two end faces of the 50-ft wide spillway monolith where the straight (unkeyed) contraction joints between the dam monoliths tend to slip during large-amplitude earthquake vibration. All nodes at the top of the pier are fixed against translation in the Z direction due to restraints provided by the spillway bridge.

## 8. EFFECTS OF DAM-WATER INTERACTION AND RESERVOIR BOTTOM ABSORPTION

Dam-water interaction and reservoir bottom absorption generally lengthen the fundamental vibration period of the dam and increase the effective damping from baseline levels corresponding to the dam on rigid foundation rock and empty reservoir. For a fixed monolith cross-section, the period lengthening and added damping can be influenced by several parameters, the more significant of which are: Young's modulus of dam concrete  $E_s$ , ratio of water depth to dam height  $H/H_s$ , and wave reflection coefficient  $\alpha$ . It has been determined from research investigation [4] that the period lengthening increases and added damping generally, but not always, increases with increasing water depth, absorptiveness of reservoir bottom materials, and concrete modulus.

## 9. EFFECTS OF DAM-FOUNDATION ROCK INTERACTION

Dam-foundation rock interaction generally lengthens the fundamental vibration period of the dam and increases the effective damping from baseline levels corresponding to the dam on rigid foundation rock and empty reservoir. For a fixed spillway monolith cross-section, the period lengthening and added damping can be influenced by several parameters, the more

significant of which are: moduli ratio  $E_f/E_s$ , where  $E_s$  and  $E_f$  are the Young's moduli of the dam concrete and foundation rock, respectively; and the constant hysteretic damping factor  $\eta_f$  for the foundation rock. It has been determined from research investigation [4] that the period lengthening and added damping increase with an increasingly flexible foundation rock and increasing hysteretic damping factor  $\eta_f$ . As a general rule recommended in reference [1], the effects of dam-foundation rock interaction can be neglected in computing the equivalent lateral earthquake loads if  $E_f/E_s > 4$ .

## 10. CONCRETE PROPERTIES

The mass concrete in the dam is assumed to be homogeneous, isotropic, and linearly elastic with the properties used for the stress analysis summarized in the following table:

Modulus of Elasticity $E_s$ Seismic Loads Considered	Modulus of Elasticity $E_s$ Seismic Loads Not Considered	Poisson's Ratio	Unit Weight $\gamma_c$
$5.9 \times 10^6$ psi	$3.6 \times 10^6$ psi	0.19	158 pcf

The above values for the modulus of elasticity and Poisson's ratio were recommended in the report prepared by Professor Jerome Raphael for the 1989 DSAP study (see Appendix D of reference [5]). The unit weight of 158 pcf was used in the DSAP study and was based on information provided by U.S. Army Corps of Engineers, Sacramento District.

Raphael's report also provided strength properties for rich and lean concrete used to assess the seismic performance of the dam. The recommended apparent dynamic tensile strength is 840 psi for rich concrete and 700 psi for lean concrete. Although recommended values for the apparent static tensile strength were not provided, they can be inferred from the report as 580 psi for rich concrete and 470 psi for lean concrete.

Direct tension tests and splitting tension tests on 12-in diameter concrete specimens were completed by the U.S. Bureau of Reclamation (USBR) laboratory in December of 2001, and the test results were summarized in a memorandum for record prepared by Stephen B. Tatro. The test results indicate an approximate splitting tensile strength of 370 psi for lean concrete, and the computed dynamic modulus of rupture is 830 psi. Note that "apparent dynamic tensile strength" used in Raphael's report is the same as "dynamic modulus of rupture" specified in Tatro's memorandum. The smaller of the two values (Raphael's and Tatro's), 700 psi, is conservatively used as the maximum allowable tensile stress for evaluation of dam performance.

Test data provided by Raphael and Tatro do not include the compressive strength. A consulting report prepared by Ernest Schrader [6] provided an estimate of static compressive strength of 4,375 psi for lean concrete and 6,000 psi for rich concrete.

## 11. FOUNDATION ROCK PROPERTIES

The ranges of expected values for the properties of the foundation rock at the dam site were provided in Appendix E of reference [5] and are summarized as follows:

	Dynamic Young's Modulus of Elasticity $E_f$	Poisson's Ratio	Unit Weight
Lower Bound	$5.8 \times 10^6$ psi	0.30	167 pcf
Average	$7.9 \times 10^6$ psi	0.25	171 pcf
Upper Bound	$11.0 \times 10^6$ psi	0.20	174 pcf

The Young's modulus of elasticity is required for computing the equivalent lateral earthquake loads using Dr. Chopra's simplified procedure, but the Poisson's ratio and unit weight are not needed. Another required property for the foundation rock is the constant hysteretic damping factor  $\eta_f$ , which can be determined

from experimental tests of appropriate rock samples subject to harmonically varying stress and strain. Since no experimental  $\eta_f$  value is available, the recommended value of  $\eta_f = 0.10$  from reference [1] is used to represent the damping properties of the foundation rock. The average value of  $E_f = 7.9$  million psi is used for the seismic stress analysis in this study. A substantially lower value of  $E_f = 1.9$  million psi was recommended in a draft memorandum prepared by URS [7]. URS will conduct studies to reconcile the significant difference in the recommended values for  $E_f$  from references [5] and [7]. Parametric studies will be performed in the final phase of stress analysis to evaluate the sensitivity of the stress results to the foundation stiffness after the range of  $E_f$  can be confirmed with reasonable confidence.

## 12. VISCOUS DAMPING RATIO OF DAM

Energy dissipation in the dam is represented by viscous damping with a damping ratio  $\xi_1$ .  $\xi_1 = 5\%$  is recommended [1] for the large motions and high stresses expected in a dam during intense earthquakes. Note that  $\xi_1 = 5\%$  is the damping ratio of the dam on rigid foundation rock with empty reservoir, and is increased to higher damping after taking into account the effects of hydrodynamic effects and foundation-rock flexibility effects.

## 13. WAVE REFLECTION COEFFICIENT

The bottom of a reservoir typically consists of layers of alluvium, silt, and other sedimentary materials. Hydrodynamic pressure waves impinging on such materials will partially reflect back into the water, and will partially be absorbed into the underlying layers of reservoir bottom materials. In general, the dynamic response of the dam decreases with increasing wave absorption at the reservoir bottom.

The absorptiveness of the reservoir bottom materials is characterized by the wave



reflection coefficient  $\alpha$ , which is defined as the ratio of the amplitude of the reflected hydrodynamic pressure wave to the amplitude of a vertically propagating pressure wave incident on the reservoir bottom. A rigid reservoir bottom ( $\alpha = 1.0$ ) indicates that pressure waves are reflected from the reservoir bottom without attenuation; whereas a completely absorptive reservoir bottom ( $\alpha = 0$ ) means that normally propagating pressure waves are fully absorbed into the reservoir bottom materials without reflection. The wave reflection coefficient  $\alpha$  can be determined according to the following equation [8]:

$$\alpha = \frac{1 - qC}{1 + qC}$$

In which  $C$  is the velocity of pressure waves in water,  $q$  is the damping coefficient of the reservoir bottom materials and is given by

$$q = \frac{\rho C}{\rho_r \sqrt{E_r / \rho_r}}$$

where  $\rho$  is the mass density of water,  $E_r$  is the Young's modulus of elasticity and  $\rho_r$  is the mass density of the materials at the reservoir bottom. Taking  $E_r = E_r = 11,000$  ksi for the foundation rock (the upper bound), the above equations lead to an  $\alpha$  value of 0.82. This  $\alpha$  value is rounded up to  $\alpha = 0.90$  for this study, as it provides conservative estimates of stresses in the dam.

#### 14. EARTHQUAKE EXCITATION

At the request of the USACE, URS Corporation conducted a study in the characterization of seismic sources and ground motion attenuation at the dam site, and performed seismic hazard analyses based on the most current seismic data available. The results of the deterministic and probabilistic seismic hazard analyses are presented in the URS's report dated 5 July 2001 [9]. The conclusions reached by URS that can potentially affect the structural analysis of this

study are summarized as follows:

- Based on probabilistic seismic hazard analysis, the Uniform Hazard Spectra associated with a 10,000-year return period should be adopted as the Maximum Design Earthquake (MDE) for the Folsom Dam modification project. The associated peak horizontal ground acceleration is 0.28g. Note that the peak horizontal acceleration of 0.35g recommended by Bolt and Seed for the DSAP study has a return period of about 20,000 years according to URS's probabilistic analysis.
- The Uniform Hazard Spectra associated with a 500-year return period should be adopted as the Operating Basis Earthquake (OBE) for the Folsom Dam modification project. The associated peak horizontal ground acceleration is 0.10g.
- The peak horizontal accelerations for the median and 84th percentile Maximum Credible Earthquake (MCE) are 0.24g and 0.38g, respectively.

URS also developed smooth response spectra for critical damping values of 10%, 12%, 14%, 16%, 18%, and 20% from the 5%-damped MDE and MCE response spectra using period dependent scaling relations derived from the model of Newmark and Hall. The MDE and MCE response spectra for various damping values are available in the URS's report. Tabulated values of spectral acceleration for the MDE and MCE at selected periods are used to compute the equivalent lateral earthquake loads for the stress analysis.

#### 15. RESPONSE COMBINATION

The two sets of equivalent lateral earthquake forces  $f_i$ ,  $f_{sc}$  produce the values  $r_i$  and  $r_{sc}$  respectively for any response quantity  $r$ , which

can be shear or normal stresses at any point in the dam. Since the maximum responses  $r_1$  and  $r_{sc}$  generally do not occur at the same time during an earthquake, they should be combined to obtain an estimate of the dynamic response using the well known modal combination rule: square-root-of-the-sum-of-squares (SRSS) of modal maxima according to the following equation:

$$r_d = \sqrt{(r_1)^2 + (r_{sc})^2}$$

To recognize that the direction of lateral earthquake forces is reversible, combinations of static and dynamic responses should consider the worst case, leading to the maximum and minimum of the total response  $r_t$ , given by

$$r_t = r_{st} + \sqrt{(r_1)^2 + (r_{sc})^2}$$

$$r_t = r_{st} - \sqrt{(r_1)^2 + (r_{sc})^2}$$

where  $r_{st}$  is the response due to initial static loads. Note that the above equations are appropriate for cases where the shear and normal stresses at any point are referenced with respect to the global coordinate system, but generally not applicable for the case of principal stresses.

## 16. CASES ANALYZED

Dynamic response history analyses are not considered at this stage of the study. A response spectrum analysis of the selected spillway monoliths is performed instead to evaluate the maximum dynamic response of the monolith to earthquake ground motion, wherein the computed earthquake lateral loads are applied as static loads in the GTSTRUDL model. The important effects of dam-water interaction, reservoir bottom absorption, and dam-foundation-rock interaction are considered in determining the earthquake loads. The following basic cases are considered in the stress analysis of the spillway monolith:

- Analysis of a completely solid monolith without any openings. The finite element mesh for Monoliths 14 without openings is shown in Figures 2. Monolith 14 is the tallest spillway monolith with an average height of 328 ft, including the pier.
- Analysis of monolith with proposed conduit enlargement and gate chambers. The conduit opening is 14-ft wide by 22-ft high at the upstream face and the cavity associated with the gate chamber approximates existing dimensions 21 ft by 30 ft by 14 ft. The 21-ft dimension is in the upstream-downstream direction, 30 ft is the height, and 14 ft is along the width of monolith. A sectional view of the finite element mesh for this case is shown in Figure 3 for Monolith 14 and in Figure 4 for Monolith 13 (two layers of finite elements are shown). Monolith 13 has an average height of approximately 310 ft, including the pier.
- Analysis of monolith with proposed conduit enlargement and gate chambers. The conduit opening is 20-ft wide by 22-ft high at the upstream face and the cavity associated with the gate chamber approximates existing dimensions 21 ft by 30 ft by 14 ft. A sectional view of the finite element mesh for Monolith 14 for this case is shown in Figure 5 (three layers of finite elements are shown).
- Analysis of monolith with proposed conduit enlargement and gate chambers. The conduit opening is 20-ft wide by 22-ft high at the upstream face. The 14-ft dimension (along the width of monolith) of the gate chamber is increased to 20 ft, and the two gate chambers are hollowed out to form one continuous cavity in the vertical direction. This case simulates a potential construction configuration



and is identified as construction case I. A sectional view of the finite element mesh for Monolith 14 for this case is shown in Figure 6 (three layers of finite elements are shown).

- Analysis of monolith with proposed conduit enlargement and gate chambers. The conduit opening is 20-ft wide by 22-ft high at the upstream face. The 14-ft dimension of the gate chamber is increased to 20 ft, and concrete is excavated vertically to provide access to the each of the conduits with the invert of the upper conduit separating the two gate chambers. This case simulates another potential construction configuration and is identified as construction case II. A sectional view of the finite element mesh for Monolith 14 for this case is shown in Figure 7 (three layers of finite elements are shown).

It is important to point out that the finite element meshes shown in Figures 3 through 7 do not represent the most current vertical alignment and dimensions of the conduit enlargement that are recommended in the Gate Size Decision Technical Memorandum [10]. The current vertical alignment is close to being horizontal through the monolith, whereas the finite element meshes show a steeper drop at the downstream outlet. The finite element meshes were completed (using preliminary data) before the vertical alignment and dimensions of the conduit enlargement could be finalized. Finite element meshes will be re-developed to conform to the current alignment and conduit dimensions in the final phase of analysis and design.

Considering different combinations of MDE, MCE, and different conduit openings, the above basic cases can be expanded to form more analysis cases, which are summarized as Cases 1 through 13 in Table 1. Cases 1, 3, 5, 12 correspond to conditions due to static loads only, which include dead weight of spillway monolith, hydrostatic pressures and uplift due

to the impounded water. Cases 7 and 8 are static construction cases I and II, respectively. Although seismic loads are not included in the construction cases, they will be considered in the final stage of the design process. URS Corporation is developing OBE design response spectra to be used for the construction cases. Cases 2, 4, 6, 9, 10, 11, 13 correspond to earthquake analysis of the monolith considering both the effects of static loads and seismic loads. For all cases analyzed, the reservoir pool elevation is at gross pool EL. 466.0 ft, and the portions of the conduits upstream of the service gates are fully pressurized with the service gates closed under normal operating condition. The exceptional cases are Cases 7 and 8, wherein the bulkhead gates are closed at the upstream face of the dam.

## **17. FUNDAMENTAL VIBRATION MODE OF DAM**

Based on GTSTRUDL eigenvalue analysis, the fundamental vibration periods of Monoliths 14 and 13 (with conduit enlargement) on rigid foundation rock with empty reservoir are found to be 0.166 sec and 0.158 sec, respectively. After taking into account the effects of water and foundation-rock flexibility using Dr. Chopra's simplified procedure, these vibration periods are lengthened to 0.314 sec and 0.299 sec for Monoliths 14 and 13, respectively. The lengthened vibration periods are used to compute the lateral earthquake loads. The fundamental vibration mode shapes of Monoliths 14 and 13 are shown in Figures 8 and 9, respectively.

## **18. LOADS IN GTSTRUDL FINITE ELEMENT MODELS**

The static loads and seismic loads incorporated into the GTSTRUDL finite element models are summarized as follows:

- The dead weight of the monolith is modeled as the sum of all finite element body forces.

- The hydrostatic pressures are input as surface forces normal to the faces of dam finite elements in contact with water.
- The uplift pressures are distributed as body forces in the dam finite elements at the bottom row adjacent to the foundation rock. Note that the uplift pressures are computed for drain effectiveness of 25% and 50% in accordance with EM 1110-2-2200 [2].
- For the two sets of earthquake forces  $f_1$  and  $f_{sc}$ , the forces due to the hydrodynamic pressures are input as surface forces on the faces of dam finite elements in contact with water, acting in the global X direction. The inertial forces associated with the mass of concrete are specified as body forces for all dam finite elements, acting in the global X direction.

The loads described above form independent load cases, which can be combined to desired load combinations. After forming load combinations, GTSTRUDL can search for the envelope maximum and envelope minimum of a response quantity from the contributing load combinations. The envelope maximum is the maximum of the values from each of the contributing load combinations. Similarly, the envelope minimum is the minimum of the values from each of the contributing load combinations.

## 19. STRESS ANALYSIS RESULTS

The stress output associated with the dam finite elements consists of normal stresses: SXX, SYY, and SZZ, as well as the shear stresses: SXY, SXZ, and SYZ. By definition, these stress components act on a unit differential volume in the X, Y, and Z global coordinate system. Positive and negative values for the normal stresses denote tensile and compressive stresses, respectively. At any point in the dam, there are three mutually perpendicular planes on which the shear

stresses vanish. The normal stress components on these three planes are principal stresses S1, S2, S3 (Note that  $S1 > S2 > S3$ ). The maximum shear stress TMAX is given by

$$TMAX = (S1 - S3) / 2$$

Stresses SXX, SYY, and SZZ, are summarized in Tables 2, 3, and 4, respectively for Cases 1 through 13. The stresses are presented at selected locations of the monolith, which include the upstream heel, downstream toe, conduit inlets, conduit outlets, and areas around the gate chambers. Because of the variation in stresses along the 50-ft width of the monolith (especially around openings), highest stresses are searched in this direction and reported in the tables. For Cases 1, 3, 5, 7, 8, 12, the stresses shown are total static stresses due to dead weight of spillway monolith, hydrostatic pressures, and uplift. For Cases 2, 4, 6, 9, 10, 11, 13, the stresses shown are total stresses due to dead weight of spillway monolith, hydrostatic pressures, uplift, plus the dynamic response due to earthquake loads. It should be noted that Tables 2 through 4 are intended to present the highest tensile stresses (envelope maximum) at the selected locations. At locations where no tensile stresses are found, the highest compressive stresses (envelope minimum) are reported. Principal stress computations for the downstream face show the maximum compressive stress of 985 psi (for Case 11) at the soffit of the upper conduit outlet, which is well within the compressive strength of the dam concrete. Comparing the stress results in Tables 2 through 4 for Case 10 to those for Case 11, it is apparent that the effects of larger conduit openings generally lead to higher tensile and compressive stresses at the soffit and invert of each conduit, but slightly lower stresses at the upstream heel of the monolith. Since Case 11 represents a condition with the conduit dimensions significantly larger than those recommended in the Gate Size Decision Technical Memorandum, stress results from this case will not be used for discussion in the following paragraphs.

The damage that concrete gravity dams may experience due to intense earthquake ground motions is primarily in the form of cracking in areas subjected to large tensile stresses. Therefore, attention will now be focused only on the high tensile stresses developed in the dam. Color-coded stress contour plots are used to display the distribution of stresses in the spillway monolith. Selected contour plots showing the distribution of stresses SXX, SYY, and SZZ, are included in this report only for Cases 3 and 10. Contour plots for other cases are on file in Structural Design Section and will be available for review upon request. For Case 3, the distribution of stresses SXX, SYY, and SZZ, at  $Z = 25$  ft are displayed in Figures 10 through 12. The highest tensile stress (principal stress S1) corresponding to this case is 342 psi at the upstream heel is well below the strength capacity of the dam concrete. For Case 10, the contour plots showing the envelope maximum of these stress components at  $Z = 25$  ft, 18 ft, and 12 ft are shown in Figures 13 through 21.

The stress contour plots consistently show a high stress concentration in the isolated heel area of the spillway monolith. The highest tensile stress (principal stress S1) at the heel is 1,024 psi for Case 10. This stress drops sharply to 680 psi within a distance of 10 ft up from the base of the heel. The stress concentration, which was also predicted by Dr. Chopra's previous research work and his case study for Pine Flat Dam [8], and the steep stress gradient are, in part, due to the fixed boundary condition assumed at the base. The high stresses and the steep stress gradient are expected to be less severe if the flexibility effects of the foundation rock are incorporated into the finite element model. The stress contour plots also reveal some significant tensile stresses at the upstream and downstream faces of the monolith. For Case 10, the highest tensile stress developed on the upstream face, away from the heel area, is 494 psi at a location near the lower conduit inlet. The highest tensile stress on the downstream face is 533 psi at the soffit of the upper conduit outlet, and drops rapidly over a short distance

away from the opening.

The analytical procedure described in this report is appropriate for stress analysis of the spillway monolith but not for the pier. The pier should be analyzed as a reinforced concrete structure subjected to the earthquake forces due to upstream-downstream ground motion, computed by Dr. Chopra's simplified procedure, and the forces associated with earthquake excitation along the dam axis. Since the latter set of forces is not considered in the simplified procedure, the stress results computed for the pier, as shown in the contour plots, should not be used for design or seismic safety evaluation.

## 20. CONCLUSIONS

Based on the linearly elastic stress analysis performed in this study, the prevalent level of computed tensile stresses is within the apparent dynamic tensile strength of 700 psi, except for the stress concentration of 1,024 psi at the upstream heel of the monolith. This stress drops sharply to less than 700 psi within a distance of 10 ft up from the base. The stress concentration is, in part, a consequence of the assumed fixed boundary condition at the dam base where a discontinuity between the dam base and the foundation rock exists. The high stress could not be realized in the actual monolith because consideration of rock flexibility in the finite element analysis would alleviate this stress concentration. Even if cracking occurs in the heel area, it is very localized and is considered as acceptable performance for the Maximum Credible Earthquake (MCE). Although tensile stresses (in the order of 500 psi) developed at the conduit inlets and outlets during the MCE event are less than the concrete tensile strength, it is prudent to have steel reinforcement around the conduit openings to resist the tensile stresses. This is consistent with the assumption that concrete tensile strength is neglected in flexural strength design.

The following, as a minimum, will be

considered in the final phase of analysis and design. First, to conform to the alignment and dimensions of the conduit enlargement recommended in the Gate Size Decision Technical Memorandum [10], finite element meshes will be re-developed for stress analysis. Secondly, an important issue that should be resolved is the uncertainty associated with the modulus of elasticity for the foundation rock. The extent of any concrete cracking and its implications to the seismic safety of the dam cannot be determined with confidence until the new finite element meshes are analyzed with more accurate foundation stiffness. Finally, seismic loads corresponding to the Operating Basis Earthquake (OBE) will be incorporated into the construction cases.

Considering the level of computed stresses from this study, rigorous response history analysis in which the reservoir is treated as a continuum governed by the wave equation is not justified, because this type of analysis will be very computationally intensive for the three-dimensional finite element meshes of practical size and will require use of special purpose computer programs.

## 21. REFERENCES

1. A.K. Chopra and T. Hanchen, "Simplified Earthquake Analysis of Gated Spillway Monoliths of Concrete Gravity Dams," Technical Report SL-89-4, U.S. Army Corps of Engineers, Waterways Experiment Station Structures Laboratory, Vicksburg, Mississippi, March 1989.
2. U.S. Army Corps of Engineers, "Engineering and Design – Gravity Dam Design," EM 1110-2-2200, Department of the Army, Washington DC, 30 June 1995.
3. Georgia Institute of Technology, "GTSTRUDL User Reference Manual – Volume 3," June 1999.
4. G. Fenves and A.K. Chopra, "Simplified Earthquake Analysis of Concrete Gravity Dams: Combined Hydrodynamic and Foundation Interaction Effects," *Journal of Engineering Mechanics*, ASCE, Vol. 111, No.6, June 1985, pp.736-756.
5. R.L. Hall, S.C. Woodson, and J.M. Nau, "Seismic Stability Evaluation of Folsom Dam and Reservoir Project," Technical Report GL-87-14 Report 3, U.S. Army Corps of Engineers, Waterways Experiment Station Structures Laboratory, Vicksburg, Mississippi, March 1989.
6. E.K. Schrader, "Estimated Mass Concrete Material Properties for Folsom Dam," Consulting Report Prepared for U.S. Army Corps of Engineers Sacramento District, Schrader Consulting, May 2001.
7. G. Lawton, D. Young, and M. Schmoll, "Draft Memorandum – Folsom Dam Modifications Evaluation of Rock Mass Properties," URS Corporation, June 2001.
8. G. Fenves and A.K. Chopra, "Earthquake Analysis and Response of Concrete Gravity Dams," Report No. UCB/EERC-84/10, Earthquake Engineering Research Center, University of California, Berkeley, August 1984.
9. URS Corporation, "Deterministic and Probabilistic Seismic Hazard Analyses for Folsom Dam," July 2001.
10. U.S. Army Corps of Engineers, Sacramento District, "Gate Size Decision Technical Memorandum," November 2001.

TABLE 1 SUMMARY OF CASES ANALYZED

Case No.	Monolith No.	Conduit Dimensions W x H	Gate Chamber Dimensions W x H x L	Earthquake	Foundation Rock Young's Modulus E
1*	14	-	-	-	7.9 x 10 <sup>6</sup> psi
2*	14	-	-	MDE	7.9 x 10 <sup>6</sup> psi
3	14	14' x 22'	21' x 30' x 14'	-	7.9 x 10 <sup>6</sup> psi
4	14	14' x 22'	21' x 30' x 14'	MDE	7.9 x 10 <sup>6</sup> psi
5	14	20' x 22'	21' x 30' x 14'	-	7.9 x 10 <sup>6</sup> psi
6	14	20' x 22'	21' x 30' x 14'	MDE	7.9 x 10 <sup>6</sup> psi
7	14	20' x 22'	21' x H• x 20'	-	7.9 x 10 <sup>6</sup> psi
8	14	20' x 22'	21' x H•• x 20'	-	7.9 x 10 <sup>6</sup> psi
9*	14	-	-	MCE	7.9 x 10 <sup>6</sup> psi
10	14	14' x 22'	21' x 30' x 14'	MCE	7.9 x 10 <sup>6</sup> psi
11	14	20' x 22'	21' x 30' x 14'	MCE	7.9 x 10 <sup>6</sup> psi
12	13	14' x 22'	21' x 30' x 14'	-	7.9 x 10 <sup>6</sup> psi
13	13	14' x 22'	21' x 30' x 14'	MCE	7.9 x 10 <sup>6</sup> psi

\* solid monolith without any openings

• the two gate chambers are hollowed out to form one continuous cavity in the vertical direction

•• concrete is excavated vertically to provide access to the each of the conduits with the invert of the upper conduit separating the two gate chambers

TABLE 2 SUMMARY OF NORMAL STRESSES SX (PSI)

TABLE 2. SUMMARY OF RUMINAL STRESSES SCA (PSI)																
CASE No.	OPENINGS AROUND GATE CHAMBERS			UPSTREAM FACE						DOWNSTREAM FACE						
	UPPER	LOWER	HEEL	UPPER INLET		CONDUIT INLET		LOWER INLET		CONDUIT TOE	UPPER OUTLET		CONDUIT OUTLET		LOWER OUTLET	CONDUIT INVERT
				SOFFIT	INVERT	SOFFIT	INVERT	SOFFIT	INVERT		SOFFIT	INVERT	SOFFIT	INVERT		
1	-	-	56	-	-	-	-	-	-	-24	-	-	-	-	-	-
2	-	-	159	-	-	-	-	-	-	-44	-	-	-	-	-	-
3	-105	3	55	-72	-90	-96	-128	-91	-72	-21	-91	-72	5	-67	5	-67
4	31	38	156	-120	-157	-150	-205	-41	10	-41	10	6	8	-126	8	-126
5	-99	5	54	-73	-93	-102	-136	-18	-116	-18	-116	-91	56	-75	56	-75
6	37	48	152	-131	-172	-164	-224	-38	13	-38	13	7	105	-141	105	-141
7	24	20	59	-95	-101	-115	-126	-34	-114	-34	-114	-89	55	-74	55	-74
8	24	18	59	-94	-104	-115	-126	-34	-113	-34	-113	-89	55	-74	55	-74
9	-	-	202	-	-	-	-	6	-	6	-	-	-	-	-	-
10	77	75	198	38	31	-173	-237	6	54	6	54	42	21	18	21	18
11	83	68	194	44	39	-191	-265	6	69	6	69	45	127	20	127	20
12	-105	2	52	-70	-90	-95	-129	-23	-88	-23	-88	-73	4	-51	4	-51
13	77	75	193	41	43	29	-235	4	53	4	53	38	17	11	17	11

TABLE 4 SUMMARY OF NORMAL STRESSES SZZ (PSI)																			
OPENINGS AROUND CHAMBERS			GATE			UPSTREAM FACE						DOWNSTREAM FACE							
CASE No.	UPPER	LOWER	HEEL	UPPER INLET		CONDUIT		LOWER INLET		CONDUIT	TOE	UPPER OUTLET		CONDUIT		LOWER OUTLET			
				SOFFIT	INVERT	SOFFIT	INVERT	SOFFIT	INVERT			SOFFIT	INVERT	SOFFIT	INVERT				
1	-	-	56	-	-	-	-	-	-	-	-24	-	-	-	-	-	-		
2	-	-	159	-	-	-	-	-	-	-	-45	-	-	-	-	-	-		
3	-47	1	55	8	7	6	30	51	94	-21	-60	-63	24	24	-51	-	-		
4	-65	12	155	34	52	1	9	22	-21	123	32	290	17	-	-	-	-		
5	-58	20	54	3	1	88	78	108	-38	257	55	549	40	-	-	-	-		
6	3	70	152	97	41	26	16	7	-24	121	35	287	35	-	-	-	-		
7	105	136	59	41	25	17	7	-24	120	34	287	36	-	-	-	-	-		
8	106	118	59	41	25	17	7	-24	120	34	287	36	-	-	-	-	-		
9	-	-	202	-	-	-	-	-	-	4	-	-	-	-	-	-	-		
10	12	21	198	41	70	64	121	4	37	37	55	13	-	-	-	-	-		
11	16	92	194	137	130	116	145	4	315	56	659	60	-	-	-	-	-		
12	-46	2	52	15	11	24	48	-17	-63	-70	21	-59	-	-	-	-	-		
13	12	23	193	43	72	71	157	3	36	35	48	9	-	-	-	-	-		

TABLE 3 SUMMARY OF NORMAL STRESSES SYX (PSI)																			
OPENINGS AROUND CHAMBERS			GATE		UPSTREAM FACE								DOWNSTREAM FACE						
CASE No.	UPPER	LOWER	HEEL	UPPER INLET		CONDUIT		LOWER INLET		CONDUIT		TOE	UPPER OUTLET		CONDUIT		LOWER OUTLET		
				SOFFIT	INVERT	SOFFIT	INVERT	SOFFIT	INVERT	SOFFIT	INVERT		SOFFIT	INVERT	SOFFIT	INVERT			
1	-	-	239	-	-	-	-	-	-	-	-103	-	-	-	-	-	-	-	
2	-	-	676	-	-	-	-	-	-	-	-190	-	-	-	-	-	-	-	
3	24	20	235	-95	-91	-99	-103	-91	5	20	63	5	-	-	-	-	-	-	
4	58	46	663	82	107	118	187	-176	27	32	117	42	-	-	-	-	-	-	
5	19	17	231	-104	-97	-106	-114	-89	22	14	82	10	-	-	-	-	-	-	
6	56	50	649	106	162	154	254	-162	44	21	153	22	-	-	-	-	-	-	
7	32	33	253	23	17	7	-132	-89	22	17	81	11	-	-	-	-	-	-	
8	32	41	253	23	16	7	-132	-89	21	16	81	11	-	-	-	-	-	-	
9	-	-	861	-	-	-	-	-	-	-	-	-	-	-	-	-	-	-	
10	114	67	844	156	191	208	290	-17	111	76	141	50	-	-	-	-	-	-	
11	112	78	827	200	269	273	379	-16	142	92	184	31	-	-	-	-	-	-	
12	18	21	220	-96	-89	-100	-116	-45	5	21	56	20	-	-	-	-	-	-	
13	116	98	823	156	195	228	373	-10	109	73	123	44	-	-	-	-	-	-	

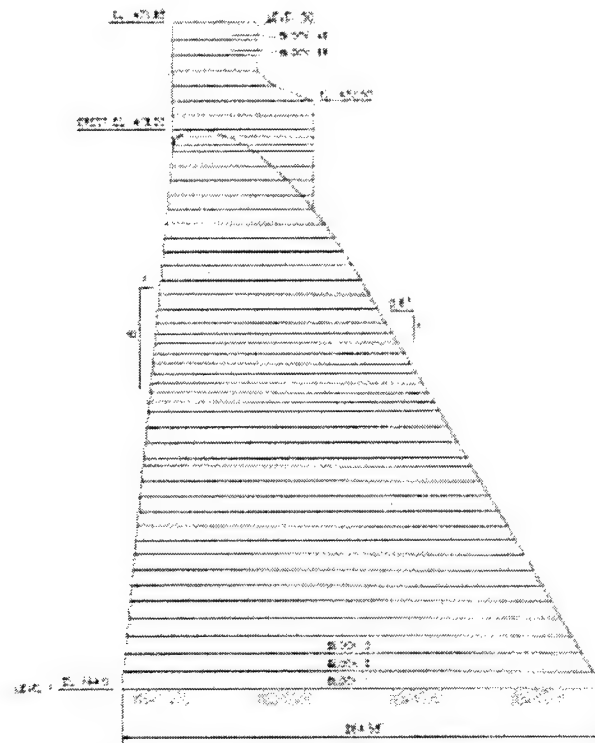


FIGURE 1 IDEALIZED BLOCK MODEL FOR SPILLWAY MONOLITH 14

Figure 1. Idealized block model for spillway monolith 14

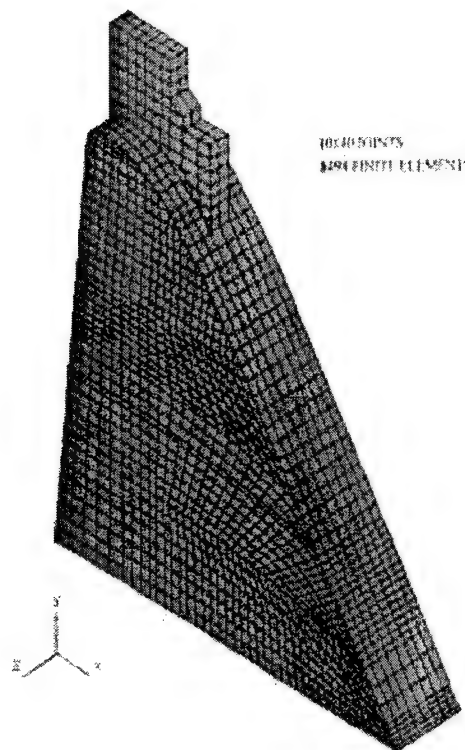


Figure 2. FE mesh for monolith 14 without openings

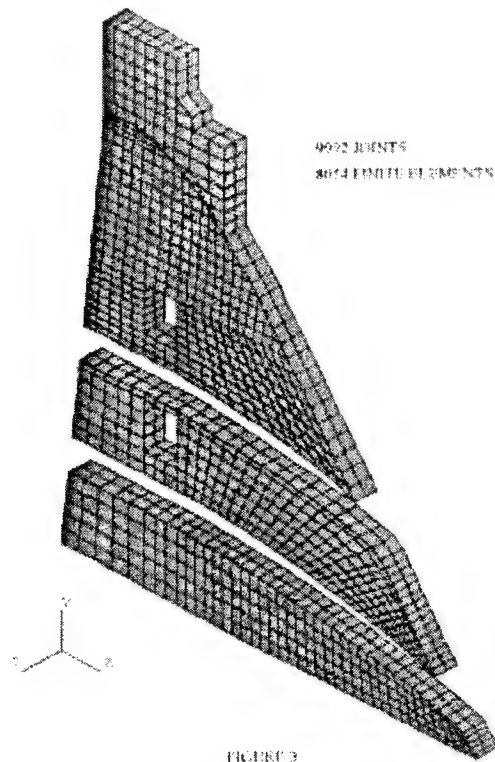


FIGURE 3

Figure 3. Sectional view of FE mesh for monolith 14 with 14' W x 22' H openings at upstream face

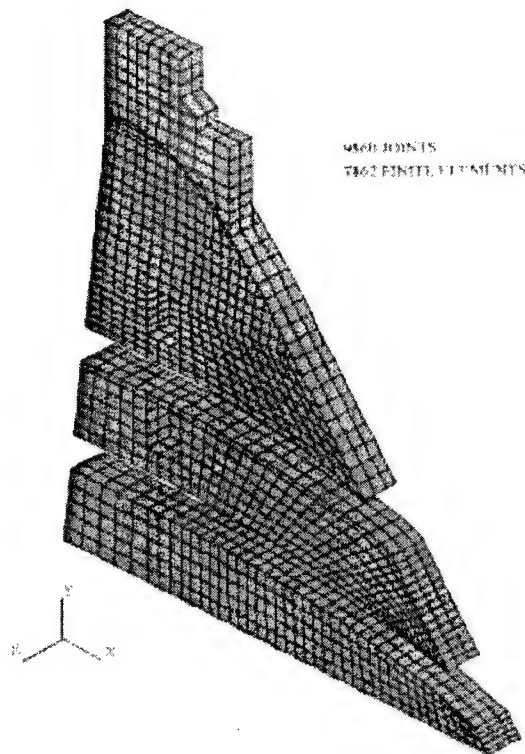


Figure 4. Sectional view of FE mesh for monolith 13 with 14' W x 22' H openings at upstream face



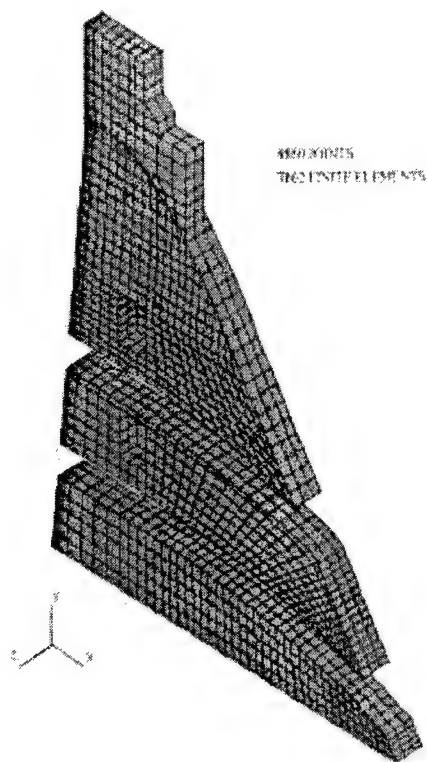


Figure 5. Sectional view of FE mesh for monolith 14 with 20' W x 22' H openings at upstream face

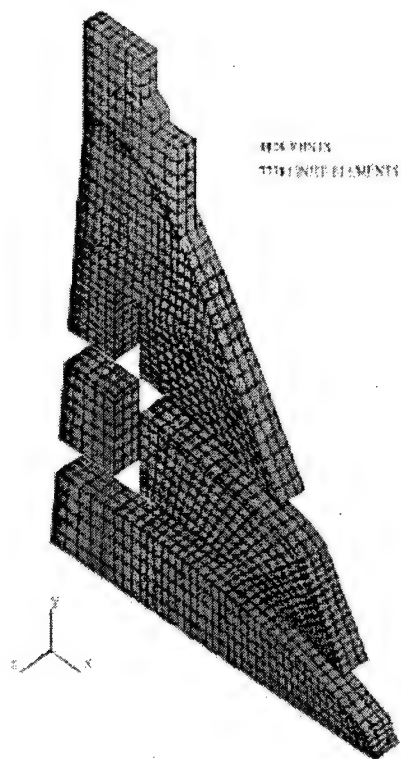


Figure 6. Sectional view of FE mesh for monolith 14 with 20' W x 22' H openings at upstream face for construction case I

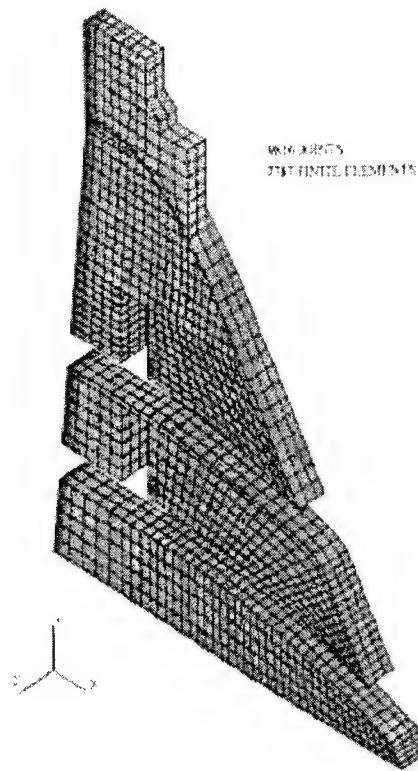


Figure 7. Sectional view of FE mesh for monolith 14 with 20' W x 22' H openings at upstream face for construction case II

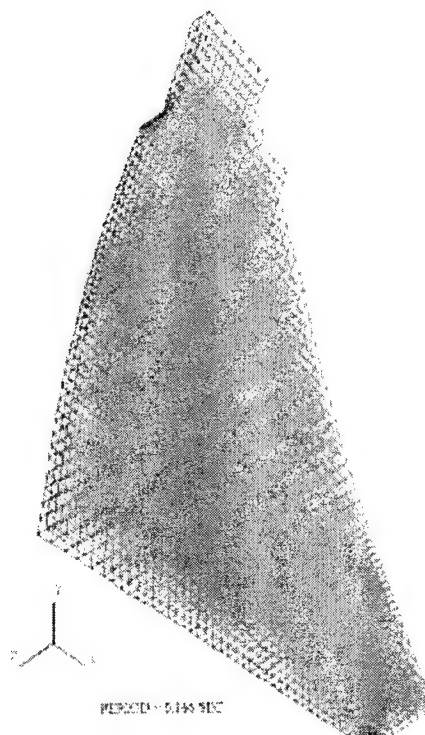


Figure 8. Fundamental vibration mode of monolith 14

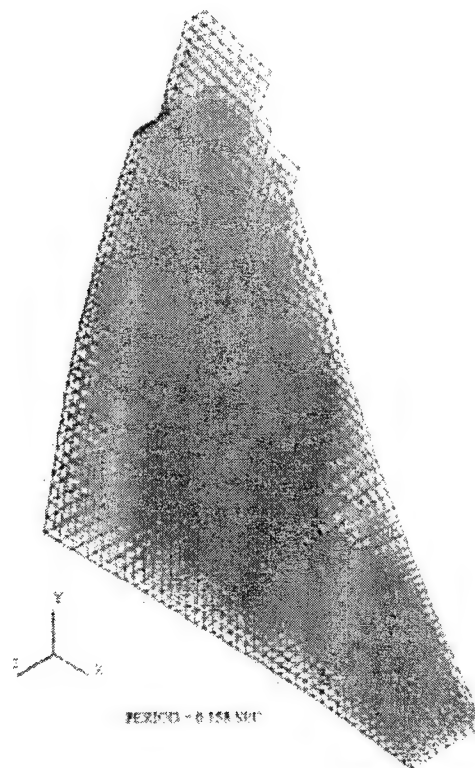


Figure 9. Fundamental vibration mode of monolith 13

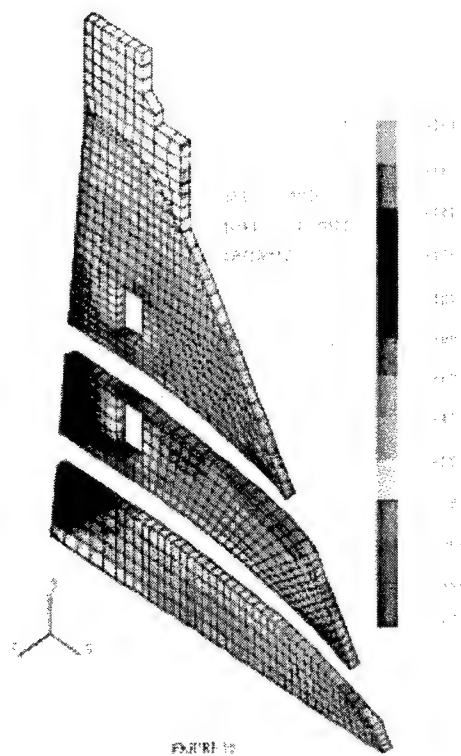


Figure 10. Normal stresses  $S_{xx}$  (psi) at  $z = 25$  ft (case 3)

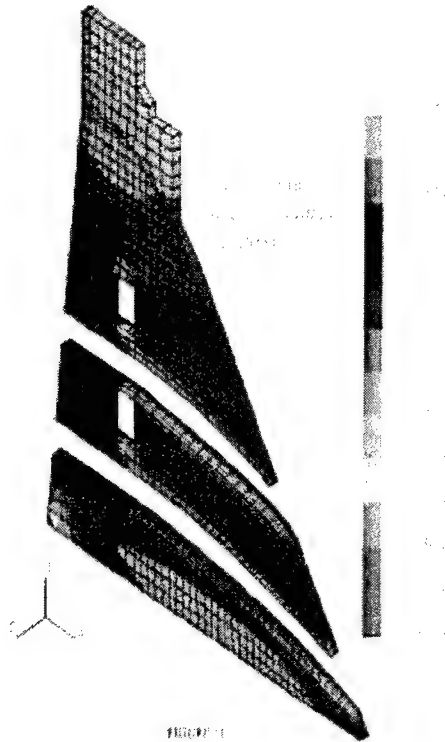


Figure 11. Normal stresses  $S_{yy}$  (psi) at  $z = 25$  ft (case 3)

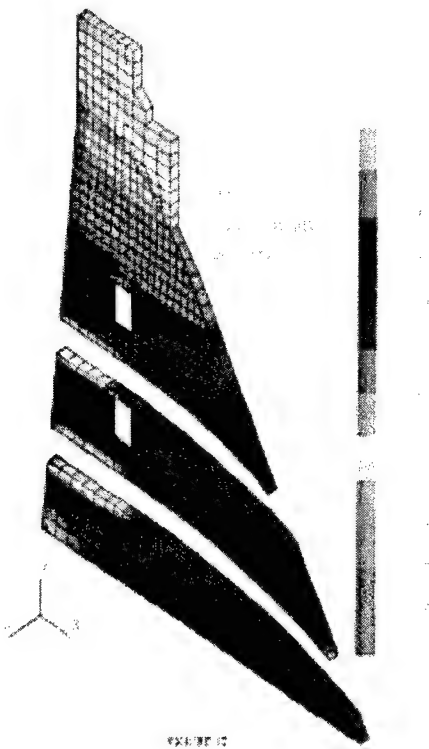


Figure 12. Normal stresses  $S_{zz}$  (psi) at  $z = 25$  ft (case 3)

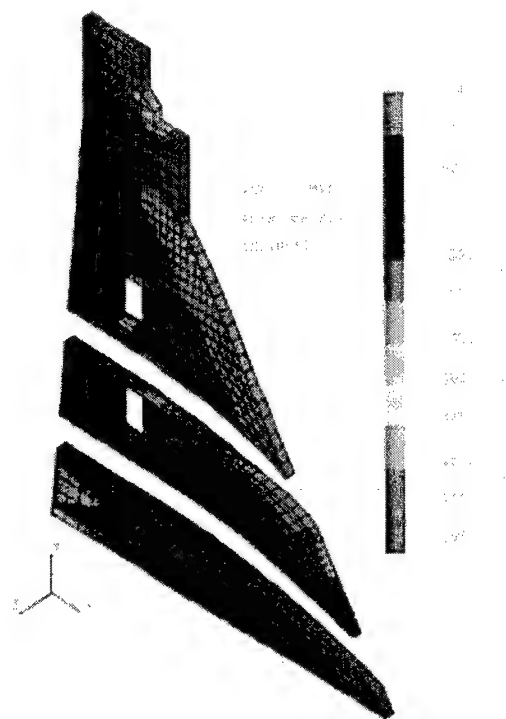


Figure 13. Envelope of maximum normal stresses  $S_{xx}$  (psi) at  $z = 25$  ft (case 10)

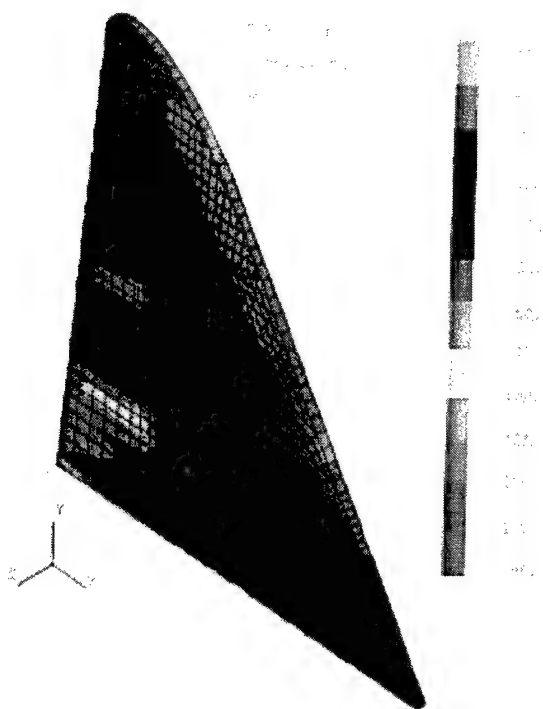


Figure 14. Envelope of maximum normal stresses  $S_{xx}$  (psi) at  $z = 18$  ft (case 10)

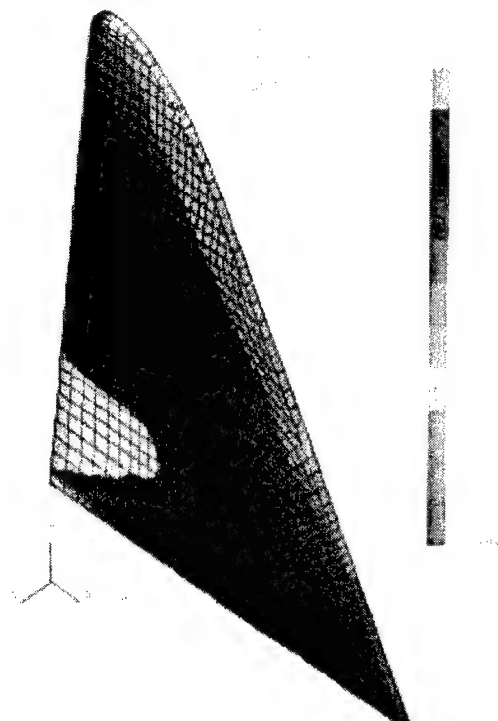


Figure 15. Envelope of maximum normal stresses  $S_{xx}$  (psi) at  $z = 12$  ft (case 10)

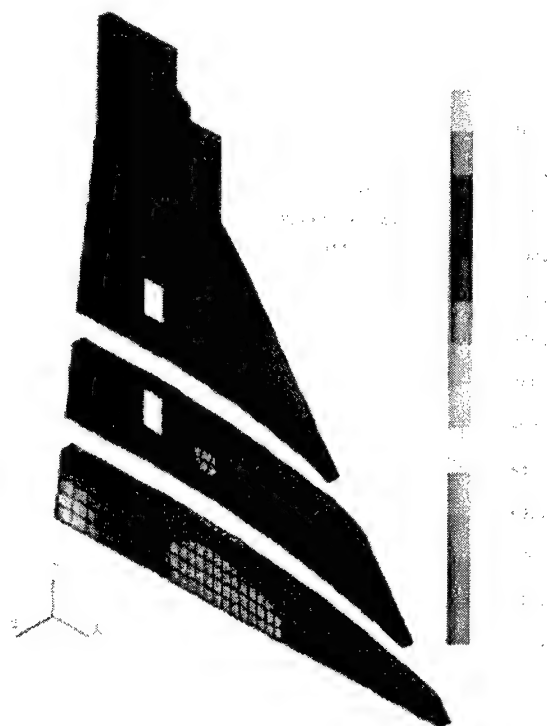


Figure 16. Envelope of maximum normal stresses  $S_{yy}$  (psi) at  $z = 25$  ft (case 10)

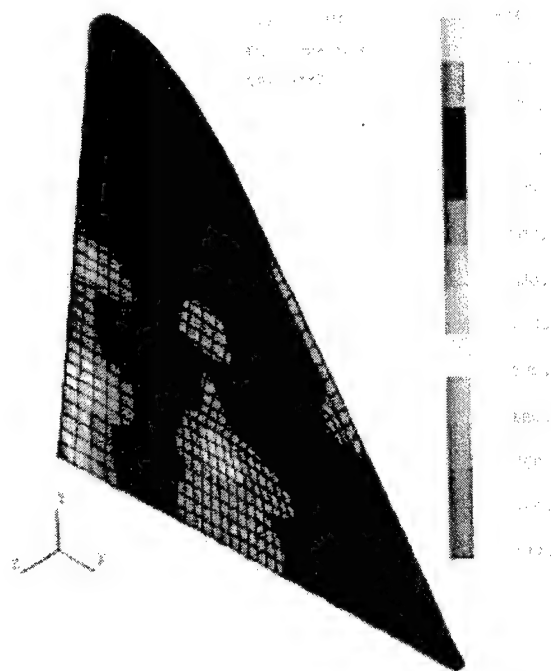


Figure 17. Envelope of maximum normal stresses  $S_{yy}$  (psi) at  $z = 18$  ft (case 10)

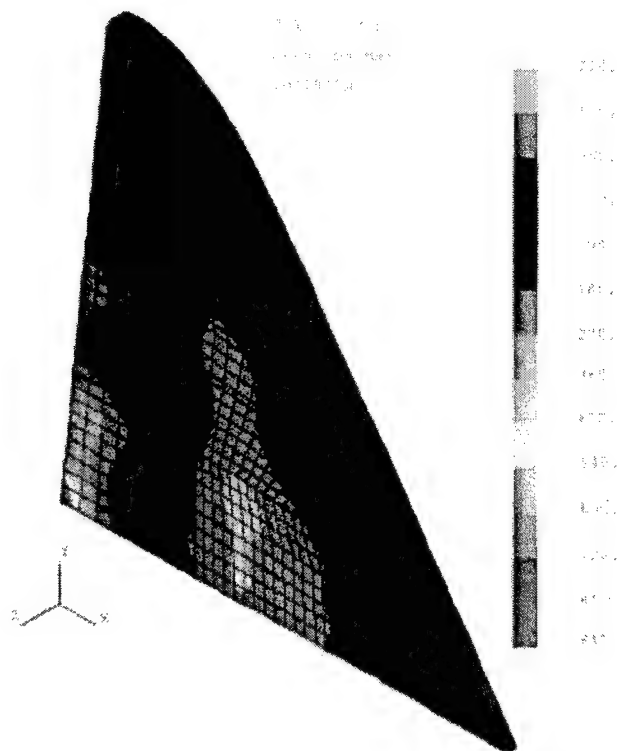


Figure 18. Envelope of maximum normal stresses  $S_{yy}$  (psi) at  $z = 12$  ft (case 10)

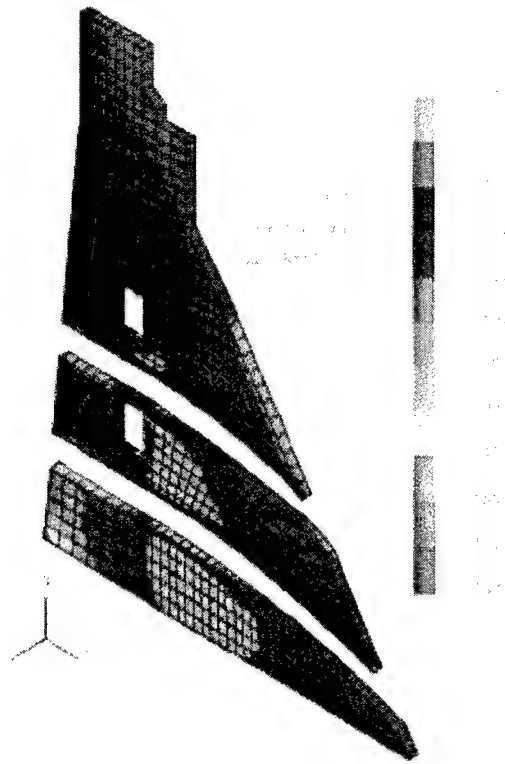


Figure 19. Envelope of maximum normal stresses  $S_{zz}$  (psi) at  $z = 25$  ft (case 10)

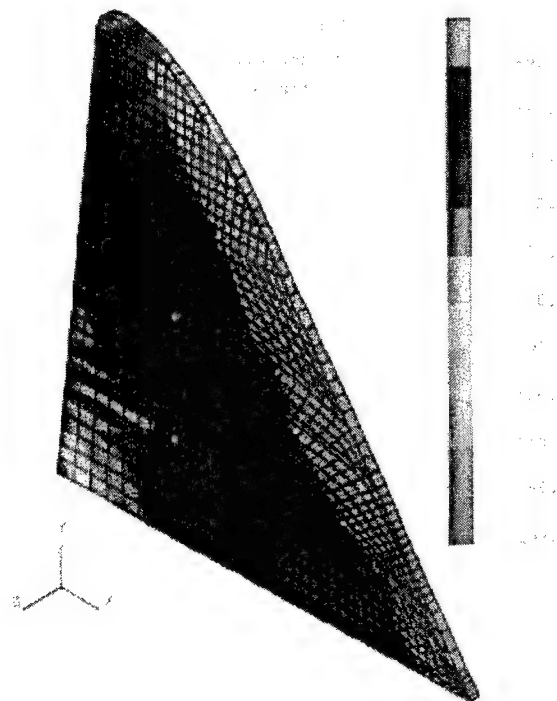


Figure 20. Envelope of maximum normal stresses  $S_{zz}$  (psi) at  $z = 18$  ft (case 10)



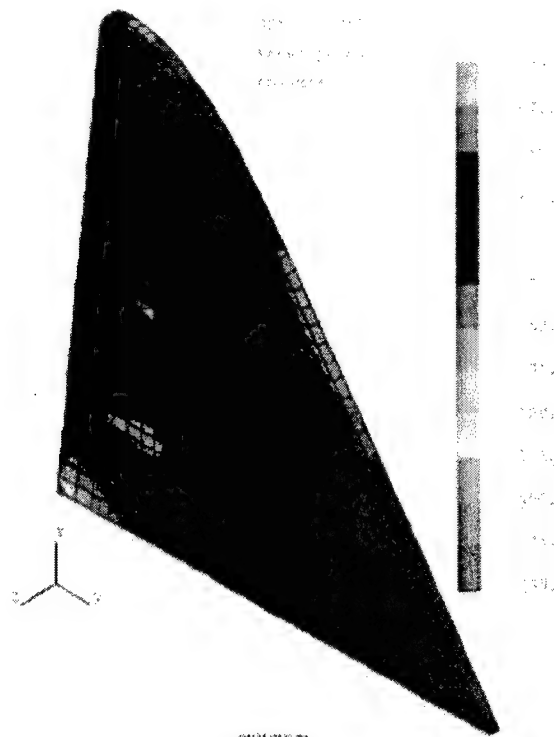


FIGURE 21

Figure 21. Envelope of maximum normal stresses  $S_{zz}$  (psi) at  $z = 12$  ft (case 10)

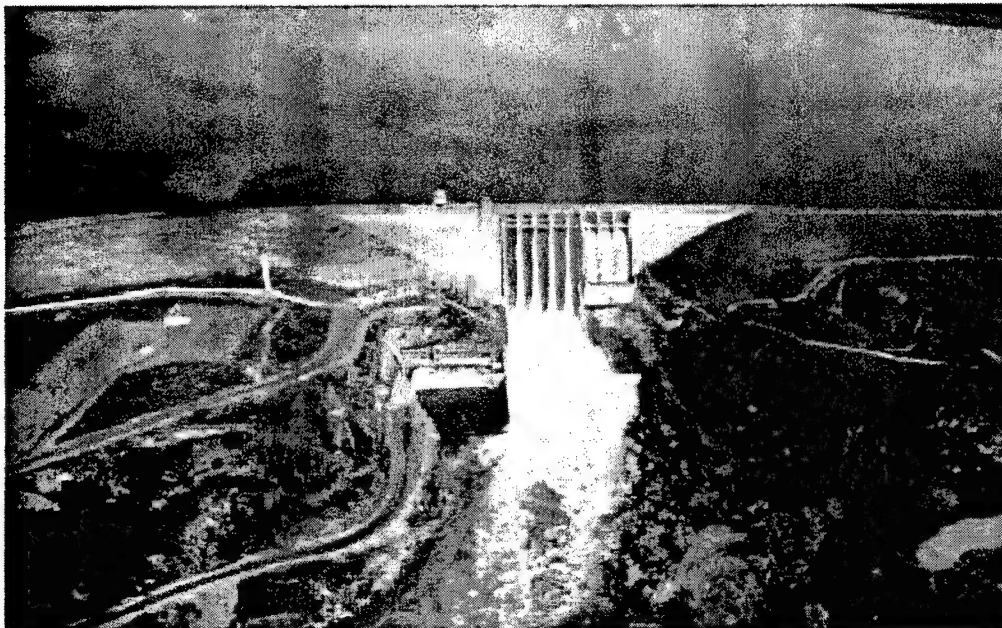


Figure 22. Aerial view of Folsom Dam

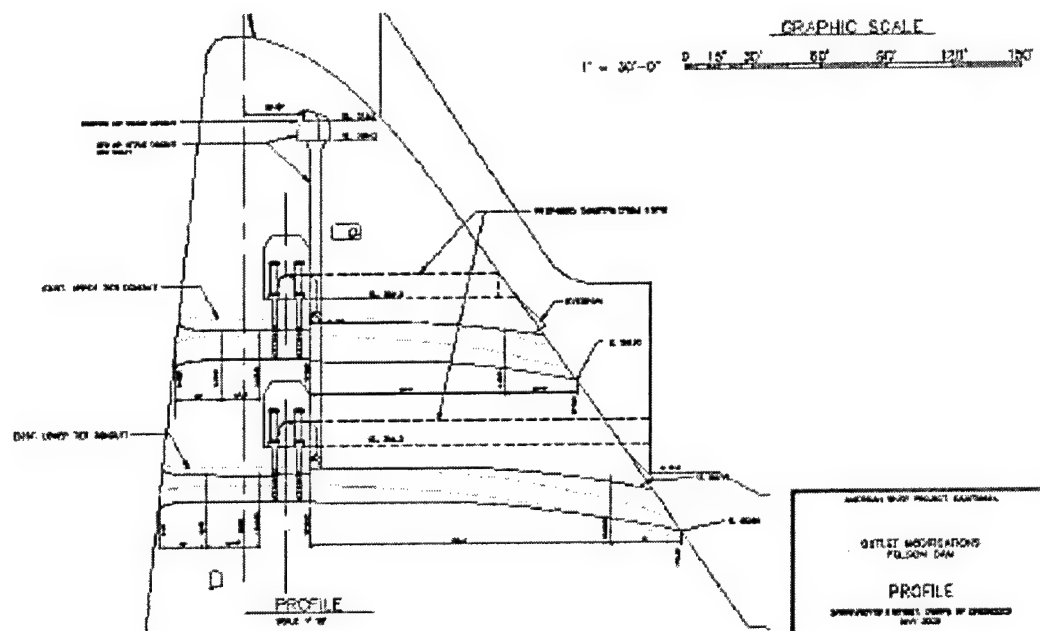


Figure 23. Typical section of Folsom Dam spillway monolith

## Comparison of the Nonlinear Behavior of Concrete Arch Dams using Physical and Numerical Models

by

David W. Harris<sup>1</sup>, Terry L. Payne<sup>2</sup>, and Larry K. Nuss<sup>3</sup>

### ABSTRACT

This report presents results from laboratory shake table tests performed on scale concrete arch dam models and computer analyses of these models using the nonlinear finite element code ABAQUS Explicit. Comparisons are made for models with various combinations of vertical and horizontal joints. The purpose of the study was twofold. First, failure mechanisms of an arch dam with various joint combinations were observed. Second, the ability of a nonlinear computer code to predict failure and failure modes of the arch dam model was tested. Because modeling the precise similitude for all the parameters for a scale test is very difficult, the purpose of this study was not to model the response of an actual arch dam.

### INTRODUCTION

Concrete arch dams have performed very well when subjected to earthquake loadings with no reported failures and only minor damage. However, there are only a limited number of arch dams that have experienced strong dynamic loadings. Without historical evidence of the seismic failure modes for this type of dam, a comparison of historical cases for verification of numerical methods is simply not possible.

For this reason, a series of physical model vibration tests of an arch dam were made for the

following purposes:

- 1) Test the ability of a nonlinear computer code to predict failure and failure modes of the arch dam model.
- 2) Observe the failure mechanisms of an arch dam with various geometric nonlinearities.

For the conference, actual video presentations of the model tests and subsequent numerical analyses will be shown; the paper shows photos which summarize the results. The full data set and selected scenes from the physical model tests are being prepared and will be made available for use by other researchers to make their own comparisons. The purpose of both the physical and numerical models was to compare directly one to the other, a process referred to as calibration modeling. Although it was not critical using this approach to accomplish precise similitude modeling, there is a need to model parameters so that the physical model reasonably represents conditions which may be observed in the field. To this end the model and model parameters were carefully selected to fulfill similitude to the extent possible.

---

<sup>1</sup>Materials Engineering and Research Laboratory Group, Bureau of Reclamation, P. O. Box 25007, D-8180, Denver, CO (USA), Office: 303-445-2375, Fax: 303-445-6341, dharris@do.usbr.gov.

<sup>2</sup>Structural Analysis Group, Bureau of Reclamation, P. O. Box 25007, D-8110, Denver, CO (USA), Office: 303-445-3230, Fax: 303-445-6489, tpayne@do.usbr.gov

<sup>3</sup>Structural Analysis Group, Bureau of Reclamation, P. O. Box 25007, D-8110, Denver, CO (USA), Office: 303-445-3231, Fax: 303-445-6489, lnuss@do.usbr.gov.

**KEYWORDS:** Concrete arch dams, scaled model experiments, nonlinear response, ABAQUS, contraction joint modeling

## 1. PHYSICAL MODEL CONSTRUCTION AND EXECUTION

A 1/150 scale model of a typical arch dam was constructed on a shake table used for horizontal accelerations, see Figure 1. The material for the dam was scaled for stiffness and strength properties and cast into a stiff foundation. A detailed description of the mix components used in this and previous studies has already been published (Harris, et al., 2000; Harris and Travers, 2002).

For these models a sinusoidal motion of 14 Hz. was used which approximated the third fundamental mode of the monolithic arch numerical model. The loading was begun at an acceleration of 0.25 g and ramped by 0.25 g every 30 seconds until a complete failure was achieved. A earthquake pulse, scaled to time, was not used in any tests. The input of a ramped up sinusoidal wave guaranteed the production of a complete failure in the arch model. The reservoir was modeled with water. Instrumentation consisted of accelerometers located throughout the height of the dam at the centerline and at the left (looking downstream) 1/4 point. Video tapes were made from downstream and overhead.

A series of models were constructed with varying joint conditions:

1. Monolithic with no joints (M),
2. One mid-height horizontal joint (H1),
3. One vertical joint at the crown (V1),
4. 17 vertical joints equally spaced across the dam (V17),
5. 17 vertical joints across the dam with 2 horizontal joints at 1/3 and 2/3 height (V17H2).

There were 2 laboratory tests for each joint configuration.

## 2. PHYSICAL MODEL RESULTS

Initially, all models responded elastically, irrespective of the constructed joints. The elastic response is characterized by a typical first mode response of the upper portions of the dam displacing an increasing amount from bottom to top. Displacements increased as the base accelerations increased. No permanent displacements occurred at low levels of shaking.

Once cracking initiated, the crack patterns were, in general, controlled by the joint pattern, as were the final failures. Figures 4a through 8a show the downstream view of final failures of the monolith, 1 horizontal joint, 1 vertical joint, 17 vertical joints, and 17 vertical with 2 horizontal joint models. Of note is that all models failed by forming multiple blocks which ultimately collapsed downstream. The blocks which formed generally aligned with dynamic mode shapes of a typical structure, see figures 2 and 3. As has been noted previously (Niwa and Clough, 1982), the final collapse occurred after considerable shaking (approximately 30 seconds of test time scales to minutes of duration for an actual earthquake). The suggestion that abrasion and considerable damage is required for the final collapse to occur appeared consistent with the Niwa and Clough model results. The arch steadily vibrated out of shape and lost arching action. Individual blocks formed by the preformed joints and/or by cracking, rotated, and then fell downstream like saloon doors opening.

Once a horizontal through crack formed, reservoir water spirted from the crack on the downstream face. This showed that reservoir water had time to enter the crack during shaking. The spirting indicated the uplift pressure increased as the crack closed.

## 3. NUMERICAL MODELING

All analyses were made using ABAQUS Explicit (Hibbitt 2001) on a Hewlett-Packard J2240 Unix workstation.

The nonlinear material model used in ABAQUS Explicit for the concrete allows tensile failure at a tensile cutoff and a post-peak tension stiffening degradation defined by either stress versus displacement criteria or stress versus mode I fracture energy. In compression, the material model is linear-elastic and does not model crushing. This is generally appropriate for concrete dams since the compressive strength of the concrete is normally 10 times the tensile strength. Cracks are modeled using smeared cracking techniques at the integration points of the finite elements. Crack orientation is remembered, so a crack maintains its orientation throughout the analysis. The 3 cracks allowed at an integration point have to be orthogonal. Cracking is initiated when the maximum principal stress exceeds a pre-described tensile limit.

Table 1 - Material properties

Study	Static Modulus MPa (lb/in <sup>2</sup> )	Compressive Strength kPa (lb/in <sup>2</sup> )	Tensile Cutoff kPa (lb/in <sup>2</sup> )
M Analysis	16 (2,300)	172 (25)	103 (15)
Test 2	16 (2,303)	159 (23)	--
Test 5	21 (3,088)	262 (38)	33 (4.8)
V1 Analysis	26 (3,760)	290 (42)	145 (21)
Test 1	26 (3,759)	290 (42)	30 (4.4)
H1 Analysis	36 (5,170)	359 (52)	165 (24)
Test 1	36 (5,172)	359 (52)	--
V17 Analysis	19 (2,800)	179 (26)	103 (15)
Test 1	15 (2,147)	186 (27)	--
Test 2	24 (3,462)	159 (23)	25 (3.6)
V17H2 Analysis	27 (3,950)	145 (21)	90 (13)
Test 1	21 (3,099)	138 (20)	21 (3.1)
Test 2	27 (3,948)	145 (21)	28 (4.1)

Since the foundation model was reused for every test, the concrete for the dam models was specially designed to be much weaker than the model foundation. The foundation was standard concrete with a modulus of about 20 684 MPa (3,000,000 lb/in<sup>2</sup>). Tests on the arch model concrete measured an average modulus of elasticity of 25 MPa (3,600 lb/in<sup>2</sup>), compressive strength of (33 lb/in<sup>2</sup>), and splitting tensile strength of 28 kPa (4 lb/in<sup>2</sup>). Comparisons between analyses using various tensile strengths of concrete with the monolithic model physical test indicated a tensile strength of 172 kPa (18 lb/in<sup>2</sup>) matched when cracks initiated the best. This tensile strength corresponds to Raphael's (Raphael 1981) static splitting tensile strength ( $1.7f_c^{2/3}$ ) equation. Table 1 lists the material properties used for each analyses.

Gravity and reservoir pressure loads were applied to the dam model over numerous analysis steps prior to applying the dynamic loading. Low viscous pressure, applied along the contact surfaces to reduce numerical chatter only during the static analysis, aided the explicit algorithm.

Each finite element model had 6 elements through the thickness (upstream to downstream direction) of the dam model. Elements were 8-noded bricks with one integration point at the center of the element. The models consisted of 1988 nodes in model M, 2058 nodes in model V1, 2165 nodes in model H1, 2821 nodes in model V17, and 9055 nodes in model V17H2 (see figures 4b, 5b, 6b, 7b, and 8b).

Since the foundation was significantly stiffer than the dam, only the dam was modeled in the analysis and the foundation was assumed to be fixed. This greatly reduced the solution time in the explicit algorithms. Accelerations were applied in the upstream to downstream direction only at nodes along the dam to foundation contact.

Westergaard's added mass was added to the upstream wet nodes to simulate hydrodynamic interaction. However, accounting for the curvature of the dam model by computing generalized Westergaard's mass components was

not be done because ABAQUS Explicit only allows one component of mass.

Damping was incorporated in the analysis when the material cracks and when contact surfaces interact. Rayleigh damping with mass proportional damping ( $\alpha=3$ ) and no stiffness proportional damping ( $\beta=0$ ) provided some general damping at approximately 5 percent of critical between 7 Hz and 15 Hz. Artificial energy levels were checked during the analysis and were very low compared to the real energies such as kinetic energy and strain energy.

Contact surfaces were used to simulate vertical and horizontal joints. Contact surfaces in ABAQUS Explicit have a master and slave surface that can open, close, and translate in relationship to each other with the ability for large displacements. Frictionless interaction was specified. Nodes along the surfaces were not allowed to penetrate the opposing surface. Compression was reestablished as the contacts touched and tension was relieved as the contacts separated.

Acceleration and displacement time-histories measured during the laboratory tests were on the order of 300 seconds long. The time to run an analysis using these long time records was not practical so each 0.25 g segment was trimmed to 10 cycles each producing a more manageable input record of less than 5 seconds.

#### 4. OBSERVATIONS AND FINDINGS

Table 2 lists the acceleration at which cracking initiated and the acceleration at failure for the physical model tests and the analyses. The computed accelerations at crack initiation and failure are approximately at the same magnitude in all the tests except the 17 vertical joint model.

Results of the ABAQUS smeared crack analyses corresponded well with the laboratory cracking patterns. Some engineering judgement is required when looking at the computed crack patterns, because the analysis using material nonlinearity

(concrete cracking) failed to converge before the analysis model indicated kinematic failure. The analyses modeled the failure modes and cracking patterns relatively well (see figures 4c, 4d, 5c, 5d, 6c, 6d, 7c, 7d, 8c, and 8d).

When independent concrete blocks were built into the analysis model with contact surfaces in the V17H2 model (linear material model), ABAQUS modeled the kinematic failure well.

Table 2 - Acceleration at crack initiation and failure

Model	Acceleration at Crack Initiation (g)	Acceleration at Failure (g)
M Analysis	1.25	2.0
	Test 0.75	5.0
	Test 1.50	1.5
V1 Analysis	1.25	1.50
	Test 0.70	0.85
	Test 1.20	1.20
H1 Analysis	0.75	1.75
	Test 0.95	1.75
	Test 1.65	1.65
V17 Analysis	1.5	2.0
	Test 0.6	0.6
	Test 0.5	0.5
V17H2 Analysis	N/A	0.75
	Test 1.00	1.25
	Test 0.75	0.75

The laboratory tests all resulted in similar failure modes. The models cracked along the crown, then diagonally downward from the arch quarter points, and then horizontally near the base. Independent blocks formed, rotated, and displaced downstream. The arch fell downstream. The different joint configurations affected the size and number of independent blocks that formed. Models M, V1, and H1 formed larger independent blocks than the V17 and V17H2 models. The monolithic (M) and single horizontal joint (H1) models were able to withstand higher accelerations than the other models.

In the analyses, horizontal cracking occurred on the upstream face first and progressed through to the downstream face. The analysis was not able to simulate water pressures in the cracks.

Variation in the selection of the concrete tensile strength significantly affected the initiation of cracking and the dynamic analysis results.

The selection of a tension stiffening scheme of course did not affect when the cracks initiated, but did affect the number of cracks that developed as the analysis continued.

The extend of cracking was affected in the laboratory and in the analysis by the presence of geometric nonlinearities. In the laboratory, the monolithic model (M) cracked vertically 2/3 of the dam height down where the crack joined diagonal cracks. This formed two large separate blocks in the dam. The single vertical joint model (V1) opened the joint down to the base where diagonal cracks formed very close to the base. Again, two large independent blocks formed. Eventually one block swung downstream. The one horizontal joint model (H1) formed diagonal cracks at the quarter points and then formed a vertical crack along the crown. Once the vertical crack at the crown formed along with the diagonal cracks, the failure mode was similar to the other tests. The seventeen vertical joint model (V17) had all the vertical joints open up. Diagonal cracks developed at the quarter points and progressed through the vertical joints in a stair-stepped fashion. This formed many small independent blocks that rotated downstream once arching action was lost. The 17 vertical and 2 horizontal joint model (V17H2) had most of the vertical joints open. Diagonal cracks at the quarter points formed but only extended down to the upper horizontal joint. The upper independent blocks failed and then diagonal cracks progressed to the lower horizontal joint. These lower blocks then failed.

All the analyses resulted in similar deflected shapes that matched the observed laboratory model deflected shapes. The magnitude of the measured and computed deflections and accelerations from the models did not match, with the measured magnitudes an order of magnitude higher. Analyzing only the dam and not the entire test apparatus may have resulted in the small computed displacements.

## 5. REFERENCES

Harris, David W., Nathan Snorteland, Timothy Dolen, and Fred Travers, 2000, "Shaking Table 2-D Models of a Concrete Gravity Dam," *Earthquake Engineering and Structural Dynamics* 2000; 29: 769-787.

Harris, David W., and Fred Travers, 2002, "Investigation of the Failure Modes of Concrete Arch Dams using Physical Model Tests," Submitted for publication *Earthquake Engineering and Structural Dynamics*.

Niwa, A. and R.W. Clough, 1982, "Non-Linear Seismic Response of Arch Dams," *Earthquake Engineering and Structural Dynamics*, Vol. 10, 267-281.

Hibbitt, Karlsson, & Sorensen, 2001, "ABAQUS /Explicit - Version 6.1," Pawtucket, Rhode Island.

Raphael, Jerome, 1984, "Tensile Strength of Concrete," *ACI Journal*.

Payne, Terry L., 2003, "Shaking Table Study to Investigate Failure Modes of Arch Dams," 12<sup>th</sup> European Conference on earthquake Engineering, Paper 145.



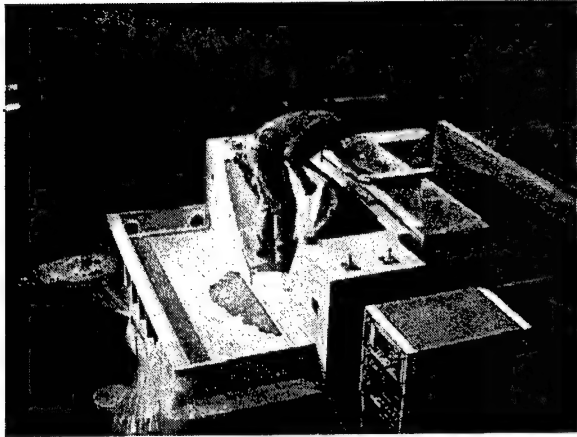


Figure 1 - Arch Model under Construction

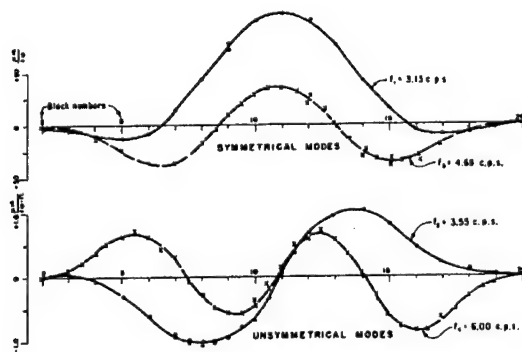


Figure 14.—Radial deflections of crest.

Figure 2 - Typical Mode Shapes Measured in Field on Arch Dam.

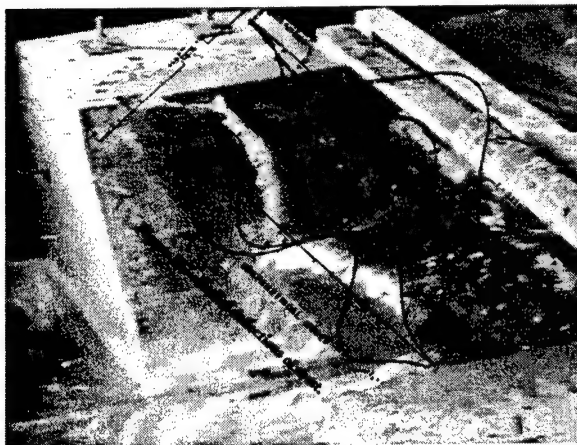


Figure 3 - Typical failure of models (5 large blocks) and typical mode shapes overlaid

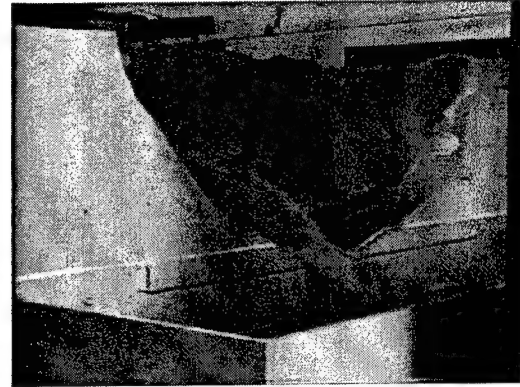


Figure 4a - Monolithic (M) final crack.

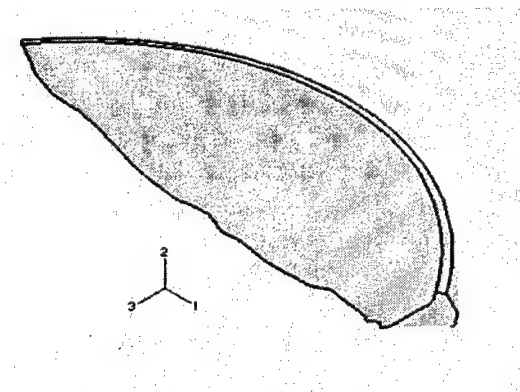


Figure 4b - Analysis model (M)

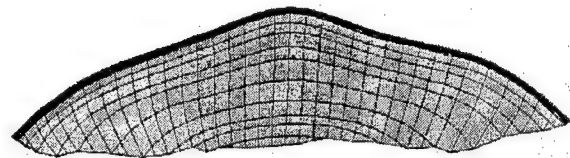


Figure 4c - Deflected shape (M)

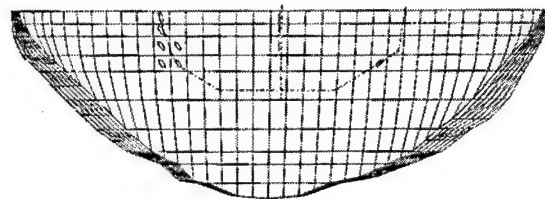


Figure 4d - Computed cracking pattern (M)



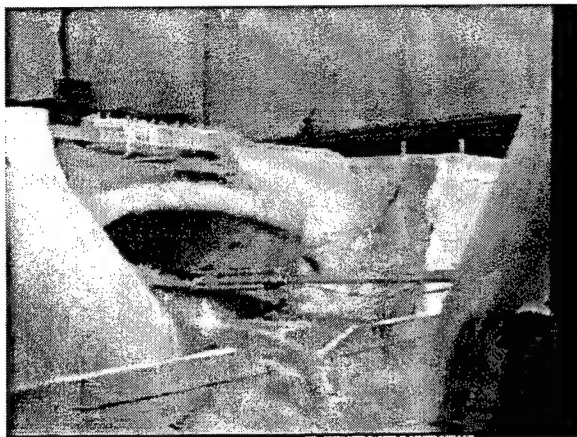


Figure 5a - Failure 1 horizontal joint (H1)



Figure 6a - Failure 1 vertical joint (V1)

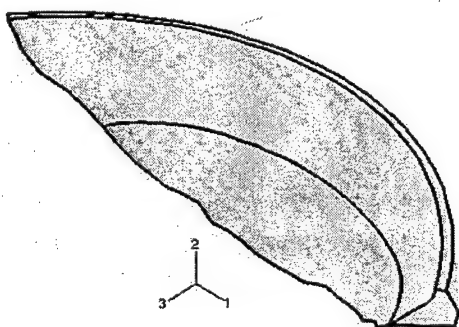


Figure 5b - Finite element model (H1)

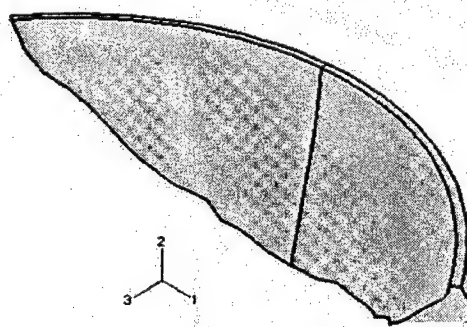


Figure 6b - Finite element model (V1)

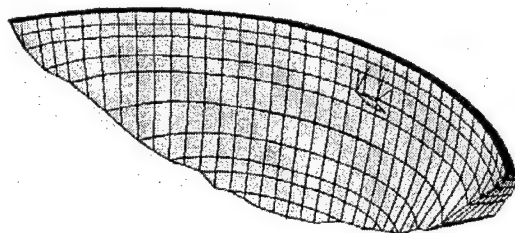


Figure 5c - Deflected shape (H1)

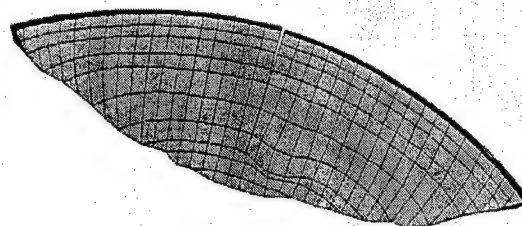


Figure 6c - Deflected shape (V1)

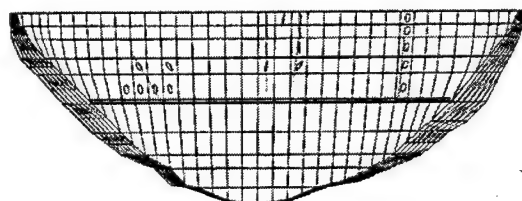


Figure 5d - Computed crack pattern (H1)

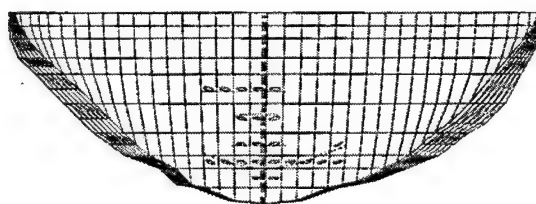


Figure 6d - Computed crack pattern (V1)

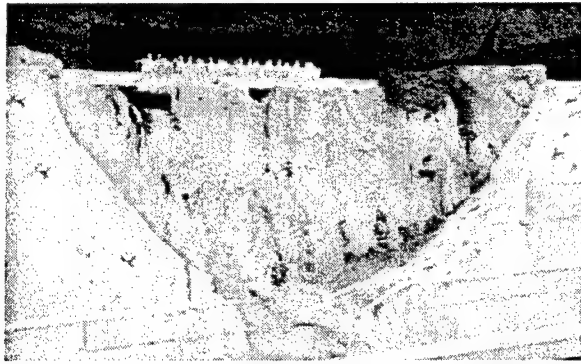


Figure 7a - Failure of 17 vertical joint (V17)

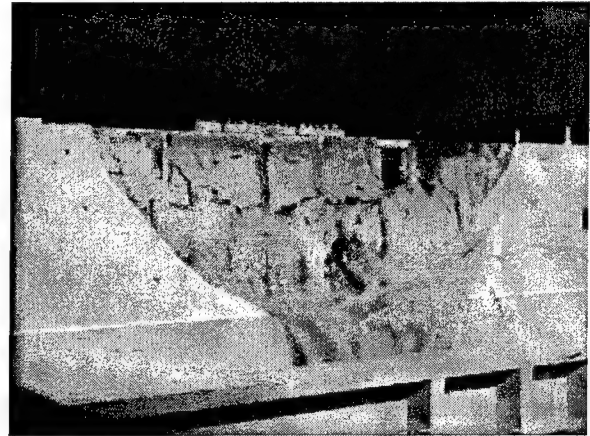


Figure 8a - Failure of model V17H2

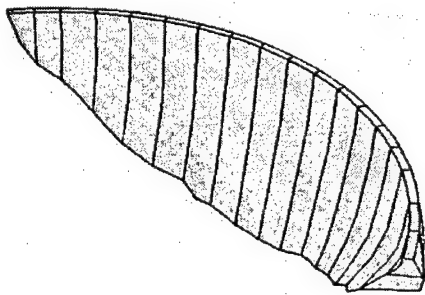


Figure 7b - Analysis model (V17)

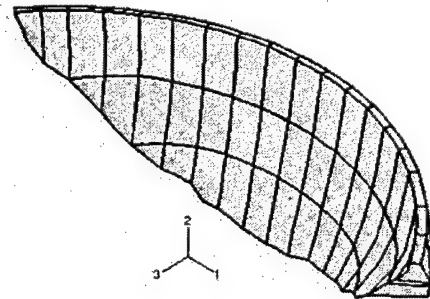


Figure 8b - Analysis model (V17H2)

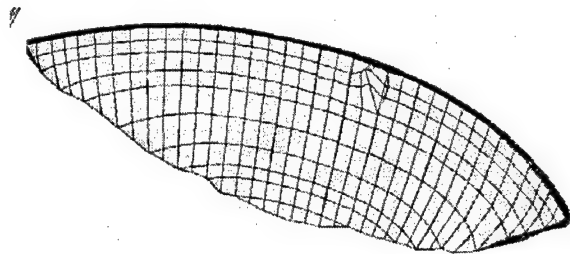


Figure 7c - Deflected shape (V17)

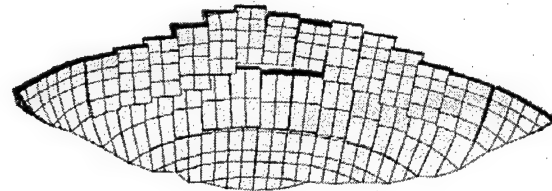


Figure 8c - Deflected shape (V17H2)

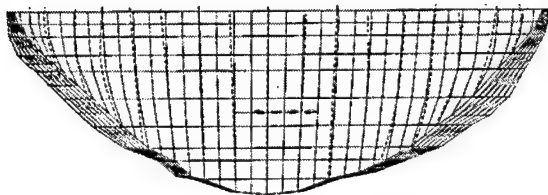


Figure 7d - Computed crack pattern (V17)

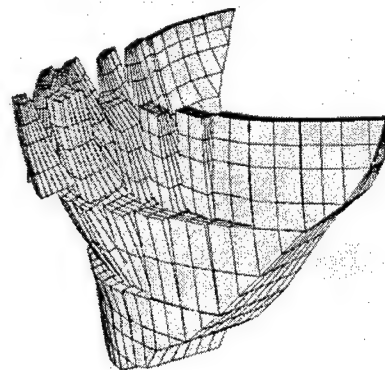


Figure 8d - Deflected shape (V17H2)

## Non-linear Seismic Analysis of Stony Gorge Dam

by

Barbara L. Mills/Bria<sup>1</sup>

### ABSTRACT

Stony Gorge Dam is a concrete slab and buttress (Ambursen type) dam built in 1928, located on Stony Creek about 64 km (40 miles) southwest of Orland, California. The crest length is 264 m (868 ft) and the structural height is 42 m (139 ft). The dam consists of three components: buttresses (spaced on 5.5-m (18-ft) centers), slabs, and struts. Special care was taken during construction to ensure that each slab rests simply supported on corbels located on the buttresses. The cast in place struts, which provide lateral support to the structure, are also simply supported, resting in tapered recesses coated with water gas tar. The struts are located on a 7.3-m (24-ft) grid between the buttresses.

To address seismic concerns, a finite element model of the structure was created and analyzed using ABAQUS/Explicit. The model consisted of 42 buttresses with slabs between them. Slabs were connected to the buttresses using multiple point constraints (mpc). These mpc's allowed the slabs to move relative to the buttresses without developing shear forces along the edge of the buttresses and at the same time allowed loads to be transferred from the slabs into the buttresses. The model included 254 struts providing lateral support between buttresses. These were modeled using non-linear springs with a very low tensile stiffness and a compressive stiffness based on the concrete properties and cross section of the struts. The buttresses were fixed against displacement at the base in three directions.

Five sets of ground motions representing various return intervals were used in the analyses. The compressive forces experienced by the struts

were studied to gain an understanding of the likelihood of compressive failure of the struts. Maximum principal tensile stresses in the buttresses were also considered. Finally, for one earthquake record, "failed" struts were removed and the analysis was re-run to see how this affected the remaining structure.

Conclusions based on the results of these analyses were used in a risk analysis to determine recommendations for further action to reduce failure probabilities and risk associated with seismic failure of the dam.

**KEYWORDS:** Concrete dams, non-linear analysis, seismic response, slab and buttress

### 1 INTRODUCTION

This paper presents non-linear three-dimensional time-history seismic analyses of Stony Gorge Dam, an Ambursen type slab and buttress dam. The model included 42 buttresses and the slabs supported by them. In this model the slabs were connected to the buttresses using multiple point constraints (mpc) that keep a node on a straight line defined by two other nodes but allow the possibility of moving along the line. The behavior of this mpc is similar to a ring sliding along a rod. Struts were modeled using non-linear springs. Linear concrete material properties were used.

### 2 DESCRIPTION OF DAM

Stony Gorge Dam, constructed from 1926 to 1928, is a concrete slab and buttress (Ambursen type) dam, located on Stony Creek about 64 km

<sup>1</sup> Structural Analysis Group, Technical Service Center, United States Bureau of Reclamation, Denver, CO 80225 (USA).

(40 miles) southwest of Orland, California (see Figure 1). The crest length is 264 m (868 ft) and the structural height is 42 m (139 ft).

The dam consists of three components: buttresses, slabs, and struts. (See Figures 2 through 4) The buttresses are spaced on 5.5-m (18-ft) centers, are 45.7 cm (18 in.) thick at the top elevation of 258 m (846 ft), and increase in thickness 5.1 cm (2 in.) for every 3.7-m (12-ft) drop in elevation. The slabs are 38.1 cm (15 in.) thick at the elevation of 257.9 m (846 ft). The upstream face of the slab tapers 8.9 cm (3.5 in.) for every 3.7 vertical meters (12 ft) down, increasing the thickness of the slab at the base of each buttress from 38.1 cm (15 in.) at the top.

Special care was taken during construction to ensure that the slab acts as a simply supported beam. This was accomplished by coating contraction joints between the slab and buttresses with asphalt putty. The cast-in-place struts have a cross section of 45.7 cm (18 in.) by 61.0 cm (24 in.) and are 4.7 m (15.5 ft) long. These struts are also simply supported, resting in tapered recesses coated with water gas tar. The struts are located on 7.3-m (24-ft) centers between the buttresses. All three structural concrete components are reinforced.

For the most part, the dam and its foundation are in good condition although some spalling of concrete and deterioration of reinforcing steel has been observed on the downstream face of some of the slabs and buttresses.

### 3 MODEL DESCRIPTION

The model, which is shown in Figures 5 through 9, consisted of 42 buttresses (buttress 13 through buttress 54) modeled using shell elements, 41 slabs, modeled using shell elements, and 254 struts.

Shell elements were used for the slabs on the upstream face of the dam. For simplicity, downstream portions of the spillway section slabs were modeled using compression-only springs similar to those used to model the struts. (See

Figure 6). The use of shell elements in this larger model allowed the mass of most of the slabs to be included. The mass of the downstream portion of the spillway slabs was neglected. However, because the downstream portion of the spillway section slabs represents a relatively small portion of the mass of the entire model, neglecting it in this area did not impact the response of the model greatly.

Slabs were connected to the buttresses using multiple point constraints (mpc). The type of mpc used, a slider, keeps a node on a straight line defined by two other nodes but allows the possibility of moving along the line and allows the line to change length. The behavior of this mpc is similar to a ring sliding along a rod. This allowed the slabs and buttresses to deform without shear or moment transfer between the slabs and buttresses. Gravity and water loads, as well as cross-canyon loads, were transferred through the slabs into the buttresses so that the structural response is well represented. Figure 7 shows the locations of the sliders. The slabs were fixed against displacement in three directions at the base but were free to rotate.

The struts, which provide lateral support between buttresses, were modeled using springs with a compressive stiffness based on the concrete properties and cross section of the struts and a very low tensile stiffness. The tensile forces can be related to displacements by dividing them by the tensile spring constant, 126 N/cm (72 lb/in.). In the following discussion about this model, these displacements will be called "tensile displacements." The actual struts rest in tapered notches that are 6.4 cm (2.5 in.) deep at elevation 250.5 m (822 ft), 14 cm (5.5 in.) deep at elevation 243.2 m (798 ft), 21.6 cm (8.5 in.) deep at elevation 235.9 m (774 ft) and 25.4 cm (10 in.) deep at elevation 228.6 m (750 ft). Care was taken during construction to eliminate any bond between a strut and the buttress into which it is set. A tensile displacement close to or greater than the notch depth at any elevation would indicate that support for a strut could be lost leading to the loss of a strut.

The buttresses were fixed against displacement at the base in three directions. Rotations were not fixed. When a buttress displaces in the cross-canyon direction, it is expected that any bond developed between the concrete and the rock would be soon lost or joints in the rock would open to relieve tensions. In reality the connection between any given buttress and the foundation is somewhere between a totally fixed and a pinned condition. Assuming a pinned condition results in higher stresses throughout most of the buttress as opposed to higher stresses at the base of the buttress for the completely fixed condition.

The gate hoist house and steel sliding gates were modeled as lumped masses at the top of buttresses 26, 28, 30 and 32. Because the floor slab, which is fairly massive, rests simply supported on the top of the buttresses, it was decided that this portion of the structure would contribute little stiffness and considerable mass to the structure model.

#### 4 MATERIAL PROPERTIES

The average compressive strength based on testing of cores taken in 1982 was 26.5 MPa (3840 lb/in.<sup>2</sup>). The dynamic modulus of elasticity was assumed to be  $2.52 \times 10^4$  MPa ( $3.66 \times 10^6$  lb/in.<sup>2</sup>). This value is somewhat lower than the measured values of  $3.2 \times 10^4$  MPa ( $4.65 \times 10^6$  lb/in.<sup>2</sup>) described in the 1982 report. However, because there are existing cracks in nearly all of the buttresses, a reduced value for the modulus is considered to be appropriate. The unit weight of concrete was assumed to be 2400 Kg/m<sup>3</sup> (150 lb/ft<sup>3</sup>) and Poisson's ratio was assumed to be 0.15. Because Stony Gorge Dam is a reinforced concrete structure, the dynamic tensile strength of the concrete was assumed to be 2.65 Mpa (384 lb/in.<sup>2</sup>), 10 percent of the compressive strength.

It should be noted that the concrete cores tested were taken from the buttresses and not the struts. While most of the struts within viewing distance appear sound, some have moss growth and visible deterioration of the concrete. The axial

compressive strength of each strut was determined using ACI 10.3.5:

$$\phi P_n = 0.80 \phi [0.85 f'_c (A_g)] = 3.5 \times 10^6 \text{ Newtons} \\ (790,000 \text{ lbs})$$

where  $\phi = 0.70$  (ACI 9.3.2.2, to account for variation in materials and workmanship) and  $f'_c = 2.65$  MPa (3840 lb/in.<sup>2</sup>),  $A_g = 2787$  cm<sup>2</sup> (432 in.<sup>2</sup>). The factor of 0.80 accounts for eccentricity of the axial load. The tie steel in the struts, which serves to counteract any tendency of the compression-loaded bars to buckle out of the concrete, consists of #5 bars spaced at 61 cm (24 in.). This is much less than the recommended tie steel (ACI 10.3.5.2). Therefore, the axial compressive capacity could be less than this value.

The springs modeling the struts were non-linear, compression only members. The spring stiffness was input in terms of force and displacement. The compressive stiffness was determined by calculating  $EA/L$ , where  $E$  is the modulus of elasticity,  $L$  is the cross canyon length of a strut and  $A$  is the cross sectional area of a strut. The area of each strut was constant and the springs were modeled in the strut locations. However, because the strain computations were of importance in the determination of failure, the compressive stiffness was varied to match the slope of an average concrete stress-strain curve for concrete with  $f'_c = 27.6$  MPa (4000 lb/in.<sup>2</sup>). Normally, it is assumed that the concrete will remain in the elastic portion of the stress-strain curve. Therefore, a constant slope or modulus of elasticity is assumed. However, in reality, as the strain increases the slope of the stress-strain curve changes, indicating a change in modulus. The stress-strain curve assumed for this analysis and the spring stiffness curve are shown in Figure 8.

The "Final Report on Construction of Stony Gorge Dam" states that reinforcing "bars to be bent were of structural steel grade, and straight bars of hard rerolled rails." The yield strength of the structural steel from this time period was probably 227.5 MPa (33,000 lb/in.<sup>2</sup>) according



to the Concrete Reinforcing Steel Institute. The "rerolled rails" could have a yield strength of up to 344.8 MPa (50,000 lb/in.<sup>2</sup>). For these analyses, a conservative value of 227.5 MPa was assumed due to the uncertainty.

Linear concrete material properties were assumed in this analysis. Therefore it was necessary to assume some damping. The following Rayleigh damping values were assumed:  $\alpha = 1.743584$  (mass damping) and  $\beta = 0.000797$  (stiffness damping) resulting in a combined damping percentage of approximately 6.5 percent for the fundamental mode and ranging between 3.75 and 4.5 percent for higher modes.

## 5 LOADS

Hydrodynamic loads were neglected in this analysis. An accepted convention is to model the hydrodynamic loads using Westergaard's theory of added mass, with modifications as suggested by Zangar. Neglecting the hydrodynamic interaction action has the most effect on the slabs. Therefore, this model was not used to evaluate the slabs. The additional force causing compression in the downstream side of the buttress and tension in the upstream side of the buttress, is eliminated, resulting in a slightly less conservative analysis of the buttresses.

The static water pressure on the upstream face slabs was applied as a varying pressure load based on a normal water surface elevation of 267.8 m (841 ft). Gravity was applied as a body force.

Four earthquake records were used in these analyses. These are shown in Figure 11 along with the response spectra for each record. In the following description, the acceleration spectral intensity (ASI), defined as the area under the acceleration response spectrum between periods of 0.1 and 0.5 sec, is a measure of the energy content of the record in the general frequency range of interest to concrete dams.

The Saratoga station record, from the 1989 M 7.0 Loma Prieta earthquake, with an

acceleration spectral intensity of 148 cm/sec for the vertical record and 288 cm/sec for the two horizontal records, represents a return interval of approximately 5000 years. The peak acceleration for the record used in the cross canyon direction was 0.51 g. The peak acceleration for the record used in the upstream/downstream direction was 0.32 g and for the record used in the vertical direction the peak acceleration was 0.36 g. For this ground motion, a second analysis was performed that assumed that some struts had failed. These were removed and the analysis re-done.

The Branciforte record, also from the 1989 M 7.0 Loma Prieta earthquake, with an ASI of 348 cm/sec for the vertical record and 530 cm/sec for the two horizontal records, represents a return interval of approximately 14,000 years. The peak acceleration for the record used in the cross canyon direction is 0.44 g. The peak acceleration for the record used in the upstream/downstream direction is 0.50 g and for the record used in the vertical direction the peak acceleration is 0.50 g.

The Pleasant Valley record, from the 1983 M 6.5 Coalinga earthquake, with an ASI of 263 cm/sec for the vertical record and 578 cm/sec and 555 cm/sec for the two horizontal records, represents a return interval of approximately 25,000 years. The peak acceleration for the record used in the cross canyon direction is 0.65 g. The peak acceleration for the record used in the upstream/downstream direction is 0.71 g and for the record used in the vertical direction, the peak acceleration is 0.53 g.

The Chi Chi record, from the 1999 M 7.6 Chi-Chi, Taiwan earthquake, with an ASI of 186 cm/sec for the vertical record and 678 cm/sec for the two horizontal records, represents a return interval of approximately 60,000 years. The peak acceleration for the record used in the cross canyon direction is 0.64 g. The peak acceleration for the record used in the upstream/downstream direction is 0.83 g and for the record used in the vertical direction, the peak acceleration is 0.26 g.

## 6 RESULTS

### 6.1 Modes

A modal analysis was performed on the model to determine the fundamental frequency and mode shapes of this model of the dam. The fundamental frequency is 2.654 cycles/sec. Figures 10 and 11 show that this mode shape involves contributions from most of the buttresses and slabs. Note that the magnification of the bottom plot (slabs) is 10 times the magnification of the top plot (buttresses). Thirty-nine additional mode shapes were also determined, resulting in frequencies ranging from 4.08 to 12.23 cycles/sec.

### 6.2 Struts

Of the 153 struts for which output was requested, two representative struts were selected, one from each side of the dam. The compressive and tensile forces were plotted over time for these struts. This helped in gaining understanding of both the likelihood of compressive failure and the extent to which "hammering" was experienced by the struts. A tensile force of 320 Newtons (72 lb) corresponds to a displacement of 2.54 cm (1 in.).

Figure 12 and 13 are looking downstream and show the force in struts during two time steps: one when the cross canyon motion of the dam was to the left and one when the cross canyon motion of the dam was to the right. These plots show in general the number of struts that experienced high compressive forces and their location in the model.

Figures 14 through 21 show time history plots of the axial forces for struts number 7048 and 7126 for each of the input ground motions (compression is negative). From these plots one can see how many times the compressive capacity of a strut was exceeded and by how much.

When the model was analyzed for the Saratoga ground motions, the compressive strength of the struts was exceeded in 36 percent of the struts. Figures 14 and 15 are typical plots of the force

in the struts when the Saratoga record was input. For the entire record model, there were an average of four excursions over the compressive strength and the maximum compressive force experienced by a strut was  $4.98 \times 10^6$  Newtons ( $11.2 \times 10^5$  lb). The subsequent analysis with some struts removed indicated that once struts had failed, the load would be re-distributed causing additional struts to fail.

The Branciforte, Pleasant Valley Pumping Plant and Chi Chi ground motion records all had a similar effect on the structure (see Figures 16 through 21). In each analysis the maximum compressive force experienced by a strut was  $7.3 \times 10^6$  Newtons ( $16.4 \times 10^5$  lb) (the maximum compressive force allowed by the material properties), and more than 80 percent of the 153 struts considered experienced loads in excess of the compressive capacity of the struts. This capacity was exceeded an average of 11.3 to 17.5 times, depending on the input record.

Figures 22 and 23 show the extent and duration of the tensile forces experienced in two typical struts. Most of the struts experienced fairly low tensile values, not exceeding 89 to 133 Newtons (20 to 30 lb), or 0.6 to 1.0 cm (0.25 to 0.375 in.) displacement. A few experienced higher values around 400 to 489 Newtons (90 to 100 lb), or 3.18 to 3.81 cm (1.25 to 1.5 in.) displacement. This indicates that some hammering is possible, but dislodging of the struts is not likely.

The struts for which these data were plotted were chosen because they were representative of the behavior of a large number of the struts considered, and because they experienced relatively high compressive forces and tensile displacements.

### 6.2 Buttresses

Several views of the typical displaced shape of a buttress, which involved some twisting of the buttress, are shown in Figure 24. This behavior appeared to cause planar concrete cracking which would lead to spalling of the concrete and loss of cover for the reinforcing steel. Because

there is no tie steel in the buttresses to help support the reinforcing steel, if the cracking extends completely through the buttress, a shear failure of the buttress could be expected. This is because the static water pressure and gravity loads of the slabs are transferred through the buttresses to the foundation.

The following discussion focuses on the response of buttress 25, one of the taller buttresses in the dam.

### 6.2.1 Saratoga ground motions

For the Saratoga set of ground motions, comparisons of the maximum principal tensile stresses prior to removal of some of the struts and following the removal of these struts were made to see the effect of loss of struts. Prior to removal of some of the struts, the maximum principal tensile stresses remained below the assumed dynamic tensile capacity of 2.76 MPa (400 lb/in.<sup>2</sup>), with the exception of a few elements for which the maximum principal tensile stress exceeded the capacity for one pulse. Following the removal of the struts, the maximum principal tensile stresses in many elements exceeded the dynamic tensile capacity. Loss of the struts caused the downstream, unsupported edge of the buttresses to displace farther in the cross canyon direction. Stresses were higher indicating that cracking of the concrete resulting in an increase in spalling of concrete and possible shear failure through a buttress would be likely.

### 6.2.2 Branciforte, Chi Chi and Pleasant Valley Pumping Plant ground motions

The principal tensile stresses greatly exceeded the tensile capacity in many locations during these analyses. Most of the elements of buttress 25 experienced tensile stresses that exceeded 2.76 MPa (400 lb/in.<sup>2</sup>) for more than 10 excursions and the capacity was exceeded by up to 3 times. Figures 26-28, 30-32 and 34-36 are time history plots of maximum principal stress for three typical elements in buttress 25, for each of these sets of ground motions.

Figures 29, 33 and 37 are contour plots of maximum principal tensile stresses. Output from the Branciforte earthquake analysis is shown in Figure 29, and the maximum principal tensile stress, represented by the red area, is 9.3 MPa (1350 lb/in.<sup>2</sup>). In Figure 33, output from the Chi Chi earthquake analysis is shown and the maximum principal tensile stress, represented by the red area, is 9.3 MPa (1350 lb/in.<sup>2</sup>). Finally, output from the Pleasant Valley earthquake analysis is shown in Figure 37 and the maximum principal tensile stress, represented by the red area, is 7.1 MPa (1030 lb/in.<sup>2</sup>). The area of stresses greater than 2.76 MPa (400 lb/in.<sup>2</sup>) extends from the downstream edge to the upstream edge for the top half of the buttress. The stresses reach capacity near the upstream edge and exceed the capacity by 2 to 4 times near the downstream edge. The highest stresses are in the vicinity of the top downstream struts.

## 6.3 CONCLUSIONS

When Stony Gorge Dam was analyzed for ground motions with return intervals greater than 1 in 14,000 years, more than 80 percent of the struts were over-stressed, potentially eliminating lateral support of portions of the dam leading to probable failure of the dam. In addition high tensile stresses that occurred in the buttresses could lead to loss of cover on the buttress reinforcement.

Because the face slabs hold the upstream edge of the buttresses in a plane and the foundation holds the lower edge of the buttresses in a plane, the dynamic displaced shape is due to warping and twisting. This displaced shape and resulting high principal tensile stresses indicate that concrete could spall off the reinforcement in a torsion failure mode. If the cover is lost, because there is no tie steel present and because the gravity and static water loads are carried by the buttresses to the foundation, the buttress could fail in shear through the weakened sections. This analysis indicates that under large seismic loading a progressive failure of the dam is possible.



## 7 REFERENCES

Gault, H. J., *Final Report on Construction of Stony Gorge Dam, 1927-1928*, Ambursen Dam Company, Dept of Interior, Bureau of Reclamation, Orland Project, California, November, 1928.

*Evaluation of Reinforcing Steel Systems in Old Reinforced Concrete Structures*, Concrete Reinforcing Steel Institute, 1981.

O'Connell, D. R. H., Ground Motions Analysis for Stony Gorge Dam, Bureau of Reclamation, Seismotectonic Report 2001-3, Technical Service Center, Denver, Colorado, October, 2001.

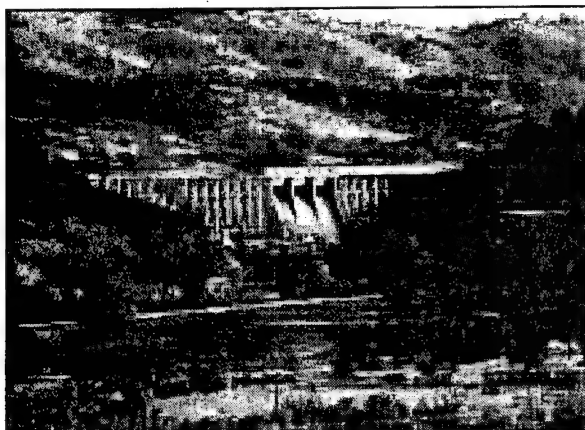


Figure 1 Stony Gorge Dam

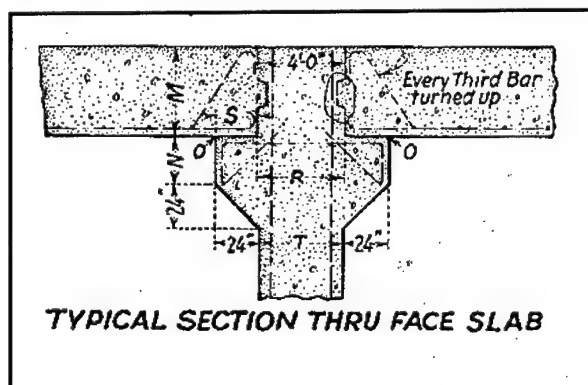


Figure 2 Slab-Corbel Detail

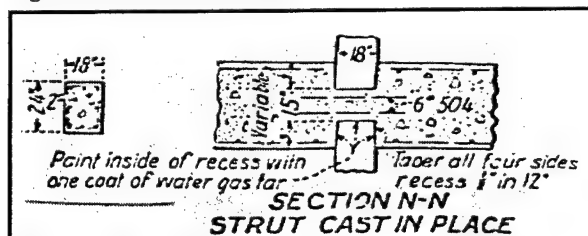


Figure 3 Strut Detail

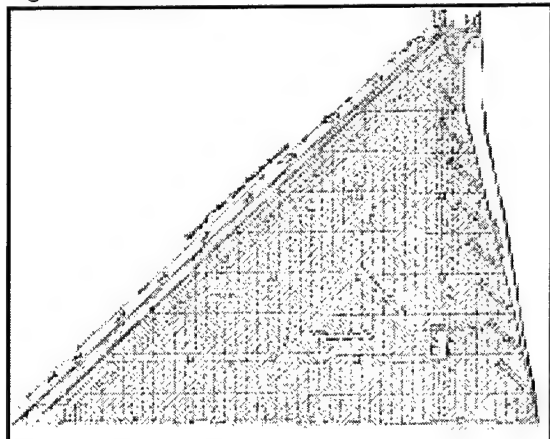


Figure 4 Typical Buttress

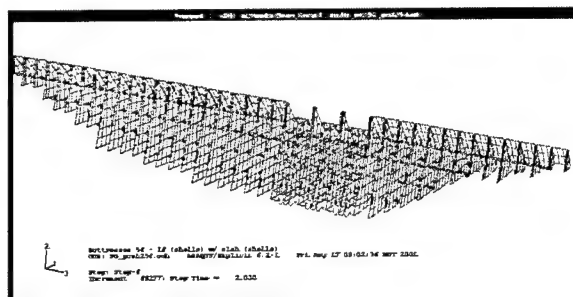


Figure 5 Finite Element Model

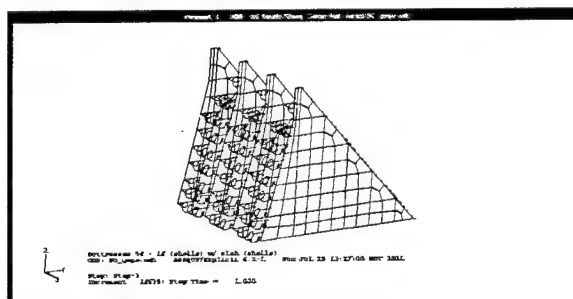


Figure 6 Spillway section of the Model

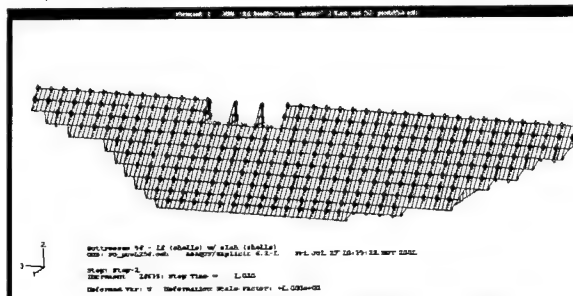


Figure 7 Location of Multiple Point Constraints

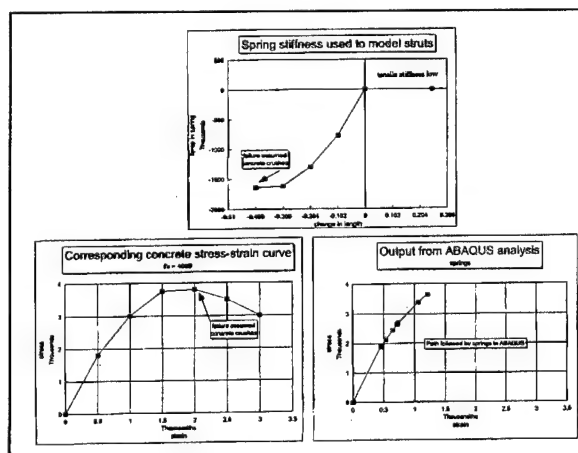
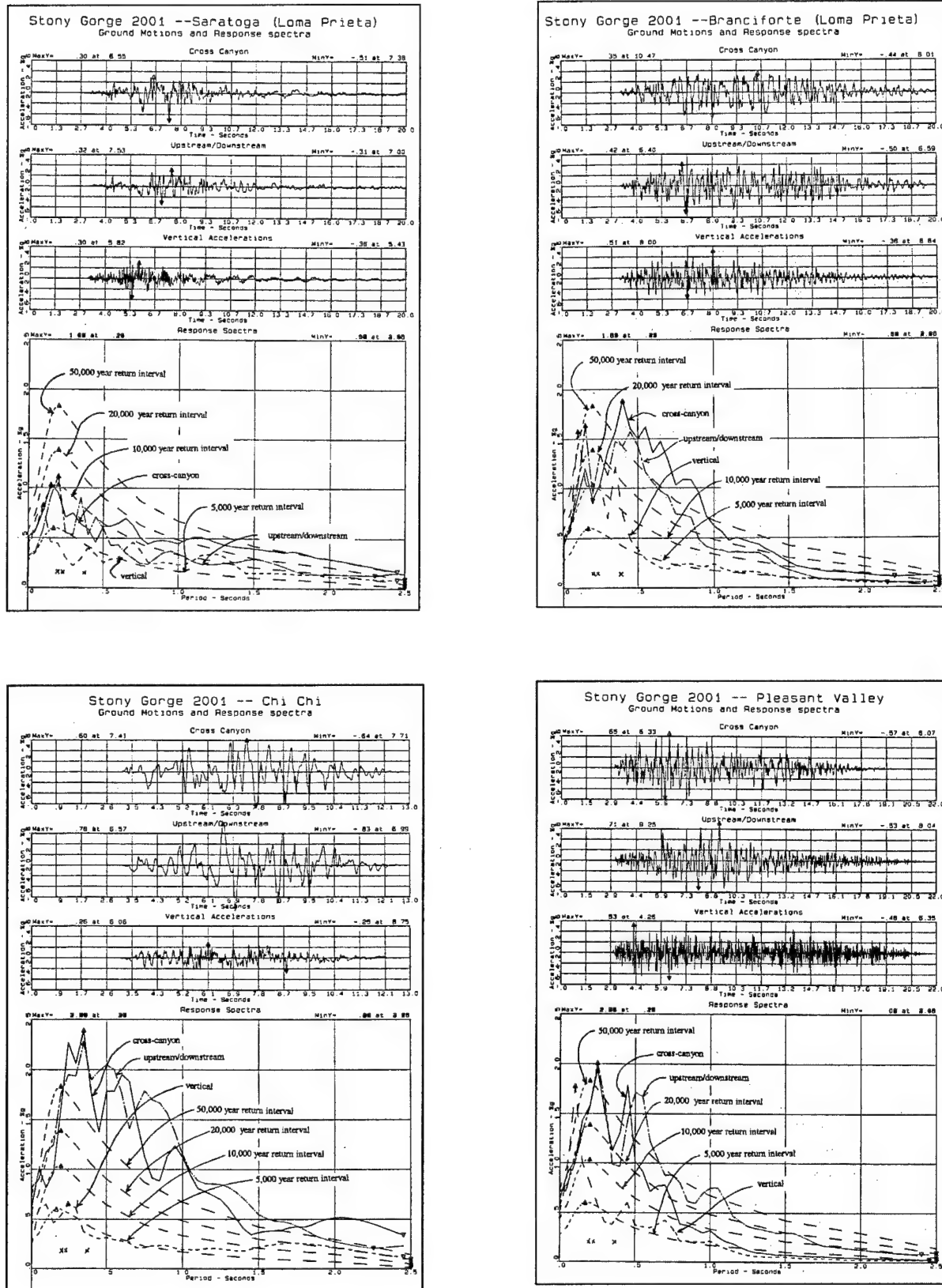


Figure 8 Concrete Material Properties

Figure 9 Ground Motions



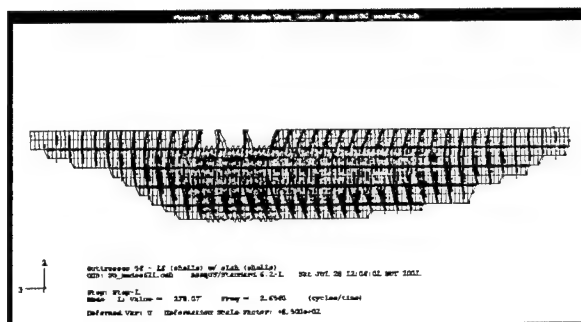


Figure 10 Fundamental Mode – Looking Upstream

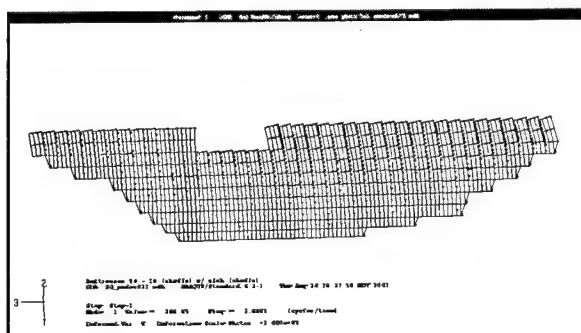


Figure 11 Fundamental Mode – Looking Downstream

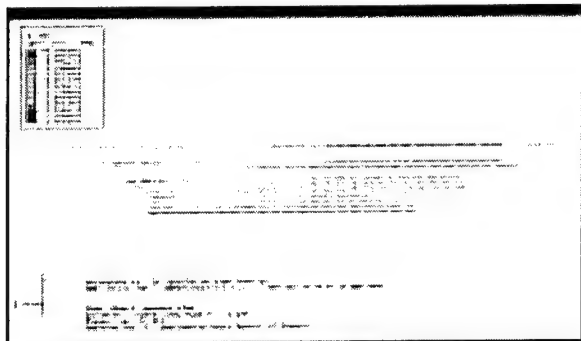


Figure 12 Typical Distribution of Force in Strut, Displacement toward Left Abutment

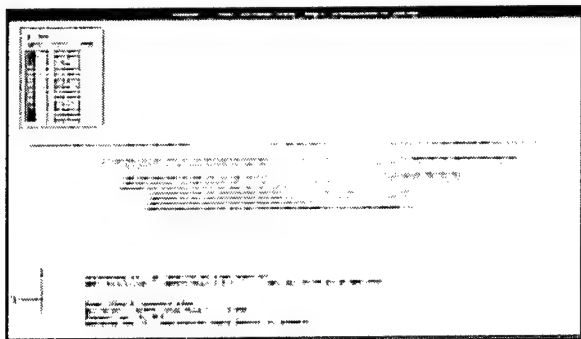


Figure 13 Typical Distribution of Force in Strut, Displacement toward Right Abutment

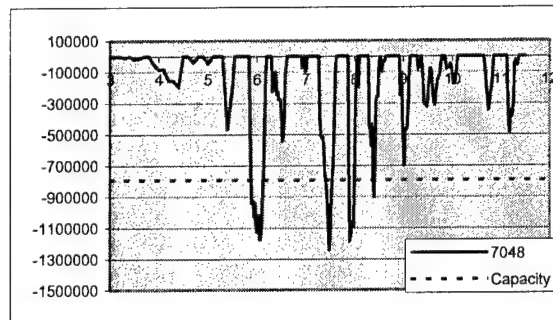


Figure 14 Force in Strut, Top Left Side – Saratoga Motions

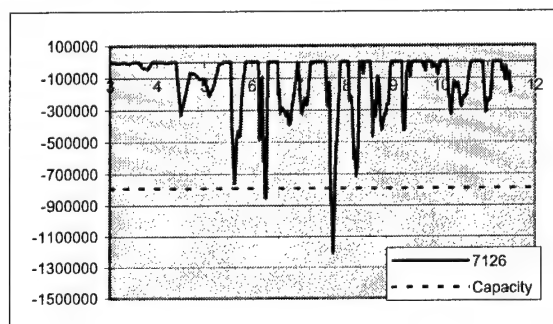


Figure 15 Force in Strut, Middle Right Side – Saratoga Motions

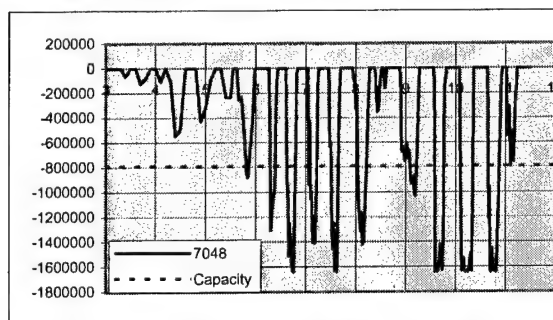


Figure 16 Force in Strut, Top Left Side – Branciforte Motions

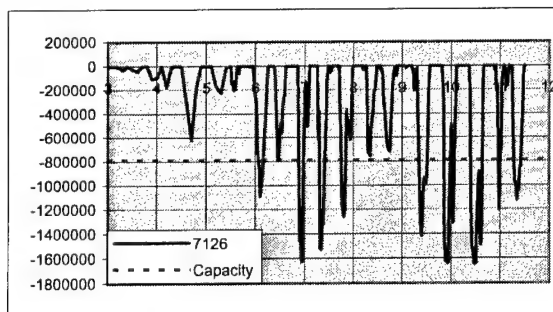


Figure 17 Force in Strut, Middle Right Side – Branciforte Motions

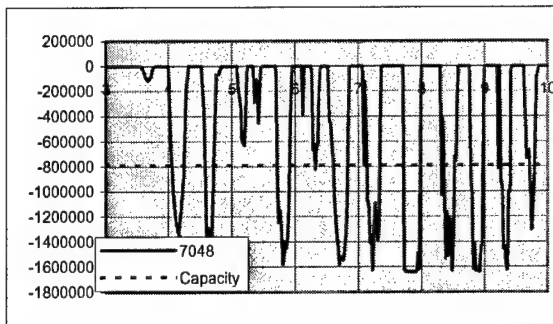


Figure 18 Force in Strut, Top Left Side – Chi Chi Motions

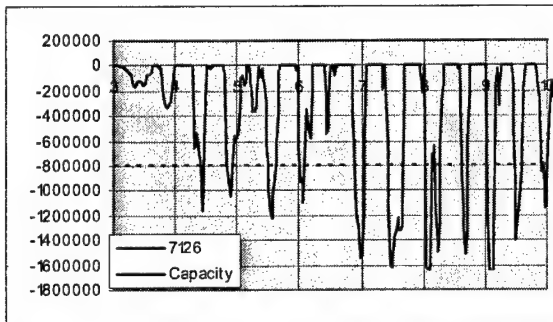


Figure 19 Force in Strut, Middle Right Side– Chi Chi Motions

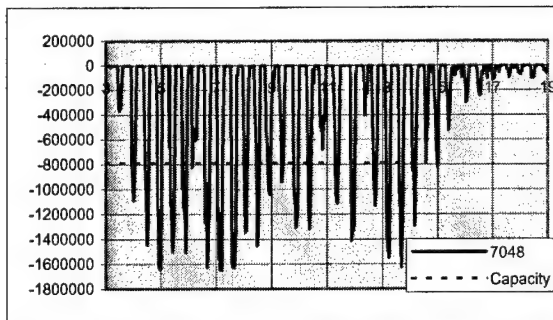


Figure 20 Force in Strut, Top Left Side –Pleasant Valley Motions

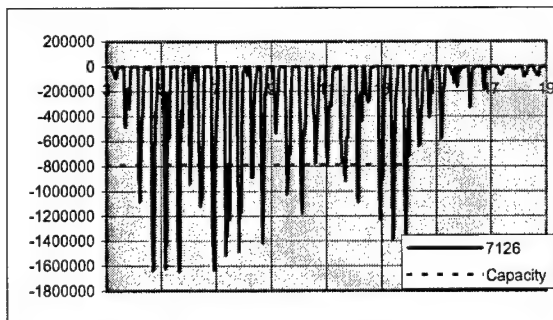


Figure 21 Force in Strut, Middle Right Side Pleasant Valley Motions

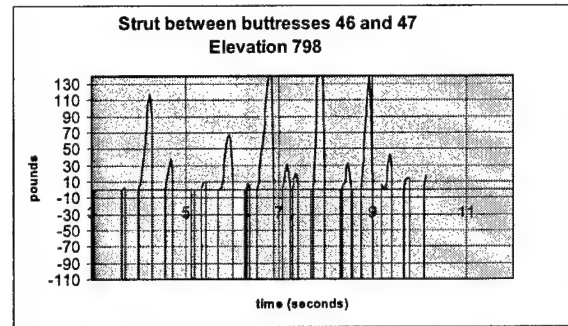


Figure 22 Tension Force in typical strut – Chi Chi Ground Motions

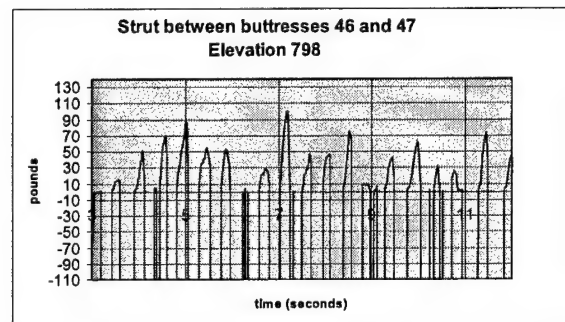


Figure 23 Tension Force in typical strut – Pleasant Valley Ground Motions

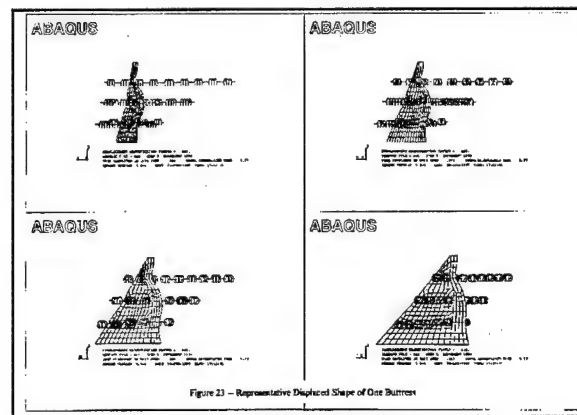


Figure 24 Typical Displaced Shape of a Buttress

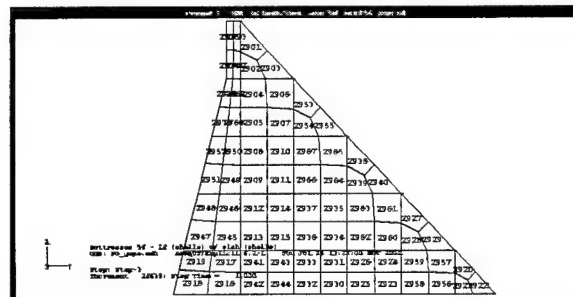


Figure 25 Element Locations in Buttress

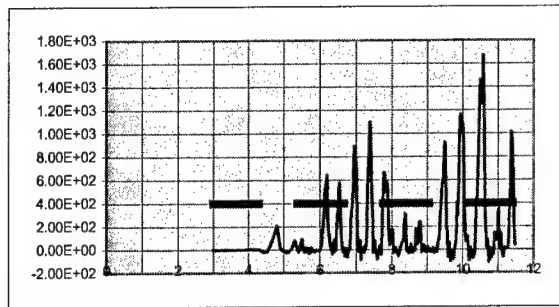


Figure 26 Maximum Principal Stress Near Top of Buttress - Branciforte Ground Motions

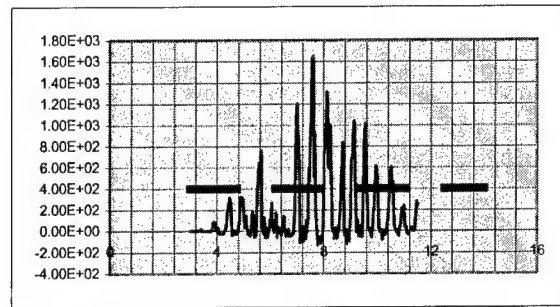


Figure 30 Maximum Principal Stress Near Top of Buttress Chi Chi - Ground Motions

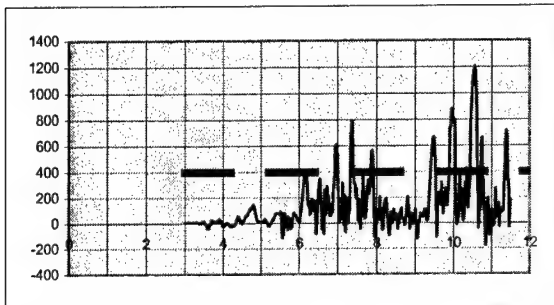


Figure 27 Maximum Principal Stress Near Center of Buttress - Branciforte Ground Motions

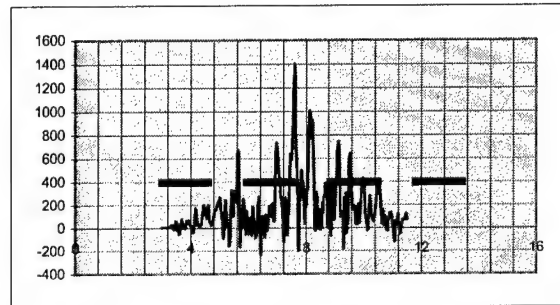


Figure 31 Maximum Principal Stress Near Center of Buttress - Chi Chi Ground Motions

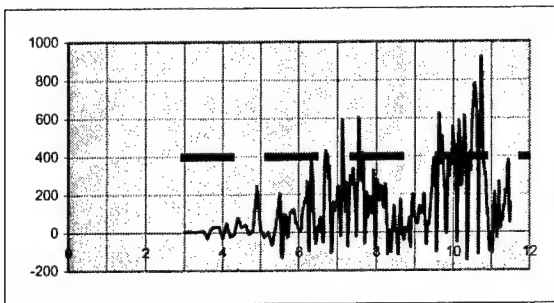


Figure 28 Maximum Principal Stress Near Base of Buttress - Branciforte Ground Motions

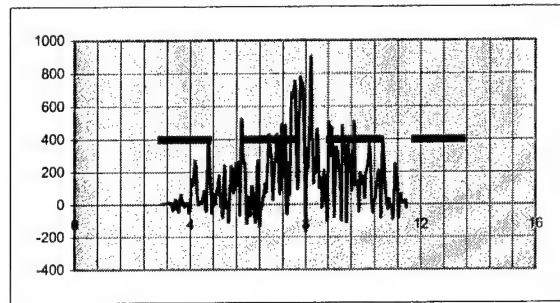


Figure 32 Maximum Principal Stress Near Base of Buttress - Chi Chi Ground Motions

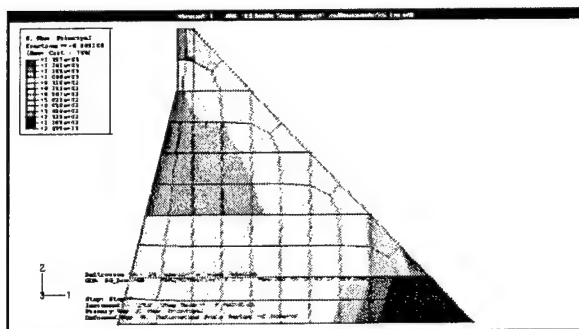


Figure 29 Contour Plot of Maximum Principal Stresses at time = 10.6 seconds - Branciforte Ground Motions

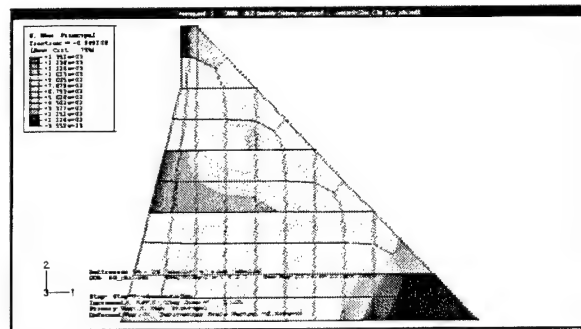


Figure 33 Contour Plot of Maximum Principal Tensile Stresses at time 7.6 seconds - Chi Chi Ground Motions

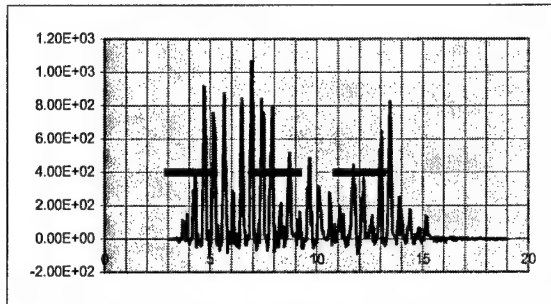


Figure 34 Maximum Principal Stress Near Top of Buttress  
Pleasant Valley Pumping Plant - Ground Motions

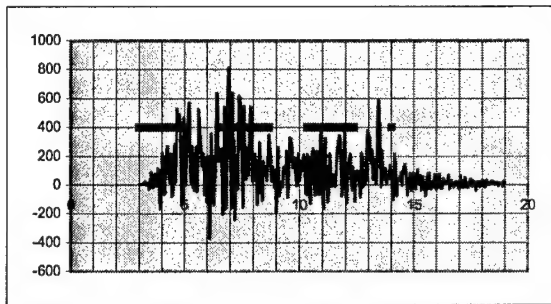


Figure 35 Maximum Principal Stress Near Center of  
Buttress - Pleasant Valley Pumping Plant Ground Motions

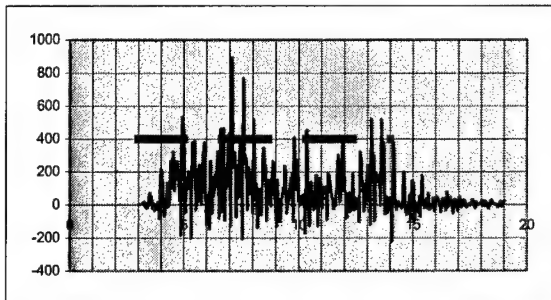


Figure 36 Maximum Principal Stress Near Base of Buttress  
- Pleasant Valley Pumping Plant Ground Motions

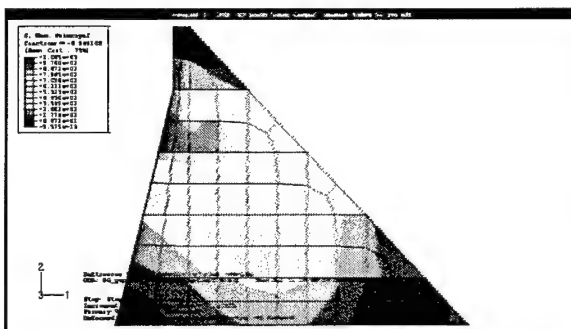


Figure 37 Contour Plot of Maximum Principal Tensile  
Stresses at time 6.9 seconds - Pleasant Valley Pumping  
Plant Ground Motions

This page intentionally left blank.



## Properties Obtained from Dam Cores

by

David W. Harris<sup>1</sup>, Timothy P. Dolen<sup>1</sup>, Caroline E. Mohorovic<sup>1</sup>, and Phoebe Mitchell<sup>1</sup>

### ABSTRACT

A series of laboratory tests were performed at the U.S. Bureau of Reclamation Laboratories on concrete cores obtained from a number of dams. The approximately 500 cores were tested using ASTM standard tests C39 Standard Test for Compressive Strength of Cylindrical Specimens, C 469 Standard Test for Modulus of Elasticity and Poisson's Ratio, and C 496 Splitting Tension Strength of Cylindrical Concrete Specimens. In addition to the static tests, tests were conducted at a strain rate typical of earthquake loading rates. A technique is suggested to display multiple tests as a method to understand nonlinear behavior of concrete. Conclusions drawn are as follows: 1. mass concrete has strains at ultimate strengths lower than conventional concrete, data from different sites produced different results – generalizations from site to site are not recommended, biaxial stress conditions produce higher tensile strength than uniaxial stress testing, ratios of dynamic properties to static properties were 1.1 for compressive strength, 1.4 for tensile strength, and 0.9 for Modulus of Elasticity, larger cores generally yielded lower strength values and higher Modulus, and cores tested at dynamic strain rates exhibited nearly linear behavior throughout the stress-strain range to failure.

**KEYWORDS:** Materials, Material Properties, Dynamic Properties, Concrete Dams

### 1 INTRODUCTION

This paper is presented to show numerical values of tests made on cores obtained from dams that were tested both statically and dynamically.

The data was previously analyzed and presented in summary form.<sup>1</sup> A detailed analysis of results and comparison with work of other authors was presented in this previous work. An emphasis in this paper is to show the amount of material variation inherent in cores from a single dam, and particularly the variation of data taken from several dams. An approach to interpret the various behaviors which may occur in concrete and to report the lowest value at which the behavior may occur is presented.

### 2 TEST PROGRAM

In 1999, a series of tests of over 470 mass concrete test specimens was conducted. The data combined with other published data to serve as a resource for use of properties of materials in dams. This effort concentrated exclusively on conventional properties, of compressive strength, tensile strength, Modulus of Elasticity, and failure strains tested both statically and at a strain rate of  $10^{-3}$ , considered a rate similar to dynamic loadings such as earthquakes. All tests were conducted in accordance with ASTM<sup>2</sup> C 39 Standard Test for Compressive Strength of Cylindrical Specimens, ASTM C 469 Standard Test for Modulus of Elasticity and Poisson's Ratio in Compression, and ASTM C 496 Splitting Tension Strength of Cylindrical Concrete Specimens. Once combined, the data set represented tests from a number of dams as shown in Table 1. A comprehensive study of the trends of the data, and a comparison to other data<sup>3,4</sup> has been published<sup>1</sup>. Note that some data was drawn from previous publications<sup>5,6,7,8</sup> and in some cases, noted by the average equaling the maximum, were based on a single test.

<sup>1</sup> Materials Engineering and Research Laboratory, P.O. Box 25007, D-8180, U.S. Bureau of Reclamation, Denver, CO 80225 (USA) Office 303-445-2375, [dwharris@do.usbr.gov](mailto:dwharris@do.usbr.gov).

The reported values from these tests are shown in Figures 1 through 9. Figures 1 through 6 show data tested at slower, static rates. Figures 7 through 9 show data obtained at the dynamic loading rate. All figures were designed to display all data points so that the variation in the data and the clustering towards certain values is readily apparent. Compressive strength values and Modulus of Elasticity values, although there is considerable range, are generally typical of other published values. Of particular note are the strain values at ultimate stress; most values are below, and in some projects well below, 2000 microstrain. These values for mass concrete tests are generally less than would be expected for more conventional, structural concrete and suggest that analyses for failure need to check for cases where strain may control. Average values of the data with maximums and minimums are shown in Table 2. From this table it can be observed that taking the average values from all projects, the range of values as a ratio is approximately 7:1 for strength, 10:1 for Modulus of Elasticity, and 4:1 for strain. The maximum range if taken project by project is 3.5x for strength, 8x for Modulus of Elasticity, and 2x for strain. Or stated another way, the potential for error based on the variation of properties within any given structure is lessened by estimating properties from at least some tests, versus estimating properties from a broad population of tests.

Comparisons have also been made with the data to compare dynamic to static ratios.<sup>1</sup> The ratio of dynamic to static compressive strength was found to increase by approximately 1.1, split cylinder tension tests were found to increase by 1.4, and the Modulus of Elasticity calculated by the ASTM<sup>2</sup> recommended method decreased to a ratio of 0.9. It is noted that the ASTM recommended method to calculate Elastic Modulus is a chord method, discounting lesser slopes typically shown in the beginning of the data. As noted by other authors<sup>3</sup>, and observed in this study, there may be a difference with calculated ratios when a secant method of calculation is used for Modulus of Elasticity. This difference owes to the more linear nature of dynamic stress-strain data throughout the entire testing

range. The less stiff behavior observed at low stress during static testing is not observed. The ASTM chord calculation uses more consistent data by offsetting from zero stress in the calculation. Thus, the difference is particularly exaggerated when comparing static to dynamic results.

The data was also used to compare the results of the static tension tests: the static stress split cylinder test with the direct tension test, a resulting average ratio of 1.75. This is an expected result owing to the biaxial stress state at failure for split cylinder tests and a uniaxial stress state at failure for direct tension results. Comparisons of stresses calculated analytically to tension strengths should account for the in-situ stress state for a correct comparison.

In the test series it was noted that<sup>1</sup> values did vary somewhat as a function of the size of the core sample being tested. Large diameter core generally produced lower strength and strain values and higher moduli values. It is difficult, practically impossible, to obtain core samples in mass concrete dams, which in many cases have maximum sized aggregate of 6 in. or more, that comply with the guide for samples of at least three times the maximum aggregate size.

All of these comparisons are for properties traditionally considered as linear, elastic properties.

### 3 USE OF DATA SETS TO DETERMINE LIMITS OF NONLINEAR BEHAVIOR

Variation in tests is inherent due to multiple factors of placement and aging of concrete in field conditions. Figure 10 illustrates typical compressive stress-strain curves measured from fifteen core samples from Deadwood Dam in Idaho and tested at the Reclamation Laboratories according to ASTM standards. Concrete cores, 6 in. (150 mm) were drilled perpendicular to the top surface of the dam and sealed in plastic once extracted to preserve the in-situ moisture content during shipping. The maximum aggregate size of the concrete was approximately 6.0 in. (150 mm).

A tool to distinguish the possible nonlinear material behavior in the samples can be developed. To encompass all possible model conditions, a circumferential boundary that includes all plausible data is made, as shown in Figure 11. Also shown in Figure 11 are the maximum and minimum values of Modulus of Elasticity. Figure 12 shows the establishment of a range of stress-strain values which may be considered as exhibiting linear, elastic behavior. The upper boundary stress for this region is calculated as 0.40 times the average of the ultimate strengths of the entire population, that is, the average upper value recommended by ASTM for the calculation of linear, elastic Modulus of Elasticity, based on a chord calculation. This strength value fundamentally represents the proportional limit, or end of the linear region. Conditions within this region, region FGO in Figure 12, are referred to as working stress. The average Modulus of Elasticity is also shown in Figure 12 and generally would be used in analysis methods.

Directly above the working stress zone are stress-strain states that represent the transition between from elastic behavior to nonrecoverable strains as the loading accumulates. This zone is named the accumulating strain zone, see region HBFG in Figure 13. That is, permanent deformations or plasticity effects may be present but may not exhibit severe nonlinearity such as cracking. Standard linear, elastic analysis may not be appropriate when stresses are in this zone. Static cyclic tests would be required to identify the plastic strain offset from stress states in this zone, and all subsequent zones discussed.

Since stress-strain pairs in the accumulating strain zone do not represent failure, the upper boundary for this region is established at the first indication of failure experienced by any of the test samples. This will occur at the least ultimate stress or least ultimate strain value calculated for the sample population. Often these values do not correspond, due to material variations. Accordingly, the upper bound of the accumulating strain region is established at the lower stress value corresponding to either of the following failure conditions: (1) the minimum ultimate

strength of the sample population (stress-based criteria), or (2) the stress value defined at the intersection of the minimum ultimate strain value (strain-based criteria).

The remaining portion of the diagram, Figure 14, is defined as the cracking zone. Stress-strain conditions that fall to the right of the least failure strain line in the cracking zone, region BICDE, have presumably cracked and failed. Data in this region can only be modeled with nonlinear cracking models. Stress-strain conditions to the left of the least failure strain, region AHBI, have experienced varying degrees of micro-cracking, but have not necessarily failed. The probability of failure increases as the values rise (increased stress) and/or move to the right (increased strain) within this region. Stress-strain conditions in this latter region, referred to as cracking onset, adhere to both plastic and cracking nonlinear models.

As would be expected, diagrams produced from different data sets would be quite different, as the data itself is quite different. Figure 15 shows data produced from Warm Springs stress-strain data. Here the data obtained from laboratory tests shows a very low working stress or linear zone and cracking occurring at fairly low stresses. Figure 16 shows data produced from test specimens from Warm Springs Dam tested dynamically. In these data note that the prediction is that there is essentially no plasticity effect, the material transitions directly from linear, elastic behavior to cracking behavior. Also note that the stress-strain boundaries, noted by the maximum and minimum outside boundaries of the zones are nearly straight, demonstrating very linear behavior of samples when tested dynamically. This was a trend observed in all dynamic testing within this series.

Use of the stress-strain diagrams to produce descriptions of the possible material response from various stress-strain states appears to be a systematic method to study the possible failure mechanisms of concrete structures and apply linear and nonlinear analysis appropriately.

## 4 CONCLUSIONS

1. Properties for static and dynamic testing of approximately 500 dam cores are shown.
2. Strains at ultimate strength are low compared to more conventional, structural concrete. Strain as the controlling failure mechanism should be considered in the analysis of critical structures.
3. Samples taken from different sites produce data which show site-specific characteristics and spatial variations within the cores tested. Generalization of properties is not recommended for analysis of critical structures. Use of general averaged values raises the uncertainty of the result by a factor of 2.
4. Biaxial stress testing (split cylinder) generally produces higher tensile strengths than uniaxial stress (direct) tests. Results for the mass concrete specimens tested in this series provided a ratio of split to direct tension strength of approximately 1.75 to 1.
5. Tests run with rapid test rates vary from tests run with slower, static loading. The ratio of this difference, based on the tests reported, are 1.1 for compression strength, 1.4 for split tension tests, and 0.9 for Modulus of Elasticity.
6. Larger diameter cores when tested generally yield lower strength and strain values and higher moduli.
7. Samples tested at dynamic strain rates exhibited nearly linear behavior throughout the stress-strain range to failure.
8. A diagram produced using data from multiple stress-strain diagrams provides a systematic method to study the possible failure mechanisms of concrete structures and check that linear and nonlinear approaches have been applied correctly.

## 5 RECOMMENDATIONS FOR FUTURE DIRECTIONS IN SEISMIC EVALUATION OF DAMS

1. Dam properties need to be established on a site-specific basis for analysis of critical structures.
2. Dynamic properties for concrete need to be established based on tests using the correct equivalent strain rates.
3. Evaluations based on analytical results compared to strength results need to assure that the appropriate failure condition, stress or strain, and the appropriate stress state, biaxial versus uniaxial, are used.
4. Emphasis needs to be given to producing reliable test protocols and test data from dam cores to provide input data into ongoing and planned nonlinear static and dynamic analyses. These analyses are becoming more common as techniques are developed and older structures are being evaluated for more severe conditions.

## 6 ACKNOWLEDGEMENTS

The authors would like to thank the U.S. Bureau of Reclamation Dam Safety Office, Denver, CO, for funding these studies and publication of this paper. Thanks to all employees of the Materials Engineering and Research Laboratory Group for contributions to and support of this study.

## 7 REFERENCES

1. Harris, David W., Caroline E. Mohorovic, and Timothy P. Dolen, "Dynamic Properties of Mass Concrete Obtained from Dam Cores," Title No. 97-M35, ACI Materials Journal, May-June 2000.

2. Annual Book of ASTM Standards, 1998, V. 4.02, Concrete and Aggregates, American Society for Testing and Materials, West Conshohocken, PA, 1998.

3. Bishoff, P.H. and Perry, S.H., "Compressive Behavior of Concrete at High Strain Rates," Materials and Structures, V. 24 pp. 425-450, 1991.

4. Raphael, J. M., "The Nature of Mass Concrete in Dams," Douglass McHenry International Symposium on Concrete and Concrete Structures, SP-55, B. Besler, ed. American Concrete Institute, Farmington Hills, Mich, pp. 133-159.

5. Gaeto, T.A., "Stewart Mountain Dam Concrete Analysis - 1983," REC-ERC-84-5,

Division of Research and Laboratory Services, Engineering and Research Center, U.S. Bureau of Reclamation, Denver, CO, 1983, pp. 1-4.

6. Peabody, M. and F. Travers, "Testing of Englebright Dam Cores under rapid Loading Conditions," Memo reporting results, U.S. Bureau of Reclamation, Denver, CO, 1986.

7. Peabody, M. and F. Travers, "Testing of Cores from Folsom and Pine Flat Dams under Rapid Loading Conditions," Memo reporting results, U.S. Bureau of Reclamation, 1986.

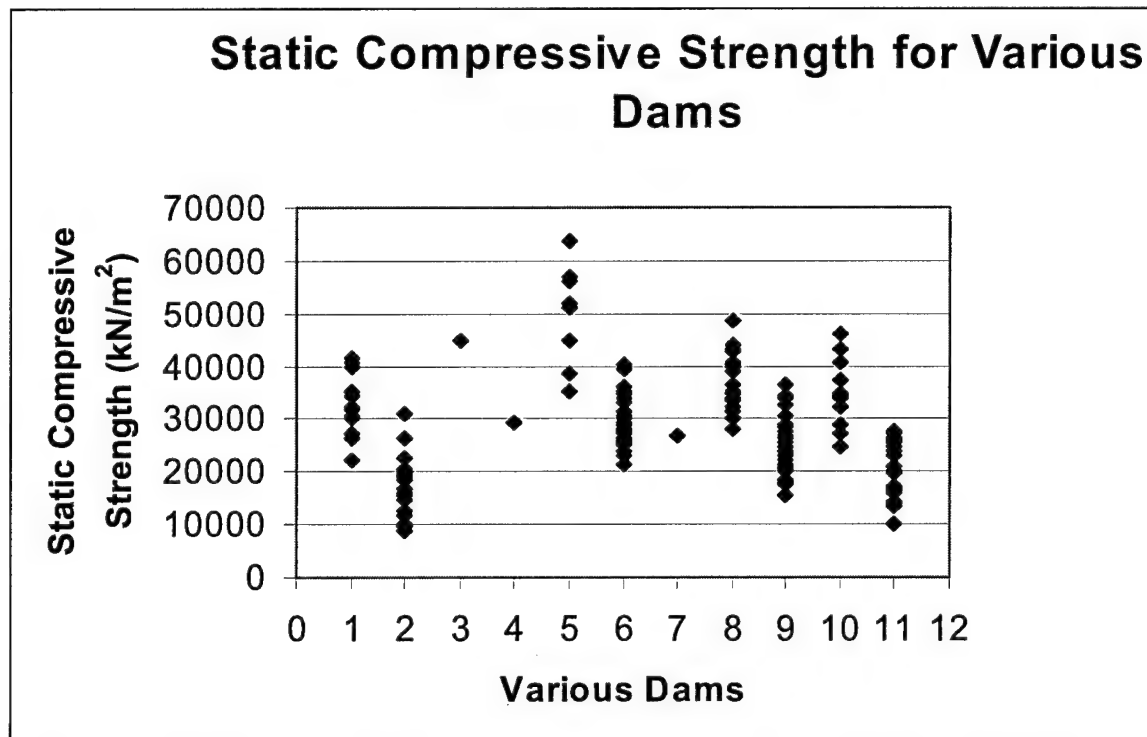
8. Raphael, J.M., "Tensile Strength of Concrete," ACI Journal, Proceedings V81, No. 2 Mar-Apr, pp 158-65.

**Table 1.** Concrete Dams Represented in this Study

Dam Name, Location (USA)	Dam Type	Date Completed	Structural Height (m)	Nominal maximum aggregate size (mm)
Deadwood Dam, ID	Thick Arch	1931	50.3	153
Elephant Butte, NM	Gravity	1916	91.8	90
Monticello, CA	Thick Arch	1957	92.7	153
Warm Springs, OR	Thin Arch	1919	32.3	153
Hoover, AR/NV	Thick Arch	1936	221.3	228.6
Stewart Mtn, AR	Thin Arch	1930	63.1	
Folsom, CA	Gravity	1956	103.7	
Roosevelt(Mod),AZ	Mod-Buttress	Mod-1995	85.4	101.6
Englebright, CA	Variable Arch	1941	85.4	
Pine Flat, CA	Gravity	1954	134.1	

**Table 2.** Summary of Static Compression Tests

Project	Average			Maximum			Minimum		
	Strength (MPa)	E GPa	Strain $\times 10^{-6}$	Strength	E	Strain	Strength	E	Strain
Deadwood	32.4	24.1	1785	41.5	29.7	2240	22.1	20.7	1103
Elephant Butte	17.4	19.1	1450	31.1	30.3	2055	8.8	10.3	
Englebright	45.0	32.4		45.0	32.4				
Folsom	29.3	14.5		29.3	14.5				
Hoover	47.5	38.6		63.6	51.7		29.3	14.5	
Monticello	30.5	35.6	1183	40.1	49.6	1400	41.9	26.9	
Pine Flat	26.8	26.9		26.8	26.9				
Roosevelt	37.3	37.9	1175	48.8	55.2	1625	28.2	18.6	
Seminole	24.1	11.7	951	36.4	22.4	2880	15.6	6.9	
Stewart Mountain	34.8	26.9		46.0	40.0		24.8	14.5	
Warm Springs	20.2	23.4		46.0	46.2		10.2	5.5	
All Projects	31.4	26.2		63.6	55.1		8.8	5.5	



Index: 1. Deadwood, 2. Elephant Butte, 3. Englebright, 4. Folsom, 5. Hoover, 6. Monticello  
7. Pine Flat, 8. Roosevelt, 9. Seminoe, 10. Stewart Mountain, 11. Warm Springs

**Figure 1.** Static compressive strength of tested dam cores

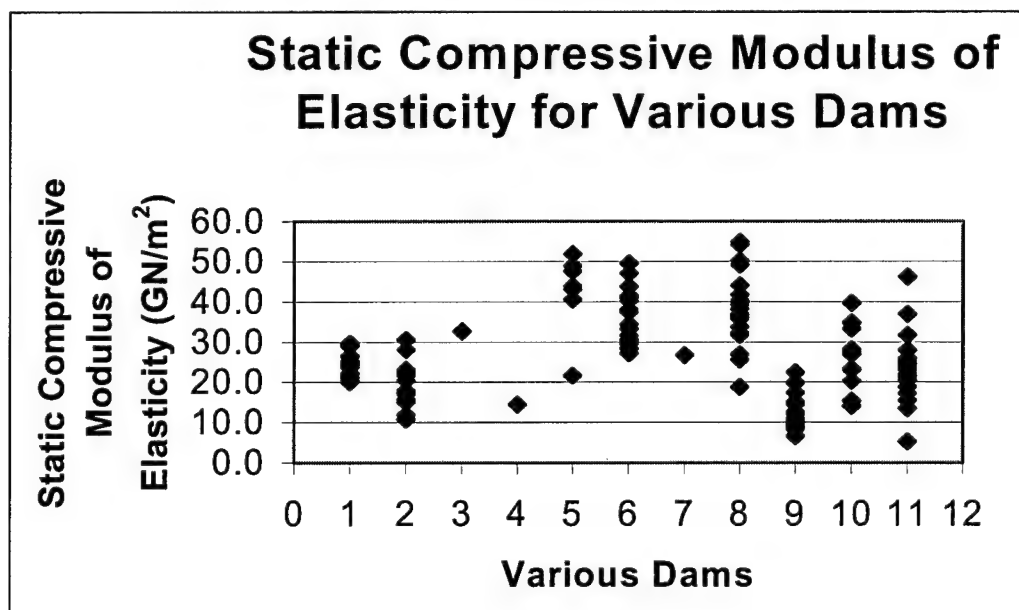


**Figure 2.** Elastic modulus calculated from static tested dam cores (Index see Figure 1)

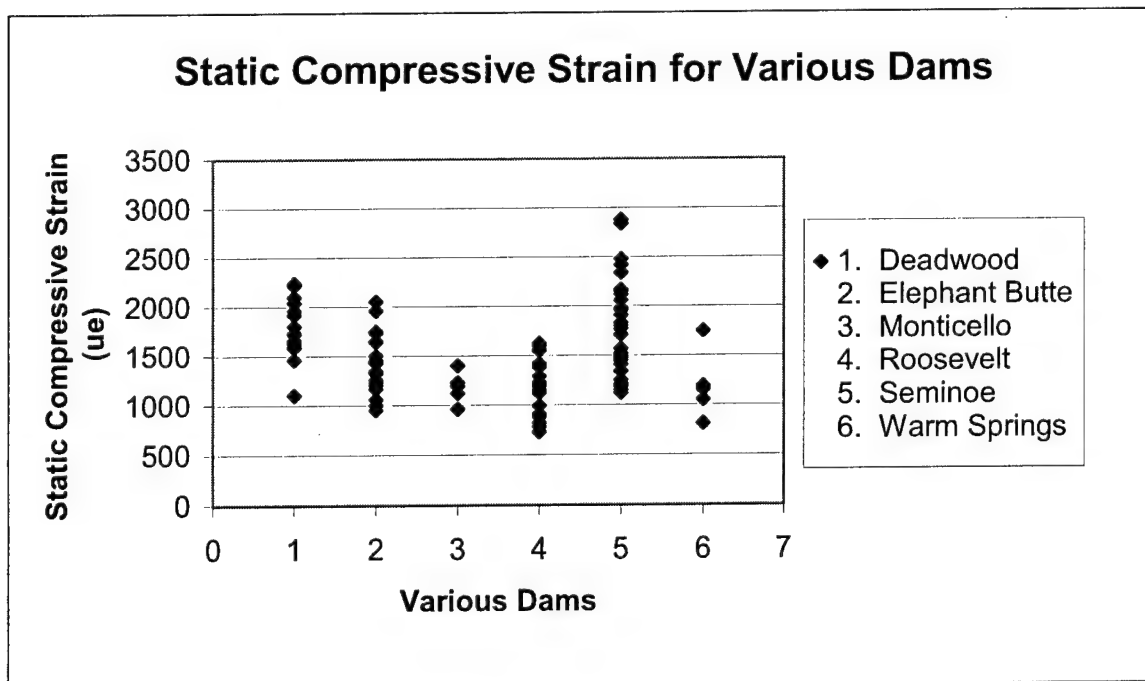


**Figure 3.** Static compressive strain at ultimate stress

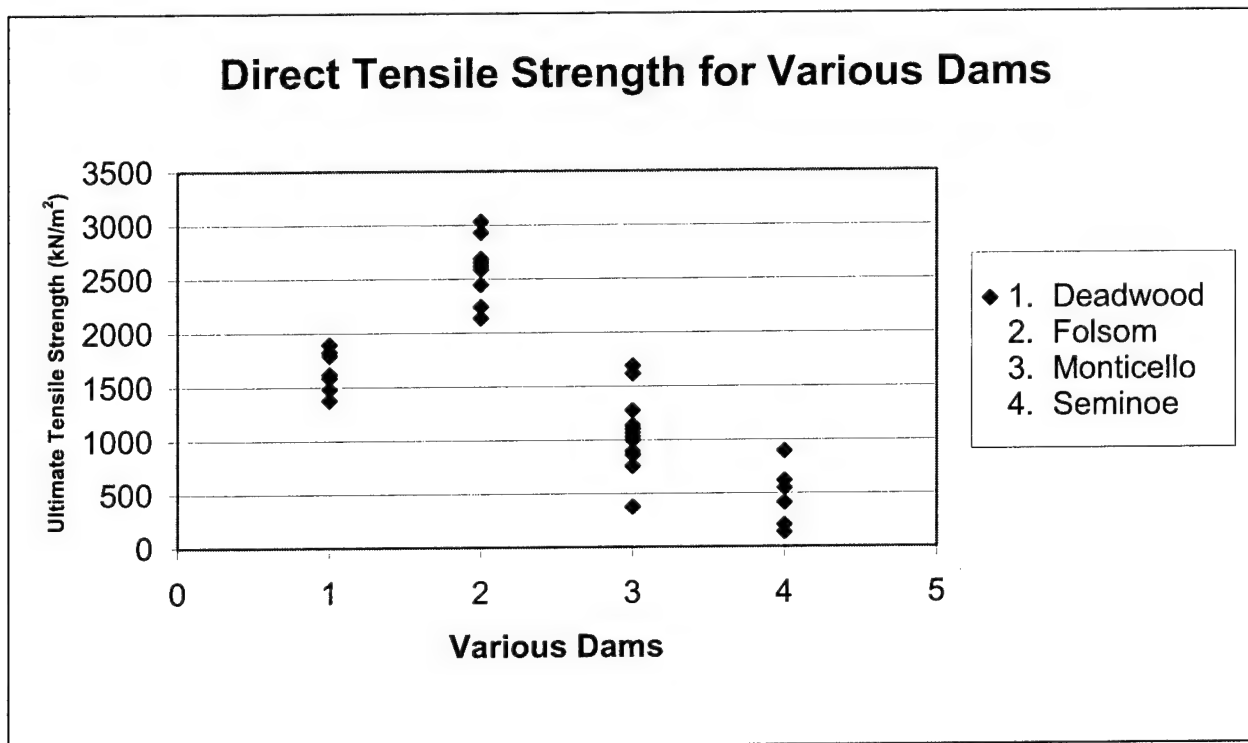


**Figure 4.** Static direct tension tests of dam cores



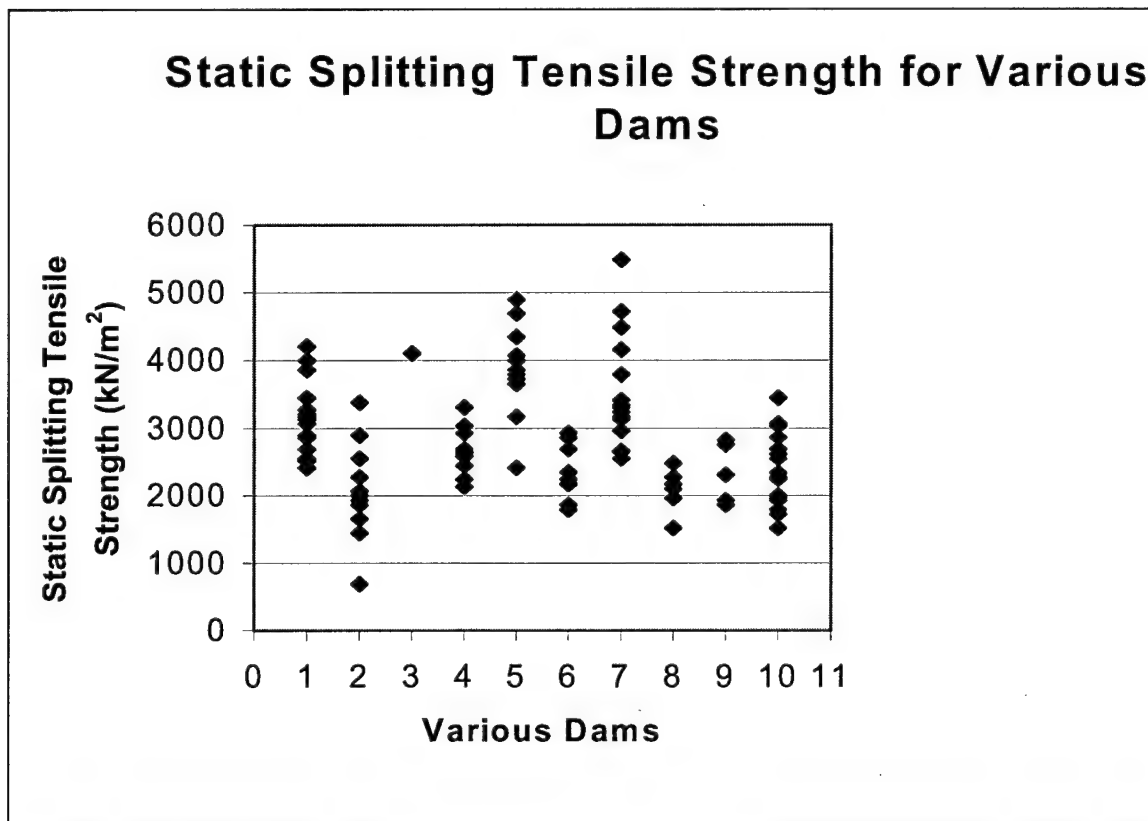


**Figure 5.** Static splitting tension tests for dam cores (Index see Figure 1)

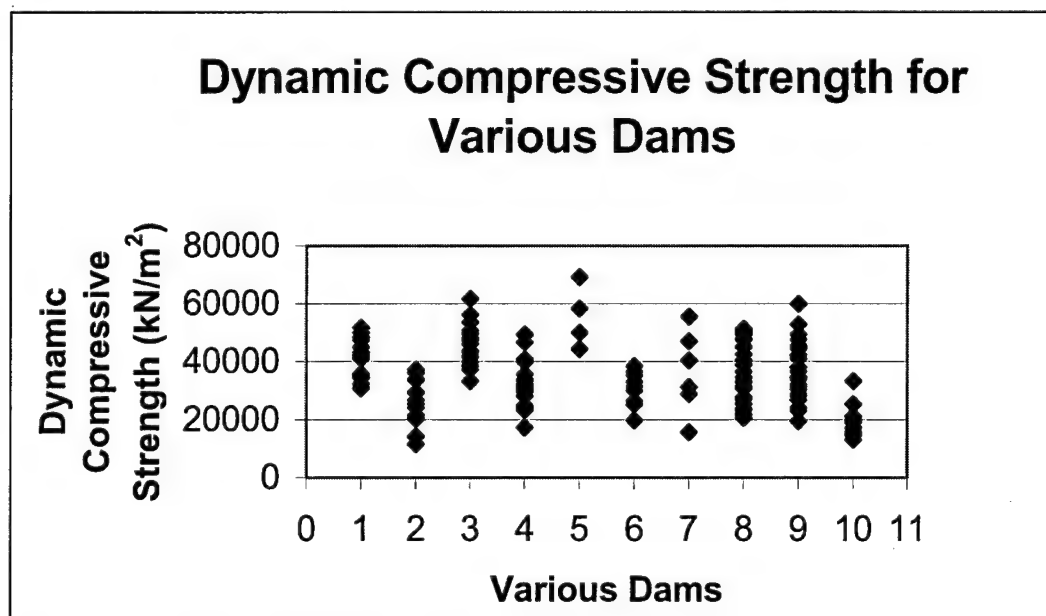


**Figure 6.** Dynamic compressive strength of tested dam cores

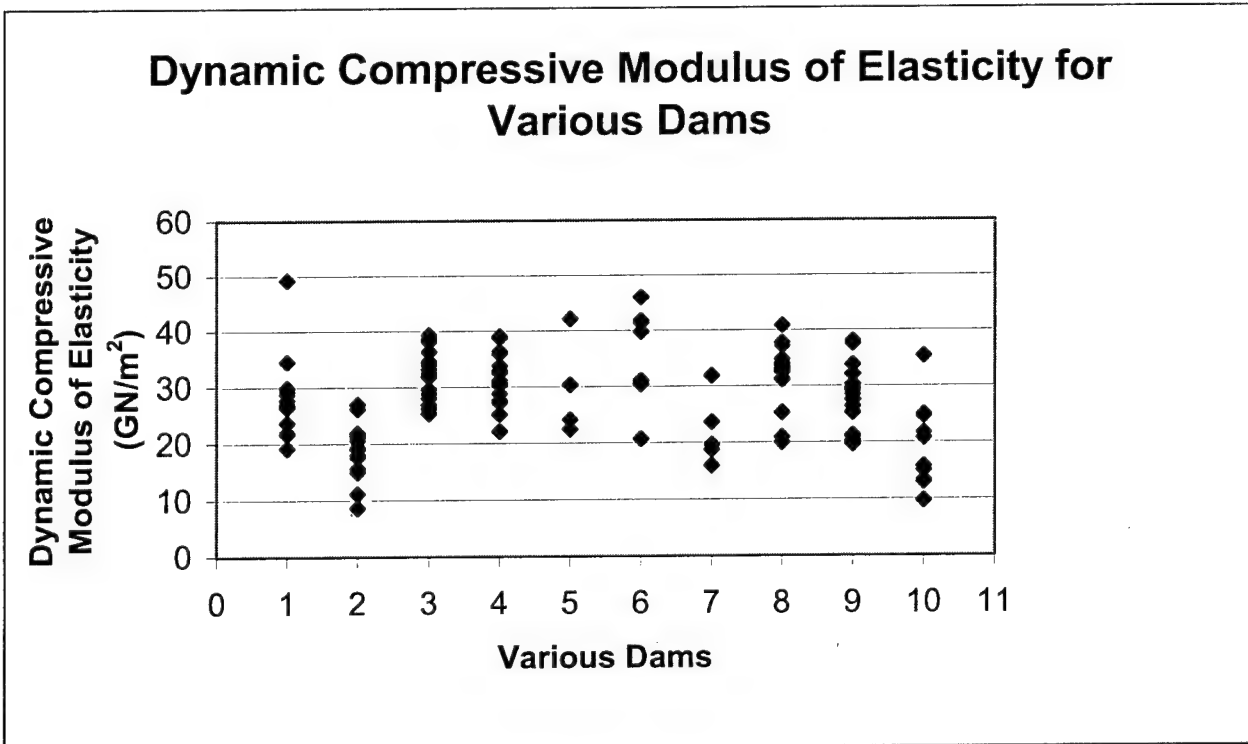


Figure 7. Dynamic modulus calculated from tested dam cores (Index see Figure 1)

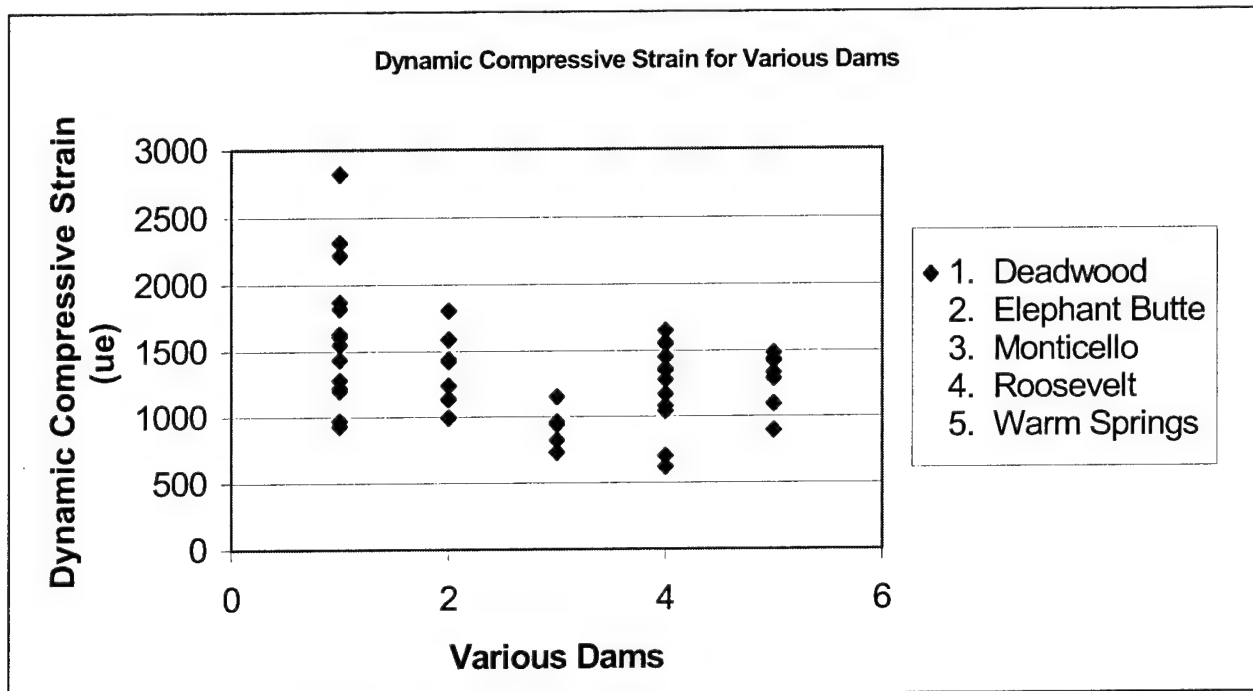
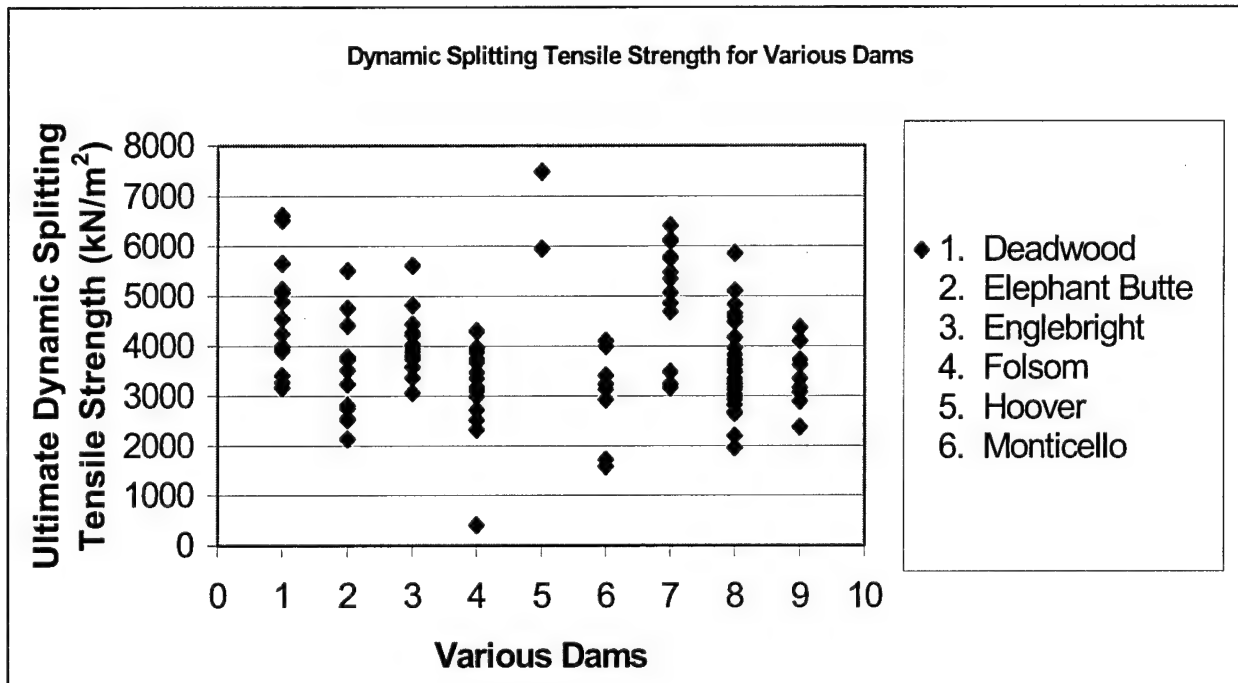
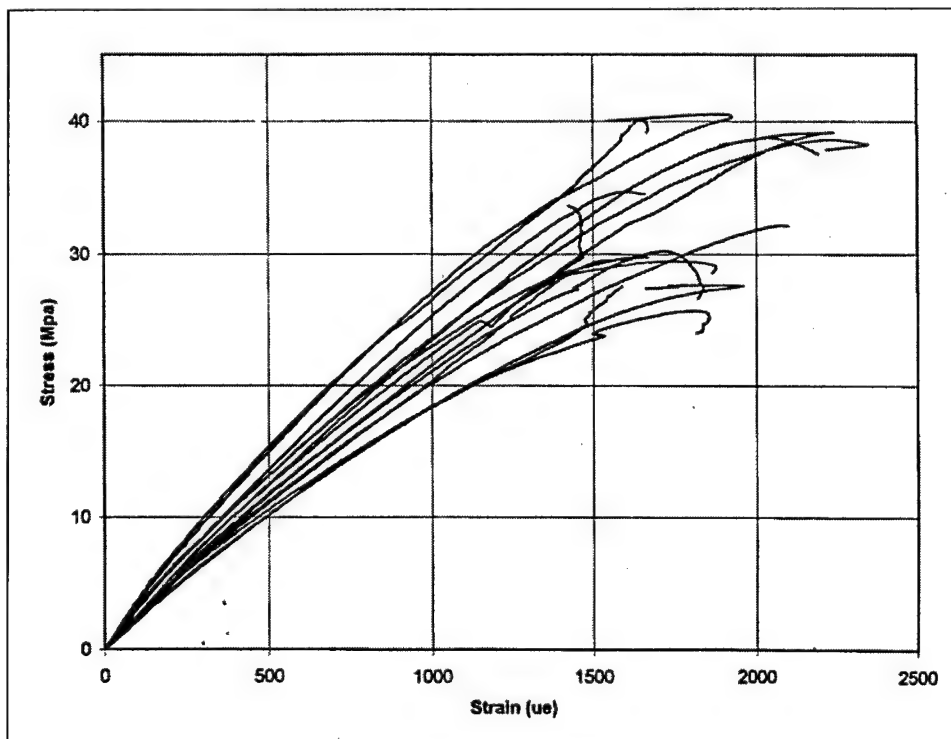


Figure 8. Dynamic compressive strain at ultimate stress



**Figure 9.** Dynamic splitting tension for dam cores



**Figure 10.** Typical stress-strain curves Deadwood Dam, ID

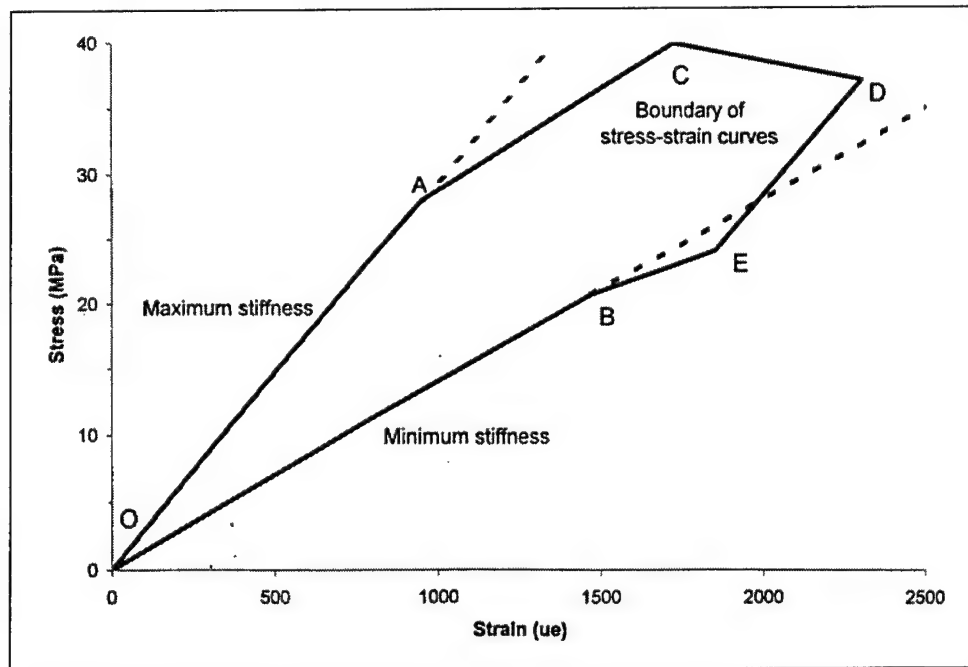


Figure 11. Boundary of stress- strain curves

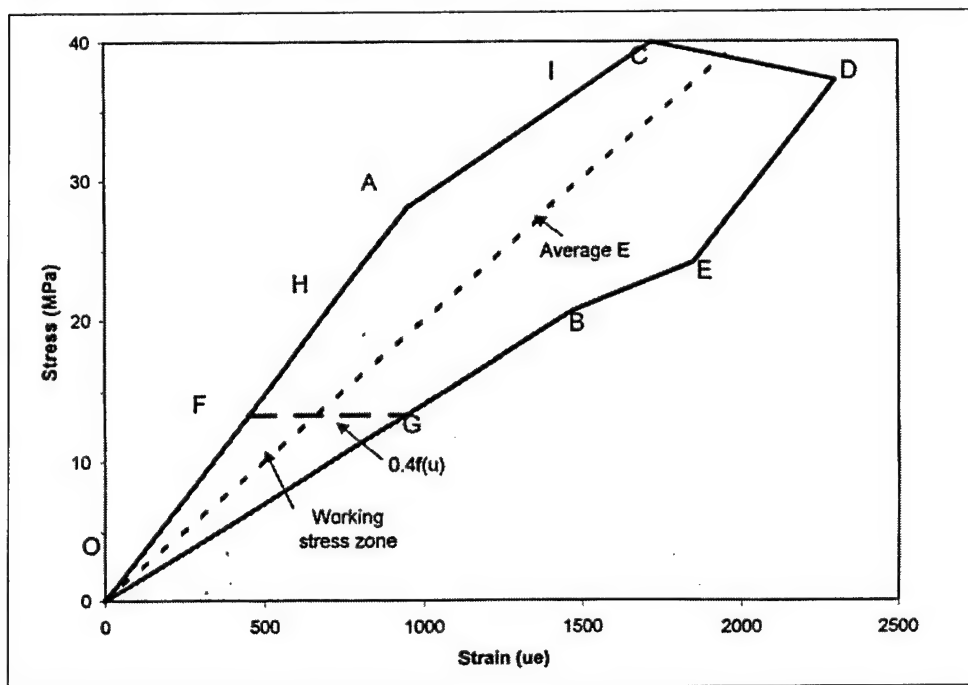


Figure 12. Working stress (linear, elastic) zone

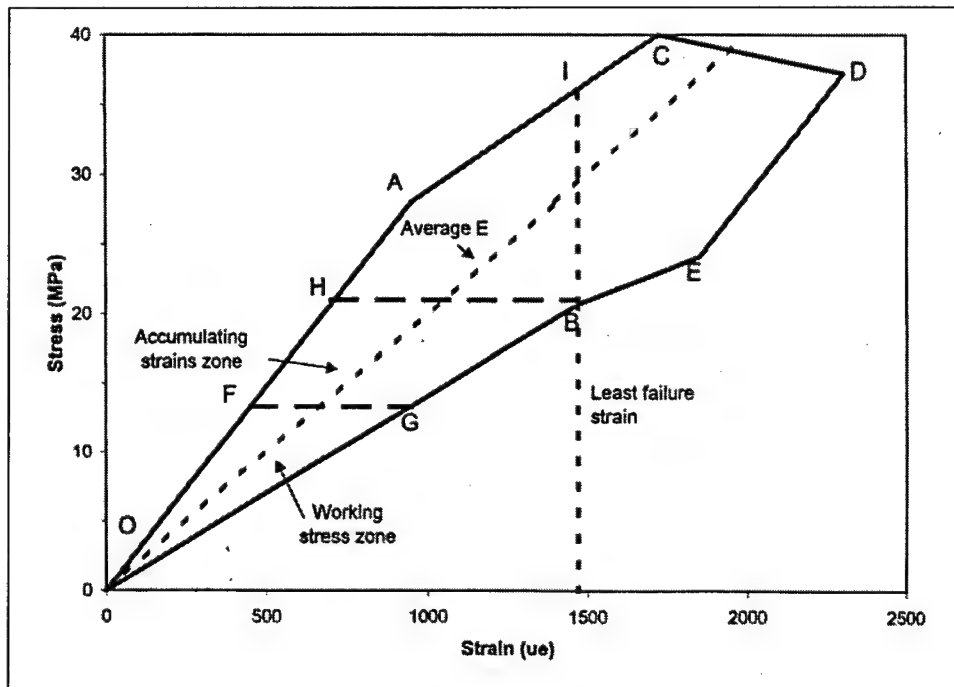


Figure 13. Stress-strain data showing accumulating (plastic) strain

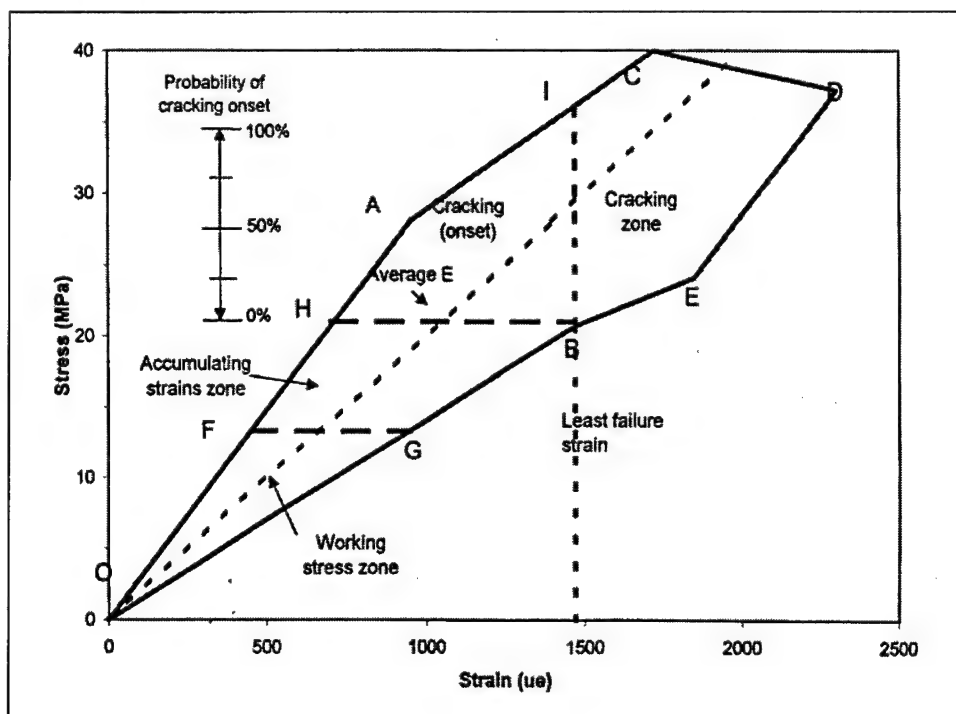


Figure 14. Stress-strain data showing nonlinear behavior

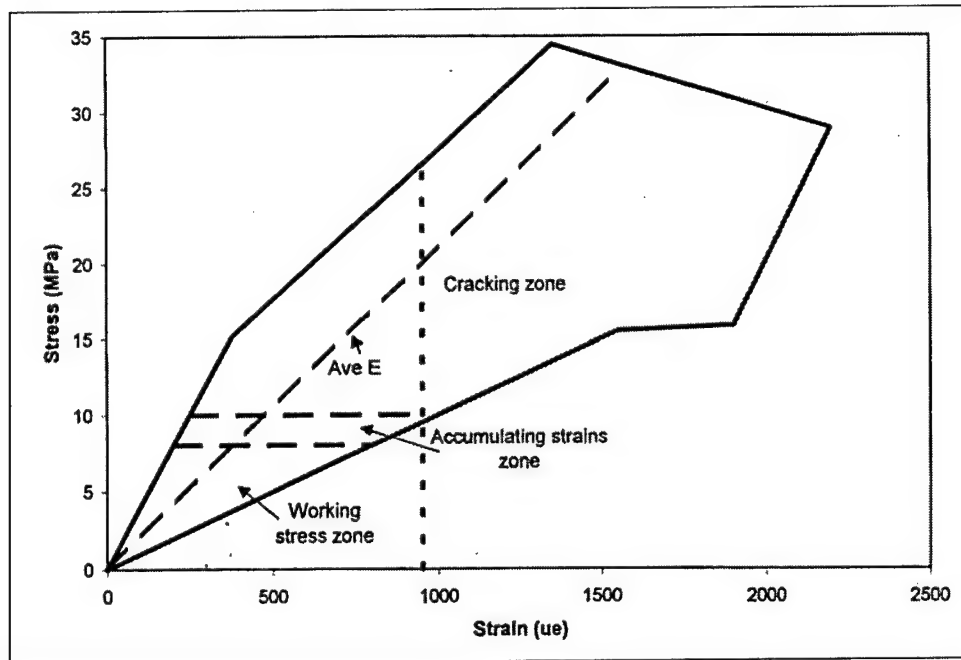


Figure 15. Stress-strain data for Warm Springs Dam

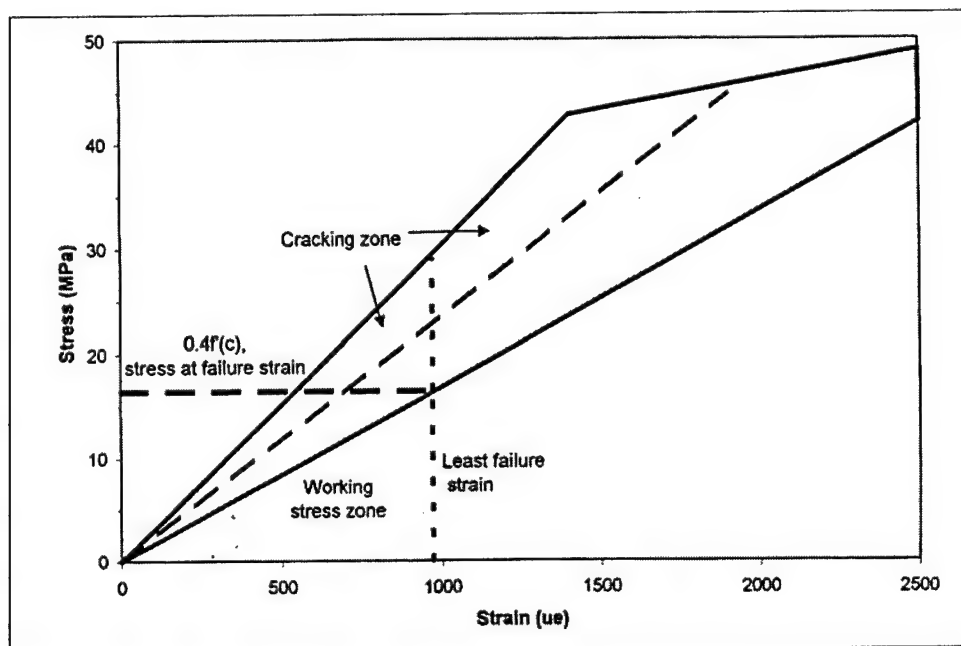


Figure 16. Dynamic stress-strain data for Warm Springs Dam

## Earthquake Damage and its Remedial Measure for Earth Dam with an Asphalt Facing

by

Yoshio OHNE<sup>1)</sup>, Kunitomo NARITA<sup>2)</sup>, Tetsuo OKUMURA<sup>3)</sup> and Yoshio NAKAMURA<sup>4)</sup>

### ABSTRACT

An asphalt facing was constructed along the upstream face of an earth dam, consisting of a volcanic sand material, in order to control seepage through the dam. A medium-scale earthquake happened to take place to cause severe damages on the facing, and many cracks appeared especially near the crest of the dam. It was inferred that dynamic deformation developed near the crest during the response to the earthquake exceeded an allowable strain of asphalt concrete used as the facing material. Laboratory cyclic shear tests were conducted in this paper on these materials of asphalt mixture, to investigate such dynamic deformation characteristics as strain dependency of the modulus of rigidity and a critical strain to cause cracking. According to the test results, the critical strain against cracking was more than about  $10^{-3}$ , and an asphalt mixture with high ductility and strength was newly developed as an earthquake resistant facing material.

**Key Words:** *Earthquake, Asphalt facing, Asphalt mixture, Dynamic test, Dynamic strain*

### 1. INTRODUCTION

This dam was constructed for the purpose of agriculture at the eastside foot of Mt. Fuji in 1971 and is called 「Higashifuji Dam」.

Because of topographical and geological restrictions, the dam was constructed with the excavated materials from the hillside as shown in Fig.-1. This material was used as embankment material for dam body and most of them are consisted of volcanic sandy soil (scoria) with high water permeability. For this reason, the asphalt facing was constructed not only on the dam body but also on the entire bottom area of the reservoir. Typical cross section of the dam is shown on Fig.-2 and asphalt structures for the slope and the bottom are shown respectively on (a) and (b) of the same Fig. On March 6, 1996, at about 23:35 hours, an earthquake with its epicenter located at a point about 15 km north of this dam had occurred and caused numerous cracks on the asphalt facing as shown on Fig.-3. Seismograph capable of observing maximum acceleration only had been installed one at the dam bottom and another at the dam crest. According to the record of these observations, at the dam bottom ( $\alpha_B$ ) and at the dam crest ( $\alpha_t$ ) were observed as  $\alpha_B = 85$  gal and  $\alpha_t = 380$  gal respectively.

- 
- 1), 2), 3) Department of Civil Engineering  
AICHI INSTITUTE OF TECHNOLOGY  
Yachikusa, Yagusa, Toyota, Aichi, JAPAN  
4) Department of Environment  
TOKAI TECHNOLOGY CENTER  
Nagoya, Aichi, JAPAN

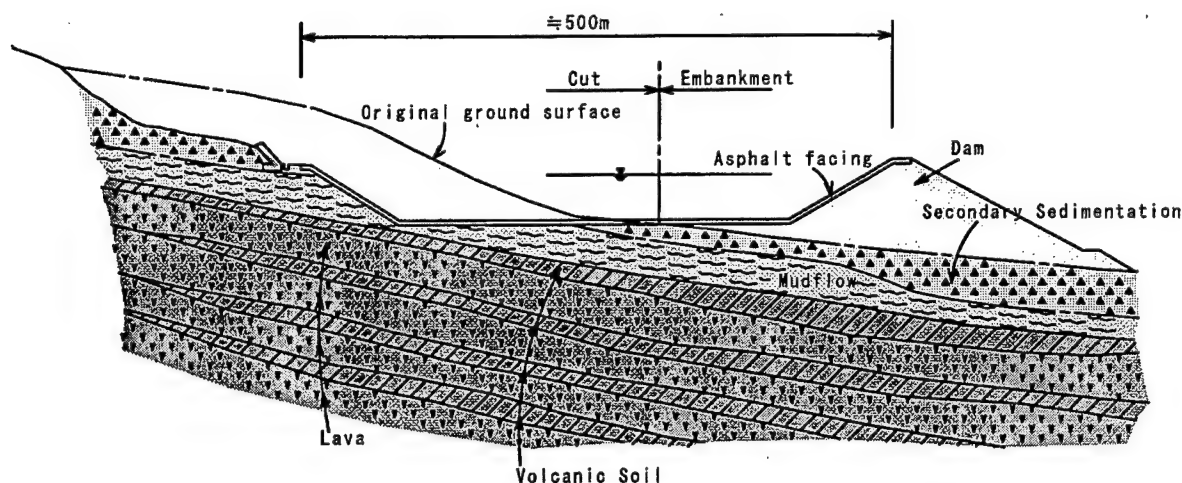


Fig.-1 Schematic Cross Section of Dam

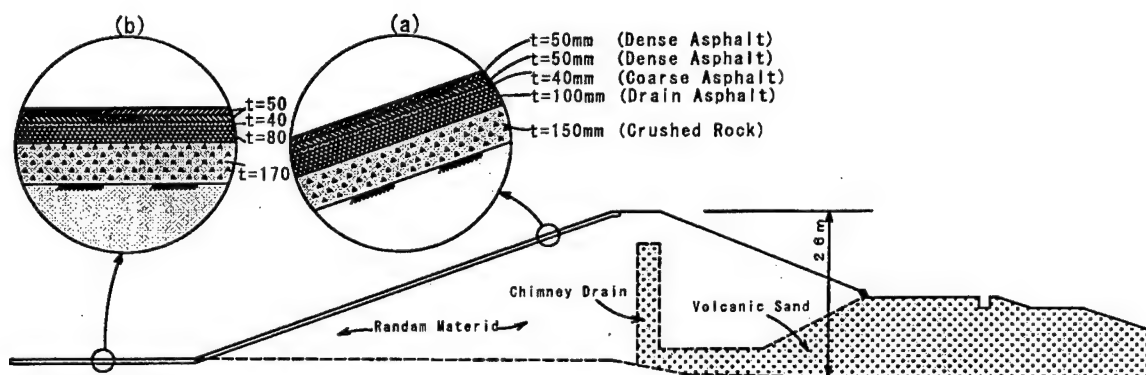


Fig.-2 Standard Cross Section of Dam and Structure of Facing

Fig-4 is showing the relation between  $\alpha_B$  and  $\alpha_t$  as obtained from the large fill type dams and large scale model experiments. According to the record of these observations, responded acceleration that corresponds to  $\alpha_B = 85$  gal is  $\alpha_t \approx 190$  gal and  $\alpha_t / \alpha_B \approx 2.3$ . As against this figure, in case of this dam is  $\alpha_t / \alpha_B \approx 4.5$  which can be noticed as remarkably large.

## 2.AN INVESTIGATION OF EARTHQUAKE DAMAGE

Water level in the reservoir at the time of earthquake occurrence was approximately  $2/3$

of full level of the reservoir. After the earthquake occurrence, the water level in the reservoir was drawn down and inspection was conducted for possible damages in and around the reservoir, on dam body and on bottom of the reservoir. As a result of this inspection, no damage was found on the dam body. However, as shown on the Fig.-3, many cracks were recognized on asphalt pavement of the dam slope and the bottom of the reservoir. Scale of crack is reaching maximum of 10 mm, and many of them are stretching to entire thickness of the pavement as shown on the Photograph-1.



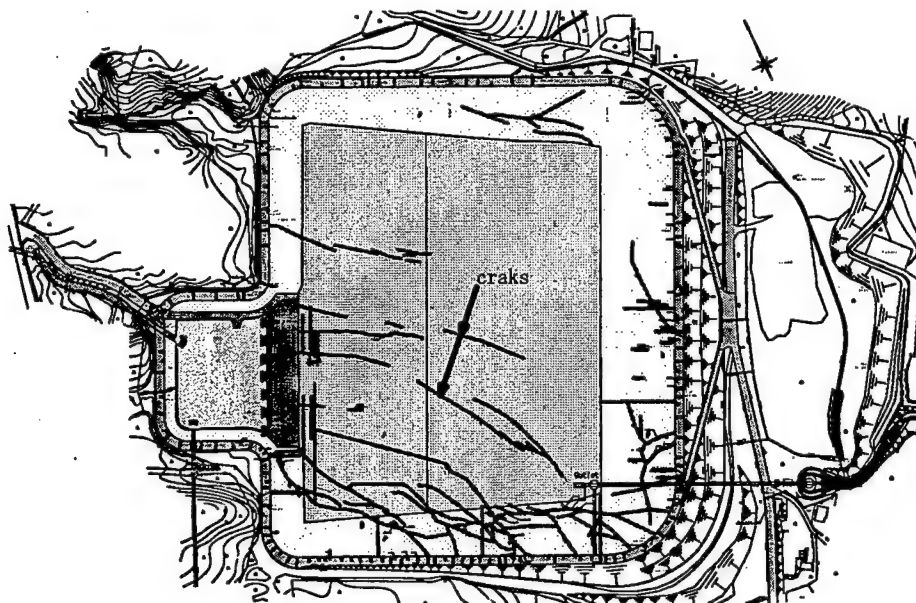


Fig.-3 Plan view of reservoir

▲ Tadaragi Dam	64.5m	• Large Scale Model test	2.5m
● Ainono Dam	40.8m	• Sannokai Dam	37.5m
▲ Tadaragi Dam Model test		▲ Makio Dam	104.5m
● Hsinfengkiang Dam	105m	* Togo Dam	31m
▲ Namioka Dam	60m	* Isaka Dam	30m
		● Kiseniyama Dam	95m

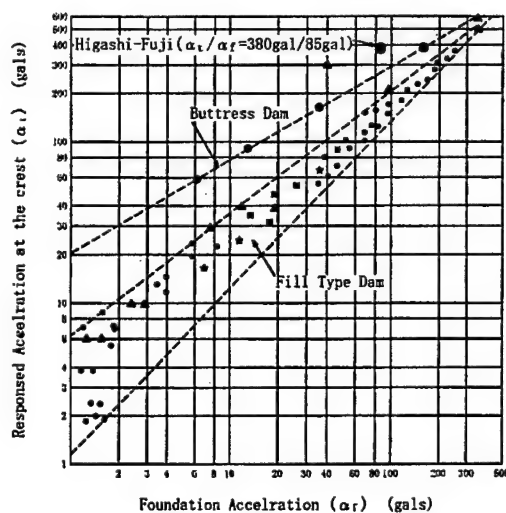


Fig.-4 Relation between Foundation and Responded Acceleration at crest

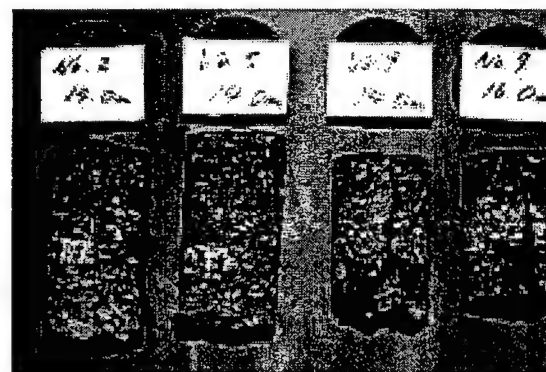


Photo.-1 Cracks of Asphalt Facing

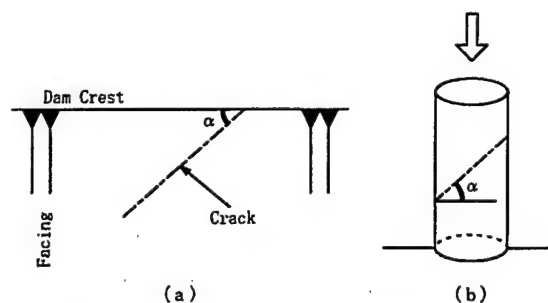


Fig.5 Direction of Cracks generated on Asphalt Facing

Cracks developed on the asphalt facing are distributed with the angles of 35~80 degrees against the direction of the dam crest. Its

mean angle ( $\alpha_{\text{mean}}$ ) was approximately  $64^\circ$  and this angle almost coincides with the angle of cracks developed on the test piece of

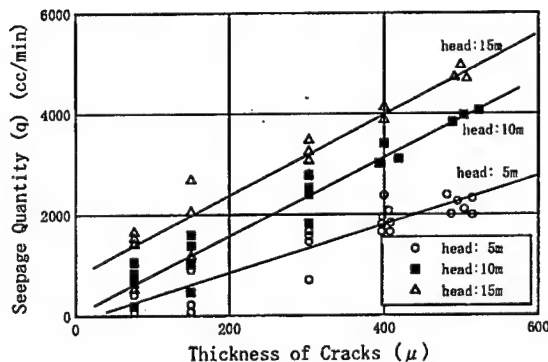


Fig.-6 Relation between  $q$  and  $\mu$



Photo.-2 Percolation Test on Asphalt Facing

asphalt pavement when simple-axial compression test was conducted. That is, as shown on Fig.-5, failure angle ( $\alpha$ ) against the maximum principal stress is formulated by formula (1)

$$\alpha = 45 + \phi/2 \text{ -----(1)}$$

So, when finding the value of  $\phi$  (internal friction angle) by the formula (1),  $\phi = 38^\circ$  is obtained and it can be known that this value almost coincides with the value of  $\phi$  of general sandy soil. It is considered that this means that the asphalt facing was compressed toward the direction of the slope and was led to developing the cracks. Relations between the width of cracks ( $\mu$ ) and water permeability ( $q$ ) has been tested by using a permeability apparatus which is used for ordinary permeability test with a partial improvement made to it. Such test

(Photograph-2) and the result thereof are shown on Fig.-6. This amount of leakage is so great and suggests a necessity of overall repair of asphalt facing.

### 3.EARTHQUAKE RESPONSE ANALYSIS

#### (1) Analysis and dynamic character of material

For the analysis against maximum two-dimensional cross section of dam body, a program almost identical to QUAD-IV was used, and for dynamic character of material, it was formulated by Hardin-Drnevich model.

$$G/G_0 = \frac{1}{1 + (\gamma/\gamma_r)\gamma} \text{ -----(2)}$$

$$h/h_0 = \frac{\gamma/\gamma_r}{1 + (\gamma/\gamma_r)} + 0.12 \quad (=h) \text{ -----(3)}$$

Here,  $\gamma_r = 4.8 \times 10^{-3} \cdot \sigma^{0.75}$  has been established.

Regarding  $G_0$ , trial analysis was done under the harmonic wave and made variations within the range of  $G_0 = (400 \sim 500) \cdot \sigma^{0.47}$  in searching for value that can obtain  $\alpha_t / \alpha_B \approx 4.5$ . Such value was found and adopted and as a result of this trial, at  $G_0 = 450 \cdot \sigma^{0.47}$ ,  $\alpha_t / \alpha_B$  becomes 4.5 and predominant period( $T_0$ ) is 0.5 sec.

Further, seismograph was installed on this dam shortly after the occurrence of the earthquake and small-scale earthquakes were recorded. By using earthquake waves from this seismograph and having  $G_0 = 450 \cdot \sigma^{0.47}$ , earthquake response analysis was conducted and the result of the analysis is shown on Fig.-7. As is made clear on this Fig., the responded acceleration value is almost in coincidence with the value of observation and an appropriateness of the value  $G_0 = 450 \cdot \sigma^{0.47}$  is inferred.

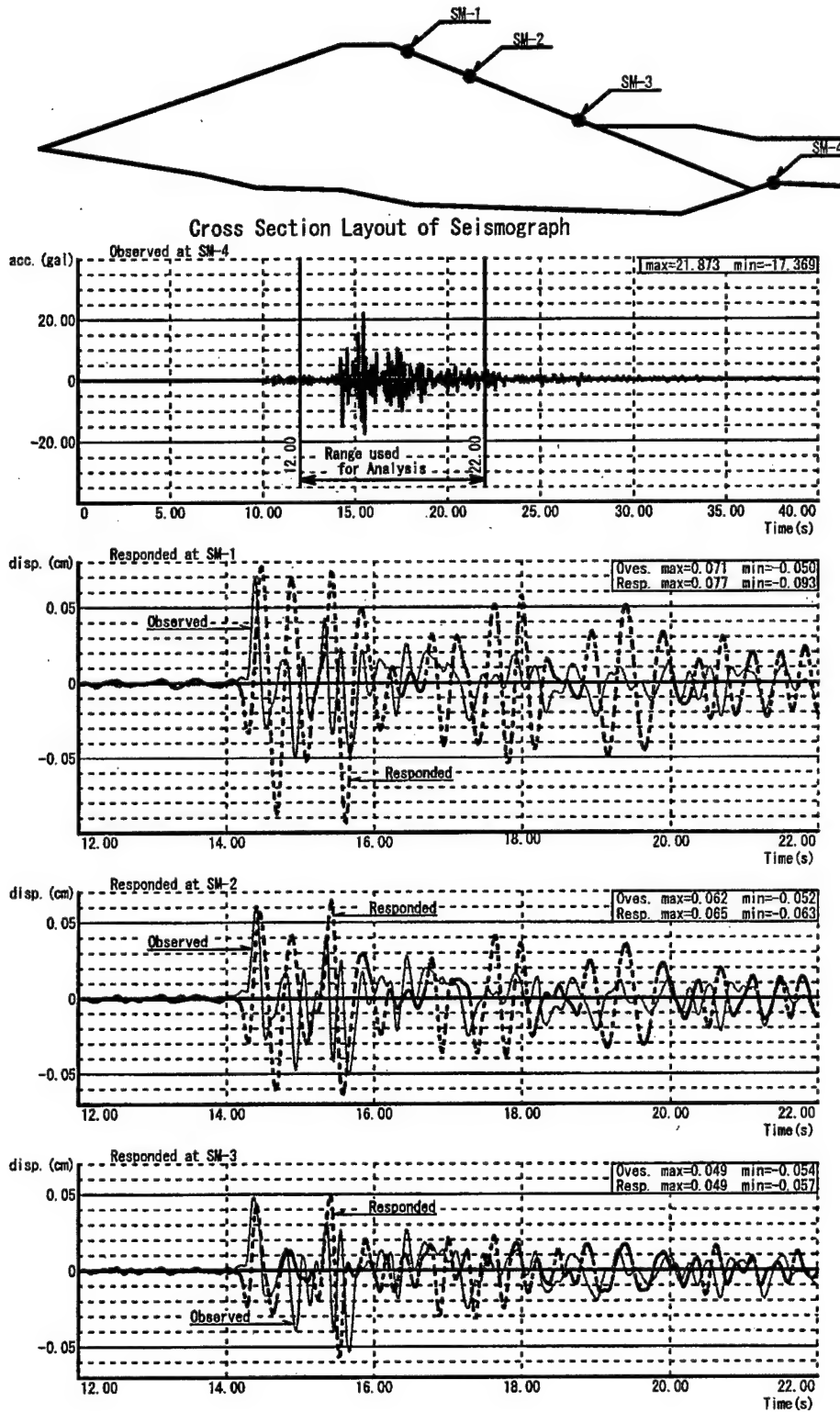


Fig.-7 Observed and Calculated Displacement

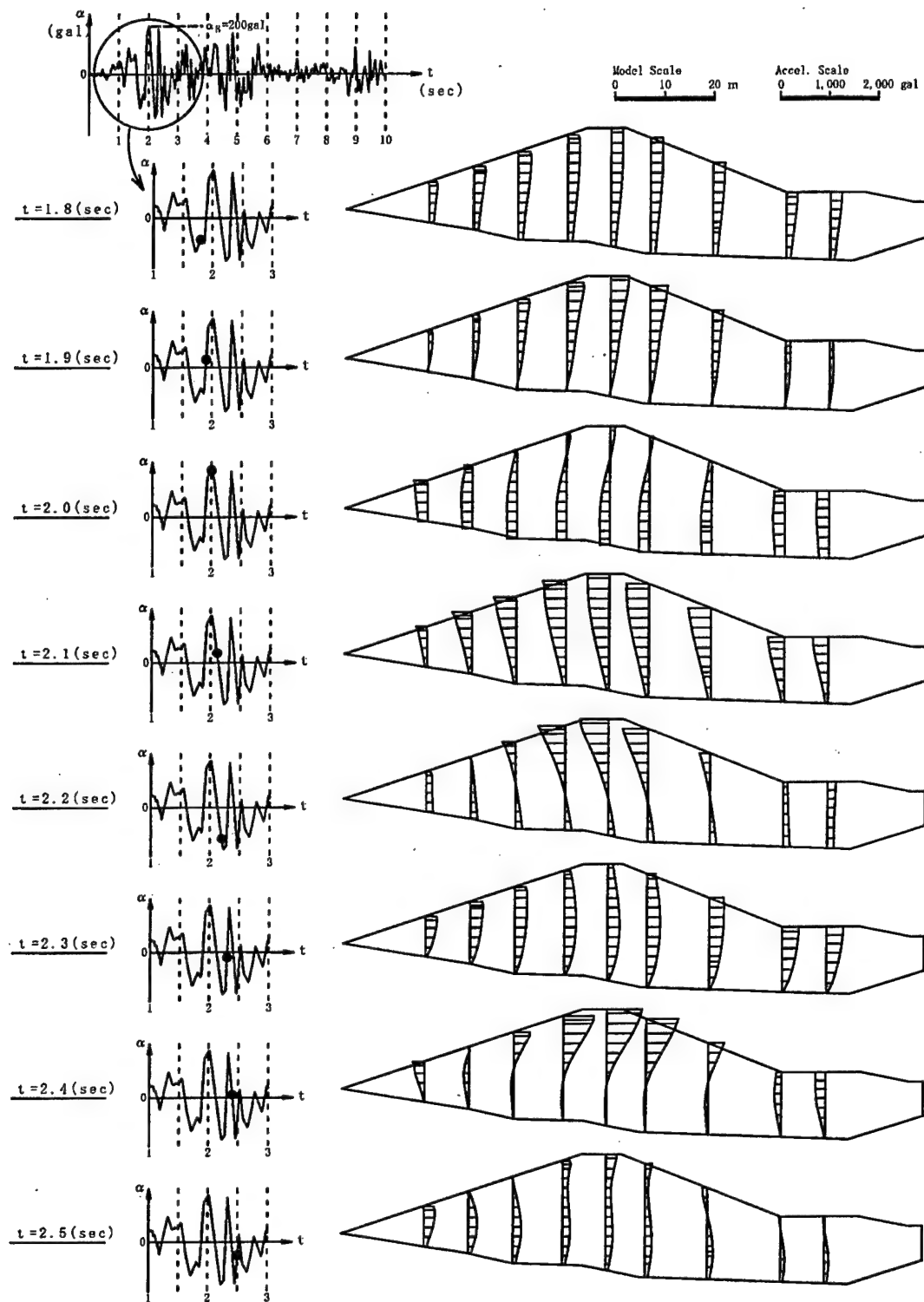


Fig.-8 Horizontal Acceleration mode (El Centro:  $\alpha_B = 200\text{gals}$ )

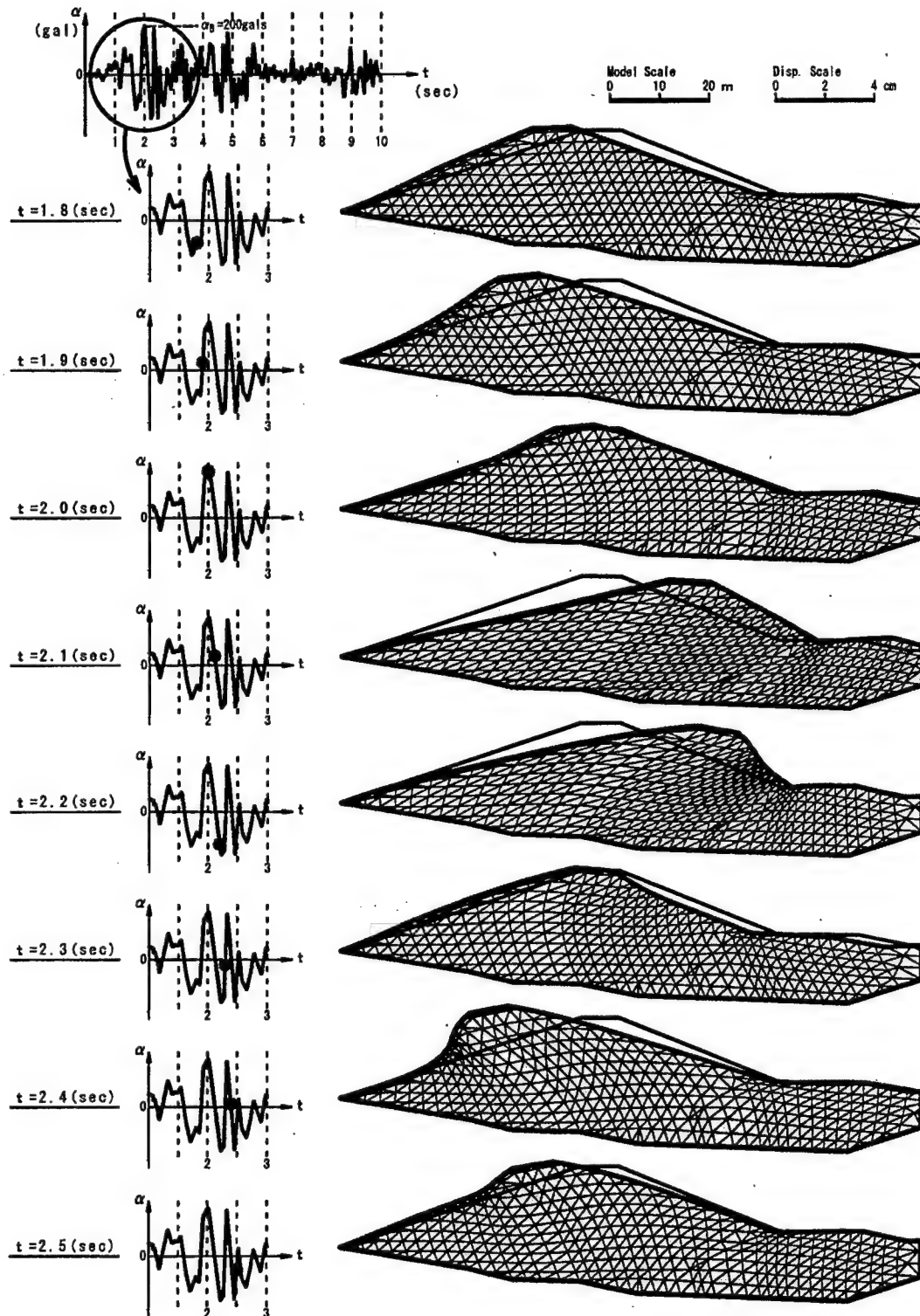


Fig-9 Deformation mode (El Centro:  $\alpha_B = 200\text{gals}$ )

## (2) Response analysis

The response analysis of dam body was carried out in 2 cases using Elcentro earthquake wave; ① acceleration at the bottom of dam  $\alpha_B=85$  gal, and ② with  $\alpha_B=200$  gal. The former ① is for discussion on and to clarify the cause of cracks developed on asphalt facing due to the earthquake and the latter ② is for discussion of damage when design earthquake intensity ( $K=0.2g$ ) is acted upon the dam body as described later on, and for development of asphalt facing material that is sufficiently safe for such an earthquake.

## (3) The result of analysis

Responded acceleration mode at the time of a quake is shown on Fig.-8 and its deformation mode is shown on Fig.-9. Exfoliation between the asphalt pavement and the surface of the dam body does not take place at the time of earthquake. If the pavement is assumed to quake along with the dam body, the pavement is subject to the action of cyclic stress of compression and tension. If the amount of strain under the compression is defined as indicated on Fig.-10, and this value is called for along the dam slope, then, Fig.-11 is obtained.

$$\begin{pmatrix} X_1 \\ Y_1 \end{pmatrix} = \begin{pmatrix} \cos \alpha & \sin \alpha \\ -\sin \alpha & \cos \alpha \end{pmatrix} \begin{pmatrix} u_1 \\ v_1 \end{pmatrix} \quad \epsilon_d = \frac{X_1 - X_2}{L}$$

$\epsilon_d$ : Dynamic Strain  
 $u$ : Horizontal displacement  
 $v$ : Vertical displacement  
 $X$ : Parallel displacement  
 $Y$ : Normal displacement  
 $L$ : Length of nodalpoints

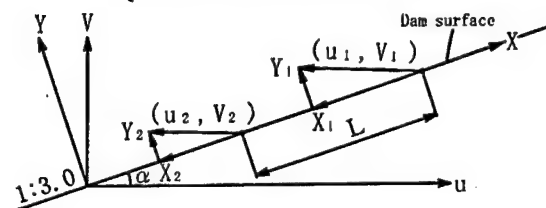


Fig.-10 Definition of Dynamic Strain along Dam Surface

As is made clear on the same Fig., the maximum strain is generated at a portion about 80% from bottom and its values are: in case of  $\alpha_B=85$  gal is  $\epsilon_{d \max.} \doteq 7.1 \times 10^{-4}$  and in case of  $\alpha_B=200$  gal is  $\epsilon_{d \max.} \doteq 1.9 \times 10^{-3}$ . Also, where responded acceleration become maximum near the dam crest;  $\epsilon_{d \max.} \doteq 4 \times 10^{-4}$  and  $1 \times 10^{-3}$  respectively.

## 4.DYNAMIC CHARACTER OF ASPHALT FACING

From the result of earthquake response analysis on dam body, a cyclic stress toward the direction of dam slope is generated on the asphalt facing of dam slope. To clarify dynamic character of the asphalt facing when such kind of cyclic stress is acted on the facing, undisturbed samples were collected from the slope pavement and from the bottom and dynamic compression test was performed on these samples.

### (1) Sampling of specimen

As shown on Fig.-2, (a) and (b), the structure of asphalt facing is consisted of 2 layers of dense asphalt on the surface layers. Sampling was done individually from the 2 upper layers in the direction of layer construction. Samples were collected not only on the slope but as similarly on the bottom also.



Photo.-3 Failure of Specimen by Cyclic Stress

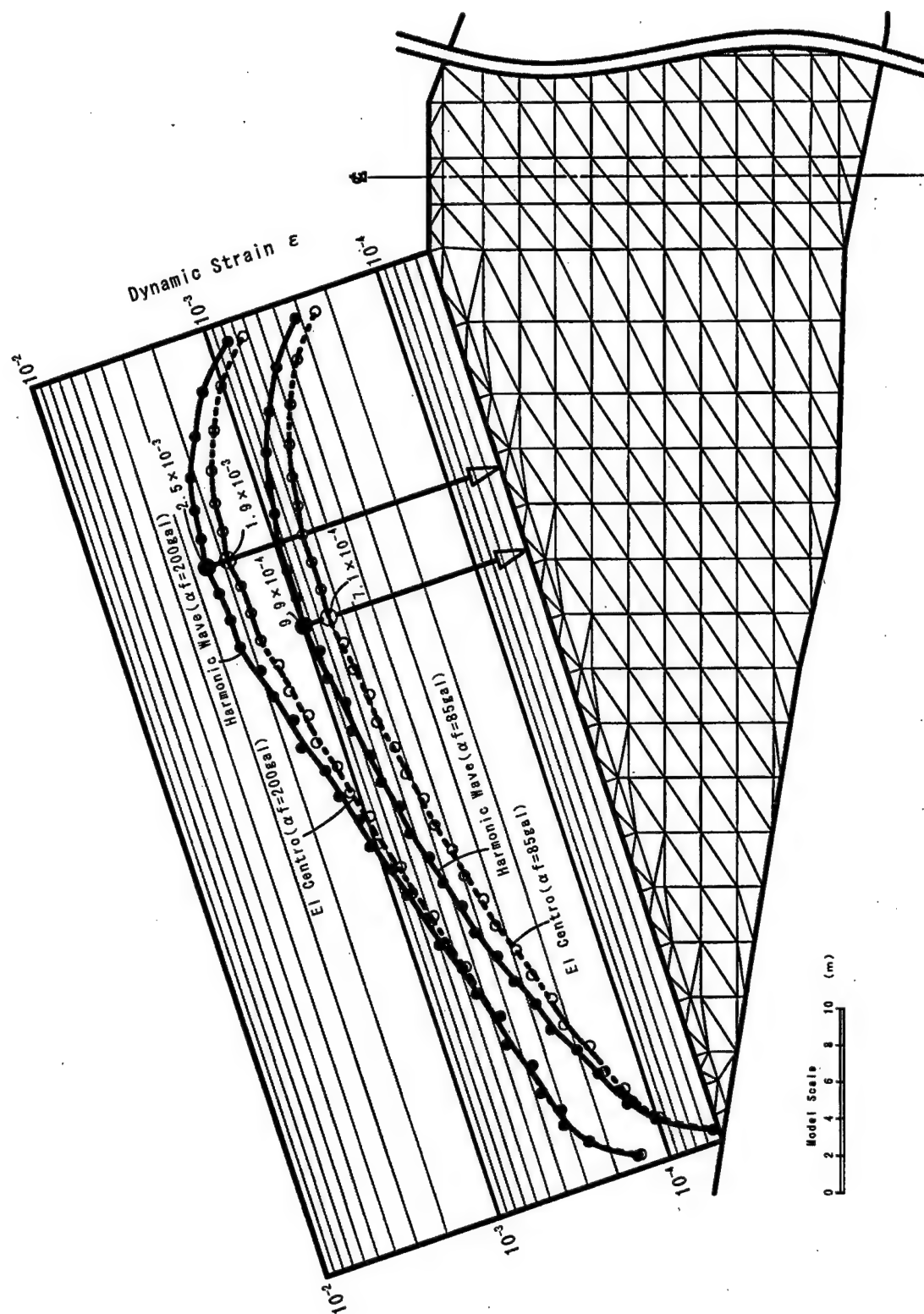


Fig.-11 Distribution of Dynamic Strain along Dam Surface



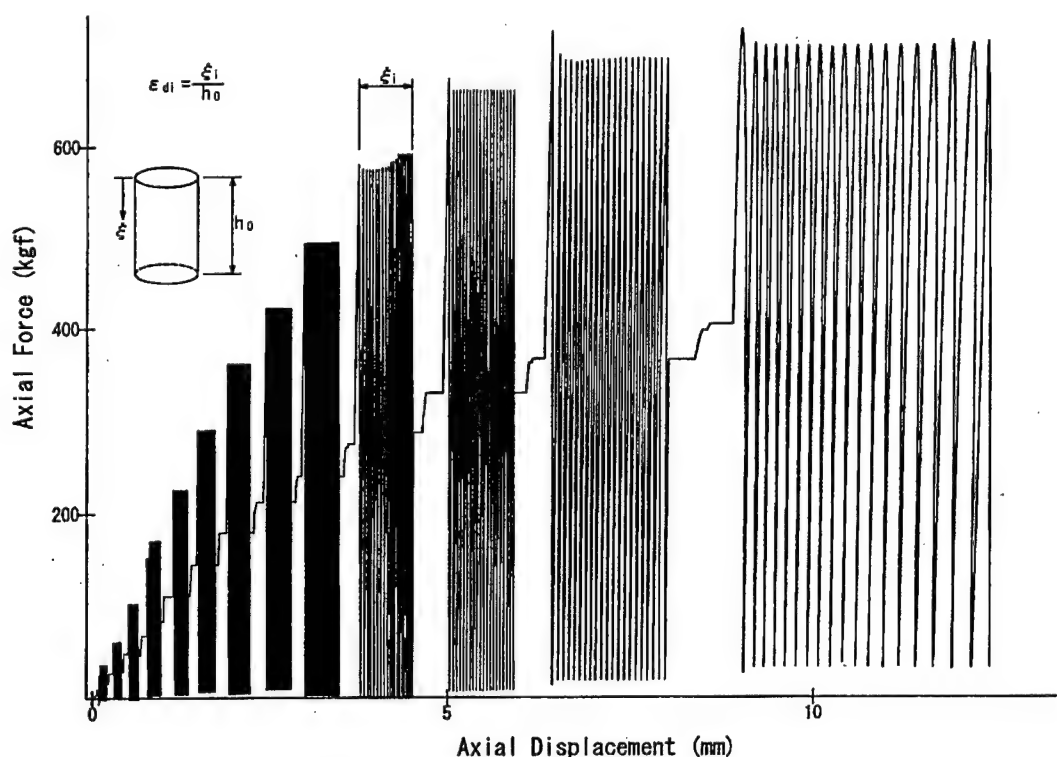


Fig.-12 Dynamic Test on Asphalt Specimen

## (2) Experimentation and its result

Experimentation was carried out by using dynamic compression testing apparatus. On the test, a constant axial stress was given to the samples in stages and harmonic wave of 20 times each under each stress were given to the samples until they reach breaking point. The result of experiment on Fig.-12 and the sample at the time of breakage on Photograph-3 are shown as one example of respective experimentation. Also, as shown on the same Fig., it was defined that the amount of deformation caused by the cyclic loading of 20 times under each stress was formulated and expressed as strain ( $\epsilon_i/h_0$ ), and was defined as 『Dynamic Strain ( $\epsilon_{di}$ )』 which has given this value under that particular stress. One example of the result of experiments that has been rearranged in relation to stress and dynamic strain is shown on Fig.-13. Here, as is shown on this Fig., that in relation to stress and dynamic

strain, the crossing point of initial straight line and stress value at the time of destruction is herewith defined as 『Dynamic Yield Strain』.

It is a known fact that the relation between stress and strain of asphalt concrete under the static condition is governed by the temperature. It is anticipated that under the dynamic condition, the similar tendency might take place also. For this reason, this experiment was undertaken with 2 conditions of temperature, one at the 16°C that is considered as general standard and another at 6 °C that is outside air temperature assumed for at the time of earthquake occurrence. These result of experiments are shown in relation with dynamic yield strain and temperature on Fig.-14, and it represents that the change in temperature of 10°C makes change in the value of yield strain by one order of digit.



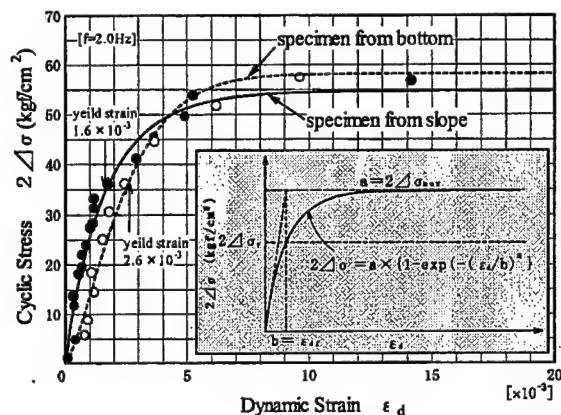


Fig. 13 Relation between  $\epsilon_d$  and  $2\Delta\sigma$

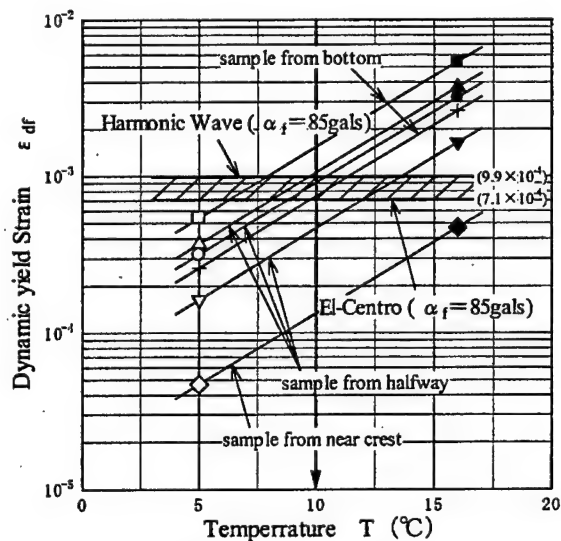


Fig. 14 Failure Strain of Specimen by Cyclic Stress

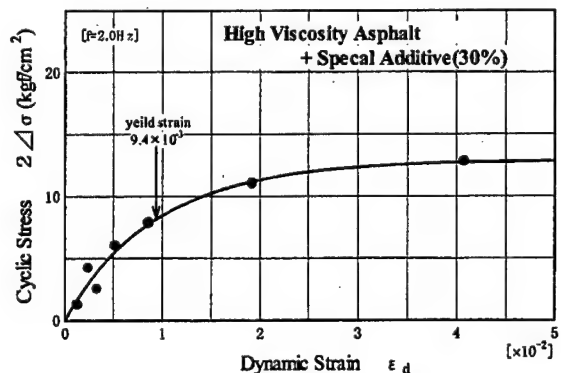


Fig. 15 Relation between  $\epsilon_d$  and  $2\Delta\sigma$

## 5.SOME CONSIDERATION ON DAMAGE FOR ASPHALT FACING

The asphalt facing of the Higashifuji Dam was damaged by a medium-scale Earthquake. The following measures were taken in order to clarify the cause of such happening:

- ① Earthquake response analysis was conducted on the dam body to make an assumption on the amount of strain of asphalt facing;
- ② Dynamic yield strain of the asphalt facing was specified.

When acceleration at the bottom was assumed to be  $\alpha_B = 85$  gal, a maximum strain of the facing, as has been described already, is generated at the part of 80% from the bottom and is valued as  $\epsilon_{dmax} \approx 7.1 \times 10^{-3}$  and in the vicinity of dam crest,  $\epsilon_{dc} \approx 4 \times 10^{-4}$ .

On the other hand, the result of dynamic compression test on the samples collected from the asphalt facing, when temperature at the time of earthquake occurrence is assumed to be around  $10^\circ\text{C}$ , the yield strains will be  $\epsilon_{df} \approx 1.5 \times 10^{-4}$  in the vicinity of dam crest,  $\epsilon_{df} \approx (5 \sim 9) \times 10^{-4}$  at the point halfway up the slope, and  $\epsilon_{df} \approx 7 \times 10^{-4} \sim 1.5 \times 10^{-3}$  at the bottom. Relationship of both has been shown on Fig. 14 and they are indicating that the amount of strain on the asphalt facing at the time of earthquake is exceeding the allowable limit of yield strains at the halfway up the dam slope and at the dam crest.

On the basis of the foregoing descriptions, it is understandable that cracking damage on the asphalt facing caused by an earthquake could possibly be judged and evaluated by the above described method.

## 6.REPAIR OF ASPHALT FACING

The asphalt facing of the Higashifuji dam was damaged by a medium-scale Earthquake. For the repair work, a facing material that

can withstand fully the design earthquake intensity for this dam must be used. Facing material must be fully safe for the amount of strain that is to be estimated through response analysis of the dam body which is using the earthquake wave equivalent of design earthquake intensity ( $K=0.2g$ ). For this earthquake response analysis, Elcentro earthquake wave has been used and maximum acceleration has been modified to 200 gal and used.

This result of analysis is shown on Fig.-11, which makes it clear that a biggest strain is generated at the point halfway up the slope with the calculation of  $\epsilon_{dmax}=2.5 \times 10^{-3}$ . At this point, as design strain amount ( $\epsilon_{da}$ ),  $\epsilon_{da}=3 \times \epsilon_{dmax} \doteq 8 \times 10^{-3}$  has been established and it was determined to develop a material with sufficient ductility ( $F_s=3$ ) withstand this strain.

As a result of dynamic compression test conducted for various mixture of asphalt material, it was found that the blending 30% of a special additive with the high viscosity asphalt mixture will increase its yield strain largely to  $\epsilon_{da} \doteq 9 \times 10^{-3}$  and will satisfy the above described  $\epsilon_{da}$  a fully. Stress and strain relation of this material under  $10^\circ\text{C}$  is shown on Fig.-15. Further, as a result of slope flow test for this material under the condition of  $10^\circ\text{C}$  and  $16^\circ\text{C}$ , no flow whatsoever was recognized and, thereby, it was confirmed that this material is suitable for repair works of this dam.

## 7.ACKNOWLEDGMENT

Repair work on Higashifuji dam is scheduled to be started from the end of the year 2002. It has been considered that the safety of the asphalt facing on the earth dam against earthquake was high. However, the facing itself was damaged by a medium-scale earthquake as experienced by this dam. On

this paper, the strain on the asphalt facing was noticed and cause of destruction was discussed. As a result thereof, it has become known that the asphalt facing destructs comparatively easy by the strain that was caused by the earthquake. For this reason, a material with the asphalt mixture with rich ductility which will withstand a large-scale earthquake has been developed for the use of repair work. This series of research works are first trial of this kind and may be a subject of criticism from every direction. Your comments and opinions are welcomed always.

## REFERENCE

- 1) Shizuoka Prefecture (in Japanese), "Design Report of Higashi Fuji Dam", 1970,3
- 2) Shizuoka Prefecture (in Japanese), "Seismic Record of Higashi Fuji Dam", 1996,5
- 3) Yoshio OHNE, "Design and construction of Dam", Technology Report of Aichi Institute of Technology.,2000,4
- 4) Shizuoka Prefecture (in Japanese), "Investigation of Disaster on Higashi Fuji Dam", 1996,6.
- 5) Yoshio OHNE et al. "Fundamental Study on Earthquake Resistant Design of Fill-Type Dam", Proceeding of The Japan Society of Civil Engineers., 1983,11.

## Evaluating Liquefaction Resistance at High Overburden Stresses

by

Ross W. Boulanger<sup>1</sup>

### ABSTRACT

This workshop paper summarizes a re-evaluation (Boulanger 2003a,b) of three factors that affect the estimation of liquefaction resistance for clean sands under high overburden stresses and sloping ground conditions (e.g., within a large earth dam): the relations used to correct penetration resistances to an equivalent overburden stress of one atmosphere (i.e.,  $C_N$ ), the adjustment factor for the effects of overburden stress on cyclic resistance ratio (i.e.,  $K_\sigma$ ), and the adjustment factor for the effects of static shear stresses on cyclic resistance ratio (i.e.,  $K_\alpha$ ). These three effects have been investigated in a number of ways and a number of different relations exist for each of them. A relative state parameter index ( $\xi_R$ ) is used to develop a consistent theoretical framework for interrelating the  $C_N$ ,  $K_\sigma$ , and  $K_\alpha$  factors. This re-evaluation shows that  $C_N$  and  $K_\sigma$  are inter-related through the sand properties and state in ways that have compensating effects on the predicted cyclic resistance. Modified relations for practice are provided that offer significant economy over some current methods when applied to very high  $\sigma_v'$  levels. Similarly, a simple method is provided for quantifying the effect of overburden stress on  $K_\alpha$  relations.

**KEYWORDS:** Liquefaction, embankment dams, overburden stress, static shear stress.

### 1. INTRODUCTION

Two important factors in the semi-empirical evaluation of liquefaction resistance at high effective overburden stresses ( $\sigma_v'$ ) are the correction of CPT and SPT penetration resistances to an equivalent overburden stress of one atmosphere (i.e.,  $C_N$ ) and the adjustment

factor for the effect of overburden stress on cyclic resistance ratio (i.e.,  $K_\sigma$ ). Overburden stress also affects the adjustment factor for the effect of static shear stress on cyclic resistance ratio (i.e.,  $K_\alpha$ ), which can be important for earth embankment dams. The  $K_\sigma$  and  $K_\alpha$  factors were introduced by Seed (1983) and are used as:

$$CRR = CRR_{\sigma=1, \alpha=0} K_\alpha K_\sigma \quad (1)$$

where  $\alpha$  is the static horizontal shear stress ratio ( $\alpha = \tau_s / \sigma_v'$ ),  $\tau_s$  is the static horizontal shear stress,  $\sigma_v'$  is the vertical effective consolidation stress,  $CRR_{\sigma=1, \alpha=0}$  is the cyclic resistance ratio for  $\sigma_v' / P_a = 1$  and  $\alpha = 0$  as obtained through a semi-empirical relation for the earthquake magnitude and other conditions under consideration, and  $P_a$  is atmospheric pressure.

This workshop paper summarizes a re-evaluation of  $C_N$ ,  $K_\sigma$ , and  $K_\alpha$  relations for clean sands with specific attention to the high overburden stress levels pertinent to large dams. The details of this re-evaluation are provided in two forthcoming publications:  $K_\alpha$  relations in Boulanger (2003a), and  $K_\sigma$  and  $C_N$  relations in Boulanger (2003b). Note that this workshop paper has been condensed from a preprint version that contained considerably more detail.  $C_N$  relations were re-evaluated based on: (1) a cone penetration theory that has been validated against calibration chamber tests data for  $\sigma_v' / P_a$  up to about 7, and (2) a nonlinear weighted regression analysis of previously published SPT calibration chamber test data for  $\sigma_v' / P_a$  up to about 5.5. The theoretical solutions for  $C_N$  as a function of relative density ( $D_R$ ) fit the SPT and CPT data well, and were used to extend these relations to larger  $\sigma_v' / P_a$  values. The trends in the published  $C_N$ ,  $K_\sigma$  and  $K_\alpha$  relations were

<sup>1</sup> Department of Civil & Environmental Engineering, University of California, Davis, CA 95616 (USA).

shown to be consistent with critical state concepts. Subsequently, a consistent theoretical framework for inter-relating the  $C_N$ ,  $K_o$ , and  $K_\alpha$  relations for clean sands was developed.

## 2. PENETRATION RESISTANCE

### 2.1. Solutions for CPT Tip Resistance from Penetration Theory

Salgado et al. (1997a) performed numerical analyses of  $q_c$  for about 400 calibration chamber tests on clean sands. Details of the theory and its implementation are presented in Salgado et al. (1997a). The numerical analyses were shown to provide excellent agreement with the experimental data, providing reasonable validation of the theory for predominantly silica sands of medium compressibility.

Solutions for  $q_c$  as a function of  $D_R$ ,  $\sigma'_v$ , and the lateral earth pressure coefficient at rest ( $K_o$ ) were subsequently presented by Salgado et al. (1997b) for typical, upper bound, and lower bound sets of soil properties. Those solutions are closely approximated as (Boulanger 2003b):

$$\frac{q_c}{P_a} = C_0 C_I \left( \frac{\sigma'_v}{P_a} \right)^m \left( \frac{K_o}{0.45} \right)^{m-0.077} \quad (2a)$$

$$m = 0.7836 - 0.5208 D_R \quad (2b)$$

$$C_0 = 25.7 + 39.7 D_R + 212.3 D_R^2 \quad (2c)$$

$$\begin{aligned} C_I &= 1.0 \text{ typical soil property set} \\ &0.64 \text{ lower bound property set} \\ &1.55 \text{ upper bound property set} \end{aligned} \quad (2d)$$

with  $K_o=0.45$  being considered as reasonable for most normally consolidated sands.

### 2.2. Overburden Correction for CPT & SPT

The correction (or normalization) of  $q_c$  to an effective overburden stress of 1  $P_a$  is performed as:

$$q_{cI} = C_N q_c \quad (3)$$

which from (2) becomes:

$$C_N = \left( \frac{P_a}{\sigma'_v} \right)^m \quad (4)$$

The  $C_N$  relation in (4), as plotted in Fig. 1, is independent of the material property set (as represented by  $C_I$ ) and matches the widely used relation by Liao and Whitman (1985):

$$C_N = \left( \frac{P_a}{\sigma'_v} \right)^{0.5} \quad (5)$$

at a  $D_R$  of 54%.

The dependency of  $C_N$  on  $D_R$  is similar to that obtained for the SPT calibration chamber tests on four sands by Marcuson and Bieganousky (1977a,b) with  $\sigma'_v/P_a = 0.68, 2.72$ , and  $5.44$ . A weighted nonlinear regression analysis of that data set showed that the  $C_N$  expression in (4) appears to provide a reasonable approximation for both the CPT and SPT data (Boulanger 2003b).

### 2.3 A Corresponding Relative State Parameter Index

A key feature of the CPT penetration theory by Salgado et al. (1997a) is that the peak friction and dilatancy angles are based on Bolton's (1986) relative dilatancy index ( $I_{RD}$ ):

$$I_{RD} = D_R \left( Q - \ln \frac{100 p'}{P_a} \right) - R \quad (6)$$

where  $p'$  = mean effective normal stress,  $Q$  = an empirical constant, and  $R$  = a fitting parameter that was taken as 1.0 for the test data that was evaluated. The value of  $Q$  determines the value of  $p'$  at which dilatancy is suppressed (i.e.,  $I_{RD} = 0$ ). Bolton indicated that  $Q$  depends on the grain type, with  $Q \approx 10$  for quartz and feldspar, 8 for limestone, 7 for anthracite, and 5.5 for chalk.

The  $I_{RD}$  index is necessarily empirical in nature, but has a functional form that is reasonable for describing the combined effects of relative density and confining stress on the dilatancy or volume change characteristics of clean sands.

Boulanger (2003a) used the  $I_{RD}$  relation in (6) to derive an equivalent state parameter ( $\xi$ ).  $\xi$  is the difference between the current void ratio and the critical state void ratio for the current value of  $p'$  (Been and Jeffries 1985). The definition of  $\xi$  is shown on Fig. 2, along with the critical state lines produced from the  $I_{RD}$  relation with  $Q=9$ , 10, and 11 (i.e., critical state corresponds to  $I_{RD} = 0$ ). The curvature of the critical state line reflects the onset of significant particle crushing, and its position is controlled by the parameter  $Q$ .  $\xi$  can be further normalized by the difference in the maximum and minimum void ratios ( $e_{max} - e_{min}$ ) to arrive at a relative state parameter ( $\xi_R$ ) that provides better correlations to the shear behavior of sand (Konrad 1988). This leads to (Boulanger 2003a):

$$\xi_R = \frac{1}{Q - \ln\left(\frac{100p'}{P_a}\right)} - D_R \quad (7)$$

where this  $\xi_R$  is an empirical index that has a functional form consistent with critical state concepts, just like the empirical  $I_{RD}$  index from which it is derived. The advantage of  $\xi_R$  for this study is that it provides a consistent link to the penetration theory of Salgado et al. (1997a).

### 3. EVALUATING CRR- $\xi_R$ RELATIONS FOR RECONSTITUTED SPECIMENS

The effect of  $D_R$  and  $\sigma_v'/P_a$  on the cyclic resistance ratio (CRR) of clean sand would intuitively be related to the sand's position relative to critical state or some other reference state. Relating cyclic behavior to a critical state framework in engineering practice is hampered by the difficulty in defining an appropriate critical state or other reference line without recourse to advanced sampling and testing of representative field samples. Consequently, the  $\xi_R$  index was

evaluated as a practical substitute for representing the combined influence of  $D_R$  and  $\sigma_v'$  on CRR.

The CRR -  $\xi_R$  relation is illustrated by the laboratory tests on reconstituted clean Fraser Delta sand by Vaid and Sivathayalan (1996) and Vaid and Thomas (1995). The data includes simple shear and triaxial tests on specimens at  $D_R$  of 31 to 72% and consolidation stresses ( $\sigma_v'/P_a$  for simple shear,  $\sigma_{3C}'/P_a$  for the isotropically consolidated triaxial tests) of 0.5 to 4. The simple shear and triaxial test data collapse onto single CRR- $\xi_R$  relations, with the quality of fit being better for  $Q=9$  than for  $Q=10$ , as shown in Fig. 3. In either case, these data suggest that  $\xi_R$  can reasonably represent the combined effects of  $D_R$  and  $\sigma_v'$  on CRR.

A CRR- $\xi_R$  relation has a unique corresponding  $K_\sigma$  relation that can be expressed as:

$$K_\sigma = \frac{CRR(\xi_R)}{CRR(\xi_{R1})} \quad (8)$$

where  $\xi_{R1}$  = value of  $\xi_R$  for the same  $D_R$  at  $\sigma_v'/P_a = 1$ . The  $K_\sigma$  curves derived in this manner for reconstituted Fraser Delta sand are in excellent agreement with the curves derived directly from the experimental data, as expected. These data show that  $K_\sigma$  is dependent on  $D_R$ , with  $K_\sigma$  values at  $\sigma_v'/P_a > 1$  becoming smaller with increasing  $D_R$ , and that  $K_\sigma$  is different for simple shear versus triaxial loading conditions. The results of the simple shear tests are shown on Fig. 4 along with other data and  $K_\sigma$  relations from Seed and Harder (1990), Harder and Boulanger (1997), and Hynes and Olsen (1998). The wide scatter in these data and relations may be due to many factors, including the differences between reconstituted specimens and field samples.

### 4. DERIVING CRR- $\xi_R$ RELATIONS FOR IN SITU CONDITIONS

CRR- $\xi_R$  relations may be significantly different for in situ conditions than for laboratory tests on freshly reconstituted specimens because CRR is

strongly affected by factors such as fabric (deposition), age, stress-strain history, and cementation. Furthermore, laboratory test data are always subject to certain limitations, such as the unavoidable effects of boundary conditions.

CRR- $\xi_R$  relations are consequently derived from the penetration test-based semi-empirical liquefaction relations, thereby retaining consistency with the field data and the eventual application of the findings to practice. For simplicity, it is assumed that the semi-empirical liquefaction correlations pertain exactly to  $\sigma_v'/P_a = 1$  with  $K_o = 0.45$ . Two CRR- $q_{c1}$  correlations for clean sands in  $M=7.5$  earthquakes are shown in Fig. 5 (Robertson and Wride 1998; Idriss 1999, personal communication). These CRR- $q_{c1}$  relations were mapped onto corresponding CRR- $\xi_R$  relations by mapping  $q_{c1}$  to  $\xi_R$ . This mapping only requires the selection of a  $C_1$  value for (2), after which each  $q_{c1}$  value corresponds to a unique  $D_R$  value, which in turn produces a unique  $\xi_R$  value (with  $Q=10$  for consistency with the CPT analyses). For calibration to the semi-empirical liquefaction correlations,  $C_1$  was based on the value of  $D_R$  that corresponds to a CRR of 0.6 (roughly the limit at which liquefaction might be triggered) when  $\sigma_v'/P_a \approx 1$  (called  $D_{R,lim}$  hereafter). CPT derivations are presented for  $C_1 = 1.0$  and  $C_1 = 0.817$ , which correspond to  $D_{R,lim}$  of 75% and 85% at  $q_{c1}/P_a = 174$ , respectively. For SPT tests, a common correlation is:

$$\frac{(N_1)_{60}}{(D_R)^2} = C_d \quad (9)$$

SPT derivations are presented for  $C_d = 53.3$  and 41.5, which correspond to  $D_{R,lim}$  of 75% and 85% at  $(N_1)_{60} = 30$ , respectively.

Three of the resulting CRR- $\xi_R$  relations, covering a range of  $D_{R,lim}$  are shown in Fig. 6. The differences in these relations are due to both the choice of  $D_{R,lim}$  value and the shapes of the underlying semi-empirical liquefaction correlations. These CRR- $\xi_R$  relations can be used to derive a corresponding consistent set of

$K_\sigma$  relations, as will be illustrated in the following section.

## 5. EXTENDING THE FIELD CRR- $\xi_R$ RELATIONS TO HIGH OVERBURDEN STRESSES

The effect of overburden stress on a liquefaction analysis is illustrated by tracking its effects on both penetration resistance and CRR. The effect of  $\sigma_v'$  on  $q_c$  is accounted for using the relations in (2) and (3), such that the corresponding  $q_{c1}$  values are properly independent of  $\sigma_v'$ ; Note that if  $C_N$  is truly dependent on  $D_R$ , then the use of a  $D_R$ -independent  $C_N$  relation [such as in (5)] would result in calculated  $q_{c1}$  values that are not actually independent of  $\sigma_v'$ . The effect of  $\sigma_v'$  on CRR is accounted for by assuming that the CRR- $\xi_R$  relation is applicable for all values of  $\sigma_v'$  (as was previously shown to be an acceptable approximation in Fig. 3). Thus, for clean sand at a given  $D_R$ , a change in  $\sigma_v'$  causes a change in  $\xi_R$  [via (7)], which results in a change in CRR (Fig. 6). The combined effects of  $\sigma_v'$  are illustrated in Fig. 7 showing how the Idriss (1999) CRR- $q_{c1}$  relation would be modified for  $\sigma_v'/P_a = 0.25, 4$ , and 10 for the case with  $C_1 = 1.0$ . Very similar results are obtained with  $C_1 = 0.817$  because the  $C_1$  parameter affects both the derivation of the CRR- $\xi_R$  relation and its mapping back onto CRR- $q_{c1}$  plot for different overburden stresses. Increasing  $\sigma_v'$  not only causes a decrease in CRR for a given  $q_{c1}$  (shifting the curves downwards), but also increases the limit at which triggering can develop (shifting the curves to the right). This increase in  $q_{c1,lim}$  (where CRR exceeds 0.6) with  $\sigma_v'$  occurs because the limiting state at which triggering of liquefaction can occur is actually tied to a limiting value of  $\xi_R$ . With  $\xi_{R,lim}$  being a constant, it follows that an increase in  $\sigma_v'$  causes an increase in both  $D_{R,lim}$  and  $q_{c1,lim}$ .

The CRR- $q_{c1}$ - $\sigma_v'$  relations shown in Fig. 7 can also be expressed in terms of implied  $K_\sigma$  relations as:

$$K_\sigma = \frac{CRR}{CRR_i} \quad (10)$$



where  $CRR_1$  = the CRR at  $\sigma'_v/P_a = 1$  for the same  $q_{c1}$  value. Note that the identical  $K_\sigma$  relations can also be obtained directly from the  $CRR-\xi_R$  relation using (8).  $K_\sigma$  relations derived in this way are illustrated in Fig. 8 for  $C_1=1.0$  and with the Robertson and Wride (1998) and Idriss (1999) baseline correlations. The resulting  $K_\sigma$  relations are dependent on  $D_R$ , with  $K_\sigma$  values at  $\sigma'_v/P_a > 1$  becoming smaller with increasing  $D_R$ . Note that  $K_\sigma$  values cannot be derived if  $CRR_1$  is undefined, which happens for  $D_R > 71\%$  in the first case and  $D_R > 75\%$  in the second case. The relative positions of the  $K_\sigma$  curves are directly related to the slopes of the  $CRR-q_{c1}$  correlations and the corresponding  $CRR-\xi_R$  curves. These results simply illustrate the fact that  $CRR-q_{c1}$  [or  $CRR-(N_1)_{60}$ ] and  $K_\sigma$  relations are not uncoupled, but rather there is a direct correspondence between them that depends on the material properties. In addition, the  $K_\sigma$  curves in Fig. 8 are in reasonable agreement with the available experimental data (e.g., Fig. 4), given the scatter that is undoubtedly related to numerous factors such as grain characteristics, fabric, age, cementation, and stress-strain history.

Lastly, it is worth noting that the  $\xi_R$ -based procedure for calculating CRR, as described in this section, does not explicitly involve use of a  $K_\sigma$  factor. The  $\xi_R$ -based procedure first requires an estimate of  $D_R$  from the measured penetration resistance, perhaps with the interim step of estimating the corrected  $q_{c1}$  or  $(N_1)_{60}$  value. Either way, this is an iterative process because the penetration resistances, measured or corrected, are nonlinearly dependent on  $D_R$ . Once  $D_R$  has been obtained,  $\xi_R$  would be calculated using (7) and CRR would be calculated via the  $CRR-\xi_R$  relation that corresponds to the desired semi-empirical liquefaction correlation.

## 6. SIMPLIFIED IMPLEMENTATION & COMPARISON TO PRACTICE

### 6.1. Method A: Representing Current Practice

First, a reasonable adaptation of current practice (hereafter called Method A) is presented for subsequent comparisons. The measured penetration resistance will be corrected using the  $C_N$  relation by Liao and Whitman (1986) in (5) and the  $CRR_1$  will be multiplied by the  $K_\sigma$  relation proposed by Harder and Boulanger (1997), which can be closely approximated as:

$$K_\sigma = 1 - C_\sigma \ln \left( \frac{\sigma'_v}{P_a} \right) \quad (11)$$

with  $C_\sigma = 0.185$ .

### 6.2 Method B: Simple Implementation of $\xi_R$ -based Findings

The  $\xi_R$ -based approach requires an iterative estimation of  $D_R$  that, while not mechanistically difficult, does add another element of complexity to the liquefaction analysis. Consequently, a simplified approximation (hereafter called Method B) that uses  $D_R$ -independent  $C_N$  and  $K_\sigma$  relations is also introduced. The key observation that makes this simplification possible is that both  $C_N$  and  $K_\sigma$  are actually dependent on  $D_R$ , but in ways that produce opposing effects on the predicted CRR. For example, at  $\sigma'_v/P_a > 1$ , an increase in  $D_R$  causes both an increase in  $C_N$  and a decrease in  $K_\sigma$ . A single  $D_R$ -independent  $C_N$  relation was therefore derived that tracked the limiting condition at which liquefaction can be triggered (i.e.,  $\xi_{R,lim}$ ). This relation can be reasonably approximated as:

$$C_N = \left( \frac{P_a}{\sigma'_v} \right)^{m_{lim}} \quad (12)$$

where  $m_{lim}$  depends on the baseline liquefaction correlation and the parameters that relate penetration resistance to  $D_R$  (i.e.,  $C_1$  for CPT and  $C_d$  for SPT). Values of  $m_{lim}$  are summarized in Boulanger (2003b) for the two CPT liquefaction correlations (with  $C_1=0.817$  and  $1.0$ ) and the one SPT liquefaction correlation (with  $C_d=41.5$  and  $53.3$ ). Values for  $m_{lim}$  varied from  $0.37$  to  $0.46$

over the entire range of possibilities considered. Note that  $m$  and  $m_{lim}$  are not equal for equal values of  $D_R$  and  $D_{R,lim}$  respectively, because  $m_{lim}$  tracks the effects of  $\sigma'_v$  on CRR as well as on penetration resistance.

The second part of Method B is the choice of a compatible  $D_R$ -independent  $K_\sigma$  relation. The  $K_\sigma$  relation was assumed to follow (11) because it reasonably approximates the curves in Fig. 8. A single  $C_\sigma$  value was chosen (for the given  $m_{lim}$ ) that predicts CRR values that remain conservative relative to the  $\xi_R$ -based values, but to the minimum extent possible.

A comparison of Method A, Method B ( $m_{lim}=0.43$ ,  $C_\sigma=0.16$ ), and the  $\xi_R$ -based method for  $\sigma'_v/P_a = 1, 4$ , and  $10$  is shown in Fig. 9 for the Idriss (1999) correlation and  $C_1=1$ . Note that CRR is plotted against the measured (not corrected)  $q_c$  value. Method B essentially matches the  $\xi_R$ -based method in this case. Method A is substantially conservative (relative to the other methods) at high  $\sigma'_v$ , particularly in setting the limit of  $q_c$  values for which triggering of liquefaction is considered possible. For example, at depths where  $\sigma'_v/P_a = 10$ , measured  $q_c$  values would have to exceed about  $550P_a$  to be nonliquefiable by Method A, compared to about  $470P_a$  by Method B.

Another comparison of Method A, Method B ( $m_{lim}=0.39$ ,  $C_\sigma=0.21$ ), and the  $\xi_R$ -based method is presented in Fig. 10, this time using the SPT-based correlation of Seed et al. (1985), as modified in Youd et al. (2001), with  $C_d=41.5$ . Method B produces CRR values that are conservative relative to the  $\xi_R$ -based method, but substantially less so than for Method A. At depths where  $\sigma'_v/P_a = 10$ , measured  $N_{60}$  values would have to exceed about 95 to be nonliquefiable by Method A, compared to about 74 by Method B.

The degree of conservatism in Method A relative to Method B (or the  $\xi_R$ -based method) depends on the  $D_{R,lim}$  value as set by  $C_1$  for the CPT and  $C_d$  for the SPT. A higher  $D_{R,lim}$  results

in a smaller  $m_{lim}$  value and hence a greater difference between Methods A and B.

## 7. RELATING $K_\alpha$ TO $\xi_R$

$\xi_R$  was also evaluated as a reasonable index for expressing the combined effects of  $D_R$  and  $\sigma'_v$  on  $K_\alpha$  for clean sands (Boulanger 2003a). Experimental data on clean sands are consistent with critical state concepts (e.g., Vaid and Chern 1985, Mohamad and Dobry 1986), but the difficulty in defining critical or quasi-steady state lines on sufficiently representative field samples has limited the use of critical state theories in practice. The alternative of estimating critical state parameters for any particular sand is seldom attempted, probably because of real and perceived difficulties in making such estimates.

The general trends in  $K_\alpha$  data are well represented by the simple shear test results by Vaid and Finn (1979) and Boulanger et al. (1991), as summarized in Fig. 11. Data are shown for Ottawa sand at  $D_R$  of 50% and 68% under  $\sigma'_{vc}$  of  $2P_a$  (Vaid and Finn 1979) and Sacramento River sand at  $D_R$  of 35% and 55% under  $\sigma'_{vc}$  of  $2P_a$  (Boulanger et al. 1991). These results correspond to 10 cycles of loading and a failure criterion of 3% shear strain. The  $\xi_R$  value for each set of test data is shown beside the corresponding  $K_\alpha$  curve in Fig. 11, based on  $Q=10$  for these uniformly-graded quartzitic sands. There is a consistent progression in  $K_\alpha$  values from less than 1.0 for the loosest sand ( $\xi_R = -0.16$ ) to greater than 1.0 for the densest sand ( $\xi_R = -0.49$ ), with the  $\xi_R$  values simply tracking the progression from  $D_R = 35\%$  to  $68\%$  since all tests were at the same confining stress.

The effects of a large variation in confining stress are best represented by the cyclic triaxial tests on tailings sand by Vaid and Chern (1985). Specimens were prepared at  $D_R=70\%$  and tested under radial consolidation stresses ( $\sigma'_{3c}$ ) of  $2P_a$  and  $16P_a$ ; Most other available studies are limited to confining stresses of  $4P_a$  or less. These results are also shown in Fig. 11, with the values of  $\alpha$  and cyclic resistance re-calculated



herein for the eventual failure plane (Seed et al. 1973). Vaid and Chern (1985) also presented consolidation curves and phase transformation states (or quasi-steady state lines) from monotonic loading tests on the tailings sand and Ottawa sand. These results show that the tailings sand (uniformly-graded, angular quartz and feldspar particles) was much more compressible and generally reached quasi-steady state conditions at much lower  $p'$  values than did the Ottawa sand (uniformly-graded, rounded quartz particles) at similar  $D_R$ . Based on these data, it appears that an appropriate value of  $Q$  would be about 9 (or slightly less) for this tailings sand.

For the  $D_R = 70\%$  tailings sand specimens at  $\sigma'_{3c}/P_a = 2$ , the value of  $\xi_R$  ranges from  $\xi_R = -0.43$  at  $\alpha = 0$  to  $\xi_R = -0.41$  at  $\alpha = 0.34$ , based on  $Q=9$ . The slight variation in  $\xi_R$  with  $\alpha$  reflects the slight change in  $p'$  between these different triaxial testing conditions. The  $\xi_R$  value is only shown for  $\alpha = 0.34$  on Fig. 11). The resulting  $K_\alpha$  relation is intermediate to the tests on Sacramento River sand at  $D_R = 55\%$  and Ottawa sand at  $D_R = 68\%$ , despite its greater  $D_R$  of 70%. The intermediate nature of its  $K_\alpha$  relation is well represented by its  $\xi_R$  value (-0.41) being intermediate to the  $\xi_R$  values for these other tests (-0.36 to -0.49), as shown in Fig. 11.

For the  $D_R = 70\%$  tailings sand specimens at  $\sigma'_{3c}/P_a = 16$ ,  $\xi_R$  ranges from  $\xi_R = -0.08$  at  $\alpha = 0$  to  $\xi_R = 0.05$  at  $\alpha = 0.34$ . This latter  $\xi_R$  value is the only positive value listed on Fig. 11, and corresponds to the lowest  $K_\alpha$  value. Thus, the  $\xi_R$  index correctly identified the  $D_R=70\%$  tailings sand to be more contractive than the  $D_R=35\%$  Sacramento River sand because of the differences in confining stress. It is also noteworthy that these triaxial tests produced  $K_\alpha > 1$  at  $\alpha \approx 0.1$ , which is related to the importance of shear stress reversal on  $K_\alpha$  relations (e.g., see Mohamad and Dobry 1986).

Vaid and Finn (1979) also studied the effect of confining stress on  $K_\alpha$  in their simple shear tests on Ottawa sand. For tests on specimens at  $D_R=50\%$  with  $\alpha = 0.093$ , the value of  $K_\alpha$  was shown to be essentially the same for  $\sigma'_{vc}/P_a$  of 2,

3, or 4. For this range of  $\sigma'_{vc}$ , the corresponding  $\xi_R$  values would only range from -0.28 to -0.31; The change in  $\xi_R$  is small because the critical state line is relatively flat over this stress range (Fig. 2). Thus,  $\xi_R$  provides a rational explanation for why these results showed no perceptible effect of  $\sigma'_{vc}$  on  $K_\alpha$ , although it is noteworthy that the results might have been more sensitive to  $\sigma'_{vc}$  if a larger  $\alpha$  value had been used.

## 8. SUMMARY AND CONCLUSIONS

The effect of overburden stress on liquefaction evaluations was re-evaluated (Boulanger 2003a,b) using a theoretical framework that provided consistency between the different components of the design process. The cone penetration theory of Salgado et al. (1997a), which had been validated against a large set of calibration chamber test data, was used to develop improved  $C_N$  relations and to relate the penetration resistance to a relative state parameter index ( $\xi_R$ ). Published SPT data (Marcuson and Bieganousky 1977a,b) were reanalyzed and shown to be in good agreement with the  $C_N$  relations derived for the CPT. Experimental data by Vaid and Sivathayalan (1996) and Vaid and Thomas (1995) on reconstituted sand specimens were used to show that CRR could be approximated as a unique function of  $\xi_R$ , thereby capturing the combined effects of  $D_R$  and  $\sigma'_v$  on CRR. Relations between CRR and  $\xi_R$  for field conditions were subsequently derived from semi-empirical liquefaction correlations, and these CRR- $\xi_R$  relations were used to calculate the effects of  $\sigma'_v$  on predicted CRR. The resulting  $\xi_R$ -based relations were compared against commonly used methods and shown to reduce the conservatism that results when certain methods are extrapolated to overburden stresses greater than they were calibrated for. In addition, it was shown that the  $C_N$  and  $K_\alpha$  relations are inter-related through the sand properties and state in ways that can have compensating effects on the predicted CRR. Subsequently, the appropriate choice of  $D_R$ -independent  $C_N$  and  $K_\alpha$  relations (eliminating the need to estimate  $D_R$  or  $\xi_R$ ) can reasonably approximate the effects of  $\sigma'_v$  on

predicted CRR. In addition,  $\xi_R$  was shown to provide a rational and practical index for describing the variation of  $K_\alpha$  with both relative density and confining stress. Modifications to existing practice were recommended that are simple to implement and reduce the excessive conservatism imposed by some of the current approaches.

The application of semi-empirical liquefaction analysis methods to large depths is inherently complicated by the shortage of case histories for such conditions, and thus considerable engineering judgment must be exercised in the procedures being used to extrapolate our shallow-depth experiences. The present study attempts to improve that extrapolation by analyzing the various components of the design process with a consistent theoretical basis, but it nonetheless remains an extrapolation with concurrent unavoidable uncertainties.

## 9. ACKNOWLEDGMENTS

The author appreciates the many discussions and insights provided by I. M. Idriss throughout this study and the constructive comments of P. Byrne and R. Salgado.

## 10. REFERENCES

- Been, K., and Jefferies, M. G. (1985). "A state parameter for sands." *Geotechnique*, 35(2), 99-112.
- Bolton, M. D. (1986). "The strength and dilatancy of sands." *Geotechnique*, 36(1), 65-78.
- Boulanger, R. W. (2003a). "Relating  $K_\alpha$  to a relative state parameter index." *J. Geotechnical and Geoenvironmental Engrg.*, ASCE, in press.
- Boulanger, R. W. (2003b). "High overburden stress effects in liquefaction analyses." *J. Geotechnical and Geoenvironmental Engrg.*, ASCE, in press.
- Cubrinovski, M., and Ishihara, K. (1999). "Empirical correlation between SPT N-value and relative density for sandy soils." *Soils and Foundations*, JGS, 39(5), 61-71.
- Harder, L. F., Jr., and Boulanger, R. W. (1997). "Application of  $K_\sigma$  and  $K_\alpha$  correction factors." *Proc. Workshop on Evaluation of Liquefaction Resistance of Soils*, NCEER-97-0022, National Center for Earthquake Engineering Research, SUNY Buffalo, N.Y., pp. 167-190.
- Hardin, B., and Black, W. (1968). "Shear modulus and damping in soils." *J. Soil Mech. and Foundations Div.*, ASCE, 94(2), 353-369.
- Hatanaka, M., Uchida, A., Oh-Oka, H. (1995). "Correlation between the liquefaction strengths of saturated sands obtained by in-situ freezing method and rotary-type triple tube method." *Soils and Foundations*, JSSMFE, 35(2), 67-75.
- Hynes, M. E., and Olsen, R. (1998). "Influence of confining stress on liquefaction resistance." *Proc., International Symposium on the Physics and Mechanics of Liquefaction*, Balkema, Rotterdam, The Netherlands, 145-152.
- Konrad, J.-M. (1988). "Interpretation of flat plate dilatometer tests in sands in terms of the state parameter." *Geotechnique*, 38(2), 263-277.
- Liao, S. C., and Whitman, R. V. (1986). "Overburden correction factors for SPT in sand." *J. Geotechnical Engineering*, ASCE, 112(3), 373-377.
- Marcusson, W. F., III, and Bieganousky, W. A. (1977a). "Laboratory standard penetration tests on fine sands." *J. Geotechnical Engineering Division*, ASCE, 103(GT6), 565-588.
- Marcusson, W. F., III, and Bieganousky, W. A. (1977b). "SPT and relative density in coarse sands." *Journal of the Geotechnical Engineering Division*, ASCE, 103(GT11), 1295-1309.
- Mohamad, R., and Dobry, R. (1986). "Undrained monotonic and cyclic triaxial strength of sand." *Journal of Geotechnical Engineering*, ASCE, 112(10): 941-958.

- Naylor, D. J., Pande, G. N., Simpson, B., and Tabb, R. (1981). *Finite elements in geotechnical engineering*, Pineridge Press, Swansea, U.K.
- Robertson, P. K., and Wride, C. E. (1998). "Evaluating cyclic liquefaction potential using the cone penetration test." *Canadian Geotechnical Journal*, 35(3), 442-459.
- Salgado, R., Mitchell, J. K., and Jamiolkowski, M. (1997a). "Cavity expansion and penetration resistance in sands." *J. Geotechnical and Geoenviron. Engrg.*, ASCE, 123(4), 344-354.
- Salgado, R., Boulanger, R. W., and Mitchell, J. K. (1997b). "Lateral stress effects on CPT liquefaction resistance correlations." *J. Geotechnical and Geoenvironmental Engineering*, ASCE, 123(8), 726-735.
- Seed, H. B. (1983). "Earthquake resistant design of earth dams." *Proc., Symposium on Seismic Design of Embankments and Caverns*, Philadelphia, PA, ASCE, pp. 41-64.
- Seed, H. B., Lee, K. L., Idriss, I. M., and Makdisi, F. (1973). "Analysis of the slides in the San Fernando Dams during the earthquake of February 9, 1971." *EERC 73-2*, Earthquake Engineering Research Center, UC Berkeley.
- Seed, H. B., Tokimatsu, K., Harder, L. F., and Chung, R. (1985). "Influence of SPT procedures in soil liquefaction resistance evaluations." *J. Geotech. Engrg.*, ASCE, 111(12), 1425-1445.
- Seed, R. B., and Harder, L. F., Jr. (1990). "SPT-based analysis of cyclic pore pressure generation and undrained residual strength." *Proc., Seed Memorial Symposium*, J. M. Duncan, ed., BiTech Publishers, Vancouver, B.C., pp. 351-376.
- Skempton, A. W. (1986). "Standard penetration test procedures and the effects in sands of overburden pressure, relative density, particle size, ageing and overconsolidation." *Geotechnique*, 36(3), 425-447.
- Vaid, Y. P., and Finn, W. D. L. (1979). "Static shear and liquefaction potential." *J. Geotech. Div.*, ASCE, 105(GT10), 1233-1246.
- Vaid, Y. P., and Chern, J. C. (1985). "Cyclic and monotonic undrained response of saturated sands." *Advances in the Art of Testing Soils under Cyclic Conditions*, ASCE, N.Y.
- Vaid, Y. P., and Thomas, J. (1995). "Liquefaction and postliquefaction behavior of sand." *J. Geotechnical Engineering*, ASCE, 121(2), 163-173.
- Vaid, Y. P., and Sivathayalan, S. (1996). "Static and cyclic liquefaction potential of Fraser Delta sand in simple shear and triaxial tests." *Canadian Geotechnical Journal*, 33, 281-289.
- Yoshimi, Y., Tokimatsu, K., and Hosaka, Y. (1989). "Evaluation of liquefaction resistance of clean sands based on high quality undisturbed samples." *Soils and Foundations*, JSSMFE, 29(1), 93-104.
- Youd, T. L., et al. (2001). "Liquefaction resistance of soils: Summary report from the 1996 NCEER and 1998 NCEER/NSF workshops on evaluation of liquefaction resistance of soils." *J. Geotechnical and Geoenvironmental Engineering*, ASCE, 127(10), 817-833.

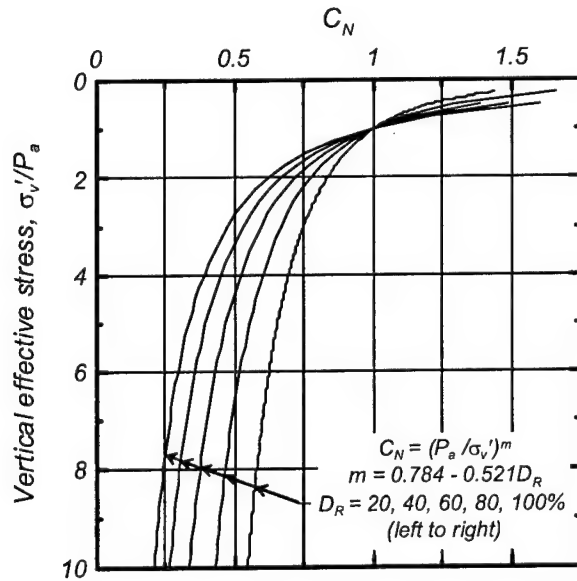


Figure 1. Overburden correction factor ( $C_N$ ) for clean sands based on Salgado et al. (1997b).

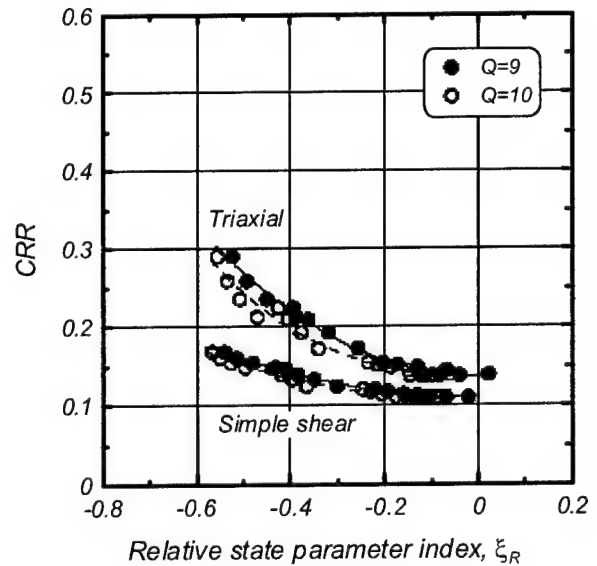


Figure 3. CRR versus  $\xi_R$  for reconstituted specimens of Fraser Delta sand: Test data by Vaid & Sivathayalan (1996) for  $D_R$  of 31, 40, 59, & 72% and  $\sigma_{v0}'/P_a$  of 0.5, 1, 2, & 4.

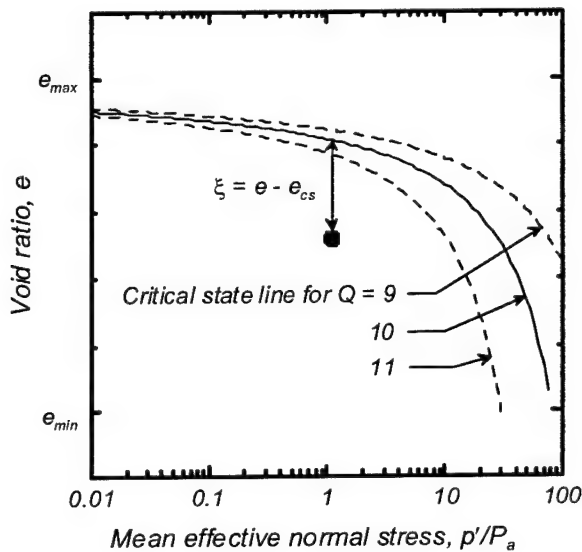


Figure 2. Critical state lines from Bolton's (1986)  $I_{RD}$  relation and the definition of state parameter.

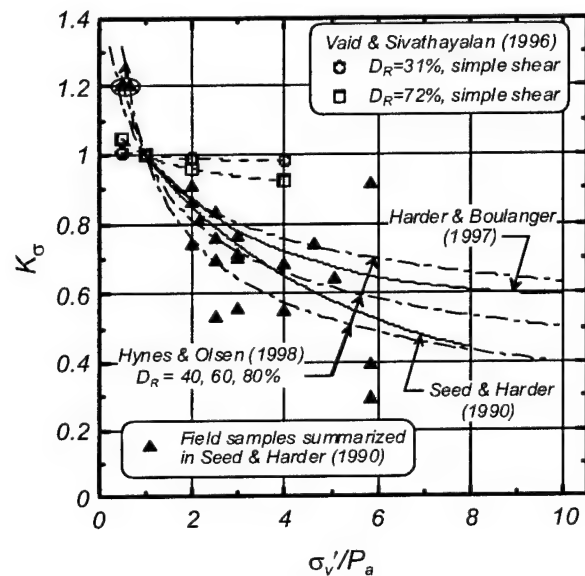


Figure 4. Comparison of  $K_\sigma$  relations with data from reconstituted Fraser Delta sand specimens (Vaid and Sivathayalan 1996) and various field samples (Seed and Harder 1990).

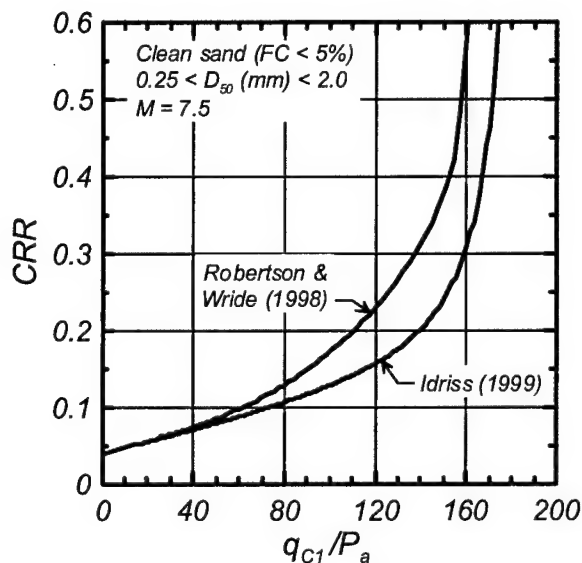


Figure 5. Semi-empirical CPT-based liquefaction Correlations.

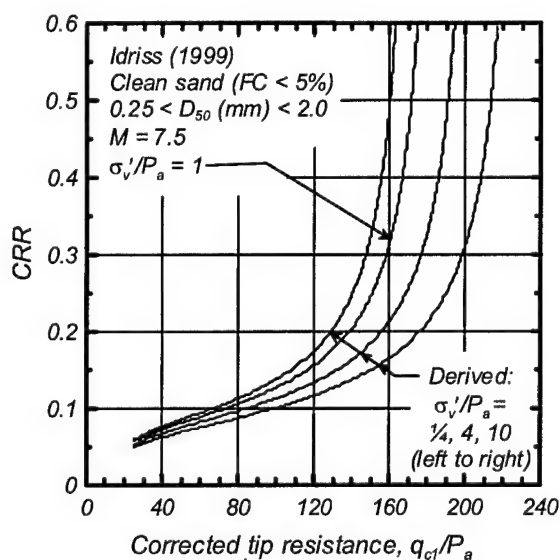


Figure 7. CRR versus  $q_{C1}/P_a$  for clean sand with different overburden stresses, using Idriss (1999) correlation for  $\sigma'_v/P_a = 1$ .

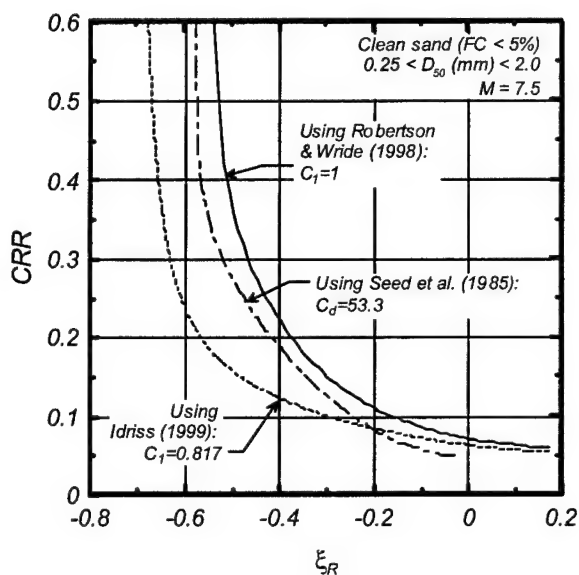


Figure 6. Field CRR- $\xi_R$  relations derived from semi-empirical liquefaction correlations.

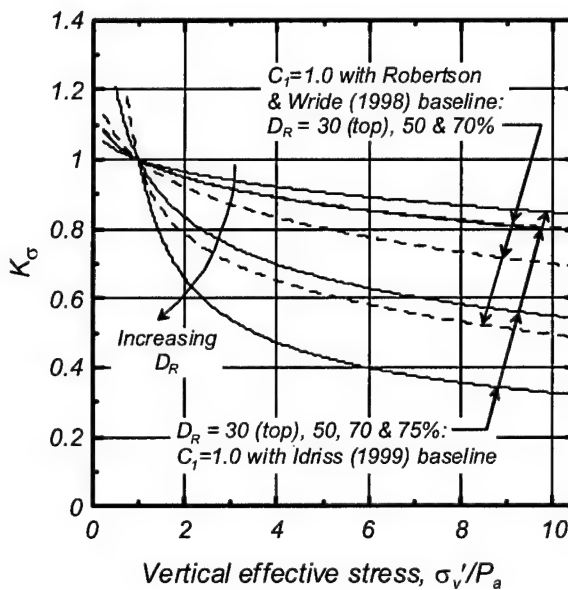


Figure 8.  $K_\sigma$  curves from CRR- $\xi_R$  relations derived from liquefaction correlations for field conditions.

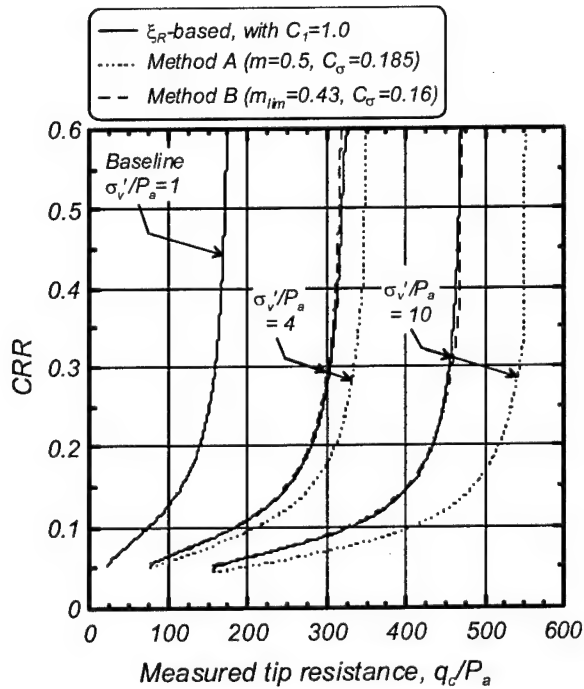


Figure 9. Comparison of  $\xi_R$ -based method, its simplified approximation (Method B), and a current method in practice (Method A) using Idriss' (1999) correlation as baseline and  $C_1=1.0$ .

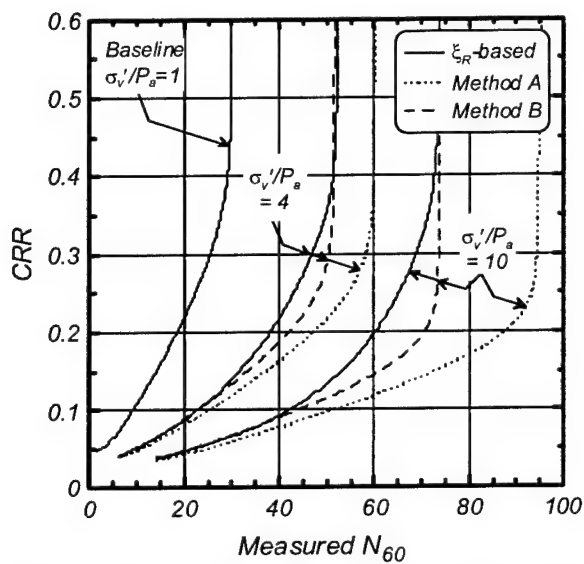


Figure 10. Comparison of  $\xi_R$ -based method, its simplified approximation (Method B with  $m_{lim}=0.39$ ,  $C_\sigma=0.21$ ), and a current method in practice (Method A with  $m=0.5$ ,  $C_\sigma=0.185$ ) using Seed et al. (1985) SPT correlation as the baseline and  $C_d=41.5$ .

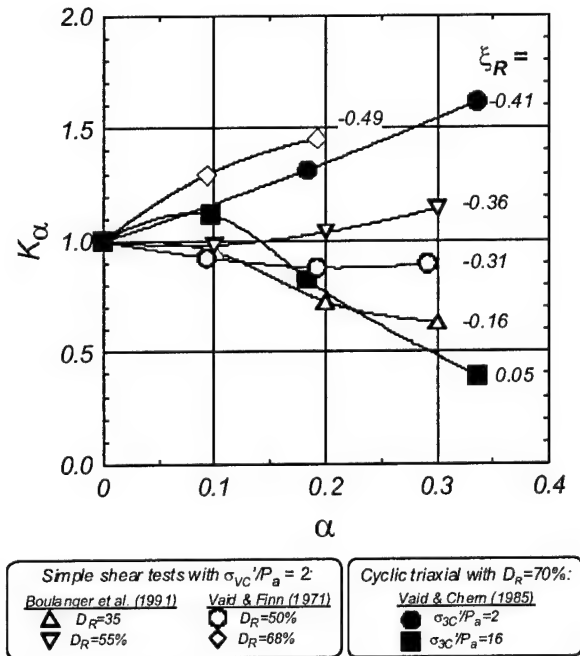


Figure 11. Effect of  $\xi_R$  on  $K_\alpha$ .

## Dynamic Centrifuge Modeling of Earth Dams on Liquefiable Foundation

By

Korhan Adalier<sup>1</sup> and Michael K. Sharp<sup>2</sup>

### ABSTRACT

Earthquake induced liquefaction is a major concern for earth dam safety in seismically active regions of the world. The failure of Sheffield dam during 1925 El Centro earthquake due to liquefaction of its foundation soil and the near catastrophic failure of the Lower San Fernando Dam during the Earthquake of February 1971 are the prime examples in U.S. Dam Engineering history. Many liquefaction induced earth dam failures or near-failures have been reported around the world during various earthquakes. Such embankment damages were particularly destructive when the underlying saturated granular soils liquefied, resulting in cracking, settlement, lateral spreading, and slumping of the embankment.

Through a series of twelve separate geotechnical centrifuge modeling tests, seismic behavior of a zoned earth dam with saturated sandy soil foundation was studied under moderate earthquake conditions. Soil response during and after shaking was monitored by many miniature accelerometers, pore pressure transducers, and displacement gauges placed throughout the soil model. The effect on the seismic behavior of the dam of different parameters such as the thickness, location, and depth of liquefiable layer is studied. This paper describes some of these tests and briefly presents the preliminary results. Valuable insights into the dynamic behavior of the employed embankment-foundation systems are provided. Currently, such testing results offer a valuable alternative to actual full-scale dynamic response, which is virtually non-existent.

**KEYWORDS:** Centrifuge modeling, earth dams, liquefaction.

### 1. INTRODUCTION

America relies on more than 75,000 dams for water supply, power generation, flood control, irrigation and recreation. They are critical to our national infrastructure. A dam failure can affect thousands of lives and cost millions of dollars. Therefore, assessment of their safety is treated with the utmost caution. One of the major hazards to the safety of dams is an earthquake.

Soil structures such as river dikes, highway embankments, and earth dams have been frequently damaged during past major earthquakes. This damage was often mainly due to liquefaction of the embankment and/or foundation soils (Seed 1968 and 1970, Matsuo 1996). In most cases, large deformations developed when the supporting loose cohesionless foundation soil liquefied (Henderson 1933, Duke and Leeds 1963, Yokomura 1966, McCulloch and Bonilla 1967, Seed 1968, Tani 1996, Krinitzsky and Hynes 2002); resulting in cracking, settlement, lateral spreading, and slumping.

The U.S. Army Corps of Engineers is responsible for the care and maintenance of over 700 embankment dams in the U.S. Many of these, over 200, are in highly seismic areas of the country. The vast majority was constructed in the 1940's and 1950's when earthquake engineering was in its infancy and seismic hazards were neither recognized nor understood, leaving some inadequate for a seismic event. It is estimated that there are many other such seismically inadequate dams around U.S. under the responsibility of federal, state and local governments, as well as the private sector. Likewise, many earth embankment dams worldwide are located in seismically active areas (Marcuson and Silver, 1987).

<sup>1</sup> Department of Civil and Environmental Engineering, Rensselaer Polytechnic Institute, Troy, NY 12180 (USA).

<sup>2</sup> Centrifuge Research Center, U.S. Army Engineer Research and Development Center, Vicksburg, MS 39180 (USA).



Some of these embankments are founded on liquefiable soils, in many cases, necessitating the development of appropriate remediation countermeasures (Ledbetter et al. 1994, Marcuson et al. 1996). However, it is not feasible to remediate all of these structures due to the considerable cost involved. A determination of how much damage such structures could tolerate and still be able to perform their primary function could alleviate the need to remediate many dams. In cases that require remediation, understanding the deformations and dynamic response mechanisms of such dam/foundation systems would enhance our ability to design remedial procedures in a more effective and economical way thus saving possibly hundreds of millions of dollars. The concern over earthquake resistance of older embankment dams drives the need for remedial construction costing hundreds of millions of dollars of public funds annually. The potential for economic savings through better understanding of the involved mechanisms can be enormous considering the high cost of remedial treatment and the volume of dams that may require treatments in the coming years. Foundation remedial projects of Sardis Dam in Northern Mississippi and Mormon Island Dam north of Sacramento, California both owned by the COE are only two recent cases, each of them costing over \$30 million. Casitas Dam, Ventura-California owned by U.S. Bureau of Reclamation is another earth dam that is currently receiving a remedial treatment against foundation liquefaction with a cost of over \$20 million. A similar \$15 million upgrade is under way at the Bureau's Bradbury Dam in the Santa Barbara-California area. Many other dams are currently under evaluation for liquefaction-induced hazards mainly by several federal and state governmental agencies.

It has been shown that the centrifuge dynamic model testing technique can play a major role in understanding the dynamic behavior of various earth structure-soil systems including earth dams (Arulanandan and Scott 1993, 1994; Kimura et al. 1995, Adalier et al. 1998). Centrifuge testing is the best, most practical, most economical, and the only method for properly investigating and verifying earthquake induced equivalent-

prototype behavior in soil, which behaves nonlinearly and is stress-state dependent. Additionally, this centrifuge experimental model response also provides a basis for calibration of design and computational modeling procedures currently being performed by the ERDC.

In a series of twelve separate centrifuge model tests, seismic behavior of a zoned earth dam with saturated sandy soil foundation was studied under moderate earthquake conditions. The effect on the seismic behavior of the dam of different parameters such as the thickness, width, and depth of liquefiable layer is studied. Currently, such testing results offer a valuable alternative to actual full-scale dynamic response, which is virtually non-existent. Soil response during and after shaking was monitored by many miniature accelerometers (in the horizontal direction), pore pressure transducers, Linear Variable Differential Transformers (LVDTs), and vertical and horizontal displacement gages, placed throughout the soil model.

This paper describes some of these tests and briefly presents the preliminary results. Valuable insights into the dynamic behavior of the employed embankment-foundation systems are provided. In these test, particular attention was given to accurate and detailed measurement of the induced deformations. In addition to the pore pressure, acceleration, and model surface displacement measurements that are commonly done in most centrifuge tests, very detailed and extensive deformation mapping was performed based on pre- and post-shake meshes of markers throughout the body of the models. Such earthquake-induced deformations and damage is the key to making well-informed seismic safety and remediation decisions for embankment dams. Practice has demonstrated that remediation measures based on displacement criteria are much more cost-effective than those based on the factor of safety approach (Finn 2000). This study is believed to significantly expand and enhance our earthquake case history database regarding the earth dam on liquefiable foundation problem with more completely known and defined conditions and earthquake responses. Such an earthquake response database will provide: (1) a basis for modification



and improvement of current methodology and assumptions, (2) realistic data for validation and improvement of numerical procedures (a current ongoing research), and (3) definitions of the physical processes and mechanisms involved in the liquefaction process and resultant effects on soil-embankment behavior. It also significantly enhances our capability to determine and define liquefaction occurrence, potential to cause damage, and need for mitigation, thereby resulting in economic savings to U.S. Corps of Engineers.

## 2. CENTRIFUGE MODELING EQUIPMENT

Geotechnical Centrifuge: The tests were done using the RPI's 100g-ton geotechnical centrifuge. This machine is an Acutronic Model 655-1. It has an in-flight radius of 3.0 m and can test a payload up to 1 ton at 100g or 0.5 ton at 200g (i.e., 100 g-ton). More details about this centrifuge can be found in Elgamal et al. (1991) and at <http://www.rpi.edu/~dobryr/centrifuge/>.

The main principle in centrifuge modeling is that a  $1/N$  scale model subject to a gravitational acceleration of  $Ng$  ( $g$  is acceleration of gravity) will feel the same stress as the prototype. Then, stress-strain relationships at all equivalent points in the model and prototype will be the same if the same soil is employed and the behavior of the model will mimic the behavior of the prototype. Consequently, with the help of scaling laws (Schofield 1981; Adalier and Sharma 2000) measurements in centrifuge tests under closely controlled conditions can be related directly to an equivalent full-scale prototype. The centrifuge modeling technique allows soil liquefaction tests to be performed at a conveniently reduced scale, and provides data applicable to full-scale problems.

In-Flight Shaker: In all tests, an in-flight shaker was employed to impart the model base shaking. Designed and built at Rensselaer, the centrifuge shaker is an electro-hydraulic, servo-controlled device with dual actuators. The total maximum force capability of the simulator is 80 kN. It can shake up to a 450 kg payload at model frequency ranges of 20 Hz to 500 Hz. The shaker accepts either standard input signals from a function

generator or arbitrary input signals synthesized by a computer (e.g., earthquake signal). Input motion is imparted (in-flight) in a direction parallel to the centrifuge axis of the RPI shaker. The vertical motion of the shake table is measured to be less than 10% of the desired horizontal motion, verifying that the base excitation produced in the tests is essentially one-dimensional. Detailed information on this shaker is provided by Van Laak et al. (1998).

Data Acquisition System: A PC - based data acquisition system with the capability of digitizing 64 channels of data at a 15 kHz sampling rate (per channel), or a smaller number of channels at correspondingly higher sampling rate was used. Transducer excitation and signal conditioning is performed on the centrifuge arm and the signals are then transmitted through slip rings to the recording system, located in the control room. These analog signals are amplified, filtered to avoid aliasing, and finally digitized in real time using array of PC - type digitizing boards. The data is then processed using the SigmaPlot data processing and graphics software. During flight, three closed-circuit television cameras monitor the centrifuge, the soil model plan, and the soil model side through a window in the model container's wall.

Instrumentation: For each test, during and after shaking, a complete set of response time histories was recorded in the form of: accelerations at 12 locations, pore pressures at 13 locations and vertical displacements (LVDTs) at 5 surface locations. In addition, the models were dissected after testing and the deformed configurations were carefully mapped with the aid of: soft vertical marker lines (embedded in the embankment and foundation layer before testing) and horizontal lines of colored sand (placed within the soil during model construction). The accelerometers are PCB Piezotronics model 303A03 with a mass of 2 grams and a range of 500g with a 0.01g resolution. The pore pressure transducers were model PDCR 81 made by Druck Inc, with pressure ranges of 690 kPa and 345 kPa. For these tests, the pore pressure transducer porous stones were removed and replaced by relatively permeable, thin, but very strong filter papers-

textile to allow easy saturation of the volume between the soil and the transducer sensing diaphragm with highly viscous pore fluid. Previous experience of the author (Adalier 1996) and others (Lee 1990) indicated that the viscous drag imposed by the PPT porous cap (standard procedure) on the pore fluid and any partial saturation of the space in front of the sensing diaphragm can significantly reduce the sensitivity of the transducer to high frequency pore pressure fluctuations. The thin and porous filters used imposed negligible drag forces and ensured transducer sensitivity to potential high-frequency pressure fluctuations. The LVDT's are Schaevitz Engineering model MHR 1000 with a nominal linear range of  $\pm 25$  mm. At the end of the LVDT rod, a circular plastic plate 1 mm in thickness and 32 mm in diameter was attached to support the LVDT core. The density of this plastic is close to the buoyant density of the soil, in order to help avoid the core sinking into the soil during liquefaction. Perforations in the plastic plate allowed for water flow. Each transducer was thoroughly calibrated before the testing series started and the calibration was checked routinely for any malfunction every other test. More detailed information about the geotechnical centrifuge modeling instrumentation used in RPI is given by Adalier (1996).

**Model Container:** A rigid model container with inner dimensions of 0.88 m length, 0.37 m width, and 0.36 m height was used. A transparent side window allowed for observation of the side of the model. Rough sand paper was glued to the inner base surface of the container to provide good interface friction between the box and the soil base.

### 3. MODEL CONSTRUCTION AND TESTING PROCEDURE

**Model Soil:** Nevada No. 120 sand with the properties listed in Table 1 was used in all tests. This is a fine, uniform, sub-round, clean sand. Extensive data about the monotonic and cyclic response characteristics of this soil has been documented by Arulmoli et al. (1992) as part of VELACS project and also can be found on the WEB at: <http://geoinfo.usc.edu/gees/velacs/> and <http://rccg03.usc.edu/velacs/Centrifuge/cntdata>.

The embankment core was made out of kaolin clay compacted at around 33% water content (3% to wet side of optimum). It had a dry unit weight of  $13.4 \text{ kN/m}^3$  and unconfined shear strength ( $S_u$ ) of 16-18 kPa.

**Table 1. Properties of Nevada No. 120 sand (after Arulmoli et al. 1992).**

Property	Value
$d_{10}$	0.08 mm
$d_{50}$	0.15 mm
Specific gravity, $G_s$	2.67
Maximum void ratio, $e_{\max}$	0.887
Minimum void ratio, $e_{\min}$	0.511
Maximum dry unit weight	$17.33 \text{ kN/m}^3$
Minimum dry unit weight	$13.87 \text{ kN/m}^3$
Water Permeability at $e = 0.736$	$6.6 \times 10^{-5} \text{ m/s}$
Water Permeability at $e = 0.661$	$5.6 \times 10^{-5} \text{ m/s}$
Int. friction angle at $D_r=40\%$	$33^\circ$
Int. friction angle at $D_r=60\%$	$36^\circ$

**Model Construction:** Oven dried Nevada sand was pluviated through a V-shaped funnel with a row of holes along the funnel tip. The sand particles drop height was adjusted to give different relative densities (e.g., 35% and 70%). Pluviation was interrupted periodically to place instrumentation in the soil model. A very thin band (about 2 cm wide in model scale) of colored Nevada sand was placed at the interface of each horizontal foundation layer (3 cm apart in model scale). Pluviation was stopped 3 to 5 mm above the desired model height and the model surface was then trimmed to the final shape by removing excess sand particles with a vacuum line. Thin spaghetti sticks were then inserted vertically (driven in a steel tube casing), at predetermined positions. When softened by the pore fluid these sticks acted as inclinometers and made it possible to measure the internal deformations during model dissection.

The dry model was carefully carried to the centrifuge with a forklift and placed on the shaker platform. Surface measurements were taken before and after this stage to make sure that no densification had been induced in the model during this transportation and installation

process. Following the conventional saturation procedure (Adalier 1996), a lid was used to seal the model box, and air inside the box was evacuated under vacuum pressure of 100 kPa applied for an hour. The vacuum was then shut off and carbon dioxide was introduced into the box to help dissolve possible remaining oxygen in the soil voids. After half an hour, vacuum of 100 kPa was applied for one hour. This negative pressure was reduced to 90 kPa and de-ionized/de-aired water/metulose solution of 50 times water viscosity was introduced very slowly to the model surface at both downstream and upstream sides of foundation layer. This highly viscous fluid slows down the rate of diffusion and dissipation and unifies time scaling factors for dynamic and consolidation events, hence gives a better simulation of the field case. Considering the fact that the tests were conducted at a 100g gravitational acceleration field, and in view of the scaling laws applicable to centrifuge experiments, about a two times more permeable foundation sand (relative to 1-g water permeability) was simulated (still a fine sand permeability). This saturation process was performed slowly over an approximate 24 to 36 hour period, to ensure good saturation and prevent local liquefaction or piping in the soil. Foundation layers on both sides were saturated with this viscous fluid to about 0.5 m (prototype) above the ground surface. Above this level, the upstream side of the embankment was saturated with a de-ionized/de-aired water, rather than a viscous fluid to simulate a coarser embankment material (as mainly found in field cases). Degree of saturation was always checked based on the measured volumes and measured weights of sand deposits and viscous fluid used, and found to be at least 98% in each test. It should be stressed that the saturation was done while the model container rested on the centrifuge swing platform to avoid any possible disturbance to the models during any transportation process. This assured high quality uniform models. After saturation, the model was opened to atmosphere, and the model geometry was measured. Vacuum suction or saturation process was found to cause no detectable settlements or deformations in any of the soil models. The LVDTs to measure

vertical displacements along the model surface at various locations were placed.

Testing Procedure: The tests were conducted in a 100g gravitational field. The centrifuge was brought to 100g very gradually in about 30 minutes in order to ensure a smooth transition of the soil model from 1g to 100g. An additional 10 minutes of spinning time was allowed at 100g before imparting the dynamic base excitation. This way the pore pressures were allowed to buildup almost statically without causing any potential instability problems. Self-weight compression of the model was monitored in each test and found to be insignificant compared to those dynamically-induced during the subsequent shaking events. All of the models were subjected to the same sinusoidal base horizontal acceleration of 30-cycles, 0.2g magnitude, and 1.5 Hz dominant frequency (prototype). In all tests, the vertical base motion was minimal (less than 10% of the horizontal input). Soil response was measured by accelerometers, LVDT's, pore pressure transducers (PPT), and deformation markers (i.e., colored sand and spaghetti noodles). During all tests, a model sampling rate of 4000 samples/second/channel with a filter cutoff frequency of 1200 Hz was used.

After the test was complete, the specimen was dissected carefully to measure final locations of the spaghetti noodles, colored sand markers, accelerometers, and pore pressure transducers. Photographs were taken before and after each test, and a detailed visual observation was conducted of the deformation of each model. The profiles of the models at dissected sections were mapped very carefully (transformed on a thin plexiglass plate) and then digitized into computer graphics. By this method, very detailed pre- and post-test mid-section profile meshes of each model was obtained.

#### 4. TESTING PROGRAM

A total of 12 dynamic tests were performed on 12 different soil models. At a 100g gravitational acceleration field, the models depicted in Fig. 1 (a setup of a typical model) simulated a prototype earth dam of 10 m in height, 39.5 m in

width, sitting on 9 m thick fine sand foundation deposit. Table 2 gives the summary of the conducted centrifuge tests. As seen in Table 2, mainly the effects of liquefiable layer i) thickness, ii) depth, and iii) location on the dynamic performance of the dam-foundation system were studied. In Series IV, the effects of longer earthquake shaking (40 cycles) and of a clay interlayer at 2.5-3.5 m depth on both downstream and upstream sides of the dam was evaluated. Full sets of horizontal accelerations, pore pressures, and deformations at different locations throughout the foundation-dam model were obtained for further analysis and interpretation. Additionally, these data are being studied numerically and used as a database for calibration and verification of several different FE codes or numerical schemes.

Due to space limitation, only selected response records of Series I tests will be presented in the following sections and preliminary results will be briefly discussed. All of the test results are presented and discussed in prototype units, unless otherwise stated.

**Table 2. Centrifuge testing program.**

Centrifuge Test Series	Model Configuration
	1DS-2DS-3DS—1US-2US-3US D: 70% $D_r$ ; L: 35% $D_r$
<b>Series I-</b>	L-L-L—L-L-L
Effect of	L-L-D—L-L-D
liquefiable layer	L-D-D—L-D-D
<b>thickness</b>	D-D-D—D-D-D
<b>Series II-</b>	D-D-L—D-D-L
Effect of	D-L-D—D-L-D
liquefiable layer	L-D-D—L-D-D
<b>depth</b>	
<b>Series III-</b>	D-D-L—D-D-D
Effect of	D-L-D—D-D-D
liquefiable layer	D-D-D—D-D-L
<b>location</b>	D-D-D—D-L-D
<b>Series IV-</b>	
Clay Interlayer	L-L-Clay-D—L-L-Clay-D
and Large	D-L-D—D-L-D
Earthquake	

$D_r$ : Relative Density; DS: Downstream; US: Upstream

## 5. SERIES-I TESTS RESULTS - EFFECT OF LIQUEFIABLE LAYER THICKNESS

### 5.1 Model 1: LLL-LLL: Entire Foundation at $D_r = 35\%$

Figure 2 depicts model response at selected transducer locations and post-test deformed shape of the model cross-section (after mid-section dissection). Figure 3 shows the model deformations in vectorial form. As seen, the induced base excitation caused very large deformations both in embankment and in the foundation. A huge embankment crest settlement of 2.4 m was measured. Essentially, most of this settlement took place during the course of the base excitation, at a nearly uniform rate with time (corresponding to approximately 0.08 m vertical settlement per cycle of base excitation). Both sides of the embankment slumped and moved laterally away from the centerline on the excess pore pressure softened foundation. The migration (mostly lateral) of underlying foundation soil towards the free field, as indicated by the post-test deformed mesh (Figs. 2 and 3), was largely responsible for the observed embankment slump. Movements as large as 4 m were observed near the toe areas. In general, the deformations on the downstream side were slightly bigger than those of upstream side. This is mainly attributed to the higher initial static shear stresses in the downstream foundation. Deep failure planes in the foundation zone are obvious in Figs. 2 and 3. The lateral deformation in the foundation soil, both at upstream and downstream sides, was found to attain its maximum near ground surface, and to decrease with depth. This deformation may be associated with an average accumulated normal lateral tensile strain of about 20% along the embankment base. Indeed, this tensile strain was clearly manifested in the form of stretching and slumping of the embankment body.

At the upstream toe-foundation, the acceleration response ( $a_3$ , Fig. 4) gradually decreased within 3-4 cycles of base excitation, reflecting the associated loss of soil stiffness and strength due to induced high excess pore pressures. However, after a few initial cycles, a very peculiar

behavior of large asymmetric acceleration spikes started to appear. Such asymmetric spiky acceleration response has been thoroughly investigated before (Dobry et al. 1995; Elgamal et al. 1996) and has been attributed to the occurrence of significant post-liquefaction cyclic down-slope (i.e., shear straining towards free-field associated mostly with initial static shear stresses) deformations and the dilation of soil as the stress state reaches the phase transformation line. Under the downstream toe, a considerably stiffer response prevailed, reflected as stronger acceleration records (Fig. 4). At this location it took about 15 cycles of excitation for the dilative acceleration spikes to appear. This is related to the distance of the initial stress state to the phase transformation line (i.e., the initial stress state of upstream toe foundation area is closer to the phase transformation line than that of downstream). Likewise, a faster build up of excess pore water pressures at the upstream side helped bring the stress state to phase transformation quicker. Notice that the direction of these spikes are in opposite directions in upstream (a3) and downstream (a10) sides, as the lateral movement, and the initial static lateral shear stresses, are actually in opposite directions. It is noteworthy that the core-/crest accelerations were significantly attenuated relative to the base input. As will be discussed later, the crest motions were largely affected by the embankment and foundation sandy soil state of strength during shaking event.

At P3 and P12, the soil built up excess pore pressures corresponding to initial liquefaction. The buildup at the upstream side was somewhat faster. Due to very large shear strains induced in the foundation and associated dilation effect the foundation excess pore pressures (P6) did not reach initial liquefaction values. The estimated excess peak pore pressure ratio at P6 is around 0.7.

### **5.2 Model 2: DLL-DLL: Top 3m Densified Foundation**

In this model the top 3 m of the entire foundation layer was densified to  $D_r = 70\%$ . In practice, various ground treatment strategies can be used to mitigate the liquefaction hazards. The

most common improvement techniques have been densification, soil replacement, or cementation. Among these, compaction or densification has been the most popular method for embankment foundation remediation projects (Adalier 1996). This model may be considered simulating a case where top 3 m of the foundation soil densified as a countermeasure or this kind of layering exist in nature.

Figure 5 depicts model response at selected transducer locations and post-test deformed shape of the model cross-section (after mid-section dissection). Figure 6 shows the model deformations in vectorial form. As seen, both the embankment and the foundation deformations were much reduced when compared with the previous model (all foundation layer is loose, i.e., LLL-LLL). Embankment crest settlement was 1.3 m (i.e., about half of that of Model 1). As in the first model, essentially all of the measured crest settlement took place during input excitation. The pattern of deformations was considerably different that that observed in the first model, as the maximum shear deformations were shifted downwards to the 6-m loose layer. From the deformed mesh (Fig. 5) one may deduce that the 3-m top dense soil plus the embankment basically translated sideways (without internally going into significant shear deformations) on the excess pore pressure softened 6-m loose underlying layer. As in the first model, the deformations on the downstream side were slightly bigger than those of upstream side. The average accumulated normal lateral tensile strain along the embankment base was about 6.5% (compared to 20% in the Model 1).

The accelerations at foundation mid-depth (a3 and a10) were both somewhat attenuated relative to base input. Also the asymmetric spiky response phenomenon was much less significant (compared to Model 1 case) as the lateral deformations were reduced. Clay core crest accelerations, although attenuated relative to base input, were higher than those of Model 1 case. This is attributed to overall stiffer and stronger foundation material surrounding the core. Both P3 and P12 at the mid-depth (in loose layer) measured excess pore pressures corresponding to initial liquefaction. P6 under



the embankment also measured excess pore pressure values corresponding to initial liquefaction. Contrary to the Model 1 case, reduced overall lateral spreading and dilation effects helped the soil to build up higher excess pore pressures.

### **5.3 Model 3: DDL-DDL: Top 6m Densified Foundation**

In this model the top 6 m of the entire foundation layer was densified to  $D_r = 70\%$ . Figure 7 depicts the Model 3 response at selected transducer locations and post-test deformed shape of the model cross-section (after mid-section dissection). Figure 8 shows the model deformations in vectorial form. As seen, embankment crest settlement was a little less than the one measured in Model 2 at about 0.8 m. Likewise the embankment and foundation internal deformations were further reduced by the increase in densified layer thickness from 3 to 6 meters. The maximum shear deformations were observed in the base 3-m loose layer. As in the previous two cases, the downstream deformations were somewhat larger. The average accumulated normal lateral tensile strain along the embankment base was about 4.5% (compared to 20% in Model 1).

The acceleration response of  $a_3$  and  $a_{10}$  were significantly stronger than those observed in Model 1 and 2, as these transducers were in dense soil. Asymmetric acceleration behavior was less significant. Clay core crest accelerations were significantly larger than the ones measured during Model 1 and 2 tests. Despite the fact that P3 and P12 were located in the dense zone, they measured excess pore pressures corresponding to initial liquefaction. Their position being close to the underlying loose layer probably helped the pore pressure buildup at these zones.

### **5.4 Model 4: DDD-DDD: All Foundation Densified**

In this model, the entire foundation layer had a  $D_r = 70\%$ . Figure 9 depicts the model response at selected transducer locations and post-test deformed shape of the model cross-section.

Figure 10 shows the model deformations in vectorial form. It is noted that, in this case, a calibration error resulted in an increase of about 20% in the input shaking accelerations. Nevertheless, the embankment and foundation deformations were reduced drastically. The pattern internal deformations were somewhat different than the ones observed in Model 2 and 3 tests, as they were more uniformly distributed through the model height in this case. The crest settled about 0.8 m uniformly during shaking. The average accumulated normal lateral tensile strain along the embankment base was about 4.0%. The foundation deformations were mostly lateral with essentially negligible vertical component, as the dense soil did not contract.

The excess pore pressure buildup was overall somewhat slower; however the dissipations were significantly faster than those observed in the other model tests. Significantly faster post-shake excess pore pressure dissipations occurred, related to the smaller bulk modulus of the dense material. Despite the high excess pore pressures, due to dilative characteristics of the initially dense soil, stiff response prevailed throughout the foundation (as suggested by strong accelerations). It should be noted that dense sand, even liquefied, does not deform excessively like loose sand because of its high residual shear strength and dilative behavior arresting large strain increments. Dilative acceleration spikes were apparent at records  $a_3$  and  $a_{10}$ , helped by the higher base input motion and higher foundation soil stiffness (dense material with high dilation potential). The relatively high overall foundation sandy soil stiffness increased the effective confining effect on the clay core resulting in relatively strong core-crest accelerations. It is interesting to note that, the densified foundation much reduced the earthquake induced deformations but at the same time increased the embankment accelerations (due to the ability of dense sand to be able to transmit shear stress due to dilative behavior). In this respect, for the dams with crest structures one may consider Model 3 case as a viable option.

### 5.5 Overall Response

The most important factor affecting the performance of an earth dam subjected to an earthquake is the movement of the structure and the ground supporting it during and after the event. In other words, although the accelerations and pore water pressures in the system may be important to fully characterize the dam-foundation behavior during earthquakes, ultimately the deformations is the most critical element for performance purposes. As such Fig. 12 depicts the normalized (relative to Model 1) crest settlements, average dam base tensile strains, maximum foundation settlements, and normalized (relative to base input motion) crest acceleration arias intensities for the four model tests (i.e., Models 1-4). Densifications to all depths are all found to reduce the embankment and foundation deformations by a range of 50% to 90%. However, the gain in deformation parameters has diminished after 6 m deep densification. The biggest gain was achieved form 3 m densification. Deeper densifications (i.e., 6 m and 9 m) further reduced the deformations however the improvement was at a diminishing rate. However, stronger foundations (denser material) have resulted in stronger embankment accelerations. The variation of dam settlement and acceleration (for the cases that the crest accelerations may be important, e.g., dams with various superstructures or auxiliary systems) with densification depth (Fig. 12) suggest it may be necessary to optimize the treatment depth to reduce the dam settlement and lateral spread to an acceptable level while at the same time ensuring that the dam accelerations are tolerable.

Preliminary examination of the dam deformations indicates that approximately 1-2 m of foundation deformation may be tolerated. Test results also indicate that wide-strong plastic core zones in zoned dams are good defensive design measures. However, dams with axiliary systems like relief wells may accommodate much less deformations. These sorts of design features must be evaluated to estimate the acceptable level of deformation for each site.

## 6. SUMMARY AND CONCLUSIONS

A series of highly instrumented dynamic centrifuge tests were performed to investigate the effects of loose foundation layer i) thickness, ii) location, and iii) depth on the dynamic behavior of a zoned earth dam with liquefiable foundations. Results of some of these tests were briefly presented herein. Centrifuge testing has proven itself as a very valuable tool to economically studying such complex geotechnical problems. The study provided many valuable insights into the dynamic behavior of earth dams sitting on alluvial soils subjected to moderate earthquake shaking. Moreover, these test results are providing a very valuable database for the calibration and verification of several numerical analysis codes and procedures modeling the dynamic behavior of liquefiable foundation-earth-dam systems.

Test results suggest that there may be an optimum depth of treatment beneath an earth dam beyond which the reduction of the earthquake-induced deformations is relatively minor. The tests results also indicate that relatively small and isolated zones (e.g., at depth) of loose material within a densified volume of soil may not impair the overall effectiveness of treatment and do not necessarily result in damaging displacements. This suggests that the remedial designs should be based on displacement criteria rather than on the factor of safety against liquefaction. The difficulty in such cases, however, is in determining the acceptable size and distribution of such zones. Further centrifuge modeling and/or calibrated numerical parametric studies in this respect will be very useful. As shown by this program, the results of such tests would be extremely effective in the development of verified design guidelines, as well as in calibration of computational procedures.

## 7. ACKNOWLEDGEMENTS

The authors would like to acknowledge the Corps of Engineers, Headquarters for their support of this research.

## 8. REFERENCES

- Adalier, K. (1996). "Mitigation of Earthquake Induced Liquefaction Hazards," Ph.D. Thesis, Department of Civil Engineering, Rensselaer Polytechnic Institute, Troy, NY, USA, 659 pp.
- Adalier, K., and Sharma, J. (2000). "Geotechnical Centrifuge Modeling for Civil Engineering Practice," Proc. of 4<sup>th</sup> Inter. Congress on Advances in Civil Engineering, Gazimagosa, Cyprus, Vol. 1, 475-484.
- Adalier, K., Elgamal, A.-W., and Martin, G.R. (1998). "Foundation Liquefaction Countermeasures for Earth Embankments," Journal of Geotechnical and Geoenvironmental Engineering, ASCE, 124(6), 500-517.
- Arulanandan, K. and Scott, R.F., eds. (1993). "Verification of Numerical Procedures for the Analysis of Soil Liquefaction Problems," Conference Proceedings, Univ. of California at Davis, CA, Volume 1, Balkema.
- Arulmoli, K., Muraleetharan, K.K., Hossain, M.M., and Fruth, L.S. (1992). "Verification of Liquefaction Analysis by Centrifuge Studies Laboratory Testing Program Soil Data," Technical Report by The Earth Technology Corporation, Irvine, California, March, 404 pp.
- Dobry R., Taboada T., Liu L. (1995). "Centrifuge modeling of liquefaction effects during earthquakes." Proc., 1<sup>st</sup> Int. Conf. on Earthquake Geotechnical Engineering, Special, Keynote and Theme Lectures, IS-Tokyo, Japan, 129-162.
- Duke, C.M., and Leeds, D.J. (1963). "Response of Soils, Foundations, and Earth Structures to the Chilean Earthquakes of 1960," Bulletin of the Seismological Society of America, 53(2).
- Elgamal A.-W., Dobry, R., Van Laak, P., and Nicolas-Font, J. (1991). "Design, Construction and Operation of 100g-ton Centrifuge at RPI," Proc. Int. Conf., Centrifuge 91, Boulder, CO, H.Y. Ko and F.G. McLean (eds.), pp. 27-34.
- Elgamal A.W., Zeghal, M., Taboada, V., Dobry, R. (1996). "Analysis of site liquefaction and lateral spreading using centrifuge testing records." Soils and Foundations, 36(2), 111-121.
- Henderson, J. (1933). "The Geological Aspects of the Hawke's Bay Earthquakes," The New Zealand Journal of Science and Technology, No.XV, July.
- Ledbetter, R.H., Liam Finn W.D., Hynes, M.E., Nickell, J.S., Allen, M.G., and Stevens, M.G. (1994). "Seismic Safety Improvement of Mormon Island Auxiliary Dam," 2<sup>nd</sup> Seismic Short Course on Evaluation and Mitigation of Earthquake Induced Liquefaction Hazards, Los Angeles, Calif.
- Lee, F.H. (1990). "Frequency Response of Diaphragm Pore Pressure Transducers in Dynamic Centrifuge Model Tests," Geotechnical Testing Journal, 13(3), 201-207.
- Finn, W.D.L. (2000) "State-of-the-art of Geotechnical Earthquake Engineering Practice," Soil Dynamics and Earthquake Engrg., 20, 1-15.
- Kimura, T., Takemura, J., Hiro-oka, A., Okamura, M., and Matsuda T. (1995). "Countermeasures against Liquefaction of Sand Deposits with Structures," 1<sup>st</sup> Int. Conf. on Earthq. Geotech. Eng., Tokyo, Japan, 163-184.
- Krinitzsky, E.L., and Hynes, M.E. (2002). "The Bhuj, India, earthquake: lessons learned for earthquake safety of dams on alluvium." Engineering Geology 2068 (in press).
- Marcuson, W.F., and Silver, M.L. (1987). "Shake-Proof Dams," Civil Eng., 57 (12), 44-47.
- Marcuson, W.F., Hadala, P.F., and Ledbetter, R.H. (1996). "Seismic Rehabilitation of Earth Dams," Journal of Geotechnical Engineering, ASCE, 122(1), 7-20.
- McCulloch, D.S., and Bonilla, M.G. (1967). "Railroad damage in the Alaska Earthquake," Journal of the Geotechnical Engineering Division, ASCE, 93(5), 89-100.



Schofield, A.N. (1981). "Dynamic and Earthquake Geotechnical Centrifuge Modeling," Proc., Int. Conf. on Recent Advances in Geotech. Earthq. Eng. and Soil Dyn., University of Missouri-Rolla, Mo., Vol. 3, 1081-1100.

Seed, H.B. (1968). "Landslides During Earthquakes Due to Soil Liquefaction," Journal of the Geotechnical Engineering Division, ASCE, 94(SM5), 1055-1123.

Seed, H.B. (1970). Soil Problems and Soil Behavior. Chapter 10 of Earthquake Engineering, Book, Wiegel R. L. (ed.), Prentice-Hall Inc., N.J.

Tani, S. (1996). "Damage to Earth Dams," Soils and Foundations, Special Issue on Geotechnical Aspects of the January 17, 1995 Hyogoken-Nambu Earthquake, 263-272.

Van Laak, P., Adalier, K., Dobry, R., and Elgamal, A.-W. (1998). "RPI's Large Centrifuge Shaker," Proc. of International Conference Centrifuge'98, Tokyo, Japan, Sept. 1998, 105-110.

Yokomura, S. (1966). "The Damage to River Dykes and Related Structures Caused by the Niigata Earthquake," Soils and Foundations, Tokyo, Japan, VI(1), 38-53.

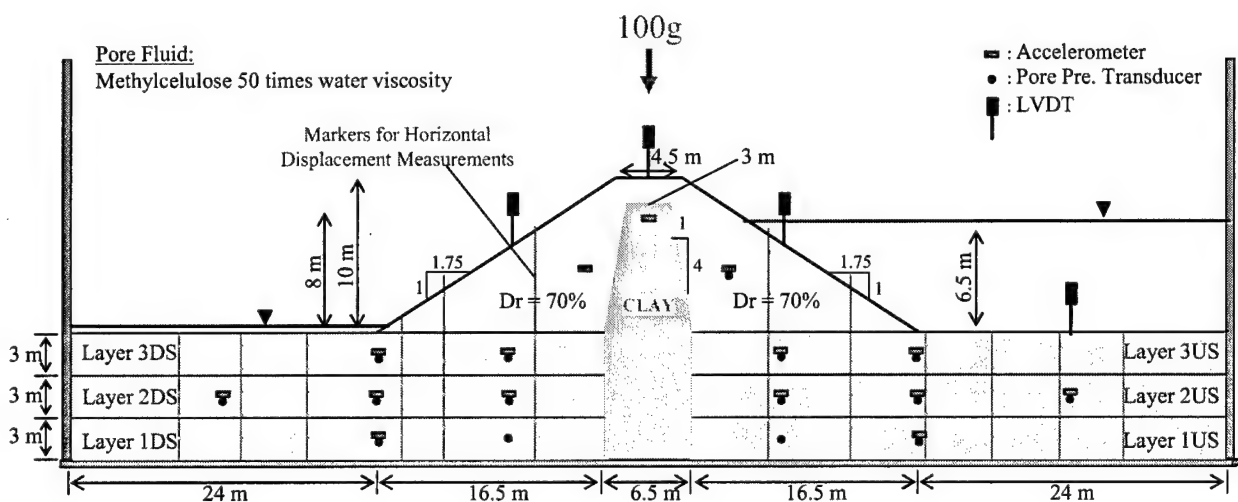


Fig.1 Schematic of a typical dam-foundation model.

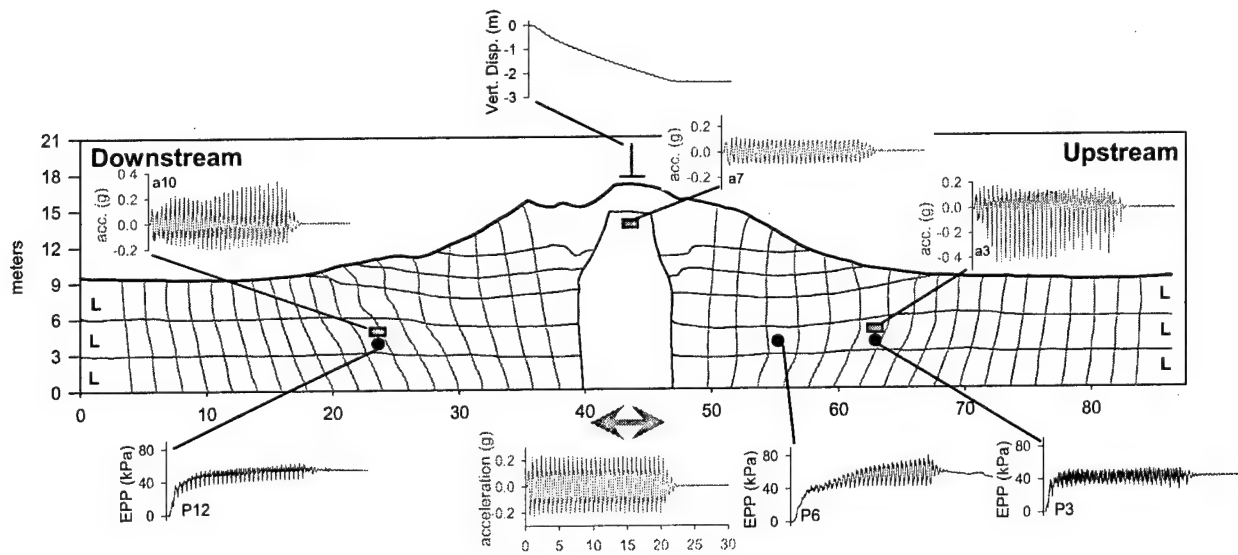


Fig. 2 Selected transducer data and post-shake deformed model (mid-cross-section)-Model 1.

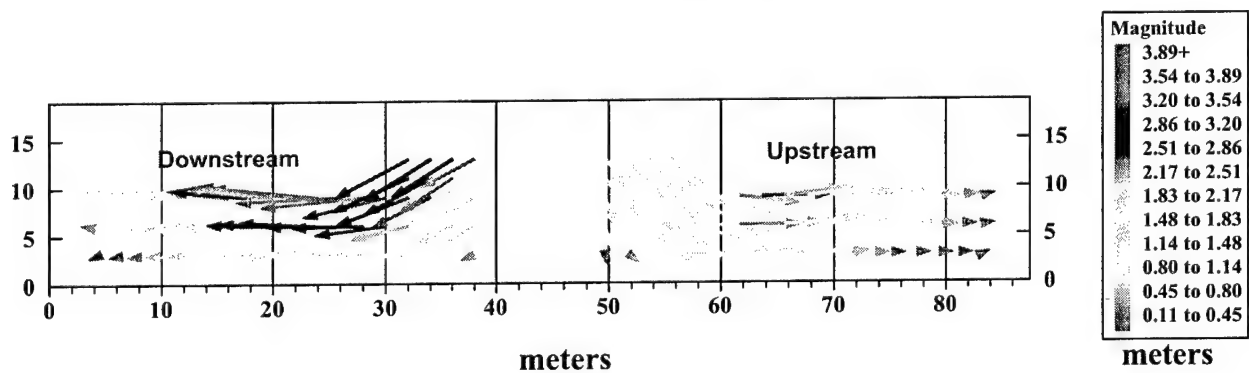


Fig. 3 Deformation vectors in Model 1.

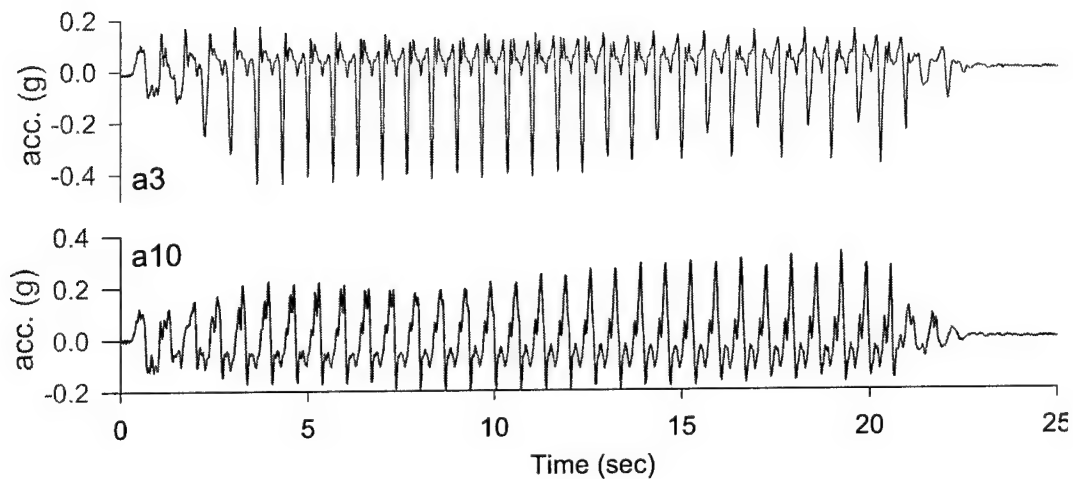


Fig. 4 Close-up of a3 and a10 acceleration time histories-Model 1.

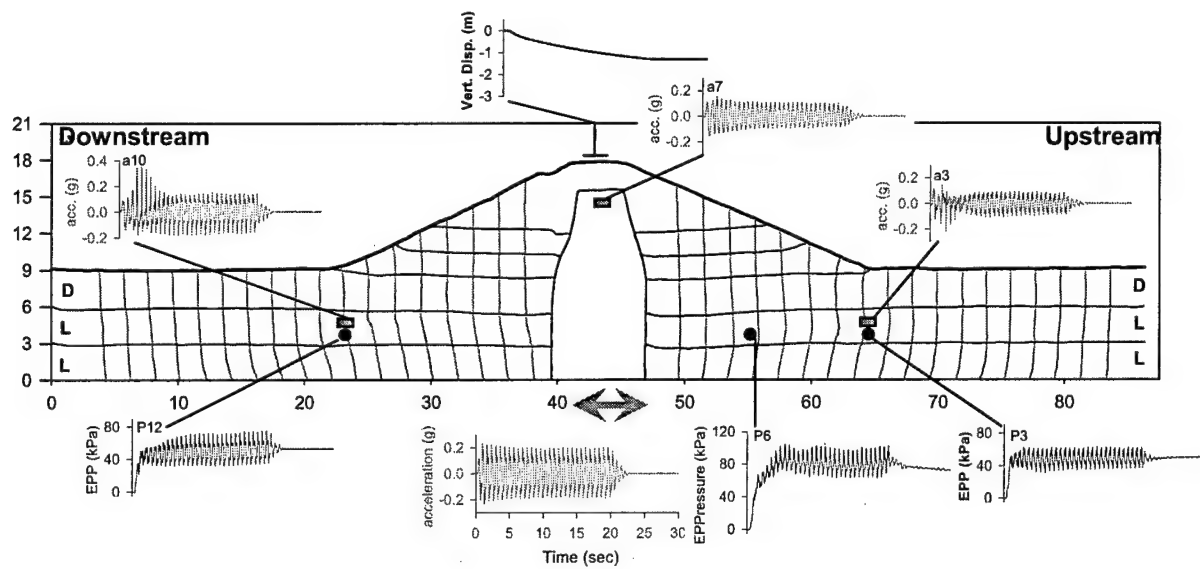


Fig. 5 Selected transducer data and post-shake deformed model (mid-cross-section)-Model 2.

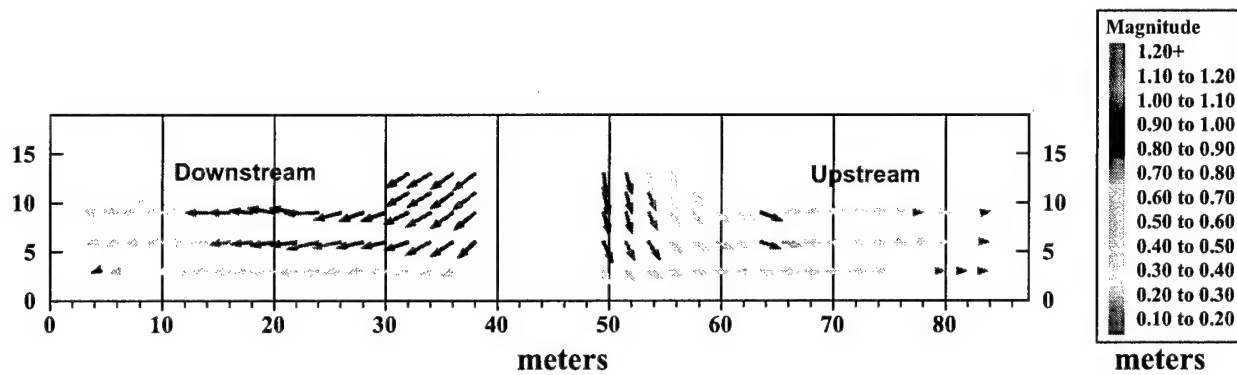


Fig. 6 Deformation vectors in Model 2.

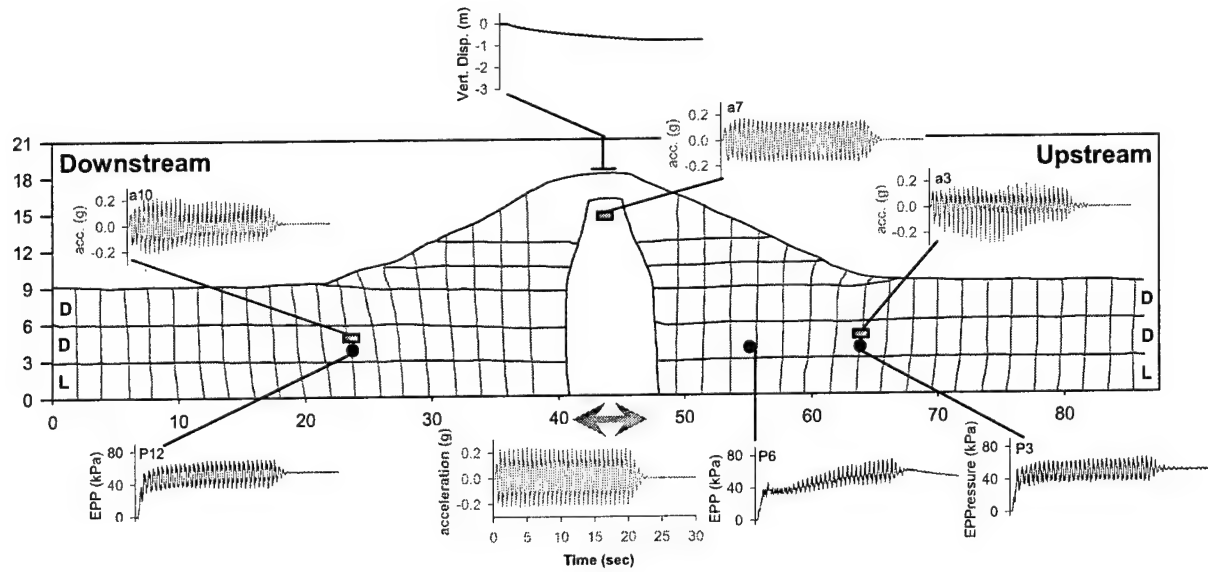


Fig. 7 Selected transducer data and post-shake deformed model (mid-cross-section)-Model 3.

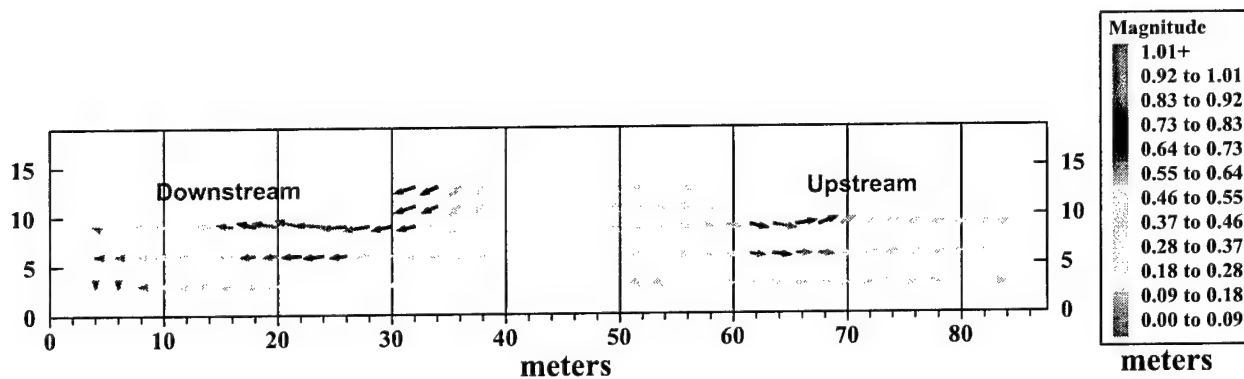


Fig. 8 Deformation vectors in Model 3.

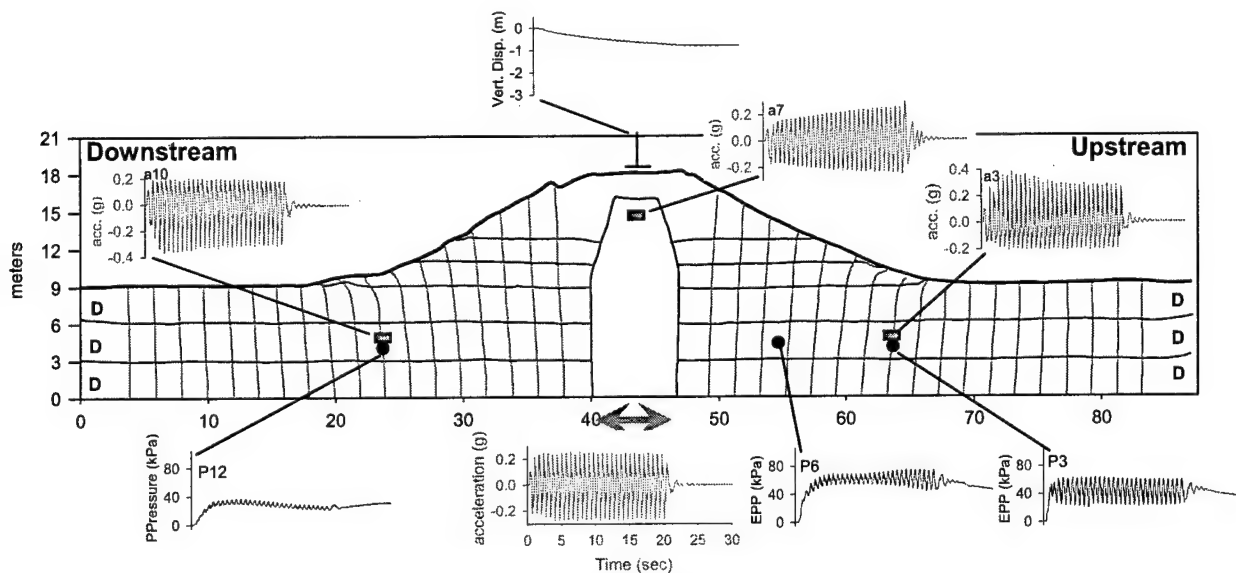


Fig. 9 Selected transducer data and post-shake deformed model (mid-cross-section)-Model 4.

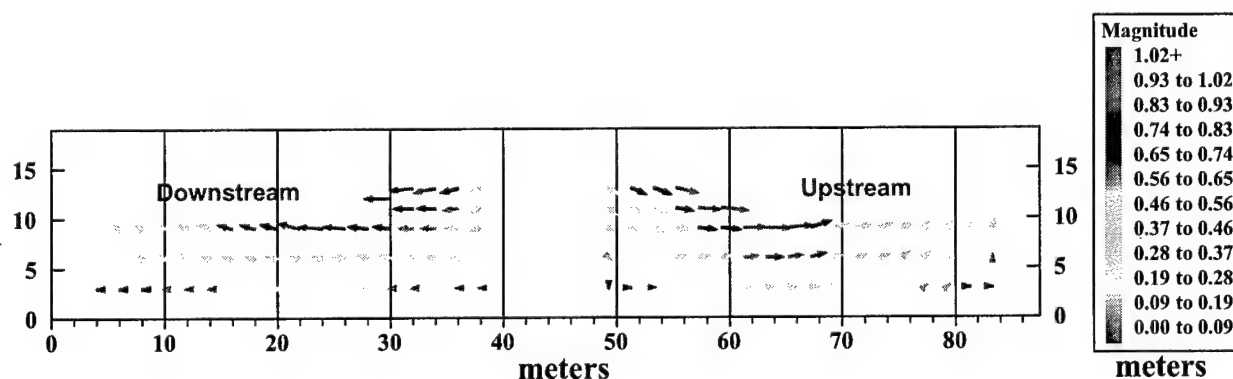


Fig. 10 Deformation vectors in Model 4.

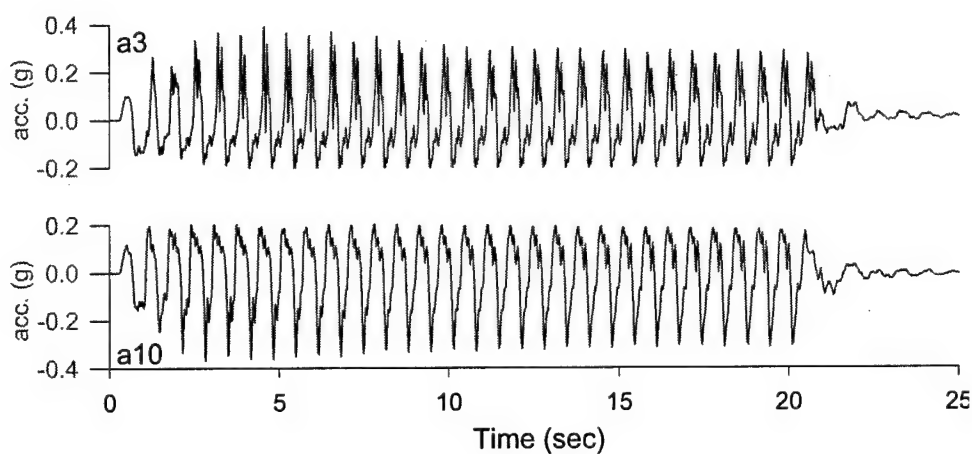


Fig. 11 Close-up of a3 and a10 acceleration time histories-Model 4.

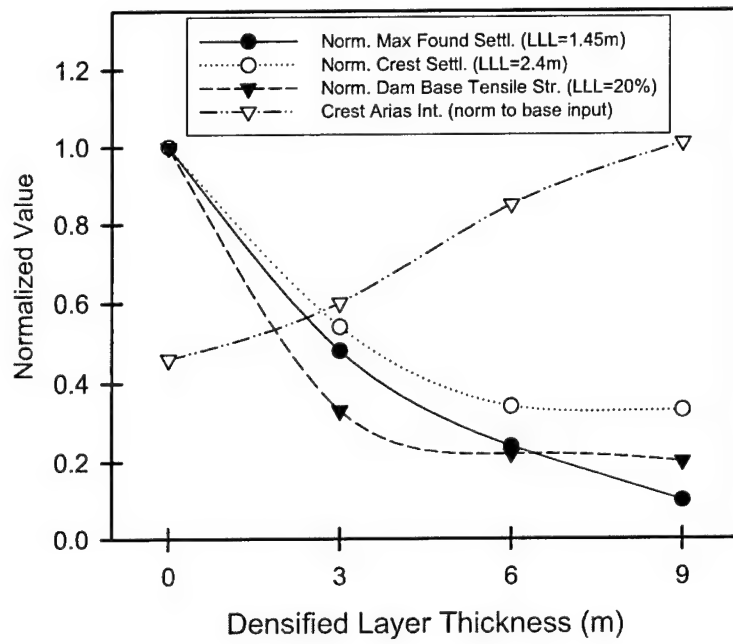


Fig. 12 Some dynamic performance parameters for the Models 1-4.

## Evaluation of Permanent Displacement in Seismic Analysis of Fill Dams

Norihisa MATSUMOTO \*

### ABSTRACT

Permanent deformations of fill dams subjected to strong earthquake shakings are discussed, by comparing the measured deformation of prototype dams, centrifuge physical model tests, and analytical results.

**Key words:** Fill dams, Seismic analysis, Permanent displacement

### 1. INTRODUCTION

Performance of fill dams to the strong earthquakes in the past indicates that significant damages were caused only in case the foundations or embankment materials lost their strength due to earthquake shakings. Therefore, if foundations or embankment materials do not have liquefaction potential, performances of fill dams subjected to strong seismic motions have been satisfactory and will be evaluated by the permanent deformation obtained from seismic analysis. Here, two questions arise. The first question is how much deformation will be acceptable. The second question is whether the permanent deformation would produce discontinuous displacements or not. If discontinuous displacements occur in the impervious zone of the embankment, one should evaluate that their effects on the internal erosion of the impervious material, and they will be repairable or not. The paper discusses the evaluation of the permanent displacements in the seismic analysis of fill dams.

### 2. MEASURED DEFORMATION

First, measured settlements of two rockfill dams are illustrated in Fig. 1. Minase Dam is 66.5 meter high concrete face rockfill dam(CFRD). The dam was constructed by dumped rockfill, and completed in 1962. The June 16, 1964 Niigata Earthquake( $M_{JMA}=7.5$ ) occurred offshore of Niigata Prefecture, facing the Sea of Japan. The dam, located 147 km from the epicenter, experienced maximum crest settlement of 14 cm. Strong motion record was not obtained. Peak ground acceleration(PGA) at Minase Dam is assumed to be 0.08g, from empirical formula. Mino-o Dam was built in 1980, and has a structure of rockfill with central clay core. The rockfill was compacted. It was subjected to January 17, 1995 Kobe Earthquake( $M_{JMA}=7.2$ ), and the settlement was minimal, with its satisfactory reaction to the earthquake. It was located 48km from the epicenter, and 11km from the causative fault. Strong motion records were obtained, with a horizontal peak acceleration(PGA) of 0.13g at the foundation inspection gallery, and 0.4g at the crest of the dam. Although Mino-o Dam was shaken more severely than Minase Dam, the settlement of Mino-o Dam was much less than Minase Dam. There is a difference of dam structure in these two rockfill dams, but the difference of settlements is mostly attributed to compaction i.e. one is dumped and the other is compacted. Another difference of two dams is the difference of elapsed time after the completion. As shown in Fig.1, settlements in

\* Japan Dam Engineering Center  
Mesonic 39 Mori Bldg, Azabudai 2-4-5, Minatoku  
Tokyo 106-0041, Japan

rockfill dams are large in first several years after completion, and tend to be very small afterward. Settlements of both dams due to earthquakes seem to have facilitated the long-term deformation in advance. Fig. 2 shows the settlements(after the completion of ten years) of eleven rockfill dams in Japan(1). Fig. 2 shows the settlements(after the completion of ten years) of eleven rockfill dams in Japan. The settlement ratio(settlement/height) depends on the dam height, and ranges from 0.1 to 0.5%.

### 3. EXPERIMENT

Yoshiaki Ariga et al. conducted centrifuge shake table model tests for rockfill dam by using the UC Davis facility(2,3,4). The model is 0.4m high, and 0.9 wide. The material of the model is crushed rock with the maximum size of 9.5mm for rockfill and the mixture of clay, sand, cement and water for impervious core. The slope is 1.8 horizontal to 1 vertical in both upstream and downstream. The model is subjected to centrifuge force of 40g, and hence the model corresponds to 16m high dam.

The peak ground acceleration of input motion was increased from 5g(equivalent to 0.0125g in prototype) to 40g(equivalent to 1.0g in prototype). Fig. 3 shows the decrease of the natural frequency of the model with the increase of the input acceleration. This indicates the modulus of rigidity of the material reduces with the increase of the strain. The permanent deformation of the model occurred prominently at the peak ground acceleration of 30g(equivalent to 0.7g in prototype) as shown in Fig.4. When the model is subjected to 40g(equivalent to 1.0g in prototype), the raveling of shoulders near dam crest occurred, but deep sides did not happen. The final configuration of the model

is depicted in Fig. 5. The response of the model is well interpreted by equivalent linear hypothesis, if the input peak ground motion is less than 30g(equivalent to 0.7g in prototype).

He performed analyses for the centrifuge model. He also computed permanent displacement of the model by using the computer code of FLAC, assuming Mohr-Coulomb failure criteria for the static analysis and Prof. Finn's model parameter for dynamic analysis. The FLAC analysis predicts the bulging of the dam and deformation of the dam crest to upstream direction that is different from centrifuge model test. The pore pressure build up assumption may not have reproduced the physical model behavior.

Tomoya Iwashita et al. conducted the centrifuge shake table model tests for rockfill dams at Public Works Research Institute(5,6,7). The height and width of the model is 0.4m, and 0.3m, respectively. The upstream slope is 2.0 horizontal to 1.0 vertical, and 1.7 horizontal to 1.0 vertical. The grain size distribution of the model material(maximum grain size is 9.75mm) is the parallel to that of prototype rockfill. The model core material is sandy clay. The tests are conducted under the centrifuge acceleration of 50g. The significant permanent deformation emerged after the input motion of 20g(equivalent to 0.4g in prototype), as shown in Fig. 6. When the input motion was 30g(equivalent to 0.6g in prototype), the downstream shoulder was stripped off from the model, and bare core appeared(see Fig. 7). The deep slides, however, did not appear. The rise of pore pressure was measured during excitation. He simulated the model dam performance by using the densification theory. In this theory, he assumed the Mohr-Coulomb failure criteria, and used the analytical code of MUDIAN. Fig.



8 gives the computational results. Comparing Fig. 8 with Fig. 7, the horizontal deformation at the middle elevation of the numerical model (Fig. 8) is larger than the physical model (Fig. 7). The three dimensional effects should be taken into account in the physical model.

#### 4. ANALYSIS

In the previous workshop, Gilles Bureau presented an excellent summary report on seismic analysis of embankment dams (8). He discussed the simplified procedures, equivalent-linear analysis, and nonlinear analysis. The simplified procedures rely on empirical correlations derived from observed and calculated seismic response. For materials not susceptible to liquefaction, response is computed by using iterated shear moduli and damping coefficients compatible with average induced strains, and permanent displacements are obtained from double integration of accelerations that exceed the yield acceleration. In his paper, Bureau placed more emphasis on nonlinear analyses, which fall into two broad categories: elastic-plastic (EPNL) and direct nonlinear (DNL). He presented the examples NL analysis on Los Leones and Los Angeles dams. He summarized that NL computer programs using quality input data, should be reliable up to calculated crest displacement to dam height ratio of about ten percent, and deformation and liquefaction estimates should be pondered by a critical assessment of factors that may impact their reliability.

In both of EQL and NL analyses, shear strength of materials has significant impact on the permanent deformation from the analysis.

In the Newmark approach to calculate the permanent deformation of fill dams, shear strength assumption has great influence on

the results. In this approach, first the slip surface of the minimum factor of safety is calculated. The friction angle decreases with the increase of confining pressure. If we assume the constant friction angle, the critical slip surface will be shallow one, and if we assume the dependency of friction angle on confining pressure, the critical surface will be deep one. One may raise an important question, whether the deep slide failure is possible mode of failure, even if the material does not lose strength during earthquakes. The aforementioned centrifuge model tests indicate that the possible mode of failure of rockfill structure is raveling of shoulders and is not deep slides. If it is true for prototype, the hypothesis of deep slide surface in Newmark approach is somewhat erroneous. If deep failure surface is true, and that surface intersects the impervious core, one should answer the seepage problem through the slip surface.

Here, the strength effect on permanent deformation is numerically tested. The model is shown in Fig. 9, with the height of 105 meter, and the assumed slip surface is given in Fig. 10.

First, the curved shear strength envelopes for rockfill materials are used as follows:

$$\tau_f = A(\sigma_n)^b \quad (1)$$

where  $\tau_f$  is shear strength, and  $\sigma_n$  is effective confining stress,  $A$ , and  $b$  are strength constants.

The computed deformation increases rapidly with the decrease of the strength parameter of  $A$ . If strength reduction after the peak strength is taken into account, deformation is amplified (see Fig. 11). Fig. 12 gives another relationship of deformation and strength parameter  $\phi$ , where  $\phi$  is average friction angle on the slip surface. The computed deformation is not significantly large, if the average friction angle is larger

than  $40^\circ$ . Another aspect of shear strength is the evaluation of shear resistance reduction from peak strength to residual strength. The strength reduction concept is shown in Fig. 13. The sinusoidal input motion was used for the same model of Fig. 9 to emphasize the strength reduction of materials. Fig. 14 illustrates the influence of strength reduction on the permanent deformation.

Stress reduction after the peak strength depends greatly on the grain size (F. Tatsuoka et al. 9). When the grain size is small, stress reduces rapidly after peak strength, but when the grain size is large, the strength decreases gradually. The permanent deformation during earthquakes depends on the stress reduction after peak strength. Therefore large size rock contributes to limiting the permanent deformation.

## 5. CONCLUSIONS

The performances of Minase and Mino-o Dam suggest the permanent deformation of rockfill dams to earthquakes would be small, especially for compacted rockfill.

In the centrifuge shake table tests plastic deformation appears when the excitation PGA reaches 0.4 to 0.7g. No definite slip surface is found in the rockfill dam model. Nonlinear analysis verifies performance of centrifuge model partly, but still needs further interpretation.

In the analysis of EQL and NL, strength parameters have great influence on the computed deformation, and strength reduction or softening of the materials should be taken into account. The grain size should be taken into account in the strength reduction.

## REFERENCES

- (1) N. Matsumoto, N. Yasuda, M. Ito, "Measured Displacements of Filldams", Technical Memorandum of PWRI, No. 3001, 1991
- (2) Yoshiaki ARIGA ; Centrifuge Shaking Test on Earthquake Response Property of Rock-fill Dam, Proceedings of 25<sup>th</sup> JSCE Earthquake Engineering Symposium No.B8-6, pp445~448, 1999
- (3) Yoshiaki Ariga, Zengyan Cao ; Examination on Earthquake Damage of Rock-fill Dam by Centrifuge Shaking Test , Proceedings of 1<sup>st</sup> JSCE Symposium for the Enhancement of Earthquake Performance of Infrastructures based on Investigation into Fracturing Process, No.e-12, pp2259~2262, 2000
- (4) Yoshiaki ARIGA, Zengyan Cao, Hiroyuki Watanabe, Examination on Earthquake Deformation of Rock-fill Dam by Centrifuge Shaking Model Test , Electric Power Civil Engineering No.291, pp46~50, 2001
- (5) T. IWASHITA, "Numerical Simulation of Sliding of an Earth Dam, during the 1995 Kobe Earthquake", Fourth International Conference on Recent Advances in Geotechnical Earthquake Engineering and Soil Dynamics, March 26-31, 2001, Paper No.5.13
- (6) Iwashita, M. Tsukuni, "Simulation of Elastic-Plastic Analysis of Centrifuge Rockfill Dam Model", 26th Symposium on Earthquake Engineering, Aug. 2001, pp. 685-688
- (7) T. Iwashita, S. Yamamoto, "Centrifuge shake table tests on Rockfill dam with central

clay core", 36th Geotechnical Engineering Symposium, 2001, pp.1345-1346,

(8) Gilles Bureau, Seismic Analysis and Safety Evaluation of Embankment Dams, Proc. of 2nd US-Japan Workshop on Advanced Research on Earthquake Engineering for Dams, May, 1999 pp311-321.

(9) Yoshida,T. ,Tatsuoka,F. ,Siddiquee,M.S.A. and Kamegai,Y.(1995), "Shear banding in sands observed in plane strain compression", *Localization and Bifurcation Theory for Soils and Rocks* (Chambon et al.,ads.), Balkema, pp.165-179

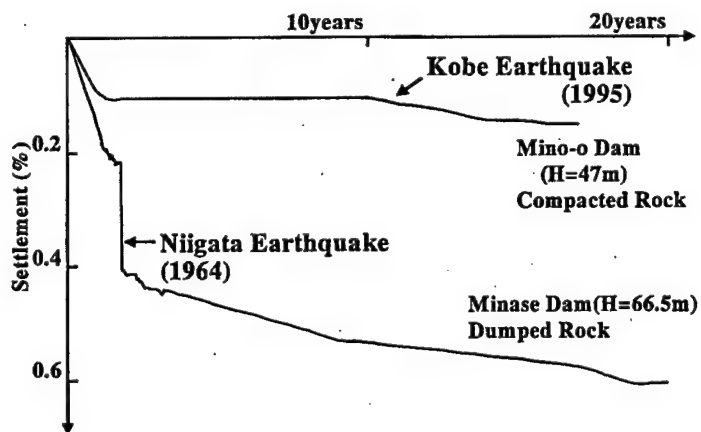


Figure 1. Settlements of Minase and Mino-o

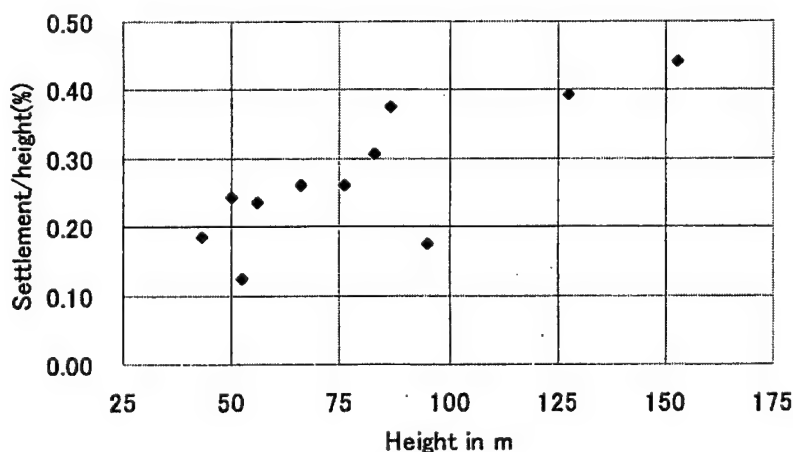


Figure 2. Settlements ratio ( ten year settlement/height ) of eleven rockfill dams

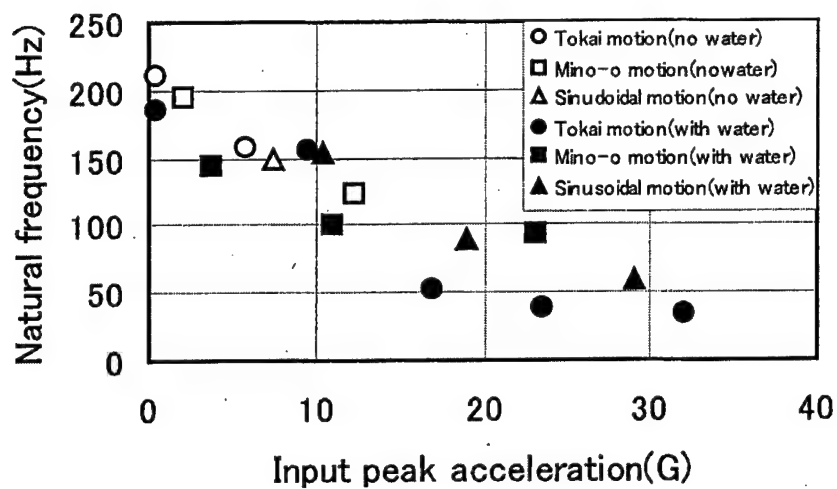


Figure 3. Relation for natural frequency and input acceleration  
(After Y. Ariga)

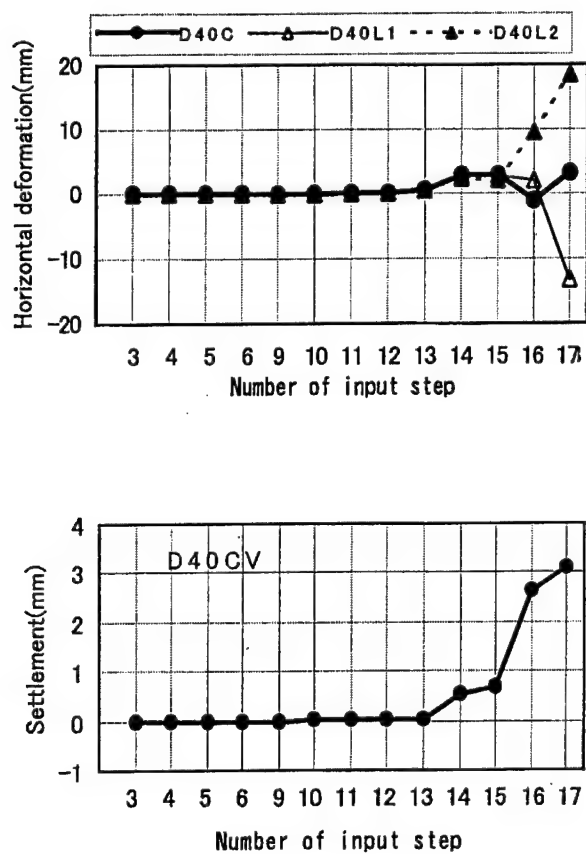


Figure 4. Development of permanent displacement  
with increase of input motion  
(After Y. Ariga)

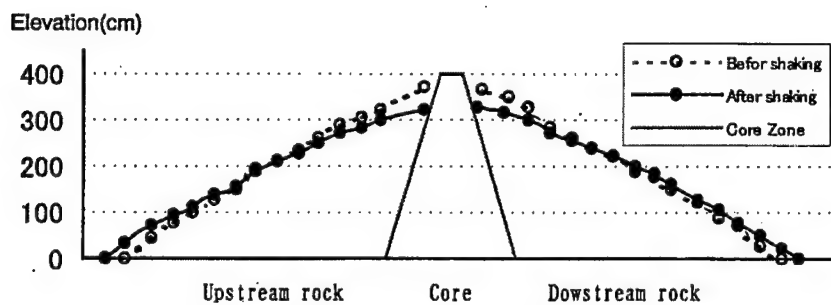


Figure 5. Final configuration after shaking  
(After Y.Ariga)

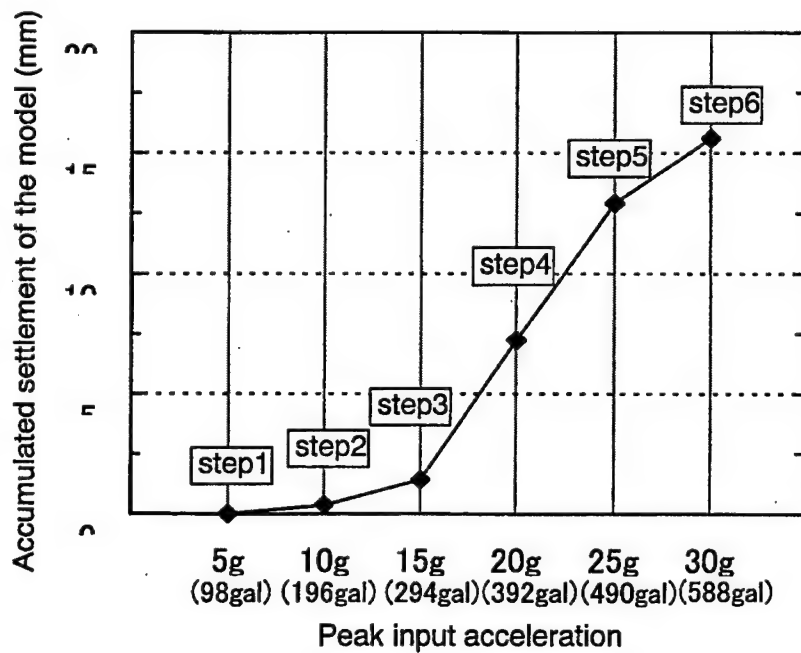


Figure 6. Accumulated settlement of dam crest  
(After T.Iwashita)

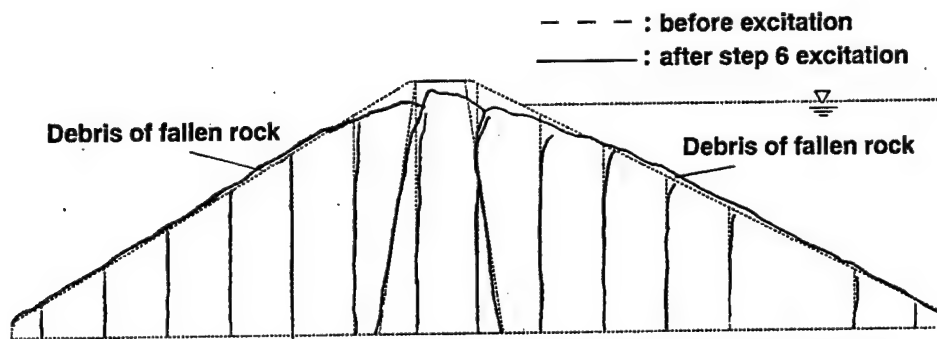


Figure 7. Deformation of the model after step 6 excitation  
(After T.Iwashita)

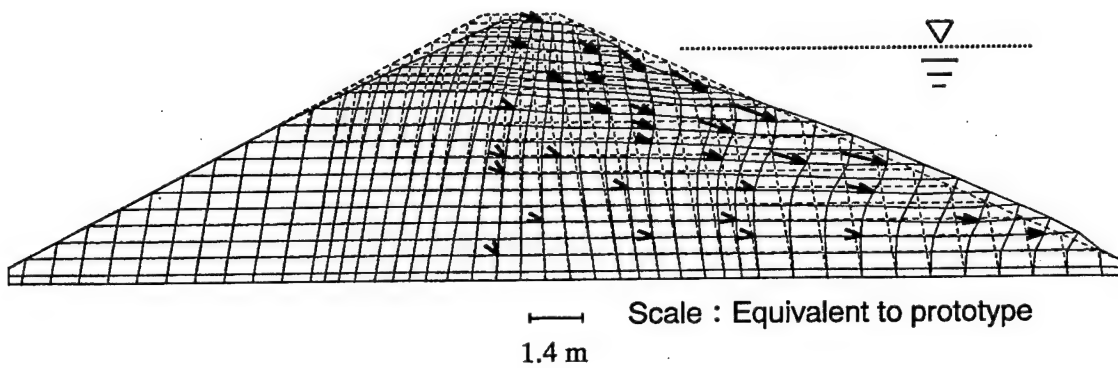


Figure 8. Deformation from elastic-plastic nonlinear analysis  
(After T.Iwashita)

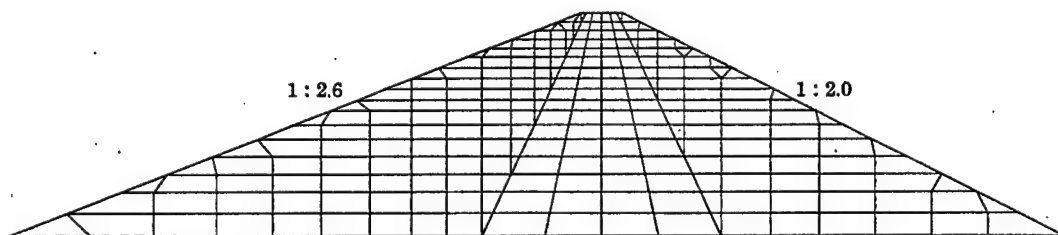


Figure 9. Finite element of the model

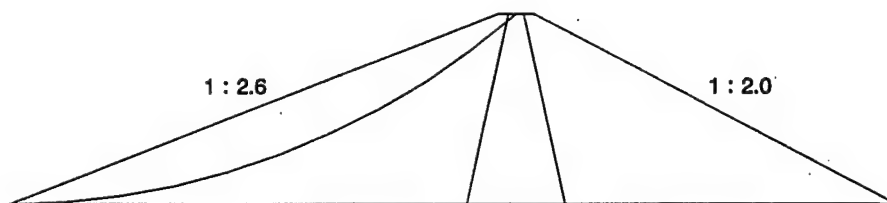


Figure 10. Assumed slip surface

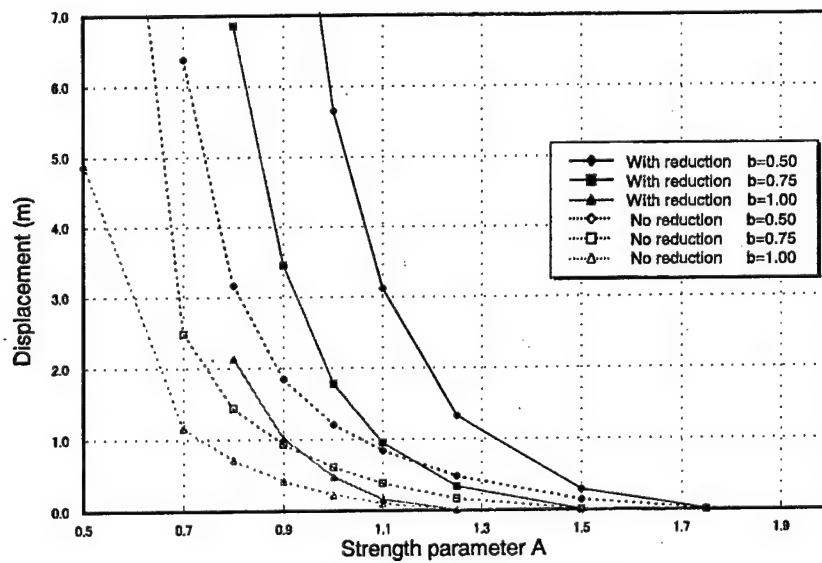


Figure 11. Cumulative displacement and strength parameter A

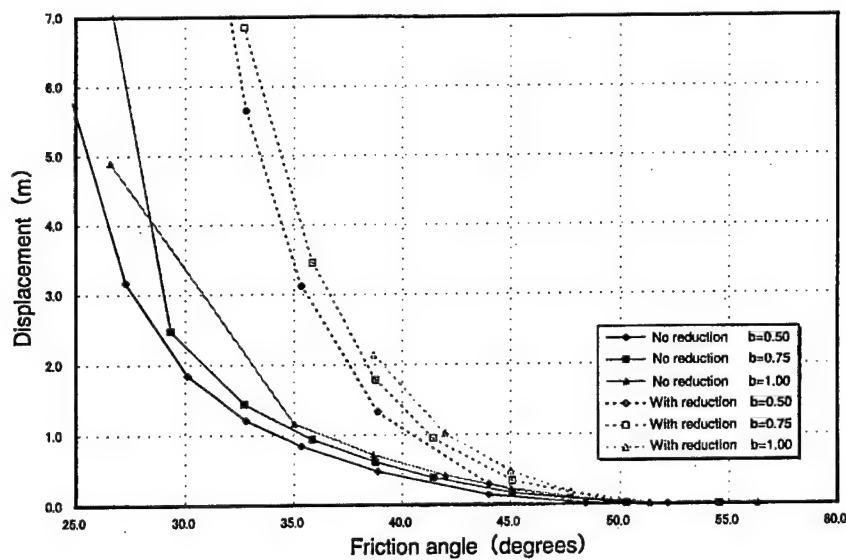


Figure 12. Cumulative displacement and friction angle



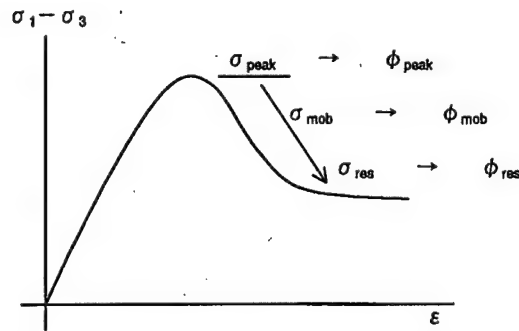


Figure 13. Friction angle of peak and residual strength

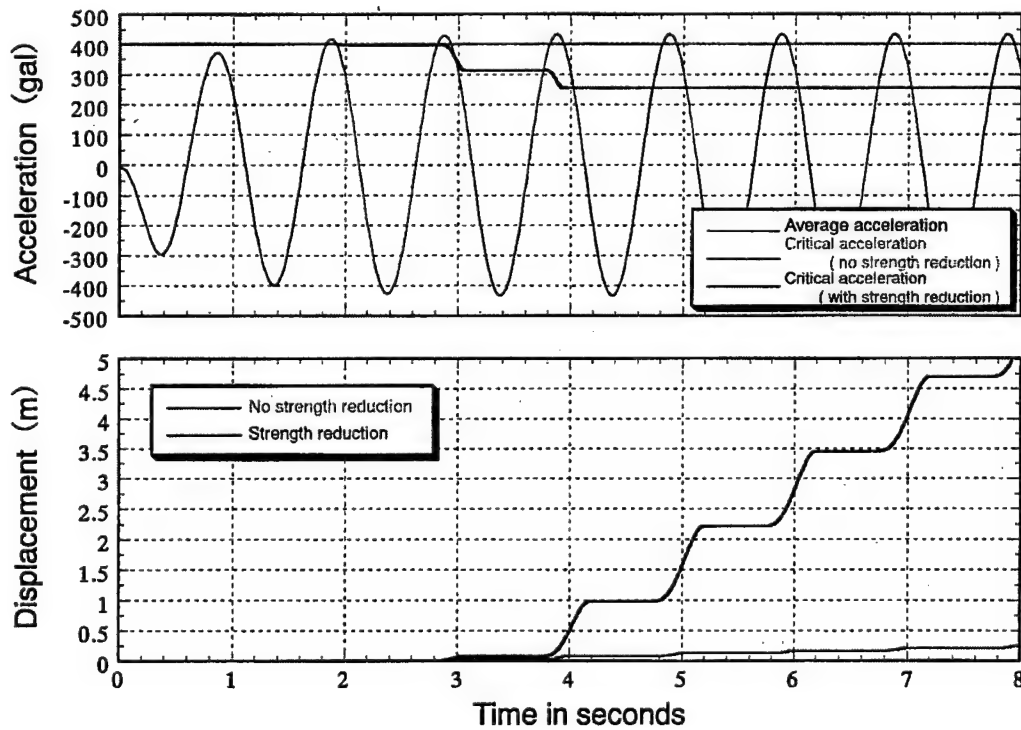


Figure 14. Cumulative deformation to sinusoidal input motion

This page intentionally left blank.

## Post Earthquake Residual Strength of Liquefiable Cohesive Soils

by

Samuel T. Stacy, P.E.<sup>1</sup>

### ABSTRACT

Static equilibrium slope stability analyses and 3-dimensional finite deformation analyses are the two major methods of predicting dam performance during major earthquake shaking. The critical element to both methods is the selection of the post earthquake residual strength of the liquefiable soil layers in the embankment and foundation. The post earthquake residual shear strength of the soils utilized in these analyses has a significant effect on calculated factors of safety, deformations computed, and to the determination of the need for remediation.

Research into the evaluation of the performance of cohesionless soils such as sands during earthquake shaking has been ongoing within the engineering community for the past 30 years and is now widely accepted. The evaluation of the performance of cohesive fine-grained soils such as silt and clay has not been investigated to the extent that sands have. Although studies concerning identifying those clays and silts subject to liquefaction are available, little research into the post earthquake strength of these soils has been investigated. The current common practice is to assume that these soils will perform like remolded clays, and the strength of these soils will degenerate to their residual or minimum strength when subject to dynamic loading.

A significant effort by the Vicksburg District, Corps of Engineers has been made to evaluate the residual strength of liquefiable cohesive soils in the foundations of Arkabutla and Enid Dams in north Mississippi as part of the seismic safety evaluation of these dams. Most of this research has utilized in-situ testing methods including cone penetration testing and field vane shear

testing, as obtaining quality undisturbed samples of the soils for laboratory testing have proven difficult. A significant database of strength information has been collected which will offer new knowledge into the residual strength of liquefiable fine-grained cohesive soils. The results of these studies will be presented.

### 1 INTRODUCTION

The seismic evaluation of large dams involves many factors and important variables. These include the determination of the maximum credible or design earthquake expected, the dynamic stresses at the dam due to the earthquake, the seismic resistant properties of the embankment, and foundation soils. However, the expected seismic response of a dam during a major earthquake is ultimately evaluated utilizing two major techniques: (1) satisfying post earthquake static equilibrium slope stability analyses and (2) evaluating dam performance during earthquake shaking utilizing state-of-the-art finite element deformation analyses. The critical parameter in both criteria is the post earthquake strength of the "liquefiable" soil layers in the embankment and foundation.

Most of the research performed by the engineering community in evaluating soil behavior during earthquakes and the post earthquake strengths of liquefiable soils has been with respect to cohesionless soils. Identification of those cohesionless soils subject to liquefaction and the post earthquake strength of those soils is presently very reliable. The procedure involves the use of Standard Penetration Testing (SPT), and correlations of SPT blow count with respect

<sup>1</sup> U.S. Army Corps of Engineers, Analytical Section, Vicksburg District, Vicksburg, Mississippi, USA.

to shear strength using Seed's empirical approach.

Research in evaluating the performance of liquefiable cohesive soils such as clays and silts is still in a relative infant stage. Although much is known regarding the criteria for determining what clays and silts are subject to liquefaction, very little is known regarding the post earthquake shear strength of these soils.

The current practice is to assume that these soils will perform like remolded clays, such that, during major earthquake shaking the strength of these soils will degenerate to their residual or minimum strength. The proper method of evaluating these soils is therefore to determine the residual strength of any liquefiable cohesive soils in the embankment or foundation.

A significant effort by the Vicksburg District has been made to evaluate the residual strength of liquefiable clays and silts in the foundations of Sardis Dam, Enid Dam and Arkabutla Dam. Many methods have been used to evaluate the residual strengths of these soils including; Standard Penetration test, Laboratory testing, Field Vane Shear testing (FVST), and Cone Penetration testing (CPT). Laboratory testing has proven unreliable in the studies of Sardis, Arkabutla and Enid, because it is very difficult to obtain quality undisturbed samples. Standard Penetration results in cohesive soils also are suspect and unreliable, and the results require conservative assumptions in strength estimates. The best tool for measuring the residual strength of these soils at least at Sardis, Enid and Arkabutla was performing Field Vane Shear testing, and using these results for site-specific correlation of the Cone Penetration Test. Cone Penetration Tests can then be performed all along the dam to evaluate residual strength trends. This paper will provide a review of the various methods of predicting post earthquake residual strengths, the evolution of the state-of-the-art in evaluating residual strengths at these dams, and recent results utilizing the Field Vane and Cone Penetration testing.

## **2 Conservatism in Seismic Evaluations Involving Liquefiable Cohesive Soils**

Common engineering practice is to make conservative assumptions in design, especially in complex problems like the seismic safety of large dams where possible loss of life could result from seismic instability. It is also common practice to make conservative assumptions when very little information or research knowledge is available. Conservatism in seismic design when dealing with liquefiable cohesive soils has been justified in the past due to lack of understanding. Engineers will be able to reduce the degree of conservatism they use in making engineering judgments as greater understanding of these soils is obtained.

In the seismic evaluation of large dams, many varied factors must be addressed before a final determination of seismic safety can be reached. Conservatism is inherently built into each factor such that when the factors are combined to form the final decision, the result is conservatism built upon conservatism.

In a seismic evaluation, the first major factor to be addressed is the development of the design earthquake. Some conservatism is inherent in the selected design earthquake, especially in dams in the central United States where very little seismic history exists as compared to seismic zones in the western United States. The next major factor in seismic analysis is propagation of the earthquake to the dam site for development of the earthquake dynamic stresses in the dam. Conservatism is again built into this due to the lack of historical records. Even the assumption that the earthquake will occur during very high lake levels (major earthquakes during low lake levels will have little effect on the dam with respect to loss of pool) has low probability and is a conservative assumption.

There is also some conservatism in the criteria for determining if a given cohesive soil is liquefiable during earthquake shaking, and in defining the soil's performance through loss of

strength estimates. Identifying those cohesive soils susceptible to liquefaction is more reliable than in the past with the present understanding of the "Chinese criteria" and with correlations with SPT and CPT data. The conservatism involving cohesive soils occurs in selection of the post earthquake residual strengths characteristic of these soils, and even in establishing the thickness and extent of the liquefiable layers for analyses. The weak layers utilized in analyses include all clays and silts identified as liquefiable and thus include the entire range of residual strengths of those soils. This is conservative since some of the soils identified as liquefiable may have residual strengths high enough that they would not negatively affect the dam's performance during an earthquake. It is also conservative to assign a residual strength ratio,  $S_r/p'$ , on the lower end of the range for the entire weak layer. This conservative assumption results in a shear strength that is at times allot lower than even the average strength throughout the weak layer.

The assumption that strength degrades all the way to residual strength in liquefiable clays is also conservative. There are many factors that could affect this such as the intensity of earthquake, earthquake duration, and even confinement pressure. In reality only partial loss of strength could occur for given events.

It is therefore important to evaluate residual strength trends all along the dam such that a good approximation of the residual strength can be made for final seismic response studies. The determination of seismic safety and/or remediation needs is highly dependent on the residual strength chosen.

### 3 Methods for Identifying Liquefiable Clays and Silts

The primary criteria utilized for identifying cohesive soils subject to strength loss at Sardis, Arkabutla and Enid has been a combination of the Chinese Criteria and SPT  $N_{1(60)}$  values. All cohesive soils with  $N_{1(60)}$  value  $\leq 4$ , and soils meeting the "Chinese criteria" with an  $N_1$  value

$\leq 10$  are deemed liquefiable. Cohesive soil with an  $N_1$  value  $\geq 10$  is deemed non-liquefiable even if it meets the Chinese criteria. At the time of writing this report the  $N_{1(160)}$  value of 10 in the Arkabutla Dam Study was being reevaluated because the 0.28 g earthquake acceleration at Arkabutla was greater than the 0.20 g used in the earthquake study of Sardis (the above criteria being developed during the Sardis Dam study). The critical  $N_{1(60)}$  value discussed above is the SPT  $N_{1(60)}$  value at which cohesive soils are expected to liquefy or experience substantial strength loss. The critical  $N_{1(60)}$  values are determined utilizing the computer program "SHAKE" in conjunction with expected earthquake intensity, duration and time histories. The Chinese criteria was developed in China in the 1970's from studies of fine-grained soils, which had liquefied during earthquakes. The Chinese criteria is commonly used in seismic evaluations today and is a good screening tool in determining liquefaction susceptibility. The Chinese criteria is of course:

$$L_L \leq 35$$

$$W_n \leq 0.9 L_L$$

$$\text{Liquidity Index} \leq 0.75$$

$$\text{Percent Passing, } 0.005\text{mm} \leq 20$$

During these studies modifications to the measured index properties were developed because of differences in laboratory technique between the United States and China. These modifications were applied to the measured properties before comparison to the Chinese criteria. Also the Liquidity Index was not used.

Another method of identifying clays and silts subject to strength loss involved use of the Cone Penetration Test. The CPT has become a very efficient screening test for locating zones of soil, which might be susceptible to significant strength loss during earthquake shaking. The Vicksburg District first utilized the CPT in the study of Sardis Dam. It is also being used in the study of Enid and Arkabutla Dams. The CPT criteria for liquefaction for fine-grained (clays and silts) soils beneath the embankment are a tip resistance ( $Q_c$ ) of  $\leq 20$  tsf and a friction ratio

( $R_F$ ) of  $\leq 2.0$ . For fine-grained soils at the toe or in the free field of the dam, the criteria is  $Q_c \leq 15$  tsf and  $R_F \leq 2.0$ .

The evaluation of these dams utilizing the above criteria indicate the existence of layers of clay and silt subject to liquefaction or strength loss in their foundation. These layers vary in thickness as much as 18 ft but generally average 5 ft to 10 ft and are located from near the original ground surface to depths of 40 ft below the original ground surface. The evaluation of post earthquake residual strength of these soils has shown that the strengths vary from a  $Sr/p'$  ratio of 0.06 to 0.28. This range was determined during the previous study of Sardis and presently in the studies of Enid and Arkabutla. Further inspection of the criteria for determining liquefaction potential in cohesive soil also indicated a range of strengths. Liquefiable soils with an SPT blow count  $N_{1(60)}$  of 10 have a larger residual strength than those with an  $N_{1(60)}$  of 1 and soils with a CPT tip resistance of 20 tsf will consequently have a higher residual strength than those with a CPT tip resistance of 5 tsf. All these soils are considered liquefiable and would be utilized in determining the thickness of the liquefiable layer. As can be seen, the residual strength could vary significantly across the layer. It had been common practice to just conservatively assume a strength on the lower bound of this range. In the study of Sardis an  $Sr/p'$  ratio of 0.075 was utilized. Later studies at Arkabutla and Enid Dams have shown that a higher residual strength has been justified.

#### **4 Evaluation of Residual Strength From Standard Penetration Test and Laboratory Testing**

The seismic evaluation of Sardis Dam was one of the first Corps of Engineers Dams in the United States evaluated for seismic response. It began in 1971, soon after the partial failure of Lower San Fernando Dam in California during an earthquake in the San Fernando Valley. There was very little understanding of the seismic response of cohesive soils at that time. Most of the early studies in the United States were in

sands. Dr. Harry Seed developed an empirical approach (Seed et al., 1983) to evaluate liquefaction susceptibility and residual strength based on the Standard Penetration Test (SPT). In developing this approach the investigators took SPT blow counts at sites that have, and have not experienced liquefaction during earthquake shaking. They then corrected these blow counts to equivalent values at one ton per square foot (tsf) over burden pressure and 60 percent hammer efficiency and associated these adjusted blow counts with the cyclic stress ratios estimated to have occurred at the site. Although most of this work was performed in sands, Dr. Seed developed correction factors for various fines contents for use in evaluating cohesive soils. Dr. Seed developed an empirical chart that relates corrected SPT blow count values to post earthquake strength. This chart presented in Figure 1 was developed from back-calculated undrained strengths required to produce factors of safety of one against sliding in an embankment that had experience liquefaction induced sliding failure.

This method of strength prediction was used in the early days of seismic evaluation to predict post earthquake residual strength in cohesive soil, using the fines content correction factors. In the seismic evaluation of Sardis Dam by the Vicksburg District in the 1980s, one section of the dam was found to be seismically unsafe and remediation using an upstream berm was constructed. Analyses utilized shear strength estimates from Seed's empirical approach and laboratory test results including triaxial tests, unconfined compression tests, and laboratory vane. Figure 2 is a graphic depiction of the cross section of Sardis utilized in the first remedial design.

The residual strengths in the weak clay/silt layer used for analysis were 300 psf beneath the centerline, 200 psf beneath the dam slopes, and 100 psf at the toe, and in the free field of the dam. In the future studies of Sardis, Arkabutla and Enid residual strength was expressed as a ratio of residual strength to overburden,  $Sr/p'$ .

## 5 Evaluation of Residual Strength of Cohesive Fine-Grained Soils Using In-situ Testing

During the seismic evaluation of Sardis Dam in the mid 1980s it became apparent that evaluating the residual strength of liquefiable fine-grained soils using laboratory testing methods was unreliable due to the difficulty of obtaining quality undisturbed samples of these soils.

In situ testing using Field Vane Shear Test (FVST) and Cone Penetration Testing (CPT) became the primary means of evaluating the residual strength. The Field Vane Shear Test is an effective tool for predicting post earthquake residual strength of soils since it is common practice to assume that fine-grained soils perform like remolded clays during seismic loading and their strengths degrade to the residual value. The Cone Penetration Test is appropriate as it can also be used to obtain undrained peak and residual strength. However, it is necessary to perform site-specific correlation of the CPT predicted strength to actual measured strengths from Field Vane Shear test or laboratory strength test. The CPT test also provides strength predictions about every one-tenth of a foot of depth.

First, the CPT is used as a screening tool to locate zones of liquefiable cohesive soil. Then, Field Vane Shear Tests are performed to obtain measured values of residual strength. Comparison of nearby CPT can then be made with the Field Vane Shear results to correlate the CPT for site-specific strength prediction. The CPT is a relatively quick, low cost test, which can be duplicated at many locations along the dam such that trends of soil strength and delineations of strength layers can be made, and more accurate assessments of the strength of the liquefiable layer can be established.

The Field Vane Shear Test is first performed to determine the measured peak strength ( $S_u$ ) and residual strength ( $S_r$ ). The sensitivity of the soil ( $S$ ) is also obtained ( $S = S_u/S_r$ ). In the Cone Penetration Test the formula  $S_u = QC/P/N_k$  is used to compute peak undrained strengths where

$QC$  is the measured tip resistance,  $P$  is the in-situ overburden pressure and  $N_k$  is the cone factor used to estimate peak undrained shear strength ( $S_u$ ). The  $N_k$  value is the factor necessary to make site-specific correlations of the CPT to Field Vane Shear Test results or even laboratory test results. The value of undrained strength ( $S_u$ ) measured in-situ by the field vane is used in the equation and a value of  $N_k$  is then back calculated. This  $N_k$  value is used in all future CPT tests to correlate strength predictions from the CPT to the measured values from the FVST. To obtain residual strength, the estimated  $S_u$  from the CPT is then divided by the sensitivity  $S$  from the Field Vane Shear Test. Figure 3 is a sample picture of the Field Vane Shear Testing at Sardis Dam.

In the Sardis Dam Study in the evaluation of the remaining unremediated portions of the dam during the late 1980s and early 1990s, residual strength of the liquefiable fine-grained soils was evaluated using the Field Vane Shear Test and CPT test. This was the first use of this technique. An  $N_k$  value of 15, and a sensitivity of 3.5 were necessary to correlate residual strength from the CPT to those obtained from the Field Vane. Predicted residual strength in the liquefiable layer ranged from a residual strength to overburden pressure ratio ( $S_r/p'$ ) of 0.06 to 0.28. In selecting the value of  $S_r/p'$  to use in seismic response analyses of Sardis, it was decided to use a conservative value of  $S_r/p' = 0.075$  which was on the lower bound of this range. This value was also partially based on static equilibrium slope stability analyses to obtain the average in-situ undrained peak strength required to give factors of safety in the range of 1.5 to 2.0. A residual strength from the slope stability analyses was obtained by dividing this undrained strength ( $S_u$ ) by the sensitivity ( $S$ ) from the field vane at Sardis. The resulting residual strength value from the slope stability analyses of 0.075 was within the range of measured values from the CPT. Although still conservative, the  $S_r/p'$  of 0.075 results in a residual strength higher than was used previously from Seed's empirical approach in the design and construction of the remediation berm. Therefore, increased



understanding of these soils resulted in a reduction in conservatism. Seismic response analyses at Sardis utilizing the residual strength ratio of 0.075 indicated that an additional 2700 ft of the dam required remediation. Construction of the driven pile foundation modification was performed in 1996. Figure 4 is a graphic depiction of the dam cross section utilized in this portion of the study.

CPT and FVST test have also been a major part of the seismic studies of Enid and Arkabutla Dams. However, more emphasis has been placed on using the CPT to map residual strength trends three dimensionally all along the dam and to use more of an average residual strength value across the liquefiable layers in final seismic response analyses. In the study of Arkabutla Dam, approximately 34 Field Vane Shear tests were performed in cohesive soils meeting the liquefaction criteria at eight locations along the dam. Corresponding CPT tests were performed near the FVST for correlation studies. Residual strength to overburden ratios from the Field Vane Shear Test ranged from 0.06 to 0.27, which are comparable to those at Sardis. The average sensitivity ( $S$ ) was found to be 4.5. An  $NK$  value of 18 was required to compute similar strengths from the CPT to those obtained from the field vane. The average residual strength from all CPT tests at Arkabutla using these parameters was 192 psf. The average measured residual strength from all field vane shear test at Arkabutla was 191 psf. This verified the use of  $NK = 18$  and  $S = 4.5$  for estimating residual strength with the cone penetrometer. Cone Penetration Tests were then performed all along the toe of the dam, the free field of the dam about 120 ft from the toe, and beneath the embankment about 85 ft downstream of the centerline. This CPT coverage provided a good representation of residual strength trends all along the dam. Figure 5 is a graphical representation of the CPT stratification of the foundation from CPT along the toe of the dam. The figure details the location of clays and silts meeting the liquefaction criteria. The figure also presents low and high CPT predicted  $Sr/p'$  ratios throughout the weak layer.

As can be seen, some sections of the dam have liquefiable clay and silt layers with  $Sr/p'$  ratios much higher than the  $Sr/p'$  of 0.075 used previously at Sardis. The average  $Sr/p'$  ratio from Field Vane Shear Tests at Arkabutla is 0.13, while the average  $Sr/p'$  ratio from all CPT is 0.15. These values justify the conclusion that some conservatism can be removed in the final selection of residual strength.

In developing the final cross sections for final seismic response analyses of Arkabutla, average strengths were looked at both parallel along the dam and in section perpendicular the dam imprint. Figure 6 is a graphic representation of the worse case section to be utilized in final analyses of Arkabutla.

Two distinct, continuous layers of liquefiable silts and clays were found in the foundation at this location of the dam. A residual strength ratio value of 0.13 was selected for the lower layer, and a  $Sr/p'$  of 0.20 was selected for the upper liquefiable soil layer. These values were based upon evaluations of the average strength trends along the weak layer, but were conservative and on the lower bound of the range of average strengths found throughout the weak layer. Although still somewhat conservative, some conservatism has been removed from previous studies due to the increase in understanding of these liquefiable fine-grained soils. Final seismic response analyses of Arkabutla are presently being performed. Similar results are also being found in the study of Enid Dam.

## 6 Final Comments

The above studies have shown that cohesive soils (clay and silt) subject to liquefaction have a range of possible residual shear strengths. This is mainly due to the range of SPT blow counts and CPT tip resistance, which are included in the criteria for liquefaction. Engineering judgment is, therefore, still a major factor in the selection of the value of residual strength to utilize in post earthquake static equilibrium slope stability and deformation analyses.



It is necessary to identify all soils subject to liquefaction in the dam and its foundation. Some soils subject to liquefaction or strength loss may not adversely affect the integrity of a given dam due to their residual strength, location, and stratification even if these soils were to liquefy or lose strength. For example, Arkabutla Dam is much shorter in height than Sardis Dam, so the effect of a liquefiable clay and silt layer in its foundation will be different, the dam's performance during an earthquake will be different, and the results of analyses will be different. The studies of Sardis, Arkabutla and Enid have shown that cohesive soils with  $N_{1(60)}$  value of 10 (in the upper bound) and meeting the Chinese criteria are subject to significant strength loss during a major earthquake. The residual strength ratio of this soil at an overburden pressure of 1 tsf is about 0.24 at Arkabutla Dam. While this soil may adversely affect some dams, it will not be a critical factor at Arkabutla. Also, a clay and silt with a tip resistance of 15 tsf and friction ratio of 2.0 has been identified as liquefiable and has a  $Sr/p'$  ratio of about 0.23. Zones of this soil at Arkabutla will have minimal effect during a major earthquake.

The accepted procedure for evaluating the seismic stability of large dams is to identify all soils in the embankment and foundation subject to strength loss and liquefaction during the earthquake, development of sections indicating these layers of earthquake susceptible soils, and then assigning a conservative residual strength for analyses. The above studies have shown that there has been significant conservatism in assigning the thickness and extent of weak foundation layers to include all liquefiable clays and silts since some of these have high enough residual strengths that they might not adversely effect the dam's seismic performance. Some conservatism could therefore be removed when assigning the residual strength in these layers for analysis and deformation performance studies.

The evaluation of the seismic response of fine-grained soils at Sardis, Arkabutla and Enid Dam evolved mainly around determining the actual residual strength of the liquefiable clays and silts. This is a value that can be measured in-situ,

or in the laboratory if quality undisturbed samples can be obtained. However, the automatic assumption that these soils degrade all the way to this residual strength during a major earthquake is most likely conservative. Only partial loss of strength is likely to happen. Many factors such as duration of the earthquake, the intensity, and the distance of the dam from the epicenter may have a big influence not only on the degradation of strength, but also on the susceptibility of liquefaction of the soil. The confinement pressure of a soil could also have a major effect. These unknowns should be addressed in both present and future studies utilizing techniques such as cyclic triaxial testing and centrifuge modeling. Under the present state-of-the-art it is still proper engineering practice to assume that cohesive soils will act like remolded clays during seismic loading.

## 7 References

- ASTM Standards, D2573-94, "Standard Test Method for Field Vane Shear Test in Cohesive Soil," (1994).
- Department of The Army, Corps of Engineers, Office of the Chief of Engineers, EM 1110-2-1907, Appendix D, "Field Vane Shear Test," 1972.
- Finn, W. D. Liam, Ledbetter, R. H., Fleming, R. L., Templeton, A. E., Forrest, T. W. and Stacy, S. T., "Dam on Liquefiable Foundation - Safety Assessment and Remediation," Proceedings, 17th International Congress on Large Dams, Vienna, pp. 531-553, June, 1991.
- Koester, J. P., "The Influence of Test Procedure on Correlation of Atterberg Limits with Liquefaction in Fine-Grained Soils," Geotechnical Testing Journal, GRJODJ, Vol. 15, No. 4, 1992, pp. 352-361.
- Olsen, R. S. and Koester, J. P., "Prediction of Liquefaction Resistance Using the CPT," Proceedings, International Symposium on Cone Penetration Testing, CPT 1995, Linkoping Sweden, October 1995.

Robertson, P. K. and Campanella, R. G., "Guidelines for Use & Interpretation of the Electronic Cone Penetration Test," Hogentogler & Company, Inc. (1984).

Salah-Mars, S., Mejia, L. H., Fleming, R. L., Forrest, T. W., and Stacy, S. T., "Seismic Rehabilitation of Sardis Dam," ASCE Specialty Conference on Geotechnical Practice in Dam Rehabilitation, Raleigh, North Carolina, April, 1993.

Schnabel, P. L., Lysmer, J. and Seed, H. B., "SHAKE: A Computer Program for Earthquake Response Analysis of Horizontally Layered Sites," Report No. EERC 71-12, University of California, Berkeley, 1972.

Seed, H. B., Indris, I. M. and Arango, I. "Evaluation of Liquefaction Potential Using Field Performance Data," *Journal of Geotechnical Engineering*, American Society of Civil Engineer, 109(3), 1983.

Seed, H. B., "Design Problems in Soil Liquefaction," *Journal of Geotechnical Engineering*, ASCE, Vol. 113, No. 7, pp. 827-845, August, 1987.

Seed, H. B., Tokimatsu, K., Harder, L. F. and Chung, R. M., "Influence of SPT Procedures in Soil Liquefaction Resistance Evaluations," *Journal of Geotechnical Engineering*, ASCE, Vol. 112, No. 11, pp. 1016-1032, November, 1986.

U.S. Army Engineer District, Vicksburg, "The Sardis Earthquake Study," Supplement No. 1 to Design Memorandum 5, Earthquake Resistant Remedial Measures Design for Sardis Dam, 1988.

U.S. Army Engineer District, Vicksburg, "The Sardis Earthquake Study," Design Memorandum 1, Introduction, Geology, Seismology and Selection of Design Earthquake (1989).

U.S. Army Engineer District, Vicksburg, "The Sardis Earthquake Study," Design Memorandum 5, Earthquake Resistant Remedial Measures Design for Sardis Dam", 1985.

Woodward-Clyde Consultants, Sardis Dam Earthquake Study, Report to U.S. Army Engineer District, Vicksburg (1989).

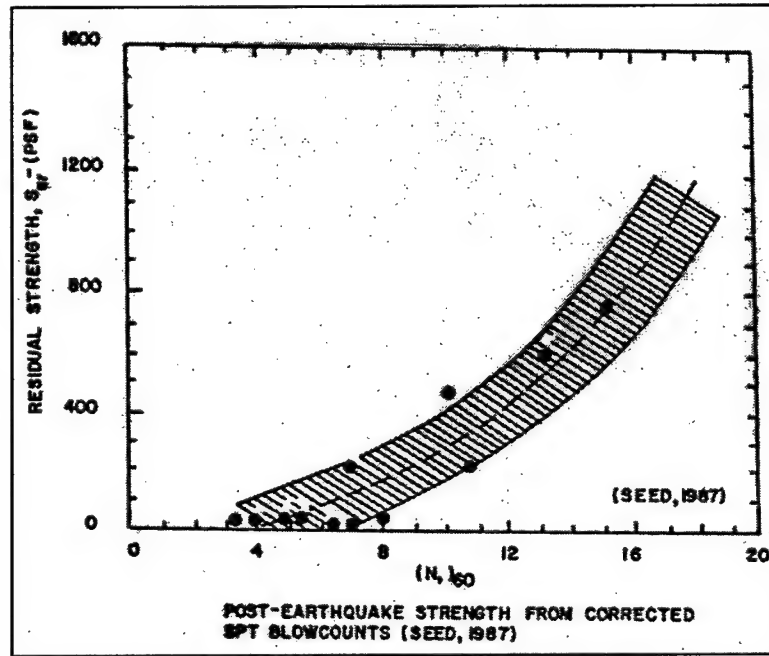


Figure 1. Post earthquake strength

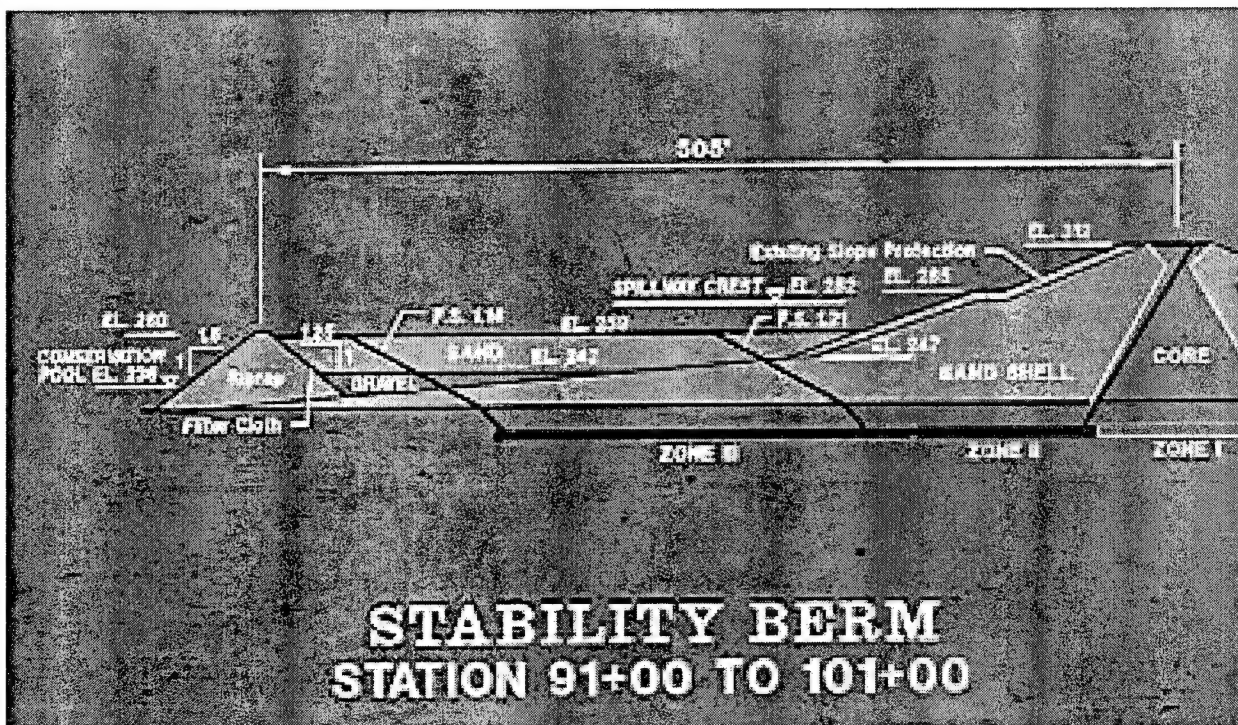


Figure 2. Cross section of Sardis utilized in the first remedial design



**Figure 3.** Field vane shear testing at Sardis Dam

## Design Criteria for Rounded/Angular Rock Riprap in Overtopping Flow

by

Humberto A. Gallegos,<sup>1</sup> and Steven R. Abt<sup>2</sup>

### ABSTRACT

A series of 9 overtopping tests were performed in a physical model of an embankment to determine design criteria for rounded/angular rock riprap in overtopping flow. A predictive equation was derived as a function of the embankment slope, coefficient of uniformity, percent rounded, failure unit discharge and the median stone size. In addition, it was determined that the hydraulic roughness, Manning's  $n$ , for rounded rock riprap on steep slopes was 25 to 28 percent smaller compared to angular rock riprap.

**KEYWORDS:** Riprap, linear regression, coefficient of uniformity, coefficient of gradation, scaled model, Colorado State University, overtopping flow, embankment, hydraulic roughness, median, empirical design equation, hydraulic resistance, alluvial material, rounded riprap, angular riprap, interstitial discharge, percent rounded.

### 1 INTRODUCTION

In the construction of new dams, rehabilitation of existing dams, and the protection of the public health and environment from the potential hazards of waste materials, rock riprap is usually the most economical material for protection. Currently, available design criteria require the use of angular stones for all riprap revetments. However, in remote locations, the cost of shipping angular riprap from the quarry to the project site may increase the project cost significantly. Large quantities of alluvial material may be locally available, but stones are often rounded in shape. Only limited design criteria

have been proposed to allow the utilization of rounded rock riprap for overtopping protection.

The objectives of this investigation were: (1) develop design criteria for rounded rock riprap in overtopping flow; (2) expand the database of rounded rock riprap to include higher embankment slopes; (3) increase the understanding of the behavior of rounded rock riprap in overtopping flow; and (4) analyze the hydraulic roughness of rounded rock riprap on steep slopes.

### 2 TEST FACILITY

A physical model of an embankment was constructed in the Hydraulics Laboratory at the Colorado State University Engineering Research Center. The testing flume consists of a wooden head box, variable slope flume (25 percent variable), and tailbox. The testing flume is 1.22 m (4 ft) wide, 1.17 m (3.85 ft) deep, and 12.60 m (32.0 ft) long (see Figure 1). The test matrix consisted of nine overtopping tests. Median rock sizes of 3.23 cm (1.27 in.) to 9.91 cm (3.9 in.) were placed on embankment slopes of 35, 40, and 45 percent.

### 3 Background

Abt et al. (1987 and 1988a) conducted an extensive testing program to devise a waste stabilization design procedure and method. The test consisted of 52 flume tests in which riprap-covered embankments were subjected to overtopping flows. Embankment slopes of 1, 2, 8, 10, and 20 percent were protected with riprap containing

<sup>1</sup> Grad Res. Asst., Dept. of Civil Engr., Colo. State Univ., Ft. Collins, CO 80523.

<sup>2</sup> Prof., Dept. of Civil Engr., Colo. State Univ., Ft. Collins, CO 80523.

median stone sizes of 2.54, 5.08, 10.16, 12.7, and 15.24 cm (1, 2, 4, 5, and 6 in.). Riprap layer thickness ranged from  $1.5 D_{50}$  to  $4 D_{50}$ . The empirical design equation for angular rock riprap is expressed as follows:

$$D_{50} = 5.23 S^{0.43} q_{design}^{0.56} \quad (1)$$

$$q_{design} = 1.35 q_f \quad (2)$$

The rounded riprap required oversizing of about 40 percent to provide the same level of protection as the angular riprap.

Ullman (2000) developed a design criteria for rounded riprap in overtopping flow by conducting a series of 12 flume tests in which rounded riprap of median stone diameter ranging from 2.39 cm (0.94 in.) to 9.91 cm (3.9 in.) were placed on embankment slopes of 20, 25 and 30 percent and subjected to overtopping flow conditions. The design equation for rounded rock riprap in overtopping flow is:

$$\frac{D_{50}}{C_u^{0.25} (1.12\%R + 0.39)} = 6.48 S^{0.43} q_f^{0.56} \quad (3)$$

#### 4 ROUNDED/ANGULAR ROCK RIPRAP ANALYSIS

The test findings from this study, Ullman (2000) and Abt et al. (1988a) are presented in Table 1.

Equation 1 developed by Abt et al. (1988a) was used as the basis for the analysis of the rounded and angular rock riprap data. To adjust the data for rock riprap gradation, the median rock riprap size was divided by  $C_u^{0.25}$ . The adjustment collapsed the data set for the current, Ullman (2000) and the Abt et al. (1988a) data into a single relationship. The riprap sizes used in this study and the Ullman (2000) study indicate that the percent rounded rock increases with median stone size (see Table 1). Equation 4 is used to adjust the difference observed in percent rounded as median stone diameter increases:

$$\frac{D_{50}}{C_u^{0.25} (1.0805\%R + 0.4428)} = 5.23 S^{0.43} q_f^{0.56} \quad (4)$$

Equation 4 is plotted for all data presented in Table 1 to produce Figure 2.

Safety factors were included in Equation 4 to account for the scatter in Figure 2 and the maximum expected unit discharge was multiplied by a factor of 1.35 to reduce movement of stones that would compromise the riprap stability. The recommended design equation is:

$$\frac{D_{50}}{C_u^{0.25} (1.0805\%R + 0.4428)} = 6.58 S^{0.43} q_f^{0.56} \quad (5)$$

Equation 5 was developed from a database with the following constraints: (1) embankment slopes of 10 to 45 percent, (2) median rock sizes of 2.39 cm (0.94 in.) to 15.24 cm (6 in.), (3) rounded rock 55 to 95 percent rounded (4) riprap layer thickness of  $1.5 D_{50}$  to  $3 D_{50}$  and (5) coefficient of uniformity from 1.21 to 4.

#### 5 HYDRAULIC ROUGHNESS ANALYSIS FOR ANGULAR/ROUNDED ROCK RIPRAP IN OVERTOPPING FLOW

To calculate the hydraulic resistance the Manning equation was used:

$$n = \frac{k}{V} R^{\frac{2}{3}} S^{\frac{1}{2}} \quad (6)$$

To determine Manning's  $n$ , the surface flow was utilized. The interstitial velocity through the riprap layer was estimated using Equation 7 developed by Abt et al. (1988a):

$$V_i = 0.23 \sqrt{g D_{10} S} \quad (7)$$

The surface discharge is the difference between the total and the interstitial discharge. The average surface flow velocity was obtained by dividing the surface flow discharge by the surface



**Table 1. Test Results**

			$D_{50}$	$D_{50}$	$C_u$	Rounded	S	$q_r$	$q_r$	Mode Of
			(cm)	(in)		%	decimal	$m^3/s/m$	$ft^3/s/ft$	Failure
Current Study	1	Round	5.87	2.31	1.21	79	0.35	0.042	0.455	Exposure
	2	Round	3.23	1.27	1.32	60	0.35	0.014	0.154	Catastrophic
	3	Round	9.91	3.90	1.24	92	0.35	0.086	0.935	Exposure
	4	Round	5.87	2.31	1.21	79	0.40	0.031	0.335	Channel
	5	Round	3.23	1.27	1.32	60	0.40	0.014	0.157	Channel
	6	Round	9.91	3.90	1.24	92	0.40	0.051	0.552	Exposure
	7	Round	3.23	1.27	1.32	60	0.45	0.012	0.131	Exposure
	8	Round	5.87	2.31	1.21	79	0.45	0.036	0.394	Catastrophic
	9	Round	9.91	3.90	1.24	92	0.45	0.065	0.708	Exposure
Ulman (2000)	10	Round	2.39	0.94	1.24	55	0.20	0.019	0.20	Channel
	11	Round	2.39	0.94	1.24	55	0.30	0.015	0.16	Channel
	12	Round	3.23	1.27	1.32	60	0.20	0.030	0.33	Channel
	13	Round	3.23	1.27	1.32	60	0.25	0.021	0.22	Channel
	14	Round	3.23	1.27	1.32	60	0.30	0.019	0.21	Channel
	15	Round	4.50	1.77	1.33	76	0.20	0.035	0.39	Channel
	16	Round	4.50	1.77	1.33	76	0.25	0.035	0.38	Channel
	17	Round	4.50	1.77	1.33	76	0.30	0.029	0.32	Channel
	18	Round	5.87	2.31	1.21	79	0.20	0.053	0.58	Catastrophic
	19	Round	5.87	2.31	1.21	79	0.30	0.048	0.53	Catastrophic
	20	Round	5.87	2.31	1.21	79	0.25	0.052	0.57	Catastrophic
	21	Round	9.91	3.90	1.24	92	0.30	0.096	1.04	Catastrophic
Abt et al. (1988 a)	22	Round	10.42	4.10	2.12	95	0.20	0.087	0.95	Unk nown
	23	Round	10.42	4.10	2.12	95	0.20	0.087	0.95	Unk nown
	24	Round	10.42	4.10	2.12	95	0.10	0.183	1.99	Unk nown
	25	Round	10.42	4.10	2.12	95	0.10	0.192	2.09	Unk nown
	26	Round	5.21	2.05	2.14	95	0.10	0.063	0.69	Unk nown
Abt and Johnson (1991)	1	Angular	2.59	1.02	1.75	0	0.02	0.102	1.11	Unk nown
	2	Angular	2.59	1.02	1.75	0	0.01	0.138	1.50	Unk nown
	3	Angular	2.59	1.02	1.75	0	0.10	0.033	0.36	Unk nown
	4	Angular	2.59	1.02	1.75	0	0.10	0.031	0.34	Unk nown
	5	Angular	2.59	1.02	1.75	0	0.10	0.028	0.31	Unk nown
	6	Angular	2.59	1.02	1.75	0	0.10	0.039	0.42	Unk nown
	7	Angular	5.08	2.00	2.40	0	0.10	0.078	0.85	Unk nown
	8	Angular	5.08	2.00	2.40	0	0.10	0.092	1.00	Unk nown
	9	Angular	5.08	2.00	2.40	0	0.10	0.102	1.11	Unk nown
	10	Angular	5.59	2.20	2.09	0	0.10	0.103	1.12	Unk nown
	11	Angular	5.59	2.20	2.09	0	0.10	0.115	1.25	Unk nown
	12	Angular	5.59	2.20	2.09	0	0.10	0.115	1.25	Unk nown
	13	Angular	5.59	2.20	2.09	0	0.08	0.166	1.81	Unk nown
	14	Angular	5.59	2.20	2.09	0	0.02	0.416	4.53	Unk nown
	15	Angular	5.59	2.20	2.09	0	0.20	0.046	0.50	Unk nown
	16	Angular	10.16	4.00	2.30	0	0.10	0.322	3.51	Unk nown
	17	Angular	10.16	4.00	2.30	0	0.10	0.348	3.79	Unk nown
	18	Angular	10.16	4.00	2.30	0	0.10	0.378	4.12	Unk nown
	19	Angular	10.41	4.10	2.15	0	0.20	0.166	1.81	Unk nown
	20	Angular	12.95	5.10	1.62	0	0.20	0.327	3.56	Unk nown
	21	Angular	15.75	6.20	1.69	0	0.20	0.407	4.43	Unk nown

flow area. The surface flow depth was inserted in the hydraulics radius term in Manning's equation. The Abt et al. (1988b) data for Manning's  $n$  using angular and rounded rock riprap and the rounded rock riprap data for Manning's  $n$  from the current and the Ullman (2000) study are presented in Table 2.

**Table 2.** Manning's  $n$  Data

Manning's $n$ data from Abt et al. (1988a)					
Test #	$D_{50}$ (in)	$D_{50}$ (cm)	$S$ (%)	$n$	$D_{50}S$ (in)
24	1.02	2.59	1	0.024	0.010
10	1.02	2.59	2	0.024	0.020
25	1.02	2.59	10	0.034	0.102
8	2.2	5.59	2	0.025	0.044
32	2.02	5.13	8	0.036	0.162
31	2.2	5.59	10	0.036	0.220
18	2.2	5.59	20	0.035	0.440
7	4.1	10.41	20	0.043	0.820
10A	5.1	12.95	20	0.044	1.020
15	6.2	15.75	20	0.055	1.240
21	4	10.16	20	0.022	0.800
22	4	10.16	20	0.033	0.800
36	4	10.16	10	0.041	0.400
38	4	10.16	10	0.049	0.400
46	2	5.08	10	0.048	0.200
Manning's $n$ data from Ullman (2000)					
4	1.27	3.23	20	0.041	0.254
5	2.31	5.87	20	0.048	0.462
6	1.77	4.50	20	0.034	0.354
7	0.94	2.39	20	0.029	0.188
8	2.31	5.87	30	0.052	0.693
9	1.77	4.50	30	0.034	0.531
10	3.9	9.91	30	0.058	1.170
11	1.27	3.23	30	0.031	0.381
12	0.94	2.39	30	0.012	0.282
13	1.27	3.23	25	0.030	0.318
14	1.77	4.50	25	0.021	0.443
15	2.31	5.87	25	0.041	0.578
Manning's $n$ data from current study					
1	2.31	5.87	35	0.012	0.809
2	1.27	3.23	35	0.121	0.446
6	3.9	9.91	40	0.015	1.560
8	2.31	5.87	45	0.047	1.040
9	3.9	9.91	45	0.046	1.755

Abt et al. (1988b) found that combining the median stone size and the embankment slope in one parameter reduces the data scatter observed when Manning's  $n$  values are plotted against the median stone size. The Manning's  $n$  values are plotted against the product of the median stone size and embankment slope in Figure 3.

Figure 3 presents the best-fit lines for angular and rounded stones. The power equations for angular and rounded riprap are:

$$y = 0.0457x^{0.1579} \quad (\text{Angular}) \quad (8)$$

$$y = 0.0328x^{0.0973} \quad (\text{Rounded}) \quad (9)$$

Equation 9 provides smaller Manning's  $n$  values for a specified median stone size and embankment slope for rounded rock riprap. Manning's  $n$  values for rounded rock riprap were 25 to 28 percent smaller compared to angular rock riprap.

## 6 Conclusions

The recommended design relationship for rounded/angular rock riprap in overtopping flow is:

$$\frac{D_{50}}{C_u^{0.25}(1.0805\%R + 0.4428)} = 6.58S^{0.43}q_f^{0.56} \quad (10)$$

It was found that Manning's  $n$  values for rounded rock riprap were 25 to 28 percent smaller compared to angular rock riprap.

## 7 ACKNOWLEDGMENT

Information presented herein was obtained from the research conducted under Abt et al. (1987, 1988a, and 1988b) and Ullman (2000). The Colorado State Agricultural Experiment Station funded the study.

## 8. REFERENCES

- Abt, S. R., Khattak, M. S., Nelson, J. D., Ruff, J. F., Shaikh, A., Wittler, R. J., Lee, D. W., and Hinkle, N. E. (1987). Development of riprap design criteria by riprap testing in flumes: Phase I. NUREG/CR-4651, U.S. Nuclear Regulatory Commission, Vol 1.
- Abt, S. R., Wittler, R. J., J. D., Ruff, LaGrone, D. L., Khattak, M. S., Nelson, J. F., Hinkle, N. E., and Lee, D. W. (1988a). Development of riprap design criteria by riprap testing in flumes:



Phase II. NUREG/CR-4651, U.S. Nuclear Regulatory Commission, Vol 1.

Abt, S. R., Wittler, R. J., Ruff, J. F., and Khattak, M. S. (1988b). Resistance to flow over riprap in steep channels. Water Resources Bulletin, 24 (6), 1193-1200.

Ullman, C. (2000). Rounded riprap in overtopping flow. Masters Thesis, Dept. of Civil Engineering, Colorado State University, Ft. Collins, CO.

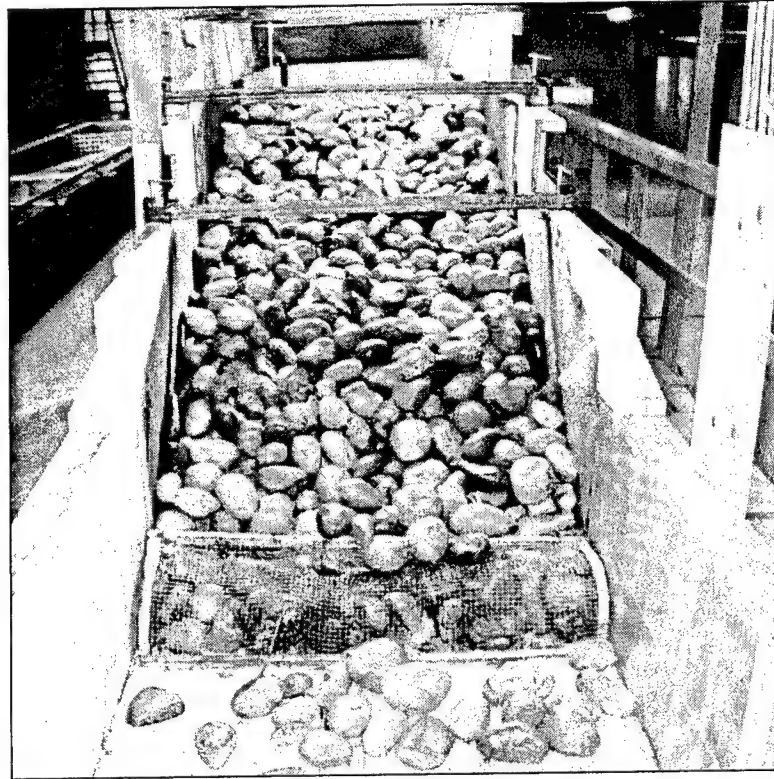


**Figure 1.** Testing flume

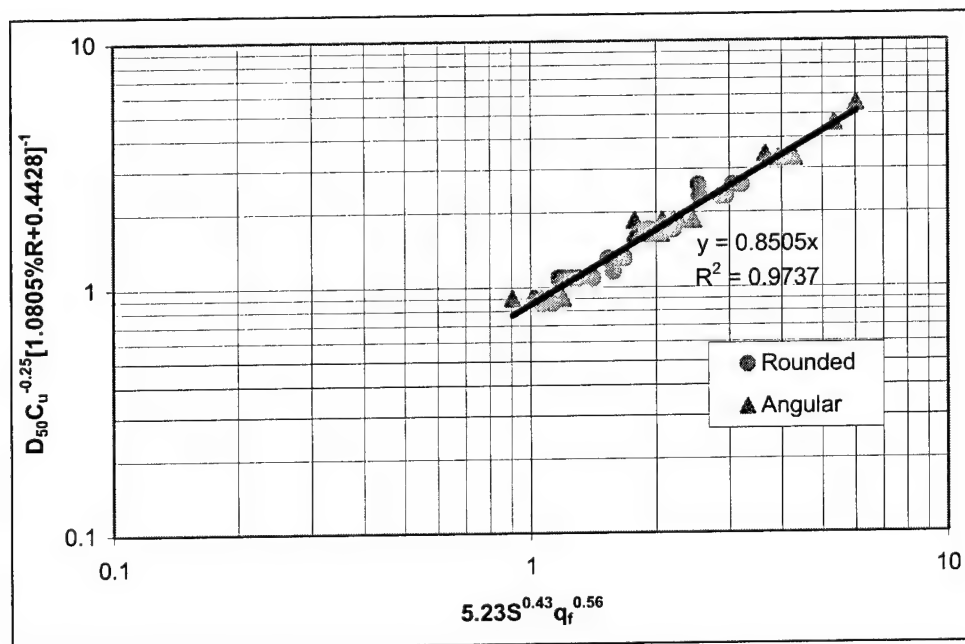


**Figure 2.** Rounded and angular rock riprap data adjusted for  $C_u$  and percent rounded rock

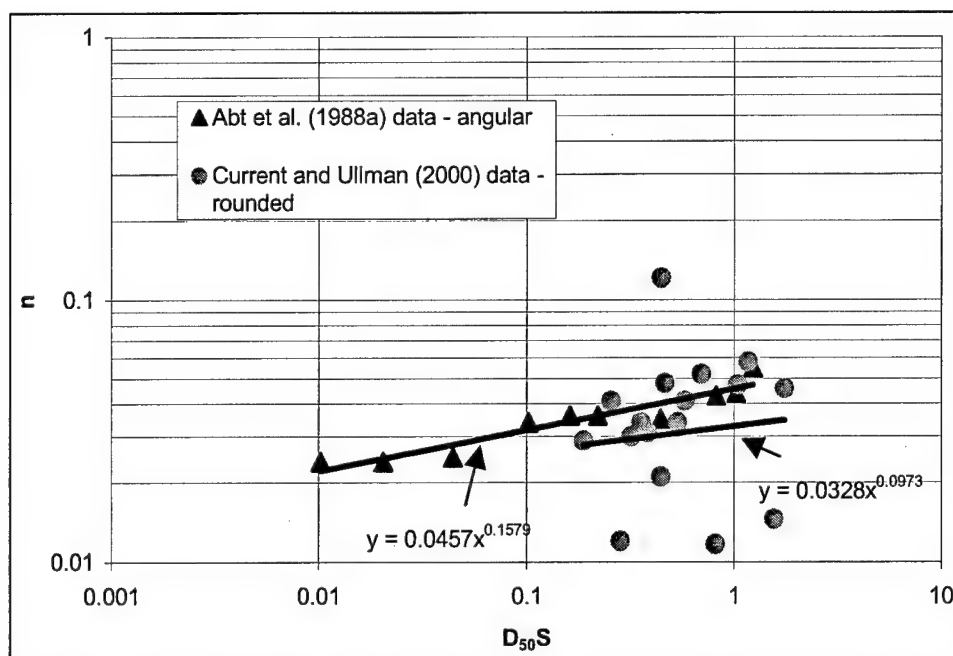


**Figure 3.** Manning's  $n$  values for angular and rounded riprap with best-fit lines

This page intentionally left blank.

## Dynamic Response of Lightly Reinforced Concrete Intake Towers

by

Richard C. Dove<sup>1</sup> and Enrique E. Matheu<sup>2</sup>

### ABSTRACT

In the event of an earthquake, it is vitally important that the catastrophic failure of a dam and subsequent sudden release of the reservoir be prevented. An important part of the prevention of such a failure is maintaining the ability to control the release of water after the earthquake. For most earthen dams, and some concrete dams, the release of water is controlled through a reinforced concrete intake tower. The functional survival of such towers has been the main concern of a multi-year research effort sponsored by the U.S. Army Corps of Engineers (USACE). Most intake towers in the current USACE inventory are lightly reinforced. The functional survival of such lightly reinforced structures is thus the main concern of this research effort. The ultimate objective of this research work is the development of analysis procedures for seismic evaluation of these structures. This paper presents some of the results of this effort.

**KEYWORDS:** Reinforced concrete, ductility, intake towers, seismic evaluation, displacement-based approach, shaking table tests

### 1 INTRODUCTION

Earthquake engineering research efforts in the area of reinforced concrete intake towers are currently focused on understanding the nonlinear response of lightly reinforced intake towers. The ultimate objective is the evaluation and/or development of simplified analysis procedures for the seismic evaluation of these structures. The work presented in this paper is part of a

larger research effort that began with a statistical analysis of the USACE inventory of existing intake towers. This tower inventory analysis quantified the distribution and variation of the structural characteristics of the towers as relating to their earthquake location hazard (Dove, 1996). The information collected was used in planning the second phase of this research program, referred to as the Intake Tower Substructure (ITS) experimentation series (Figure 1), which was conducted during 1996 and 1997 (Dove, 1998) at the Geotechnical and Structures Laboratory (Vicksburg, Mississippi).

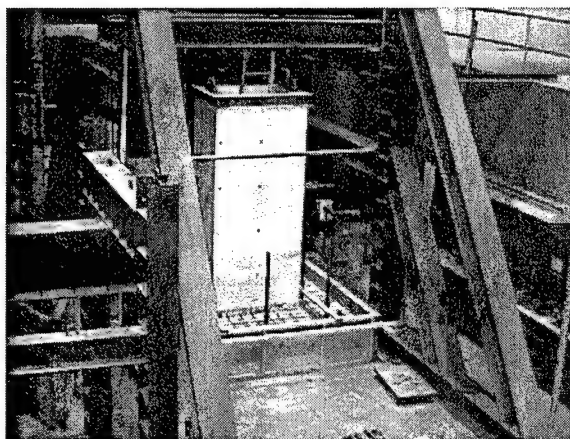


**Figure 1.** Typical 1/8-scale static experiment

The results from this experimental effort, which included monotonic and cyclic loading tests of 1/8-scale models, showed that substantial ductility is available (Figure 2). The objectives of these experiments were not only to observe the response of reduced scale models of typical intake towers and quantify the ductility available, but also to use the information generated for the development of approximate and/or

<sup>1</sup> Geotechnical and Structures Laboratory, U.S. Army Engineer Research and Development Center, Vicksburg, MS 39180 (USA).

<sup>2</sup> Department of Civil and Environmental Engineering, Louisiana State University, Baton Rouge, LA 70803 (USA).

simplified evaluation procedures for existing intake towers.

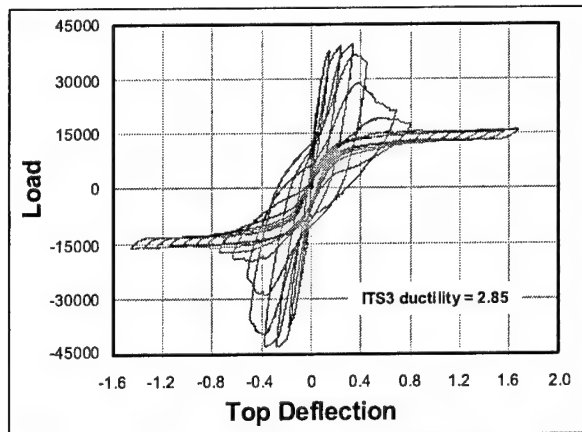


**Figure 2.** Typical load-deflection curve exhibiting substantial ductility

Based on the results of the ITS experiments, it was concluded that additional information was required for the application of the simplified analysis procedures under development. Specifically, a method was needed to properly estimate the ultimate deflection capacity of existing intake towers. During 1999 and 2000, fourteen 1/2-scale experiments were conducted to provide a statistically significant basis for the development of an empirical estimation of the parameters needed (Dove, 2000). As a result of these tests, a modified displacement-based analysis procedure was generated incorporating the available experimental information. This analysis procedure is discussed in the next section. Some discussion will be presented of the fourteen 1/2-scale experiments conducted to provide the empirical parameters used in the procedure. More recent research efforts have mainly focused on the validation and calibration of the proposed analysis procedure and its underlying assumptions by means of an extensive series of shaking table tests. The first series of tests were recently performed at the facilities of the Construction Engineering Research Laboratory (Urbana, Illinois). The corresponding results and preliminary conclusions are discussed in following sections.

## 2 DISPLACEMENT-BASED ANALYSIS

The nonlinear response and ductility of lightly reinforced intake towers has been the focus of recent analytical and experimental efforts. It has been shown that lightly reinforced intake towers can exhibit ductility but with a very localized failure. When a lightly reinforced intake tower is excited by a seismic event, a single crack forms at the base of the tower or at the location of a major stiffness change. Experimentation has shown that ultimate failure is dependent on the response of the rebar within the crack (Dove, 2000). An analysis technique has been developed that reflects this localized failure mode and includes explicit consideration of the earthquake-induced displacements of a structure. It also attempts to account for the shift of the fundamental frequencies with formation of plastic regions in the structure. The proposed analysis procedure will be presented by applying it to a representative rectangular intake tower.

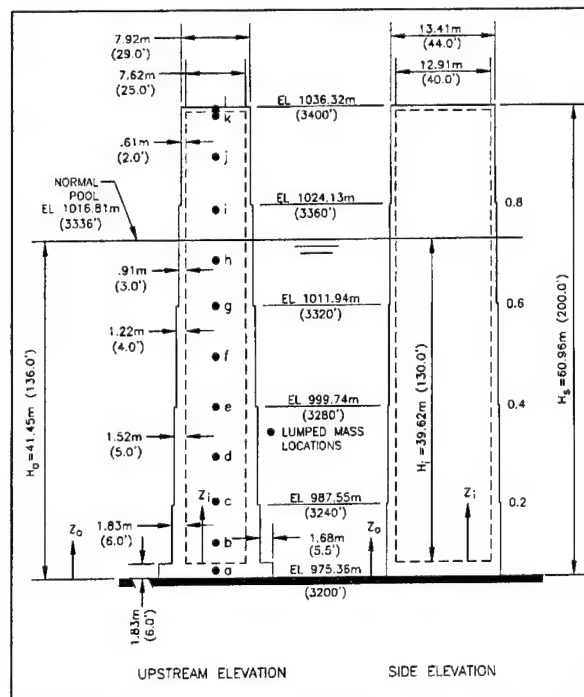


**Figure 3.** Layout of example intake tower

The structure analyzed has been used as an example problem in past and current USACE guidance documents (U.S. Army Corps of Engineers, 2002). The analysis presented here is essentially a modification of the prior analysis presented in this reference. The structure is a generic tapering rectangular tower about 61 m tall, 14.6 m by 11.6 m wide with a wall thickness 1.83 m at the base, as shown in Figure 3. Primary reinforcement consisted of #11 bars at 30.48 cm on center.

The assumed analytical model consists of a simple cantilever beam attached to a rotational spring. The spring approximates the response of the cracked region. The beam models the response of the uncracked tower above the base. The definition of the rotational spring stiffness requires the calculation of the moment-curvature ( $M-\phi$ ) relationship. Based on this relationship, it is then possible to calculate the corresponding moment-rotation relationship ( $M-\theta$ ), which is obtained by multiplying the curvature by an assumed plastic hinge length. The  $M-\theta$  relationship represents the stiffness of the rotational spring.

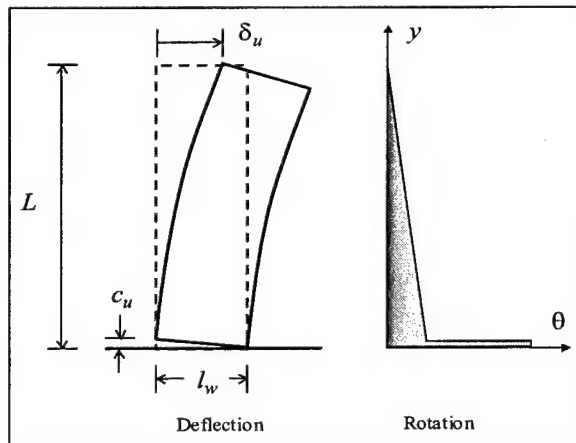


**Figure 4.** Deflection capacity

The  $M-\theta$  relationship is often strongly bilinear, and therefore a simplification is required in order to conduct a response spectrum analysis. The  $M-\theta$  relationship is linearized such that it encloses the same area for the same maximum rotation. This approximation allows the calculation of the expected deflection under the given

earthquake loads. Given the linear spring stiffness, the element properties, and any added mass due to water, a response spectrum analysis can be readily conducted. The maximum deflection calculated represents the deflection demand of the tower under the input earthquake.

In order to complete the analysis, it is necessary to determine the ultimate deflection capacity  $\delta_u$  (Figure 4), which is calculated as follows:

$$\delta_u = \frac{\phi_E L^2}{3} + \delta_{cu} \quad (1)$$

where  $\phi_E$  is the ultimate elastic curvature at the base of the tower, also known as the cracking curvature;  $\theta_P$  represents the plastic rotation at failure;  $l_w$  denotes the depth of the section,  $L$  is the height of the intake tower; and  $\delta_{cu}$  represents the deflection contribution caused by the base crack.

This model assumes that the ultimate lateral deflection consists of the sum of two parts. The first part is the elastic response of the body of the intake tower above the cracked section. The elastic curvature  $\phi_E$  can be computed as

$$\phi_E = \frac{M}{EI_g} \quad (2)$$

where  $M$  denotes the yielding moment,  $E$  the elastic modulus, and  $I_g$  the uncracked moment of inertia. The second part is a rigid body rotation of the tower as the crack opens at the base of the elastic section, and the tower rotates about the neutral axis of the cracked section. It is conservative to assume that the neutral axis is coincident with the edge of the tower. Hence, the lateral rigid-body deflection at the top of the tower varies directly with the crack width, and its maximum value is as a ratio of the tower height and the tower width, times the ultimate crack width. Therefore,

$$\delta_{cu} = \theta_P L = \frac{c_u}{l_w} L \quad (3)$$

The principal unknown in the above equation is  $c_u$ , i.e., the ultimate crack width at failure, which is a function of the ultimate strain of the rebar and the strain penetration. Experiments have indicated that for a single crack response, the crack widths are largely predicted by the ultimate strain capacity of the rebar and rebar diameter. An empirical equation for  $c_u$  was generated as follows:

$$c_u \text{ (mm)} = 1.17 + 24.68\varepsilon_u + 0.312d_b \quad (4)$$

where  $\varepsilon_u$  is the ultimate strain at failure of the rebar as measured over the standard gage length (20.3 cm or 8 in.) and  $d_b$  is the diameter of the reinforcing bar in millimeters.

Application of the proposed displacement-based procedure to the design example begins with the calculation of the  $M-\phi$  relationship for the bottom section of the tower in two directions (weak and strong axis). This follows the assumption that the failure mechanism of the tower will be the formation of a single crack at the base of the bottom section. The vertical dead load of the tower self weight was included. Assuming an 18 percent ultimate strain, the ultimate crack width calculated from the above empirical equation to be 1.40 cm. The strain penetration length ( $L_s$ ) can be calculated from the following equation:

$$L_s = \frac{c_u}{\varepsilon_u} \quad (5)$$

This gives a strain penetration length of 7.52 cm. Multiplying the  $M-\phi$  diagram by this strain penetration length gives the corresponding  $M-\theta$  relationship. Proceeding as described above, the equivalent rotational spring stiffness is calculated such that the total area under the equivalent rotational spring is the same as that for the corresponding weak and strong axis  $M-\theta$  relationships. The resulting equivalent spring constants are given by  $2.107\text{E}+12$  N-m/rad and  $3.561\text{E}+12$  N-m/rad for the weak and strong axes, respectively. Based on these properties, and assuming a finite-element discretization of the structure using standard beam elements, a response

spectrum analysis was conducted using the MDE response spectrum for 5 percent damping indicated in Figure 5. The results of this analysis indicate a top deflection of 9.6 cm for rotation about the strong axis and 10.1 cm for rotation about the weak axis.

Finally, it is necessary to calculate the ultimate deflection capacity  $\delta_u$ . Given the ultimate crack width and section width at the base of the model, the ultimate base rotation  $\theta_P$  can be calculated. The elastic curvature  $\phi_E$  at the base of the intake tower (also known as the cracking curvature) is determined from the  $M-\phi$  relationship for the section. Based on these parameters, the deflection capacity of the tower is calculated as 9.6 cm for rotation about the strong axis and 12.6 cm about the weak axis. Therefore, the tower passes the analysis.

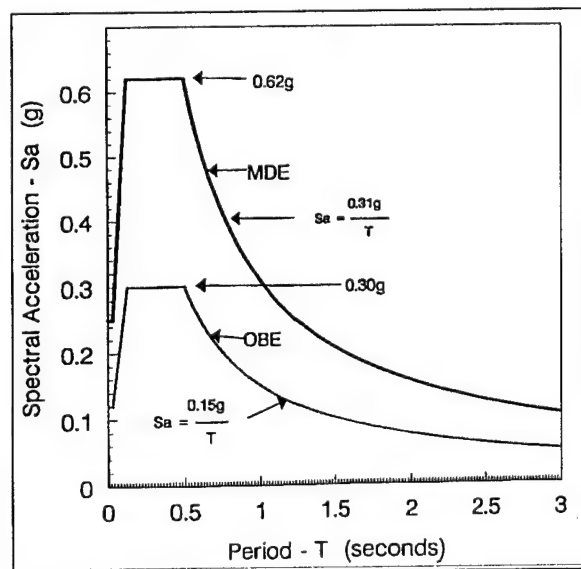


Figure 5. Standard spectra used in analysis

### 3 STRAIN PENETRATION EXPERIMENTS

Determining the ultimate deflection capacity of lightly reinforced intake towers is pivotal in the deflection-based analysis technique. Fourteen 1/2-scale experiments were conducted to provide a statistically significant basis for the development of an empirical estimation of the



parameters needed to calculate the ultimate deflection capacity (Dove, 2000). A commercial statistical analysis program STAGRAPHS was used to design the experimental program. Initially, the experimental design was based on a modified full-factorial variation of the three main variables of interest. The three variables were, concrete strength, reinforcing steel strength, and reinforcing steel diameter. A full-factorial design includes all the combinations of the extremes on each variable. With three variables, the number of combinations is two raised to the third power, or eight. In addition to the eight combinations, proper experimental design includes an experiment consisting of the combination of the middle values of the variables. This allows for a check of the linearity of the model. Inclusion of the middle values assumes that the variables are continuous.

In this specific design the reinforcing steel strength variable of nominal yield strength was only available in 413685 kPa and 275790 kPa. Thus, two middle experiments were designed consisting of the middle values of the concrete strength and reinforcing steel diameter and the high and low values of the steel strength, for a total of ten experiments. After these initial experiments, four additional experiments with larger diameter bars were conducted.

### 3.1 Model configuration

The primary concern of this experiment design was the proper modeling of the response of an individual reinforcing bar found in an existing intake towers during an earthquake. In prior experimentation it was shown that the response of these lightly reinforced structures was dominated by the localized failure of the reinforcing in a single crack. The dimensions, configuration, and structural parameters of the strain penetration experimental components were selected to model this failure mode for typical prototype rectangular intake towers (Figure 6). The experimental specimen consisted of a 1.83 m tall, 0.609 m by 0.609 m concrete monolith reinforced with vertical reinforcing bars. The vertical bars modeled the vertical reinforcement across the single crack failure plane in the

prototype tower. The vertical bars in the various models consisted of high and low strength 0.95 cm, 1.27 cm, 1.59 cm, 1.90 cm, 3.18 cm and 3.49 cm diameter bars. The actual properties of the reinforcement were determined by conducting tensile tests of a minimum of three samples from each size and strength.

Concrete strength was varied from 19457 kPa to 37116 kPa. Unconfined compressive tests were conducted on standard concrete cylinders on the day of the experiments to determine the actual concrete properties. The concrete mix designs used were successful in obtaining a consistent variation of high, medium and low strengths. All post-experimental analysis was conducted using actual material properties.

Each model included a construction joint with a typical lap splice detail. This construction joint was painted with a joint release compound to assure failure at that location.

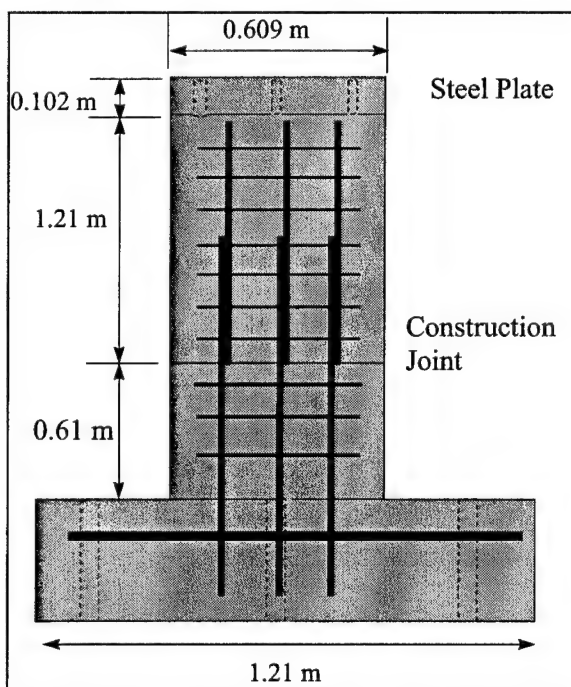


**Figure 6.** Schematic view of strain penetration experimental specimen indicating model dimensions

Deflection gages were mounted directly on the specimen spanning the construction joint. The

probes of these Linearly Varying Deflection Transducers (LVDT) gages were attached to rigid links via flexible couplings. The couplings allowed for limited lateral displacement while measuring vertical displacement. These gages were expected to give a direct measurement of the crack width up to failure at this critical section.

### 3.2 Experimental results

Each specimen was mounted in the load frame (Figure 7). Vertical force was applied to the each model with a servo-controlled 889 kN hydraulic loader. An initial vertical compression load of 222 kN was applied to the structure. This vertical load was applied in each experiment to simulate the dead load of a full-scale tower. After application of the initial dead all strain gages and deflection gages were reset to zero. Thus the initial condition of the model included dead load effects as in a prototype structure.

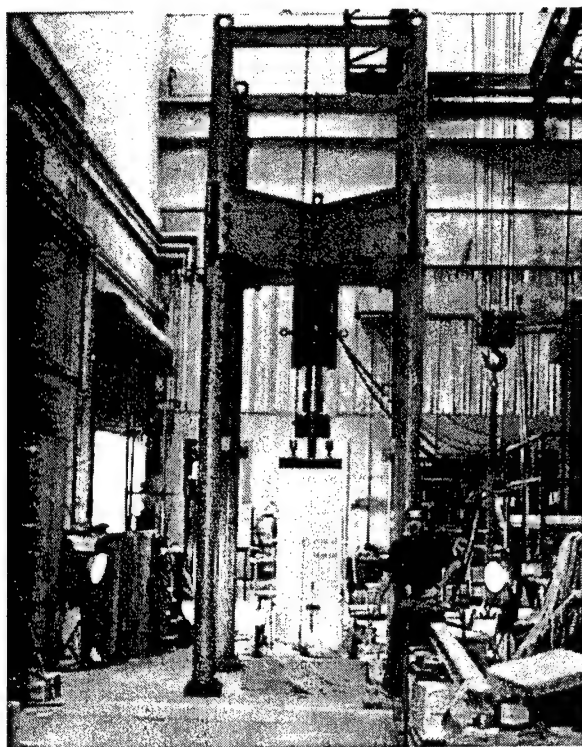


**Figure 7.** Strain penetration experimental specimen mounted in load frame, Geotechnical and Structures Laboratory, (Vicksburg, Mississippi)

The load measurement was not reset to zero. From this compressed condition the experiment proceeded with the application the deflection controlled vertical tension load. The load head was moved upward at a rate of 0.254 mm/sec to a deflection of 2.54 mm as measured by the ram's internal deflection gage. At this point the load head was returned to zero. This was repeated for a total of three repetitions. After the three repetitions the next load cycle began and the total deflection applied was increased by 2.54 mm to a total of 3.048 mm. Again, three cycles were applied. This process of the application of increasing deflections, repeated three times, was continued until failure occurred. As longer deflections were applied the load rate was increased in order to complete the experiment in a reasonable time.

Figure 8 shows the load-deflection curve for a small-diameter (0.95 cm) low-strength (404 mPa yield strength) bar in high-strength (37116 kPa) concrete. This is a fairly typical response.

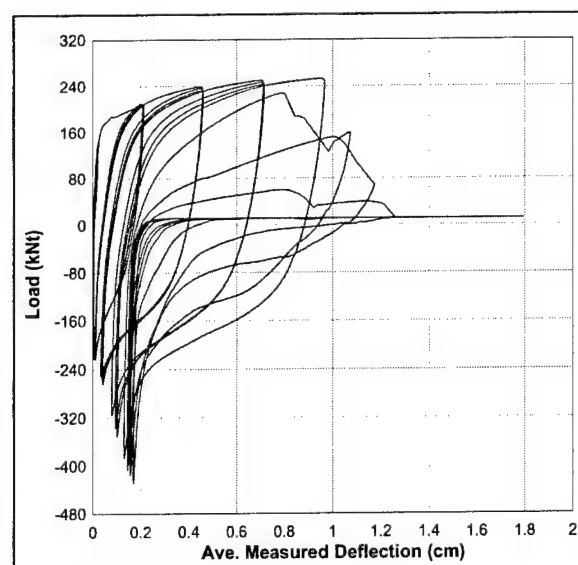


**Figure 8.** Typical load-deflection curve for strain penetration experiment

The maximum measured deflection was taken to be the last deflection for which a cycle of three load reversals was completed. This is the same as the ultimate crack width at failure that

appears in Equations 3 and 4 of the deflection-based analysis technique. The photograph in Figure 9 shows a typical specimen after completion of the experiment. It should be noted that some of the larger bar experiments exhibited a multi-crack failure. In these cases it was observed that all the cracks were of the same width at failure. Hence, the ultimate single crack width was taken as the measured deflection divided by the number of cracks. This multi-crack failure mode is thought to be an artifact of the uniform tensile load in the experiment and does not reflect the expected failure in an intake tower.

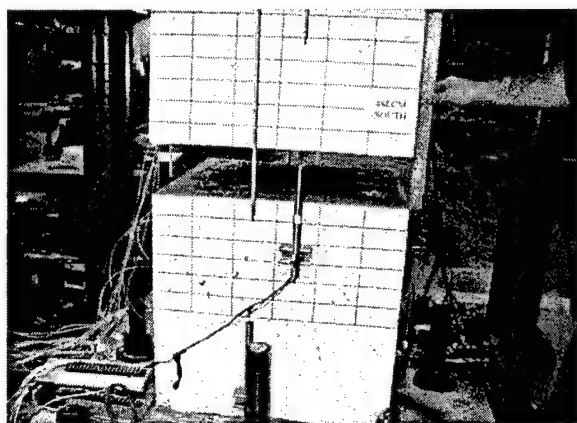


**Figure 9.** Typical single crack failure zone of strain penetration experiment

A statistical analysis was conducted of the results of the initial small diameter bar experiments. The values of parameters included in the statistical model included those associated with the steel (bar diameter, bar area, yield strength, yield strain, hardening strain, ultimate strength, ultimate rupture strain) as well as the concrete (density, compressive strength, modulus of elasticity) and finally the response (number of cracks, ultimate crack width, cycles to failure).

An analysis of variance was conducted and the results were somewhat surprising. The only input parameters that showed significant correlation to the crack width were those associated with the steel material properties of strength and strain. It is especially interesting to note that there was not a significant correlation to bar diameter. It was recognized that the variation of

the bar diameter may not have been large enough to expose the importance of this parameter. Four further experiments were conducted with larger bar sizes and the results included in the statistical analysis. Given the inclusion of the larger bars the bar diameter was shown to be significant. The final equation generated for ultimate crack width at failure is Equation 4. The crack widths are largely predicted by the ultimate strain capacity of the rebar and rebar diameter. Given the crack width the ultimate deflection capacity can be calculated the displacement-based analytical procedure completed.

#### 4 SHAKING TABLE EXPERIMENTS

As part of a continuing effort to validate the displacement-based analytical procedure, a series of shaking table experiments was performed. The experiments were conducted on a 1/8-scale model of a typical intake tower, of the same design as used for the ITS3 cyclic loading tests. The objective of these tests was to compare the failure mode under dynamic conditions with the failure mechanism previously observed under monotonic and cyclic loading. These tests also served the purpose of providing additional data for the evaluation and validation of current analytical models.

The tests were completed by early July 2001. The intake tower model (Figure 10) was tested laterally with uniaxial sinusoidal support motions, near the tower's natural frequency in the short direction of the tower. Test levels were increased until failure occurred. Pre- and post-failure responses of the model as well as the corresponding failure mechanism were systematically documented. The extensive results collected from this testing program will facilitate a direct comparison between the measured responses and the behavior predicted by numerical models and previous static cyclic tests. The intake tower model was 3.05 m tall with a hollow rectangular cross-section that was 1.32 m wide in the east-west direction and 1.02 m wide in the north-south direction. The walls were 0.14 m thick, constructed of normal strength

concrete with scaled aggregate and reinforcing steel. The weight of the tower was calculated as 4.29 metric tons. Figure 11 shows a schematic drawing of the intake tower model, which was placed on top of a heavily reinforced base beam. The base beam was square, with a width of 2.74 m and a thickness of 0.46 m.



**Figure 10.** Intake tower model on top of shaking table at the Construction Engineering Research Laboratory (Urbana, Illinois)

The model was extensively instrumented with accelerometers attached to the base beam and the external faces, linear variable differential transducers (LVDT) installed between the base beam and tower, and several deflection gages. In addition, the vertical reinforcing steel was instrumented with strain gages. Progression of damage was extensively documented with digital photographs and video. Two digital camcorders were used: one recorded the overall model response from the east-north-east side, whereas the other camcorder zoomed in on the cold joint at the bottom of the model on the west face of the model (Figure 7).

Table 1 displays the scaling relationships that govern this type of problem, in terms of 3 main scaling factors:  $\lambda_L$  (geometry),  $\lambda_E$  (modulus of elasticity), and  $\lambda_\rho$  (density). The model geometry was 1/8 of the prototype, that is,  $\lambda_L = 8$ .

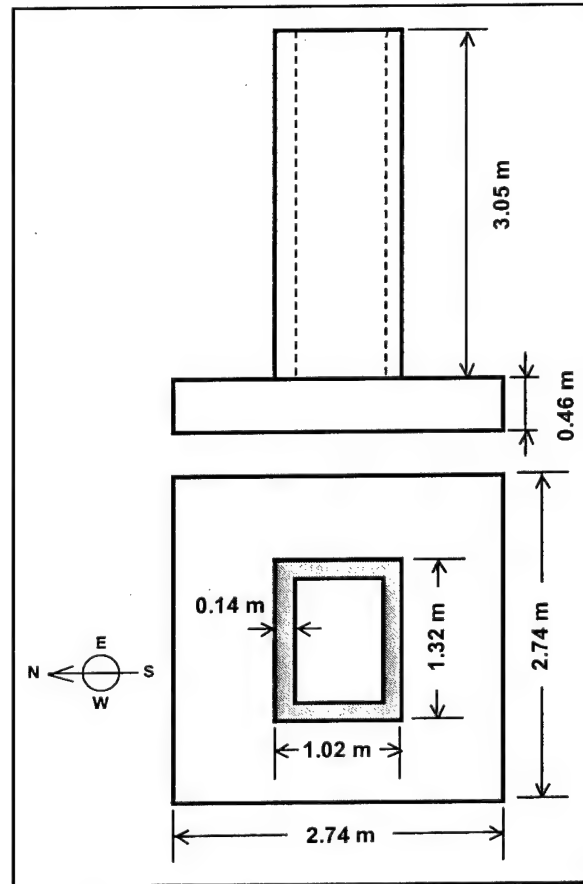


**Figure 11.** Schematic view indicating intake tower model dimensions.

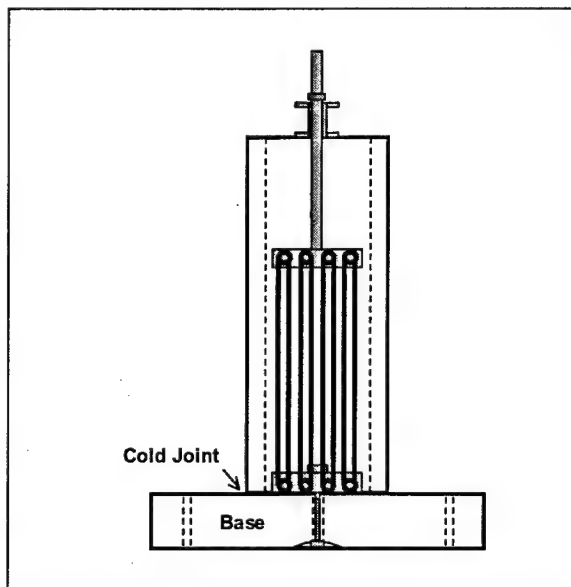
Standard strength concrete was used for the model, and therefore  $\lambda_E = \lambda_\rho = 1$ . The third column of the table contains the resulting scaling relationships for this case, which is characterized by an acceleration scaling factor that is the reciprocal of the geometric scaling factor.

Therefore, inertial and gravity effects for the model should be increased  $\lambda_L = 8$  times with respect to prototype conditions. The scaling of inertial effects was achieved by increasing the magnitude of the imposed base accelerations by a factor of 8.

The scaling of gravity effects was achieved by means of 80 loops of 2.54 cm diameter elastic cord connected between the top and the base of the tower model (Figure 12). The extremely flat load-deflection characteristics of these elastic cords allowed them to be used in such a way that

**Table 1.** Scaling Relationships

Variable	Scaling factors	
	$\lambda_L, \lambda_E, \lambda_p$	$\lambda_L, \lambda_E = \lambda_p = 1$
Time	$\lambda_t = \lambda_L \sqrt{\frac{\lambda_p}{\lambda_E}}$	$\lambda_t = \lambda_L$
Frequency	$\lambda_f = \frac{1}{\lambda_L} \sqrt{\frac{\lambda_E}{\lambda_p}}$	$\lambda_f = \frac{1}{\lambda_L}$
Force	$\lambda_F = \lambda_E \lambda_L^2$	$\lambda_F = \lambda_L^2$
Stress	$\lambda_\sigma = \lambda_E$	$\lambda_\sigma = 1$
Strain	$\lambda_\epsilon = 1$	$\lambda_\epsilon = 1$
Displacement	$\lambda_u = \lambda_L$	$\lambda_u = \lambda_L$
Velocity	$\lambda_{\dot{u}} = \sqrt{\frac{\lambda_E}{\lambda_p}}$	$\lambda_{\dot{u}} = 1$
Acceleration	$\lambda_{\ddot{u}} = \frac{\lambda_E}{\lambda_L \lambda_p}$	$\lambda_{\ddot{u}} = \frac{1}{\lambda_L}$

**Figure 12.** Schematic view depicting modeling of gravity load effects

the corresponding vertical loads did not vary significantly with the rocking response of the tower with respect to the base. The cords were designed to provide an additional vertical load equal to 30 metric tons. Including this load, the resulting vertical compressive stresses at the

base of the model due to gravity effects were 575 kPa.

The model was initially tested with low-level random motions to measure natural frequencies, mode shapes and damping. These tests were conducted in the X (north-south) and Y (east-west) directions. The amplitude of the input motions was initially very low (0.02 g). The random motion tests were then repeated at increasing amplitudes until clear modal information was acquired in both horizontal directions.

The model was initially excited using sinusoidal base motions in the X direction at a frequency of 28 Hz (3.5 Hz, prototype scale). The imposed base motions ramped up to full amplitude in 0.5 sec; held a constant amplitude for 2.0 sec; and ramped down in 0.5 sec, for a total test duration of 3.0 sec. For each test run, the amplitude of the sinusoidal support motion was gradually increased with respect to the previous one while keeping the excitation frequency constant. Previous static tests performed on similar 1/8-scale models indicated that the base of the model cracked at a value of top lateral deflection between 1.3 and 1.8 mm, with applied lateral loads between 130 and 170 kN.

The model failed by cracking at the cold joint at the base. Once it cracked across the entire cold joint surface, the model softened significantly. The change in the fundamental frequency was a very effective damage indicator. Damage evolution was carefully monitored by the LVDT measurements along the base of the model. Figures 13 and 14 show acceleration responses measured during test run 18, corresponding to an excitation level of 2.04 g (0.255 g, prototype scale). These responses correspond to sensors A6x and A14x, located at the bottom and top of the north face of the model, respectively.

Figure 15 shows the time history measured by one of the deflection gages installed at the top of the model (D5x). The amplitude of oscillation is about 2 mm.

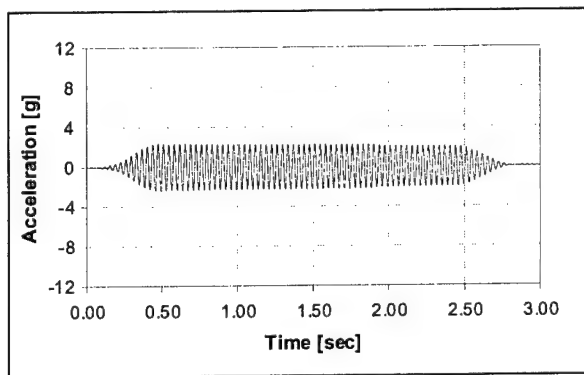


**Figure 13.** Base acceleration, A6x (run 18)

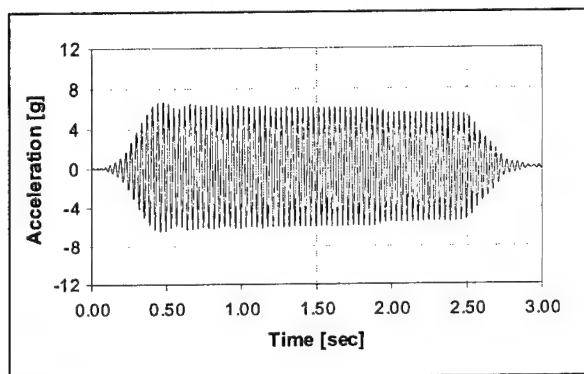


**Figure 14.** Top acceleration, A14x (run 18)

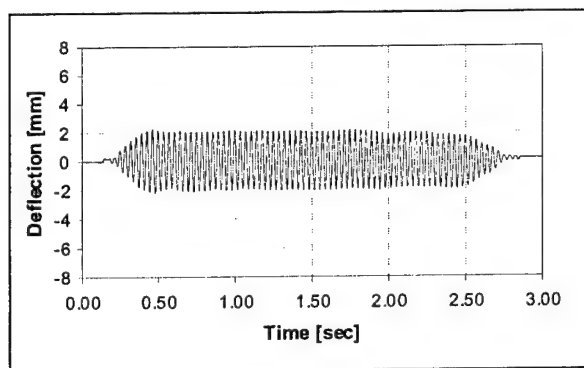


**Figure 15.** Top deflection, D5x (run 18)

After significant damage was identified, the model was again tested with random motions to determine updated modal properties associated with the damaged condition. Cracking of the model across the entire cold joint surface softened the structure, as evidenced by the shift in the fundamental vibration frequency. Figure 16 shows the transfer functions between the top model acceleration (A14x) and the base beam

acceleration (A1x) corresponding to two different series of random motion tests. As shown in the figure, the fundamental frequency decreases from 29 Hz to 24 Hz.

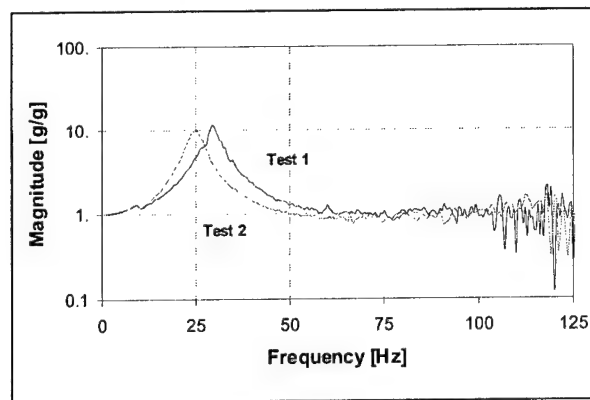


**Figure 16.** Transfer functions A14x/A1x for different series of random excitation tests

Additional sinusoidal tests were conducted with an excitation frequency of 22 Hz (2.75 Hz, prototype scale), gradually increasing the amplitude of the motions as in the previous case. Figure 17 shows the top deflection of the model during test run 37, corresponding to an excitation level of 6.00 g (0.75 g, prototype scale). The behavior of the model at this stage exhibits different response characteristics that are induced by the significant damage and rotation at the base.

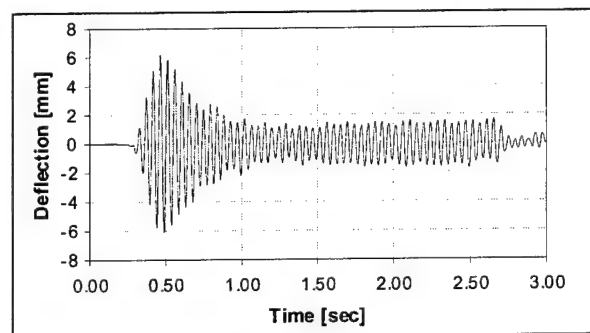


**Figure 17.** Top deflection, D5x (run 37)

Extensive quantitative information regarding the behavior of the failure surface (cold joint at the base of the model) was gathered by the vertical LVDT gages at that location. Figure 18 shows



the time history for the sensor L2Z, illustrating the opening and closing of the single base crack.

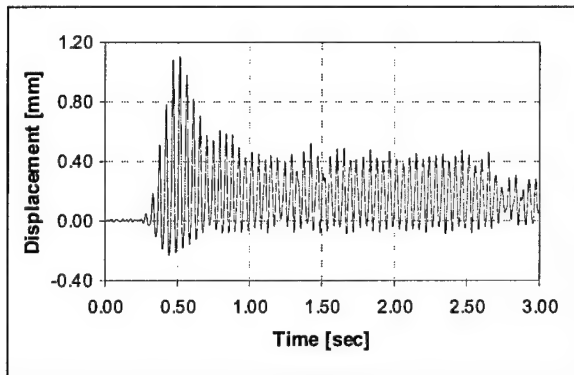


**Figure 18.** Base LVDT, L2z (run 37)

#### 4 CONCLUSIONS

We now have an experimentally and analytically validated deflection-based analysis procedure accounting for available ductility in lightly reinforced rectangular intake towers. The analytical technique was developed based on the observed response of statically loaded models. Shake table experiments demonstrated that the failure mode under dynamic conditions was very similar to the failure mode under monotonic and cyclic static loading. The natural frequency of the model decreased substantially after cracking. The same single crack response with significant ductility was witnessed in both the static and dynamic experiments. The experiment validates the calculation of the deflection capacity based on the results of static experimentation. Future dynamic experiments will model the response of a tower to an individual earthquake. This will further validate the complete displacement-based analysis process.

#### 5 ACKNOWLEDGEMENTS

This work was sponsored by the Direct-Allotted Civil Works Earthquake Engineering Research Program of the U.S. Army Engineer Research and Development Center (ERDC) in Vicksburg, Mississippi. The authors appreciate the cooperation of the authorities at the ERDC, which permitted the presentation and publication of this study.

#### 6 REFERENCES

- Dove, Richard C. (1996). "Structural Parameter Analysis of U.S. Army Corps of Engineers Existing Intake Tower Inventory," Technical Report SL-96-1, U.S. Army Engineer Waterways Experiment Station, Vicksburg, MS.
- Dove, Richard C. (1998). "Performance of Lightly Reinforced Concrete Intake Towers under Selected Loadings," Technical Report SL-98-1, U.S. Army Engineer Waterways Experiment Station, Vicksburg, MS.
- Dove, Richard C. (2000). "Performance of Lightly Reinforced Concrete Intake Towers under Selected Loadings," Technical Report ERDC/SL TR-00-6, U.S. Army Engineer Research and Development Center, Vicksburg, MS.
- Headquarters, U.S. Army Corps of Engineers (2002). "Structural Design of Spillways and Outlet Works," Engineer Manual EM 1110-2-2400, Washington, DC (in publication).

This page intentionally left blank.



## Earthquake Analysis of Radial Gates/Dam Including Fluid-Structure Interaction

by

Mohammad Aslam<sup>1</sup>, Edward L. Wilson<sup>2</sup>, Martin Button<sup>3</sup>, Charles Ahlgren<sup>1</sup>

### ABSTRACT

A limited amount of experimental and analysis research has been conducted on the dynamic behavior of spillway radial gates including fluid structure interaction during earthquake loading. A common method of dynamic analysis is to use added mass to approximate the dynamic interaction of the gate or the dam with the reservoir based on the Westergaard theory. This added mass approach generally predicts natural frequencies which do not match with the measured data on the radial gates. For the analysis of the radial gates, the added mass approach in some cases may be overly conservative and vice versa in others.

The added mass method is generally based on the assumption that the gate is rigid and that the water is incompressible. One of the purposes of this paper is to evaluate the added mass approximation and compare the results with a reservoir, modeled with three-dimensional, compressible fluid elements. Therefore only one model, including the dam, the radial gate and the reservoir is generated for the static or earthquake analysis of the complete structural system. The hydrostatic loading on the dam and the gate can be applied as normal pressure loads on the upstream shell elements without the reservoir present. An alternate method to apply the hydrostatic loading as used in this investigation, is to give the three dimensional reservoir elements dead load and allow the lateral forces to develop between the reservoir and the structural system consisting of the dam and the gate in this case. A close comparison between the results of these

two different methods assured the accuracy of the present methodology for the static and the dynamic analysis of the radial gate or the dam.

In addition to the analysis, extensive amount of testing was performed on 13 different radial gates to determine the natural frequencies and to compare the test results with the analytical results.

### 1 INTRODUCTION

A common method of modeling fluids, for earthquake loading, is to use the "added mass" approach which is based on the assumption that part of the mass of the fluid moves with the same displacement as the structure. This approximation is based on many assumptions that cannot be applied to most fluid-structure systems. The purpose of this paper is to review the limitations of the added mass approach and to propose an alternate finite element model for fluids subjected to dynamic loads. The proposed displacement-based finite element method considers the flexibility of the structure, compressibility of the fluid and arbitrary geometry and boundary conditions. The analysis of radial gates has been mandated by regulatory agencies since the failure of Folsom Dam radial gate in California in 1995.

#### 1.1 The Westergaard Paper

Westergaard published the classical paper on "Water Pressures on Dams During Earthquakes" [1]. This work was based on the solution of a

<sup>1</sup> Pacific Gas and Electric Co., San Francisco, CA 94105.

<sup>2</sup> Professor of Civil Engineering, University of California, Berkeley, CA 94720.

<sup>3</sup> Eng Analysis Corp., 300, Frank Ogawa Plaza, Oakland, CA 94612.

two-dimensional reservoir/dam system subjected to a horizontal earthquake displacement motion of  $u_x(t) = u_{x0} \sin(\omega t)$  at the base of the dam. Since simple harmonic motion is assumed, the displacement is related to the acceleration by the following equation:

$$\ddot{u}_x(t) = -\omega^2 u_{x0} \sin(\omega t) \quad \text{or, } u_{x0} = -\frac{\ddot{u}_{x0}}{\omega^2} \quad (1)$$

Westergaard concluded (based on a 1.3-sec period measured during the great earthquake in Japan in 1923) that the period of earthquake motions (displacements) could be assumed to be greater than one second. Most of his conclusions and equations presented in the paper are based on an earthquake period of 1.3 sec. The term "added mass" was never used or defined by Westergaard. Theodor von Karman, in a very complimentary discussion of the paper, used the term "apparent mass."

The rigid dam, incompressible reservoir model used by Von Karman is shown in Figure 1. He proposed an approximate equation for the pressure at the reservoir-dam vertical interface as

$$p(z) = 0.707 \sqrt{h(h-z)} \rho \ddot{u}_g = b(z) \rho \ddot{u}_g \quad (2)$$

where  $\rho$  is the mass density of water; or  $\rho = w/g$ . The term  $b(z)$  can be physically interpreted as the equivalent amount of water that will produce the same pressure for a unit value of boundary acceleration.

Based on the real compressibility of water and an earthquake period of 1.3 sec, Westergaard's equation for the pressure distribution for a rigid dam is:

$$p(z) = \frac{7}{8} \sqrt{h(h-z)} \rho \ddot{u}_g = b(z) \rho \ddot{u}_g \quad (3)$$

The term  $b(z) \rho$  has been termed the added mass by others and has been misused in many applications with flexible structures using the relative displacement formulation for earthquake loading.

## 1.2 Basic equations

From Newton's Second Law, the dynamic equilibrium equations in terms of displacement  $u$  and fluid pressure  $p$ , for an infinitesimal fluid element are:

$$p_{,x} = \rho \ddot{u}_x, \quad p_{,y} = \rho \ddot{u}_y \quad \text{and} \quad p_{,z} = \rho \ddot{u}_z \quad (4)$$

The volume change  $\mathcal{E}$  of the infinitesimal fluid element in terms of the displacements and pressure are given by the following equations:

$$\mathcal{E} = \varepsilon_x + \varepsilon_y + \varepsilon_z = u_{x,x} + u_{y,y} + u_{z,z} \quad (5)$$

$$p = \lambda \mathcal{E} \quad (6)$$

Where  $\lambda$  is the bulk or compressibility modulus. Elimination of the pressure from Equation (4) produces the following two partial differential equations for the  $xz$ -plane:

$$\rho \ddot{u}_x = \lambda (u_{x,xx} + u_{z,xx}) \quad \& \quad \rho \ddot{u}_z = \lambda (u_{z,zz} + u_{x,zx}) \quad (7)$$

The water motion at every point in time must satisfy both of these equilibrium equations. The classical "separation of variables" method is normally used to solve these equations. Only Equations (5) and (6) are required to develop an element stiffness matrix using the standard displacement finite element approach [3].

## 1.3 Horizontal wave propagation

In the horizontal direction, the one-dimensional solution for the displacement, velocity and acceleration, associated with an applied boundary displacement of  $u_0 \sin(\omega)$  at  $x = 0$  in a semi-infinite domain, is given by

$$\begin{aligned} u_x(x, t) &= u_{x0} \sin\left(\omega t - \frac{\omega x}{V}\right) \\ \dot{u}_x(x, t) &= u_{x0} \omega \cos\left(\omega t - \frac{\omega x}{V}\right) \\ \ddot{u}_x(x, t) &= -u_{x0} \omega^2 \sin\left(\omega t - \frac{\omega x}{V}\right) \\ u_z(x, t) &= \dot{u}_z(x, t) = \ddot{u}_z(x, t) = 0 \end{aligned} \quad (8)$$

where  $x$  is the distance from the boundary and  $V$  is the wave propagation speed given by  $V = \sqrt{\lambda/\rho}$ . The wave propagation speed for water is 1438 m/sec (4,719 ft/sec). The strain, or volume change, can be calculated from Equation (8) as

$$\varepsilon = u_{x,x} = -u_0 \frac{\omega}{V} \cos(\omega t - \frac{\omega x}{V}) \quad (9)$$

At  $x=0$  the internal pressure, associated with the boundary displacement, is expressed by

$$p(t) = \lambda \varepsilon = -\lambda u_0 \frac{\omega}{V} \cos(\omega t) \quad (10)$$

For harmonic displacement response,  $u_0 = \frac{\ddot{u}_0}{\omega^2}$ ;

hence, the maximum internal pressure that can be developed at a boundary due to harmonic horizontal displacement input is:

$$p_{MAX} = \frac{\lambda \ddot{u}_0}{\omega V} \quad (11)$$

#### 1.4 Radiation boundary condition

From Equations (6), (8) and (9) the pressure as a function of time and space can be written, for one-dimensional wave propagation, as

$$p(x,t) = \lambda \varepsilon = -V \rho \dot{u}_x(x,t) \quad (12)$$

Hence, the pressure is related to the absolute velocity by a viscous damping constant equal to the  $V\rho$  per unit area. Therefore, linear viscous dashpots can be inserted at the upstream nodes of the reservoir that will allow the wave to pass and the strain energy in the water to "radiate" away from the dam. This is an approximation since the water near the upstream boundary of the reservoir is not 100 percent confined in the vertical direction.

#### 1.5 Vertical wave propagation

Due to the existence of the free surface of the reservoir, water can move vertically due to

horizontal boundary displacements. These vertical waves are coupled with the horizontal displacements since the water pressure is equal in all directions. If no horizontal motion exists, vertical waves can still exist with a displacement given by the following equation:

$$u_z(z,t) = \alpha_n \sin\left(\frac{2n-1}{2h}\pi z\right) \sin(\omega_n t) \quad (13)$$

Note that the vertical shape function satisfies the boundary conditions of zero displacement at the bottom and zero pressure at the surface of the reservoir. Substitution of Equation 13 into the vertical wave equation,  $\rho \ddot{u}_z = \lambda u_{z,zz}$ , produces the following vertical frequencies of vibration:

$$\omega_n = \frac{2n-1}{2h}\pi V \quad \& \quad f_n = \frac{2n-1}{4} \frac{V}{h} \quad (14)$$

Therefore, for a reservoir depth of 30.5 m (100 ft) the first frequency is 11.8 cps and the second frequency is 34.4 cps. The excitation of these vertical modes by horizontal earthquake motions is very significant for many dam-reservoir systems.

Since Westergaard believed that only periods longer than one second were important he concluded that these vertical modes of vibration were not important and neglected their contribution to the dynamic water pressures acting on the dam.

## 2 MECHANICAL PROPERTIES OF FLUIDS

Many different isotropic materials that have a very low shear modulus compared to their bulk modulus, have fluid-like behavior. These materials are often referred to as nearly incompressible fluids. The incompressible terminology is misleading since the compressibility, or bulk modulus, of these materials is normally lower than other solids. The bulk modulus  $\lambda$  and shear modulus can be written in terms of Young's modulus  $E$  and Poisson's ratio  $\nu$  as:

$$\lambda = \frac{1}{3(1-2\nu)}E \quad \& \quad G = \frac{1}{2(1+\nu)}E \quad (15)$$

For isotropic materials the bulk modulus and shear modulus are known as Lamé's elastic constants and are considered to be fundamental material properties for both solids and fluids. Given the bulk modulus and shear modulus, Poisson's ratio and Young's modulus can be calculated from the following equations:

$$\nu = \frac{3-2R}{6+2R} \quad \& \quad E = 2(1+\nu)G \quad (16)$$

where the ratio of shear modulus to bulk modulus is  $R = G/\lambda$ . If a material has a very small shear modulus, Poisson's ratio  $\nu \approx 0.50$  and Young's Modulus  $E \approx 3.0G$ . In order to illustrate the relative mechanical properties of fluids and solids, Table 1 summarizes approximate values for several common materials.

**Table 1.** Mechanical Properties of Steel, Concrete and Water

Material	E Young's Modulus	$\nu$ Poisson's Ratio	G Shear Modulus	$\lambda$ Bulk Modulus
Steel	207 mpa	0.25	83 mpa	83 mpa
Concrete	27.6 mpa	0.20	11.5 mpa	7.6 mpa
Water	0	0.50	0	2.1 mpa
Water	0.6 kpa	0.49995	0.21 kpa	2.1 mpa

Note that the ratio of shear modulus to bulk modulus for normal solids is very close to 1.0. It should be pointed out that the shear modulus for real fluids is not zero. Under dynamic loading viscosity and boundary layer effects allow fluids to resist shearing strains. Hence, a small value of shear modulus is physically justifiable. It is apparent that water is not incompressible compared to other materials. In fact the compressibility of water is three times of that of concrete.

Table 1 also presents approximate mechanical properties for water assuming a very low shear modulus and a consistent value of Poisson's ratio. The bulk modulus of the water-like

material will be identical to water and the shear modulus will be very small.

### 3 FINITE ELEMENT MODEL FOR FLUIDS

During the past 30 years considerable research has been conducted on the development of special purpose finite elements for the analysis of fluids. Most of this work has been based on the pressure formulation and has been restricted to the dynamic response of linear systems.

Within the past 15 years, however, an eight-node, three-dimensional element has been developed that can be used to model both solids and fluids. This element contains internal displacement modes that prevent locking for materials with low shear modulus. This is the standard solid element used in both SAP2000 and SADSAP structural analysis programs and is documented in Reference 3. It will be demonstrated in this section that this new element can be used to accurately model dam/reservoir systems subjected to dynamic loads.

The 30.5 m (100 ft) depth, infinite-length reservoir is approximated by  $30.5 \times 91.5$  m ( $100 \times 300$  ft) finite element mesh shown in Figure 2 and the steady state harmonic displacement associated with one g acceleration is applied to the right boundary. The water elements have a bulk modulus of 21126 kgf/cm<sup>2</sup> (300,000 psi) and a shear modulus of 2.1 kgf/cm<sup>2</sup> (30 psi). The upstream boundary of the reservoir is fixed horizontally or is modeled by pressure transmitting dashpots with a viscous constant of  $c = \rho V = 0.15 \text{ Kg} - \text{sec}/\text{cu.cm.} (5.296 \# \text{sec}/\text{in}^3)$  per unit of boundary area. The "radiation boundary" solution was produced by a transient nonlinear analysis using the Fast Nonlinear Analysis method [3].

Table 2 summarizes the maximum pressure obtained using different boundary conditions at the upstream face of the reservoir and different values for modal damping. Since the loading is simple harmonic motion many different

frequencies of the reservoir tend to be excited by all loadings. The maximum reservoir pressure using added mass approach or Equation 3 is determined to be 2.6 Kg/cm<sup>2</sup>.

**Table 2.** Pressure vs. Load Frequency for a 91 × 30 m Reservoir (Note: Westergaard Pressure is 2.6 Kg/cm<sup>2</sup> for all frequencies)

Loading Frequency CPS	Modal Damping Percent	2-D Finite Element Models (Pressure in units of Kg/cm <sup>2</sup> )	
		Fixed Upstream Boundary	Radiation Upstream Boundary
2	5.0	2.8	2.6
5	5.0	2.4	2.4
10	5.0	4.3	3.8
20	5.0	4.0	4.1
30	5.0	1.0	0.8

#### 4 ANALYSIS OF TIGER CREEK DAM AND RADIAL GATE USING FLUID-STRUCTURE INTERACTION MODEL

The following numerical example uses the finite element method to establish an integrated model incorporating the dam, the gate and the reservoir. The model is excited by a horizontal (upstream-downstream) displacement time history applied at the base of the dam, and a vertical acceleration time history applied at the base of the dam and reservoir. Cross-channel excitation will result in very low forces on the radial gates, and is ignored in this analysis.

The development of the combined dam-gate-reservoir finite element model started with a "dry" gate model. The gate model was then connected to the crest of a gate-width dam model. Finally, the reservoir was explicitly included to produce an integrated dam-gate-reservoir model. All models were developed and analyzed using SAP2000 [4].

##### 4.1 Gate model

The SAP2000 computer analysis software was used to develop a detailed linear model of the gate structure. Two element types were used to

form this model: FRAME elements were used to model the fifteen vertical ribs, the bracing members, and the double angles forming the flanges of the built-up main girder and arm members and their stiffeners; SHELL elements were used to model the face plate 9.5 mm thickness as-built [7,8]) and the webs of the main girders and arms (both 9.5 mm in thickness. The centerlines of the vertical rib elements were offset from the faceplate elements. The rib and faceplate nodes were appropriately constrained to represent composite action between the ribs and faceplate. Similar constraints were used between the ribs and the two horizontal girders.

The gate model was supported vertically along the bottom of the faceplate, and with full restraint (three translations and three rotations) at each of the two trunnions. The complete gate model consists of 248 frame and 150 shell elements, and is shown in Figure 5. The weight of the gate computed by SAP2000 is 8950 kg.

##### 4.2 Dam model

The concrete arch dam at Tiger Creek Afterbay was modeled in 3-D using plan, elevation and cross-section geometry taken from [8]. The 3-D model was founded along both abutments and at its downstream base, assumed at (PG&E) elevation 677 m. For modeling purposes, the dam was assumed symmetrical about its upstream-downstream axis. The dam model had an arc length of approximately 104 m between abutments, and a height of 30.5 m from spillway crest to bottom of foundation. A total of 300 3-D solid elements were used to form the model, shown in Figure 6.

The first six frequencies from the 3-D dam model without any water are presented in Table 3. The frequencies producing significant upstream-downstream (U/D) motion near the center of the dam are also noted in Table 3.

A 2-D model of a gate-width slice of the dam, located on the axis of the dam, was then constructed using the dam axis cross section shown in PG&E Drawing No. 46585. The 2-D model is shown in Figure 7. The material properties of the

**Table 3.** Lowest Six Frequencies of Tiger Creek Afterbay Dam 3-D Model (Dry Condition)

Mode	Frequency (Hz)	Description of Modes	Center U/D Motion
1	8.4	First anti-symmetric	—
2	8.6	First symmetric	✓
3	11.0	Second symmetric	✓
4	14.2	Second anti-symmetric	—
5	18.4	Third symmetric	—
6	18.8	First rotation mode of top of arch	✓

2-D slice model were identical to those in the 3-D dam model. The stiffening effect of the horizontal arches was accounted for by the addition of a horizontal spring at a model location corresponding to 3.0 m below the crest of the dam. The stiffness of this spring was adjusted so that the frequencies of the 2-D slice model closely matched those frequencies from the 3-D dam model producing significant upstream-downstream motion near the axis of the dam. The frequency match is presented and the corresponding mode shape comparison is shown in Figure 8. Figure 8 indicates excellent agreement between the 2-D and 3-D shapes for mode 1. For mode 2., the general form of the shapes are consistent, but the 2-D dam model shows higher modal amplitudes near the crest of the dam, and will therefore produce conservative (larger than 3-D) motions at the crest of the dam at approximately 18 Hz.

### 4.3 Dam–gate model

The gate model described in Section 4.1 was connected to the crest of the dam model described in Section 4.2, and the combined model was analyzed for frequencies and mode shapes. The geometry of the connection in the model is such that the bottom edge of the gate faceplate is coincident with the upstream face of the dam. In reality, the bottom of the gate is set back about 1.2 m from the upstream face of the dam near the crest. Ignoring this set-back greatly simplifies the modeling of water in this region,

and has previously been shown to be a conservative assumption. The set-back creates a local region of “dead” water near the bottom of the gate for vertically propagating pressure waves. Ignoring the set-back results in a slight over-estimation of total hydrodynamic force on the gate. The gate trunnions were rigidly connected to the fins mounted near the crest of the dam, mimicking the physical connection between gate and dam.

As expected, the dry gate frequencies were reproduced in the combined dam–gate model, providing confidence that the connection between the two structures had been appropriately established in the model.

### 4.4 Dam–gate–reservoir model

Water elements representing the reservoir were added to the dam–gate model to produce an integrated model representing the dam, the gate and the water in the reservoir behind the dam. The dam was also split into 14 solid elements across its slice width. This cross-channel meshing of the dam had no impact on the dam–gate frequencies.

The water was modeled using solid elements with properties set to provide water-like behavior. The material properties used to achieve this effect are described in section 2. The water elements were connected to adjacent gate or dam elements by short, stiff links, transmitting only axial force in a direction normal to the face of the connected solid. These stiff link elements allow unrestrained relative movement along the tangent of the interface between water and solid. The reservoir was modeled upstream from the face of the crest of the dam for a distance of approximately 126 m, or approximately four times the depth of the reservoir. The bottom boundary of the water was permitted only upstream-downstream displacements. The upstream boundary of the reservoir was restrained in the upstream-downstream direction, but vertical displacements on this boundary were permitted. Both sides of the water slice were restrained in the cross-channel direction.



The combined dam-gate-reservoir model is shown in Figure 9. Frequencies of this combined dam-gate-reservoir model were computed. Those modes associated primarily with gate/water movement were noted for comparison with wet gate frequencies measured in the field.

#### 4.5 Material properties

A yield strength of 2112 Kgf/cm<sup>2</sup>, was used for steel and a concrete strength of 211 Kgf/cm<sup>2</sup> was used to develop the dynamic properties of the arch dam. The relevant dynamic characteristics of the dam were shown to be relatively insensitive to variation in concrete strength.

The solid elements representing water have a bulk modulus of 21126 Kgf/cm<sup>2</sup>, and a shear modulus of 2 Kgf/cm<sup>2</sup>. The latter two properties are achieved by specifying a Young's modulus of 6 Kgf/cm<sup>2</sup> and a Poisson's ratio of 0.49995. While the actual shear modulus of water is very close to zero, total hydrodynamic force is relatively insensitive to a range of water shear moduli from 0.2 to 21 Kgf/cm<sup>2</sup>. Thus the above properties for the water-like solid elements are satisfactory.

#### 4.6 Loads and load cases

Four types of loads were considered in this analysis. The load types are as follows:

a. Dead Load – Dead load originates from gravity acting on the self-weight of the gate structure, dam concrete and water.

b. Hydrostatic Load – Hydrostatic load originates from gravity acting on the self-weight of the water in the reservoir, and results in normal pressures acting on both the radial gates and the dam.

c. Friction Load – This loading condition occurs when the gate opening is initiated, and the gate weight is transferred from the spillway sill to the hoist chains. Friction is introduced at the two side seals resisting the lifting motion.

d. Seismic Load – Digitized acceleration and displacement traces from a single earthquake were generated by PG&E. The earthquake, representative of a magnitude 6.5 event on the Gopher Gulch fault, 29 km from the Tiger Creek Afterbay Dam site and is shown in Figures 10 and 11.

These four load types were used to develop three load combinations for the gate safety evaluation. These load combinations are (1) gravity on closed gate, using load types 1 and 2 above; (2) gravity on operating gate, using load types 1, 2 and 3 above; and (3) gravity on closed gate plus seismic, using load types 1, 2 and 4 above.

### 5 DYNAMIC ANALYSIS

The combined dam-gate-reservoir model was subjected to the ground horizontal displacement traces. The absolute displacement formulation of the structural dynamics problem was used as the basis for analysis. The absolute displacement formulation allows hydrodynamic forces between the reservoir and the dam-gate to develop as the base of the dam is pushed in and out of the reservoir.

#### 5.1 Frequency analysis

In the frequency analysis, 400 modes cover a period range of 9.74 sec (0.103 Hz) to 0.0023 sec (435 Hz). The lowest modes show long period sloshing of the water in the reservoir, without deformation of the dam or gate. The mode likely to dominate the hydrodynamic forces on the gate occurs at mode 339 with a frequency of 5.2 Hz. It consists of vibration of the dam in and out of the reservoir. The gate rides along with the dam without significant gate deformation, but is pushed in and out of the reservoir.

Table 4 lists the field-measured frequencies of the Tiger Creek Afterbay wet gate with the reservoir full. The measured mode at 21.4 Hz was identified as the dominant mode by PG&E.

Table 4 also lists a set of analytical modes and frequencies. Table 4 demonstrates that the range of wet gate frequencies determined by field testing are contained in the analytical model, with analytical modes containing significant gate deformations occurring at frequencies close to the field-measured frequencies.

Figures 12 and 13 show the mode shapes of modes 339 (5.2 Hz, major contributor to gate hydrodynamic force) and 382 (20.7 Hz, analytical mode close to field-measured dominant mode).

**Table 4.** Comparison of Calculated and Measured Wet Gate Frequencies

Analytical Results		Measured Frequency (Hz)
Mode	Frequency (Hz)	
		11.3
373	11.9	
374	12.8	
		19.4
381	19.7	
382	20.7	
		21.4
391	35.2	
		39.8

## 5.2 Time history analysis of dam and radial gate

**Dam response:** A typical time history plot of the absolute accelerations at the dam base and the crest are shown in Figure 11. The maximum accelerations are 0.1 g and 0.35 g at the base of the dam and at the crest of the dam respectively.

**Radial gate response:** The maximum trunnion reactions were monitored as a means of gauging the total hydrodynamic load on the gate. The hydrodynamic loads are approximately 1.4 times the hydrostatic loads as seen in Table 5.

Figure 14 shows the first 10 seconds of the time history traces of the total horizontal and vertical forces at the trunnions for the load case 3 analysis that generates the maximum response (+ H2 earthquake, see Table 5).

**Table 5.** Total Hydrostatic and Hydrodynamic Reactions at Trunnions

Load Case	Trunnion Reaction (kips)	
	Horizontal	Vertical
EQ only: + H2	141	60
Hydrodynamic/ Hydrostatic	1.4	1.3

Figure 14 also shows two distinct frequencies in the response. The lower frequency of approximately 5 Hz is clearly visible in the response traces between 4 and 7 sec when the maximum forces on the trunnions occur. This frequency is associated with first horizontal mode of the dam and gate in and out of the reservoir (see Figure 12, mode 339, 5.2 Hz). The higher frequency of approximately 11 Hz is associated with the second horizontal mode of the dam and gate in and out of the reservoir.

The maximum earthquake-induced gate horizontal deformation occurs at the center of the bottom of the gate, and is approximately 2 mm. When combined with the hydrostatic displacement, the maximum total deformation of the gate is 4 mm at the same location.

The hydrodynamic pressure on the face plate follows an approximately trapezoidal distribution with increasing depth from the top of the gate, from zero at the water surface  $0.4 \text{ Kg/cm}^2$  at the bottom of the gate, as shown in Figure 15 at the centerline of the gate. The distribution at the edges of the gate is very similar.

## 6 CONCLUSIONS

Westergaard represented earthquake loading as a simple harmonic loading and developed pressure equations based on a vertical dam upstream face and assumed earthquake periods were greater than one second. The classical approximation of incompressibility was first introduced to simplify the mathematics in order to obtain closed form solutions of certain two-dimensional fluid problems. The added mass approximation is



valid only for low frequencies. However, these approximations are not required at the present time due to the development of three-dimensional fluid elements, inexpensive, high-speed computers and other efficient numerical method of dynamic analysis. In addition, dam/reservoir gate/foundation systems of arbitrary geometry can all be included in the same model. The radial gates and arch dams have curved geometry and the finite element method proposed here is completely general and can be easily applied to arbitrary shapes whereas Westergaard method assumes a straight face.

## 7 REFERENCES

- Westergaard, H. M., (1931), "Water Pressure on Dams During Earthquakes," ASCE Transactions, Vol. 9833, Proceedings.
- Kuo, James Shaw-Han, (1982), "Fluid Structure Interaction: Added Mass Computations for Incompressible Fluid," Report No. UCB/EERC-82/09, University of California, Berkeley.
- Wilson, E. L., (2000) "Three Dimensional Static and Dynamic Analysis of Structures," Computers and Structures, Inc., Berkeley, CA.
- Computers and Structures, Inc., (2001), "SAP2000: Three Dimensional Static and Dynamic Finite Element Analysis and Design of Structures (version 7.44)," Berkeley, CA.
- Federal Emergency Management Agency, (1997), "NEHRP Guidelines for the Seismic Rehabilitation of Buildings," Washington D.C.
- American Institute of Steel Construction, Inc., (1989), "Manual of Steel Construction Allowable Stress Design (Ninth Edition)," Chicago, IL.
- PG&E, (1931), "Tiger Creek Afterbay Dam, Mokelumne River Development," Drawing 46585, San Francisco, CA.
- PG&E, (1931), "Requirements for Radial Gates, Tiger Creek Afterbay Dam, Bear River Diversion Dam," Drawing 46413, San Francisco, CA.

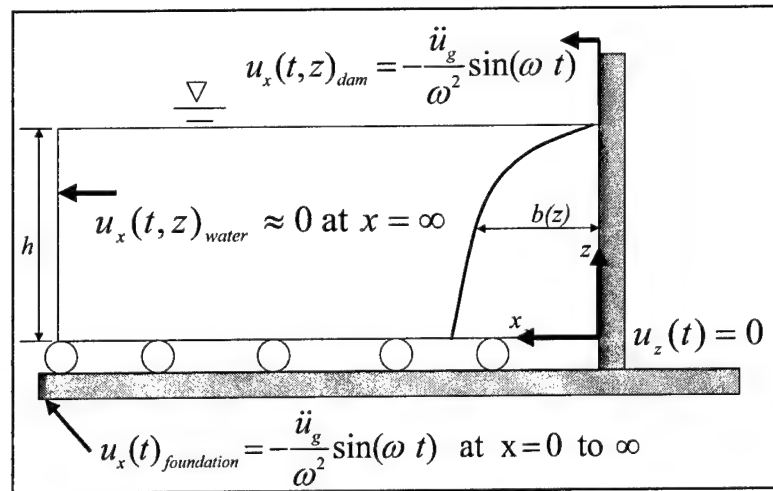


**Figure 1.** Rigid dam and reservoir model

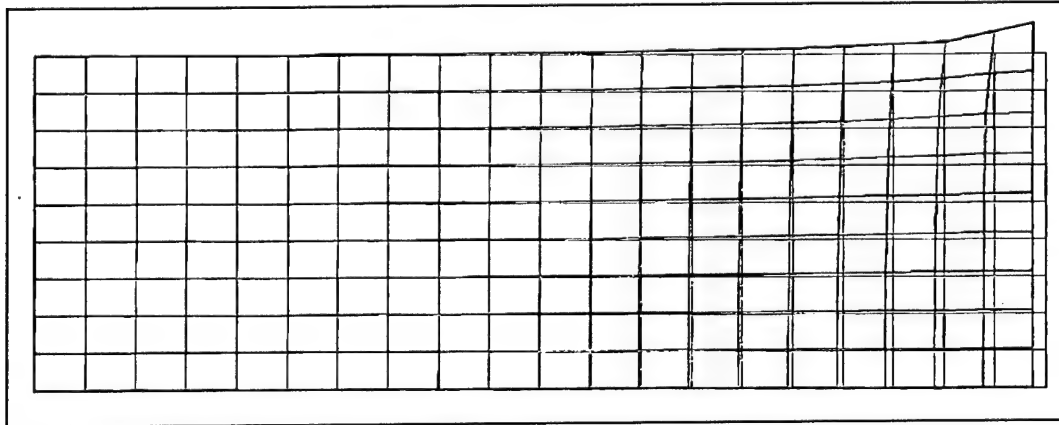


**Figure 2.** Deformed mesh for 2 cps 1 g boundary loading

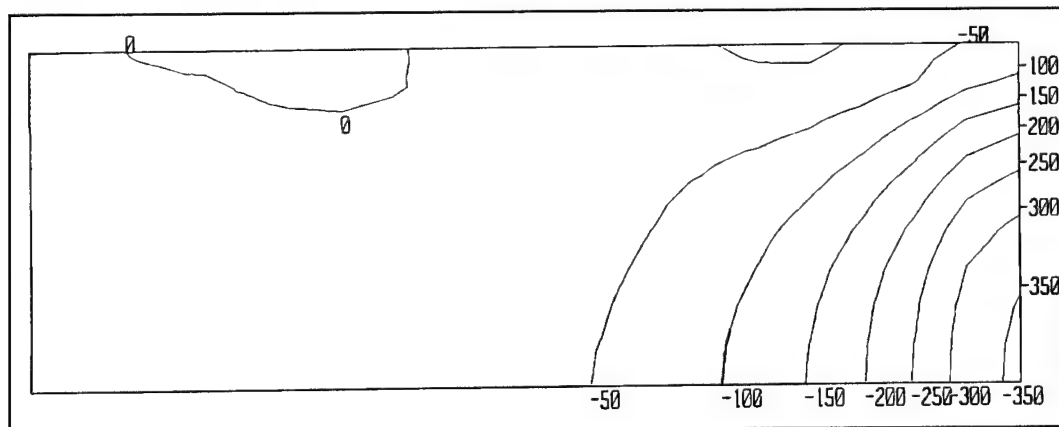


**Figure 3.** Pressure distribution (kgf/cm<sup>2</sup> H 140) for 2 cps 1 g boundary loading

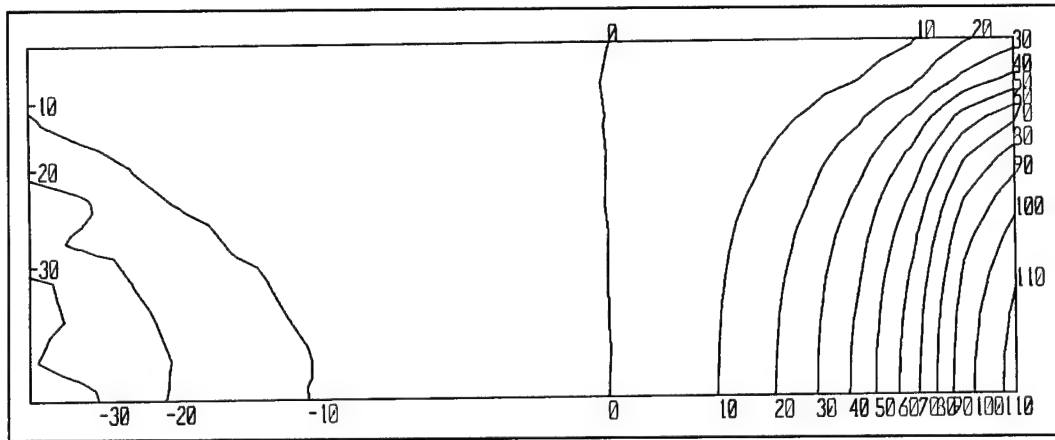


**Figure 4.** Pressure distribution ( $\text{kgf/cm}^2$  H 140) for 30 cps 1g boundary loading

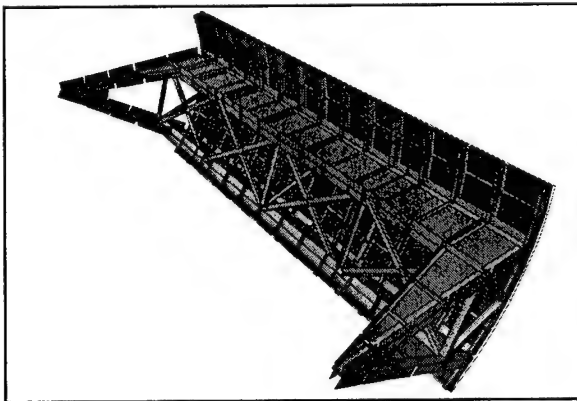


**Figure 5.** SAP2000 dry gate model

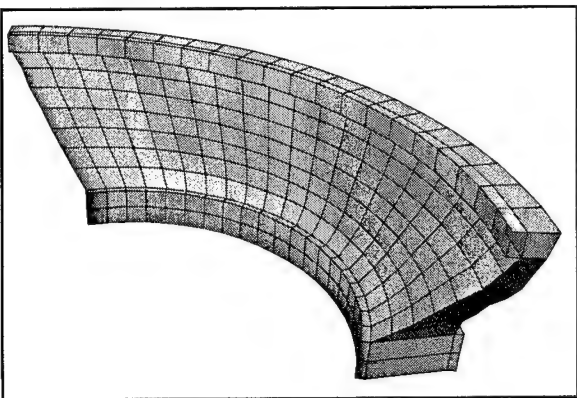


**Figure 6.** SAP2000 dry dam model

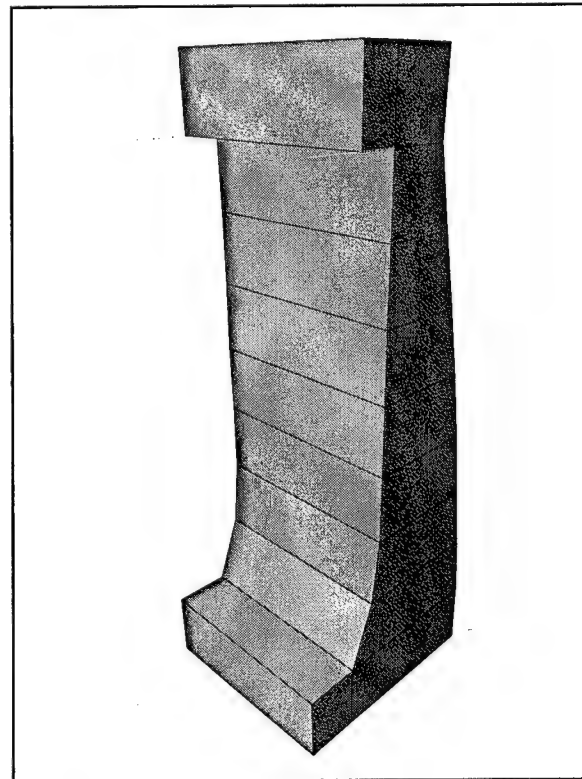


**Figure 7.** SAP2000 equivalent 2-D slice dry dam model

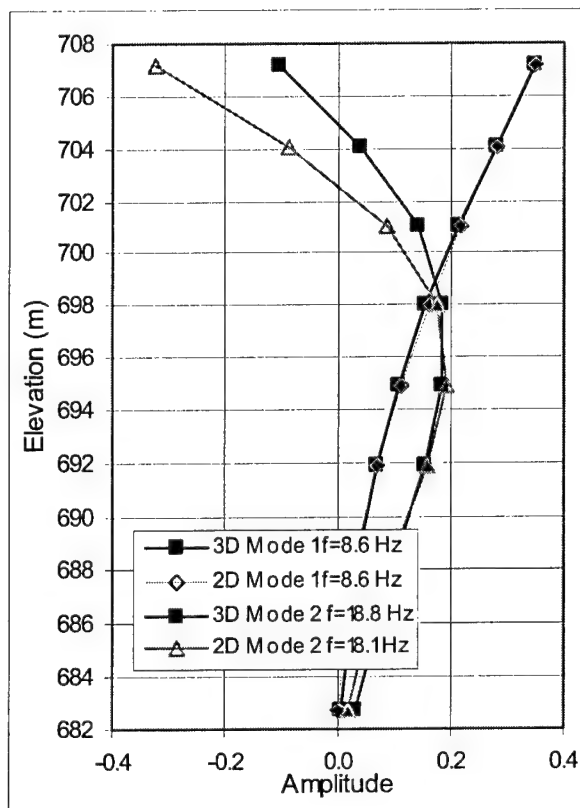


**Figure 8.** Comparison of mode shapes from 2D and 3D dam models

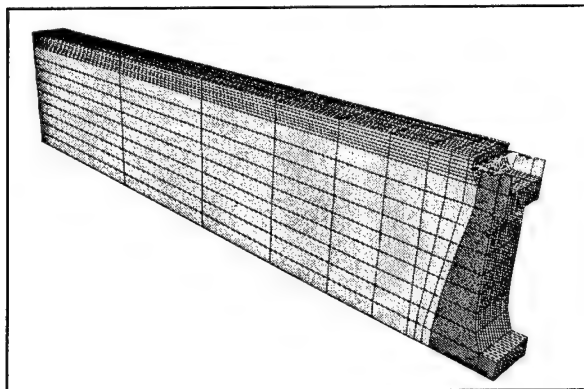


**Figure 9.** SAP2000 combined dam-gate-reservoir model

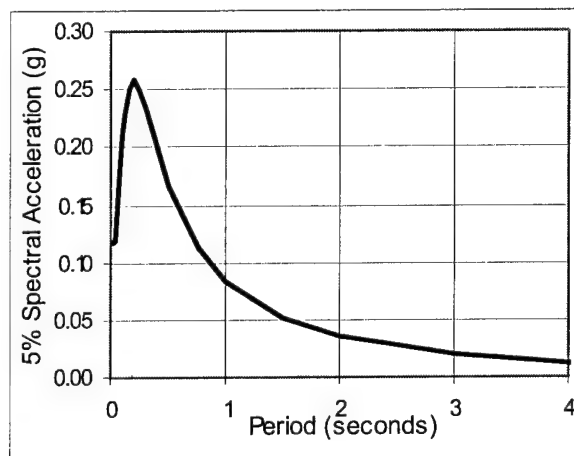


**Figure 10.** 5% damped horizontal response spectrum

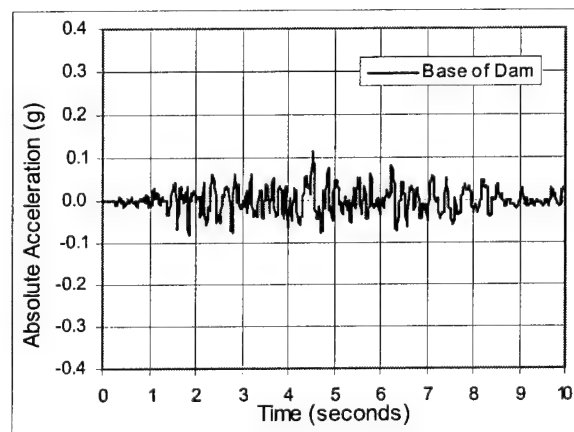
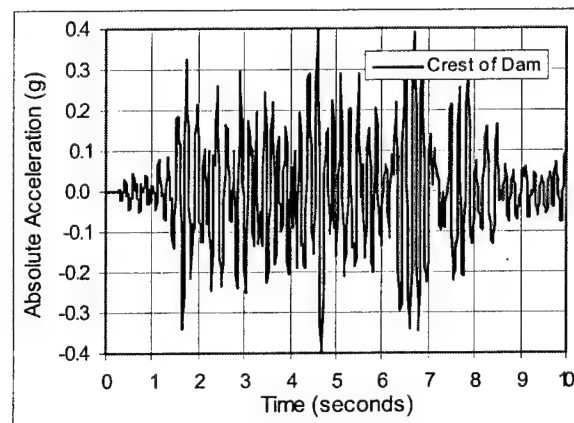


**Figure 11.** Horizontal acceleration histories at base and crest of dam

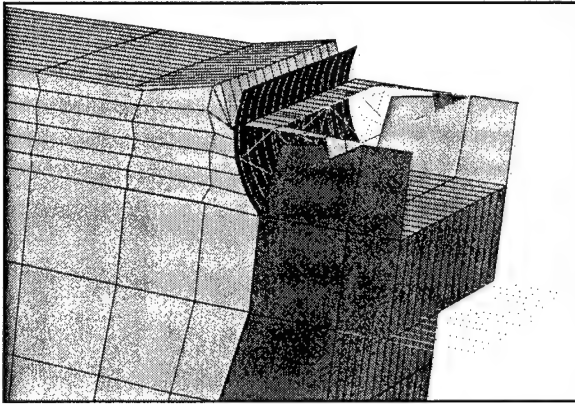


**Figure 12.** Ritz mode 339 – 5.2 Hz

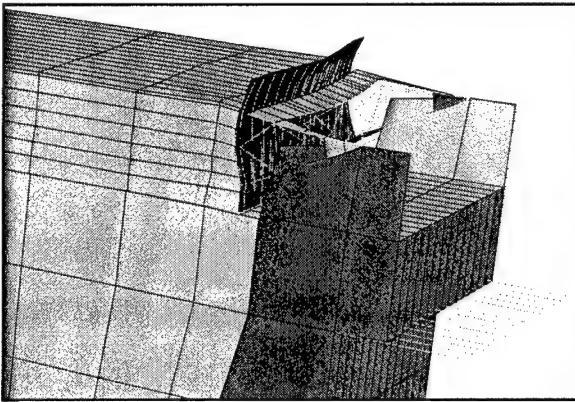


**Figure 13.** Ritz mode 382 – 20.7 Hz

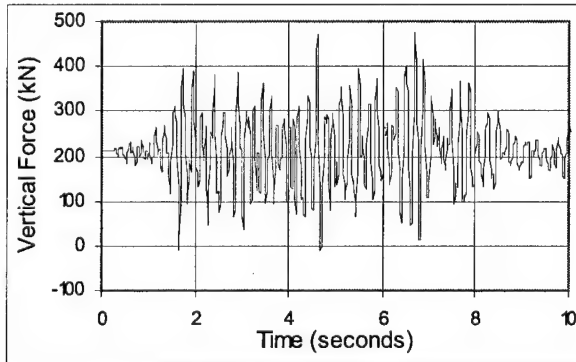
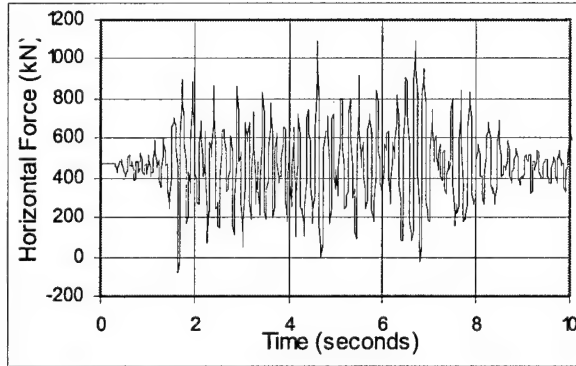


**Figure 14.** Total horizontal force at trunnions (Case 3)

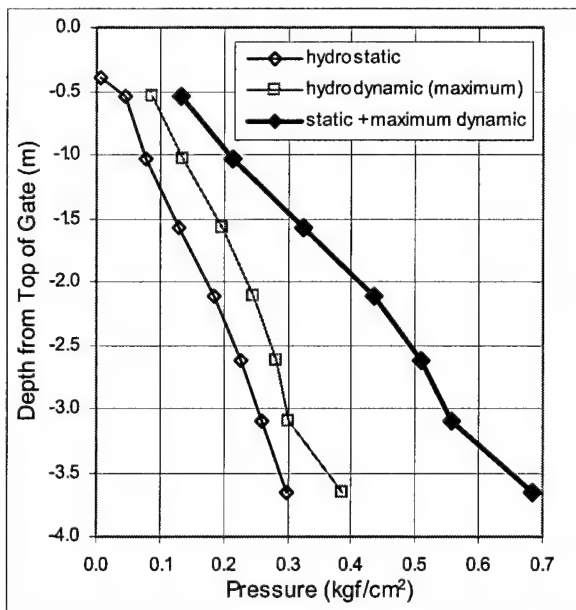


**Figure 15.** Hydrostatic and hydrodynamic pressures at gate centerline

This page intentionally left blank.

## Present State of Acceleration Measurement and Nation-wide Network of Observation at Dam Sites in Japan

by

Takashi Sasaki,<sup>1</sup> Syuji Takasu,<sup>2</sup> Hitoshi Yoshida,<sup>3</sup> and Kenji Inagaki<sup>4</sup>

### ABSTRACT

The SMAC-type strong motion recorder was installed in the Sarutani Dam in the Kinki Region, Japan in 1957, and strong motion observation on dam structures under the jurisdiction of the MLIT, the Ministry of Land, Infrastructure, and Transport (formally the Ministry of Construction) had been started. Nowadays, the 413 dams under the jurisdiction of the Ministry have seismometers and the high-density observation of earthquake records can be conducted. Furthermore, the network of observation of earthquake records at dam sites has been speeded.

This report describes the present state of seismograph arrangement and earthquake data measurement at dams under jurisdiction of MLIT, the characteristics of collected data, and the outline and the future plan of the dam-site seismograph network that is now being constructed.

**KEY WORDS:** Dam, Strong motion records, Seismometer, Network of observation of earthquake record

### 1 INTRODUCTION

Many large earthquakes struck Japan and caused severe damage on important infrastructures and private properties. Fortunately, no dams in Japan have suffered damage that threatened its safety,

but clarifying and securing the earthquake safety of dams is one of the most important missions that must be faced in densely populated Japan. To respond to a strong demand for the advancement of evaluating methods of the earthquake safety of new and existing dams, it is important to study the characteristics of seismic motion at rock foundation and the dynamic behavior of actual dams based on observed records measured at various dam sites. Installing seismographs at dams have been speeded since the 1995 Hyogo-ken Nanbu Earthquake (the Kobe Earthquake) and all dams have seismographs under jurisdiction of the MLIT now.

### 2 PRESENT STATE OF SEISMOGRAPH ARRANGEMENT AT DAMS IN JAPAN

#### 2.1 Introduction

The measurement of earthquake motion at dams of the Ministry of Construction (presently the Ministry of Land, Infrastructure and Transport) began in 1957 when the Ministry installed a SMAC-type strong motion seismograph at the Sarutani Dam to obtain data vital for dam safety management and to advance seismic resistant design. The installation of strong motion seismographs was promoted in response to a growing awareness of the need for strong motion observations following the Niigata Earthquake in 1964.

<sup>1</sup> Senior Researcher, Dam Structures Research Team, Hydraulic Research Group, Public Works Research Institute (PWRI), 1-6 Minami-hara, Tsukuba-shi, 305-8516, JAPAN.

<sup>2</sup> Group Leader, Hydraulic Research Group, PWRI.

<sup>3</sup> Research Coordinator for Watershed Management, River Department, National Institute for Land and Infrastructure Management (NILIM), Ministry of Land, Infrastructure, and Transport (MLIT), 1 Asahi, Tukuba-shi, 305-0804, JAPAN.

<sup>4</sup> Researcher, Water Management and Dam Division, River Department, NILIM, MLIT

At the Kobe Earthquake in 1995, a lot of strong motion records at dam sites were observed, but some dams near the earthquake faults didn't have seismographs, so the strong motion records at dam sites close to the earthquake faults were not got unfortunately. The Ministry, therefore, decided to place the seismographs in all dam sites under its jurisdiction, and to replace the old-fashioned analog seismographs to the new digital seismographs. By the end of 2000, all dam under MLIT's jurisdiction got the seismographs.

Other organizations that own dams, for example, the Ministry of Agriculture, and the private electronic power companies, also have made efforts to install seismographs at their dams.

## **2.2 Present state of installation of seismographs**

By the time of the Kobe Earthquake, 443 strong motion seismographs were installed at 140 dams (MLIT's dams: 48, Water Resources Development Public Corporation's dams: 10, Subsidized prefectural dams: 82), but 1,152 have now been installed at 413 dams (MLIT's dams: 78, Water Resources Development Public Corporation's dams: 20, Subsidized prefectural dams: 315). Figure 1 shows the locations of the dams where the installation of strong motion seismographs has been completed.

Strong motion seismographs that are now installed at dam sites include analog type seismographs and digital type seismographs. Figure 2 shows the state of installation of analog type and digital type seismographs. Initially, most were analog type equipped with a moving pendulum to record earthquake motion on paper, but most of those now in use are digital type that converts earthquake motion to electrical output that is then digitized by an AD converter and recorded on an IC card etc. In the case of new installation, only digital type seismographs are now selected.

Figure 3 shows the transition of the number of earthquakes during which the earthquake records were obtained at dam sites and the number of earthquake records obtained at dam sites. The number of earthquakes observed at dam sites was increased drastically after the Kobe earthquake.

## **2.3 Standard installation way of seismographs at dams**

Strong earthquake motion observations at dams play an important role in dam safety management and studies of the response of the dam to strong motion in bedrock. Therefore, in principle, installation of seismographs is done at the base and at the crest of each dam in the maximum cross section. But because differing responses appear at bridges and pier structures on dam crest, installing seismographs at these locations is avoided generally. Table 1 shows a breakdown of strong motion seismograph installation locations. Dam base mainly means the gallery near the base of concrete dams or the gallery beneath the impervious zone of rockfill dams. Other locations include rim grouting tunnels, water intake systems, and management offices. Data observed at foundations under the dam include reflected waves from on the dam body [1]. Therefore, installation of seismographs on the downstream free field is recommended.

The components measured by a seismograph are set of course as 2 horizontal components and 1 vertical component. Vibration of dam body occurs most easily at right angles to the dam axis because of the vibration characteristics of dams. Therefore, the directions of the horizontal components are, in principle, right angles to the dam axis and the dam axis direction. Earthquake observations are normally performed in trigger mode; the seismographs at one dam are all linked and begin recording simultaneously when a certain threshold value is exceeded. In general, trigger seismograph is located at dam base.



### 3 CHARACTERISTICS OF ACCELERATION AT ROCK FOUNDATION OF DAM SITE

#### 3.1 Introduction

Two reports about the collection of observed acceleration data at dam sites by the PWRI were published in January 2001. The first report [2] is about the information of the locations and the specifications of seismographs in each dam at the time of 2000. The second report [3] summarizes the acceleration data and spectrum, and information of earthquakes. The number of records dealt with in this report is 2,960 collected from 1966 to 2000.

In this paper, the characteristics of horizontal acceleration records in dam foundations have been examined based on records of observed earthquake data. Dams under the jurisdiction of the MLIT were all constructed on rock foundations. The S-wave velocities of dam foundations are therefore, expected to be at least 1,000 m/sec.

#### 3.2 Range of data used

The 143 sets of, 286 in total of horizontal acceleration records and 143 vertical acceleration records were used in this study. These data were collected during earthquakes with a magnitude of 5 or more and observed at an epicentral distance of 200 km or less. Figure 4 shows the distribution of the earthquake epicenters.

The earthquakes that occur in Japan can be classified into three types based on the location of the epicenter; i.e., inter-plate earthquake, intra-plate earthquake and moderate deep earthquake. The inter-plate earthquake means the earthquake which occurs at the interface of two tectonic plates in ocean space, and the epicenter locates 60 km or less in depth generally. The intra-plate earthquake, is also called "crustal earthquake", means the earthquake that occurs within the inland crust. The moderate deep earthquake means the earthquake which epicenter is in the somewhat deep place of inland. The depth is generally deeper than about 60 km.

Table 2 shows the number of earthquake records listed by earthquake types and magnitude. The group about the magnitude of 7.0-7.9 and intra-plate earthquake has many records, but these are mainly got in one earthquake, that is the 2000 Western Tottori Prefecture Earthquake (M7.3). The Intra-plate earthquake is object of public and technical attention in Japan because of earthquake damages by large intra-plate earthquakes which occurred recently. Figure 5 shows the relationships of peak accelerations, magnitude and hypocenter depth with the epicentral distance. The horizontal peak acceleration value is the average of values of two horizontal components. The distribution of observed results is relatively dispersive. The large peak accelerations were obtained in the intra-plate earthquakes which occurred close to the dams. The analyses of strong motion by the intra-plate earthquake are therefore, important for dams.

#### 3.3 Peak acceleration

Figure 6 shows the relationship of the epicentral distance with the horizontal peak acceleration for three magnitude ranges ( $M=5-5.9$ ,  $6-6.9$ ,  $7-7.9$ ) and the three earthquake types. The horizontal acceleration data are shown with the presumed values by the attenuation relationship equations by Fukushima et al. [4]. This equation is proposed based on the data mainly collected on hard soil foundation. The data of dam sites seem to be small as compared with the presumption value for large magnitude. Especially, the tendency is strong about the intra-plate earthquake.

Figure 7 shows the relationship the horizontal peak acceleration and the ratio of the vertical peak acceleration to the horizontal peak acceleration. The ratio is relatively low for the large horizontal acceleration. The effect of the earthquake types is not clear.

#### 3.4 Acceleration response spectra

Figure 8 shows average acceleration response spectra of 143 horizontal record sets.

For the investigation of the effect of the earthquake types on the strong motion at dam foundations, we introduce the presumption equation proposed by An-naka et al. [5]. This equation is obtained by analyses of strong motion data at hard soil sites; the  $V_s$  of those sites are ranges from 300 to 700 m/sec. Figure 9 shows the examples of acceleration response calculated by the equation by An-naka et al.

We calculate the presumed values using the magnitude, the distance to fault and hypocenter depth of 143 records at dam foundations, and obtained the ratio of the actual acceleration response to the presumed values by An-naka et al. Figure 10 shows the average ratio for each earthquake types. From this figure, the acceleration response at dam foundations of the intra-plate earthquake is relatively small those of other types of earthquake type.

Figure 11 shows average acceleration response spectra of records obtained at intra-plate earthquake for three ranges of magnitude and Figure 12 shows acceleration response magnification spectra. The locations of epicenter are 0-20 km in depth and the distance from the dam to the fault ranges 0-40 km in distance from dams. Of course, the spectrum value becomes large in all range of periods according to the size of magnitude. The larger the magnitude is, the larger the period where the spectrum is the peak value. The peak values of magnification spectra are about 2.

Next, the effect of the distance to a fault is compared. Figure 13 (a) shows average acceleration response spectra of intra-plate earthquake records in the case of magnitude of 6.0-6.9 and the depth of 0-40 km and Figure 13 (b) shows those in the case of magnitude of 7.0-7.9 and the depth of 0-40 km. In these figures, spectra lines are shown for different ranges of the distance to the fault. Figure 14(a) shows average acceleration response magnification spectra based on Figure 13(a), and Figure 14(b) shows those based on Figure 13(b). The magnification spectra in the case of magnitude 7.0-7.9 are very similar in spite of the distance from the earthquake faults as compared with the case of magnitude 6.0-6.9.

The number of records for magnitude 6.0-6.9 is not many, so it is difficult to clearly judge whether the differences of characteristic of magnification spectra result from the differences of magnitude. We have to make efforts to gather much more earthquake data in order to investigate the characteristics of the strong motions at dam sites in details.

## 4 DAM SEISMOGRAPH NETWORK

### 4.1 Standard way of data collection

Because the observed data are very valuable and indispensable for the investigation of seismic resistance of dams, the MLIT have been made a periodical collection of the data observed at dams under its jurisdiction. Now, the dam management offices should report the earthquake records to once a year and the information of observation system in the event of new installation or updating of seismographs to the National Institute for Land and Infrastructure Management (NILIM), formerly the Public Works Research Institute (PWRI). The detailed format is fixed for the report and the data in fixed format are sent to the NILIM by floppy disks.

### 4.2 Development dam seismograph network

The MLIT is connecting seismographs installed at dams in a network to construct a system that can monitor earthquakes in real time for responding to demand of earthquake disaster management. The dam seismograph network is connected by the direct microwave circuit, and enables quick collection of not only the maximum acceleration values but also time-history acceleration data. This network system is now monitoring 50 dams of the MLIT.

This system consists of earthquake information monitoring parts and a data base system. Figure 15 shows the outline of the network system.

Some of other organizations, which own their dams, also have been developing the seismograph network like the MLIT's one individually.

### **4.3 Database and monitoring**

The database consists of basic information of dam, information of seismograph, earthquake information and measured data. The following is the actual examples of the items in database.

#### **4.3.1 Basic information of dam**

Dam height, dam length, latitude, longitude, epicentral distance, dam type, slope gradient, etc.

#### **4.3.2 Seismograph information**

Seismograph model number, specification of seismograph, installation position, installation elevation, etc.

#### **4.3.3 Earthquake information**

Occurrence time, epicenter location, depth, magnitude, etc.

#### **4.3.4 Measured data**

Components, peak acceleration, number of samples, number of data, etc.

The seismograph network monitors earthquakes by connecting a server at the NILIM with relay devices installed at each dam management office using microwave circuits, which is for exclusive use of the MLIT.

At the instant that a seismograph at a dam detects an earthquake, the peak acceleration and the measured seismic intensity of the earthquake are transmitted through relay devices to the NILIM database. When the earthquake information arrives at the NILIM from a dam relay device, a message that an earthquake has occurred is displayed on a terminal screen at the same time as an alarm is sounded. And this system automatically starts the collecting of earthquake records from dams nearby the dam that firstly send a data. The dam seismograph network is connected to other seismograph networks [6] for national facilities related rivers and roads, and is sharing data such as the peak acceleration and measured SI value etc.

The shared information is utilized for immediate expectation of disaster occurrences such as the ground liquefaction the damage of bridge etc. Some kind of digital data such as the peak accelerations opens public through the Internet. For maintaining of system functions, the state of the system is constantly monitored once a day by confirmations of the soundness of each relay device, and by checking of the existence of untransmitted earthquake data.

### **5 FUTURE PLANS FOR COLLECTION DATA AND SEISMOGRAPH NETWORK**

The researches on evaluation methods of seismic safety of dams have been conducted using data are accumulated in the PWRI and the NILIM.

According as the system to collect the observed earthquake data from jurisdictional dams has been completed and networking of seismographs has been progressing, the related researches are expected to be advanced. Future plans for the seismograph network include cooperating with prefectural governments to link the network to seismographs at all prefectural dams in order to create a more precise, more highly concentrated earthquake motion monitoring environment.

The networking of seismographs enables quick collection of the earthquake information. The network is, therefore, counted on to make a big contribution to supporting an efficient and appropriate initial emergency action: evaluating the need for inspections of managed facilities, predicting the state of damage etc. immediately after the earthquake when little information is available.

It is, moreover, very important to share earthquake information each other in organizations responsible to the disaster prevention.

And the collection and accumulation of recordings of actual seismic data are essential to researches on the dynamic analysis methods of dams. Therefore, one of important subjects of the network is linkage to the database of detailed data of foundation and dam material for the

precise estimation of earthquake motion distribution and dam behavior.

When the networking of seismographs of all dams under jurisdiction of the MLIT, the collection data by the NILIM through the network will be take the place of the report of earthquake data form dam offices to the NILIM. For improvement of the reliance of the network system, the supervising function of system should be strengthened to be preventing the functional trouble and deterioration.

## REFERENCES

- [1] Y. Yamaguchi, T. Iwashita: Earthquake Motions at an Embankment Dam Site and an Estimation Method of Incident Seismic Waves Using the Observations, Proceeding of the 32<sup>nd</sup> Joint Meeting of UJNR Panel on Wind and Seismic Effects, pp. 253-262, 2001
- [2] Y. Yamaguchi, T. Iwashita, J. Matsuura: Seismometers Installed in the Dams Under the Jurisdiction of the Ministry of Land, Infrastructure and Transport, Technical Memorandum of PWRI, No.3768, 2001.
- [3] Y. Yamaguchi, T. Iwashita: Earthquake Motion at Rock Foundation and Response of Embankment Dams by Acceleration Records at Dams in Japan, Technical Memorandum of PWRI, No.3780, 2001.
- [4] Fukushima et al.: Shimizu Tech. Res. Bull., Vol.10, 1-11, 1991 (in Japanese)
- [5] An-naka, T., F. Yamazaki, and F. Katahira: A proposal of an attenuation model for peak ground motions and 5 % damped acceleration response spectra based on the JMA-87 type strong motion accelerograms, Proceedings of the 24th JSCE Earthquake Engineering Symposium, 161-164, 1997.
- [6] H. Sugita, T. Hamada: Development of Real-time Earthquake Damage Estimation System for Road Facilities, 7th U.S-Japan Workshop on Earthquake Disaster Prevention for Lifeline Systems, 1997

**Table 1.** Seismograph installation locations

Location	Number of Seismographs	Ratio (%)
Dam base	400	34.7%
Dam crest	426	37.0%
Free field	290	25.2 %
Other	36	3.1%
Total	1152	100.0 %

**Table 2.** Number of earthquake records

Earthquake Type	Magnitude			TOTAL
	5.0-5.9	6.0-6.9	7.0-7.9	
Intra-plate earthquake	36	26	112	174
Inter-plate earthquake	14	16	18	48
Moderate deep earthquake	22	26	16	64
TOTAL	72	68	146	286

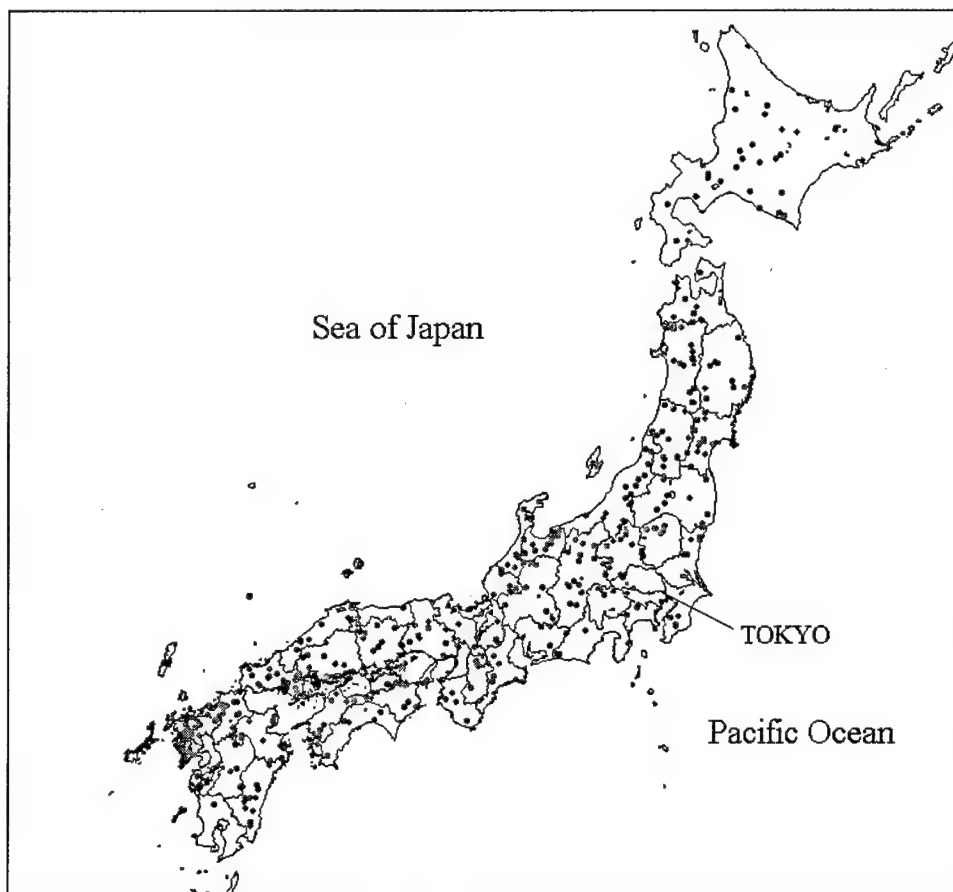


**Figure 1.** Distribution of dams where seismograph installation is completed

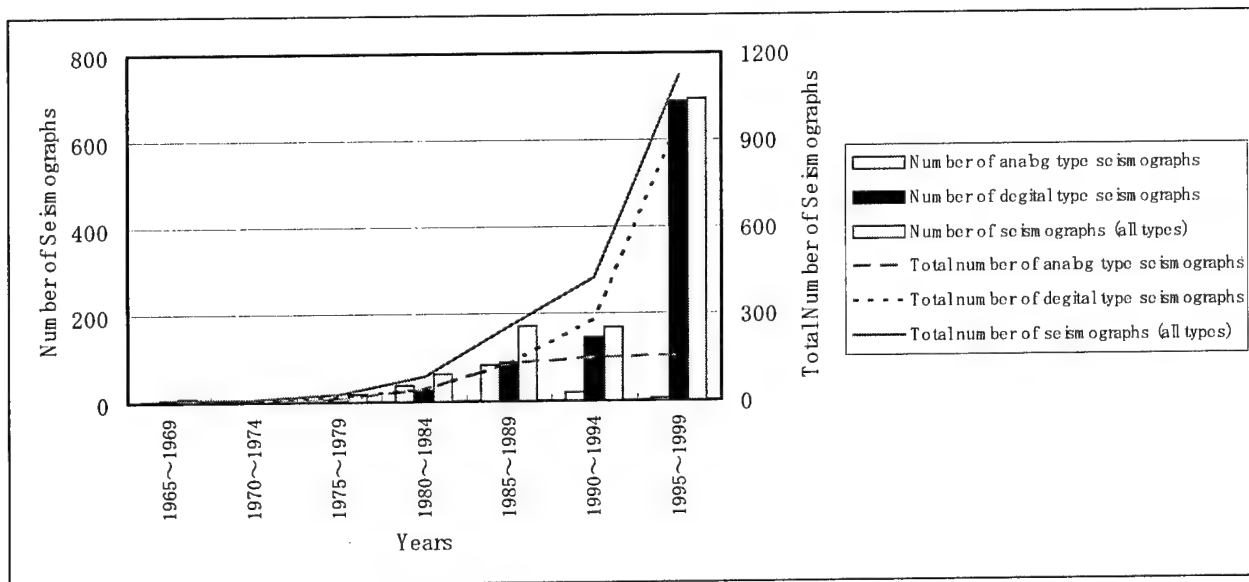


**Figure 2.** Changing number of seismographs

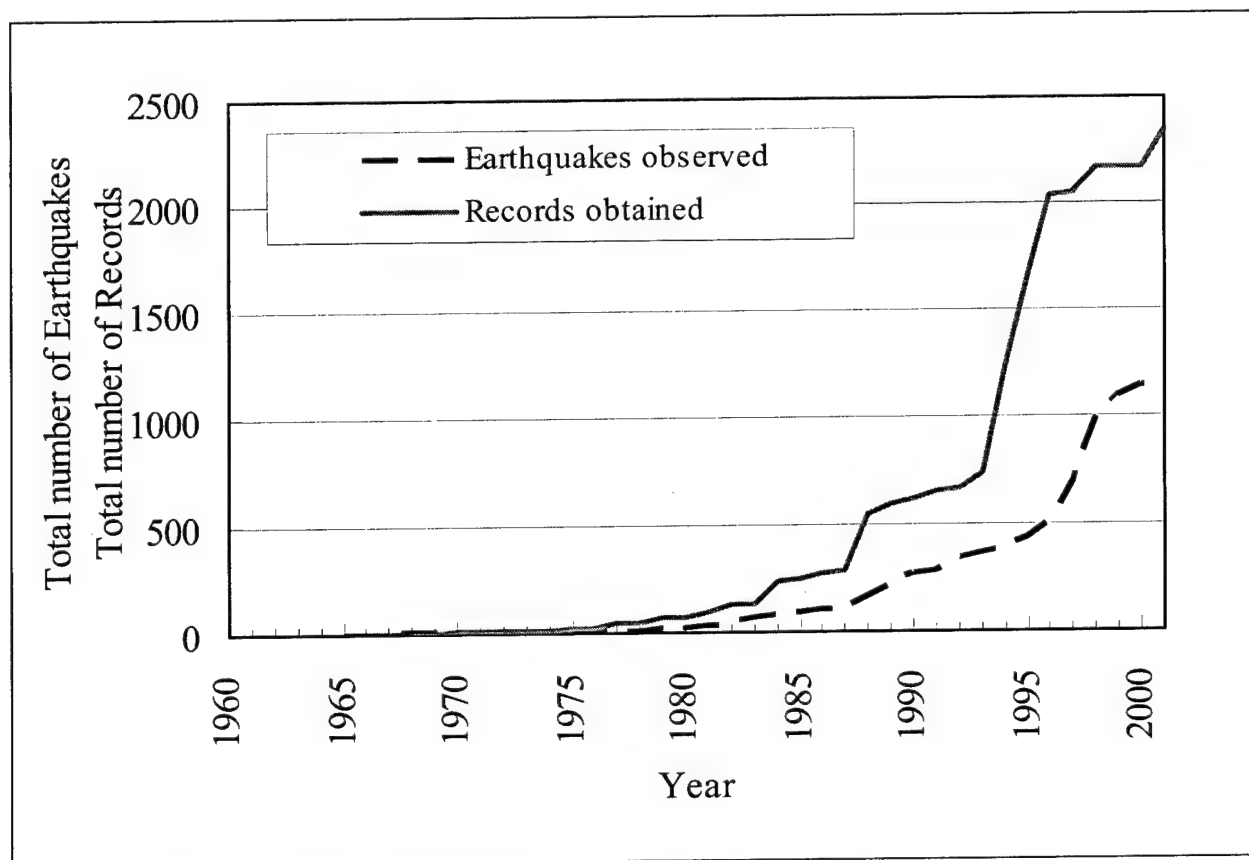


**Figure 3.** Changing number of earthquakes observed and records obtained at dam sites

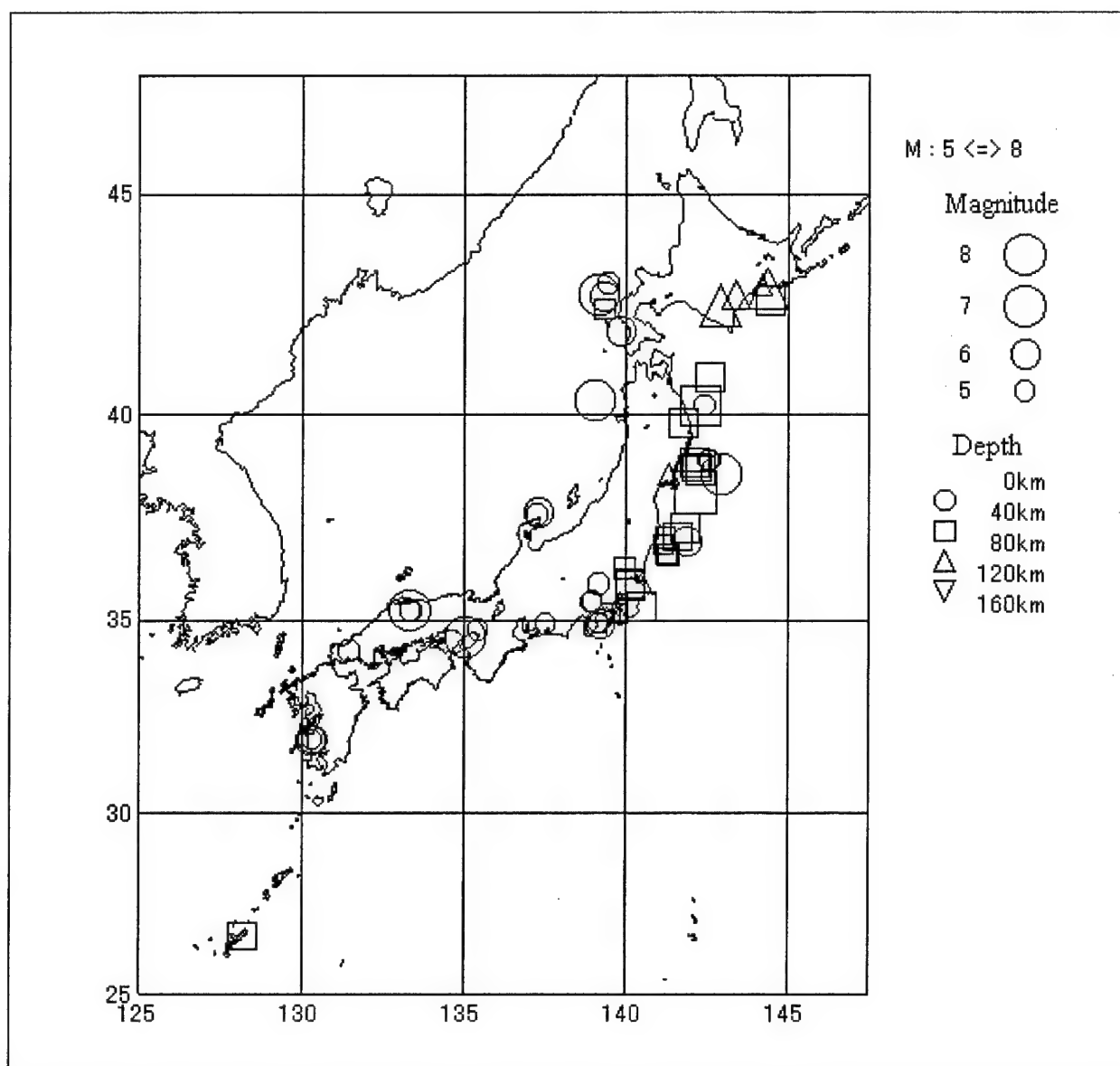


**Figure 4.** Distribution of earthquake epicenters

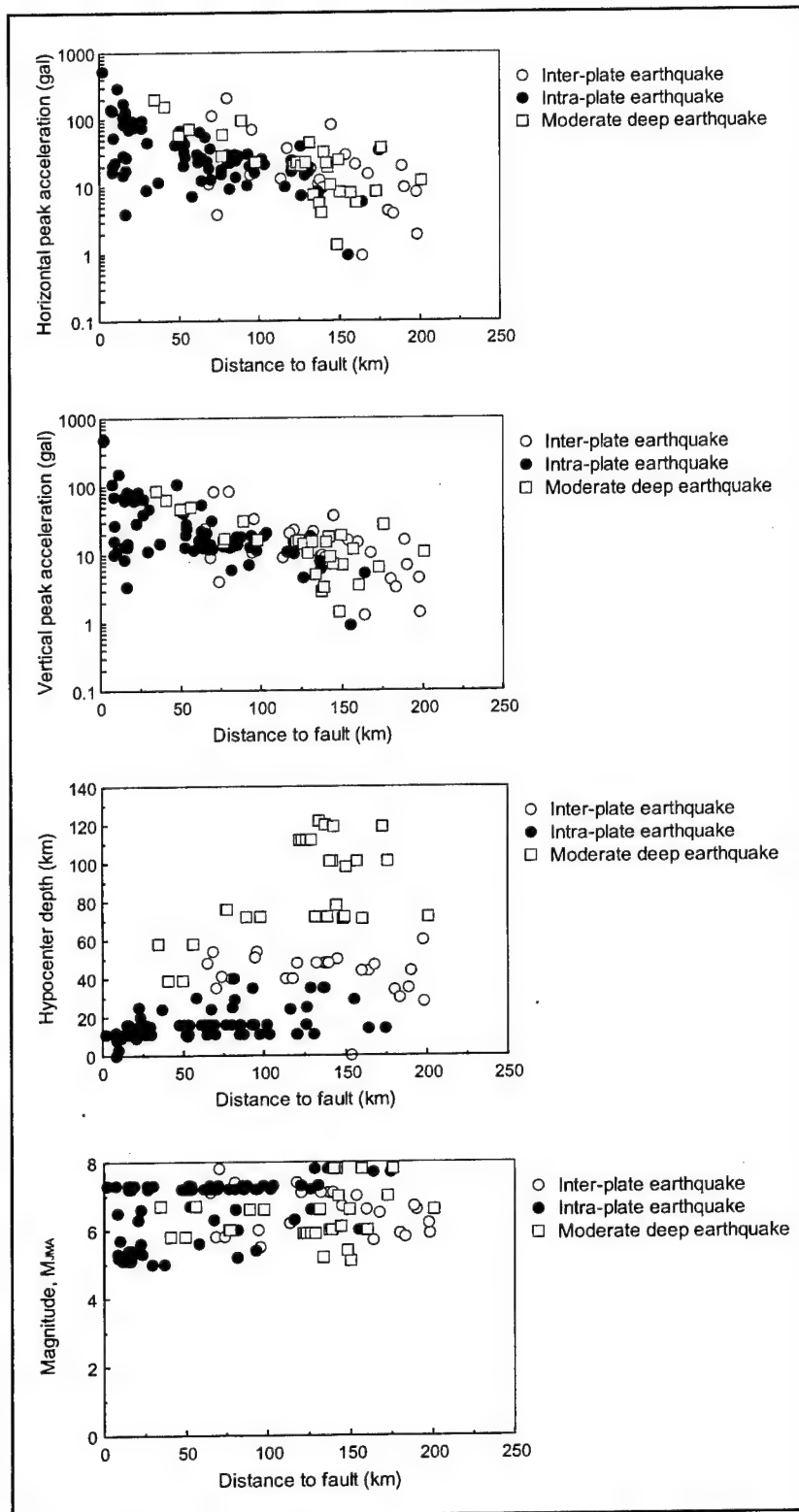


**Figure 5.** Relationship of horizontal and vertical peak accelerations, magnitude and hypocenter depth with epicentral distance



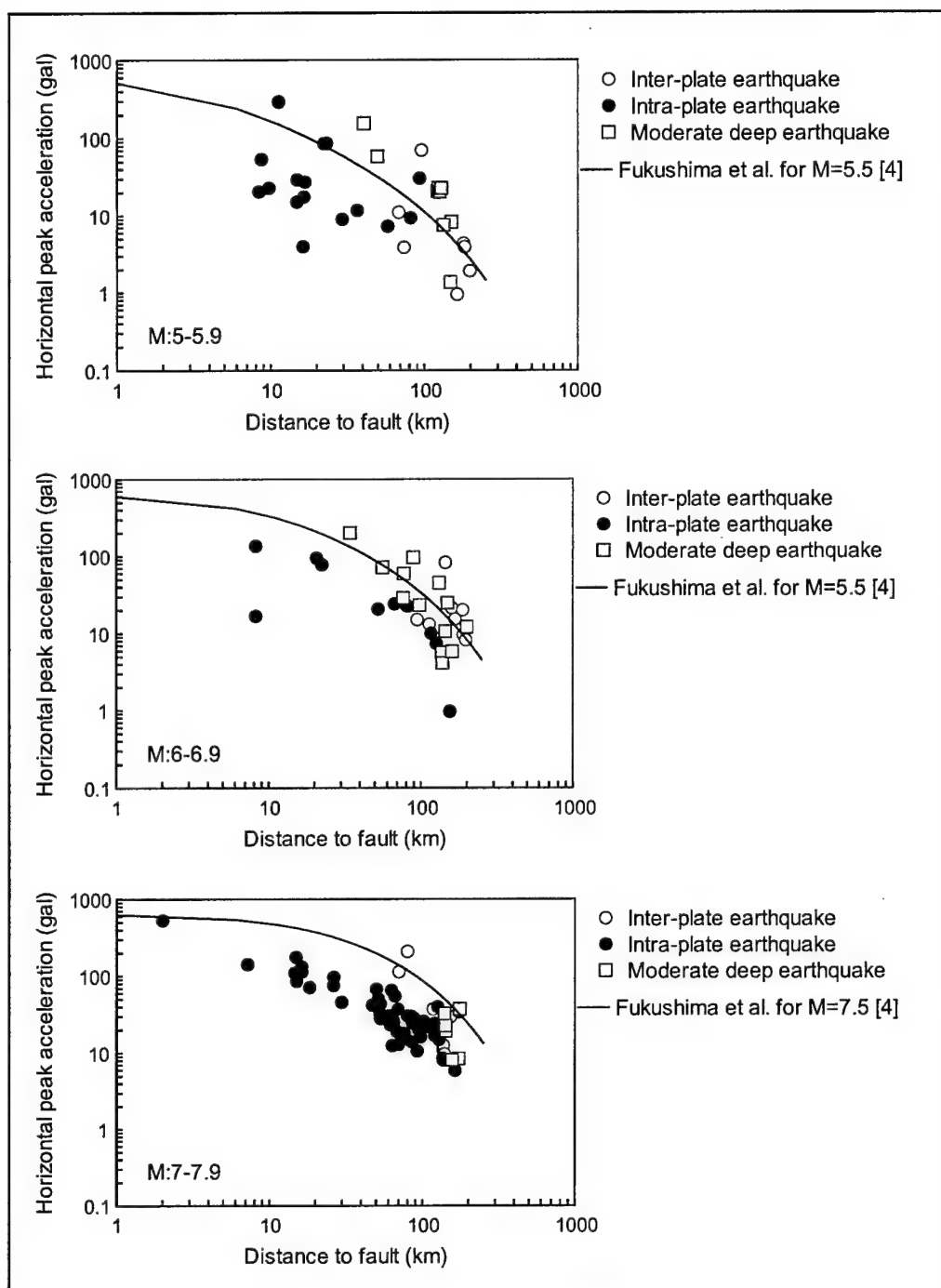


**Figure 6.** Relationship of epicentral distance and horizontal peak acceleration

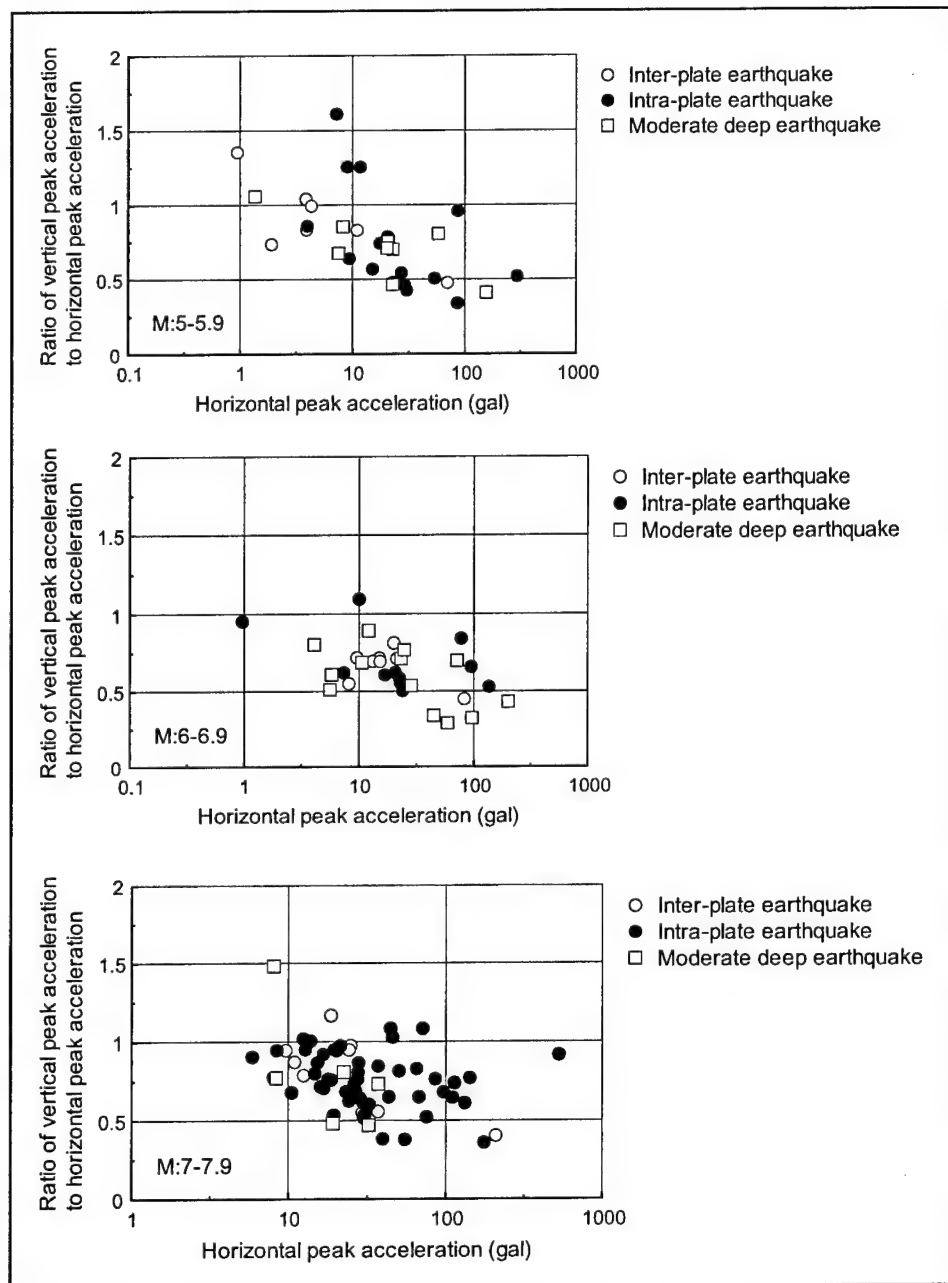


**Figure 7.** Relationship of horizontal peak acceleration and ratio of vertical acceleration to horizontal acceleration

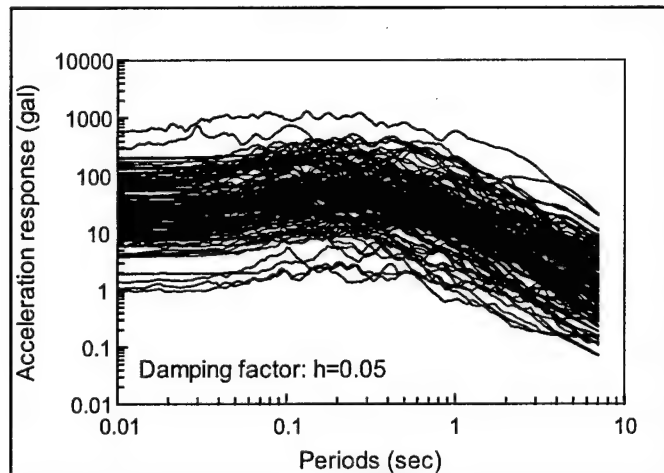


**Figure 8.** Acceleration response spectra (dam base, horizontal)

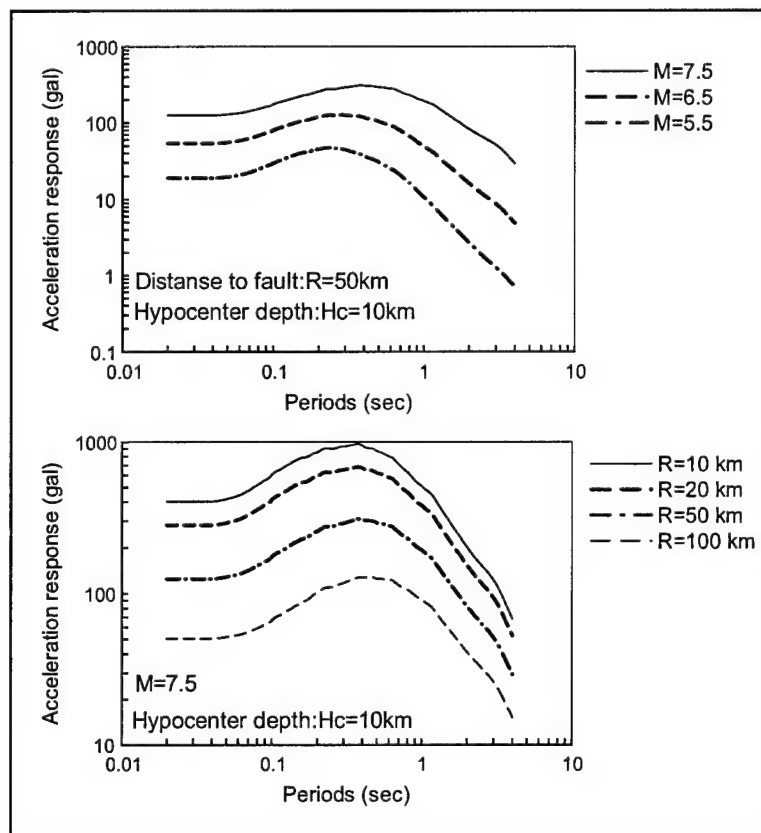


**Figure 9.** Presumed examples of acceleration responses on hard soil sites using equation proposed by An-naka et al. [5]

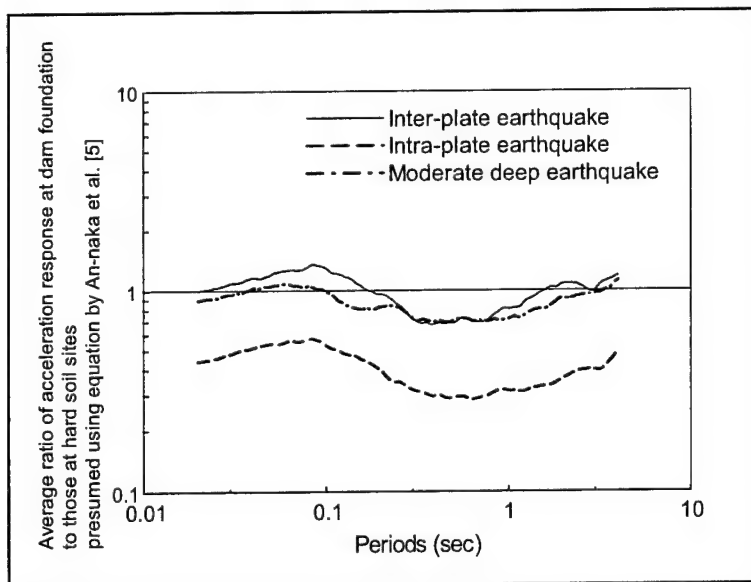


**Figure 10.** Ratio of acceleration response at dam foundation to those at hard soil sites for each earthquake type

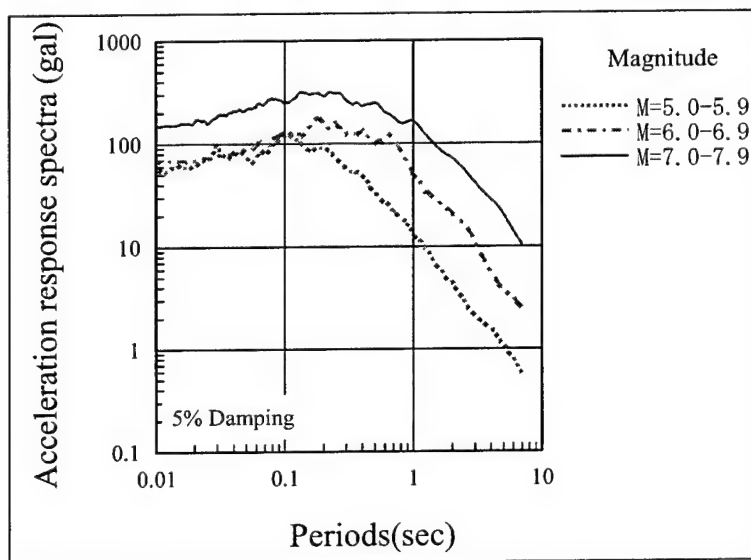


**Figure 11.** Average acceleration response spectra for different magnitude range (Intra-plate earthquake, distance to fault 0-40 km and hypocenter depth 0-20 km)

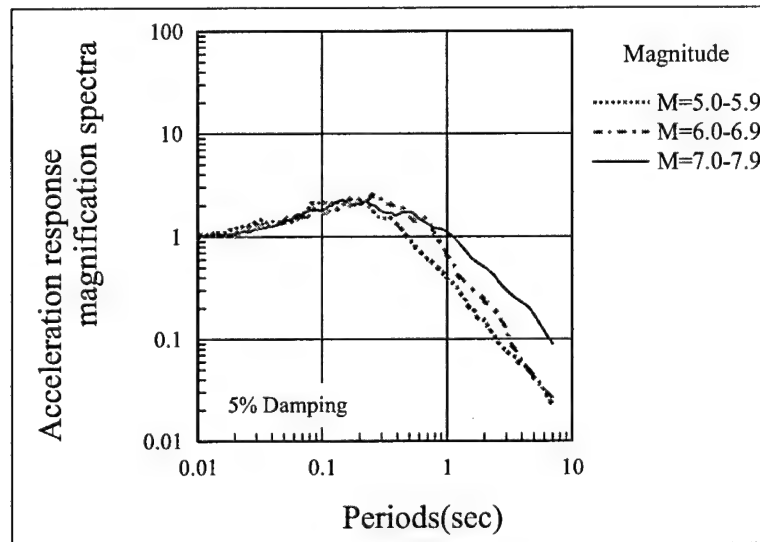


**Figure 12.** Acceleration response magnification spectra for different magnitude range (Intra-plate earthquake, distance to fault 0-40 km and hypocenter depth 0-20 km)

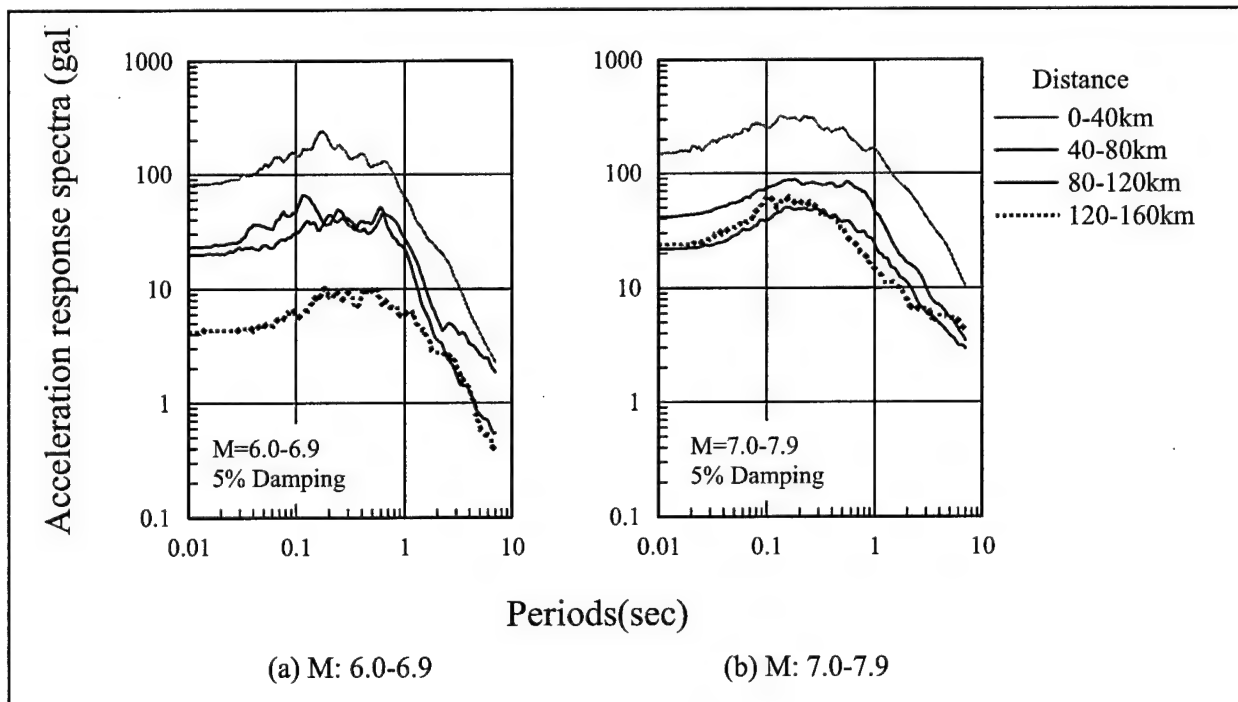


**Figure 13.** Average acceleration response spectra for different distance from fault (Intra-plate earthquake, hypocenter depth 0-40 km)

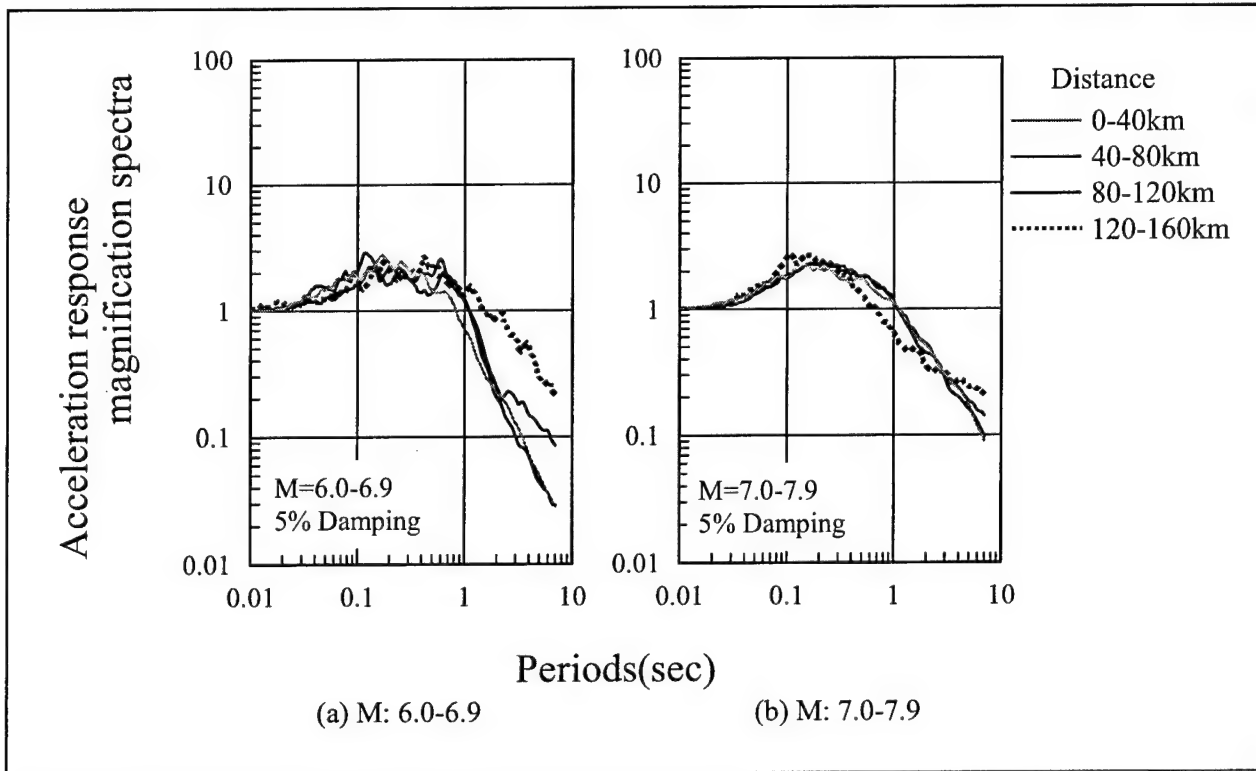


**Figure 14.** Acceleration response magnification spectra for different distance from fault (Intra-plate earthquake, hypocenter depth 0-40 km)

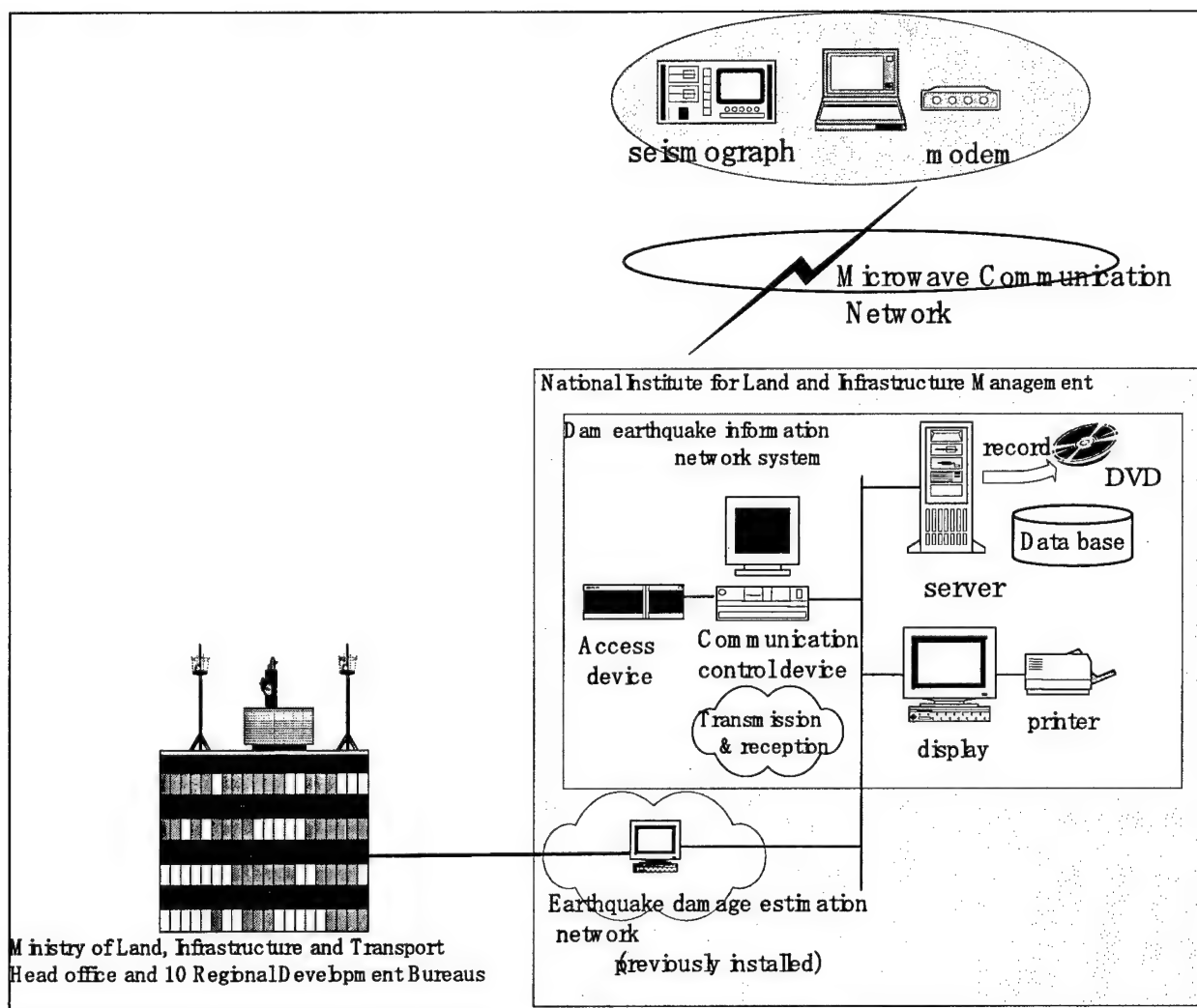


**Figure 15.** System configuration of the real-time dam seismograph network system

This page intentionally left blank.



## Seismic Hazard Analysis and Selection of Design Earthquake for a Dam in Kansas

by

Paul Somerville,<sup>1</sup> F. C. Walberg,<sup>2</sup> and Vlad Perlea<sup>2</sup>

### ABSTRACT

The sparsity of data and uncertainties in the available data make it difficult to resolve uncertainties in the seismic hazard at locations in Central United States. Under these conditions, the simple approach to seismic source characterization used by the USGS, which is to spatially smooth historical seismicity, has the advantages of being objective and avoiding reliance on uncertain assumptions. However, it suffers from the disadvantage of not including geological and tectonic models and data from the site region. Given these circumstances, the most robust approach to estimating seismic hazard was to use multiple source models in the logic tree framework, using professional judgment to assign weights to the likelihood that each alternative model represent the actual state of nature.

**KEYWORDS:** Seismic hazard, design earthquake, embankment dam.

### 1 INTRODUCTION

The seismic hazard at sites in the Midwestern United States is difficult to assess, primarily because of the lack of information on the occurrence of seismic events over a reasonably long period of time and uncertainty over causative faults. Studies that average historical seismicity data over large areas to generate seismic maps do not include important local and regional geological and tectonic features that pertain to a critical structure that is located close to a local source zone. This is the case for the seismic evaluation of a dam in Kansas that is located

within a few miles of the potentially active Humboldt fault.

### 2 SEISMIC DAM SAFETY APPROACH

In accordance with U.S. Army Corps of Engineers guidance, two approaches have to be used for conducting site-specific seismic hazard analyses:

*a.* Deterministic Seismic Hazard Analysis (DSHA) to establish the MCE (Maximum Credible Earthquake) and the MDE (Maximum Design Earthquake) for critical structures and an upper bound for the MDE for non-critical structures. For critical embankment dams the MDE is the same as the MCE. The MCE is defined as the largest earthquake that could reasonably be expected to occur along a recognized fault or within a particular seismic source.

*b.* Probabilistic Seismic Hazard Analysis (PSHA) to establish the Operating Basis Earthquake (OBE) and a lower bound of the MDE for non-critical structures. The OBE is, by definition, the level of ground motion for which there is little or no damage and no interruption of function. The OBE is an earthquake that can reasonably be expected to occur within the service life of the project. For hydraulic structures the service life is normally taken as 100 years; assuming a 50 percent probability of exceedance in 100 years results in a 144-year return period for the OBE.

In accordance with the Corps of Engineers guidance, the design earthquake ground motions for

<sup>1</sup> URS Group, Inc., Pasadena, CA (USA).

<sup>2</sup> U.S. Army Corps of Engineers, Kansas City District, MO 64106 (USA).

the seismic analysis of a high hazard embankment dam should be the 84<sup>th</sup>-percentile (mean + sigma) of the deterministic MCE. Under this very conservative but possible seismic loading the embankment dam may deform significantly but should remain functional for an extended period of time (until repairs are made or the lake is lowered sufficiently to prevent uncontrolled reservoir releases). The deformation must not result in an uncontrolled loss of pool.

### 3 STRONG EARTHQUAKE HISTORY OF NORTH-EASTERN KANSAS

The earliest, and possibly the strongest, earthquake reported within Kansas' borders occurred April 24, 1867. Several persons were injured, though not seriously. Plaster cracked, objects were thrown from shelves, and doors and windows were shaken at Lawrence. The earthquake was felt strongly at Manhattan, where stones loosened on buildings and walls cracked. A heavy wave, about 2 ft (30 cm) high, was observed on the Kansas River at Manhattan. The tremor was felt over an area of 300,000 square miles (777,000 km<sup>2</sup>) in Kansas, Missouri, Nebraska, Arkansas, Illinois, Indiana, Kentucky, and possibly Ohio (USGS, 1972). In addition, sand boils were reported at a location approximately 5 km to the south of Wamego (Stover and Coffman, 1993). Chapman (1997) estimated for this event a moment magnitude of  $M = 5.6 \pm 0.23$ , based on all available information on isoseismal area, total felt area, and maximum intensity, by means of recently developed regression models relating these parameters to seismic moment. The estimated maximum intensity, at the epicenter, was Modified Mercalli (MMI) VII.

On January 7, 1906, a strong earthquake affected an area of about 10,000 square miles (26,000 km<sup>2</sup>) in Kansas, Missouri, and Nebraska. Chimneys were thrown down and some cracks in walls were observed in Manhattan (intensity VII). Houses and buildings vibrated in Topeka, where a loud roaring sound was heard. Some towns reported feeling two or

three shocks. A series of small aftershocks of the January 7 earthquake was felt in Manhattan, the last being reported on January 23.

Four earthquakes – two on September 23, 1929, and one each on October 21 and December 7, 1929 – were reported to occur in northeastern Kansas. Houses shook over a broad area around Manhattan during the September events. The total affected area covered approximately 15,000 square miles (39,000 km<sup>2</sup>) during the strongest September event. The maximum reported intensity of all these earthquakes was V.

Although earthquakes occur along the entire Humboldt fault zone in Kansas, there appears to be greater seismic activity near Manhattan/Wamego.

### 4 DSHA APPROACH

#### 4.1 Seismic zones affecting the site

The Kansas City District (KCD) selected a panel of seismologists (Martin Chapman from Virginia Polytechnic Institute and State University, Don Steeples from University of Kansas, and Ellis Krinitzsky from Waterways Experiment Station in Vicksburg, Mississippi) to consider all known geologic features and seismic activity (including micro-earthquake records) and to define seismic zones in the region. Of these zones, the closest to the dam site are shown in Figure 1.

The defined zones were:

*a.* Humboldt Zone (HUM). The largest historical earthquake near the site, the magnitude 5.1 event of 1867 (lowest estimate of the magnitude, based on felt area, Stover and Coffman, 1993) occurred within this zone. Its western boundary lies about 20 km (12 miles) east of the site. Faults along the major Humboldt fault have segment lengths up to approximately 17 km (11 miles). The Humboldt zone was located to cover a narrow zone along the Humboldt fault extending north of the Chesapeake graben to include the recorded micro-earthquake activity.

*b.* Nemaha Zone (NEM), which includes the dam site. The relatively smaller historical seismic events of 1906 and 1929 apparently occurred within this zone. The Nemaha zone was located to include numerous faults within 40-50 km (25-31 miles) of the Humboldt fault and the pattern of micro-earthquakes 50-100 km (31-63 miles) wide that extend along the western flank of the Humboldt fault but north of the Chesapeake graben.

*c.* According to Steeples (1997) the uncertainty in the location of the 1867 and 1906 events is at least 20-25 km (12-16 miles). The mapped locations of these events are within about 10 km (6 miles) of the boundary between the Nemaha and Humboldt zones, indicating that the uncertainty in location of these events is such that they cannot be associated with the zones in which they lie with a high degree of confidence. Accordingly, a combined Nemaha-Humboldt seismic zone (NEM+HUM) was alternatively defined.

*d.* Mid-Continent Geophysical Anomaly Offset (MGA). Geologic and tectonic evidence indicate that a transform fault exists at the offset in the MGA in southeastern Nebraska and that reactivation has occurred since Precambrian. The area contains the intersections of the Humboldt and Thurman-Wilson faults with each other, a probable transform fault between, and a transform fault along the southeast side of the Kansas portion of the MGA. In addition, two MMI = VII, body-wave magnitude  $m_b = 4.7$  and five earthquakes have occurred in the zone (1935 and 1877, respectively).

*e.* Central Nebraska-Salina Basin Axis (CNS). The strongest earthquakes known to have occurred in this zone had a body-wave magnitude,  $m_b = 3.8$ .

*f.* Kansas-Nebraska Arches (KNA). The strongest known earthquake occurred in this zone in 1942 and had  $m_b = 4.2$ .

*g.* New Madrid Seismic Zone (NM). This is the most seismically active area of the eastern United States. This area includes the source of

the 1811-1812 earthquake events, estimated to have been in the range of moment magnitude  $M_w = 7.5$  to 8.2. The definition of this seismic zone was considered as presented in a Geomatrix (1997) report, with reference to a nearby site.

Probabilistic computations showed that the first two seismic zones or their combination dominate the seismic hazard at the dam site.

#### 4.2 Deterministic MCE

The panel of expert seismologists reached a consensus with reference to the MCE. Two scenarios were recommended for consideration, corresponding to the two significant seismic zones:

*a.* A moment magnitude 5.6 earthquake directly beneath the site; such an event was considered capable of occurring on relatively minor faults which could exist beneath (or very near) the site (Nemaha Zone).

*b.* A moment magnitude 6.6 earthquake at a horizontal distance of 20 km, associated with the Humboldt tectonic zone. This evaluation is based mainly on regression analysis and charts by Wells and Coppersmith (1994) showing that fault segments 17 km (11 miles) in length can produce earthquakes of moment magnitude  $M_w = 6.6$ .

The MCE associated with the other considered zones are: N+H,  $M_w = 6.6$ ; MGA,  $m_b = 5.5$ ; CNS,  $m_b = 5.5$ ; KNA,  $m_b = 5.5$ ; NM,  $m_b = 8.0$ . Although the last seismic zone (NM) is credited with the highest capable magnitude of all considered seismic sources, it is located more than 500 km (300 miles) from the dam site and has little influence on the seismic hazard at the site.

The focal depth of 10 km is characteristic for seismic events in the Midwest and was used with all estimates of MCE.

The duration of these seismic events was evaluated using the Atkinson and Boore (1997) model: 2 sec for the "M = 5.6 @ 1 km" event

and 10 sec for the "M = 6.6 @ 20 km" event. It was considered that "M = 6.6 @ 20 km" was a more critical definition of MCE than "M = 5.6 @ 1 km." The M = 5.6 event would generate somewhat higher peak ground accelerations and spectral accelerations at low periods, smaller than about 0.4 sec. Although these values are of some interest for structures, the duration of the event is an added consideration for evaluation of liquefaction potential. The M = 5.6 event has a very short duration of shaking compared to the M = 6.6 event. The longer duration is a significant factor in the seismic analysis of the dam (which is controlled by the liquefaction of the foundation soil). Therefore, the "M = 6.6 @ 20 km" was the preferred definition of the MCE.

### 4.3 Site natural period

A preliminary evaluation of the natural (fundamental) period of a uniform soil can be obtained from:

$$T = 4D / V_s \quad (1)$$

where:

- T = natural period, in seconds
- D = depth of soil/fill column, in meters
- $V_s$  = weighted average of shear wave velocity in the column (m/s)

Another approximate method used to evaluate the natural period of the dam-foundation soil system was to apply the one-dimensional model SHAKE (Schnabel et al., 1972). In comparison with the simple formula, SHAKE has the advantage of considering the actual stratification and wave velocities of various layers. The evaluation of the natural period of soil columns representative for the embankment dam, using both the simple formula (1) and the program SHAKE, is presented in Figure 2 (x-s for the formula, open circles for SHAKE). The range of values for each representative location corresponds to the variability in the thickness of the soil deposit along the dam. It is evident that the simple

formula provided satisfactory results; the natural period is essentially directly proportional to the height of the soil column, including both the embankment fill and the overburden underneath. Taking into account the most vulnerable portions of the dam (slopes on both sides) the periods of major interest were determined to lie in the range of 0.3 to 0.6 sec.

### 4.4 MCE site-specific response spectra

The database of strong motion recordings in stable continental interiors is too sparse to permit the development of empirical attenuation relationships based purely on recorded data. This necessitates the use of seismologically based methods to generate ground motion attenuation relations. We used two such ground motion models that are considered appropriate for predicting ground motions and response spectra in central United States:

- a. The Atkinson and Boore (1997) relationships, which were based on data derived mostly from earthquakes in southeastern Canada and the northeastern United States. Their authors recommend them for use in eastern North America.
- b. The Toro, Abrahamson, and Schneider (1997) relationships, which were developed for the crustal velocity structure of some central states (Wisconsin, Illinois, Indiana, and western Kentucky) and were found by their authors directly applicable to most eastern and central states, including Kansas.

The Toro et al. (1997) model is based on a single corner frequency, and the Atkinson and Boore (1997) model is based on two corner frequencies.

The response spectra for the two main definitions of the MCE are presented in Figure 3. The Atkinson-Boore model provided higher estimates than the Toro-Abrahamson-Schneider model for the peak ground acceleration at rock outcrop (PGA, equal to the spectral acceleration for zero period, 0.37 g as compared with 0.28 g). The model of Toro et al. produces higher estimates of spectral response for periods of major

interest (0.3 to 0.6 sec). It was recommended by Professor Martin Chapman to use the Toro et al. (1997) relationships for the site, as most appropriate for Kansas and hard rock conditions. The "mean plus one standard deviation" relationship recommended by Toro et al. is also included in Figure 3 (with PGA = 0.56 g).

#### 4.5 Selection of acceleration time-history

The dynamic analysis of the dam required development of acceleration time-histories of rock motions consistent with the design response spectrum. In accordance with the Corps of Engineers regulation, a high hazard dam should be evaluated for the 84-percentile MCE response spectrum. In the western United States the usual procedure involves scaling a record to the "mean + 1 $\sigma$ " PGA; however, for the Midwest no actual recordings of a strong earthquake are available and careful attention is required when records from dissimilar rock sites must be considered. Accordingly, effort was directed towards ensuring that the selected time histories contained frequencies at the natural period for the site.

Although no strong motion recording of a large earthquake in the Central United States is available, the modification of an existing record by scaling, without spectral modification, is considered more appropriate than developing a synthetic accelerogram. Although a good match with the target spectrum cannot be obtained by limiting the record modification to scaling only, the advantage is to preserve the characteristics of a "real" event.

The following four criteria were used in the first stage of selection of available records that could be used for the site specific time-history:

- a. Moment magnitude: 5.2 to 6.9 (to bracket the MCE values of 5.6 and 6.6).
- b. Epicentral distance: less than 30 km (MCE was defined by earthquakes at 20 km or less).
- c. Focal depth: less than 15 km (the depth of the MCE was postulated at 10 km).

d. Hard (rock) site (time history to be used as outcrop input motion in SHAKE or other two-dimensional models).

Thirty-nine records were identified to meet these requirements: 25 from California, 8 from Canada, 2 from China, 2 from Mexico, 1 from Montana and 1 from El Salvador.

Absolute acceleration spectra for 5 percent damping ratio were computed for each of the 39 available records, using the program WESHAK (Sykora et al., 1992). Scaling factors were determined for best fit with the 84-percentile design spectrum in the period range of interest (assumed 0.3 to 0.6 sec). In the second stage of selection of earthquake records the following restrictive criteria were considered:

- a. The scaling factor should be as close to 1.0 as possible but at least in the range 0.5 to 2.0.
- b. Ensure the selected time history had significant frequency content in the periods of major interest.
- c. The scale factor should be chosen so that the response spectra closely matches the design spectra for "mean + 1 $\sigma$ ", rather than scaled to the PGA "mean + 1 $\sigma$ ". The scaled PGA should be in the range "mean MCE PGA" to "mean + 1 $\sigma$  MCE PGA", i.e.  $0.275g < PGA < 0.561g$ .
- d. The 0.05 g bracketed duration of the scaled acceleration time history should be at least 10 sec.

Based on these criteria most of the records were eliminated. Six records met the restrictive requirements: two components each of the earthquake records listed in Table 1. The Nahanni record, from rock most comparable to the Midwest rock conditions, contains predominantly low period motions, which were not judged to be appropriate for the site.

These three accelerograms were evaluated with the one-dimensional response analysis modeled

by the WESHAKE code to determine the time history inducing the highest shear stress in the foundation of the dam. The evaluation was performed at 25 locations uniformly distributed throughout the limits of the dam (5 each along the upstream toe, mid-upstream slope, crest, mid-downstream slope, and downstream toe). The San Fernando, Castaic, N69W record induced the highest maximum shear strength in 20 cases and the second highest in the remaining 5. A preliminary deformation analysis with the Dynaflo code (performed by Dr. Radu Popescu, C-CORE, Canada) using the three records found that that one was the most critical in all of the analyses. This scaled record was therefore selected for further evaluation. The comparison of the response spectrum generated by the scaled record with the target spectra is shown in Figure 4. The scaled PGA ( $0.271 \text{ g} \times 1.107 = 0.3 \text{ g}$ ) is slightly higher than the mean PGA.

## 5 PSHA APPROACH

The main purpose of the probabilistic approach is to determine equal hazard spectra, i.e., spectra that have an equal probability of being exceeded at each period of vibration. By comparing deterministic with probabilistic spectra, an indication of the deterministic design earthquake return period is obtained. It is, however, noted that due to their different definitions, the deterministic and the probabilistic spectra have different shapes and can not be interchanged: the deterministic spectrum corresponds to a well-determined source at a specified distance from the site of interest and the probabilistic spectra represents the aggregate effect of all seismic sources.

The PSHA approach, through deaggregation of the seismic hazard, indicates the contribution of various sources to the overall seismic hazard and, consequently, can be used in the selection of the design earthquake.

PSHA takes the elements of the deterministic assessment of earthquake hazard (seismic source specifications and site conditions) and adds the

assessment of the likelihood that ground shaking will occur during a specified time period. Because of the scarcity of earthquakes in the Central United States, there are not well-defined seismic source zones and their maximum earthquake magnitude and rate of earthquake occurrence are subject to interpretation. The selected extent of seismic zones and the frequency of occurrence of earthquakes within them have a major impact on the results of PSHA.

### 5.1 Evaluation of Seismic Hazard Based on the USGS National Seismic Hazard Maps

The U.S. Geological Survey publishes probabilistic seismic hazard maps, and the probabilistic ground motion values can be obtained directly for a given location, described by the zip code: (<http://geohazards.cr.usgs.gov/eq/> "Hazard by Zip Code"). For the studied site the values listed in Table 2 are provided.

It is evident that the USGS approach, which does not recognize the concentration of some known events near the site within a small seismic zone, provides relatively low seismic hazard at the dam site. Although all known seismic events were considered in the derivation of the seismic maps, the contribution of significant events located near the dam site was spread over a large zone, resulting in "smoothing" of the maps and a lowering of the seismic hazard.

Deaggregation of the seismic hazard for some Midwest cities (among them Kansas City, Wichita, and Omaha) is also available from the USGS web site. Although the major contribution to the hazard for PGA and short periods is due to local seismicity, the USGS determined that the hazard in the period range of interest for the dam is dominated by distant, large earthquakes in the New Madrid seismic zone.

### 5.2 Methodology used for PSHA at the dam site

For each seismic zone defined for the DSHA approach, the following three factors were determined:



- a. The mean frequency per year of occurrence of each different magnitude level of earthquakes,
- b. The mean frequency per event of each possible source-to-site distance, and
- c. The mean frequency per event of each different level of ground motion from each possible magnitude-distance pair.

The PSHA code numerically integrates this information using probability theory to produce the annual frequency of exceedance of each different ground motion level for each ground motion period, i.e., seismic hazard curves that are used to construct an equal hazard response spectrum.

The response spectrum derived from the PSHA represents the aggregated contribution of a range of earthquake magnitudes occurring at various rates on each of several discrete faults or seismic source zones located at various distances from the site, and includes the effect of random variability in the ground motions for a given magnitude and distance. The response spectrum does not represent the ground motion from a single combination of magnitude and distance. However, the magnitude-distance combination that dominates the probabilistic hazard can be identified through deaggregation.

The uncertainty in ground motion level, which varies with magnitude, distance, and ground motion period, was implemented in the computer model in accordance with the Toro et al. (1997) model. The effect of uncertainty in input parameters (definition of seismic zones, their parameters, attenuation relationships) on the calculated hazard was represented using a logic tree approach.

### 5.3 Source zone definition

The same zones used for the DSHA approach were considered in the PSHA. The seismic zones as defined by the Kansas City District of the Corps of Engineers are summarized in Table 3.

The frequency of earthquake occurrence in each seismic zone was described by the "b" value in the cumulative recurrence curve given by:  $\log N = A - bm_b$ , where  $N$  = number of earthquakes with magnitude equal or smaller than  $m_b$  and  $m_b$  = earthquake magnitude. Three generally accepted values for Central United States were considered for  $b$ : 0.85, 0.92, and 1.00.

For the seismic zones characterized by an acceptable number of seismic events (this being the case for all seismic zones of interest except Nemaha and Humboldt) the preferred method was to determine first the parameter "a" of the incremental recurrence curve,  $N = a - bm_b$  and subsequently to calculate "A" using Perkins' formula:  $A = a - 0.5(b)(\Delta M) - \log(1 - 10^{-(b)(\Delta M)})$  using a least squares fit constrained to the given "b" value.

For the two most important zones, Nemaha and Humboldt, the maximum likelihood procedure (Weichert, 1980) was the preferred best fitting methodology, applied with the assistance of Dr. Martin Chapman. This methodology was applied to the combination of the two zones (N+H) where four seismic events with magnitude in excess of 4 were known. Subsequently, the parameter "A" was adjusted for the area of each source zone:  $N = 3295 \text{ km}^2$  and  $H = 1640 \text{ km}^2$ :

$$a. \text{ For Nemaha: } A_N = A_{N+H} + \log[N / (N + H)] = A_{N+H} - 0.18$$

$$b. \text{ For Humboldt: } A_H = A_{N+H} + \log[H / (N + H)] = A_{N+H} - 0.48$$

The results of these calculations are presented in Figures 5a, b, and c and Table 4.

A difficulty with the small source zones used in the KC District source model was that few earthquakes were associated with individual source zones, making it difficult to reliably estimate the seismicity rate. On behalf of the KC District, Dr. Martin Chapman used Weichert's (1980) maximum likelihood method to estimate the "A"

values of the combined Nemaha and Humboldt zones for a range of "b" values. For the maximum magnitude of the combined zones, equal weights were given to magnitudes of 5.6, 6.1, and 6.6 within the logic tree. To estimate the seismicity of the separate Nemaha and Humboldt zones, the "A" value of the combined zone was partitioned between the Nemaha and Humboldt zones in proportion to their areas. This procedure was considered to be more reliable than using the small numbers of earthquakes in the individual zones to estimate the seismicity parameters. The maximum magnitudes of the Nemaha and Humboldt zones were estimated to be 5.6 and 6.6, respectively.

An alternate definition of seismic zones by Geomatrix Inc. (1997) for the same general area is:

- a. Nemaha Ridge (NEM)
- b. Southern Mid-Continent Geophysical Anomaly (SGA)
- c. Northern Mid-Continent Geophysical Anomaly (NGA)
- d. Oklahoma Aulacogen (OAG)
- e. Central Kansas Uplift (CKU)
- f. New Madrid Seismic Zone (NMSZ)
- g. West Background Zone (WBK)
- h. East Background Zone (EBK)

Figure 6, a and b, compares the Kansas City District, Corps of Engineers (KCD) model with the Geomatrix Inc. model. It is evident that the first model assumes smaller zones, where the known seismic events are more concentrated in the vicinity of the dam, but fewer events are available to define the parameters of the seismic zones.

A third definition of seismic source zones that was used is that in the National Seismic Hazard Maps, as described in Frankel et al. (1996). Except for the New Madrid Seismic Zone, the seismicity in the site region is characterized by a

grid of "a" values derived from the smoothed historical seismicity.

#### 5.4 Attenuation relationships

Two ground motion models that were used in the hazard calculations are based largely on the stochastic ground motion model. These models, which were described above, are:

- a. Toro et al. (1997), used also in the deterministic approach, and
- b. Atkinson and Boore (1997).

Both models are based on an assumed shear wave velocity at the surface of about 6,000 fps. Since the surface velocity at the site is less than this, an adjustment factor of 1.15 was applied to the ground motion estimates derived from the two models.

#### 5.5 Logic tree

In order to address the uncertainty in the selection of: (1) seismic source models and their parameters; (2) recurrence rate for each zone, including the "b" value; and (3) ground motion attenuation relations, the logic tree in Figure 7 was used to obtain a weighted average of the seismic hazard curves.

#### 5.6 PSHA results: equal hazard response spectra

The seismic hazard spectra obtained from the detailed source model are significantly higher than those obtained from the Geomatrix and USGS source models. This is because the detailed source model concentrates the historical seismicity into small source zones that are located close to the site, whereas the Geomatrix and USGS source models smooth the historical seismicity over broader regions.

The response spectra resulting from the logic tree weights are presented in Figure 8. The response spectra for three return periods (475-, 975-, and 2475-year) are based directly on weighted averages using the USGS results, which are only available for these three return



periods. The spectra for the other return periods were obtained by extrapolation, using the recommended procedure by CECW-ED (1996):

a. For any spectral acceleration ( $S_A$ ) a power curve in respect to return period ( $T_r$ ) is assumed:  $S_A = b (T_r)^m$ .

b. Two equations are solved simultaneously to obtain "m" and "log b":

$$\log S_{A(475)} = m \log 475 + \log b$$

$$\log S_{A(2475)} = m \log 2475 + \log b$$

c. This gives:

$$m = (\log S_{A(2475)} - \log S_{A(475)}) / (\log 2475 - \log 475)$$

$$\log b = \log S_{A(475)} \log 2475 / (\log 2475 - \log 475) - \log S_{A(2475)} \log 475 / (\log 2475 - \log 475)$$

### 5.7 PSHA results: deaggregation of seismic hazard

Deaggregation results for the weighted combination of all models shown in the logic tree are presented in Figures 9, a and b, for the 2,475-year average return period (ARP) for peak ground acceleration and spectral response at a period of 1 sec, respectively. It is evident that the hazard at the site is controlled by earthquakes in the magnitude range of 5.5 to 6.0 and the distance range of 0 to 20 km, reflecting earthquakes occurring in the Nemaha and Humboldt source zones. The deterministic MCE is a magnitude 6.6 earthquake occurring at a distance of 20 km; the predominant magnitude from the deaggregation of the hazard for the return period of 2,475-year consists of a smaller magnitude earthquake. However, a smaller magnitude earthquake (5.7) was determined to be capable of inducing liquefaction of sands in the foundation. This indicates a high probability of damage for this return period.

For comparison purposes, Figures 10, a and b, show the deaggregation for the same parameters as Figure 9, as published by the U.S. Geological Survey (Frankel et al. 1996) for Topeka, Kansas.

The contribution of distant earthquakes generated by the New Madrid Seismic Zone is much more important, especially for the 1.0 sec spectral period.

## 6. CONCLUSIONS

This paper presents a methodology for determining the seismic hazard at a dam site in Kansas. The methodology is considered to be appropriate for the present state of knowledge of a region where there are relatively few historical earthquakes.

The sparsity of data and uncertainties in the available data make it difficult to resolve uncertainties in the seismic hazard at locations in Central United States. Under these conditions, the simple approach to seismic source characterization used by the USGS, which is to spatially smooth historical seismicity, has the advantages of being objective and avoiding reliance on uncertain assumptions. However, it suffers from the disadvantage of not including geological and tectonic models and data from the site region. The more detailed source models developed by Geomatrix Inc. and Kansas City District of the Corps of Engineers have the advantage of making use of local and regional geological and tectonic data and models, but these are subject to a considerable degree of uncertainty. Given these circumstances, the most robust approach to estimating seismic hazard was to use multiple source models in the logic tree framework, using professional judgment to assign weights to the likelihood that each alternative model represents the actual state of nature.

## 7 REFERENCES

- Atkinson, G.M., 1993. "Source Spectra for Earthquakes in Eastern North America," *Bull. Seism. Soc. Am.* Vol. 83, 1778-1798.
- Atkinson, G.M. and D.M. Boore, 1997. "Some Comparisons Between Recent Ground-Motion Relations," *Seismological Research Letters*, Vol. 68, No. 1, Jan-Feb, 22-40.

- Boatwright, J. and G. Choy, 1992. "Acceleration Source Spectra Anticipated for Large Earthquakes in Eastern North America," *Bull. Seism. Soc. Am.*, Vol. 82, 660-682.
- CECW-ED, 1996. "Earthquake Design Guidance for Structures," Corps of Engineers publication dated 30 October 1996.
- Chapman, M. 1997. "Letter-Report on Maximum Credible Earthquake Magnitude, Location, and Ground Motion," dated July 20, 1997 (unpublished).
- Frankel, A., C. Mueller, T. Barnhard, D. Perkins, E.V. Leyendecker, N. Dickman, S. Hanson, and M. Hooper, 1996. "Documentation," *National Seismic Hazard Maps*.
- Geomatrix, 1997. "Geologic Evaluation of Fort Riley, Kansas," (unpublished).
- Schnabel, P.B., J. Lysmer, and H.B. Seed, 1972, "SHAKE: A Computer Program for Earthquake Response Analysis of Horizontally Layered Sites," *Report No. EERC 72-12*, UC Berkeley, California.
- Steeple, D.W., 1997, "Letter-Report on Historical Earthquake Locations, Geologic Structure, and Micro-Earthquake Information," dated June 19, 1997 (unpublished).
- Stover, C.W. and J.L. Coffman, 1993, "Seismicity of the United States, 1568-1989 (Revised)," *U.S. Geological Survey Professional Paper 1527*, 418 p.
- Sycora, D.W., R.E. Wahl, and D.C. Wallace, 1992, "USACE Geotechnical Engineering Software: WESHAK for personal computers," IR GL-92-4, Report 1, U.S. Army Engineer Waterways Experiment Station, Vicksburg, MS.
- Toro, G.R., N.A. Abrahamson, and J.F. Schneider, 1997, "Model of Strong Ground Motions from Earthquakes in Central and Eastern North America: Best Estimates and Uncertainties," *Seismological Research Letters*, Vol. 68, No. 1, Jan-Feb, 41-57.
- USGS, 1972, "Earthquake History of Kansas," *Earthquake Information Bulletin*, Vol. 4, No. 6, November-December. Abridged in [http://neic.usgs.gov/neis/states/kansas/kansas\\_history.html](http://neic.usgs.gov/neis/states/kansas/kansas_history.html).
- Weichert, D.H., 1980, "Estimation of Earthquake Recurrence Parameters for Unequal Observation Periods for Different Magnitudes," *Bull. Seism. Soc. Am.* 70, 1337-1346.

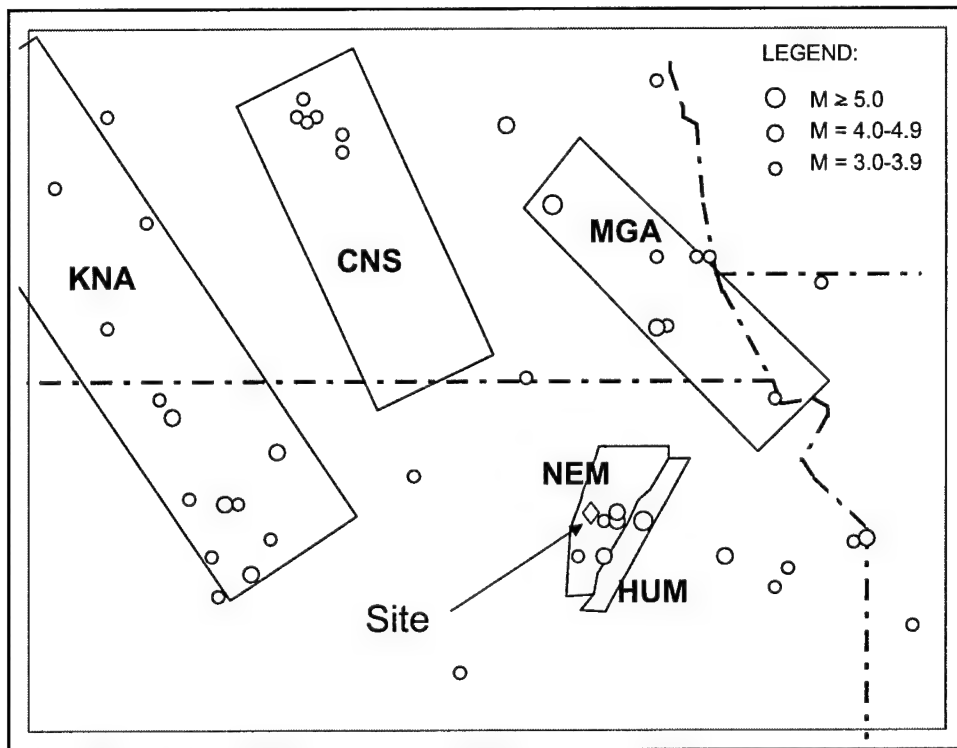


**Figure 1.** Seismic source zones in vicinity of the dam site

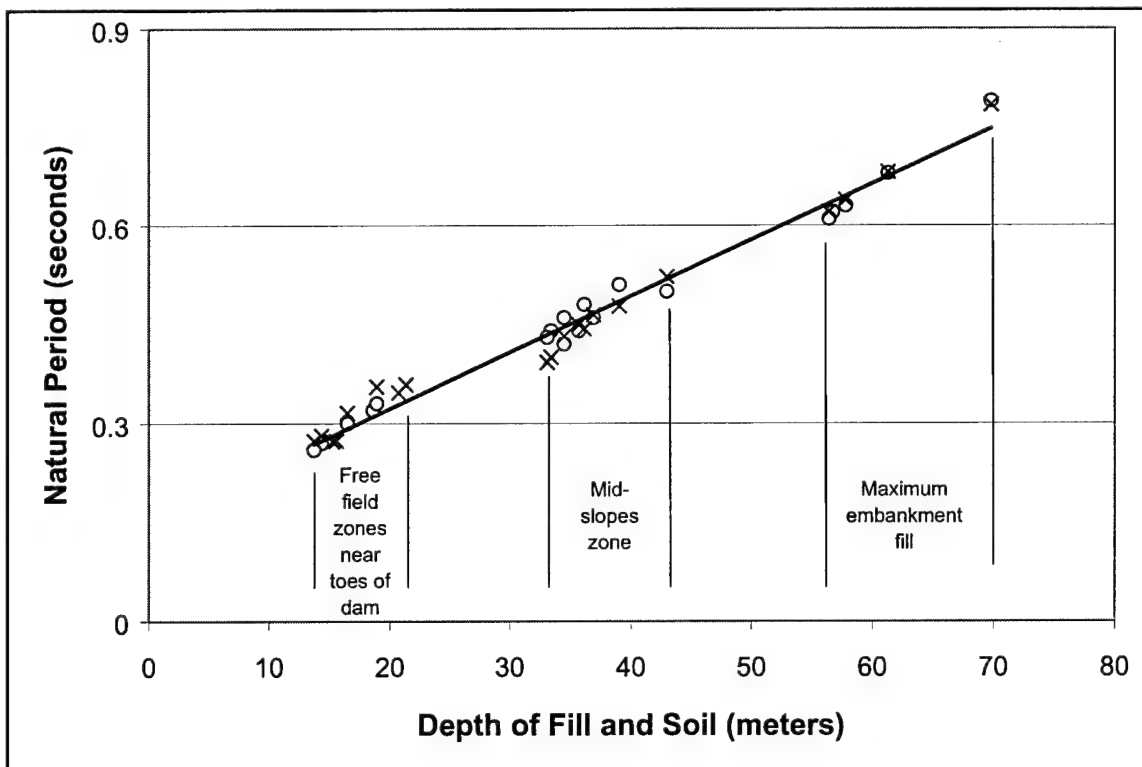


**Figure 2.** Natural period of soil columns (embankment and soil foundation)

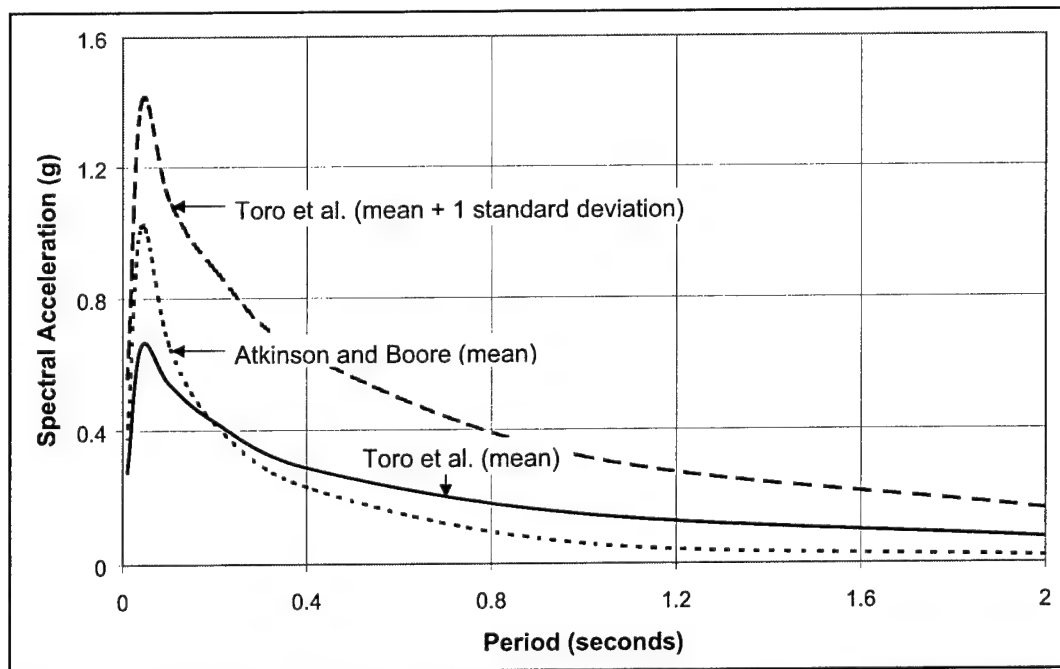


Figure 3. Comparison of MCE response spectra ( $M = 6.6$  at 20 km)

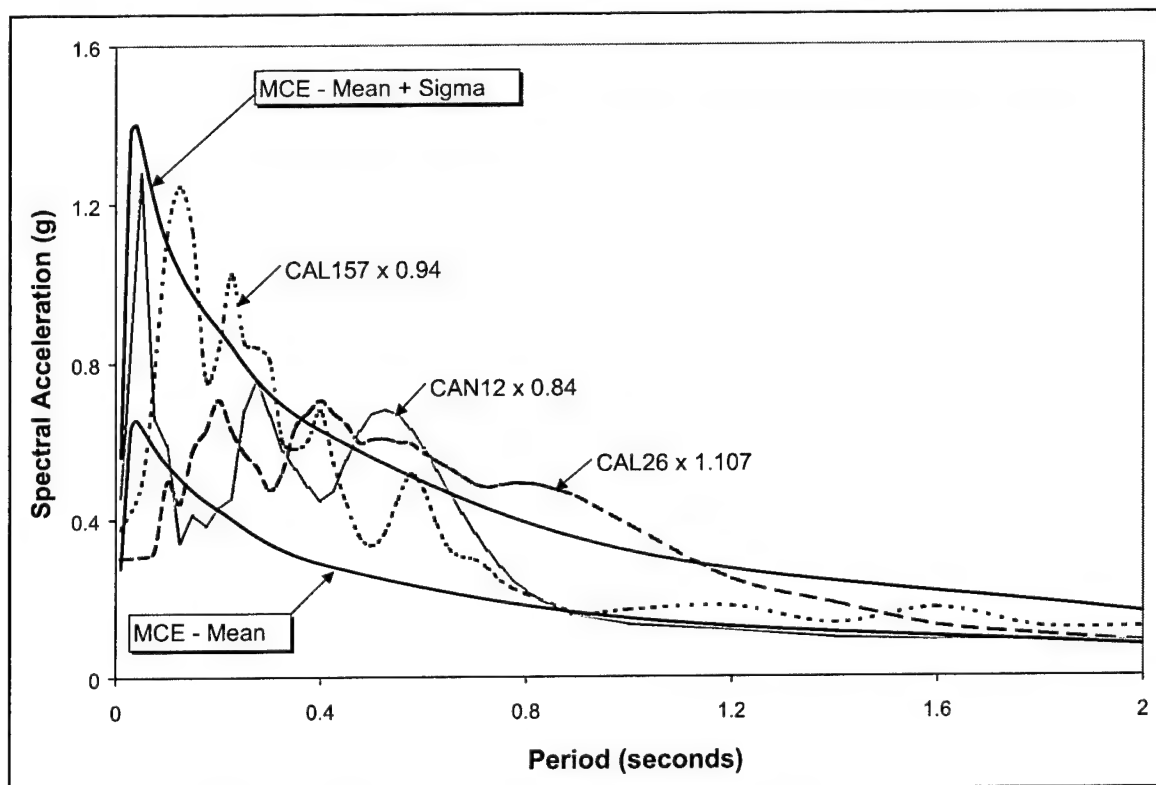
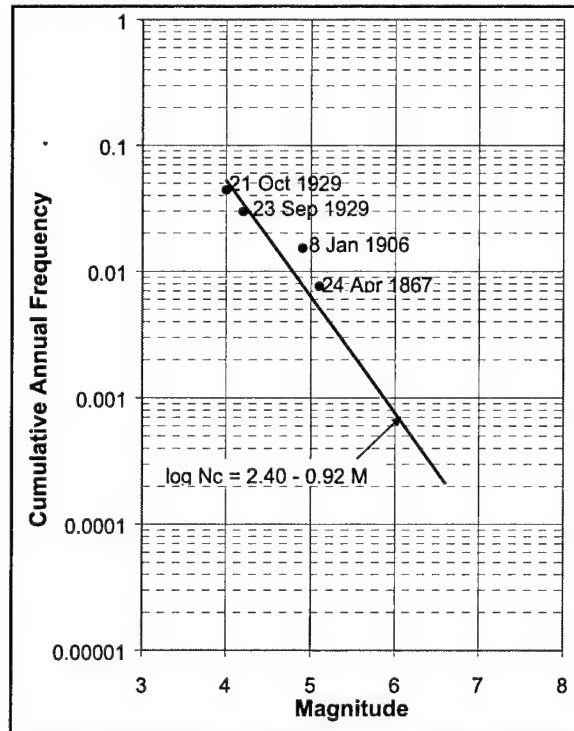
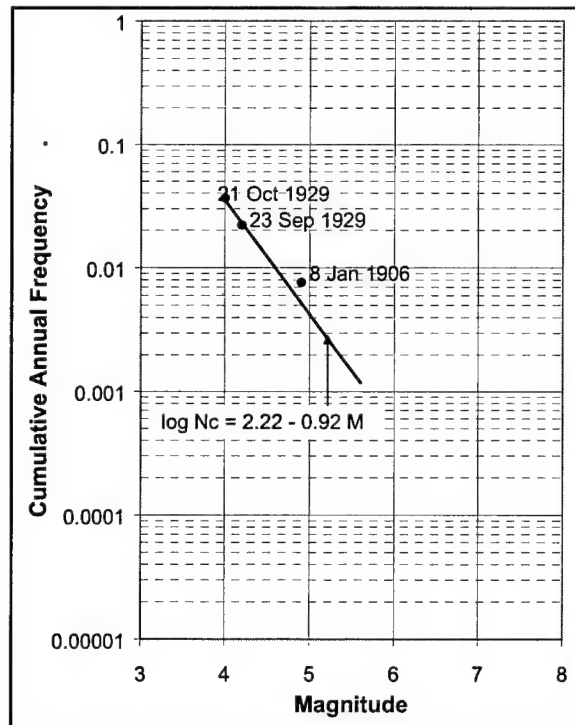


Figure 4. Comparison of design and scaled recorded response spectra



**Figure 5a.** Cumulative recurrence relationship for the combined N+H zone



**Figure 5b.** Cumulative recurrence relationship for NEM seismic source zone

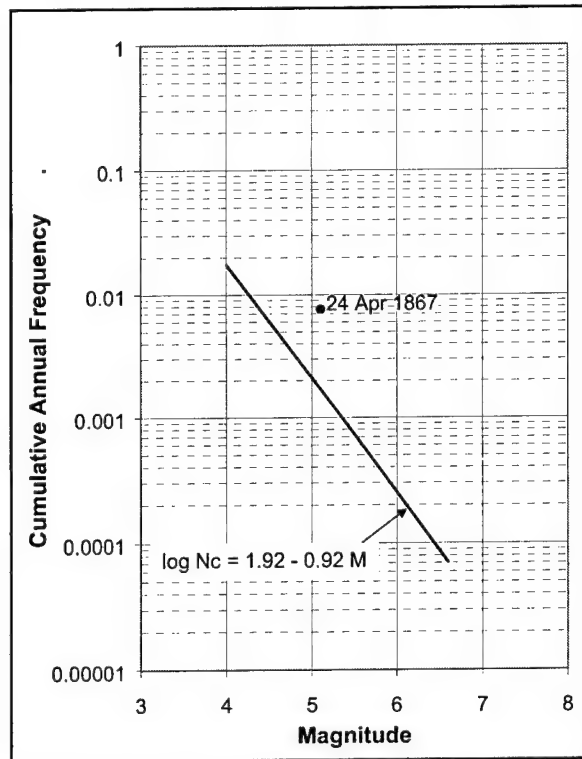


**Figure 5c.** Cumulative recurrence relationship for HUM seismic source zone

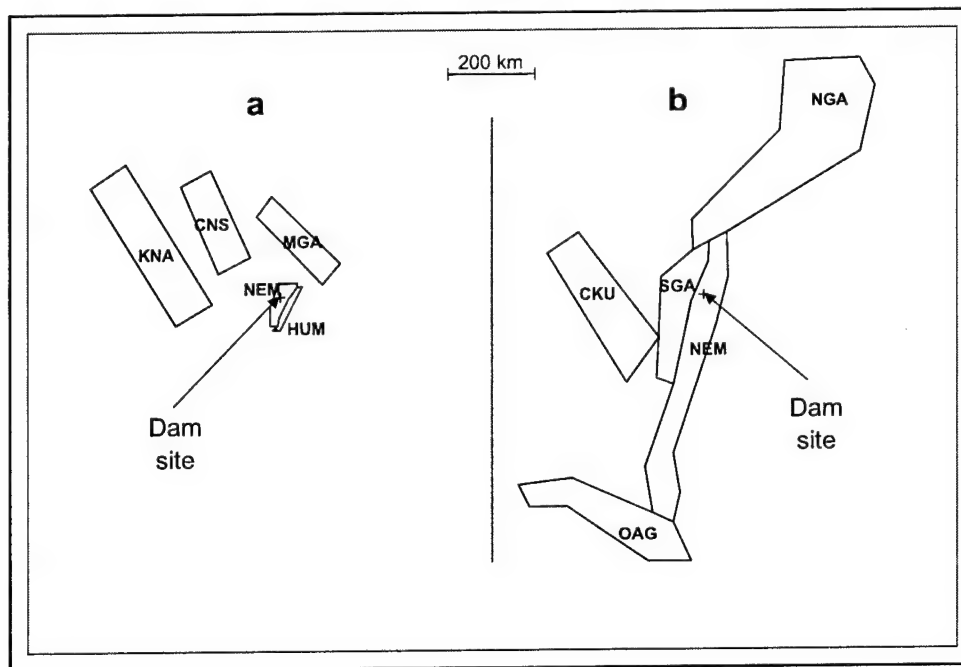


**Figure 6.** Seismic source zones considered by: (a) KCD; (b) Geomatrix

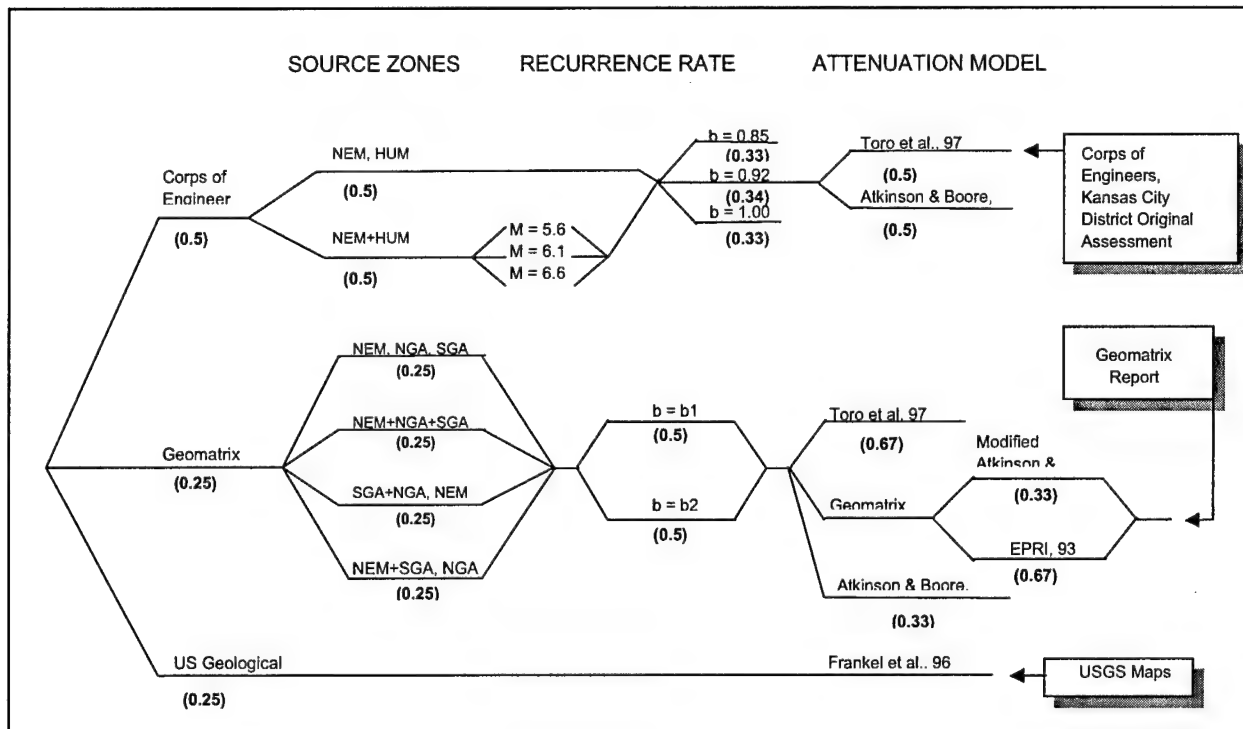


Figure 7. Logic tree

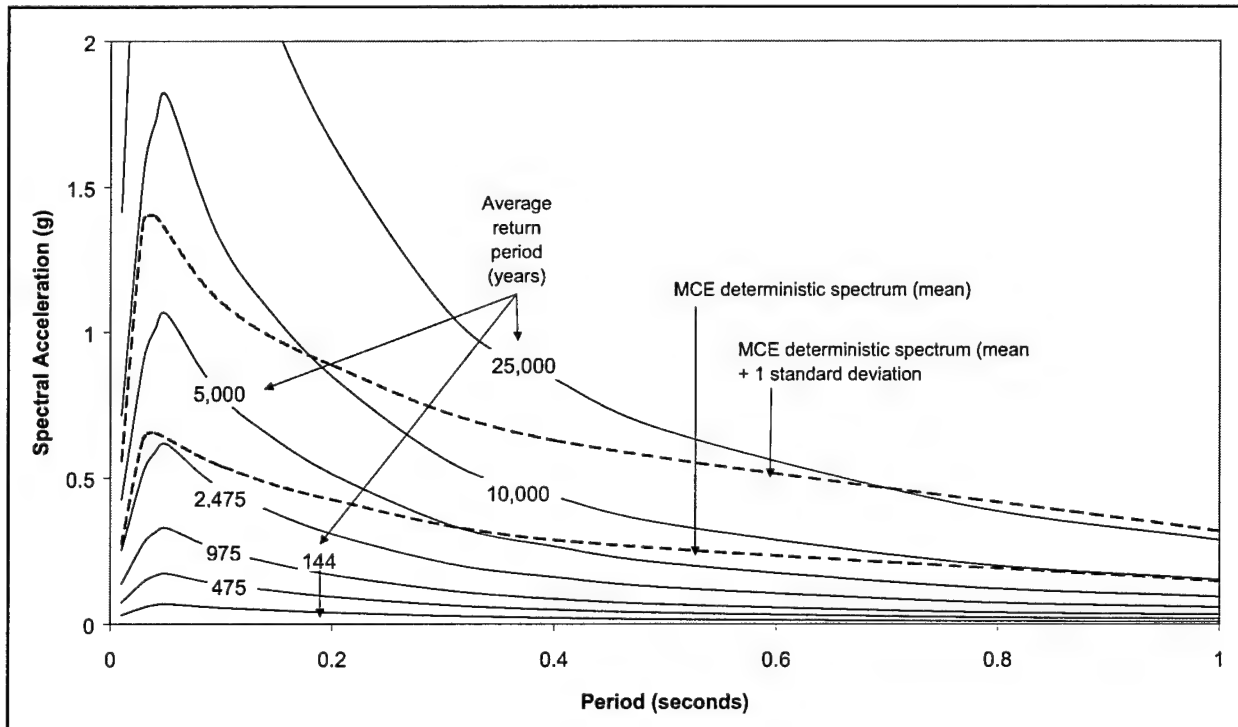
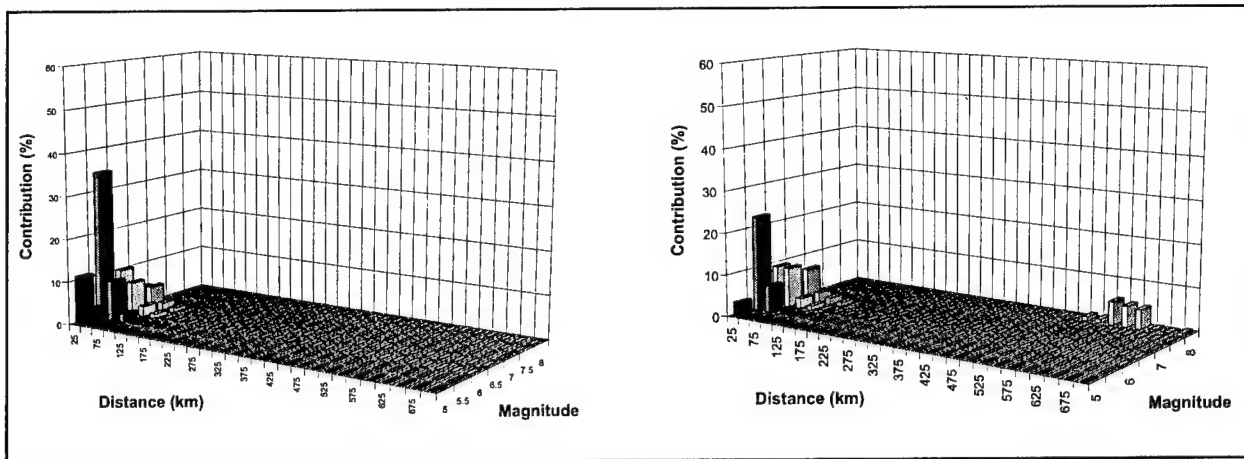
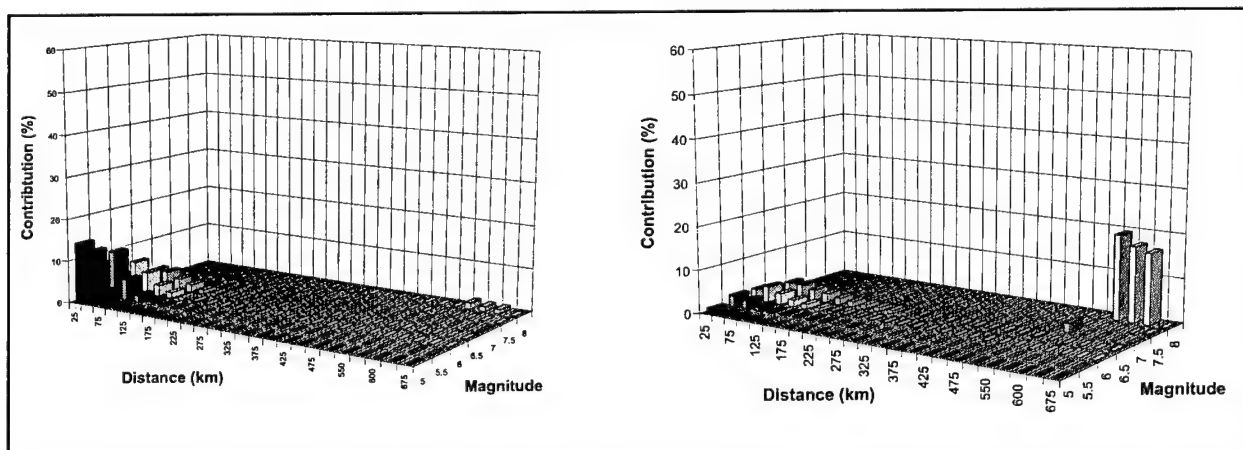


Figure 8. Weighted average response spectra



**Figure 9.** Seismic hazard deaggregation at the dam site for 2,475-year average return period. Left: for peak ground acceleration; Right: for 1.0 second spectral period



**Figure 10.** Seismic hazard deaggregation for 2,475-year average return period for Topeka, KS, by USGS. Left: for peak ground acceleration; Right: for 1.0 second spectral period



**Table 1.** Selected Acceleration Records

Earthquake	Date	Location/ Component (record)	M	Depth (km)	Epicentral Distance (km)	A <sub>max</sub> (g)	Duration (s)	Scaling Factor
San Fernando, California	02/09/71	Castaic N69W (CAL26 record)	6.5	14	29	0.271	18.5	1.107
		N21E (CAL25 record)				0.315	13.8	1.06
Nahanni, NWT Canada	12/23/85	Slide Mt., 240° (CAN12 record)	6.9	6	7	0.545	14.1	0.84
		330° (CAN11 record)				0.390	14.5	0.99
Mammoth Lake, California	05/25/80	Conv. Ck 180° (CAL157 record)	6.5	9	2	0.400	13.8	0.94
		90° (CAL158 record)				0.410	13.8	0.87

**Table 2.** Site Seismicity Based on USGS Maps/Zip Code Search

Seismic Parameter	Probability of Exceedance		
	10% in 50 years	5% in 50 years	2% in 50 years
Peak ground acceleration (PGA)	0.026 g	0.053 g	0.123 g
0.2 sec spectral acceleration	0.057 g	0.111 g	0.229 g
0.3 sec spectral acceleration	0.047 g	0.082 g	0.164 g
1.0 sec spectral acceleration	0.017 g	0.031 g	0.058 g

**Table 3. Known Seismic Events**

Source Zone	Abbreviation	Seismic Events			
		Date M / D / Y	Magnitude $m_b$	West Longitude	North Latitude
Nemaha	NEM	01/08/1906	4.9	96.5	39.2
		09/23/1929	4.2	96.6	39.0
		10/21/1929	4.0	96.5	39.2
		10/23/1929	3.2	96.8	39.0
		12/07/1929	3.6	96.6	39.2
Humboldt	HUM	04/24/1867	5.1	96.3	39.2
Mid-Continent Geophysical Anomaly Offset	MGA	04/28/1867	3.8	95.9	40.7
		12/09/1875	3.4	95.8	40.7
		11/15/1877	5.0	97.0	41.0
		03/18/1927	3.9	95.3	39.9
		03/01/1935	4.7	96.2	40.3
		06/06/1963	3.2	96.2	40.7
Central Nebraska- Salina Basin Axis	CNS	10/14/1927	3.8	98.9	41.6
		05/11/1934	3.8	98.8	41.5
		02/25/1955	3.8	98.6	41.3
		09/09/1966	3.5	98.6	41.4
		10/09/1981	3.3	98.87	41.47
		07/18/1990	3.0	98.95	41.5
Kansas- Nebraska Axis	KNA	14 events between 1879 and 1992 with magnitude in the range 3.0 to 4.2			
New Madrid	NMSZ	Numerous events with magnitude in the range 3.0 and 7.5			

**Table 4.**

Seismic Source Zone	“a” value of incremental recurrence			“A” value of cumulative recurrence		
	b = 0.85	b = 0.92	b = 1.00	b = 0.85	b = 0.92	b = 1.00
NEM		1.85		1.94	2.22	2.54
HUM		1.86		1.64	1.92	2.24
N+H		2.34		2.12	2.40	2.72
MGA	1.83*	2.13*	2.48*	1.59	1.85	2.15
CNS	2.31**	2.61**	2.95**	1.25	1.46	1.70
KNA	2.68**	2.98**	3.32**	1.62	1.83	2.07
NMSZ	b-value as determined by Geomatrix, Inc. (1997)					
Notes:	* ΔM = 0.8;    ** ΔM = 2.5.					

## Simulation of Strong Ground Motion at the Kasyo Dam Site During the 2000 Tottori Seibu Earthquake

by

Nobuteru Sato<sup>1</sup> and Fumio Yonezaki<sup>2</sup>

### ABSTRACT

The Water Resources Development Public Corporation (hereafter referred to as WARDEC) has been studying the simulation methods of strong ground motion at dam sites by taking into consideration the fault ruptures in order to evaluate dams' earthquake resisting capabilities. Seismic ground motion having the peak acceleration of  $531 \text{ cm/s}^2$  was observed at the Kasyo Dam Site (under the management of Tottori Prefecture) during the 2000 Tottori-ken Seibu Earthquake. To examine the appropriateness of the ground motion characteristics evaluation method and strong ground motion simulation method, the authors conducted the simulation analysis of the seismic waveform at the Kasyo Dam Site by using the hybrid method. As a result, it became clear that the simulated seismic waveform well agreed with the observed record. The appropriateness of the strong ground motion evaluation method was confirmed.

**KEYWORDS:** 2000 Tottori-Ken Seibu Earthquake, Kasyo Dam, Strong Ground Motion Simulation, Hybrid Method

### 1. INTRODUCTION

A very strong ground motion having the maximum intensity of VII occurred during the 2000 Hyogo-ken Nanbu Earthquake. The earthquake inflicted serious damage on many structures and caused a loss of more than 6,000 lives. Strong ground motion occurred in wide areas along the

source faults in the northern part of Awaji Island and Kobe City. From these phenomena, it became clear that the prediction of strong ground motion by taking into consideration widely distributed fault ruptures, but not a single source fault that used to be considered as a cause of an earthquake, would be necessary. The Japan Society of Civil Engineers suggested the adoption of Level 1 and Level 2 earthquake motion in the "Proposal on Earthquake Resistance for Civil Engineering Structures" and proposed the necessity of examining structures' earthquake resisting capabilities against the Level 1 and Level 2 earthquake motion [1]. No damage was inflicted on dams by the Southern Hyogo Earthquake [2]. But, WARDEC started a study on the simulation of strong seismic ground motion at dam sites based on fault models by taking into consideration the importance of the examination of the earthquake resisting capabilities of dams against strong ground motion near fault ruptures.

On October 6, the 2000 Tottori-Ken Seibu Earthquake occurred. Kasyo Dam is located very close to the source faults. Strong motion having the peak acceleration of  $531 \text{ cm/s}^2$  (horizontal direction) was observed in the lower inspection gallery of the dam [3]. This figure was the largest one ever observed at a dam foundation in Japan. This paper presents the appropriateness of the evaluation method of seismic ground motion characteristics and the strong ground motion simulation method at dam site that are being studied at WARDEC.

<sup>1</sup> Senior Research Engineer, Fill Dam Division, Research Institute, Water Resources Development Public Corporation, 936 Jinde, Saitama City, Saitama Pref., 338-0812, JAPAN.

<sup>2</sup> Chief, Fill Dam Division, Research Institute, Water Resources Development Public Corporation, 936 Jinde, Saitama City, Saitama Pref., 338-0812, JAPAN.

## 2 2000 Tottori-Ken Seibu Earthquake and Kasyo Dam

The Tottori-Ken Seibu Earthquake occurred at 13:30 on October 6, 2000. Its epicenter was located in a mountainous region in the western Tottori Prefecture as shown in Figure 1. Its magnitude was 7.3. Hino Observation Station located near the epicenter observed the peak acceleration of 927 Gal on the ground surface layer [4].

The earthquake caused no death tolls but 141 were wounded and 393 houses were destroyed. Although the ground motion was strong, damage was relatively small [5].

The epicenter of the earthquake was close to Kasyo Dam. The dam is a 46.4 m tall concrete gravity dam as shown in Figure 2. A strong ground motion having the peak acceleration of  $531 \text{ cm/s}^2$  was observed by the seismograph installed in the lower inspection gallery of the dam. The seismograph on the dam crest observed the peak acceleration of  $2,051 \text{ cm/s}^2$  [6]. The earthquake caused cracks in the concrete walls of the auxiliary gate room, but the dam's mechanical functions were not damaged [6].

The relationship between the peak acceleration observed in the dam foundation during the Tottori-Ken Seibu Earthquake and the distance from the source fault is shown in Figure 3 [6].

The epicenter of the earthquake was only several hundred meters from the Kasyo Dam. Thus, it is believed that the tremendously strong ground motion having the peak acceleration of  $531 \text{ cm/s}^2$  was observed in the inspection gallery.

## 3 Analysis Method

In order to learn whether or not WARDEC's strong ground motion simulation method is applicable to the strong ground motion observed at the Kasyo Dam Site, the authors tried to simulate the strong ground motion.

The strong ground motion simulation at the Kasyo Dam Site was made by using the hybrid method [7,8]. The procedures of the hybrid method are as shown by the flowchart in Figure 4.

Each simulation process can be outlined as follows: If a record of seismic ground motion observed during a small or medium-sized earthquake having its hypocenter in a concerned fault is available, ground motion to be caused by a large earthquake may be simulated by using the empirical Green's function method [9,10]. The idea is based on an assumption that there is the scaling law between ground motion caused by observed small earthquake and ground motion to be caused by an expected large earthquake.

As shown in Figure 5, this analysis method divides a source fault into the meshes of small faults. By rupturing small faults, small earthquakes can be created as same as the occurrence process of a large earthquake. By superimposing the small earthquakes at a concerned dam site, a large earthquake can be synthesized. However, there would be no chance to observe ground motion caused by an earthquake having its hypocenter in a concerned fault. In this case, ground motion to be caused by a small earthquake having its hypocenter in a concerned fault can be synthesized by the stochastic Green's function method [11]. By superimposing the ground motion as the same method as used by the empirical Green's function method, ground motion to be caused by a large earthquake can be synthesized by the stochastic Green's function method [12].

Small ground motion in a short period range should be synthesized by the above-mentioned stochastic Green's function method. Small ground motion in a long period range having the period of longer than 1 sec should be synthesized by the theoretical method that takes into consideration the underground structure. In other words, the theoretical analysis for horizontal multi-layers [13] should be used. By superimposing the obtained small ground motion having a short period and a long period

respectively as the same method as used by the empirical Green's method, strong ground motion having a short period and a long period should be separately obtained. By superimposing the strong ground motion having a short period and a long period on a time scale, a strong ground motion can be synthesized.

#### 4 Ground Motion Characteristics to be Used for Analysis

##### 4.1 Source model

Several fault rupture models are proposed for the Tottori-Ken Seibu Earthquakes in 2000. By taking into account the frequencies in a wide range, including the high-frequency range, the authors used the Ikeda et al.'s model for superimposing the empirical Green's functions [14]. The source fault location, the fault rupture model, and the fault rupture characteristics are as shown in Figure 6, Figure 7 and Table 1 respectively.

The shortest distance from Kasyo Dam to the source fault was only approximately 1 km. Parameters used for the ground motion analyses were as shown in Table 2.

Underground velocity structure to obtain long period ground motion was set up as shown in Table 3 by referring to Ito et al. [15].

##### 4.2 Path effects

It is believed that the  $Q$ -value, that indicates the attenuation factor of a ground motion propagation path, relates to the hypocenter depth and distance from a concerned location as well as to the area characteristics. Thus, it is desirable to evaluate the  $Q$ -value by using the earthquake record observed at a concerned location and by the spectrum inversion method [16]. However, in the Tottori-Ken Seibu area, seismic activities, except the Tottori-Ken Seibu Earthquake, are not so frequent and there is no sufficient data for the spectrum inversion analysis. Thus, it was decided upon to use characteristics shown by Equation (1) judging from the past study results. The characteristics were obtained by analyzing

earthquake records observed at Tokuyama Dam Site in Gifu Prefecture and the surrounding areas. The average source distance used for the analysis was approximately 22 km.

$$Q_s(f) = 28.4 \times f^{1.04} \quad (1)$$

#### 4.3 Site Amplification Effects

The site amplification effects at the Kasyo Dam Site were evaluated based on the record of the aftershock observed at the Dam Site by using the method proposed by Tsurugi et al. [17]. The amplification effects of the dam foundation rock for the seismological bedrock were obtained from 10 aftershock records. Observation locations are as shown in Figure 8. The site amplification effects of the horizontal direction ground motion caused by the aftershocks and their average values are shown in Figures 9 and 10 respectively. It is clear that the figures show 1.5 to 2 times of the amplification effects in the entire frequency range and that there are no conspicuous peak values.

WARDEC has been conducting earthquake observation at various existing dam sites and planned dam construction sites by using a velocity meter in order to learn the site amplification effects of the base rock. The average values of the observed site amplification effects are also shown in Figure 10. Rock at observation sites has  $V_s$  values in the range of 1.0 to 1.5 km/s indicating a strong rock at all the sites. Thus, it was decided upon to examine seismic ground motion that corresponds to the average amplification effects at these dam sites.

#### 5 Spectrum Characteristics of High Frequency Range

It is known that spectral characteristics in the high frequency range attenuates greater than the spectral characteristics that are ruled by the theoretical source spectrum ( $\omega^2$  law) in the frequency range higher than one called as a high cut-off frequency [18]. As shown in Figure 11 it can be seen that the record of the Tottori-Ken Seibu

Earthquake observed at the Kasyo Dam Site attenuated in the high frequency range higher than 5 to 6 Hz. On the other hand, the attenuation in the high frequency range of the after-shock record that was used for the evaluation of the site amplification effects was not so conspicuous as shown in Figure 12. In addition, as shown in Figure 10, the site amplification effects at the Kasyo Dam Site did not attenuate in the frequency range higher than 5 Hz when they are compared to the average site amplification effects at WARDEC's other dam sites. Thus, the site amplification effects obtained from after-shock records may not be used as is for the simulation site amplification effects because they may simulate too large figures of site amplification effects in the high frequency range.

Ikeda et al. (2000) corrected  $f_{\max}$  based on the concept on the hypocenter in the analysis of K-net and KiK-net waveform analysis of the Tottori-Ken Seibu Earthquake by using the empirical Green's function method [14]. Thus,  $f_{\max}$  for the analysis at the Kasyo Dam Site was corrected based on the same concept. For the case of the Kasyo Dam Site, it was analyzed by setting  $f_{\max} = 5.5$  Hz in the same way as Ikeda et al.

## 6 Results of the Strong Ground Motion Analysis

The high frequency ground motion was obtained by the stochastic Green's function method and the low frequency ground motion was obtained by the theoretical analysis for horizontal multi layers. By superimposing the obtained ground motions on the time scale having the frequency range of 0.8 to 1.0 Hz, the strong ground motion in the wide frequency range was synthesized. Two types of simulation waves of the site amplification effects at the Kasyo Dam Site and the average site amplification effects at WARDEC's various dam sites were obtained.

The peak acceleration ( $A_{\text{peak}}$ ), peak velocity ( $V_{\text{peak}}$ ) and the peak dislocation ( $D_{\text{peak}}$ ) of the

observation record and the simulated waves are as shown in Table 4.

### 6.1 A Case When the Site Amplification Effects at Kasyo Dam Site were Used:

As for EW components of the accselerogram shown in Figure 13, the peak acceleration of the observed record was  $531 \text{ cm/s}^2$  while that of the simulated result was  $552 \text{ cm/s}^2$ . On the other hand, the acceleration response spectrum of the observed record and the simulated waveform corresponded with each other as shown in Figure 14. The NS component of the simulated acceleration response spectrum relatively well corresponded with that of the observed record although it was relatively smaller than the latter value.

### 6.2 A Case When Average Site Amplification Effects were Used:

Both EW and NS components for the average site amplification effects at various dam sites were relatively smaller than those for the site amplification effects at the Kasyo Dam Site. As shown in Figure 10, the reason is considered to be that the former components varied more than 5 Hz compared to the latter components.

## 7. CONCLUSION

Strong ground motion was simulated for the earthquake record observed during the 2000 Tottori-Ken Seibu Earthquake at Kasyo Dam Site by using the hybrid method. As a result, the simulated strong ground motion well corresponded to the observation record and the appropriateness of the evaluation method of seismic ground motion characteristics and the strong ground motion simulation method was confirmed. The authors intend to continue the study on the earthquake resisting capabilities of WARDEC's various dams against the simulated strong ground motion based on the fault model.

## ACKNOWLEDGEMENT

The authors would like to express sincere appreciation to Professor Kenzo Toki (former professor of the Kyoto University) for his useful advice on the simulation analysis of the strong ground motion at Kasyo Dam Site. The authors also would like to express appreciation to the Land Protection and Water Resources Division, the Civil Engineering Department of Tottori Prefectural Government for providing the observation record of the 2000 Tottori-Ken Seibu Earthquake and its aftershocks.

## REFERENCES

- [1] Japan Society of Civil Engineers, Special Committee for Earthquake Resistant Design of Civil Structures (2000). "Third Proposal and Explanation Regarding Seismic Resisting Design of Civil Structures," 2-6.
- [2] Committee on Evaluation of Earthquake Resistance of Dams (1995). "Report of Committee on Evaluation of Earthquake Resistance of Dams," 1995. (in Japanese)
- [3] Tottori Prefectural Government, Erosion and Sediment Control and Water Resources Division, Civil Engineering Department (2000). "Seismic Waveform Data Recorded at Kasyo Dam Site during Tottori-Ken Seibu Earthquake."
- [4] National Research Institute for Earth Science and Disaster Prevention (2000). Waveform of the 2000 Tottori-Ken Seib Earthquake, Digital Strong-Motion Seismograph Network(KiK-net), <http://www.kik.bosai.go.jp/kik,2000>.
- [5] Tottori Prefectural Government (2000). "The 2000 Tottori-Ken Seib Earthquake damage," <http://www.pref.tottori.jp/bosai/seibujisinigai.htm>. (In Japanese)
- [6] Ministry of Construction, Dam Division of the Public Works Research Institute (2000). "Dam Survey After 2000 Tottori-Ken Seibu Earthquake (Interim Report)." Dam Engineering Report No. 170. (In Japanese)
- [7] Irikura, K. (1996). "Assumed Earthquakes and Prediction of Strong Seismic Motion for Earthquake Disaster Prevention in Osaka and the Adjacent Areas." Proceedings of 24th Symposium of Earthquake Ground Motion, 91-100 (in Japanese).
- [8] Irikura, K. (2000). "Prediction of Strong Motions from Future Earthquakes Caused by Active Faults - Case of the Osaka Basin." Proceedings of 12th World Conference of Earthquake Engineering Symposium, Paper No. 2687.
- [9] Hartzell, S. H. (1978). "Earthquake Aftershocks as Green's Function." Geophysical Research Letters, Vol. 5, 1-4.
- [10] Irikura, K. (1986). "Prediction of Strong Acceleration Motion Using Empirical Green's Function." Proceedings of 7th Japan Earthquake Engineering Symposium, 151-156.
- [11] Boore, D. M. (1983). "Stochastic Simulation of High-frequency Ground Motion Based on Seismological Models of the Radiated Spectra." Bull. Seism. Soc. Am., Vol. 73, 1865-1894.
- [12] Kamae, M. and Irikura, K (1991). "Prediction of Strong Ground Motion based on the Scaling Law of Earthquake by Stochastic Synthesis Method." Architectural Institute of Japan, Journal of Structure and Construction Engineering, Vol. 430, 1-9 (in Japanese).
- [13] Bouchon, M. (1981). "A Simple Method to Calculate Green's Functions for Elastic Layered Media." Bull. Seism. Soc. Am., Vol. 71, 959-971.
- [14] Ikeda, T., Miwa, K. Kamae, K. and Irikura (2000). "Source Modeling and Strong Motion Simulation of Tottori-Ken Seibu Earthquake Using the Empirical Green's Function Method (in Japanese)." Internet 10.<http://www.tobishima.co.jp/>.

[15] Ito, K. et al. (1998). "Seismogenic layer of the crust in the inner zone of southwest Japan," *Annals of Disaster Prevention Research Institute, Kyoto University*, No.41, B-1.

[16] Iwata, T. and K.Irikura (1988). "Source parameters of The 1983 Japan Sea earthquake," *Journal of Physics of Earth*, Vol.36, pp.155-184.

[17] Tsurugi, M., M.tai, A.Kowada, Y. Tatsumi, K. Irikura (1999). "Estimation of

Empirical Site Amplification Effects Using Observed Records," *12th World Conference on Earthquake Engineering*.

[18] Hanks, T. C. (1982). *Bull. Seism. Soc. Am.*, Vol. 72, 1867-1879.



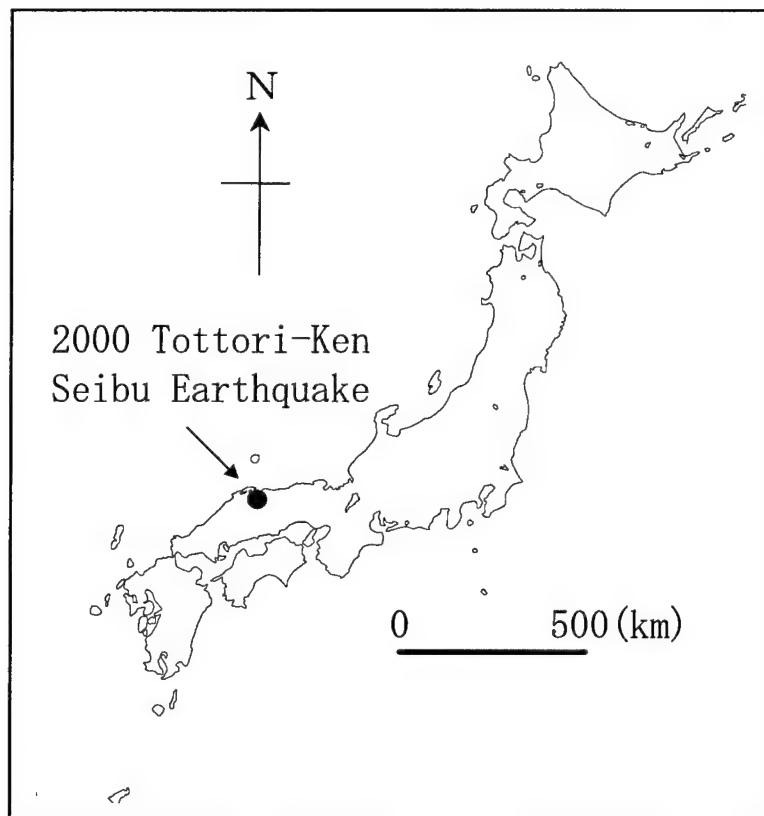


**Figure 1.** Location of 2000 Tottori-Ken Seibu earthquake

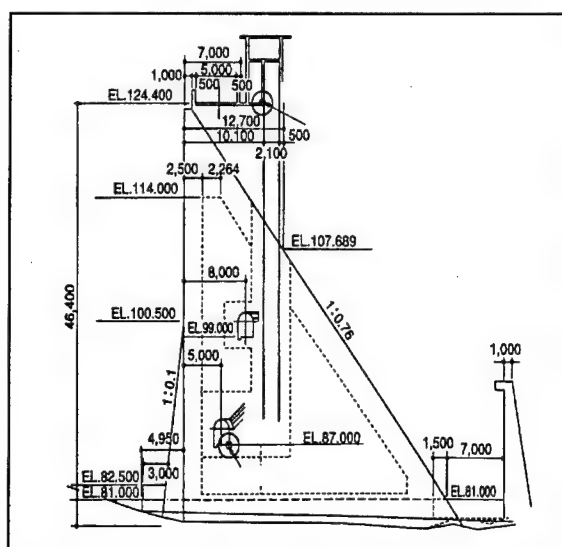


**Figure 2.** Section of Kasyo Dam

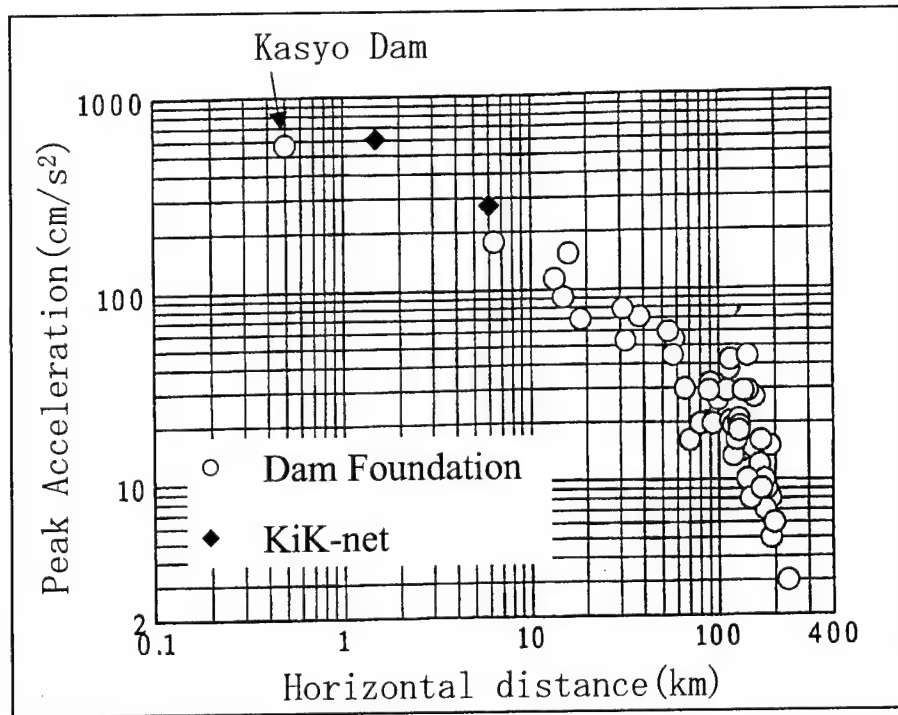


**Figure 3.** Peak acceleration at dam foundation and the shortest distance from source fault [5]

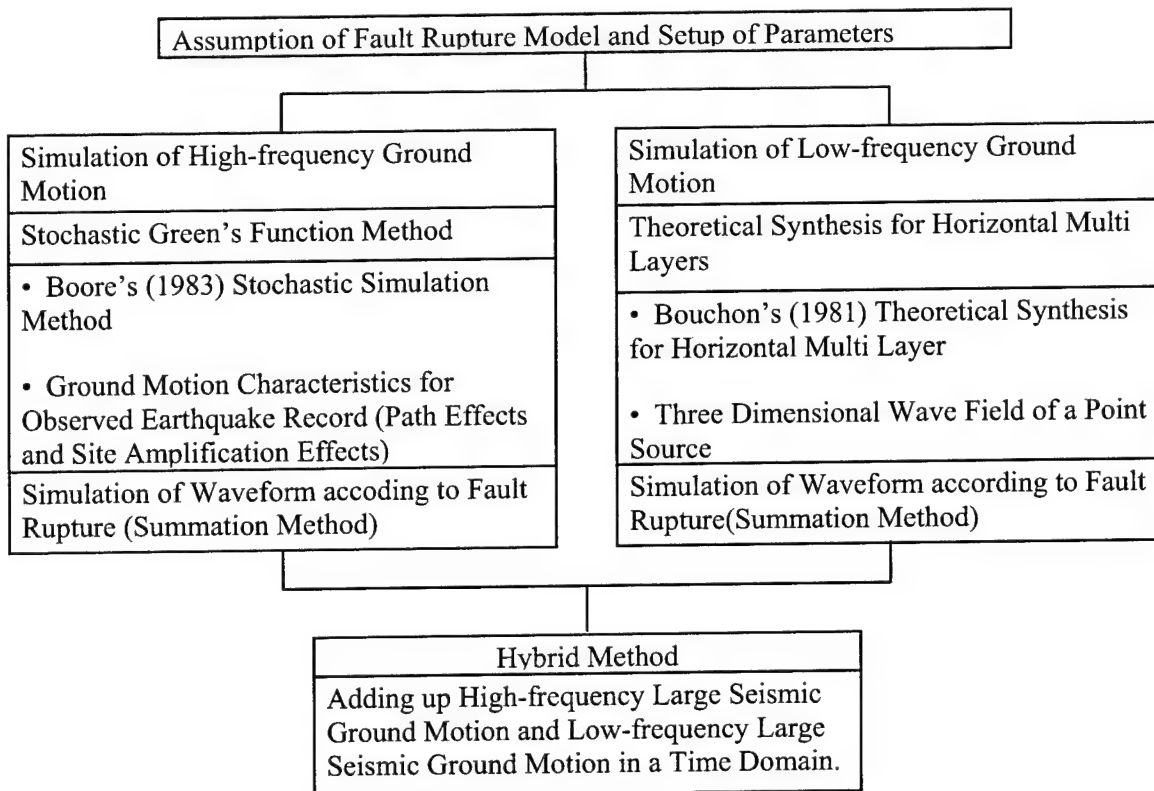


**Figure 4.** Flowchart of ground motion simulation procedures by the hybrid method

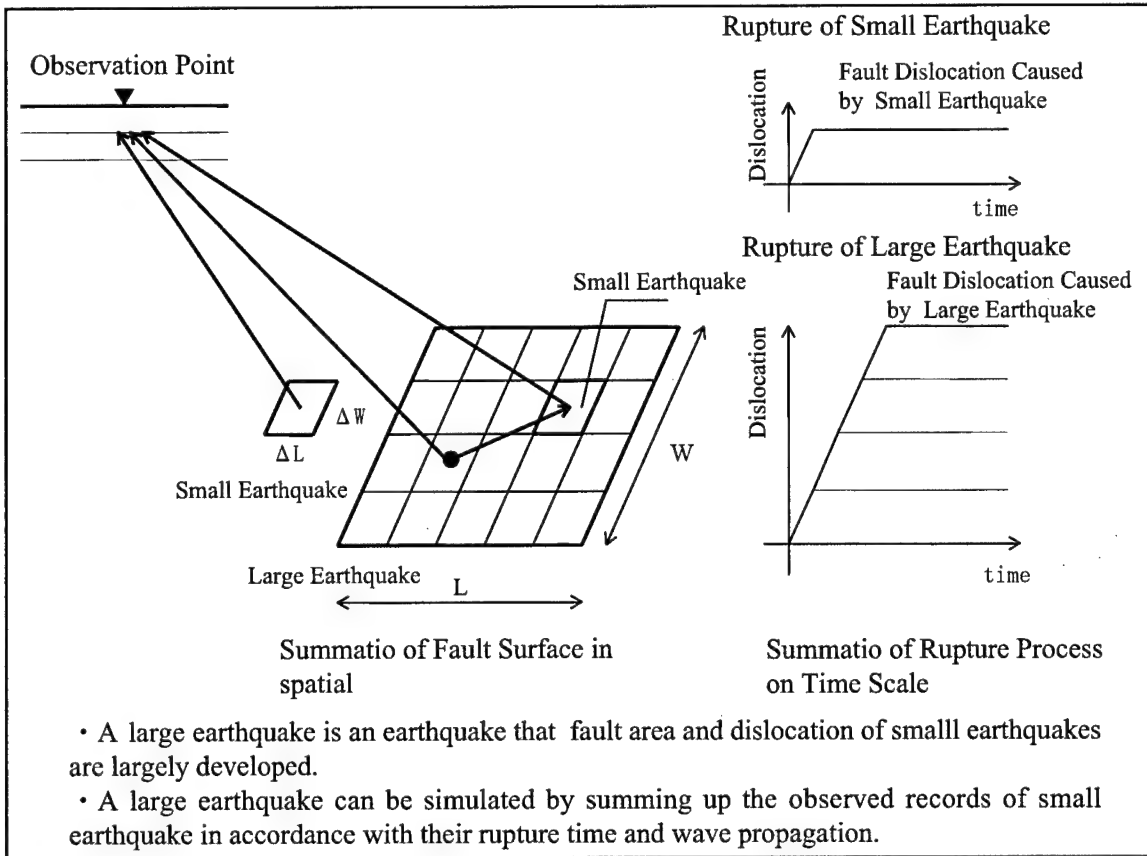


**Figure 5.** Concept of the empirical Green's function method

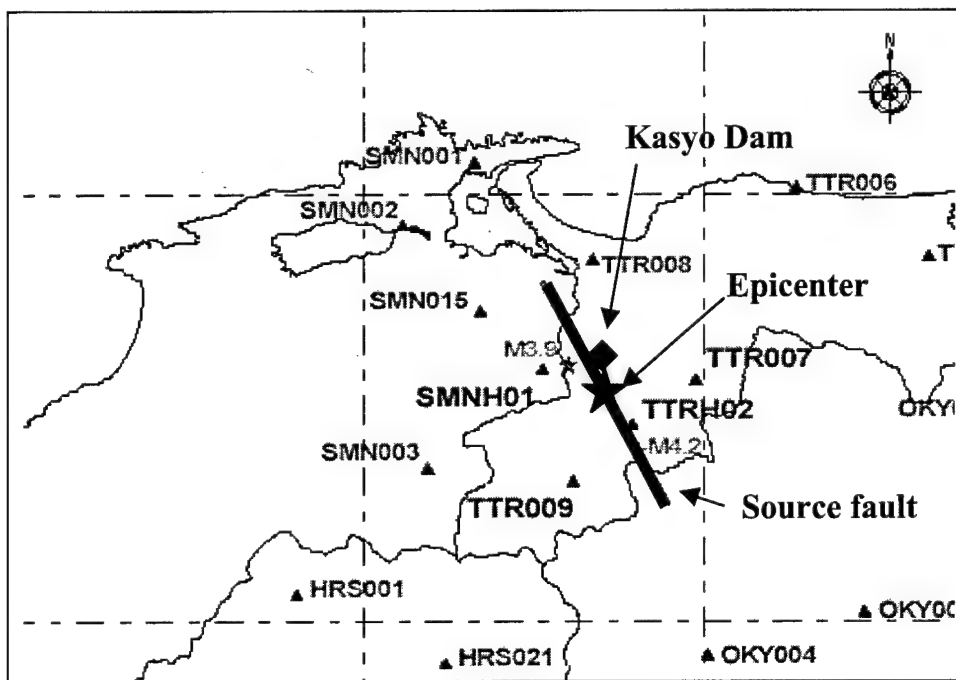


**Figure 6.** Location of source fault and Kasyo Dam site [14]

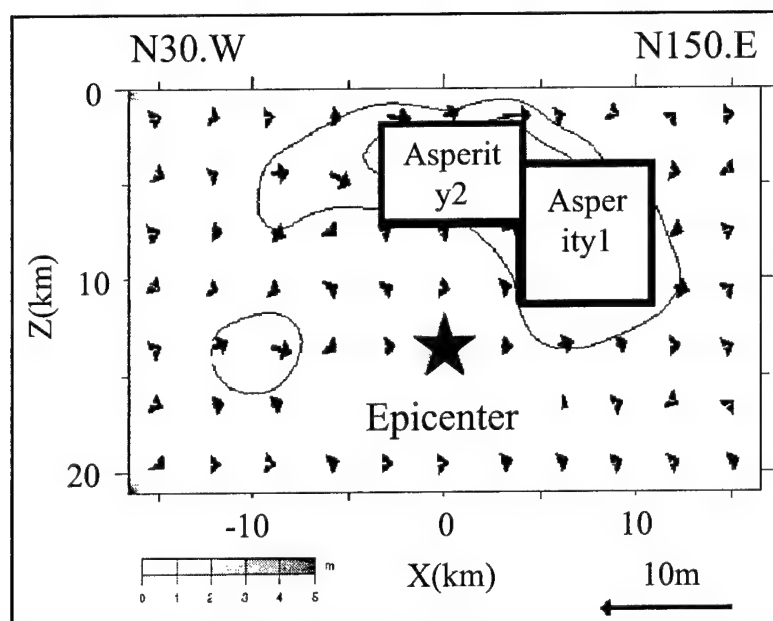


**Figure 7.** Fault model prepared by Ikeda, et al. [14]

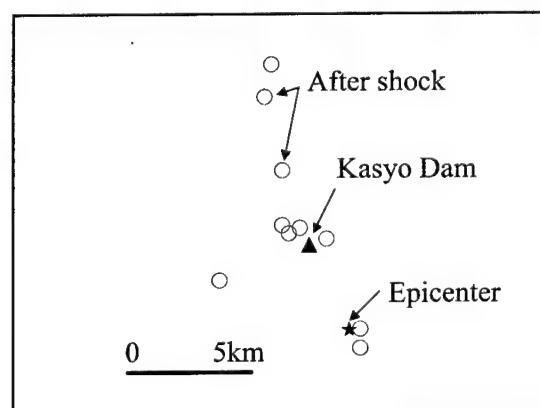


**Figure 8.** Aftershock locations

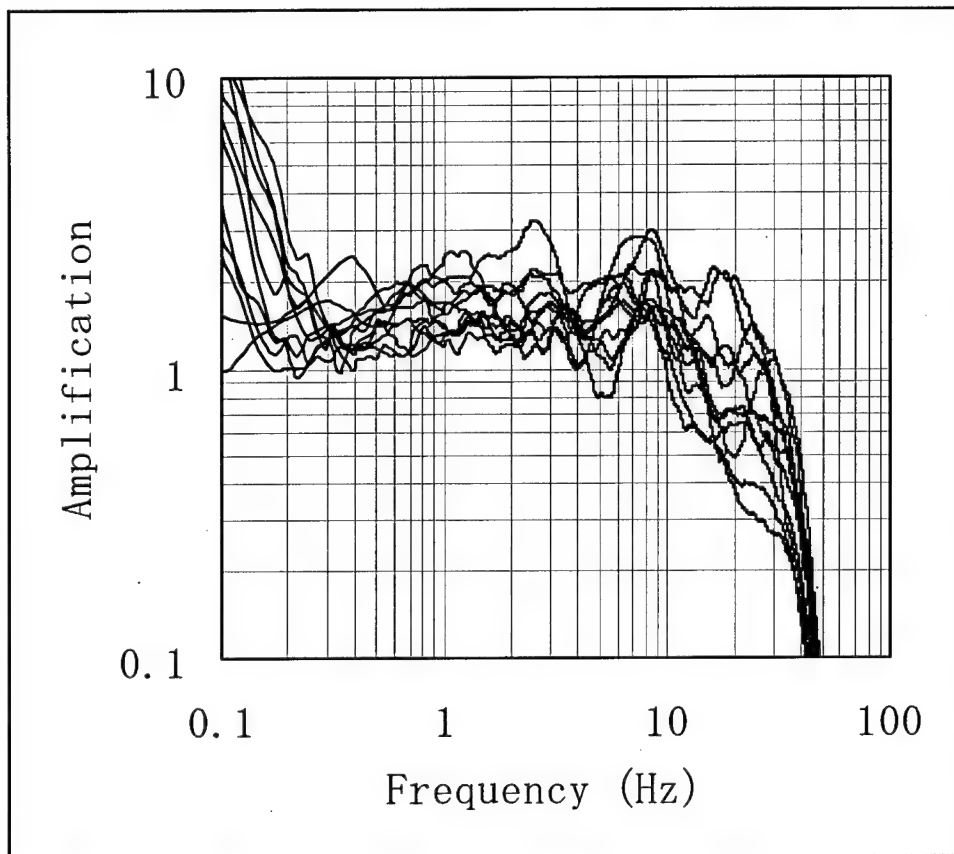


**Figure 9.** Aftershocks' site amplification effects

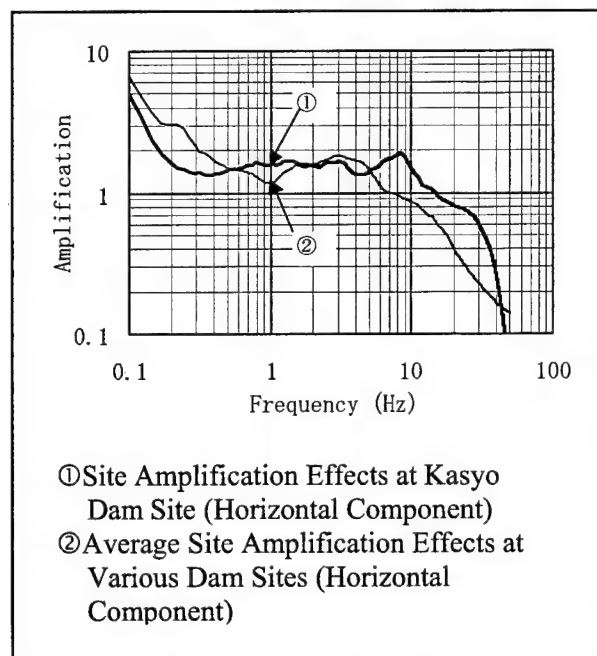


**Figure 10.** Site amplification effects

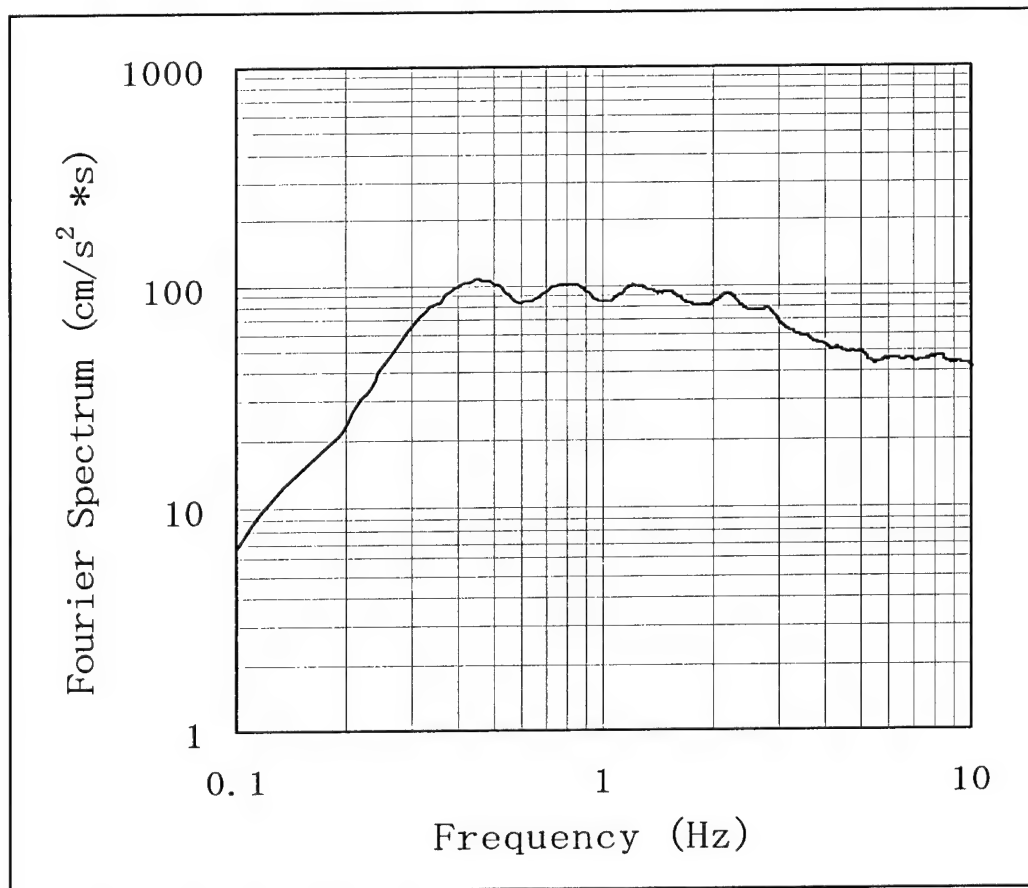


**Figure 11.** Fourier spectrum of the 2000 Tottori-Ken Seibu earthquake record

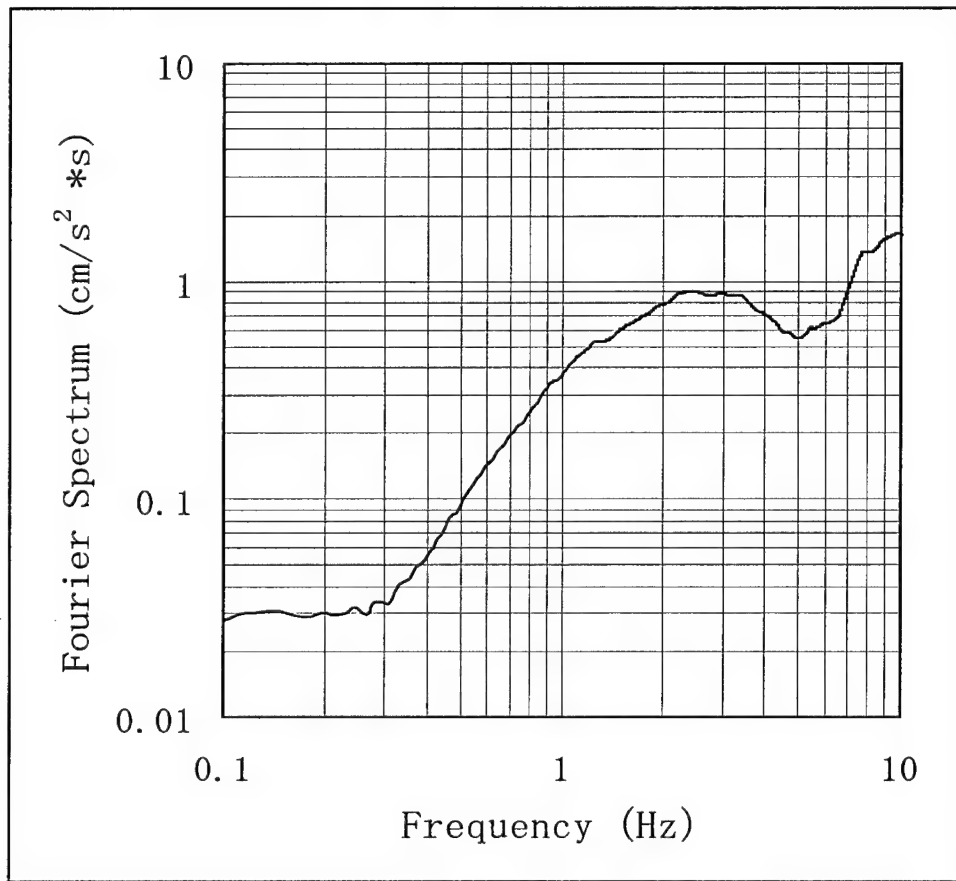


**Figure 12.** Fourier spectrum of the aftershock record

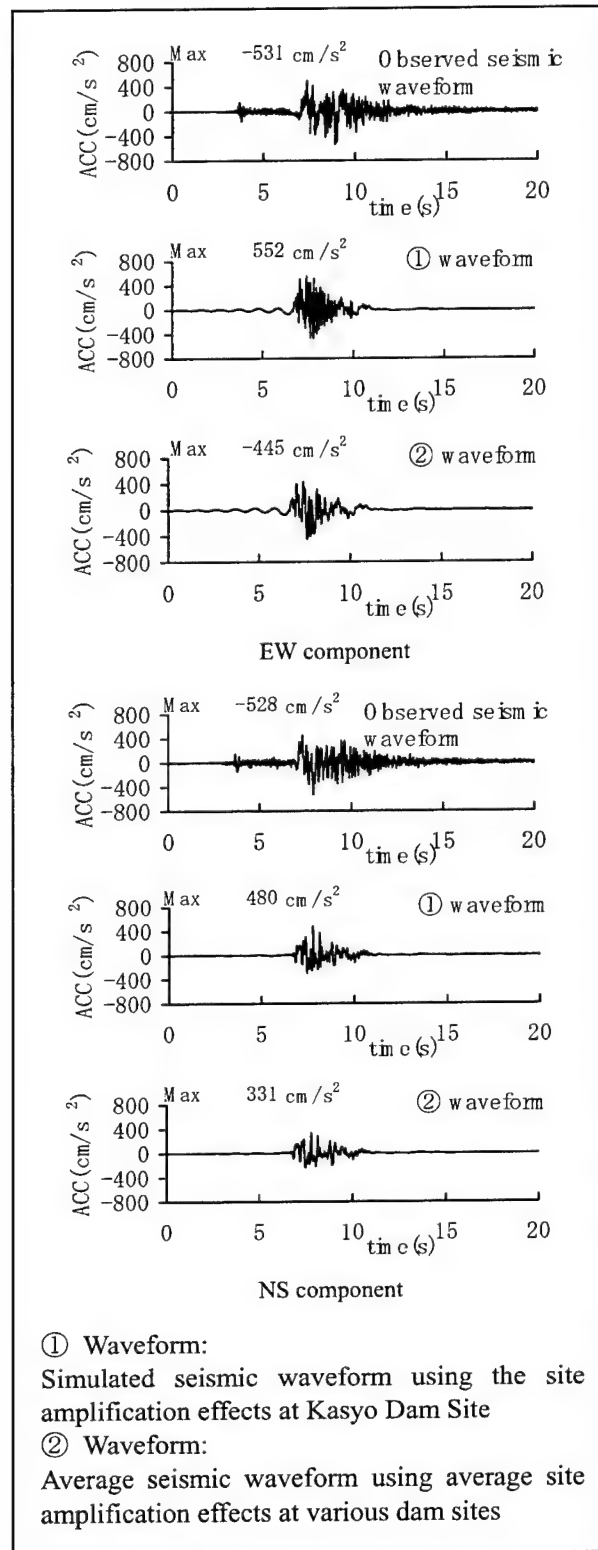


**Figure 13.** Comparison of the acceleration for time-history waveforms



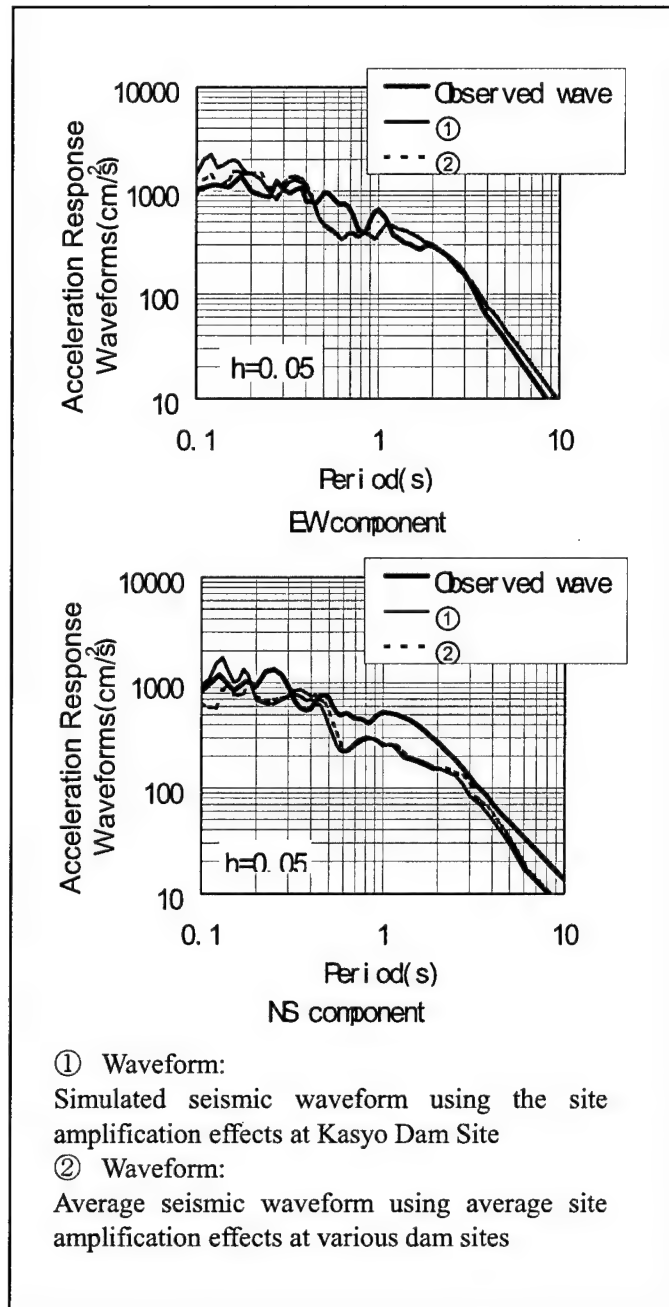


**Figure 14.** Comparison of the acceleration response spectrum

**Table 1.** Fault Rupture Characteristics [14]

	Asperity 1	Asperity 2
Northern End Latitude (°)	35.2407	35.2950
Northern End Longitude (°)	133.3723	133.3331
Southern End Latitude (°)	35.7864	35.2407
Southern End Longitude (°)	133.4114	133.3723
Fault Classification	Left Lateral	Left Lateral
Strike Angle (°)	150.0	150.0
Dip Angle (°)	90.0	90.0
Rake Angle (°)	0.0	0.0
Depth of Fault Top (km)	4.2	2.1
Fault Length (km)	7.0	7.0
Fault Width (km)	7.0	5.0
Fault Area (km <sup>3</sup> )	49.0	35.0
Seismic Moment (dyn·cm)	$2.72 \times 10^{26}$	$1.52 \times 10^{25}$
Moment Magnitude	6.4	
Rise Time (s)	0.61	0.50
Rupture Velocity (km/s)	2.8	2.0

**Table 2.** Analysis Parameter

	Asperity 1	Asperity 2
Fault Element Moment (dyn·cm)	$7.930 \times 10^{22}$	$7.238 \times 10^{22}$
Fault Element Corner Frequency (Hz)	2.17	2.23
Fault Element Stress Drop (bar)	160.0	160.0
Number of Fault Division(Longitudinal Direction), NL	7	7
Number of Fault Division(Width Direction), NW	7	6
Number of Fault Division(Dislocation), ND	7	6
Subdivision Number, NND	8	8
Length of Small Fault (km)	1.0	1.0
Width of Small Fault (km)	1.0	1.0
Shear-wave Velocity (km/s)	3.5	
Density (1/m <sup>3</sup> )	2.8	

**Table 3.** Velocity Structure Model

	Depth G.L.-(km)	$V_p$ (km/s)	$V_s$ (km/s)
1st Layer	0.0	2.2	1.3
2nd Layer	1.0	3.8	2.2
3rd Layer	1.5	5.5	3.2
4th Layer	2.0	6.05	3.5
5th Layer	16.0	6.6	3.8
6th Layer	38.0	8.0	4.6
$V_p$ : P-wave velocity $V_s$ : S-wave velocity			

**Table 4.** Comparison of the Peak Acceleration, Peak Velocity and Peak Dislocation

Component	Item	Observation Record	Simulation Result	
			①	②
EW	$A_{peak}$	531.1	552.0	444.9
	$V_{peak}$	49.3	62.4	62.8
	$D_{peak}$	16.4	16.3	16.3
NS	$A_{peak}$	528.4	480.3	330.7
	$V_{peak}$	54.4	42.0	41.7
	$D_{peak}$	15.0	10.0	10.1
① Effects at Kasyo Dam Site ② Average Effects at Various Dams Sites $A_{peak}$ :cm/s/s, $V_{peak}$ :cm/s, $D_{peak}$ :cm				

This page intentionally left blank.

## Permanent Ground Displacement at a Dam-site and Change in Reservoir Water Level Caused by the 2000 Western Tottori-prefecture, Japan Earthquake

by

Tatsuo OHMACHI<sup>1)</sup>, Naoyuki KOJIMA<sup>2)</sup> and Atsushi MURAKAMI<sup>3)</sup>

### ABSTRACT

During the 2000 Western Tottori-prefecture earthquake, strong motion accelerometers at Kasho Dam recorded 2051gal and 531gal at the upper and lower parts of the dam, respectively. Integration of the records resulted in permanent displacement of 28cm to the north, 7cm to the east and uplift of 5cm. The 46m-high concrete gravity dam survived the earthquake without damage, but its reservoir water level showed sudden drop of 6cm followed by damped free vibration. Numerical simulation has proved that these phenomena are direct influence of the seismic faulting underlying the dam site.

**Key Words:** 2000 Western Tottori-prefecture earthquake, Kasho Dam, seiche, strong motion, ground displacement.

### 1. INTRODUCTION

The 2000 Western Tottori-prefecture Japan earthquake (M<sub>j</sub>7.3) occurred at 13h30m (local time) on October 6, 2000. In the near field of the earthquake is located Kasho Dam, and strong motion records at the dam showed 2051gal and 531gal at the upper and lower parts of the dam, respectively. Despite such large acceleration, the dam survived the earthquake without any damage to the dam body, but with minor damage such as concrete cracking on the side-wall of an elevator shaft. There was also no report on the increase in the leakage water after the earthquake. In the meantime, the reservoir water level recorded at the dam showed sudden drop of 6cm immediately after the main shock, followed by damped free vibration lasting for hours. Questions were raised about causes and effects of the change in the reservoir water level.

As for the seismic fault, any traces of the fault rupturing were not discovered on the ground surface in the near field including the dam site. Even with the state-of-the-art knowledge and technology, it is thought impossible to predict when and where such earthquakes due to hidden faults will take place. However, earthquake engineers have to try to secure safety of lives and properties from any future earthquakes. To the authors' belief, the first step to cope with this kind of unpredictable earthquakes is a case study on causes and effects of such earthquakes. The case of Kasho Dam in the 2000 Western Tottori-prefecture earthquake will give us good lessons on what happens to civil engineering structures in the event of seismic rupturing of a hidden fault underlying the structures.

### 2. GROUND DISPLACEMENT INFERRED FROM STRONG MOTION RECORDS

Kasho Dam is a concrete gravity dam with the height of 46.4m and the crest length of 174m, constructed in 1989. The location of the dam is shown in Fig. 1, in which locations of the main shock and aftershocks of the 2000 Western Tottori-prefecture earthquake are also shown. In Fig.1, it is evident that the seismic faulting took place just below the dam site of Kasho Dam. The full water level of the dam reservoir is EL. 118m, while the water level was EL. 112m when the main shock occurred.

---

<sup>1)</sup>Professor, Department of Built Environment, Tokyo Institute of Technology, Yokohama, Japan

<sup>2)</sup>Engineer, Metropolitan Expressway Public Corporation, Tokyo, Japan (Former Graduate Student, Ditto)

<sup>3)</sup>Graduate Student, Ditto

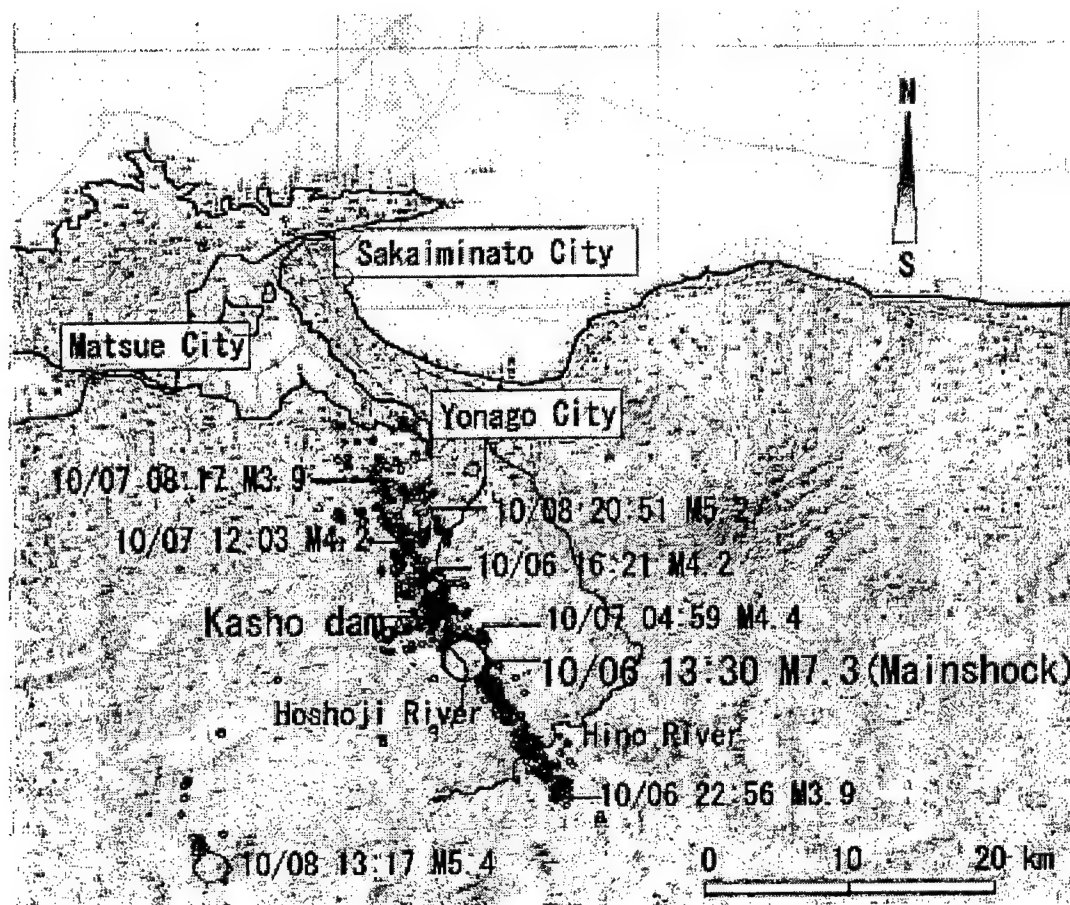


Fig. 1. Location map showing the main shock, aftershocks and Kashiwa Dam.

At Kashiwa Dam, several monitoring systems are installed. Among them, two sets of three-component strong motion accelerometers (seismometers) are installed at two places. One at the upper part is fixed on the concrete floor of the upper elevator room near the dam crest, and the other at the lower part is on the concrete floor of the lower inspection gallery, as shown in Fig. 2. Although the azimuth of the dam axis is  $N110^{\circ} E$ , horizontal components of both seismometers are installed in the N-S and E-W directions. A reservoir water level meter of a floating type is also installed in a concrete cottage next to the dam crest, as shown in Fig. 2. A downstream view of the dam is shown in Fig. 3, in which the elevator shaft and the concrete cottage are shown. Peak accelerations recorded during the main shock of the 2000 earthquake are listed in Table 1. Time histories recorded at the lower inspection gallery of the dam are shown in Fig. 3, in which

N-S, E-W and U-D components are shown in order from the top. The acceleration data were sampled at 100Hz with 24bit numbers. A reliable range of frequency is said to be as wide as from DC to 41 HZ. Thus, to estimate seismic ground displacement, the acceleration time histories were carefully integrated twice with respect to time, with the results shown in Fig. 5.

According to Fig. 5, it seems reasonable to think that the dam base was displaced in three directions in different manners. In N-S direction, the displacement occurred almost monotonously to the north and permanent displacement of 27.6cm to the north remained after the shaking. In E-W direction, the displacement was like a single sine-wave with a permanent displacement of about 6.5cm to the west. In U-D direction, the displacement was like a single pulse with a permanent uplift of about 4.7cm.

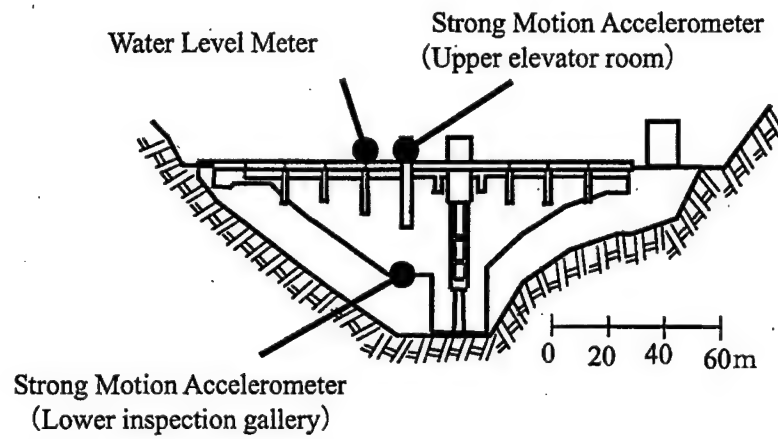


Fig. 2. Location of seismometers and water level meter.  
(Viewed from downstream side)

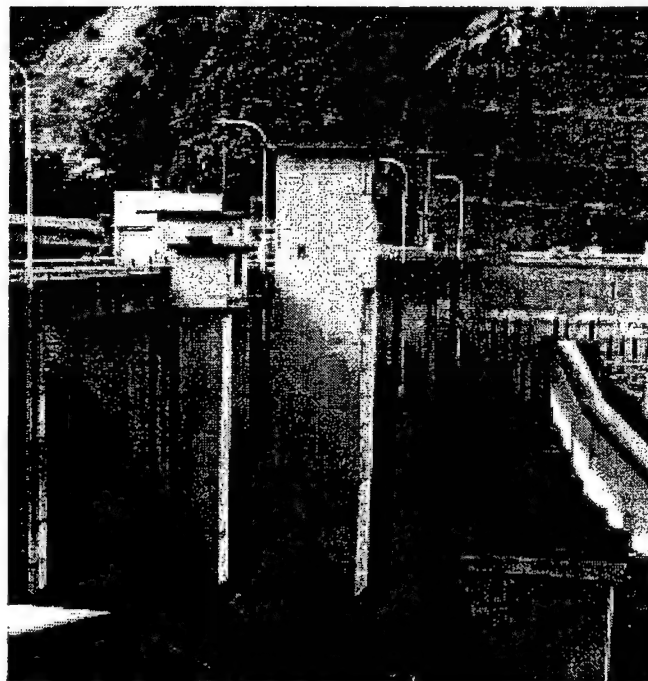


Fig. 3. Kasho Dam viewed from the downstream right bank.

Table 1. Peak acceleration at Kasho Dam.

	Lower inspection gallery	Upper elevator room
N-S Component	529 gal	2051 gal
E-W Component	531 gal	1406 gal
U-D Component	485 gal	884 gal

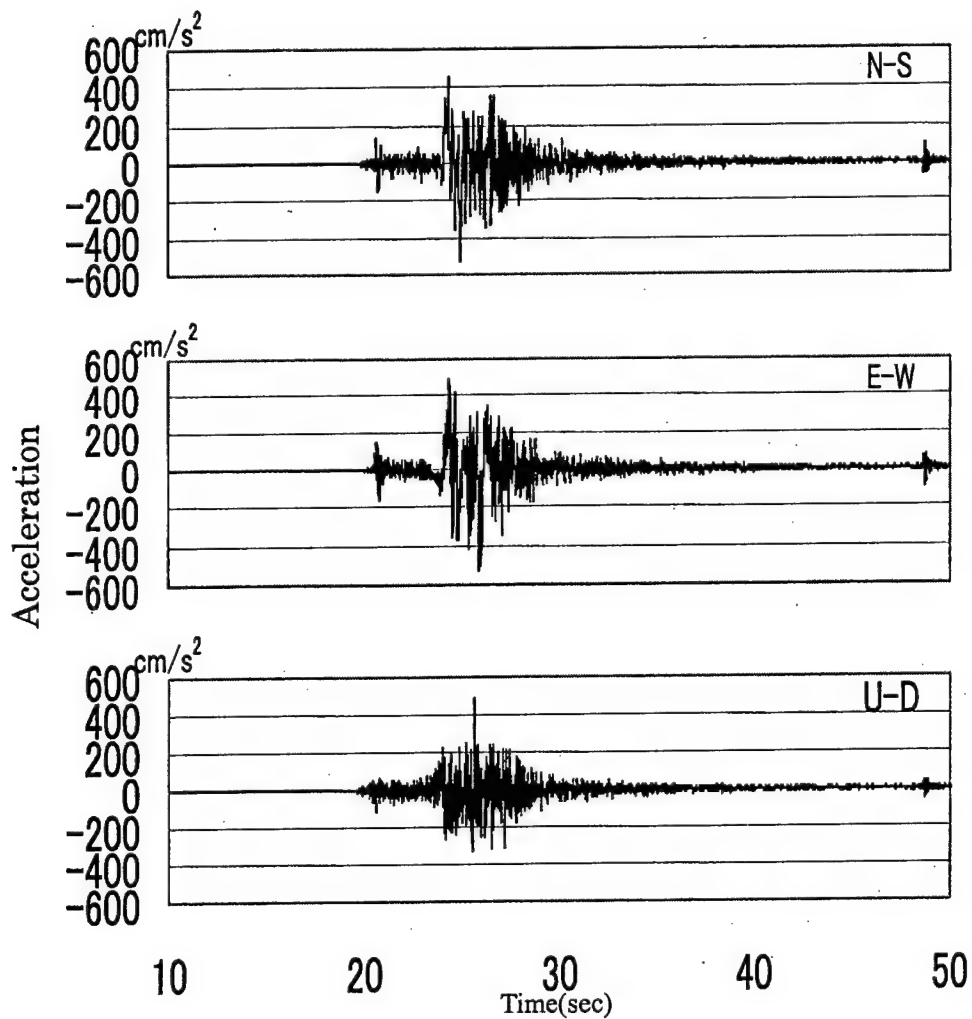


Fig. 4. Strong motion acceleration recorded at the dam base.



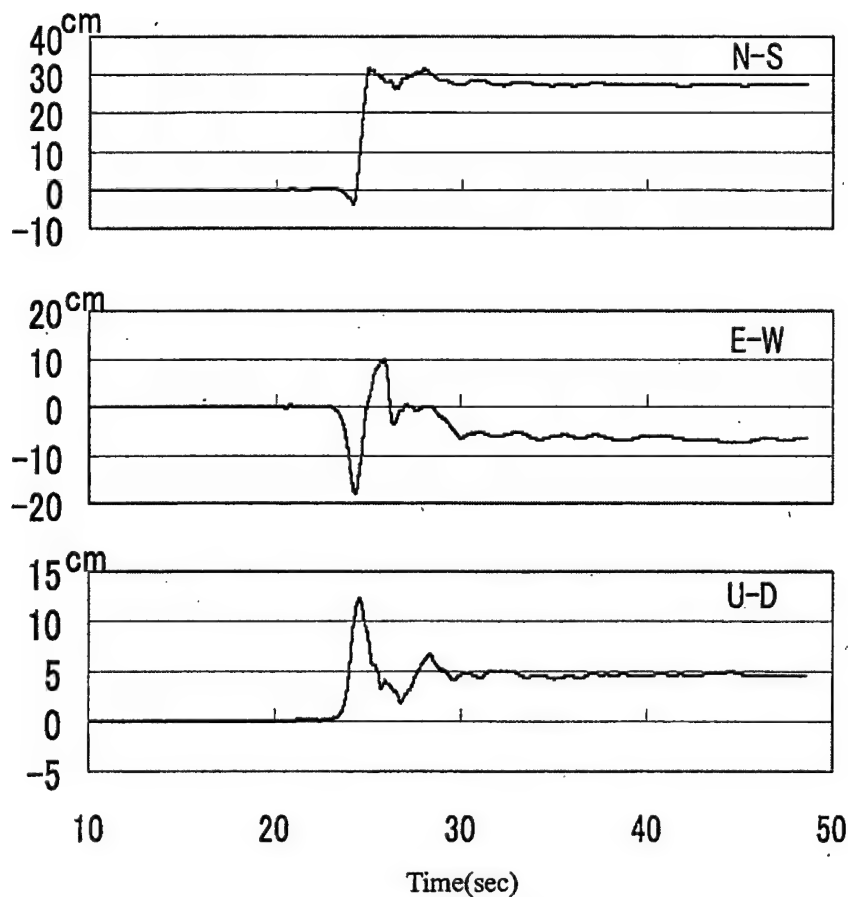


Fig. 5. Displacement time histories obtained by integration of acceleration in Fig. 4.

### 3. GROUND DISPLACEMENT FROM NUMERICAL SIMULATION

#### (1) Numerical Simulation by BEM

Using fault parameters shown in Table 2, ground displacement due to the seismic faulting was simulated by means of the 3-D boundary element method (BEM). The seismic fault of the main shock is of a left lateral strike slip with the strike of  $N152^{\circ} E$ . The rupture pattern was supposedly as simple as that shown in Fig. 6, having a rupture velocity of 3 km/s and a rise-time of 1sec. The ground was assumed to be a half-space of homogenous elasticity with a shear wave velocity of 4 km/s.

The numerical simulation was conducted for the square area of 23km long in NS direction and 17km wide in EW direction, in which Kasho Dam and its reservoir are included. In the simulation, seismic ground displacement was first calculated at every node of 500m x 500m meshes, with a result shown in Fig. 7(a). In Fig. 7(a), thick broken lines indicate a projection of the fault plane, and the reservoir is in a small square drawn with thick solid lines. Kasho Dam is located at the north end of the reservoir. As shown in Fig. 7(a), the simulated ground displacement indicates a general trend of uplift to the north-east of the reservoir, and settlement to the south-west of the reservoir.

Since the thin solid lines indicating the equal displacement in Fig. 6(a) are almost parallel to the fault line in the area near the reservoir, the

displacement in the area surrounded by the thick solid lines are interpolated based on the simulated displacement, with a result shown in Fig. 6(b). In Figs. 6(a) and (b), the profile of the reservoir was drawn along an altitude of EL. 123.2m which is the design flood water level of the dam. According to Fig. 6, due to the seismic faulting, the dam is uplifted about 2.5cm, which is about a half of the permanent displacement of the U-D component shown in Fig. 5.

Time histories of the simulated displacement at the dam were also obtained from the interpolation of the simulated ones at some of the nearest mesh nodes, with a result shown in Fig. 8. The time histories shown in Fig. 8 are somewhat similar to their counterparts shown in Fig. 5, though they are not exactly the same one another. The simulated ground displacement at the dam is 10.9cm to the north, 0.1cm to the west, and 2.5cm of uplift

Table 2. Fault parameters used in the simulation.

Item	Value
Strike (degree)	152
Dip (degree)	86
Rake (degree)	-7
Dislocation (m)	1.4
Depth of the fault (km)	1.0
Fault length (km)	20
Fault width (km)	10

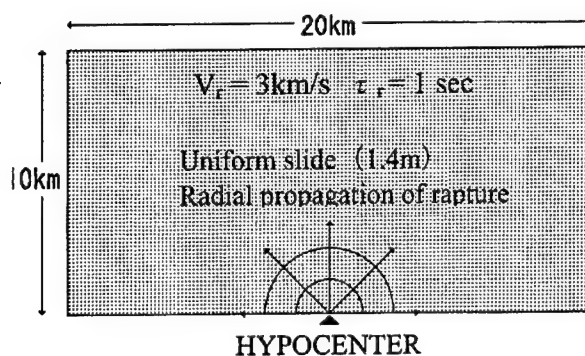


Fig.6. Fault model used in the simulation.

## (2) Comparison with Ground Survey Results

After the main shock, a ground survey was conducted at 65 points along the reservoir shown in Fig. 9. In Fig. 9, lines A to D are straight lines drawn in parallel to the fault line shown in Fig. 7. When the distance from the line A is taken as a reference, the vertical displacements from the simulation and the survey are compared as shown in Fig. 10 where lines A to D correspond to those in Fig. 9.

Obviously in Fig. 10, the displacements from the survey are larger than the simulated displacements. The former is almost three times as large as the latter, and especially larger between the lines B and C. The differences could be attributed to several factors such as inaccuracy of the simulation parameters, local site effects that were not considered in the simulation, and effects of many aftershocks. Although some rooms still remains for further discussion, two kinds of the displacements seem to indicate a similar trend as a whole, demonstrating that the dam site was somewhat displaced by the seismic faulting of the main shock, as was inferred from the integration of the strong motion acceleration.

## 4. CHENGE IN THE RESERVOIR WATER LEVEL

### (1) Sudden Drop of the Reservoir Water Level Followed by Damped Free Vibration

The record of the water level before and after the main shock is shown in Fig. 12, in which a sudden drop of the water level amounting to about 6cm is seen on both time histories with high and low resolutions, shown at upper and lower parts respectively. The records also indicate that, following the sudden drop, the water level showed damped free vibration for hours.

To analyze the water level record, it was roughly reproduced from readings of the peaks and troughs as shown in Fig. 12(a). From the digitized data shown in Fig. 12(a), the free vibration characteristics such as the period and the damping factor were estimated from the Fourier spectrum of the data shown in Fig. 12(b). The period and the damping ratio were found to be 6.5min and 2%, respectively.

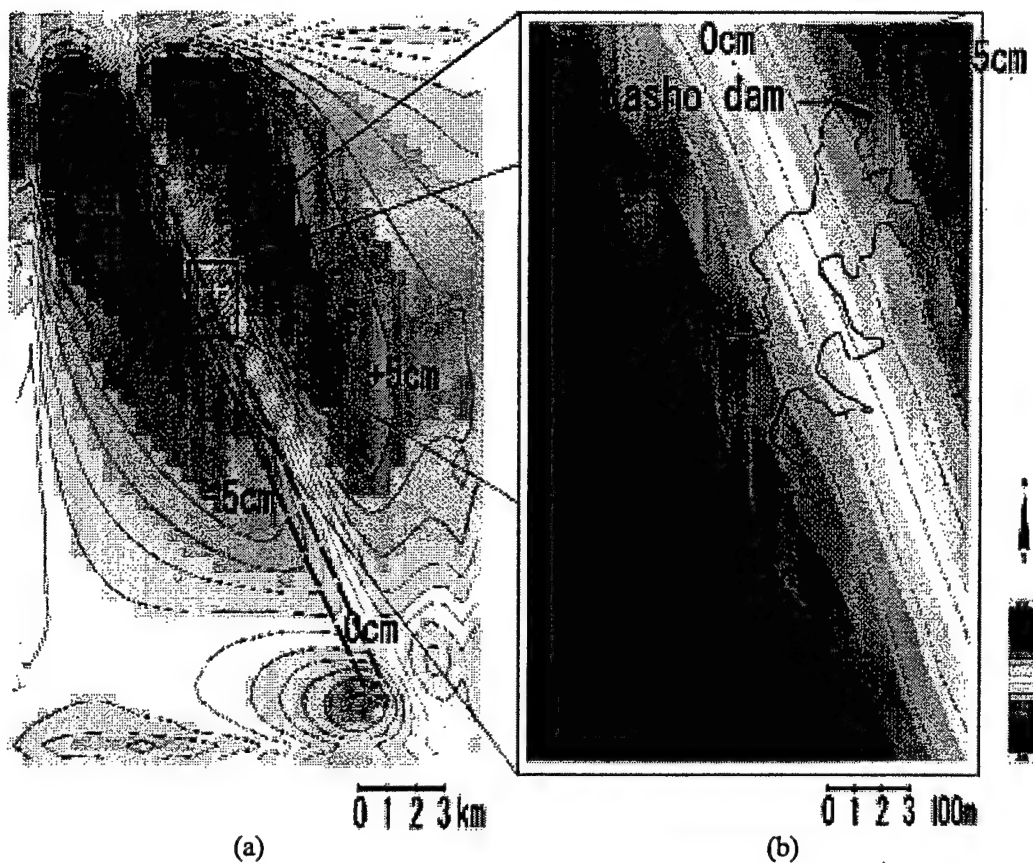


Fig. 7. Vertical displacement of the ground simulated by BEM (a), and its interpolation (b).

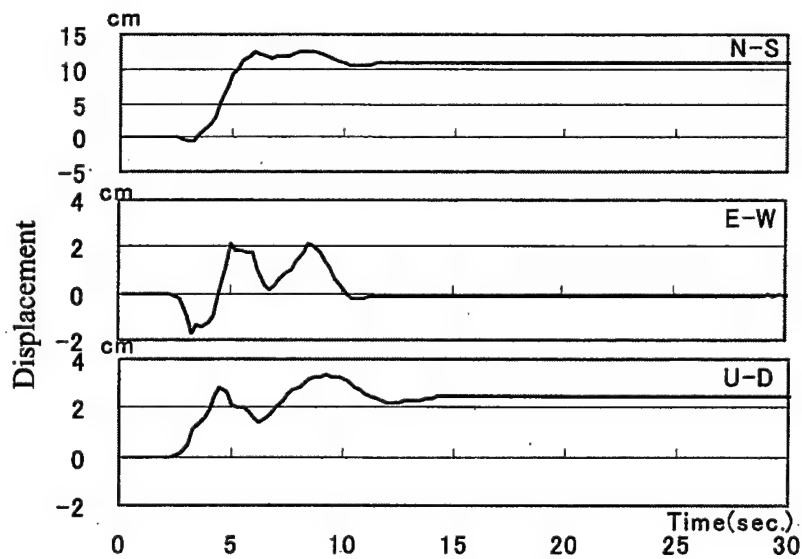


Fig.8. Ground Displacement at Kasho Dam estimated from numerical simulation

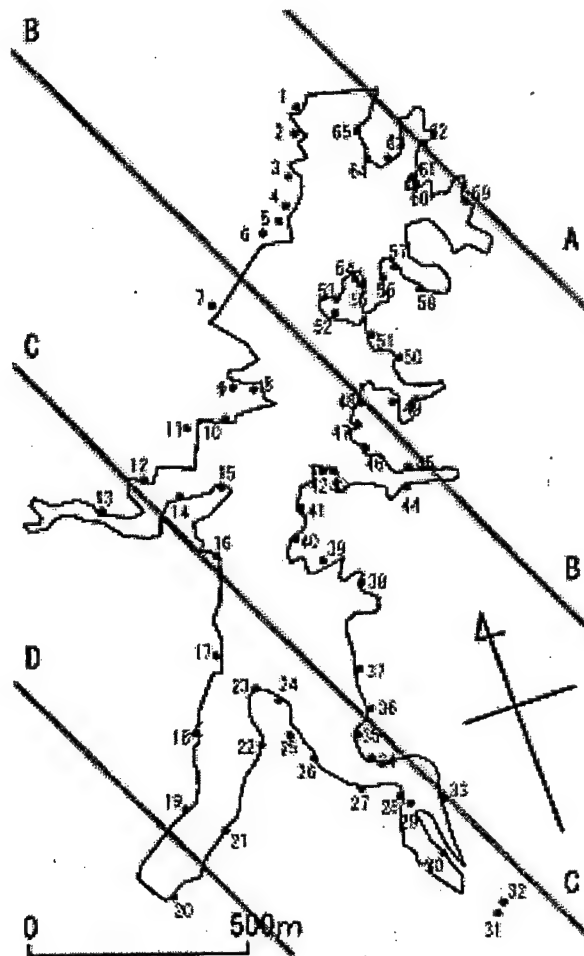


Fig. 9. Observation points where the ground survey was conducted along the reservoir.

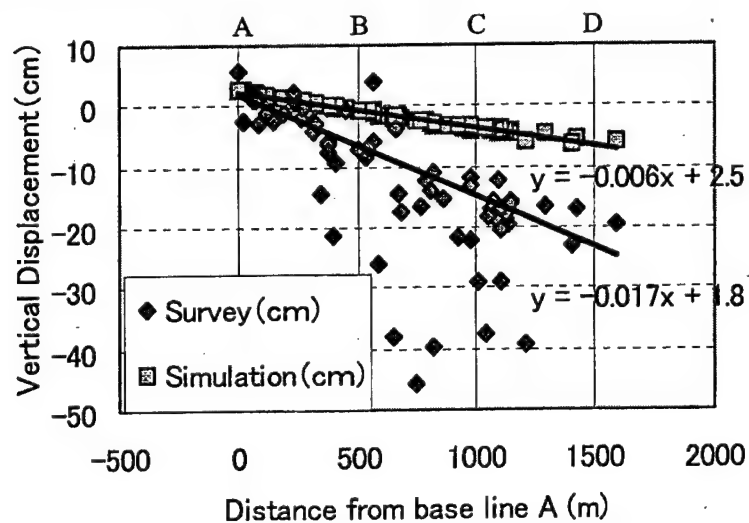


Fig. 10. Comparison of vertical displacements obtained from the simulation and the survey.

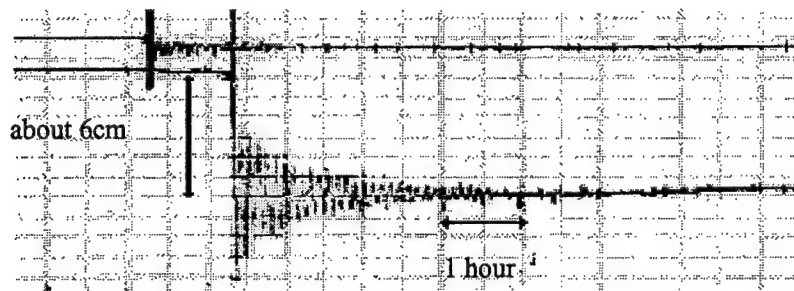


Fig. 11. A copy of the record of the reservoir water level.

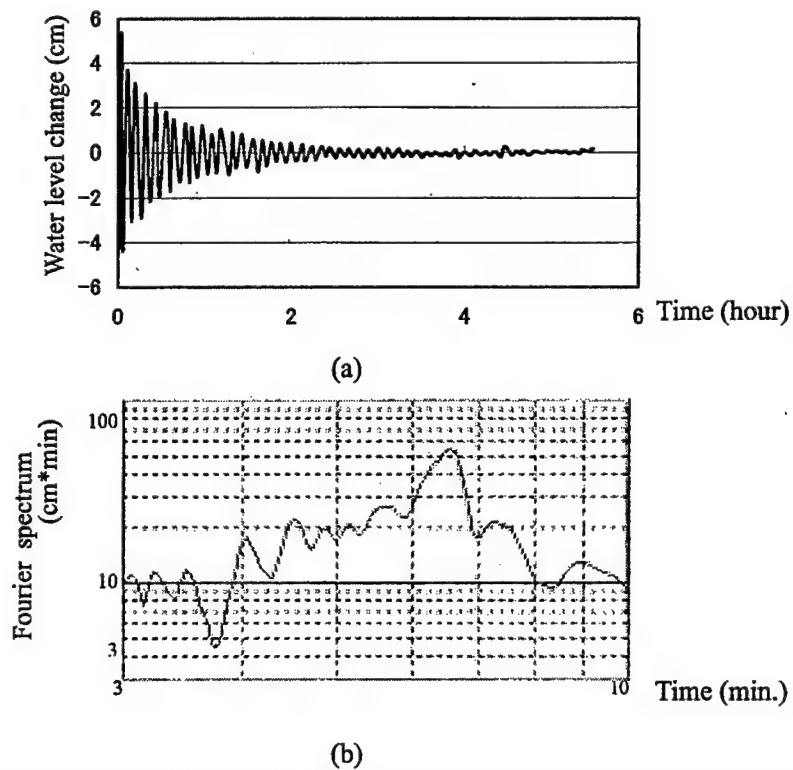


Fig. 12. Reproduced free vibration data of the reservoir water level (a) and its spectrum (b).

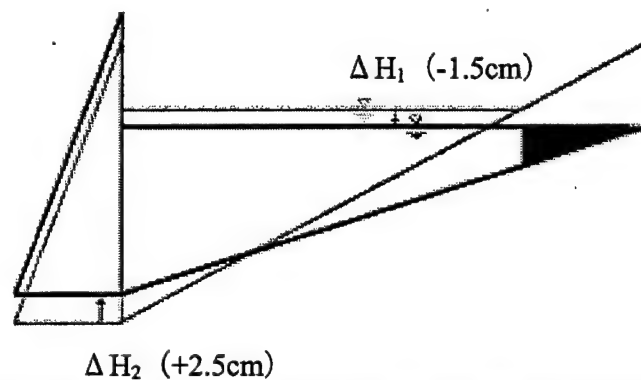


Fig. 13. Schematic explanation of the water level change caused by the ground displacement.

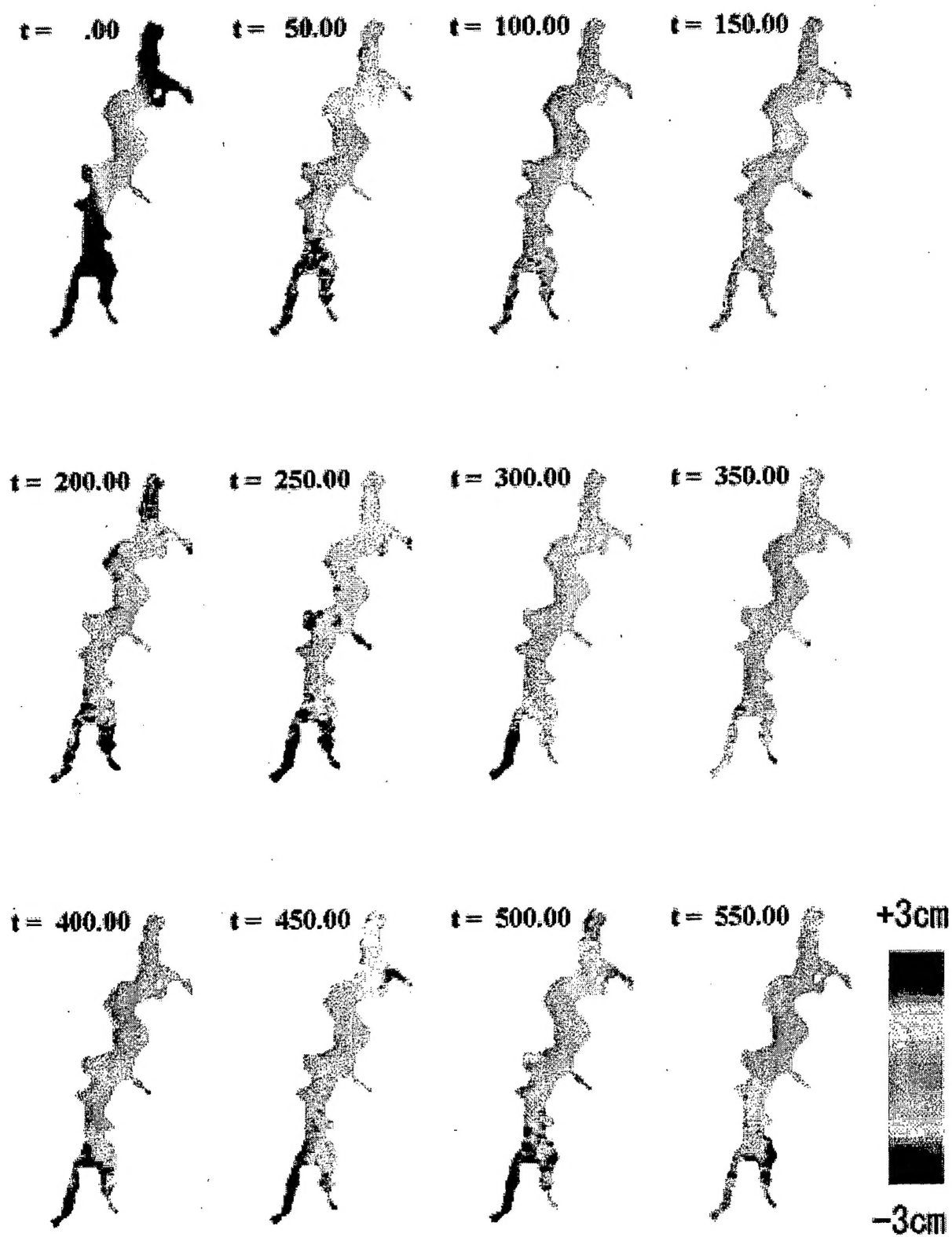


Fig. 14. Snap shots of the simulated seiche of the reservoir water.

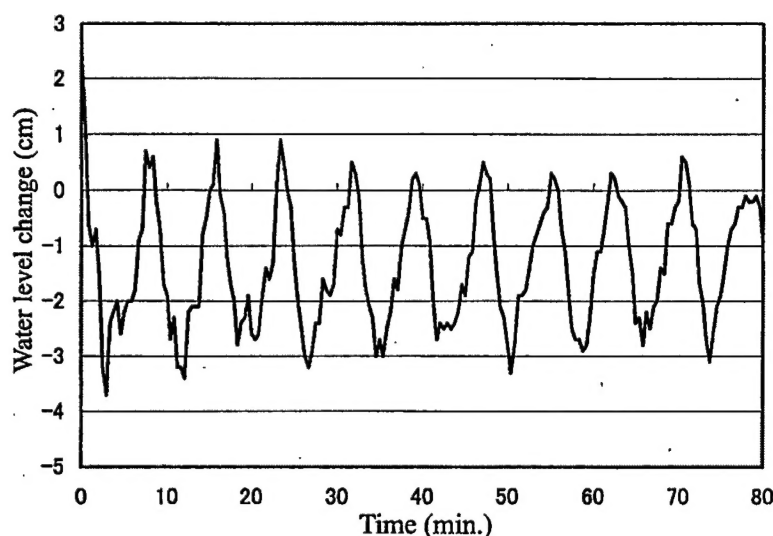


Fig. 15. Time history of simulated water level at Kasho Dam.

## (2) Causes of the Sudden Change in the Reservoir Water Level

As described earlier, the dam site was displaced by the seismic faulting, giving rise to uplift of the dam body and incremental reservoir capacity that resulted from the change in the ground slope under the reservoir. These are regarded as the main causes of the sudden drop of the reservoir water level. A schematic explanation is shown in Fig. 13, in which the dam and ground conditions before and after the earthquake are shown by thin and thick lines, respectively. In Fig. 13,  $\Delta H_1$  is the water level change due to the incremental water capacity, which is roughly estimable from an average settlement of the reservoir area, and  $\Delta H_2$  is the water level change due to the uplift of the dam. When the simulated displacement shown in Fig. 7 is used,  $\Delta H_1$  and  $\Delta H_2$  are found to be  $-1.5\text{cm}$  and  $2.5\text{cm}$ , respectively, as shown in the Fig. 13. Accordingly, the water level change resulting from the simulation given by  $\Delta H = \Delta H_1 + \Delta H_2$  is expected to be  $-4.0\text{cm}$ , which seems to agree fairly well with the observation.

## (3) Seiche of the Reservoir Water and its Simulation

Free vibration of the reservoir water is often referred to as seiche or seiching. The

fundamental period  $T$  for a rectangular reservoir is approximately given by

$$T = \frac{2a}{\sqrt{gh}} \quad (1)$$

where  $a$  and  $h$  are the length and the depth of the reservoir, respectively, and  $g$  is acceleration of gravity. Introducing  $a=2\text{km}$  and  $h=10\text{m}$  into Equation (1) as approximations for Kasho Dam leads to  $T=7.0\text{min}$ , which is close to the observed period of the free vibration  $6.5\text{min}$ . Hence, it seems reasonable to think that the free vibration of the reservoir is the seiche. On this basis, the simulation of the seiche was conducted using a numerical technique recently developed for tsunami simulation (Ohmachi et al, 2001). The technique is basically to solve the Navier-Stokes equation, using the 3-D finite difference method (FDM).

In the present simulation, for the sake of simplicity, the dam and the ground were assumed to be rigid. The initial water surface was supposed to be the same as that given from the simulated ground displacement, and then it was released under the action of gravity, which induced free vibration of the reservoir water. Snap shots of the simulated water surface of the whole reservoir are shown in Fig. 14 at every 50sec from  $t=0\text{sec}$  to  $t=550\text{sec}$ . A time history of the water level at the dam is shown in Fig. 15, from which the period of the simulated seiche is found to be

7.5min (450sec).

As shown in Fig. 14, the reservoir water surface has a uniform inclination at  $t=0$ , with the highest water level at the dam and the lowest water level at the upstream end. At 200sec which is almost a half of the period, the highest is seen at the upstream end and the lowest is at the dam. At 450sec, the water surface is similar to the initial one. Thus, the change of the water surface is like a see-saw movement with an axis at the middle of the reservoir, and evidently it is the free vibration motion mainly of the fundamental mode of the seiche.

## 5. CONCLUSIONS

During the 2000 Western Tottori-prefecture earthquake ( $M_J7.3$ ), strong motion records at Kasho Dam showed as large acceleration as 2051gal at the top and 531gal at the base. Despite such large acceleration, the dam survived the earthquake without damage to the dam body. However, as the dam was located just above the seismic fault, permanent displacement of the ground was observed over the dam site including the dam and the reservoir. The permanent displacement at the dam was 28cm to the north, 7cm to the west and uplift of about 5cm. The sudden drop of the water level observed immediately after the main shock is attributed to the permanent displacement of the ground under the reservoir.

Following the sudden drop of the reservoir water level, free vibration of the water level was observed with the period of 6.5min and a damping ratio of 2%. The free vibration is attributable to what is called the seiche of the reservoir water.

As fault traces of the main shock did not appear on the ground surface, the seismic fault of the 2000 earthquake is said to be a hidden fault. The case of this earthquake is full of lessons for us to learn what happens to civil engineering structures, when earthquakes are triggered by hidden seismic faults underlying themselves.

## ACKNOWLEDGMENT

Authors would like to express their thanks to Department of Civil Engineering, Tottori Prefecture for providing a variety of valuable information about effects of the 2000 earthquake on Kasho Dam. This study was partially supported by the Ministry of Education, Science, Sports and Culture, Grant in Aid for Scientific Research No.13480119 (Ohmachi, T.) and No.12555134 (Kawashima, K.).

## REFERENCE

- Ohmachi, T., Tsukiyama, H. and Matsumoto, H. (2001). "Simulation of tsunami induced by dynamic displacement of seabed due to seismic faulting", *BSSA* Vol. 91, NO.6, 1898-1909.



**REPORT DOCUMENTATION PAGE**Form Approved  
OMB No. 0704-0188

Public reporting burden for this collection of information is estimated to average 1 hour per response, including the time for reviewing instructions, searching existing data sources, gathering and maintaining the data needed, and completing and reviewing this collection of information. Send comments regarding this burden estimate or any other aspect of this collection of information, including suggestions for reducing this burden to Department of Defense, Washington Headquarters Services, Directorate for Information Operations and Reports (0704-0188), 1215 Jefferson Davis Highway, Suite 1204, Arlington, VA 22202-4302. Respondents should be aware that notwithstanding any other provision of law, no person shall be subject to any penalty for failing to comply with a collection of information if it does not display a currently valid OMB control number. **PLEASE DO NOT RETURN YOUR FORM TO THE ABOVE ADDRESS.**

<b>1. REPORT DATE (DD-MM-YYYY)</b> August 2003		<b>2. REPORT TYPE</b> Final report		<b>3. DATES COVERED (From - To)</b>	
<b>4. TITLE AND SUBTITLE</b>  Third U.S.-Japan Workshop on Advanced Research on Earthquake Engineering for Dams, San Diego, California, 22-23 June 2002				<b>5a. CONTRACT NUMBER</b>	
				<b>5b. GRANT NUMBER</b>	
				<b>5c. PROGRAM ELEMENT NUMBER</b>	
<b>6. AUTHOR(S)</b>  Robert L. Hall, Yoshikazu Yamaguchi, Enrique E. Matheu, and Ziyad H. Duron				<b>5d. PROJECT NUMBER</b>	
				<b>5e. TASK NUMBER</b>	
				<b>5f. WORK UNIT NUMBER</b> TE004	
<b>7. PERFORMING ORGANIZATION NAME(S) AND ADDRESS(ES)</b> U.S. Army Engineer Research and Development Center, Geotechnical and Structures Laboratory, Vicksburg, MS 39180-6199; Public Works Research Institute, 1-6, Minamihara, Tsukuba, Ibaraki, 305-8516, JAPAN; Louisiana State University, Department of Civil Environmental Engineering, Baton Rouge, LA 70803; Harvey Mudd College, Department of Engineering, 301 E. 12th Street, Claremont, CA 91711				<b>8. PERFORMING ORGANIZATION REPORT NUMBER</b>  ERDC/GSL TR-03-13	
<b>9. SPONSORING / MONITORING AGENCY NAME(S) AND ADDRESS(ES)</b>  U.S. Army Corps of Engineers Washington, DC 20314-1000				<b>10. SPONSOR/MONITOR'S ACRONYM(S)</b>	
				<b>11. SPONSOR/MONITOR'S REPORT NUMBER(S)</b>	
<b>12. DISTRIBUTION / AVAILABILITY STATEMENT</b>  Approved for public release; distribution is unlimited.					
<b>13. SUPPLEMENTARY NOTES</b>					
<b>14. ABSTRACT</b>  This report summarizes a workshop organized by the U.S. Army Engineer Research and Development Center (ERDC), Vicksburg, MS, and the Public Works Research Institute of Japan (PWRI) under the auspices of the Task Committee on Dams of the Panel on Wind and Seismic Effects, part of the U.S.-Japan Cooperative Program in Natural Resources. The workshop was held in San Diego, CA, 22-23 June 2002, as part of the preconference activities of the 22 <sup>nd</sup> U.S. Society on Dams Annual Meeting and Conference held at the same location 24-28 June 2002. Dr. Robert L. Hall, Chief, Geosciences and Structures Division, Geotechnical and Structures Laboratory (GSL), ERDC; Dr. Yoshikazu Yamaguchi, PWRI; Dr. Enrique E. Matheu, Louisiana State University, Baton Rouge, LA; and Dr. Ziyad H. Duron, Harvey Mudd College, 301 E. 12th Street, Claremont, CA, contributed in the organization of this workshop.					
<b>15. SUBJECT TERMS</b> Dam engineering Seismic Conference proceedings					
<b>16. SECURITY CLASSIFICATION OF:</b>			<b>17. LIMITATION OF ABSTRACT</b>	<b>18. NUMBER OF PAGES</b>  416	<b>19a. NAME OF RESPONSIBLE PERSON</b>
<b>a. REPORT</b> UNCLASSIFIED	<b>b. ABSTRACT</b> UNCLASSIFIED	<b>c. THIS PAGE</b> UNCLASSIFIED			<b>19b. TELEPHONE NUMBER (include area code)</b>